MAJOR TO GREAT EARTHQUAKES: MULTIDISCIPLINARY GEOPHYSICAL ANALYSES FOR SOURCE CHARACTERIZATION

EDITED BY: Debora Presti, Sebastiano D'Amico and Ioannis Kassaras
PUBLISHED IN: Frontiers in Earth Science

frontiers Research Topics

Frontiers eBook Copyright Statement

ISSN 1664-8714
ISBN 978-2-88971-540-4
DOI 10.3389/978-2-88971-540-4

About Frontiers

Frontiers is more than just an open-access publisher of scholarly articles: it is a pioneering approach to the world of academia, radically improving the way scholarly research is managed. The grand vision of Frontiers is a world where all people have an equal opportunity to seek, share and generate knowledge. Frontiers provides immediate and permanent online open access to all its publications, but this alone is not enough to realize our grand goals.

Frontiers Journal Series

The Frontiers Journal Series is a multi-tier and interdisciplinary set of open-access, online journals, promising a paradigm shift from the current review, selection and dissemination processes in academic publishing. All Frontiers journals are driven by researchers for researchers; therefore, they constitute a service to the scholarly community. At the same time, the Frontiers Journal Series operates on a revolutionary invention, the tiered publishing system, initially addressing specific communities of scholars, and gradually climbing up to broader public understanding, thus serving the interests of the lay society, too.

Dedication to Quality

Each Frontiers article is a landmark of the highest quality, thanks to genuinely collaborative interactions between authors and review editors, who include some of the world's best academicians. Research must be certified by peers before entering a stream of knowledge that may eventually reach the public - and shape society; therefore, Frontiers only applies the most rigorous and unbiased reviews.
Frontiers revolutionizes research publishing by freely delivering the most outstanding research, evaluated with no bias from both the academic and social point of view.
By applying the most advanced information technologies, Frontiers is catapulting scholarly publishing into a new generation.

What are Frontiers Research Topics?

Frontiers Research Topics are very popular trademarks of the Frontiers Journals Series: they are collections of at least ten articles, all centered on a particular subject. With their unique mix of varied contributions from Original Research to Review Articles, Frontiers Research Topics unify the most influential researchers, the latest key findings and historical advances in a hot research area! Find out more on how to host your own Frontiers Research Topic or contribute to one as an author by contacting the Frontiers Editorial Office: frontiersin.org/about/contact

MAJOR TO GREAT EARTHQUAKES: MULTIDISCIPLINARY GEOPHYSICAL ANALYSES FOR SOURCE CHARACTERIZATION

Topic Editors:
Debora Presti, University of Messina, Italy
Sebastiano D'Amico, University of Malta, Malta
Ioannis Kassaras, National and Kapodistrian University of Athens, Greece

Citation: Presti, D., D'Amico, S., Kassaras, I., eds. (2021). Major to Great Earthquakes: Multidisciplinary Geophysical Analyses for Source Characterization. Lausanne: Frontiers Media SA. doi: 10.3389/978-2-88971-540-4

Table of Contents

frontiers in Earth Science

EDITORIAL
published: 08 September 2021
doi: 10.3389/feart.2021.749603

Editorial: Major to Great Earthquakes: Multidisciplinary Geophysical Analyses for Source Characterization

Debora Presti[1]*, *Sebastiano D'Amico*[2] *and Ioannis Kassaras*[3]

[1]Department of Mathematics, Computer Science, Physics, and Earth Sciences, University of Messina, Messina, Italy, [2]Department of Geosciences, University of Malta, Msida, Malta, [3]Department of Geology and Geoenvironment, National and Kapodistrian University of Athens, Athens, Greece

Keywords: major to great earthquakes, geophysical inversion methods, physical and numerical modelling, instrumental data, seismogenic sources

Editorial on the Research Topic

Major to Great Earthquakes: Multidisciplinary Geophysical Analyses for Source Characterization

In recent years, the study of Major to Great earthquakes is strongly supported by the increase of technological and scientific capabilities such as dense global networks of seismic sensors, GPS stations and satellite imaging, tsunami gauges, geophysical surveying of the gravity of the Earth and more and more accurate techniques of data analysis. This enhancement in earthquake research facilitates unprecedented analyses of precursory, co-seismic, post-seismic processes, as well as their impact through comprehensive modelling of their consequences. Nevertheless, there are cases that information for significant earthquakes like location, moment tensor, rupture propagation, relation with secondary effects are to date poorly known and both the causative sources and triggering forces are still debated. Such ambiguities are often the source of misleading seismic hazard estimates that may result in unexpected adverse impacts.

The main goal of this Research Topic was to assemble studies of seismogenic sources able to produce major to great earthquakes, mainly focusing on their nature and rupture properties, interactions with nearby sources, spatiotemporal arrangement of aftershocks, and induced secondary effects. The works published herein are based on the application of various geophysical techniques such as inversion methods, processing of seismological, geodetic and gravimetric data, remote sensing, physical and numerical modelling. We believe that the overall effort, apart from shedding light at active regions of interest could provide a multidisciplinary framework for future research as well.

The mini review by Funiciello et al., presents the current state of knowledge achieved from application of empirical analysis of global-scale natural data and experimental data from analogue modelling to the study of cause-effect relationships between subduction zone parameters and the megathrust seismogenic behavior. The combination of the two approaches allows drawing conclusions about the geodynamic conditions that may favor the occurrence of giant megathrust earthquakes such as the Indonesia 2004, Chile 2010, and Japan 2011 earthquakes.

During the last 2 decades, space geodesy allowed mapping accurately rupture areas, slip distribution, and seismic coupling by obtaining refined inversion models and greatly improving the study of great megathrust earthquakes. Álvarez et al., by performing direct modeling of satellite GOCE, analyzed seismic rupture behavior for recent and for historical earthquakes along the Sunda subduction margin and the relationship of the degree of interseismic coupling.

The study by Singh and Khan, deals with the computations and mapping of the basement configuration, sediment thickness, Moho depth, and residual isostatic gravity anomaly, in the eastern

OPEN ACCESS

Edited and reviewed by:
Mourad Bezzeghoud,
Universidade de Évora, Portugal

****Correspondence:***
Debora Presti
dpresti@unime.it

Specialty section:
This article was submitted to
Solid Earth Geophysics,
a section of the journal
Frontiers in Earth Science

Received: *29 July 2021*
Accepted: *25 August 2021*
Published: *08 September 2021*

Citation:
Presti D, D'Amico S and Kassaras I
(2021) Editorial: Major to Great
Earthquakes: Multidisciplinary
Geophysical Analyses for
Source Characterization.
Front. Earth Sci. 9:749603.
doi: 10.3389/feart.2021.749603

Indian shield and adjoining regions. Main findings were interpreted in terms of stress field distribution generating great earthquakes in the Nepal-Bihar-Sikkim Himalaya, and causing deformation and seismicity in the adjacent areas.

Romano et al., investigated the source model of the 2010 Chile, Mw 8.8, earthquake by benchmark the method of Optimal Time Alignment of the tsunami waveforms in the joint inversion of tsunami (DART and tide-gauges) and geodetic (GPS, InSAR, land-leveling) observations for this event. The results obtained show that the first-order modeling correction introduced by OPT confirms the bilateral rupture pattern around the epicenter and shifts the inferred northern patch of slip to a shallower position consistent with the slip models obtained by applying more complex physics-based corrections to the tsunami waveforms.

The subject of rupture mechanism of deep-focus (>300 km) earthquakes in subducting slabs of oceanic lithosphere is addressed by Zhang et al. The rupture model for the 2013, Mw 8.3, deep Okhotsk Sea earthquake, is constrained by a multi-array and multi-frequency combined back-projection method as well as a global P-wave train inversion technique for discrete subevents. The earthquake is found to rupture at different speeds to the north and to the south, respectively, of the epicenter. This evidence newly supports dehydration embrittlement as a viable and possible unifying mechanism for the majority of deep earthquakes.

A physics-based earthquake simulator is implemented by Kourouklas et al. in the Southern Thessaly Fault Zone (Greece), aiming to provide insights about the recurrence behavior of earthquakes with Mw ≥ 6.0 in six major fault segments in the study area. The application of the algorithm produced a seismic catalog for 10 kyr containing 254 events with Mw ≥ 6.0 implying both single and multi-segment ruptures. The large number of simulated ruptures provides the ability of a thorough investigation of their recurrence properties.

Major seismicity of southern Italy is analyzed in four contributions. Bello et al., use various geological and revised seismological data in order to reconstruct the surface and depth geometry, the kinematics and stress tensor related to the Campania–Lucania 1980 earthquake (Mw 6.9). Three main fault alignments are identified. Strain and stress analyses show NNE extension. The proposed seismotectonic model includes a deep graben-like structure.

Neri et al. (a) find that very strong shallow seismicity of southern Calabria, imputed to normal faulting, corresponds to relatively low values of local, geodetic horizontal strain rate, and note that this situation apparently contrasts with observations in the Apennines, from central Italy to northern Calabria, where normal faulting earthquake activity of lower magnitude corresponds to relatively large values of extensional strain rate. The authors suggest a possible explanation of this somewhat unusual situation.

A detailed study of the Messina Straits area is proposed by Neri et al. (b), based on high-quality hypocenter locations and waveform inversion focal mechanisms of recent earthquakes. Seismicity in the area of the major, 1908 earthquake has mainly occurred below the east-dipping north-striking fault proposed by most investigators as the source of the 1908 earthquake, while it has been substantially absent in correspondence of the fault and above it. This distribution of seismicity suggests the existence of a huge, low-fractured shallow block resting on a somewhat fractured medium, with the separation surface between them corresponding to the 1908 earthquake fault.

Finally, marine seismic reflection data coupled with on-land structural measurements allowed Gambino et al. to achieve new information about active deformation pattern of the northern sector of the Malta Escarpment, a bathymetric and structural discontinuity capable of major earthquakes in the near-offshore of Eastern Sicily. Dimensional parameters of detected faults were then used to estimate expected magnitudes and their reactivation propensity.

AUTHOR CONTRIBUTIONS

All authors listed have made a substantial, direct, and intellectual contribution to the work and approved it for publication.

frontiers in Earth Science

ORIGINAL RESEARCH
published: 11 September 2020
doi: 10.3389/feart.2020.579846

Major Earthquakes of Southern Calabria, Italy, Into the Regional Geodynamic Context

Giancarlo Neri, Barbara Orecchio, Silvia Scolaro and Cristina Totaro*

Department of Mathematical and Computer Science, Physical Sciences and Earth Sciences, University of Messina, Messina, Italy

We analyze the seismicity of southern Calabria, the most active area of Italy from the seismic point of view, and compare it with geodetic data available from literature. Our analysis focuses both on the strongest earthquakes of the last centuries reported in the Italian historical seismic catalog and on seismicity recorded in the last decades by instrumental networks. The data highlight that strong shallow seismicity of southern Calabria, imputed to normal faulting by previous investigators, corresponds to low values of local, geodetic horizontal strain rate. This situation is quite different from that observed along the Apennines from central Italy to northern Calabria, where normal-faulting strong earthquake activity corresponds to relatively large values of extensional strain rate. On the other hand, the strong earthquake activity of southern Calabria corresponds to marked variation of vertical displacement rates detected from west to east in the same area. We frame these evidences into the regional geodynamic model assuming the coexistence of Africa-Europe NNW-trending plate convergence and SE-ward residual rollback of the Ionian lithospheric slab subducting underneath the Tyrrhenian-Calabria unit. Taking also benefit from the recently found relationship between the two strongest earthquakes of the 20th century in Italy (the southern Calabria earthquakes of 1905 and 1908 of magnitude 7.5 and 7.1, respectively), we propose that instabilities of the upper bending part of the subduction slab may perturb shallow normal faults in the overriding plate and concur to shallow seismicity of southern Calabria jointly with the dynamics of differential vertical motion marked by geodetic data. The opposite action of lithosphere convergence and rollback may justify low values of horizontal strain rate in the low coupling scenario of the Ionian and Tyrrhenian-Calabria units.

Keywords: earthquakes, geodetic strain, geodynamics, southern Calabria, Italy

OPEN ACCESS

Edited by:
Ioannis Kassaras,
National and Kapodistrian University of Athens, Greece

Reviewed by:
Mimmo Palano,
Istituto Nazionale di Geofisica e Vulcanologia (INGV), Italy
David Iacopini,
University of Naples Federico II, Italy

****Correspondence:***
Barbara Orecchio
orecchio@unime.it

Specialty section:
This article was submitted to Solid Earth Geophysics, a section of the journal Frontiers in Earth Science

Received: *03 July 2020*
Accepted: *19 August 2020*
Published: *11 September 2020*

Citation:
Neri G, Orecchio B, Scolaro S and Totaro C (2020) Major Earthquakes of Southern Calabria, Italy, Into the Regional Geodynamic Context. Front. Earth Sci. 8:579846. doi: 10.3389/feart.2020.579846

INTRODUCTION

In the last decade, taking benefit from large improvement of geophysical datasets and methods, researchers have much deepened the knowledge of the structure and dynamics of the Calabrian Arc subduction zone (**Figures 1** and **2**), the most active area of Italy from the seismic point of view. Neri et al. (2009, 2012) have found that southern Calabria is the only place in the Calabrian Arc subduction zone where the subduction slab is still continuous over depth, while detachment of the deepest portion of subducting lithosphere has already occurred beneath the Arc edges (northern Calabria and northeastern Sicily, respectively; **Figure 1**). Other investigators (see, e.g., Presti et al.,

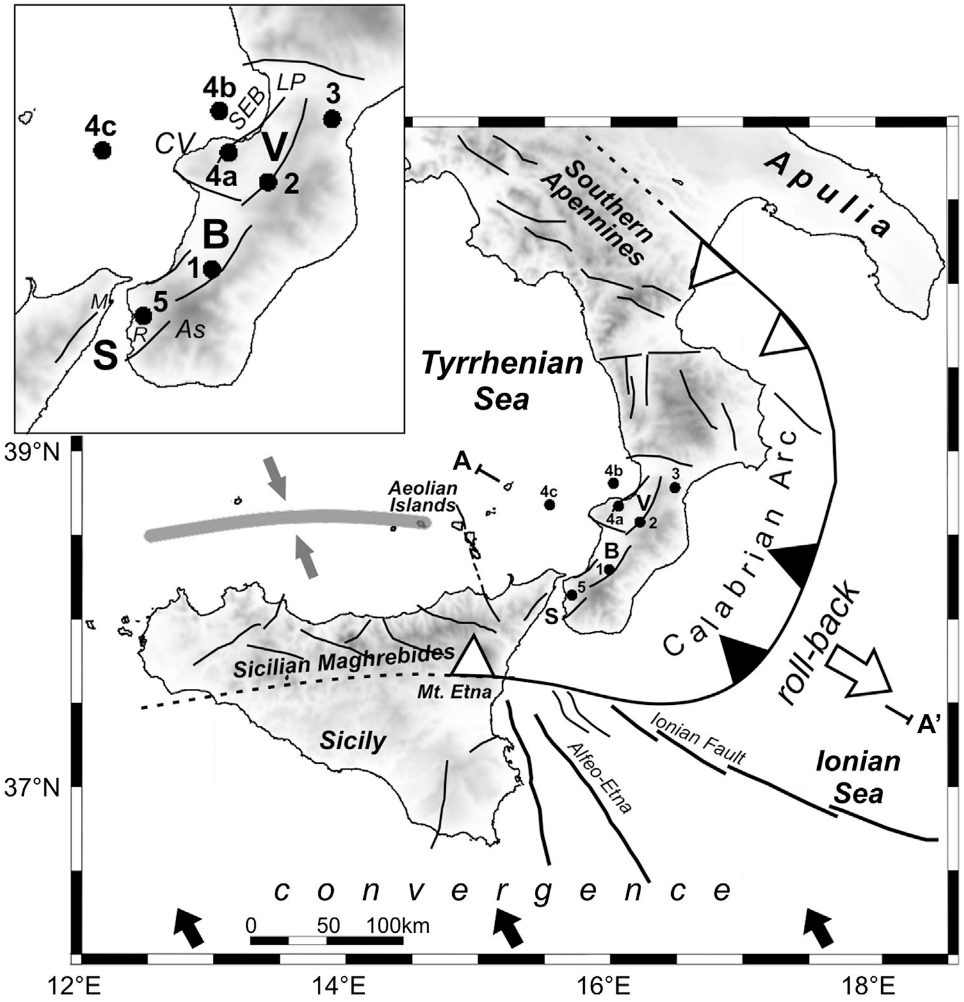

FIGURE 1 | Simplified tectonic map of the Calabrian Arc region redrawn with modifications from Cadet and Funiciello (2004) and Polonia et al. (2011), with additional data from Dellong et al. (2018). The solid curve with the sawtooth pattern, pointing in the direction of subduction, indicates the present-day location of the Ionian subducting system. Black sawteeth indicate the location of the in-depth continuous subducting slab, white sawteeth show locations where the slab has already undergone detachment (Neri et al., 2009; Neri et al., 2012; Orecchio et al., 2014). The white arrow shows the sense of the gravity-induced subducting slab rollback. The black arrows schematize the sense of motion of Nubia relative to Europe in the study area (velocities of the order of 3–5 mm/yr; D'Agostino and Selvaggi, 2004; Devoti et al., 2008; Nocquet, 2012 and references therein). The gray belt and the converging arrows west of the Aeolian Islands in the southern Tyrrhenian sea show the present-day site of accommodation of convergence at the longitude of Sicily after detachment of the subduction slab and tectonic reorganization of the plate boundary. AA′ approximately indicates the NW-SE profile used for the cross-section sketch view of **Figure 2**. S, B, and V stand for Messina Straits, Gioia Basin, and Mesima Valley, respectively. Dots with numbers 1 to 5 show the epicenters of the earthquakes of magnitude M over 6.5 which occurred since 1600 in the southern Calabria segment of the Arc (see **Table 1** for details). As = Aspromonte, CV = Capo Vaticano, LP = Lamezia Plain, M = Messina, R = Reggio Calabria, SEB = S. Eufemia basin.

2013; Totaro et al., 2016) have distinguished the main compressional domain west of Calabrian Arc due to NNW-trending Africa-Europe plate convergence from the subduction domain where plate convergence and gravity-induced rollback of the Ionian subducting slab coexist (**Figure 1**). Joint analyses of geophysical and geologic data collected in the wide offshore sectors of the subduction zone have led Polonia et al. (2016, 2017) to identify an incipient rifting process at the southwestern edge of the Ionian subducting slab. A 3D reconstruction of the interface between the subducting and the overriding plates beneath southern Calabria has been performed by Maesano et al. (2017) who have also debated whether this subduction interface may be locked or not. On their hand, Carafa et al. (2017) have suggested high interseismic coupling with low seismic coupling on the subduction interface, assuming that elastic strain accumulating on the interface is released episodically in creep events. The dynamics of plate interaction at the subduction interface remains a major topic of debate in the study region. Finally, Presti et al. (2017, 2019) have focused on the dynamics of the Ionian subducting slab and proposed a revision of the traditional view of down-dip compression throughout the whole slab. In particular, Presti et al. (2019) stated that the upper part of the descending slab (located above a necking zone detected at 150 km depth) is subjected to down-dip

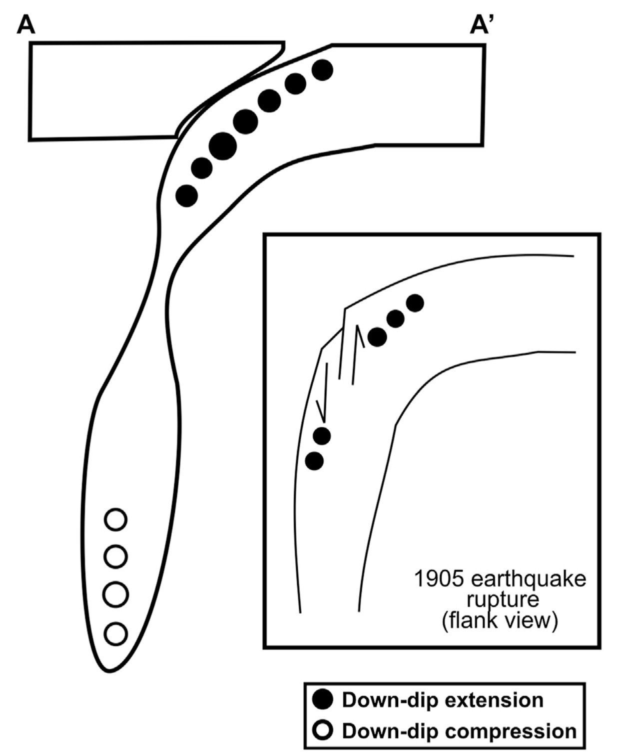

FIGURE 2 | Cross-section sketch view of the subduction system along a NW-SE profile crossing southern Calabria approximately indicated as AA′ in **Figure 1**. The figure shows the present-day state of subduction beneath Southern Calabria in the reconstruction given by Presti et al. (2019). Clear necking of the founding slab has occurred at a depth of ca. 150 km but slab detachment has not happened, yet. The upper part of the slab located above the necking zone is subjected to down-dip extension under its own weight. This may generate seismic effects like those observed in 1905 when the upper, elbow zone of the slab ruptured, producing the magnitude 7.5 earthquake of southern Calabria [a sketch of this process redrawn from Presti et al. (2017), with modifications, is reported in the inset of this figure]. The 1905 rupture occurred on a high-dip plane parallel to the SW-NE subduction trench orientation, with the most advanced northwestern part of the slab slipping down with respect to the southeastern part (Presti et al., 2017).

extension under its own weight, and this stress regime would produce seismic effects of great relevance in the upper bending zone of the slab and, in turn, in the shallow normal faults of the Tyrrhenian-Calabria overriding plate.

In the present study, we are going i) to examine data of historical and recent seismicity of southern Calabria and ii) to compare the main features of seismicity with geodetic data and geodynamic information available from literature. We attempt to give a unifying view of the data available and to identify future strategies for the solution of the still existing model uncertainties and ambiguities.

GEODYNAMIC FEATURES OF THE STUDY REGION

As described more widely in previous papers (see, e.g., Presti et al., 2013), the Calabrian Arc is a curved orogeny corresponding to the sector of maximum curvature of the Apennine-Maghrebian chain in the central Mediterranean (**Figure 1**). Many investigators (Malinverno and Ryan, 1986; Faccenna et al., 1996, among others) have suggested that geologic and geophysical data in the Calabrian Arc region can be interpreted in the framework of a geodynamic model assuming the co-existence of i) NNW-SSE convergence of Nubia and Europe plates and ii) gravity-induced SE-ward rollback of the Ionian lithospheric slab subducting to NW beneath the Tyrrhenian lithosphere (**Figure 1**). Nubia has been slowly converging toward Europe during the last ca. 80 Myr and NW-dipping subduction and ensuing rollback are thought to have started about 35–30 Myr ago (see, e.g., Dellong et al., 2020 and references therein). Current plate convergence velocity in this region is estimated to be on the order of 3–5 mm/yr (see, e.g., D'Agostino and Selvaggi, 2004; Devoti et al., 2008), rollback of the subducting slab is also believed to be quite slow (a couple of mm/yr; see, e.g., Hollenstein et al., 2003; Devoti et al., 2008; Nocquet, 2012). Much faster rollback (velocity was ~8 cm/yr about 5 Myr ago and has been progressively decreasing in more recent times) is believed to have been the primary tectonic source for SE-ward kinematics of the southern Tyrrhenian unit and its overthrusting onto the Ionian lithosphere (Faccenna et al., 1996). The Calabrian Arc curved segment of the margin (**Figure 1**) has been recognized as a low coupling zone (Hsu, 2001).

Geologic data evidence that the Calabrian Arc (**Figure 1**) includes strongly contrasting vertical movements, such as mountain chain uplifting of 0.5–1.2 mm/yr in the last 1–0.7 Myr and relative-to-chain subsidence in the major tectonic troughs on the western side (same figure; Monaco et al., 1996; Faccenna et al., 2011). Normal faults located closely west of the chain are considered to be major seismogenic faults, with particular reference to the NE-trending fault systems of the Messina Straits, Gioia Basin and Mesima Valley (S, B, and V in **Figure 1**) believed to have generated the major earthquakes of December 28, 1908 (magnitude 7.1 according to the CPTI15 catalog; Rovida et al., 2019; Rovida et al., 2020), February 5, 1783 (7.1) and February 7, 1783 (6.7), respectively, (see, e.g., Monaco et al., 1996; Neri et al., 2006). Seismogenic stress inversion of recent earthquake fault plane solutions (Neri et al., 2004; Neri et al., 2005; Totaro et al., 2016) and analyses of geostructural data (Tortorici et al., 1995) provided evidence that these fault systems are subjected to a relatively uniform extensional stress regime with a nearly NW-SE orientation of the minimum compressive stress σ_3.

Detachment of the Ionian lithospheric slab subducting beneath the Calabrian Arc was suggested by Monaco et al. (1996) to explain the uplift of the Arc in the past 1–0.7 Myr. The question on whether and eventually where the subduction slab is still continuous in depth or already detached beneath the Calabrian Arc has continued to be a primary subject of debate in more recent years (e.g., Spakman and Wortel, 2004; Neri et al., 2009). A more recent analysis of different geophysical data (gravity anomalies, seismotomographic structure, and seismicity of crust and uppermost mantle) has led Neri et al. (2012) to propose that the subducting slab is still continuous over depth beneath the central part of Calabrian Arc (southern Calabria; black sawteeth in **Figure 1**) while detachment of the deepest portion of subducting lithosphere has already occurred beneath the Arc edges (northern Calabria and northeastern Sicily, respectively; white sawteeth in **Figure 1**). On the other hand, Finite Element Modeling of lithosphere motions and strains on a regional scale (Negredo et al., 1999) has proven that the coexistence of plate convergence and rollback of an in-depth continuous subducting slab beneath the Calabrian Arc is compatible with geodetic displacement fields and chain uplift observed in Calabria. Lithospheric structures accommodating slab segmentation and roll-back have been proposed in the onshore and offshore areas around northern Calabria and northeastern Sicily (Argnani and Bonazzi, 2005; Govers and Wortel, 2005; Rosenbaum et al., 2008; Orecchio et al., 2015; Gutscher et al., 2016; Polonia et al., 2016; Dellong et al., 2018; Dellong et al., 2020).

Seismogenic stress inversion by Totaro et al. (2016) evidenced a more or less perpendicular-to-chain extensional process along the Apennine-Maghrebian chain and compressional effects of Africa-Europe slow convergence in all other sectors in the region. More in detail, the well constrained NNW-trending σ_1 in the main E-trending seismogenic belt located offshore northern Sicily, and the quite diffused transcurrent regime in southeastern Sicily and Ionian offshore driven by NW- to NNW-trending σ_1, mark clearly continental plate convergence (**Figure 1**). These results match well with the recent Nijholt et al. (2018) conclusion according to which in this south-central part of the Mediterranean region "the Calabrian Arc is now further transitioning toward a setting dominated by Africa-Europe plate convergence, whereas during the past 30 Myr slab retreat continually was the dominant factor." In a very recent analysis based on earthquake relocations and stress inversion in the western Ionian, Presti (2020) confirmed that Africa-Europe convergence is the primary tectonic action in that sector but found also local stress heterogeneity imputable to the incipient rifting process at the southwestern edge of the subducting slab hypothesized by Polonia et al. (2017). In particular, SW-NE opening in the NW-trending belt comprised between the Alfeo-Etna and Ionian Fault Systems (**Figure 1**) is believed to add an extensional stress component to convergence-related compression in the offshore of Eastern Sicily (Presti, 2020).

STRONG EARTHQUAKE ACTIVITY OF SOUTHERN CALABRIA

Normal faulting appears to be the dominant faulting mechanism in southern Calabria (**Figure 1**; see, e.g., Ghisetti, 1984; Tortorici et al., 1995; Valensise and Pantosti, 2001). In particular, normal faulting mechanisms have been proposed for some devastating earthquakes which occurred in this part of the Calabrian Arc during the last centuries, those of February 5, 1783 and February 7, 1783 and December, 28 1908 (see locations in **Figure 1** and detailed descriptions given later on in this section). For these earthquakes, however, the debate concerning the causative faults is still open (see below). Even larger is the spreading of hypotheses concerning the other devastating earthquake of September 8, 1905 for which all data of location, magnitude and mechanism are still very debated (more details below). We next discuss the sources proposed in the literature for the earthquakes of magnitude over 6.5 which occurred in southern Calabria since 1600 according to the CPTI15 catalog (Rovida et al., 2019; Rovida et al., 2020). These earthquakes are listed in **Table 1** and indicated by numbering in the map of **Figure 1**. We are going to comment on the individual earthquakes following a geographical order from south to north.

The earthquake of December 28, 1908 (no. 5 in **Figure 1** and **Table 1**) has been imputed to E-dipping faults with top located beneath the western side of Messina Straits (e.g., Amoruso et al., 2002; DISS Working Group, 2018) or to W-dipping faults with top located beneath the eastern side of the Straits (e.g., Tortorici et al., 1995; Aloisi et al., 2013). In particular, by joint inversion of leveling and seismic data associated to this earthquake Amoruso et al., (2002, 2006) obtained a nearly N-trending E-dipping source plane passing through Messina (M in **Figure 1**). On their hand, Aloisi et al. (2013) proposed a NE-striking NW-dipping fault located east of Reggio Calabria (R in **Figure 1**) on the grounds of geologic evidence of Holocene activity, geodetic strain, and seismicity recorded in the last decades. For the same earthquake, the DISS catalog (DISS Working Group, 2018) reports a NE-trending SE-dipping fault with top located a couple of km beneath the Sicilian coast of the Straits (**Figure 1**) mainly derived by work of Valensise (1988) and Valensise and Pantosti (1992). In spite of the different opinions still existing in the scientific community concerning the causative fault of this event, there is a general consensus concerning its normal faulting mechanism and the depth of the source assumed to be confined to the upper 15 km of crust. Magnitude M_s values between 6.9 and 7.2 are reported for this event in the literature (Pino et al., 2009).

Several investigators (Tortorici et al., 1995; Bosi and Galli, 2000; Jacques et al., 2001) related the earthquake of February 5, 1783 (number 1 in **Figure 1** and **Table 1**) to a W-dipping NNE-trending normal fault separating the Aspromonte chain from the Gioia basin (**Figure 1**). On the other hand, an E-dipping NNE-trending blind normal fault with top beneath the Tyrrhenian shoreline of the Gioia basin was proposed as the source of the same earthquake by Valensise and D'Addezio (1994) and in the DISS catalog (DISS Working Group, 2018). Both sources are, however, confined to the upper 15–20 km of crust. A very similar situation occurs concerning the source of the earthquake of February 7, 1783 (no. 2 in **Figure 1** and **Table 1**) for which the DISS catalog (DISS Working Group, 2018) suggests an

TABLE 1 | Earthquakes of magnitude over 6.5 which occurred in southern Calabria since 1600 according to the CPTI15 catalog (Rovida et al., 2019; Rovida et al., 2020). *N* is the order number of the earthquake used also in the map of **Figure 1**. The other columns report the date of the earthquake (year, month, day) and its epicentral coordinates and magnitude M taken from the bibliography indicated in the last column. Three different solutions (a–c) are reported for the earthquake no. 4 of September 8, 1905.

N	Year	Month	Day	Latitude	Longitude	M	Source
1	1783	02	05	38.297	15.970	7.1	CPTI15
2	1783	02	07	38.580	16.201	6.7	CPTI15
3	1783	03	28	38.785	16.464	7.0	CPTI15
4a	1905	09	08	38.667	16.067	6.8	Boschi et al. (2000)
4b	1905	09	08	38.811	16.000	7.0	CPTI15
4c	1905	09	08	38.640	15.540	7.5	Presti et al. (2017)
5	1908	12	28	38.146	15.687	7.1	CPTI15

E-dipping NNE-trending normal fault with top on the western side of the Mesima Valley (**Figure 1**), while Tortorici et al. (1986) and Jacques et al. (2001) proposed a NW-dipping, NNE striking normal fault separating the crystalline bedrock of the chain from the sedimentary Plio-Pleistocenic clastic sequence of the eastern side of the valley (**Figure 1**).

The source of the earthquake of September 8, 1905 (no. 4a–c in **Figure 1** and **Table 1**) is even more debated: i) epicenter location onshore in the Capo Vaticano promontory area (4a in **Figure 1**) or offshore in the Tyrrhenian sea (4b and 4c, same figure); ii) depth estimates in the upper crust of the overriding plate (in the case of locations 4a and 4b) or at the top of the Ionian subducting slab (4c); iii) magnitude values between 6.7 and 7.5 (DISS Working Group, 2018, and references therein). Onshore or near-to-coast shallow locations and lower magnitude values come in general from macroseismic analyses of the earthquake (see, e.g., Boschi et al., 2000). The DISS catalog (DISS Working Group, 2018) reports the solution proposed by Loreto et al. (2013) on the basis of multibeam and seismic reflection analysis carried out in the S. Eufemia basin (SEB in **Figure 1**), i.e., a NE-striking SE-dipping normal fault defined as S. Eufemia fault. By a Bayesian non-linear location method based on use of seismic wave arrival times, Presti et al. (2017) stated that the 1905 earthquake occurred in the Tyrrhenian offshore of Calabria, a few tens km west of Capo Vaticano (4c in **Figure 1**), at a depth between 35 and 55 km. The same authors intervened in the current debate on location, magnitude and generation process of this major earthquake, by stating that it had a magnitude of the order of 7.5 and originated from rupture of the bending zone of the Ionian subduction slab (**Figure 2B**). According to Presti et al.'s reconstruction, rupture occurred on a nearly vertical plane parallel to the SW-NE subduction trench orientation, with the most advanced, northwestern part of the slab slipping down with respect to the southeastern part (**Figure 2B**). This process was framed by the same authors in the geodynamic model of the study region assuming slow SE-ward rollback of the Ionian subducting slab pulled by gravity (Malinverno and Ryan, 1986; Faccenna et al., 1996; Wortel and Spakman, 2000; among many others). Presti et al. (2017) showed also that the 1905 earthquake caused positive Coulomb Stress Changes on the hypothesized sources of the 1908 earthquake in the Messina Straits area, therefore favoring the occurrence of the latter at very short distance only 3 years later.

Finally, the earthquake of March 28, 1783 (no. 3 in **Figure 1** and **Table 1**) was possibly related to a fault located in the Lamezia plain attributable to the ESE-trending, left-lateral transtensional structural system that dissects and advances the southern Calabrian Arc toward ESE (DISS Working Group, 2018). According to Jacques et al. (2001) the trace and nature of the fault that slipped during this earthquake are unclear as well as the source depth which may have been greater than in the cases of the earthquakes of February 1783 (no. 1 and 2 in **Figure 1** and **Table 1**).

DATA AND ANALYSIS

Figure 3 (built with the data available in the Italian earthquake catalog, CPTI15; Rovida et al., 2019; Rovida et al., 2020) clearly shows that the Calabrian Arc is one of the most active areas of

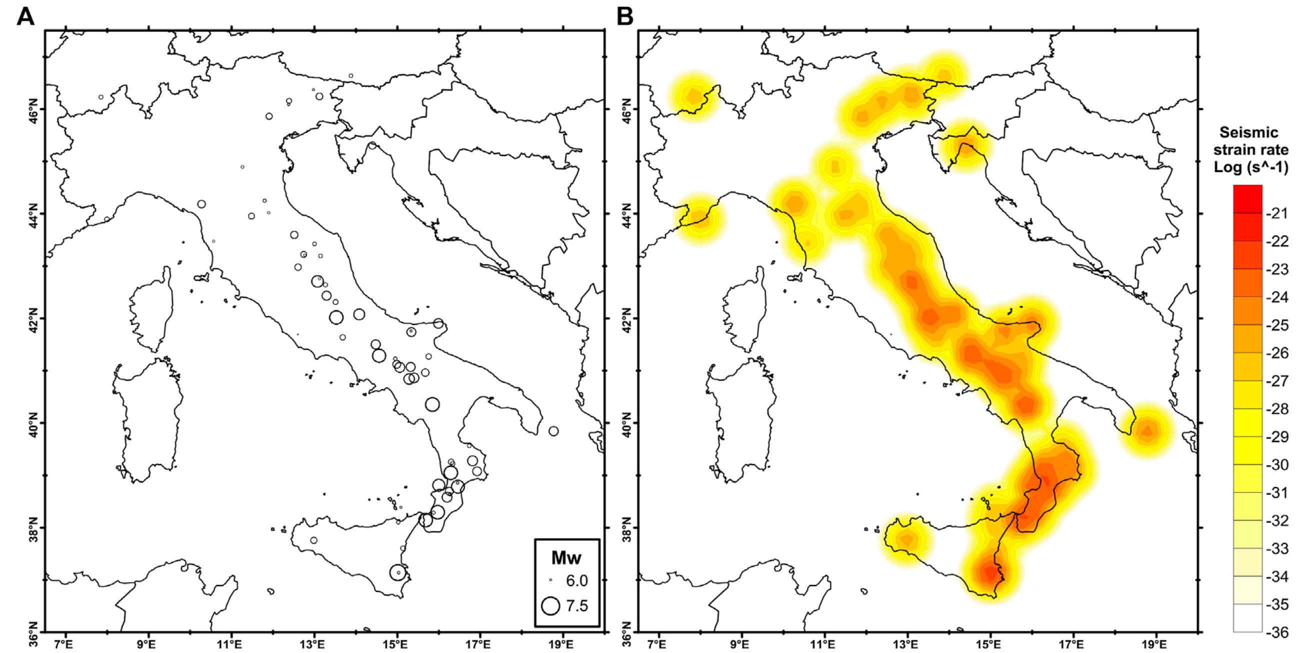

FIGURE 3 | Panel **(A)** shows the epicentral map of the earthquakes of magnitude over 6.0 which occurred in Italy since 1600 (CPTI15; Rovida et al., 2019; Rovida et al., 2020). The corresponding spatial distribution of seismic strain is displayed in panel **(B)**. The values of seismic strain rate have been estimated on a 0.2° × 0.2° grid by using the approach proposed by Jimenez-Munt et al. (2001).

Italy from the seismic point of view. This feature is evident from the epicenter map of the earthquakes of magnitude ≥6.0 which occurred since 1600 (panel **A**) as well as from the space distribution of the corresponding seismic strain rate (panel **B**). Time interval and magnitude threshold used for drawing this figure allow us to guarantee the completeness of the catalog over a relatively long period of time (Stucchi et al., 2011). The seismic strain rate has been estimated on a 0.2° × 0.2° grid by using the approach proposed by Jimenez-Munt et al. (2001). These authors started from the basic Kostrov (1974) relationship and assumed that each earthquake involves a strain rate effect following a Gaussian function:

$$\dot{\varepsilon}_{\text{seismic}} = \frac{1}{2\pi\mu L_S b^2 \Delta t} \sum_{n=1}^{N} \left[M_0\,(N\cdot m)\right]_n \cdot \exp\left(-\frac{r_n^2}{b^2}\right)$$

where $L_S = 25$ km, r_n is the distance to the earthquake n-th, and Δt is the investigated time interval. The b parameter is the width of the Gaussian function. High values of b tend to smooth too much the horizontal gradient of the calculated strain rate, whereas small values of it restrict the deformation to the close vicinity of each epicenter. Several trials have been performed to choose the most appropriate value of b in the study case and this was fixed to 20 km.

The panel **A** of **Figure 4** displays the space distribution of recent shallow seismicity occurring in southern Italy. The plot reports, in particular, the earthquakes of magnitude ≥3.0 occurring at depth less than 30 km between January 1, 2005 and March 31, 2020. We have located the hypocenters of these earthquakes by the Simulps standard linearized method (Evans et al., 1994) using the P and S arrival times available from the INGV bulletin database (http://terremoti.ingv.it/) and the 3D local velocity model estimated by Neri et al. (2012) by integration of crustal (Orecchio et al., 2011) and sub-crustal (Neri et al., 2009) seismotomographic models of the Tyrrhenian region. The linearized procedure of location based on time residual minimization has led to location error estimates of the order of 1 km (ERH) and 2 km (ERZ) for earthquakes located in the Calabrian Arc. Slightly larger errors of the order of 2 km (ERH) and 3 km (ERZ) were obtained in the same area by Presti et al. (2017) using the Bayloc Bayesian non-linear location algorithm. This algorithm computes a cloud of probability density for each hypocenter location and was shown to provide more reliable hypocentral uncertainties with respect to standard linearized algorithms in suboptimal network conditions (Presti et al., 2004; Presti et al., 2008). We take Bayloc's error estimates by Presti et al. (2017) as more conservative estimates of hypocenter uncertainty in the present study. The magnitude threshold of 3 (plot A) should guarantee the completeness of the INGV seismic catalog (http://terremoti.ingv.it/) since 2005 in southern Italy and the concerned Tyrrhenian and Ionian offshores (Schorlemmer et al., 2010). Plot A shows greater density of epicenters i) near the Etna volcano in eastern Sicily, ii) in the southern Tyrrhenian sea offshore Sicily, iii) in northern Calabria, and iv) along the southern Apennines. Very low activity can be noted in the Ionian offshore of southern Calabria. To better explore this situation, we have decided to analyze for hypocentral locations all the earthquakes occurring at depth between 0 and 250 km in the rectangular area indicated in **Figure 4B** and to report in **Figure 4C** the cross section of these earthquakes taken along the

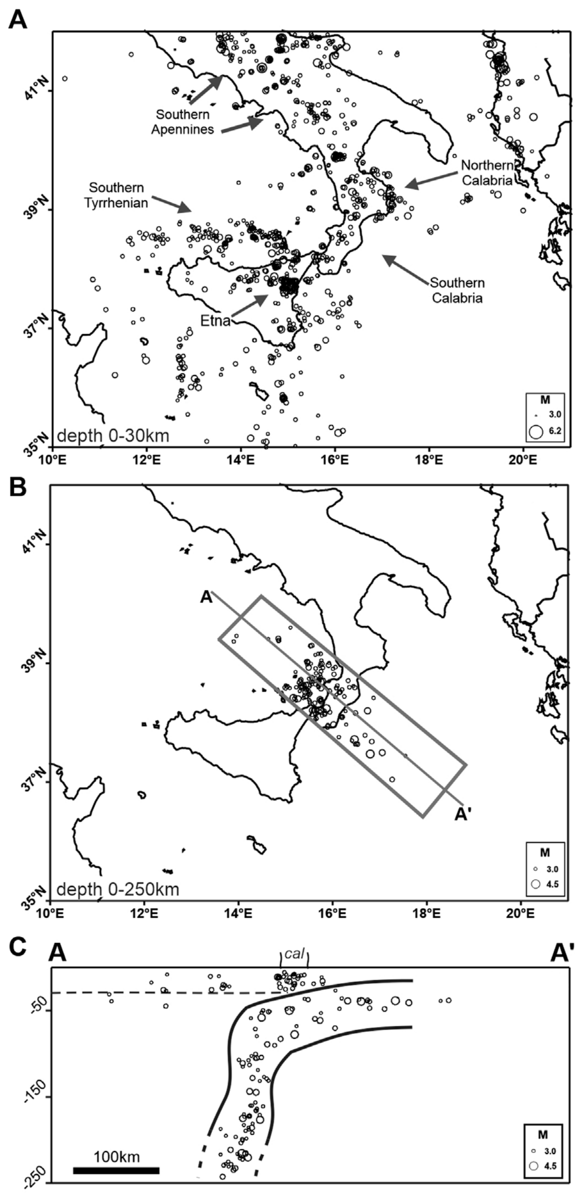

FIGURE 4 | The panel **(A)** shows the epicentral map of earthquakes of magnitude M ≥ 3.0 which occurred at depth less than 30 km in southern Italy between January 1, 2005 and March 31, 2020. Hypocenter locations have been performed using the P- and S-readings available from INGV Bulletin database (http://terremoti.ingv.it/), the standard location method of Evans et al. (1994) and the local seismic velocity model of Neri et al. (2012). The panel **(B)** shows the epicentral map of the earthquakes of magnitude over 3.0 which occurred in the same period at depth less than 250 km in a NW-trending rectangular area crossing southern Calabria. The panel **(C)** displays the hypocenter vertical section along the profile AA′ of the earthquakes of panel **(B)**. For comparison, the location of the Ionian subducting slab derived from data published in previous works (Lucente et al., 1999; Barberi et al., 2004; Cassinis et al., 2005; Montuori et al., 2007; Neri et al., 2009; Piana Agostinetti et al., 2009) is also reported in panel **(C)**.

profile AA′ indicated in **4B**. Considering the location errors of 1 km (ERH) and 2 km (ERZ) obtained for the shallow earthquakes by the Simul linearized method, and also the more conservative values of 2 and 3 km estimated by non-linear methods (see above), we are led to conclude from **Figure 4C** that no significant seismicity is located at the top of the subducting slab (or subduction interface) shown in the vertical section for comparison, while seismicity is clearly detectable at shallow depth in the overriding plate and at deeper depths in the interior of the subducting slab.

Figure 5 shows the horizontal strain rate in Italy estimated by Palano (2015) using global positioning system (GPS) data collected between 1994 and 2013. Palano's dataset included 379 continuous GPS stations and 80 episodic GPS sites located in Sicily and the Northern Apennines in the framework of specific Projects. Palano (2015) aligned estimated GPS velocities to a fixed Eurasian reference frame, derived a continuous velocity gradient tensor on a regular 0.35° × 0.35° grid and then computed the average 2-D strain-rate tensor reported in **Figure 5** (see Palano, 2015 for further details). The figure evidences clear difference between low values of 0–15 nanostrain/yr of extensional horizontal strain in southern Calabria and quite larger values of 35–55 nanostrain/yr along the rest of the Apennine extensional belt in the Italian peninsula from northern Calabria to central Italy. This finding was further evidenced in the more recent paper by Chiarabba and Palano (2017).

Figure 6 displays the vertical displacement rates estimated by Serpelloni et al. (2013) using 2.5–14 years long position time series from more than 800 continuous GPS stations of several networks operating in the Euro-Mediterranean and African regions (see Supplementary Table S1 of Serpelloni et al., 2013). Starting from raw data the same authors analyzed the absolute IGS08 position time series to estimate tridimensional velocities. **Figure 6** reports both the observed (colored circles) and the interpolated vertical velocity fields for the southern Tyrrhenian region (see Serpelloni et al., 2013 for further details). The inset displays the values of vertical displacement rates along the profile MM′ perpendicular to southern Calabria. Both representations show significant variations of vertical displacements on the territory of southern Calabria, with the eastern side of this

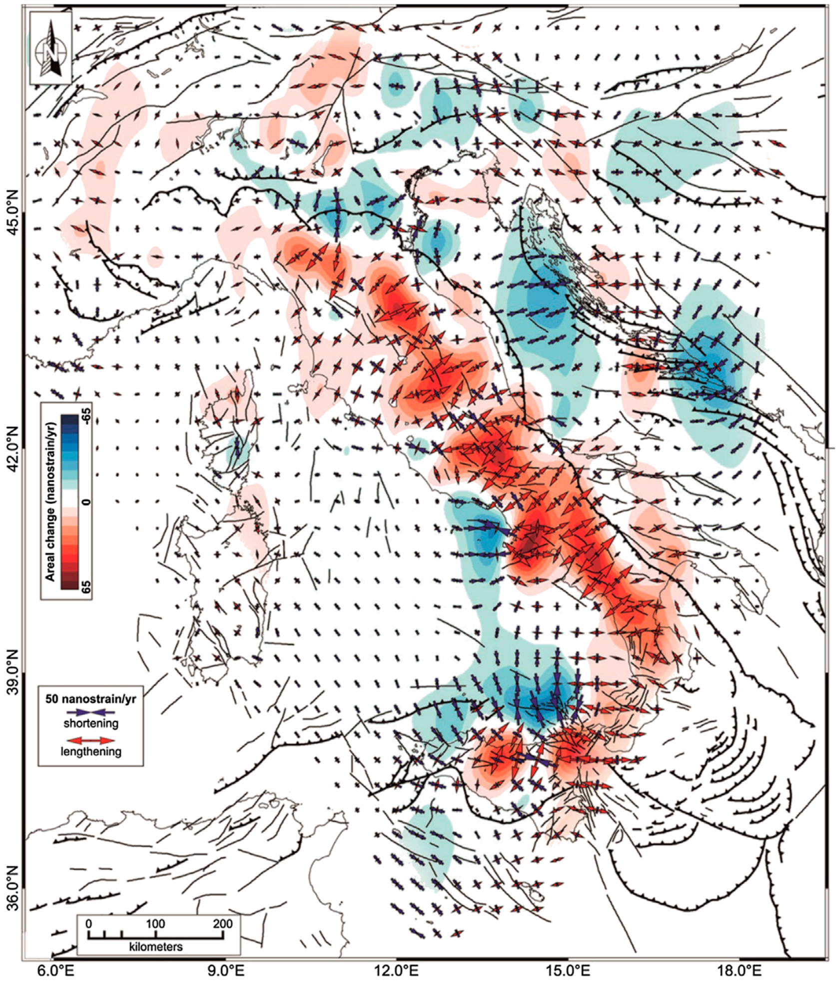

FIGURE 5 | Map of geodetic horizontal strain rate in Italy reproduced from Palano (2015). The color in background shows the rate of areal change, the arrows represent the greatest extensional (red) and contractional (blue) horizontal strain rates.

area uplifting with respect to the western one at a rate of 1–2 mm/yr.

Even considering the approximations of the data available, the vertical displacements reported in the inset of **Figure 6** appear to match well with local geologic data which indicate mountain chain uplifting of 0.5–1.2 mm/yr in the last 1–0.7 Myr and relative-to-chain subsidence in the major tectonic troughs on the western side (Monaco et al., 1996; Faccenna et al., 2011). As reported in a previous section, the zones of uplift in Calabria are predicted by numerical modeling of lithosphere motions and strains based on the assumption of coexistence of continental plate convergence and rollback of an in-depth continuous subducting slab beneath the Calabrian Arc (Negredo et al., 1999).

DISCUSSION

The coexistence of plate convergence and subducting slab rollback in the Calabrian Arc area (more precisely in the southern Calabria segment of Calabrian Arc; Neri et al., 2012) may explain the low values of horizontal strain rate estimated by geodetic measurements in southern Calabria (**Figure 5**). As said in a previous section, NNW-trending plate convergence with velocity of 3–5 mm/yr is reported in the literature for this part of the Mediterranean region (see, e.g., D'Agostino and Selvaggi, 2004; Devoti et al., 2008; Nocquet, 2012). Velocity values of the order of a couple of mm/yr are reported for SE-ward rollback of the Ionian slab subducting beneath the Tyrrhenian-Calabria unit (see, e.g., Hollenstein et al., 2003; Devoti et al., 2008; Nocquet, 2012). We note that plate convergence and rollback are not parallel. With the respective values of velocity, the oblique, opposite action of lithosphere convergence and rollback in southern Calabria may justify the low value of horizontal strain rate as well as the low level of shallow seismicity detected in the Ionian offshore of southern Calabria (**Figure 4**). Also, it can be noted the very low level of seismicity at the top of the subducting slab in the hypocenter vertical section of **Figure 4C**, compatible with the thesis of weak coupling in the Calabria subduction zone (Hsu, 2001).

We attempt to frame the strong earthquake activity of southern Calabria into the geodynamic context presented above. We have said in a previous section that the strong shallow earthquakes of December 28, 1908 and February 5, 1783 and February 7, 1783 can be imputed to NE-trending normal fault systems located closely west of the chain, i.e., the Messina Straits, Gioia Basin, and Mesima Valley fault systems (S, B, and V in **Figure 1**). The horizontal strain rate in this area of normal-faulting strong earthquakes is low and this situation is quite different from that observed in the normal-faulting earthquake belt of the Apennine chain from central Italy to northern Calabria where horizontal strain rates are relatively large (**Figure 5**). Starting from Presti et al., (2017) findings concerning the magnitude 7.5 southern Calabria earthquake of 1905 (summarized in the previous section) we hypothesize that ruptures and instabilities of the upper bending part of the Ionian subducting slab may contribute to shallow seismicity of southern Calabria. Presti et al. (2017) stated that the 1905 earthquake originated at 35–55 km depth in the Tyrrhenian offshore of Calabria (epicenter location 4c in **Figure 1**) and was due to rupture in the elbow zone of the subducting slab occurring on a

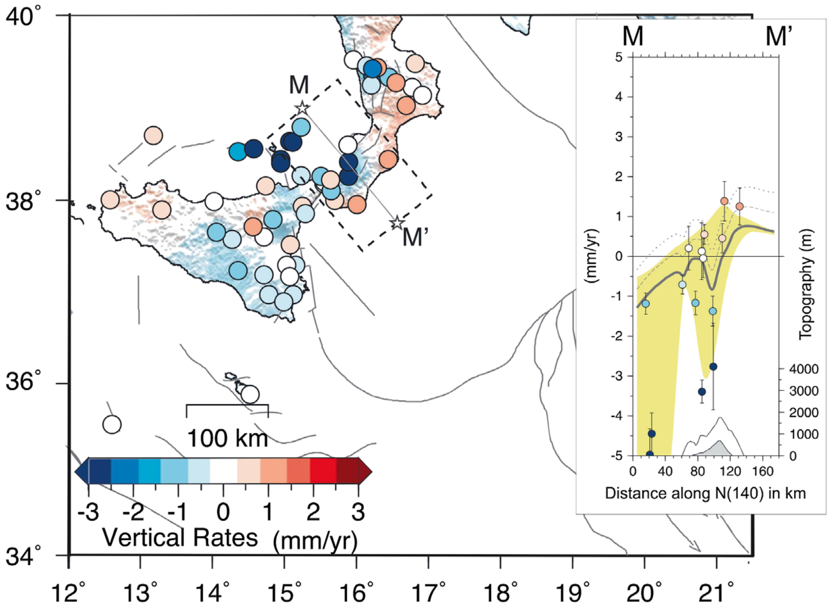

FIGURE 6 | This figure is redrawn from Serpelloni et al. (2013) with combination of their Figures 10 and 13. The main plot shows the observed vertical velocity field (colored circles) over the Italian and surrounding regions. The color scale is saturated at ±3 mm/yr. Positive (red) and negative (blue) values represent uplift and subsidence vertical velocities, respectively. The inset displays the vertical velocities observed along the MM′ profile shown in the main plot (southern Calabria). See Serpelloni et al. (2013) for more details.

nearly vertical plane parallel to the subduction trench orientation (**Figure 2B**). The same authors related this rupture process to gravity pull of the Ionian subducting slab and found also that it caused significant, positive Coulomb Stress Changes on the source of the 1908 earthquake in the Messina Straits area. In a more recent paper, Presti et al. (2019) analyzed the magnitude 4.5 southern Calabria earthquake of July 14, 2018, identified as the only earthquake of magnitude over 4.0 occurring in the last three decades in the same area and depth range (30–70 km) of the 1905 earthquake. The 2018 earthquake was located at about 60 km depth in the seismogenic core of the descending slab. Based on necking of the descending slab and seismicity increase detected at depths around 150 km, Presti et al. (2019) proposed that i) the slab is approaching detachment at this depth and ii) the part of the slab above necking may be subjected to down-dip extension under its own weight, that is, under gravity pull due to the same mass located above the necking zone. The same authors concluded that down-dip extension of the upper slab produces diffused seismogenic stress acting in the inner core of the slab (2018 event) and in the top-elbow zone of it (1905).

We suggest that relatively deep dynamics may concur to normal-faulting shallow seismicity in southern Calabria. Gravity-pull of the upper part of the Ionian subducting slab (that located above necking) may cause ruptures and instabilities in the shallowest portion of the descending slab which, in turn, may perturb stress acting on the normal faults in the Calabria-Tyrrhenian overriding plate (**Figure 7**) favoring the occurrence of shallow earthquakes. These processes of rupture/instability in the upper slab and the related seismicity in the overriding plate (strong normal-faulting earthquakes) may occur in the presence of low horizontal strain rate.

3D reconstruction of the Calabrian Subduction Interface (CSI) led Maesano et al. (2017) to estimate a maximum moment magnitude of ~8 in the CSI framework, corresponding to seismic rupture over the whole length of the trench under condition of full coupling. The same authors claim that the dearth of shallow seismicity related to the CSI can either suggest that it is enduring interseismic locking or is aseismic, with the second hypothesis implying that plate convergence is spent through other mechanisms rather than interplate earthquakes. On their hand, Carafa et al. (2017) suggested high interseismic coupling with low seismic coupling on the same subduction interface, i.e., elastic strain accumulating on the interface would be released episodically in creep events.

Our reconstruction of the dynamic processes occurring in the study region includes the reduction of convergence-related compressional effects due to the opposite action by rollback (**Figure 7**). Coupling would be gradually decreasing at the subduction interface and this may explain the dearth of thrust seismicity on the CSI. This view matches well with the above mentioned findings of Hsu (2001) according to which the Calabria subduction zone represents a weak plate coupling zone. It can also be speculated that the long period of completeness of the historical catalog of Italian earthquakes (estimated to be of the order of 7 and 5 centuries for M7 and M6 earthquakes, respectively; Stucchi et al., 2011) may, at some extent, weaken the hypothesis of enduring interseismic locking on the CSI. Analyses of displacements on the subduction interface by inversion of geodetic data, similar to those proposed for Japan by Yokota et al. (2016, 2018), would be useful in this connection, but the location of our subduction zone including the western Ionian sea, Calabria, and the southeastern Tyrrhenian sea (**Figure 1**) does require contribution by offshore monitoring of crustal displacements, that is not available at present. Finally, we remark that our reconstruction of the local geodynamics based on coexistence of convergence and rollback processes in a low-coupling scenario appears to be coherent with inferences from comparisons between crustal strain fields and Fast Polarization Directions of seismic wave propagation below the crust (Palano, 2015). Along-Arc Fast Polarization Directions attitudes revealing maximum horizontal extension perpendicular to orientation found by geodetic strain analyses in the upper crust was proposed as an evidence of different deformation mechanisms of crust and mantle in the framework of the ongoing subduction and rollback of the Ionian slab (Palano, 2015).

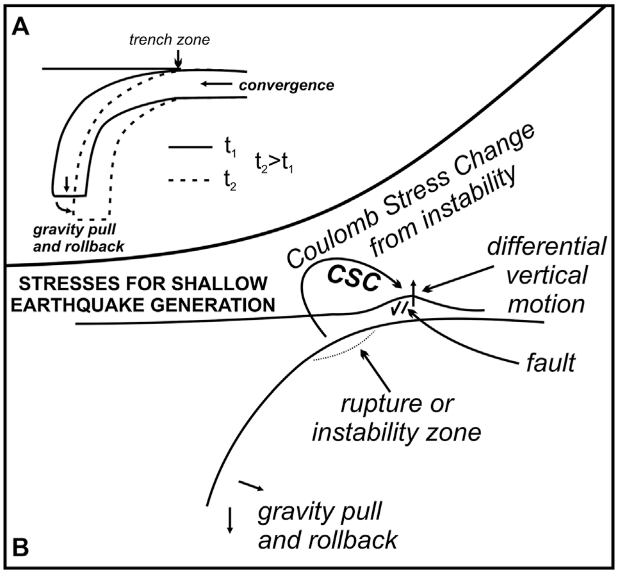

FIGURE 7 | Panel **(A)** reports a sketch representation of the gravity-induced subduction slab rollback and plate convergence in southern Calabria. The continuous and dashed lines indicate the location of the rollbacking slab at different times t_1 and t_2, with $t_2 > t_1$. Rollback and convergence are oriented SE- and NNW-ward, respectively. Their almost opposite motions tend to balance each other, what causes very low horizontal strain rate at Earth's surface and gradually decreasing coupling between the subducting and overriding plates. The detail of the contact zone between subducting slab and overthrusting plate shown in panel **(B)** furnishes a schematic view of seismogenic processes occurring at shallow depth in the overriding plate (Tyrrhenian-southern Calabria unit). In our reconstruction, instabilities of the upper part of the Ionian subducting slab (such as the 1905 major earthquake; see also **Figure 2**) and chain-to-valley differential vertical motion detected at surface would play the role of dynamic sources of normal-faulting earthquake activity occurring at shallow depth in southern Calabria. Basically, major shallow earthquakes of southern Calabria result from complex interaction between different dynamic factors (subduction slab rollback and plate convergence) and, finally, from vertical dynamics produced by this interaction.

CONCLUSION

Low horizontal strain rate associated with the main features of seismicity and marked spatial variation of vertical displacement in southern Calabria suggest a new view of dynamic processes and seismogenesis in one of the highest seismic hazard areas in Italy. While marked extension is observed along the Apennine chain between central Italy and northern Calabria with areal change values as large as 55–35 nanostrain/yr, and this closely corresponds to normal-faulting strong seismicity, the southern Calabria segment of the chain displays relatively low extension between 0 and 15 nanostrain/yr although normal-faulting earthquake activity is here even stronger than along the rest of the Apennine chain. Based also on recent results concerning relationships between intermediate and shallow earthquakes occurring in southern Calabria, we suggest that the observed patterns of ground deformation and seismicity in this specific segment of the chain may be explained with low coupling between the Ionian subducting slab and the Tyrrhenian overriding plate. The opposite action of plate convergence and subduction slab rollback, leading to low coupling, may justify low values of horizontal strain rate. Also, the coexistence of lithosphere convergence and rollback is compatible with GPS and geologic evidence of marked spatial variation of vertical displacement rate in southern Calabria. Ruptures or instabilities in the upper bending part of the Ionian subducting slab due to slab gravity pull are able to perturb shallow normal faults located in the overriding Tyrrhenian plate and may concur to shallow seismicity of southern Calabria. In other words, normal-faulting earthquakes occurring at shallow depth in southern Calabria would be produced by the joint action of i) the dynamics of chain/valley differential vertical movements and ii) the Coulomb Stress Changes due to ruptures or instabilities of the upper bending zone of the subducting slab. New work for comprehensive quantitative description of these processes, based on Finite Element Modeling of the plate boundary in southern Calabria, is being planned as the next step of this research.

DATA AVAILABILITY STATEMENT

Publicly available datasets were analyzed in this study. These data can be found here: www.ingv.it.

AUTHOR CONTRIBUTIONS

GN and BO: coordination of the study. SS and CT: data collection and analysis, and contributions to interpretation of results.

REFERENCES

Aloisi, M., Bruno, V., Cannavò, F., Ferranti, L., Mattia, M., Monaco, C., et al. (2013). Are the source models of the M 7.1 1908 Messina Straits earthquake reliable? Insights from a novel inversion and a sensitivity analysis of levelling data. *Geophys. J. Int.* 192 (3), 1025–1041. doi:10.1093/gji/ggs062

Amoruso, A., Crescentini, L., Neri, G., Orecchio, B., and Scarpa, R. (2006). Spatial relation between the 1908 Messina Straits earthquake slip and recent earthquake distribution. *Geophys. Res. Lett.* 33 (17), L17309. doi:10.1029/2006GL027227

Amoruso, A., Crescentini, L., and Scarpa, R. (2002). Source parameters of the 1908 Messina Straits, Italy, earthquake from geodetic and seismic data. *J. Geophys. Res.* 107 (B4), ESE 4-1–ESE 4-11. doi:10.1029/2001JB000434

Argnani, A., and Bonazzi, C. (2005). Malta escarpment fault zone offshore eastern Sicily: Pliocene-quaternary tectonic evolution based on new multichannel seismic data. *Tectonics* 24 (4), TC4009. doi:10.1029/2004tc001656

Barberi, G., Cosentino, M. T., Gervasi, A., Guerra, I., Neri, G., and Orecchio, B. (2004). Crustal seismic tomography in the Calabrian Arc region, south Italy. *Phys. Earth Planet. In.* 147 (4), 297–314. doi:10.1016/j.pepi.2004.04.005

Boschi, E., Guidoboni, E., Ferrari, G., Mariotti, D., Valensise, G., and Gasperini, P. (2000). Catalogue of strong Italian earthquakes, 461 B.C. to 1997. *Ann. Geofisc.* 43, 609–868 (with database on CD-ROM). doi:10.4401/ag-3668

Bosi, V., and Galli, P. (2000). "Paleoseismic investigation along the February 5, 1783 earthquake ruptures (Cittanova fault, Calabria, southern Italy)," in Proceedings of the XXVII General Assembly of the European Seismological Commission (ESC), Lisbon, Portugal, September 10–15, 2000 (European Seismological Commission), 69. Available at: http://www.esc-web.org/the-esc-general-assembly/164-xxvii-lisbon-portugal.html.

Cadet, J.-P., and Funiciello, R. (2004). *Carte géodynamique de la Méditerranée.* Paris, France: Commission for the Geological Map of the World.

Carafa, M. M., Valensise, G., and Bird, P. (2017). Assessing the seismic coupling of shallow continental faults and its impact on seismic hazard estimates: a case-study from Italy. *Geophys. J. Int.* 209 (1), 32–47. 10.1093/gji/ggx002

Cassinis, R., Scarascia, S., and Lozej, A. (2005). "Review of seismic wide-angle reflection-refraction (WARR) results in the Italian region (1956–1987)," in *Crop project: deep seismic exploration of the central Mediterranean and Italy.* Editor I. R. Finetti (Amsterdam, Netherlands: Elsevier), 31–55.

Chiarabba, C., and Palano, M. (2017). Progressive migration of slab break-off along the southern Tyrrhenian plate boundary: constraints for the present day kinematics. *J. Geodyn.* 105, 51–61. doi:10.1016/j.jog.2017.01.006

D'Agostino, N., and Selvaggi, G. (2004). Crustal motion along the Eurasia-Nubia plate boundary in the Calabrian Arc and Sicily and active extension in the Messina Straits from GPS measurements. *J. Geophys. Res. Solid Earth* 109 (B11), B11402. doi:10.1029/2004JB002998

Dellong, D., Klingelhoefer, F., Dannowski, A., Kopp, H., Murphy, S., Graindorge, D., et al. (2020). Geometry of the deep Calabrian subduction (central Mediterranean Sea) from wide-angle seismic data and 3-D gravity modeling. *Geochem. Geophy. Geosy.* 21, 3. doi:10.1029/2019GC008586

Dellong, D., Klingelhoefer, F., Kopp, H., Graindorge, D., Margheriti, L., Moretti, M., et al. (2018). Crustal structure of the Ionian Basin and eastern Sicily margin: results from a wide-angle seismic survey. *J. Geophys. Res. Solid Earth* 123, 2090–2114. doi:10.1002/2017jb015312

Devoti, R., Riguzzi, F., Cuffaro, M., and Doglioni, C. (2008). New GPS constraints on the kinematics of the Apennines subduction. *Earth Planet Sci. Lett.* 273, 163–174. doi:10.1016/j.epsl.2008.06.031

DISS Working Group (2018). Database of individual seismogenic sources (DISS), version 3.2.1: a compilation of potential sources for earthquakes larger than M 5.5 in Italy and surrounding areas (Rome: Istituto Nazionale di Geofisica e Vulcanologia). Available at: http://diss.rm.ingv.it/diss/ (Accessed May, 2020).

Evans, J. R., Eberhart-Phillips, D., and Thurber, C. H. (1994). Open File Report. User's manual for simulps12 for imaging Vp and Vp/Vs: a derivative of the "Thurber" tomographic inversion simul3 for local earthquakes and explosions. Menlo Park, CA: USGS, Menlo Park, 94–431.

Faccenna, C., Davy, P., Brun, J.-P., Funiciello, R., Giardini, D., Mattei, M., et al. (1996). The dynamics of back-arc extension: an experimental approach to the opening of the Tyrrhenian Sea. *Geophys. J. Int.* 126, 781–795. doi:10.1111/j.1365-246x.1996.tb04702.x

Faccenna, C., Molin, P., Orecchio, B., Olivetti, V., Bellier, O., Funiciello, F., et al. (2011). Topography of the Calabria subduction zone (southern Italy): clues for the origin of Mt. Etna. *Tectonics* 30, TC1003. doi:10.1029/2010TC002694

Ghisetti, F. (1984). Recent deformations and the seismogenic source in the Messina Strait (southern Italy). *Tectonophysics* 109, 191–208. doi:10.1016/0040-1951(84)90140-9

Govers, R., and Wortel, M. J. R. (2005). Lithosphere tearing at STEP faults: response to edges of subduction zones. *Earth Planet Sci. Lett.* 236, 505–523. doi:10.1016/j.epsl.2005.03.022

Gutscher, M.-A., Dominguez, S., de Lepinay, B. M., Pinheiro, L., Gallais, F., Babonneau, N., et al. (2016). Tectonic expression of an active slab tear from high-resolution seismic and bathymetric data offshore Sicily (Ionian Sea). *Tectonics* 35(1), 39–54. doi:10.1002/2015tc003898

Hollenstein, C., Kahle, H. G., Geiger, A., Jenny, S., Goes, S., and Giardini, D. (2003). New GPS constraints on the Africa-Eurasia plate boundary zone in southern Italy. *Geophys. Res. Lett.* 30 (18), 1935. doi:10.1029/2003gl017554

Hsu, S. K. (2001). Lithospheric structure, buoyancy and coupling across the southernmost Ryukyu subduction zone: an example of decreasing plate coupling. *Earth Planet Sci. Lett.* 186 (3–4), 471–478. doi:10.1016/s0012-821x(01)00261-8

Jacques, E., Monaco, C., Tapponnier, P., Tortorici, L., and Winter, T. (2001). Faulting and earthquake triggering during the 1783 Calabria seismic sequence. *Geophys. J. Int.* 147, 499–516. doi:10.1046/j.0956-540x.2001.01518.x

Jiménez-Munt, I., Fernàndez, M., Torne, M., and Bird, P. (2001). The transition from linear to diffuse plate boundary in the Azores-Gibraltar region: results from a thin-sheet model. *Earth Planet Sci. Lett.* 192, 175–189. doi:10.1016/s0012-821x(01)00442-3

Kostrov, V. (1974). Seismic moment and energy of earthquakes, and seismic flow of rock. *Izv. Acad. Sci. USSR Phys. Solid Earth.* 1, 23–44.

Loreto, M. F., Fracassi, U., Franzo, A., Del Negro, P., Zgur, F., and Facchin, L. (2013). Approaching the seismogenic source of the Calabria 8 September 1905 earthquake: new geophysical, geological and biochemical data from the S. Eufemia Gulf (S Italy). *Mar. Geol.* 343, 62–75. doi:10.1016/j.margeo.2013.06.016

Lucente, F. P., Chiarabba, C., Cimini, G. B., and Giardini, D. (1999). Tomographic constraints on the geodynamic evolution of the Italian region. *J. Geophys. Res.* 104 (B9), 20307–20327. doi:10.1029/1999JB900147

Maesano, F. E., Tiberti, M. M., and Basili, R. (2017). The Calabrian Arc: three-dimensional modelling of the subduction interface. *Sci. Rep.* 7, 8887. doi:10.1038/s41598-017-09074-8

Malinverno, A., and Ryan, W. B. F. (1986). Extension in the Tyrrhenian Sea and shortening in the Apennines as result of arc migration driven by sinking of the lithosphere. *Tectonics* 5 (2), 227–245. doi:10.1029/TC005i002p00227

Monaco, C., Tortorici, L., Nicolich, R., Cernobori, L., and Costa, M. (1996). From collisional to rifted basins: an example from the southern Calabrian arc (Italy). *Tectonophysics* 266 (1–4), 233–249. doi:10.1016/S0040-1951(96)00192-8

Montuori, C., Cimini, G. B., and Favali, P. (2007). Teleseismic tomography of the southern Tyrrhenian subduction zone: new results from seafloor and land recordings. *J. Geophys. Res.* 112, B3. doi:10.1029/2005JB004114

Negredo, A. M., Carminati, E., Barba, S., and Sabadini, R. (1999). Dynamic modelling of stress accumulation in central Italy. *Geophys. Res. Lett.* 26 (13), 1945–1948. doi:10.1029/1999GL900408

Neri, G., Barberi, G., Oliva, G., and Orecchio, B. (2004). Tectonic stress and seismogenic faulting in the area of the 1908 Messina earthquake, south Italy. *Geophys. Res. Lett.* 31 (10), L10602. doi:10.1029/2004GL019742

Neri, G., Barberi, G., Oliva, G., and Orecchio, B. (2005). Spatial variations of seismogenic stress orientations in Sicily, south Italy. *Phys. Earth Planet. In.* 148, 175–191. doi:10.1016/j.pepi.2004.08.009

Neri, G., Marotta, A. M., Orecchio, B., Presti, D., Totaro, C., Barzaghi, R., et al. (2012). How lithospheric subduction changes along the Calabrian Arc in southern Italy: geophysical evidences. *Int. J. Earth Sci.* 101, 1949–1969. doi:10.1007/s00531-012-0762-7

Neri, G., Oliva, G., Orecchio, B., and Presti, D. (2006). A possible seismic gap within a highly seismogenic belt crossing Calabria and eastern Sicily, Italy, *Bull. Seismol. Soc. Am.* 96, 1321–1331. doi:10.1785/0120050170

Neri, G., Orecchio, B., Totaro, C., Falcone, G., and Presti, D. (2009). Subduction beneath southern Italy close the ending: results from seismic tomography. *Seismol. Res. Lett.* 80 (1), 63–70. doi:10.1785/gssrl.80.1.63

Nijholt, N., Govers, R., and Wortel, R. (2018). On the forces that drive and resist deformation of the south-central Mediterranean: a mechanical model study. *Geophys. J. Int.* 214 (2), 876–894. doi:10.1093/gji/ggy144

Nocquet, J.-M. (2012). Present-day kinematics of the Mediterranean: a comprehensive overview of GPS results. *Tectonophysics* 579, 220–242. doi:10.1016/j.tecto.2012.03.037

Orecchio, B., Presti, D., Totaro, C., D'Amico, S., and Neri, G. (2015). Investigating slab edge kinematics through seismological data: the northern boundary of the Ionian subduction system (south Italy). *J. Geodyn.* 88, 23–35. doi:10.1016/j.jog.2015.04.003

Orecchio, B., Presti, D., Totaro, C., Guerra, I., and Neri, G. (2011). Imaging the velocity structure of the Calabrian Arc region (south Italy) through the integration of different seismological data. *Boll. Geofis. Teor. Appl.* 52, 625–638. doi:10.4430/bgta0023

Orecchio, B., Presti, D., Totaro, C., and Neri, G. (2014). What earthquakes say concerning residual subduction and STEP dynamics in the Calabrian arc region, south Italy. *Geophys. J. Int.* 199 (3), 1929–1942. doi:10.1093/gji/ggu373

Palano, M. (2015). On the present-day crustal stress, strain-rate fields and mantle anisotropy pattern of Italy. *Geophys. J. Int.* 200 (2), 969–985. doi:10.1093/gji/ggu451

Piana Agostinetti, N., Steckler, M. S., and Lucente, F. P. (2009). Imaging the subducted slab under the Calabrian Arc, Italy, from receiver function analysis. *Lithosphere* 1 (3), 131–138. doi:10.1130/L49.1

Pino, N. A., Piatanesi, A., Valensise, G., and Boschi, E. (2009). The 28 December 1908 Messina Straits earthquake (M_w 7.1): a great earthquake throughout a century of seismology. *Seismol Res. Lett.* 80 (2), 243–259. doi:10.1785/gssrl.80.2.243

Polonia, A., Torelli, L., Artoni, A., Carlini, M., Faccenna, C., Ferranti, L., et al. (2016). The Ionian and Alfeo-Etna fault zones: new segments of an evolving plate boundary in the central Mediterranean Sea? *Tectonophysics* 675, 69–90. doi:10.1016/j.tecto.2016.03.016

Polonia, A., Torelli, L., Gasperini, L., Cocchi, L., Muccini, F., Bonatti, E., et al. (2017). Lower plate serpentinite diapirism in the Calabrian Arc subduction complex. *Nat. Commun.* 8 (1), 1–13. doi:10.1038/s41467-017-02273-x

Polonia, A., Torelli, L., Mussoni, P., Gasperini, L., Artoni, A., and Klaeschen, D. (2011). The Calabrian Arc subduction complex in the Ionian Sea: regional architecture, active deformation, and seismic hazard. *Tectonics* 30 (5), TC5018. doi:10.1029/2010TC002821

Presti, D. (2020). Seismicity supports the theory of incipient rifting in the western Ionian Sea, central Mediterranean. *Ann. Geophys.* 63 (2), 225. 10.4401/ag-8360

Presti, D., Billi, A., Orecchio, B., Totaro, C., Faccenna, C., and Neri, G. (2013). Earthquake focal mechanisms, seismogenic stress, and seismotectonics of the Calabrian Arc, Italy, *Tectonophysics* 602, 153–175. doi:10.1016/j.tecto.2013.01.030

Presti, D., Neri, G., Orecchio, B., Scolaro, S., and Totaro, C. (2017). The 1905 Calabria, southern Italy, earthquake: hypocenter location, causative process, and stress changes induced in the area of the 1908 Messina Straits earthquake. *Bull. Seismol. Soc. Am.* 107 (6), 2613–2623. doi:10.1785/0120170094

Presti, D., Orecchio, B., Falcone, G., and Neri, G. (2008). Linear versus non-linear earthquake location and seismogenic fault detection in the southern Tyrrhenian Sea, Italy, *Geophys. J. Int.* 172, 607–618. doi:10.1111/j.1365-246x.2007.03642.x

Presti, D., Totaro, C., Neri, G., and Orecchio, B. (2019). New earthquake data in the Calabrian subduction zone, Italy, suggest revision of the presumed dynamics in the upper part of the subducting slab. *Seismol Res. Lett.* 90 (5), 1994–2004. doi:10.1785/0220190024

Presti, D., Troise, C., and De Natale, G. (2004). Probabilistic location of seismic sequences in heterogeneous media. *Bull. Seismol. Soc. Am.* 94, 2239–2253. doi:10.1785/0120030160

Rosenbaum, G., Gasparon, M., Lucente, F. P., Peccerillo, A., and Miller, M. S. (2008). Kinematics of slab tear faults during subduction segmentation and implications for Italian magmatism. *Tectonics* 27 (2), TC2008. doi:10.1029/2007tc002143

Rovida, A., Locati, M., Camassi, R., Lolli, B., and Gasperini, P. (2019). Catalogo parametrico dei terremoti Italiani (CPTI15), versione 2.0 (Rome: Istituto Nazionale di Geofisica e Vulcanologia (INGV)). Available at: https://emidius.mi.ingv.it/CPTI15-DBMI15/.

Rovida, A., Locati, M., Camassi, R., Lolli, B., and Gasperini, P. (2020). The Italian earthquake catalogue CPTI15. *Bull. Earthq. Eng.* 18 (7), 2953–2984. doi:10.1007/s10518-020-00818-y

Schorlemmer, D., Mele, F., and Marzocchi, W. (2010). A completeness analysis of the National Seismic Network of Italy. *J. Geophys. Res. Solid Earth* 115 (B4), B04308. doi:10.1029/2008jb006097

Serpelloni, E., Faccenna, C., Spada, G., Dong, D., and Williams, S. D. P. (2013). Vertical GPS ground motion rates in the Euro-Mediterranean region: new evidence of velocity gradients at different spatial scales along the Nubia-Eurasia plate boundary. *J. Geophys. Res. Solid Earth* 118 (11), 6003–6024. doi:10.1002/2013jb010102

Spakman, W., and Wortel, R. (2004). "A tomographic view on western Mediterranean geodynamics," in *The TRANSMED Atlas. The Mediterranean region from crust to mantle*. Editors W. Cavazza, F. Roure, W. Spakman, G. M. Stampfli, and P. A. Ziegler (Heidelberg, Germany: Springer-Verlag), 31–52.

Stucchi, M., Meletti, C., Montaldo, V., Crowley, H., Calvi, G. M., and Boschi, E. (2011). Seismic hazard assessment (2003–2009) for the Italian building code. *Bull. Seismol. Soc. Am.* 101 (4), 1885–1911. doi:10.1785/0120100130

Tortorici, L., Monaco, C., Tansi, C., and Cocina, O. (1995). Recent and active tectonics in the Calabrian Arc (southern Italy). *Tectonophysics* 243, 37–55. doi:10.1016/0040-1951(94)00190-k

Tortorici, L., Tapponnier, P., and Winter, T. (1986). Faulting during the 1783 Calabria earthquakes and tectonics of the Messina Strait. *EOS Trans. AGU* 67, 1188.

Totaro, C., Orecchio, B., Presti, D., Scolaro, S., and Neri, G. (2016). Seismogenic stress field estimation in the Calabrian Arc region (south Italy) from a Bayesian approach. *Geophys. Res. Lett.* 43 (17), 8960–8969. doi:10.1002/2016GL070107

Valensise, G. (1988). Low angle normal faulting during the 1908, Messina, earthquake revealed by geodetic data analysis. *Eos Trans. AGU* 69 (44), F1433.

Valensise, G., and D'Addezio, G. (1994). I.N.G. Internal Report. Il contributo della geologia di superficie all'identificazione delle strutture sismogenetiche della Piana di Gioia Tauro, 559.

Valensise, G., and Pantosti, D. (1992). A 125 Kyr-long geological record of seismic source repeatability: the Messina Straits (southern Italy) and the 1908 earthquake (Ms7/2). *Terra. Nova* 4 (4), 472–483. doi:10.1111/j.1365-3121.1992.tb00583.x

Valensise, G., and Pantosti, D. (2001). Database of potential sources for earthquakes larger than M 5.5 in Italy. *Ann. Geofisc.* 44 (Suppl. 1), 180, 2001 (with database on CD-ROM).

Wortel, M. J. R., and Spakman, W. (2000). Subduction and slab detachment in the Mediterranean-Carpathian region. *Science* 290, 1910–1917. doi:10.1126/science.290.5498.1910

Yokota, Y., Ishikawa, T., and Watanabe, S. (2018). Seafloor crustal deformation data along the subduction zones around Japan obtained by GNSS-A observations. *Sci. data* 5, 180–182. doi:10.1038/sdata.2018.182

Yokota, Y., Ishikawa, T., Watanabe, S., Tashiro, T., and Asada, A. (2016). Seafloor geodetic constraints on interplate coupling of the Nankai Trough megathrust zone. *Nature* 534, 374–377. doi:10.1038/nature17632

Conflict of Interest: The authors declare that the research was conducted in the absence of any commercial or financial relationships that could be construed as a potential conflict of interest.

frontiers in Earth Science

MINI REVIEW
published: 17 December 2020
doi: 10.3389/feart.2020.600152

Empirical Analysis of Global-Scale Natural Data and Analogue Seismotectonic Modelling Data to Unravel the Seismic Behaviour of the Subduction Megathrust

Francesca Funiciello[1]*, *Fabio Corbi*[2], *Arnauld Heuret*[3], *Claudia Piromallo*[4] *and Matthias Rosenau*[5]

[1]*Department of Science, University "Roma TRE", Roma, Italy,* [2]*Istituto di Geologia Ambientale Geoingegneria—CNR C/o Dipartimento Scienze della Terra, Sapienza Università di Roma, Roma, Italy,* [3]*Université De Guyane / Géosciences Montpellier, Cayenne, France,* [4]*Istituto Nazionale Di Geofisica e Vulcanologia, Roma, Italy,* [5]*Helmholtz Centre Potsdam–GFZ German Research Centre for Geosciences, Potsdam, Germany*

OPEN ACCESS

Edited by:
Debora Presti,
University of Messina, Italy

Reviewed by:
Magdala Tesauro,
Utrecht University, Netherlands
Luis E. Lara,
Servicio Nacional de Geología y Minería de Chile (SERNAGEOMIN), Chile

***Correspondence:**
Francesca Funiciello
francesca.funiciello@uniroma3.it

Specialty section:
This article was submitted to Structural Geology and Tectonics, a section of the journal Frontiers in Earth Science

Received: *28 August 2020*
Accepted: *17 November 2020*
Published: *17 December 2020*

Citation:
Funiciello F, Corbi F, Heuret A, Piromallo C and Rosenau M (2020) Empirical Analysis of Global-Scale Natural Data and Analogue Seismotectonic Modelling Data to Unravel the Seismic Behaviour of the Subduction Megathrust. Front. Earth Sci. 8:600152. doi: 10.3389/feart.2020.600152

Subduction megathrusts host the Earth's greatest earthquakes as the 1960 Valdivia (M_w 9.5, Chile), the largest earthquake instrumentally recorded, and the recent 2004 Sumatra-Andaman (M_w 9.2, Indonesia), 2010 Maule (M_w 8.8, Chile), and 2011 Tohoku-Oki (M_w 9.1, Japan) earthquakes triggering devastating tsunamis and representing a major hazard to society. Unravelling the spatio-temporal pattern of these events is thus a key for seismic hazard assessment of subduction zones. This paper reviews the current state of knowledge of two research areas–empirical analysis of global-scale natural data and experimental data from an analogue seismotectonic modelling—devoted to study cause-effect relationships between subduction zone parameters and the megathrust seismogenic behavior. The combination of the two approaches overcomes the observational bias and inherent sampling limitations of geological processes (i.e., shortness of instrumental and historical data, decreasing completeness and resolution with time into the past) and allows drawing appropriately from multiple disciplines with the aim of highlighting the geodynamic conditions that may favor the occurrence of giant megathrust earthquakes.

Keywords: analogue seismotectonic modelling, analysis of global-scale natural data, mega-earthquakes, interplate seismicity, subduction megathrust

INTRODUCTION

Most of the global seismicity and the largest earthquakes occur at subduction zones where oceanic lithosphere is recycled as it sinks into the underlying mantle. The downgoing movement of the subducting plate and friction acting at the shallow part of the interface between the subducting and overriding plate (aka megathrust) cause shear stresses to accumulate slowly over centuries. When the frictional shear strength of the interface is overcome, these stresses are released episodically by a variety of seismic and aseismic slip modes, including "mega-earthquakes": seismic megathrust rupture causing earthquakes with magnitudes (M_W) ≥ 8.5. Stress accumulation and release occurs in cycles known as seismic cycles. In the last 15 years, a cluster of mega-earthquakes occurred at an increased rate with respect to the last century (e.g., Ammon et al., 2010) often revealing unexpected characteristics (e.g., Stein and Okal 2011; Yue and Lay 2013) and resulting in catastrophic direct but also indirect (e.g., tsunamis) effects as in Sumatra (2004) (e.g., Subaraya et al., 2006), and Tohoku-Oki 2011 (e.g., Romano et al., 2012). The attention for these events has thus recently increased, raising interest on factors controlling their spatio-temporal pattern, including their potential maximum magnitude and return periods which are fundamental parameters in earthquake and tsunami hazard assessment. This is a challenging goal not only because each subduction zone has unique characteristics (e.g., Kopp, 2013) but also because the seismogenic portion of the megathrust is located offshore, below the sea-level (Heuret et al., 2011), and direct observation is restrained to shallow drilling (e.g., Japan Trench Fast Drilling Project; Chester et al., 2012) and the study of exhumed prototypes (e.g., Remitti et al., 2011). Moreover, the instrumental seismic record is limited to the last century, a very short time interval compared to the recurrence time of great earthquakes, which ranges from centuries to millennia (e.g., McCaffrey, 2008). In some cases, seismic records of megathrust ruptures can be extended back in time with paleoseismological investigations (e.g., Philibosian and Meltzner 2020), however such data typically lack the spatio-temporal completeness and resolution needed for rigorous statistical analysis.

One of the empirical research strategies that allow overcoming limited records consists in trading time with space at the global scale: given that different subduction zones are at individual stages of their seismic cycle, we may be able to infer the general seismogenic behavior of subduction zones by integrating information from worldwide seismicity (e.g., Schafer and Wenzel, 2019). The second approach, somehow complementary to the first one, is comparing the seismic character of individual megathrusts with the widest range of geological, geophysical and geodynamical parameters, with the aim of statistically identifying the combination of factors controlling subduction seismicity (e.g., Ruff and Kanamori, 1980; Peterson and Seno, 1984; Heuret et al., 2011; Schellart and Rawlinson, 2013; Brizzi et al., 2018).

Results from such a global-scale natural data analysis approach can be then tested against experimental and modelling data in order to validate inferred causal relationships by means of ad hoc parametric studies. Analytical (e.g., Ruff, 1992), numerical (e.g., van Dinther et al., 2013), physical (e.g., Den Hartog and Spiers 2013) and analog models (e.g., Rosenau et al., 2017) can reproduce a long series of seismic cycles and, by tuning ad hoc boundary conditions, they allow testing the role played on seismicity by the different parameters deduced from the analysis of natural data (e.g., Corbi et al., 2017b). Despite models are only simplified representations of the complexity of the natural prototype due to the unavoidable computational and experimental limitations, their results are inspiring for the interpretation of the limited and sparse natural data, thus enhancing our current understanding of subduction seismicity.

We focus our brief overview on the state of the art of the analysis from global-scale natural data and experimental data from analogue seismotectonic modelling, highlighting the advantages of their use and the great potential for future developments in the study of the earthquake process that can be drawn from the close interaction and reciprocal feedback between the two methods. Very recently, also numerical methods have been developed to setup simulations which capture both the long-term and the short-term evolution of the subduction process. While numerical simulations proved particularly useful for testing hypothesis and mapping a wide parameter space, it is the emergent behavior of analogue models which makes them appealing for an empirical analysis as addressed in this review.

OBSERVATIONS AND INFERENCES FROM NATURAL DATA

There is a noteworthy variability in the maximum moment magnitude of earthquakes originated at the subduction megathrust during the instrumental era (e.g., Dixon and Moore, 2007 **Figure 1A**): some subduction zones–e.g., Alaska, Chile, Sumatra, NE Japan–experienced mega-earthquakes, while others–e.g., Tonga Mariana–did not (**Figure 1A**). What is unclear and still debated is if this dichotomy results only from the short observational time span and therefore all the worldwide subduction zones could host mega-earthquakes given a long enough observation period (e.g., McCaffrey, 2008) or if specific local conditions are responsible for the diversity of the interplate seismicity (e.g., Ruff and Kanamori, 1980). It is thus tempting to identify which geological/geophysical features, individually or in combination, possibly have a cause-effect relationship with megathrust seismicity (e.g., Pacheco et al., 1993; Heuret et al., 2011; Schellart and Rawlinson, 2013) and to quantify the likelihood for great earthquakes along worldwide subduction megathrusts (e.g., Marzocchi et al., 2016).

The “comparative subductology” was the intuition to disentangle the overall behavior of subduction by comparing a wide range of observables (i.e., subducting plate age and dip, convergent velocity, backarc tectonic style, characteristics of arc volcanism and seismicity, accretionary/erosional character of the margin) with seismicity characteristics of convergent margins (Uyeda, 1982) with the aim of deducing possible causal relationships (**Figure 1B**). This space-time trade-off approach allowed to overcome limitations due to uniqueness of local conditions (e.g., Suárez and Albini, 2009; Becker and Meier, 2010; Hayes and Furlong, 2010) and to the undersampling of the modern seismicity record.

Early on, two end–members subduction types — Mariana and Chilean — have been proposed, showing also significant difference in the degree of mechanical coupling (i.e., the ability to accumulate stresses) along the plate interface and in the consequent capability to host mega-earthquakes (Uyeda and Kanamori, 1979). The Chilean–type boundaries seemed more coupled and prone to trigger mega-earthquakes than the rather aseismic Marianas, with the different behaviors likely tuned by both different densities of the subducting plate and motions of the upper plate (Uyeda and Kanamori, 1979).

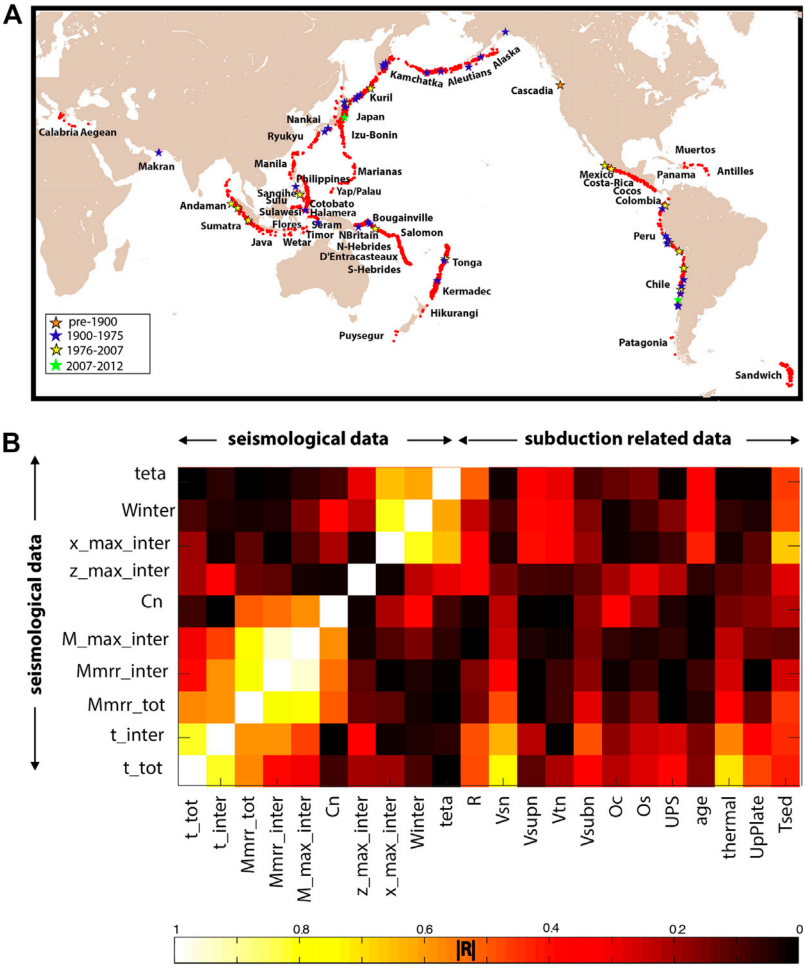

FIGURE 1 | (A) Map of the subduction interface seismicity (redrawn from Heuret et al., 2011). $M_w \geq 8.0$ subduction interface events are plotted by stars of different colours, representing the interval of occurrence of the events. The largest events are not homogeneously distributed in space and time along the worldwide subduction zones; **(B)** Correlation matrix used to show the dependence between multiple variables at a glance. The table contains the modulus of the Pearson's product moment correlation coefficient R of linear bivariate regressions between seismogenic zone parameters (t_tot: total seismic of subduction zones; t_inter: seismic rate due to interplate earthquakes; Mmrr_tot: total moment release rate of subduction zones; Mmrr_inter: moment release rate due to interplate events; Mmax_inter: maximum magnitude of interplate events; Cn: seismic coupling coefficient; zmax_inter: downdip limit of the subduction thrust fault; zmin_inter: updip limit of the subduction thrust fault) and other independent subduction parameters (Tsed: thickness of sediments at the trench; UpPlate: nature of the upper plate; thermal: thermal parameter; age: age of the subducting lithosphere at the trench; Vsn: normal component of the subduction velocity; Vsupn: normal component of the overriding plate velocity; Vts: normal component of the trench velocity; Vsubn: normal component of the subducting plate velocity; Oc: convergence obliquity; Os: subduction obliquity; R: radius of bending of the slab) as attempt to unravel the overall behavior of subduction by comparing a wide range of observables (see Heuret et al., 2011 for additional details).

Based on this idea, Ruff and Kanamori (1980) looked at the maximum M_w recorded in the instrumental era and they found a striking correlation between the convergence rate and plate age. It was thus proposed that mega-earthquakes preferentially occur where a young lithosphere is converging fast with the overriding plate, allowing for a high mechanical plate coupling along the megathrust. This relationship has long been supported by studies involving larger, progressively updated and refined datasets (e.g., Peterson and Seno, 1984; Jarrard, 1986; Pacheco et al., 1993; Scholz and Campos, 1995). However, variations of coupling found within individual subduction zones (Scholz and Campos, 2012), the identification of different moment release rates in subduction zones sharing similar lithospheric ages and speeds (Peterson and Seno, 1984) and, last but not least, updated data (e.g., Heuret et al., 2011; Stein and Okal, 2007; Stein and Okal, 2011) initiated skepticism in the acknowledgement of the Ruff and Kanamori (1980) model (e.g., McCaffrey, 1994) that was finally challenged by recent mega-earthquakes occurring in locations assumed to be weakly coupled (e.g., Wang, 2013). Among these, the Tohoku-Oki earthquake stands out not only for exceeding the regional maximum magnitude earthquake for that region according to Ruff and Kanamori (1980) model, but also as case of extreme violation of commonly accepted scaling laws (e.g. Okal, 2015).

A new phase of the comparative subductology involved not only the use of large dataset (e.g., Heuret et al., 2012; Schellart and

Rawlinson 2013) but also of more sophisticated statistical analysis to treat them (e.g., Heuret et al., 2012; Marzocchi et al., 2016; Brizzi et al., 2018; Schafer and Wenzel, 2019). Cause-effect relationships between geodynamical and seismological parameters, have inspired physical models of seismically active convergent margins highlighting the possible role of numerous factors in triggering mega-earthquakes: trench sediments (Kostoglodov, 1988; Ruff, 1989; Heuret et al., 2011; Heuret et al., 2012; Scholl et al., 2015; Seno, 2017; Brizzi et al., 2018), plate roughness (Morgan et al., 2008; Kopp, 2013; Wang and Bilek, 2014; Bassett and Watts, 2015; Lallemand et al., 2018; van Rijsingen et al., 2018) upper plate strain (Conrad et al., 2004; Heuret et al., 2011; Heuret et al., 2012; Schellart and Rawlinson, 2013), plate age (Nishikawa and Ide, 2014), forearc structure (Song and Simons, 2003; Wells et al., 2003; Fuller et al, 2006; Rosenau and Oncken, 2009), along–strike (Schellart and Rawlinson, 2013) and along-dip (Bletery et al., 2016) curvature of subduction zones, slab dip (Schafer and Wenzel, 2019), downdip width of the seismogenic zone (e.g., Kelleher et al., 1974; Pacheco et al., 1993; Hayes et al., 2012; Schellart and Rawlinson, 2013; Schafer and Wenzel, 2019) and propensity to produce large rupture in the trench–parallel direction (Bilek and Lay, 1999; Brizzi et al., 2018). The proposed models highlight ingredients able to produce a homogeneous and strong subduction megathrust allowing ruptures to easily propagate along–strike and, thus, to grow into mega-earthquakes.

Such a physical understanding may re-evaluate traditional probabilistic seismic-hazard assessment, suggesting that, irrespective of the geodynamic context, many subduction zones (Berryman et al., 2015) if not all (McCaffrey, 2008; Rong et al., 2014) may have the potential of producing mega-earthquakes (McCaffrey, 2008; Rong et al., 2014) but they are likely characterized by a difference in the average rate of occurrence of these events (Marzocchi et al., 2016).

INSIGHTS FROM ANALOG MODELLING OF SUBDUCTION MEGATHRUST SEISMIC CYCLES

To overcome limitations of natural records and test cause-effect relationships suggested by global-scale data analysis we promote an analog modelling approach. Analog models are down-scaled and simplified versions of natural subduction zones used in experiments that allow reproducing the essence of a variety of geological phenomena, in convenient spatial and temporal scales (e.g., Hubbert, 1937; Funiciello and Corbi, 2017). Despite analog models might appear oversimplified with respect to high performance computational modelling strategies anticipated in the introduction (for example, no efficient control on temperature and water content has been implemented so far), they have the advantage of evolving spontaneously on the basis of the physics of the process, which can be easy to tune and to interpret. Moreover, analog models are intrinsically three-dimensional and occur in a space-time continuum, both keys in allowing across-scale processes to emerge, as e.g. the growth of mega-earthquakes (e.g., Brizzi et al., 2018). The recent advances in characterization of rheological (e.g., Di Giuseppe et al., 2014; Rudolf et al., 2016) and frictional properties (Klinkmüller et al., 2016) of analog materials and the improvement in monitoring techniques (Rudolf et al., 2019) supported the development of so-called "seismotectonic" analog models (Rosenau et al., 2017). Those models reproduce the elastic loading and sudden release in a cyclic fashion similarly to the seismic cycle of subduction megathrusts (**Figure 2**). All seismotectonic analog models developed so far share the common characteristics listed below:

- *Kinematic boundary condition*: deformation of the overriding plate is imposed by underthrusting of the subducting plate at a constant rate.
- *Wedge geometry*: elastic stresses are stored into the analog overriding plate which might be elastic or elastoplastic while the subducting plate is assumed being rigid; the initial wedge surface and the analog megathrust are flat (i.e., with no downdip- and along trench curvature).
- *Rate-state friction*: the analog megathrust includes both (aseismic) velocity-strengthening and (seismogenic) velocity-weakening frictional regions.
- *Spontaneous earthquake nucleation*: slip episodes occur spontaneously when elastic stress overcomes the frictional strength of the megathrust locally (i.e., there is no external triggering).
- *Laboratory geodetic monitoring*: models are monitored via cross-correlation of images of the top or side surfaces or the interior of the model (e.g., with the Particle Image Velocimetry, PIV method; Sveen 2004). Applied to the top surface this technique is equivalent to having a dense network of continuous GPS stations (hence the name "laboratory geodesy models") which allow inverting for relevant earthquake source parameters (e.g., Rosenau et al., 2019; Corbi et al., 2013; Kosari et al., 2020).

The first articles about analog modelling of megathrust seismic cycling focused on reporting rheological and frictional properties of analog materials (Corbi et al., 2011) and their implementation into a scale model (Rosenau et al., 2009). The experimental behavior was composed of the archetypical pattern of alternating relatively longer periods of low, landward deformation rates with sudden, higher, trenchward velocities reversals as in the seismic cycle of subduction megathrusts (Rosenau et al., 2009; Corbi et al., 2013; **Figure 2** panels c–f). Follow-up studies focused on applications demonstrating the capabilities of analog models in studying a variety of earthquake phenomena, including recurrence pattern (Rosenau and Oncken, 2009; Rosenau et al., 2019) and the moment-duration proportionality (Corbi et al., 2013). Analog models have been used for investigating extrinsic parameter control, for example how the width of the seismogenic zone (Corbi et al., 2017a), the upper plate rheology (Brizzi et al., 2016), the subduction velocity (Corbi et al., 2017a) or the subduction megathrust roughness (van Rijsingen et al., 2019) influence the seismic behavior. Analog models helped in constraining the intrinsic variability of earthquake ruptures and associated tsunamis, validating empirical tsunami forecast

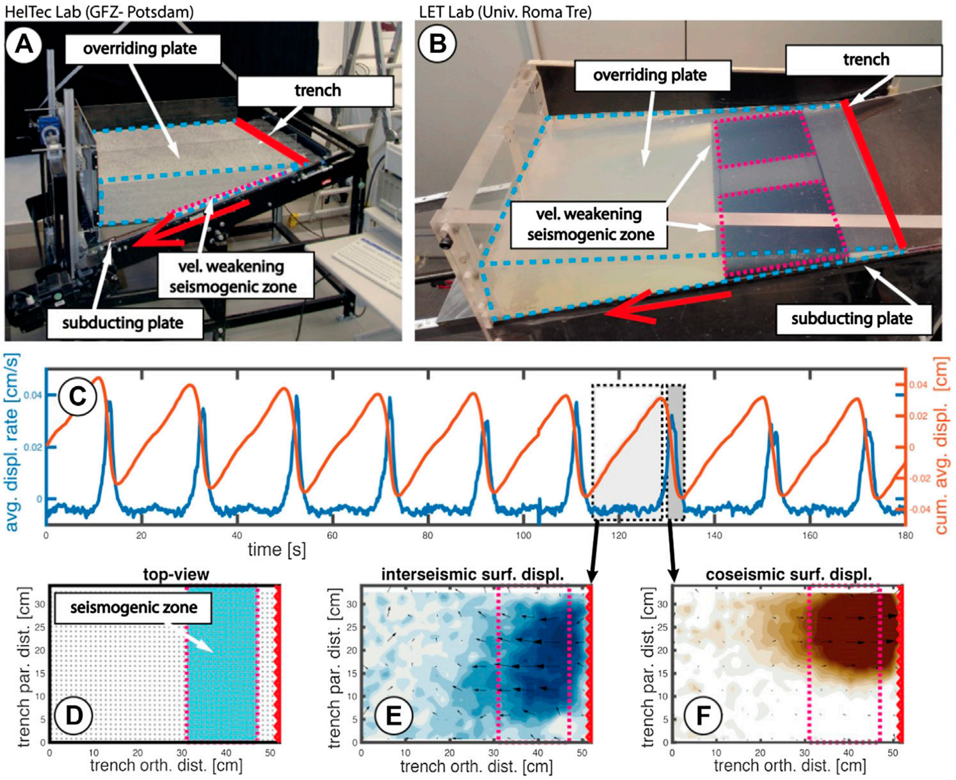

FIGURE 2 | Digital photos of seismotectonic analog model setup from the HelTec **(A)** and LET **(B)** labs (modified from Rosenau et al., 2017; Corbi et al., 2017a, respectively). Both setups are made of a glass-sided, wedge shaped box whose base is inclined 10°–15° in agreement with natural observables of subduction mega thrusts (Heuret et al., 2011). Both are equipped with a basal conveyer plate moved by a motor-driven piston with variable velocities of the order of 10^4–10^{-5} m/s as analogue, analog of the downgoing subducting plate. HetTec models use a mix of granular material composed by rice, sugar and rubber pellets to simulate an elastoplastic continental lithosphere and silicone oil to simulate the mantle. LET models are made of a visco-elastic gelatin which is deformed on the velocity-weakening seismogenic zone of the subduction thrust which simulated by sandpaper at the gelatin-basal plate interface. Both models experience stick-slip dynamics [orange time series in **(C)**] as response to subducting plate underthrusting. Particle Image Velocimetry allows monitoring the evolution of the displacement field as in a dense, homogeneously distributed geodetic network [gray dots in **(D)**], spanning also above the generally offshore seismogenic zone [cyan rectangle in **(D)**]. The average surface displacement rate time series [blue time series in **(C)**] is characterized by phases of relatively slow, landward displacement rates, analog of interseismic phases [displacement field shown in **(E)**], alternating with trenchward velocity peaks, analog of coseismic phases [displacement field shown in **(E)**].

models (Rosenau et al., 2010). Analog models have been also used for identifying the geometrical and mechanical conditions leading to synchronization of earthquakes (Corbi et al., 2017b; Rosenau et al., 2019). The process of earthquake synchronization is one of the key aspects in seismogenesis and is considered responsible for the origin of mega-earthquakes unzipping large parts of a subduction zone. Nowadays, analog models are also used for testing earthquake predictability (e.g., Corbi et al., 2019) and for identifying optimal geodetic configurations for monitoring convergent margins (Corbi et al., 2020; Kosari et al., 2020).

CHALLENGES AND FUTURE DIRECTIONS

Over the last decades, a wide range of studies have shed light on the seismogenic behavior of subduction megathrusts. This short review has recapped the contributions provided by the comparative analysis of global-scale natural data and analogue modelling.

Forecasting which subduction zone will host the next mega-earthquake and its timing remains a major challenge. The efforts to highlight which are the conditions enhancing the “productivity” of mega-earthquakes have recognized the potential role of several subduction-related parameters, but no consensus has been reached so far. For instance, empirical results point out at different parameters such as plates curvature (Bletery et al., 2016), roughness (e.g., van Rijsingen et al., 2019) or trench-parallel length of the subduction zone (Brizzi et al., 2018) and amount of trench sediments (Brizzi et al., 2020). Convergent margins are complex tectonic settings, whose diversity results from the interplay of several parameters operating at different spatial and temporal scales and whose relative importance is thus hard to assess (e.g., **Figure 1B**). Moreover, the understanding of subduction megathrusts is biased by the short instrumental seismic record and by the lack of completeness and of a homogeneous resolution of the observables characterizing subduction zones.

Is it thus really feasible to unravel the seismic behavior of the subduction megathrust or is it an impossible mission?

The continuous scientific and technological advancements allow detecting transient deformation signals occurring on short times-scales (fractions of the seismic cycle) along convergent margins and sampling the megathrust seismic cycle with progressively denser and higher quality data. For example, even if the underlying source process still has to be identified, both the 2010 Maule (Chile) and 2011 Tohoku-Oki (Japan) earthquakes have been preceded by potentially diagnostic geodetic transients lasting several months and spanning thousands of kilometers (Bedford et al., 2020). Satellite measurements (e.g., InSAR studies; Jolivet et al., 2020), dense geodetic (e.g., Michel et al., 2018) and seismic (e.g., Brodsky and Lay, 2014) monitoring - both onshore and offshore-is able to record a wide range of deformation signal frequencies (i.e., from earthquakes s.s. to low frequency earthquakes and tremors) and the improvement of the quantity, quality and accessibility of databases of convergent margin observables (e.g., geodesy.unr.edu/NGLStationPages/gpsnetmap/GPSNetMap.html; geofon.gfz-potsdam.de; www-solid.eps.s.u-tokyo.ac.jp/~sloweq) yield a promising perspective to successfully elucidate the spatio-temporal pattern of earthquake occurrence along the worldwide subduction zones and to mitigate hazard related to mega-earthquakes and tsunamis.

Another support to better understand subduction earthquakes and to advance in the forecast of earthquakes is coming from recent improvements in data analysis methods. Machine learning is an application of artificial intelligence able to automatically discover hidden patterns learning directly from analysis of large datasets, without being explicitly programmed (e.g., Bergen et al., 2019; Ren et al., 2020). This approach already succeeded for the prediction of timing (Rouet-Leduc et al., 2018), timing and locations (Corbi et al., 2019) and timing and duration (Hulbert et al., 2019) of slip episodes in laboratory experiments mimicking the basic physics of the seismic cycle.

The future is challenging also on the analogue modelling side, where the use of higher resolution and faster cameras and of optimized procedures for calculating surface velocities (Rudolf et al., 2019) permits the model monitoring with increasing detail. Thus, the detection threshold of analog earthquakes as well as the temporal resolution of the nucleation and rupture process are progressively improved. Laboratory geodetic methods will be accompanied by laboratory seismology using micro-electromechanical sensors (MEMS) measuring model accelerations with kHz sampling rates, corresponding to the frequency range of interest for earthquakes. This will soon put us in a position to detect and localize analog earthquakes which are too small to produce a surface deformation signal measurable with optical methods. Apart from such kinematic monitoring methods, dynamic monitoring of (boundary) stresses (Ritter et al., 2018) will help in detecting events but also in understanding the relationship between stress and strain during seismic cycles. Moreover, the joint use of analogue and numerical modelling is providing successful and promising results to shed light on the behavior of the subduction megathrust (Corbi et al., 2013, Corbi et al., 2017a; van Dinther et al., 2013). The combination of these two complementary approaches allows to valorize the respective strengths: analog models are physically self-consistent, and stresses/strain evolve spontaneously in response to the applied boundary conditions, while numerical models are more adaptable and effective for parametric studies.

With respect to great subduction megathrust earthquakes, our current understanding is that they show a complex but in parts deterministic pattern. Whether (mega-) earthquakes are predictable or not can be thus answered with some hopefulness in the future. Since the seismic behavior of the subduction megathrust depends on a wide combination of parameters, interdisciplinary research needs to be strengthened integrating geological, geophysical, and geodynamical constraints and contextualizing them in a physics-based modelling framework allowing to analyze and forecast mega-earthquake triggering processes in subduction zones.

Multidisciplinary studies are always challenging, but they represent the key for a substantial advancement in the understanding of this scientifically intriguing and socially hazardous issue. In this frame, collecting new data, sharing them on open platforms, networking resources and events are fundamental steps for exchanging ideas and fostering discussion towards the comprehension of the processes controlling the megathrust seismic behavior.

AUTHOR CONTRIBUTIONS

All authors listed have made a substantial, direct, and intellectual contribution to the work and approved it for publication.

ACKNOWLEDGMENTS

The authors acknowledge the Editor, DP, and two reviewers for their suggestions which help to improve the final version of the manuscript. The Grant to Department of Science, Roma Tre University (MIUR-Italy Dipartimenti di Eccellenza, ARTICOLO 1, COMMI 314—337, LEGGE 232/2016) is gratefully acknowledged by FF. FC thanks his funding from PRIME program of the German Academic Exchange Service (DAAD) with funds from the German Federal Ministry of Education and Research (BMBF). MR has been supported by the Deutsche Forschungsgemeinschaft (DFG) through grant CRC 1114 "Scaling Cascades in Complex Systems," Project Number 235221301, Project B01.

REFERENCES

Ammon, C. J., Lay, T., and Simpson, D. W. (2010). Great earthquakes and global seismic networks. *Seismol Res. Lett.* 6 (81), 965–971. doi:10.1785/gssrl.81.6.965

Bassett, D., and Watts, A. (2015). Gravity anomalies, crustal structure, and seismicity at subduction zones: 1. seafloor roughness and sub- ducting relief. *Geochem. Geophys. Geosyst.* 16, 1508–1540. doi:10.1002/2014GC005684

Becker, D., and Meier, T. (2010). Seismic dip deficit in the southwestern forearc of the hellenic subduction zone. *Bull. Seismol. Soc. Am.* 100, 325–342. doi:10.1785/0120090156

Bedford, J. R., Moreno, M., Deng, Z., Oncken, O., Schurr, B., John, T., et al. (2020). Months-long thousand-kilometre-scale wobbling before great subduction earthquakes. *Nature.* 580 (7805), 628–635. doi:10.1038/s41586-020-2212-1

Bergen, K. J., Johnson, P. A., De Hoop, M. V., and Beroza, G. C. (2019). Machine learning for data-driven discovery in solid Earth geoscience. *Science.* 363 (6433). doi:10.1126/science.aau0323

Berryman, K., Wallace, L., Hayes, G., Bird, P., Wang, K., Basili, R., et al. (2015). The GEM faulted earth subduction interface characterization project. Version 2.0. http://www.nexus.globalquakemodel.org/gem-faulted-earth/posts.

Bilek, S. L., and Lay, T. (1999). Rigidity variations with depth along interplate megathrust faults in subduction zones. *Nature.* 446 (July), 443–446. doi:10.1038/22739

Bletery, Q., Thomas, A. M., Rempel, A. W., Karlstrom, L., Sladen, A., and De Barros, L. (2016). Mega-earthquakes rupture flat megathrusts. *Science.* 354, 1027–1031. doi:10.1126/science.aag0482

Brizzi, S., Funiciello, F., Corbi, F., Di Giuseppe, E., and Mojoli, G. (2016). Salt matters: how salt affects the rheological and physical properties of gelatine for analogue modelling. *Tectonophysics.* 679, 88–101. doi:10.1016/j.tecto.2016.04.021

Brizzi, S., Sandri, L., Funiciello, F., Corbi, F., Piromallo, C., and Heuret, A. (2018). Multivariate statistical analysis to investigate the subduction zone parameters favoring the occurrence of giant megathrust earthquakes. *Tectonophysics.* 728–729, 92–103. doi:10.1016/j.tecto.2018.01.027

Brizzi, S., Zelst, I., Funiciello, F., Corbi, F., and van Dinther, Y. (2020). How sediment thickness influences subduction dynamics and seismicity. *J. Geophys. Res. Solid Earth.* 125 (8), 1–19. doi:10.1029/2019jb018964

Brodsky, E. E., and Lay, T. (2014). Recognizing foreshocks from the 1 april 2014 Chile earthquake. *Science.* 344 (May), 700–702. doi:10.1126/science.1255202

Chester, F. M., Mori, J. J., Toczko, S., Eguchi, N., Kido, Y., et al. (2012). *Integrated ocean drilling program expedition 343/343T preliminary report, Japan Trench Fast Drilling Project (JFAST)Prelim. Rep. 343*: Integrated Ocean Drilling Project.

Conrad, C. P., Bilek, S., and Lihtgow-Bertelloni, C. (2004). Great earthquakes and slab pull: interaction between seismic coupling and plate-slab coupling. *Earth Planet Sci. Lett.* 218, 109–122. doi:10.1016/s0012-821x(03)00643-5

Corbi, F., Funiciello, F., Faccenna, C., Ranalli, G., and Heuret, A. (2011). Seismic variability of subduction thrust faults: insights from laboratory models. *J. Geophys. Res.* 116 (B6), 1–14. doi:10.1029/2010JB007993

Corbi, F., Funiciello, F., Moroni, M., van Dinther, Y., Mai, P. M., Dalguer, L. A., et al. (2013). The seismic cycle at subduction thrusts: 1. Insights from laboratory models. *J. Geophys. Res. Solid Earth.* 118, 1–19. doi:10.1002/2016GL072415

Corbi, F., Funiciello, F., Brizzi, S., Lallemand, S., and Rosenau, M. (2017a). Control of asperities size and spacing on seismic behavior of subduction megathrusts. *Geophys. Res. Lett.* 44, 8227–8235. doi:10.1002/2017GL074182

Corbi, F., Herrendörfer, R., Funiciello, F., and van Dinther, Y. (2017b). Controls of seismogenic zone width and subduction velocity on interplate seismicity: insights from analog and numerical models. *Geophys. Res. Lett.* 44, 6082–6091. doi:10.1002/2016GL072415

Corbi, F., Sandri, L., Bedford, J., Funiciello, F., Brizzi, S., Rosenau, M., et al. (2019). Machine learning can predict the timing and size of analog earthquakes. *Geophys. Res. Lett.* 46, 1303–1311. doi:10.1029/2018GL081251

Corbi, F., Bedford, J., Sandri, L., Funiciello, F., Gualandi, A., and Rosenau, M. (2020). Predicting imminence of analog megathrust earthquakes with machine learning: implications for monitoring subduction zones. *Geophys. Res. Lett.* 47 (7), e2019GL086615. doi:10.1029/2019GL086615

Den Hartog, S. A. M., and Spiers, C. J. (2013). Influence of subduction zone conditions and gouge composition on frictional slip stability of megathrust faults. *Tectonophysics.* 600, 75–90. doi:10.1016/j.tecto.2012.11.006

Di Giuseppe, E., CorbiFuniciello, F. F., Massmeyer, A., Santimano, T. N., Rosenau, M., and Davaille, A. (2014). Tectonophysics Characterization of Carbopol ® hydrogel rheology for experimental tectonics and geodynamics. *Tectonophysics.* [Epub ahead of print]. doi:10.1016/j.tecto.2014.12.005

Dixon, T., and Moore, C. (2007). *The seismogenic zone of subduction thrust faults*. New York: Columbia Univ. Press, 123–146.

Fuller, W., Willett, S. W., and Brandon, M. T. (2006). Formation of forearc basins and their influence on subduction zone earthquakes. *Geology.* 34 (2), 65–68. doi:10.1130/G21828.1

Funiciello, F., and Corbi, F. (2017). "Experimental tectonics: convergent margins from a lithosphere–mantle perspective," in *Reference module in Earth Systems and environmental sciences.* (Elsevier). doi:10.1016/B978-0-12-409548-9.10019-3

Hayes, G. P., and Furlong, K. P. (2010). Quantifying potential tsunami hazard in the puysegur subduction zone, south of new zealand. *Geophys. J. Int.* 183, 1512–1524. doi:10.1111/j.1365-246x.2010.04808.x

Hayes, G. P., Wald, D. J., and Johnson, R. L. (2012). Slab1.0: a three-dimensional model of global subduction zone geometries. *J. Geophys. Res. Solid Earth.* 117, B01302. doi:10.1029/2011JB008524. b01302

Heuret, A., Conrad, C. P., Funiciello, F., Lallemand, S., and Sandri, L. (2012). Relation between subduction megathrust earthquakes, trench sediment thickness and upper plate strain. *Geophys. Res. Lett.* 39, 1–6. doi:10.1029/2011GL050712

Heuret, A., Lallemand, S., Funiciello, F., Piromallo, C., and Faccenna, C. (2011). Physical characteristics of subduction interface type seismogenic zones revisited. *Geochem. Geophys. Geosyst.* 12, 1–26. doi:10.1029/2010GC003230

Hubbert, M. K. (1937). Theory of scale models as applied to the study of geological structures. *Geol. Soc. Am. Bull.* 48, 1459–1520. doi:10.1130/gsab-48-1459

Hulbert, C., Rouet-Leduc, B., Johnson, P. A., Ren, C. X., Rivière, J., Bolton, D. C., et al. (2019). Similarity of fast and slow earth- quakes illuminated by machine learning. *Nat. Geosci.* 12 (1), 69–74. doi:10.1038/s41561-018-0272-8

Jarrard, R. D. (1986). Relations among subduction parameters. *Rev. Geophys.* 24, 217–284. doi:10.1029/RG024i002p00217

Jolivet, R., Simons, M., Duputel, Z., Olive, J.-A., Bhat, H. S., and Bletery, Q. (2020). Interseismic coupling drives long-term uplift in northern chile. *Geophys. Res. Lett.* 47, e2019GL085377. doi:10.1029/2019GL085377

Kelleher, J., Savino, J., Rowlett, H., and McCann, W. (1974). Why and where great thrust earthquakes occur along island arcs. *J. Geophys. Res.* 79, 4889–4899. doi:10.1029/JB079i032p048

Klinkmüller, M., Schreurs, G., Rosenau, M., and Kemnitz, H. (2016). Properties of granular analogue materials: a community wide survey. *Tectonophysics.* 666, 23–38. doi:10.1016/j.tecto.2016.01.017

Kopp, H. (2013). Invited review paper: the control of subduction zone structural complexity and geometry on margin segmentation and seismicity. *Tectonophysics.* 589, 1–16. doi:10.1016/j.tecto.2012.12.037

Kosari, E., Rosenau, M., Bedford, J., Rudolf, M., and Oncken, O. (2020). On the relationship between offshore geodetic coverage and slip model uncertainty: analog megathrust earthquake case studies. *Geophys. Res. Lett.* 47 (15), e2020GL088266. doi:10.1029/2020gl088266

Kostoglodov, V. (1988). Sediment subduction: a probable key for seismicity and tectonics at active plate boundaries. *Geophys. J.* 94, 65–72.

Lallemand, S., Peyret, M., van Rijsingen, E., Arcay, D., and Heuret, A. (2018). Roughness characteristics of oceanic seafloor prior to sub- duction in relation to the seismogenic potential of subduction zones. *Geochem. Geophys. Geosyst.* 19, 1–26. doi:10.1029/2018GC007434

Marzocchi, W., Sandri, L., Heuret, A., and Funiciello, F. (2016). Where giant earthquakes may come. *J. Geophys. Res. Solid Earth.* 121, 7322–7336. doi:10.1002/2016JB013054

McCaffrey, R. (1994). Dependence of earthquake size distributions on convergence rates at subduction zones. *Geophys. Res. Lett.* 21, 2327–2330. doi:10.1029/94gl02153

McCaffrey, R. (2008). Global frequency of magnitude 9 earthquakes. *Geology.* 36, 263–266. doi:10.1130/G24402A.1

Michel, S., Gualandi, A., and Avouac, J.-P. (2018). Interseismic coupling and slow slip events on the cascadia megathrust. *Pure Appl. Geophys.* 176 (10), 4641–4642. doi:10.1007/s00024-018-1991-x

Morgan, E. C., McAdoo, B. G., and Baise, L. G. (2008). Quantifying geomorphology associated with large subduction zone earthquakes. *Basin Res.* 20, 531–542. doi:10.1111/j.1365-2117.2008.00368.x

Nishikawa, T., and Ide, S. (2014). Earthquake size distribution in subduction zones linked to slab buoyancy. *Nat. Geosci.* 7 (12), 904–908. doi:10.1038/ngeo2279

Okal, E. A. (2015). The quest for wisdom: lessons from 17 tsunamis, 2004-2014. *Phil. Trans. R. Soc. A* 373, 20140370. doi:10.1098/rsta.2014.0370

Pacheco, J. F., Sykes, L. R., and Scholz, C. H. (1993). Nature of seismic coupling along simple plate boundaries of the subduction type. *J. Geophys. Res.* 98, 14133. doi:10.1029/93JB00349

Peterson, E. T., and Seno, T. (1984). Factors affecting seismic moment release rates in subduction zones. *J. Geophys. Res.* 89, 10233–10248. doi:10.1029/jb089ib12p10233

Philibosian, B., and Meltzner, A. J. (2020). Segmentation and supercycles: a catalog of earthquake rupture patterns from the Sumatran Sunda Megathrust and other well-studied faults worldwide. *Quat. Sci. Rev.* 241, 106390. doi:10.1016/j.quascirev.2020.106390

Remitti, F., Vannucchi, P., Bettelli, G., Fantoni, L., Panini, F., and Vescovi, P. (2011). Tectonic and sedimentary evolution of the frontal part of an ancient subduction complex at the transition from accretion to erosion: the case of the

Ligurian wedge of the northern apennines, italy. *Geol. Soc. Am. Bull.* 123 (1–2), 51–70. doi:10.1130/B30065.1

Ren, C., Hulbert, C., Johnson, P., and Rouet-Leduc, B. (2020). Machine learning and fault rupture: review. Preprint repository name [Preprint]. Available at: https://osf.io/g2dt8/. doi:10.31223/osf.io/xdmkq

Ritter, M. C., Santimano, T., Rosenau, M., Leever, K., and Oncken, O. (2018). Sandbox rheometry: co-evolution of stress and strain in riedel– and critical wedge–experiments. *Tectonophysics.* 722 (2), 400–409. doi:10.1016/j.tecto.2017.11.018

Romano, F., Piatanesi, A., Lorito, S., D'Agostino, N., Hirata, K., Atzori, S., et al. (2012). Clues from joint inversion of tsunami and geodetic data of the 2011 Tohoku-oki earthquake. *Sci. Rep.* 2, 385. doi:10.1038/srep00385

Rong, Y., Jackson, D. D., Magistrale, H., and Goldfinger, C. (2014). Magnitude limits of subduction zone earthquakes. *Bull. Seismol. Soc. Am.* 104, 2359–2377. doi:10.1785/0120130287

Rosenau, M., Lohrmann, J., and Oncken, O. (2009). Shocks in a box: an analogue model of subduction earthquake cycles with application to seismotectonic forearc evolution. *J. Geophys. Res.* 114 (B1), 1–20. doi:10.1029/2008JB005665

Rosenau, M., Oppelt, A., Kemnitz, H., and Oncken, O. (2008). Analogue earthquakes: friction experiments with rice and implications for the seismic cycle and earthquake nucleation. *Boll. Geofis.* 49, 104–108.

Rosenau, M., Nerlich, R., Brune, S., and Oncken, O. (2010). Experimental insights into the scaling and variability of local tsunamis triggered by giant subduction megathrust earthquakes. *J. Geophys. Res.* 115, B09314. doi:10.1029/2009jb007100

Rosenau, M., Corbi, F., and Dominguez, S. (2017). Analogue earthquakes and seismic cycles: experimental modelling across timescales. *Solid Earth.* 8 (3), 597–635. doi:10.5194/se-8-597-2017

Rosenau, M., Horenko, I., Corbi, F., Rudolf, M., Kornhuber, R., and Oncken, O. (2019). Synchronization of great subduction megathrust earthquakes: insights from scale model analysis. *J. Geophys. Res. Solid Earth.* 124 (4), 3646–3661. doi:10.1029/2018JB016597

Rosenau, M., and Oncken, O. (2009). Fore-arc deformation controls frequency-size distribution of megathrust earthquakes in subduction zones. *J. Geophys. Res. Solid Earth.* 114, 12. doi:10.1029/2009JB006359

Rouet-Leduc, B., Hulbert, C., Bolton, D. C., Ren, C. X., Riviere, J., Marone, C., et al. (2018). Estimating fault friction from seismic signals in the laboratory. *Geophys. Res. Lett.* 45, 1321–1329. doi:10.1002/2017GL076708

Rudolf, M. (2019). Velocity dependent rheologies in seismotectonic scale modelling: characterization and Implementation in a new analogue modelling scheme. PhD thesis. Berlin: Freie Universität, 135.

Rudolf, M., Boutelier, D., Rosenau, M., and Schreurs, G., and Oncken, O. (2016). Rheological benchmark of silicone oils used for analog modeling of short- and long-term lithospheric deformation. *Tectonophysics.* 684, 12–22. doi:10.1016/j.tecto.2015.11.028

Rudolf, M., Rosenau, M., Ziegenhagen, T., Ludwikowski, V., Schucht, T., Nagel, H., et al. (2019). Smart speed imaging in digital image correlation: application to seismotectonic scale modeling. *Front. Earth Sci.* 6, 248. doi:10.3389/feart.2018.00248

Ruff, L. J. (1989). Do trench sediments affect great earthquake occurrence in subduction zones?. *Pure Appl. Geophys.* 129, 263–282. doi:10.1007/bf00874629

Ruff, L. J. (1992). Asperity distributions and large earthquake occurrence in subduction zones. *Tectonophysics.* 211 (1–4), 61–83. doi:10.1016/0040-1951(92)90051-7

Ruff, L., and Kanamori, H. (1980). Seismicity and the subduction process. *Phys. Earth Planet. In.* 23, 240–252. doi:10.1016/0031-9201(80)90117-X

Schäfer, A. M., and Wenzel, F. (2019). Global megathrust earthquake hazard—maximum magnitude assessment using multi-variate machine learning. *Front. Earth Sci.* 7 (June), 1–19. doi:10.3389/feart.2019.00136

Schellart, W. P., and Rawlinson, N. (2013). Global correlations between maximum magnitudes of subduction zone interface thrust earthquakes and physical parameters of subduc- tion zones. *Phys. Earth Planet. In.* 225, 41–67. doi:10.1016/j.pepi. 2013.10.001

Scholl, D. W., Kirby, S. H., von Huene, R., Ryan, H., Wells, R. E., and Geist, E. L. (2015). Great (≥Mw8.0) megathrust earthquakes and the subduction of excess sediment and bathymetrically smooth seafloor. *Geosphere.* 11, 236–265. doi:10.1130/GES01079.1

Scholz, C. H., and Campos, J. (1995). On the mechanism of seismic decoupling and back arc spreading at subduction zones. *J. Geophys. Res.* 100, 22103. doi:10.1029/95JB01869

Scholz, C. H., and Campos, J. (2012). The seismic coupling of subduction zones revisited. *J. Geophys. Res.* 117, B05310. doi:10.1029/2011jb009003

Seno, T. (2017). Subducted sediment thickness and Mw 9 earthquakes. *J. Geophys. Res. Solid Earth.* 122, 470–491. doi:10.1002/2016JB013048

Song, T. R. A., and Simons, M. (2003). Large trench-parallel gravity variations pedict seismogenic behaviour in subduction zones. *Science.* 301, 630–633. doi:10.1126/science.1085557

Stein, S., and Okal, E. (2011). The size of the 2011 Tohoku earthquake need not have been a surprise. *EOS Trans. Am. Geophys. Union.* 92, 227–228. doi:10.1029/2011EO270005

Stein, S., and Okal, E. (2007). Ultralong period seismic study of the december 2004 indian ocean earthquake and implications for regional tectonics and the subduction process. *Seismol. Soc. Am. Bull.* 97, S279–S295. doi:10.1785/0120050617

Suarez, G., and Albini, P. (2009). Evidence for great tsunamigenic earthquakes along the mexican subduction zone. *Bull. Seismol. Soc. Am.* 99, 892–896. doi:10.1785/0120080201

Subarya, C., Chlieh, M., Prawirodirdjo, L., Avouac, J. P., Bock, Y., Sieh, K., et al. (2006). Plate-boundary deformation associated with the great Sumatra-Andaman earthquake. *Nature.* 440, 46–51. doi:10. 1038/nature04522

Sveen, J. K. (2004). An introduction to MatPIV v.1.6.1: Department of Mathematics University of Oslo.

Uyeda, S., and Kanamori, H. (1979). Back-arc opening and the mode of subduction. *J. Geophys. Res.* 84, 1049. doi:10.1029/JB084iB03p01049

Uyeda, S. (1982). Subcuction zones: an introduction to comparative subductology. *Tectonophysics.* 81 (3-4), 133–159. doi:10.1016/0040-1951(82)90126-3

van Dinther, Y., Gerya, T. V., Dalguer, L. A., Corbi, F., Funiciello, F., and Mai, P. M. (2013). The seismic cycle at subduction thrusts: 2. Dynamic implications of geodynamic simulations validated with laboratory models. *J. Geophys. Res. Solid Earth.* 118, 1502–1525. doi:10.1029/2012JB009479

van Rijsingen, E., Lallemand, S., Peyret, M., Arcay, D., Heuret, A., Funiciello, F., et al. (2018). How subduction interface roughness influences the occurrence of large interplate earthquakes. *Geochem. Geophys. Geosyst.* 19, 1–29. doi:10.1029/2018GC007618

van Rijsingen, E., Funiciello, F., Corbi, F., and Lallemand, S. (2019). Rough subducting seafloor reduces interseismic coupling and mega-earthquake occurrence: insights from analogue models. *Geophys. Res. Lett.* 46 (6), 3124–3132. doi:10.1029/2018GL081272

Wang, K., and Bilek, S. L. (2014). Invited review paper: fault creep caused by subduction of rough seafloor relief. *Tectonophysics.* 610, 1–24. doi:10.1016/j.tecto.2013.11.024

Wang, K. (2013). Megathrust surprises. *Nat. Geosci.* 6, 11–12. doi:10.1038/ngeo1682

Wells, R. E., Blakely, R. J., Sugiyama, Y., Scholl, D. W., and Dinterman, P. A. (2003). Basin-centered asperities in great subduction zone earthquakes: a link between slip, subsidence, and sub- duction erosion?. *J. Geophys. Res.* 108, 2507. doi:10.1029/2002JB002072

Yue, H., and Lay, T. (2013). Source rupture models for the Mw 9.0 2011 Tohoku earthquake from joint inversions of high-rate geodetic and seismic data. *Bull. Seismol. Soc. Am.* 103, 1242–1255. doi:10.1785/0120120119

Conflict of Interest: The authors declare that the research was conducted in the absence of any commercial or financial relationships that could be construed as a potential conflict of interest.

frontiers
in Earth Science

ORIGINAL RESEARCH
published: 22 December 2020
doi: 10.3389/feart.2020.585429

Benchmarking the Optimal Time Alignment of Tsunami Waveforms in Nonlinear Joint Inversions for the M_w 8.8 2010 Maule (Chile) Earthquake

F. Romano[1]*, S. Lorito[1], T. Lay[2], A. Piatanesi[1], M. Volpe[1], S. Murphy[3] and R. Tonini[1]

[1]Istituto Nazionale di Geofisica e Vulcanologia, Roma, Italy, [2]Department of Earth and Planetary Sciences, University of California Santa Cruz, Santa Cruz, CA, United States, [3]Ifremer, REM-GM, Plouzané, France

Finite-fault models for the 2010 M_w 8.8 Maule, Chile earthquake indicate bilateral rupture with large-slip patches located north and south of the epicenter. Previous studies also show that this event features significant slip in the shallow part of the megathrust, which is revealed through correction of the forward tsunami modeling scheme used in tsunami inversions. The presence of shallow slip is consistent with the coseismic seafloor deformation measured off the Maule region adjacent to the trench and confirms that tsunami observations are particularly important for constraining far-offshore slip. Here, we benchmark the method of Optimal Time Alignment (OTA) of the tsunami waveforms in the joint inversion of tsunami (DART and tide-gauges) and geodetic (GPS, InSAR, land-leveling) observations for this event. We test the application of OTA to the tsunami Green's functions used in a previous inversion. Through a suite of synthetic tests we show that if the bias in the forward model is comprised only of delays in the tsunami signals, the OTA can correct them precisely, independently of the sensors (DART or coastal tide-gauges) and, to the first-order, of the bathymetric model used. The same suite of experiments is repeated for the real case of the 2010 Maule earthquake where, despite the results of the synthetic tests, DARTs are shown to outperform tide-gauges. This gives an indication of the relative weights to be assigned when jointly inverting the two types of data. Moreover, we show that using OTA is preferable to subjectively correcting possible time mismatch of the tsunami waveforms. The results for the source model of the Maule earthquake show that using just the first-order modeling correction introduced by OTA confirms the bilateral rupture pattern around the epicenter, and, most importantly, shifts the inferred northern patch of slip to a shallower position consistent with the slip models obtained by applying more complex physics-based corrections to the tsunami waveforms. This is confirmed by a slip model refined by inverting geodetic and tsunami data complemented with a denser distribution of GPS data nearby the source area. The models obtained with the OTA method are finally benchmarked against the observed seafloor deformation off the Maule region. We find that all of the models using the OTA well predict this offshore coseismic deformation, thus overall, this benchmarking of the OTA method can be considered successful.

Keywords: The 2010 Maule earthquake, joint inversion, tsunami, optimal time alignment, benchmark

Edited by:
Sebastiano D'Amico,
University of Malta, Malta

Reviewed by:
Raul Madariaga,
University of Chile, Chile
Giorgio Manno,
University of Palermo, Italy
Aditya Gusman,
GNS Science, New Zealand

****Correspondence:***
F. Romano
fabrizio.romano@ingv.it

Specialty section:
This article was submitted to Solid Earth Geophysics, a section of the journal Frontiers in Earth Science

Received: *20 July 2020*
Accepted: *23 November 2020*
Published: *22 December 2020*

Citation:
Romano F, Lorito S, Lay T, Piatanesi A, Volpe M, Murphy S and Tonini R (2020) Benchmarking the Optimal Time Alignment of Tsunami Waveforms in Nonlinear Joint Inversions for the M_w 8.8 2010 Maule (Chile) Earthquake. Front. Earth Sci. 8:585429. doi: 10.3389/feart.2020.585429

INTRODUCTION

The February 27, 2010 Maule (Chile) M_w 8.8 earthquake is the third largest seismic event this century and it produced an extensive seismic sequence (e.g., Hayes et al., 2013). The rupture was located along the subduction interface between the Nazca and South America plates (**Figure 1**). It caused a large tsunami that struck along ~600 km of the Chilean coast both north and south of the epicenter (Fritz et al., 2011). Numerous studies have investigated the Maule earthquake rupture by inverting seismic (e.g., Lay et al., 2010; Koper et al., 2012; Hayes et al., 2013); geodetic (e.g., Tong et al., 2010; Pollitz et al., 2011; Vigny et al., 2011; Moreno et al., 2012); tsunami (Yoshimoto et al., 2016); joint seismic and geodetic (e.g., Delouis et al., 2010; Lin et al., 2013); joint geodetic and tsunami data (e.g., Lorito et al., 2011; Fujii and Satake, 2013; Yoshimoto et al., 2016); and joint seismic, geodetic and tsunami data (Yue et al., 2014).

These studies all find along-strike bilateral rupture from the epicenter, but vary significantly in the along-dip placement of slip on the fault, with most models that emphasize geodetic data having little slip far-offshore. It is well known that geodetic data can provide a good spatial resolution of fault slip very close to the stations, and along-strike for situations with good coastal-parallel coverage (e.g., Romano et al., 2010); but in subduction zones the resolution of offshore slip from land geodesy is typically very limited. Seismic wave models sometimes resolve offshore slip (e.g., Lay, 2018), but lacking seafloor geodetic observations, coseismic slip in the shallow region of the megathrust is usually best-constrained by tsunami data (e.g., Lorito et al., 2016) provided that accurate bathymetric models are available.

Tsunami data have long provided valuable constraints on the spatial extent of earthquake slip distributions due to them having the slowest propagation velocities of the various wave types (including seismic body and surface waves) used to study submarine sources. To exploit the absolute time information in deep-water and tide-gauge tsunami recordings for source inversions, one must trust the complete calculation of all known propagation effects through the heterogeneous bathymetric structure from the source region to the tsunami recording system. Absolute time alignments will then play a very strong role in the placement of slip in a finite-fault inversion. Errors in absolute travel time calculation due to both computational approximations (assumption of great-circle propagation for perturbation type corrections, use of inadequate bathymetry, etc.) and any clock errors in the recordings, will incorrectly align Green's functions and data, biasing the inversion results.

Deep-water seafloor pressure sensors deployed at NOAA DART buoy sites often record clear tsunami waveforms that can be well-modelled by numerous finite-difference approaches, but absolute time misalignment has long been known to increase with source to station distance for commonly-used tsunami modeling codes, with modeled waveforms usually being earlier than observed signals. This is largely attributed to neglect of

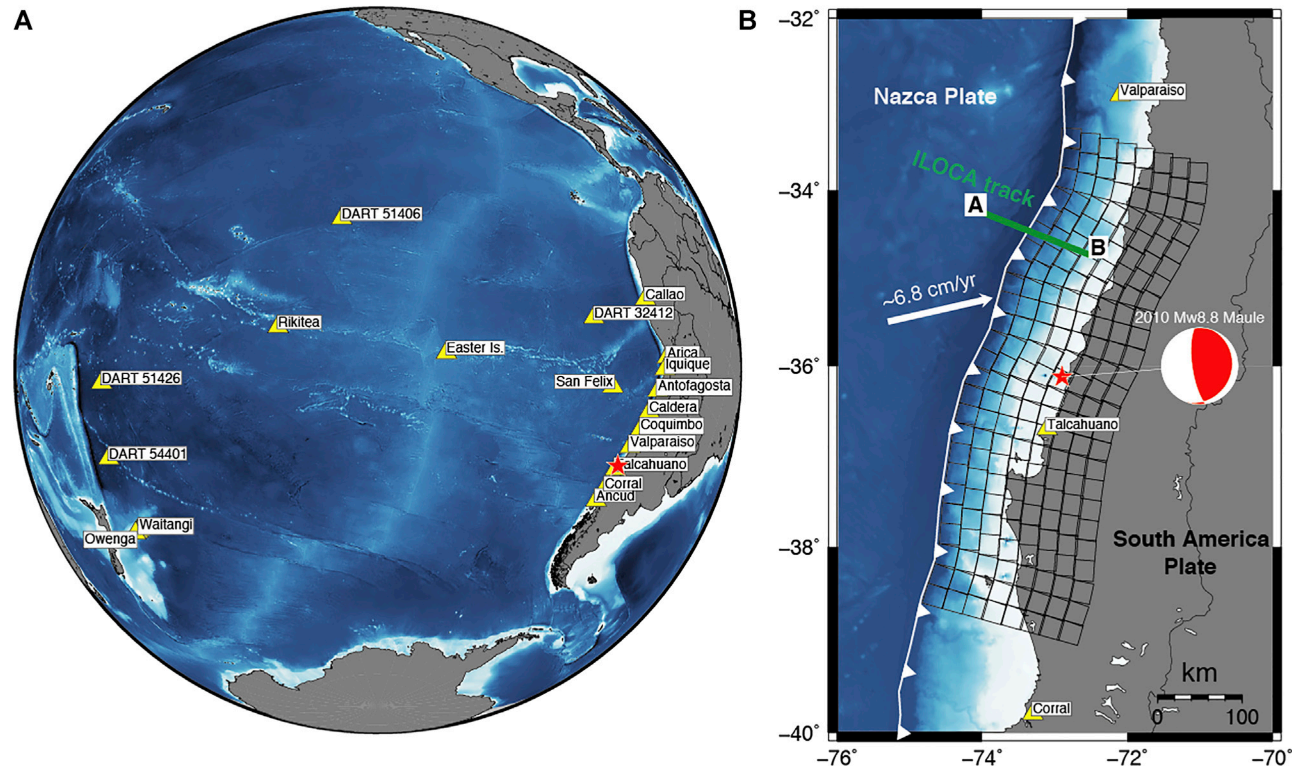

FIGURE 1 | (A) Tsunami sensors (yellow triangles); **(B)** fault geometry (black squares), epicenter (red star) and average faulting geometry (red and white focal mechanism) of the 2010 Maule earthquake. A–B segment is the ILOCA track (green line).

dispersion in the water column, neglect of elasticity of the rock substrate, neglect of water density profile, and, to a lesser extent, limitations of open ocean bathymetry models for the computed synthetics (Tsai et al., 2013; Watada et al., 2014). If uncorrected, use of absolute tsunami arrival times results in the placement of slip further from the observing stations to delay the tsunami arrivals, thus, erroneously shifting the source of slip landward. Recently, procedures have been introduced to account for some of these inadequacies of the computed tsunami signals (e.g., Tsai et al., 2013; Allgeyer and Cummins, 2014; Watada et al., 2014), which reduce the time alignment errors substantially, allowing use of absolute time information for deep-water buoy recordings in finite-fault inversions (Yue et al., 2014; Yoshimoto et al., 2016).

Time alignment shifts for tide-gauges are instead primarily attributed to clock errors or the use of inaccurate/coarse bathymetry models, mainly during the last portion of the propagation in very shallow water, and there is no set of correction procedures for the predictions to improve absolute time alignment of the tide-gauge observations. Often for tide-gauge data, the first-arrival times are picked in the data and held fixed, foregoing absolute time alignment, because the theoretical Green's functions are so far off in timing. For linearized inversions, the a priori alignments of both deep-water (absolute times) and tide-gauge (fixed picks of arrivals), can have very strong influence on the solution.

Misalignment of predicted tsunami waveforms is a long-standing issue (e.g., Fujii and Satake, 2006; Piatanesi and Lorito, 2007), and for source inversions has typically been dealt with by manually aligning observed and predicted waveforms. However, this is a very subjective approach that directly negates the sensitivity of the tsunami timing to the placement of slip. The physics-based corrections used by Yue et al. (2014) and Yoshimoto et al. (2016), which allow absolute time alignments to be used in the inversions for deep-water sensors, are still imperfect, so some timing uncertainty can still be projected into the source model. This will be the case if the bathymetric model is inaccurate or too coarse. This is a very common situation for tide-gauges, which are generally installed within harbors or closed basins. The (generally) earlier arrival time of a modeled tide-gauge waveform on a coarse bathymetry depends mainly on two factors: 1) the tide-gauge position effectively being more offshore on a coarse computational grid with respect to a finer one and 2) the depth of the grid cell being deeper in coarser bathymetric models (e.g., Satake, 1995). Station clock errors can be another source of misalignment. The timing uncertainty can lead to inconsistent source images from deep-water vs. tide-gauge tsunami data or undesired averaging of results if both data types are used (e.g., Yoshimoto et al., 2016).

Given the limited precision of regional bathymetric models, tide-gauge data are often not used or are severely down-weighted in source inversions. These recordings, being widely distributed along the global coastline, can significantly contribute to enhancing the instrumental coverage around the tsunami source, thus prospectively helping to study tsunamigenic earthquakes. This is particularly important in those regions (e.g., the Mediterranean) where deep-water ocean sensors are not present, and only coastal gauges exist.

Romano et al. (2016) proposed a new method that can automatically deal with the waveform alignment issue through a procedure embedded into the inversion algorithm called Optimal Time Alignment (OTA). The method is partially borrowed from seismology, where time shift of seismic signals can result for different reasons (e.g., inaccuracies of the Earth seismic velocity model) and it can be estimated using the cross-correlation between observed and modeled signals (e.g., Zhang and Thurber, 2003; Hauksson and Shearer, 2005). The OTA method has two strengths: 1) it eliminates the arbitrariness in the time mismatch estimation, and 2) it is independent of the cause of the misalignment. OTA does not explicitly apply corrective terms to the tsunami propagation and can be used for both deep-water (e.g., DARTs) and coastal tide-gauge data.

The OTA method, already used for a few inversions (e.g., the 2016 M_w 8.3 Illapel and the 1960 M_w 9.5 Chile earthquakes, Romano et al., 2016; Ho et al., 2019), foregoes absolute time alignments and subjective fixed picks of arrival times of tide gauge data, recognizing that there is loss of absolute timing sensitivity, but reducing the strongly biasing effect of inaccurate time prediction. This approach requires an iterative non-linear search of the solution space; a linearized inversion is not viable. The optimal time alignments are re-determined in each iteration; they are not held fixed at initial subjective values. For the optimization performed by Romano et al. (2016), waveform variations for both deep-water and tide gauge stations originating from the different placement of slip on the kinematic model provide information that allows a self-consistent model to be found without the strong influence and bias of inaccurate absolute time alignment or fixed onset specification.

In this study, with the aim of benchmarking the OTA method against documented shallow seafloor deformation for the 2010 Maule earthquake, we repeat the study of Lorito et al. (2011) leaving everything unchanged except for the application of OTA to the tsunami signals. In this way we address the effect of OTA on the absolute placement of the slip patches relative to the prior study. We estimate the slip distribution of the 2010 Maule earthquake jointly inverting geodetic (GPS, InSAR, and land-leveling) and tsunami (DART and tide-gauge) data. In particular, the slip models and the predicted seafloor deformation obtained with and without the use of OTA are compared with the Yue et al. (2014) joint inversion model and the seafloor deformation data collected by Maksymowicz et al. (2017). We also investigate the effect of OTA in the joint inversion using DART and tide-gauge tsunami waveforms separately to assess their respective resolving power on the slip distribution, and, as a consequence, optimize their relative weights for use during joint inversion. Finally, we better constrain the slip distribution of the 2010 Maule earthquake by supplementing the initially inverted data set with additional GPS data from Vigny et al. (2011) and Moreno et al. (2012).

MATERIAL AND METHODS

Data and Green's Functions

The subduction interface in the Maule region extends along the plate boundary from ~39°S to ~33°S and is parameterized

(**Figure 1**; **Figure S3, Table S1 in Supplementary Material**) with a tessellation of 200 subfaults of $25 \times 25\ \text{km}^2$ size featuring variable strike and dip values that roughly follow the best-fitting non-planar geometry built from the global CMT mechanisms in the region (https://earthquake.usgs.gov/earthquakes/eventpage/official20100227063411530_30/technical).

We use the tsunami recordings (**Supplementary Table S5**) from 15 tide-gauges (provided by the Intergovernmental Oceanographic Commission of UNESCO, http://www.ioc-sealevelmonitoring.org/, the University of Hawaii sea level center (http://ilikai.soest.hawaii.edu/uhslc/background.html), and 4 DART buoys (National Oceanic and Atmospheric Administration, http://www.ndbc.noaa.gov/dart.shtml), and the coseismic deformation observed from GPS stations, satellites, and land-leveling. In particular, we use the coseismic offsets measured at 6 GPS sites managed by the International Global Navigation Satellite Systems Service (http://igscb.jpl.nasa.gov/) and the French Centre National de la Recherche Scientifique Institut National des Sciences de l'Univers (https://gpscope.dt.insu.cnrs.fr/), the GPS coseismic offsets provided by (Vigny et al., 2011; Moreno et al., 2012), the deformation along both the ascending and descending Line-of-Sight tracks obtained from the ALOS PALSAR satellite interferograms (http://global.jaxa.jp/), and the land-level changes measured along the Chilean coast from Farías et al. (2010). Additional details about the data processing can be found in Lorito et al. (2011), whereas input data are available as **Supplementary Material** (see Data Availability Statement).

Tsunami Green's functions are computed with the nonlinear shallow water version of COMCOT (Liu et al., 1998), using a bathymetric grid model (http://topex.ucsd.edu/WWW_html/srtm30_plus.html) with 2 arc-min spatial resolution for deep-water tsunami propagation, and a system of nested grids with 30 arc-sec spatial resolution around each tide-gauge. The tsunami initial condition for each subfault (i.e., the vertical seafloor deformation) as well as the geodetic Green's functions are computed using the dislocations in a half-space model (Okada, 1992).

Inversion

We estimate the coseismic slip distribution (slip and rake angle) by performing a nonlinear joint inversion of tsunami, GPS, InSAR and land-level data by using the Heat-Bath algorithm, a particular implementation of the Simulated Annealing technique, as global optimization method (Sen and Stoffa, 2013; more details in **Supplementary Material**). We assume a circular rupture front with constant expansion velocity V_R = 2.25 km/s (Lay et al., 2010), consequently we shift the tsunami Green's functions accordingly. The same V_R value was adopted by Lorito et al. (2011), where preliminary tests had indicated that the current data configuration cannot constrain the rupture velocity for this event.

A different misfit function is used for each dataset. For geodetic data, an L2-norm is used. For tsunami data, we use a nonlinear cost-function sensitive to both waveform amplitude and period (Piatanesi and Lorito, 2007) modified for the OTA method by the introduction of the time parameter *T* (Romano et al., 2016):

$$F(T) = 1 - \frac{2\int_{t1}^{t2} obs(t)synt(t-T)dt}{\int_{t1}^{t2} obs^2(t)dt + \int_{t1}^{t2} synt^2(t-T)dt} \qquad (1)$$

In the cost function (1) *obs* and *synt* represent the observed and predicted tsunami signals, respectively, in a time window delimited by *t1* and *t2*; the time parameter *T* introduces uniform time-shifts between each observed and predicted tsunami waveform during the inversion. Positive *T* values correspond to an earlier arrival of the synthetics. Here we assume that the main error sources are the locally coarse bathymetry around the tide-gauges and the modeling approximations for the DARTs. The clock errors are considered negligible, but if any exist they will map into the values of *T*.

The inverse problem is regularized by adding smoothing (through a Laplacian operator) and seismic moment minimization (using the total slip as a proxy for the seismic moment) constraints.

Lastly, the nonlinear approach allows us to present an average slip model instead of the best one, which could be an outlier not representative of the suite of solutions; this also provides a way to deal with inversion uncertainty (further details are discussed in Piatanesi and Lorito, 2007). The average model is obtained as a weighted mean of a subset of models (ensemble) that satisfactorily fit the data; in particular, the average slip distribution is computed by weighting the models within the ensemble by the inverse of their cost function values.

RESULTS

The Effect of OTA When Inverting DARTs and/or Tide-gauge Data–A Synthetic Case

Extensive use of recordings from deep-water buoy recordings (DART) in inversions has significantly contributed to the understanding of large tsunami sources in the last decade. Being located in the open ocean, DART signals are simpler to model and contain clear waveform information about the source compared to tide-gauge observations, which are complicated by coastal and harbor effects. However, tide-gauges are more abundant than DARTs, so they are desirable for source studies. Strategies to increase their use and to overcome the modeling limitations, due, for example, to coarse bathymetry models and high computational cost of high-resolution simulations, are needed.

To address the relative importance of these two tsunami data sets for the specific case of the Maule earthquake, and to analyze the performance of OTA for different causes of misalignment, we perform a resolution test. We attempt to recover a target slip distribution featuring a checkerboard pattern (0 and 10 m slip alternating on groups of 3×3 subfaults, **Figure 2A**) by jointly inverting geodetic and either 1) all DART or 2) all tide-gauge, or 3) all DART and tide-gauge data. The checkerboard slip model is used to generate synthetic tsunami and geodetic (InSAR, GPS, land-leveling) signals that we use as

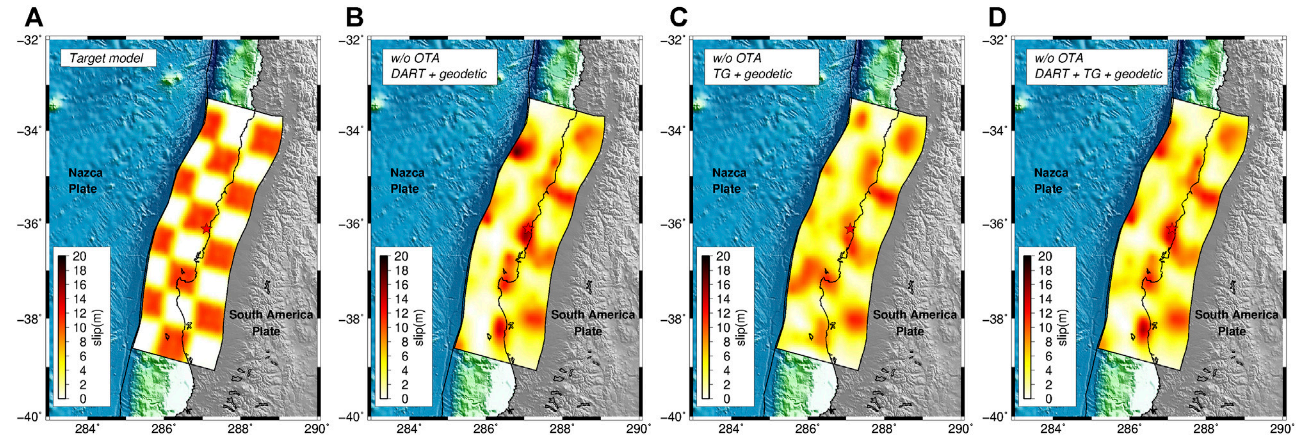

FIGURE 2 | Target slip model **(A)**; slip models estimated by jointly inverting geodetic and DART data **(B)**, geodetic and tide-gauge data **(C)**, geodetic, DART, and tide-gauge data **(D)**. All of the inversions have been performed without using OTA.

"observations" in the inversions. Each dataset is corrupted by adding Gaussian random noise with a variance of 10% of the clean data. We also shift in time the target synthetic tsunami waveforms by adding a random delay in a range of 0–15 min to mimic the typically observed early arrival of the predicted tsunami signals. An additional sensitivity test is performed using an alternative set of tsunami Green's functions computed with a bathymetric model around the tide-gauges with a lower spatial resolution (2 arc-min). This is tested against a checkerboard target model where the tsunami waveforms at the tide-gauges are produced using a bathymetry with a 0.5 arc-min spatial resolution; in this way, we do not add random delay to the tide-gauges because it is assumed to be intrinsic in the change of bathymetry, whereas we assume physics-like delays to the DARTs. In all of the cases, we perform the inversion with and without OTA.

Synthetic Test-Joint Inversions (Geodetic + DARTs and/or Tide-gauge Data) Without Using OTA

When the inversion is performed in a standard way, that is without OTA, the target slip model is never satisfactorily recovered on the entire fault (**Figure 2**). The inverted slip model is similar to the target only in the down-dip inland portion of the fault, which is where geodetic data, as expected, have a higher resolving power (Romano et al., 2020). To quantify the comparison between the estimated slip models and the target we calculate the Structural Similarity Index (SSIM; Giraud et al., 2018); we observe that all of the models have an index far from 1 (i.e., perfect match), specifically $\mathrm{SSIM}_{\mathrm{DART\_woOTA}} = 0.20$, $\mathrm{SSIM}_{\mathrm{TG\_woOTA}} = 0.39$, and $\mathrm{SSIM}_{\mathrm{JOINT\_woOTA}} = 0.25$. These discrepancies are confirmed by comparisons between the synthetic "observed" and predicted data that clearly present a time mismatch between the tsunami waveforms (**Figures S4–S6 in Supplementary Material**).

Synthetic Test-Joint Inversions (Geodetic + DARTs And/or Tide-gauge Data) Using OTA

When we apply OTA the target model is very well reconstructed independently of the data set combination used (**Figure 3**). Indeed, all SSIM values are significantly larger with respect to the previous cases ($\mathrm{SSIM}_{\mathrm{DART\_wOTA}} = 0.67$, $\mathrm{SSIM}_{\mathrm{TG\_wOTA}} = 0.63$, and $\mathrm{SSIM}_{\mathrm{JOINT\_wOTA}} = 0.70$). The results of these tests (as further documented by the very good agreement in the data comparisons in **Supplementary Material Figures S7–S9**) indicate that the joint inversion of all data sets with OTA used for the tsunami observations is the case that best reproduces the target model. We also observe that the slip distributions for inversions using only the DARTs or only the tide-gauges are similar to the joint inversion with both data sets, as indicated by the SSIM values. This indicates that OTA is equally effective for both DART and tide-gauge data, even though the reasons for the time misalignment are different. This surprisingly suggests that, in principle, there is no reason to prefer one tsunami data set over another in the inversion in this specific case and for this parameterization. However, uncertainties potentially affecting forward modeling are not fully taken into account by this type of synthetic test, since the "observed" and predicted tsunamis are modeled with the same Green's functions, in contrast to an inversion using actual tsunami observations. These uncertainties are likely smaller for open-ocean tsunami numerical modeling at DART buoys. To address this issue, we perform an additional test.

Synthetic Test-Joint Inversions (Geodetic + DARTs and Tide-gauge Data) With and Without Using OTA, Considering Tsunami Green's Functions Computed on a Lower Resolution Bathymetry

In this test the tsunami Green's functions for all of the stations (DARTs and tide-gauges) are computed by simulating the wave propagation on a bathymetric grid with 2 arc-min spatial resolution, whereas the "observed" tsunami waveforms are

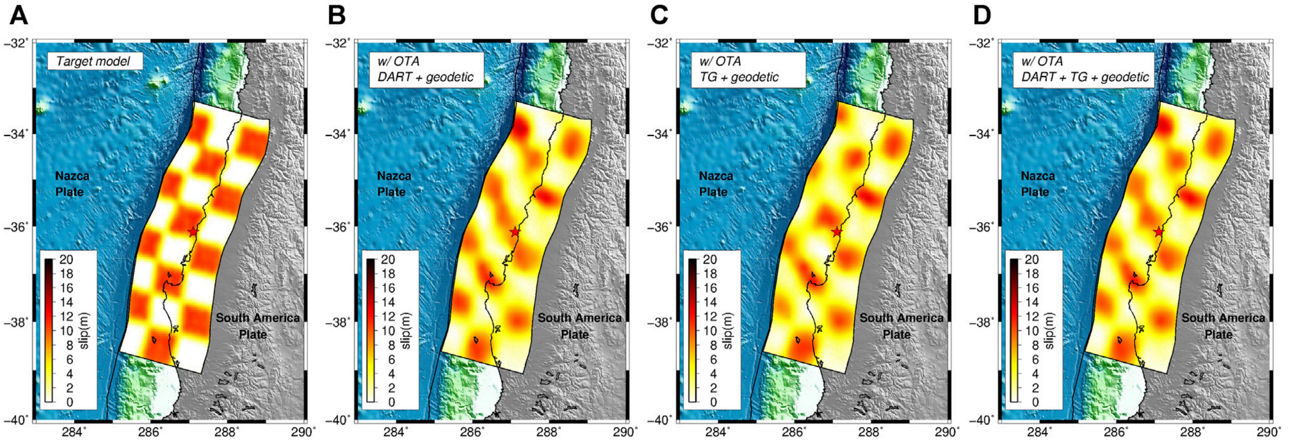

FIGURE 3 | Target slip model **(A)**; slip models estimated by jointly inverting geodetic and DART data **(B)**, geodetic and tide-gauge data **(C)**, geodetic, DART, and tide-gauge data **(D)**. All of the inversions have been performed using OTA.

computed using a 30 arc-sec bathymetry around the tide-gauges; this is a sensitivity test to check how well the OTA works using Green's functions recorded at a coarser spatial resolution with respect to the "real observations". Differently from the tests shown in the previous sections, here the target tsunami waveforms at the tide-gauges are not corrupted with a random delay because this is implicit in the different bathymetry used with respect to the one adopted for the Green's functions; on the other hand, since the possible delay to the DARTs is not related to the change of bathymetry then we add to these waveforms a "physics-like" delay that increases with the source-station distance.

The results of the tests show that without using OTA the target slip distribution is well reproduced for the portion of the fault closest to the geodetic observational points, which is consistent with the previous tests (compare **Supplementary Material Figure S10B** with **Figure 2**), whereas the resolution degrades with distance from the coastline; the comparison between observed and predicted data confirms this result (**Supplementary Material Figure S11**). When we apply the OTA then the checkerboard pattern is well recovered (**Supplementary Material Figure S10C**) and also the data fit improves (**Supplementary Material Figure S12**). It is important to notice how the change of bathymetry in some case affects the waveshape of the tide-gauges, but this appears to have a second-order effect on the target slip distribution that is nonetheless well reproduced.

The effect of OTA when inverting DARTs and/or tide-gauge data–The 2010 M_w8.8 Maule earthquake

Having verified, through the foregoing synthetic resolution test, the effectiveness of OTA in estimating the earthquake source when tsunami waveforms are affected by unmodelled time shifts alone, we now assess the performance of the method for the 2010 M_w8.8 Maule earthquake. We follow the same workflow adopted for the synthetic test.

Maule Earthquake-Joint Inversions (Geodetic + DARTs And/or Tide-gauge Data) Without Using OTA

Without using OTA, the inferred slip patterns for the three dataset combinations feature along-strike bilateral ruptures with 2 main patches of slip (**Figure 4**). The main asperity is located to the north of the epicenter and has a spatial extent of ~250 km with a maximum slip value of ~19 m at ~35°S; a second and smaller asperity is located south of the epicenter and features as maximum slip ~10 m in the area of the Arauco Peninsula, ~37°S. The average rake is ~111°, consistent with the slightly oblique relative convergence direction of the Nazca and South America plates. Visual comparison of the models in **Figure 4** highlights the first-order similarity of the slip patterns. The DART and tide-gauge data would appear to have comparable resolving power for this earthquake, as was found for the synthetic tests; however, the SSIM values indicate that the slip model from joint inversion of geodetic and DART data (**Figure 4A**, $SSIM_{DART\_woOTA} = 0.94$) is more similar to the model using geodetic and all tsunami data (**Figure 4C**; **Supplementary Table S3**) than to that using geodetic and tide-gauge data together (**Figure 4B**, $SSIM_{TG\_woOTA} = 0.74$). In all cases, comparisons between observed and predicted data highlight good agreement for the geodetic data sets, but significant time-mismatches in the tsunami waveforms (**Supplementary Material Figures S13–S15**).

Maule Earthquake-Joint Inversion With a Priori Time-Shifts Corrections for Tide-gauges

Because of the time-mismatch present in the tsunami waveforms, we decide to follow the approach presented in Lorito et al. (2011), where they jointly inverted geodetic and tsunami data after correcting the Green's functions for tide-gauges by applying a rigid time-shift to the signals. Lorito et al. (2011) conducted their work before studies on the travel time anomalies in the open ocean for distant tsunamis (Tsai et al., 2013; Watada et al., 2014). Hence, the underlying assumption of that approach was that the tsunami modeling of the tide-gauges signals, as described in the Introduction section, can be inaccurate due to several factors (e.g.,

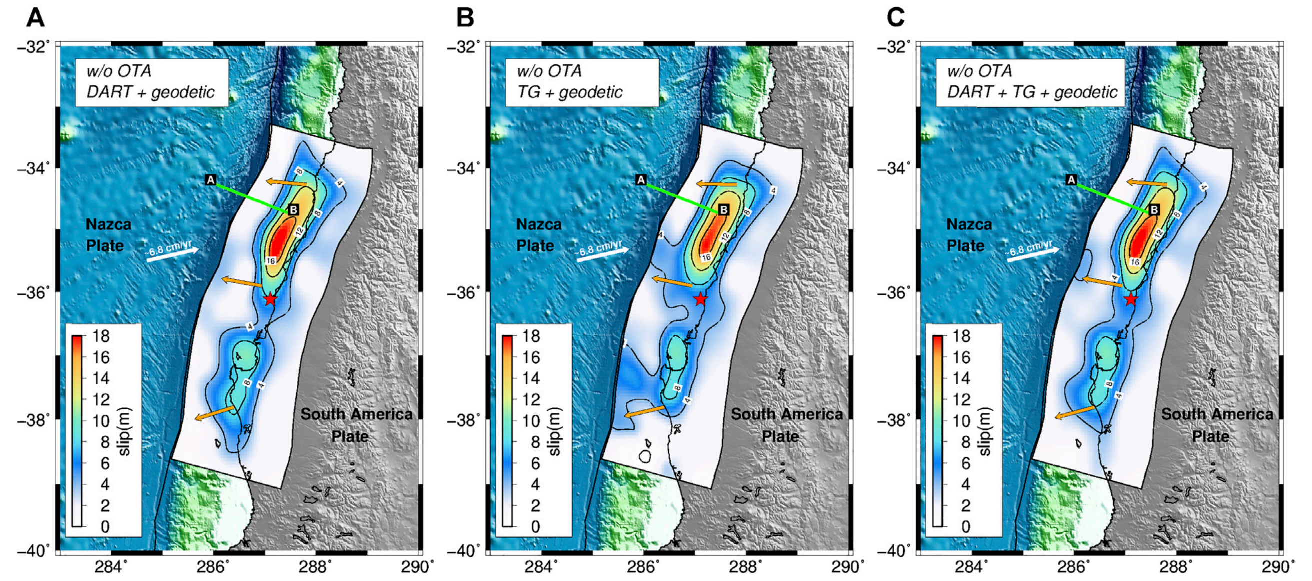

FIGURE 4 | Rupture models of the 2010 Maule earthquake. Slip models (4 m contour lines in black) are estimated by jointly inverting geodetic and DART data **(A)**, geodetic and tide-gauge data **(B)**, geodetic, DART, and tide-gauge data **(C)**. Red star represents the epicenter of the Maule earthquake; orange arrows represent the average slip directions (rake); green line represents the ILOCA track. All of the inversions have been performed without using OTA.

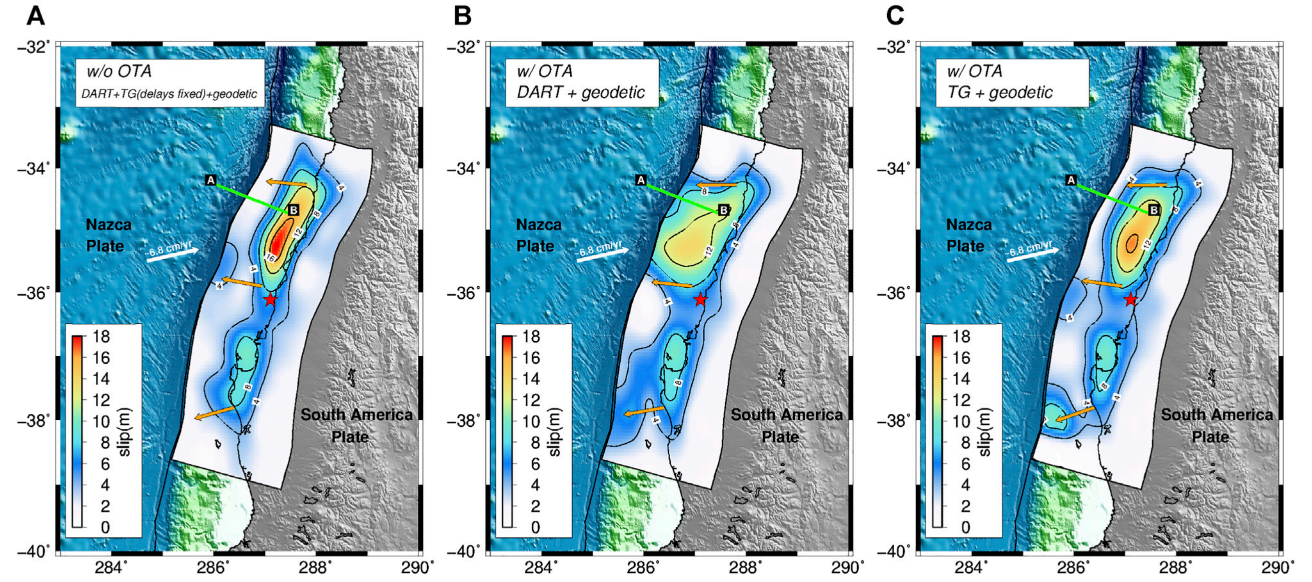

FIGURE 5 | Rupture model of the 2010 Maule earthquake. Slip model (4 m contour lines in black) estimated by repeating the study of Lorito et al. (2011), jointly inverting geodetic, DART, and tide-gauge data without OTA but applying ad hoc rigid time shifts to the tide-gauges waveforms **(A)**. Slip models estimated by joint inversion of geodetic and DART data **(B)**, and joint inversion of geodetic and tide-gauge data **(C)**. Red star represents the epicenter of the Maule earthquake; orange arrows represent the average slip directions (rake); green line represents the ILOCA track. The inversions in **(B)** and **(C)** have been performed using OTA.

the low-resolution bathymetry model around the instrument), whereas the DART signals modeling, being in principle more simple and accurate, does not necessitate any correction.

Notwithstanding the time-mismatch corrections for the tide-gauges, the slip distribution estimated following this approach (**Figure 5A**) has a rupture pattern very similar to the above slip models obtained without using OTA (**Figure 4**). Thus, the data fit continues to be very good for the geodetic data sets, whereas, apart from some tide-gauges that benefit from ad hoc time correction, the comparisons between observed and predicted

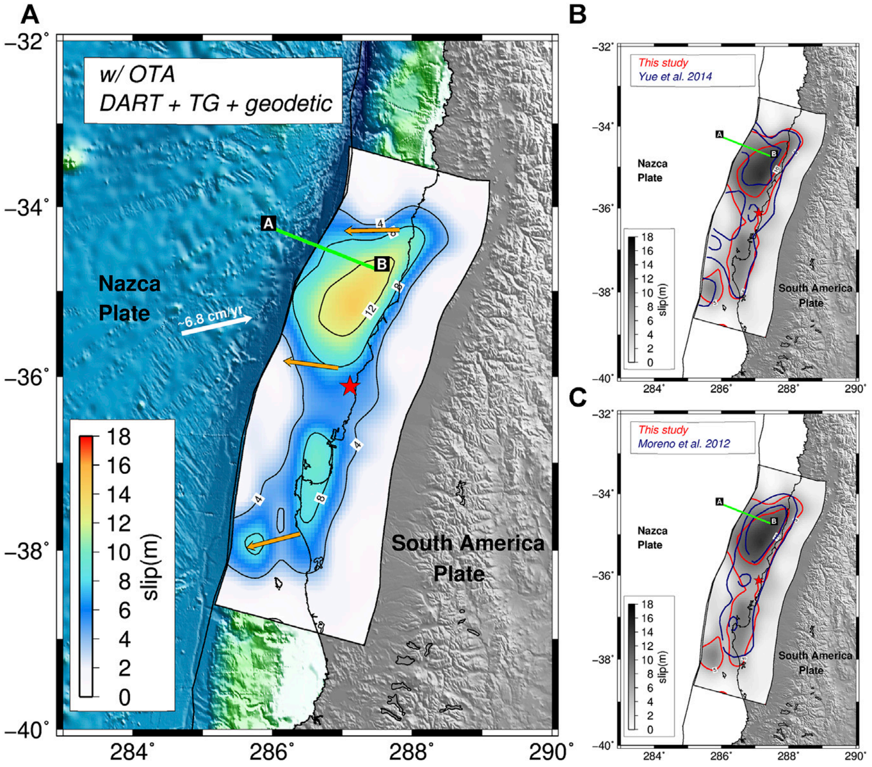

FIGURE 6 | (A) Rupture model of the 2010 Maule earthquake estimated by jointly inverting geodetic, DART, tide-gauge data, and applying OTA. Solid black lines shows the slip contour at 4 m interval; red star represents the epicenter of the Maule earthquake; orange arrows represent the average slip directions (rake); green line represents the ILOCA track. The figure also shows the comparison between the 5m slip contour lines from the model (red line) presented in panel **(A)** and the model (blue line) by **(B)** Yue et al. (2014) and **(C)** Moreno et al., (2012).

tsunami waveforms still highlight a mismatch between the signals (**Supplementary Material Figure S16**).

Maule Earthquake-Joint Inversions (Geodetic + DARTs and/or Tide-gauge Data) Using OTA

Because of the persistent time-mismatch in the tsunami signals, we incorporate OTA in the joint inversions using the geodetic data and either the DARTs or the tide-gauges. The estimated slip distributions (**Figures 5B,C**) are significantly different from the models retrieved without OTA; the rupture area is still bilaterally distributed along strike, but the northern patch now shows relatively lower and more spatially spread slip (maximum values of ~14 m and ~16 m using DARTs or tide-gauges respectively, **Figures 5B,C**). In particular, both models are characterized by shallower rupture extent, with the model using DARTs having slip that reaches the trench for both the northern and southern patches.

Despite the comparable resolving power exhibited applying the OTA for the synthetic tests, significant differences are evident between slip distributions obtained using the DARTs or the tide-gauges. We also note that the tsunami time-mismatch corrections for the OTA inversion using DARTs (**Supplementary Material Figure S17**) are larger than those for the OTA inversion using tide-gauges (**Supplementary Material Figure S18**). This is consistent with the fact that the slip distribution in **Figure 5C** is closer to the coast compared to that in **Figure 5B**.

Finally, when we invert the complete set of data using OTA, the resulting slip distribution (**Figure 6**; **Supplementary Table S2**) confirms a bilateral rupture propagation with coseismic slip that extends to the shallow part of the subduction interface near the trench with slip greater than 8 m (maximum slip value ~14 m); the second patch, around the Arauco Peninsula, features a maximum slip of ~10 m, and the average rake angle is ~113°, again consistent with the average relative plate convergence direction.

Assuming a rigidity $\mu = 30$ GPa the seismic moment is $M_0 = 1.73 \times 10^{22}$ Nm ($M_w = 8.8$). Approximately the same value of moment magnitude M_w is found for all Maule earthquake slip models retrieved in the present study, with and without OTA.

The comparison between the observed and predicted data (**Figures 7–9**) is good for all of the data sets. In particular, the comparisons of tsunami waveforms (**Figure 7**) highlight an average time-shift of ~5 min for the tide-gauges, compatible with uncertainties in the local bathymetry and tide-gauge locations (Romano et al., 2016); we also note that there is not an obvious station distance-delay relation (**Figure 10**) which supports the notion that for tide-gauges the shifts are dominated by local modeling inaccuracy near the stations. In contrast, the time mismatches found for the DART buoys increase with source-station distance (**Figure 1A**) and are on average ~1% of the first arrival time (**Figure 10**), as observed by Watada et al. (2014). This is consistent with unmodeled features

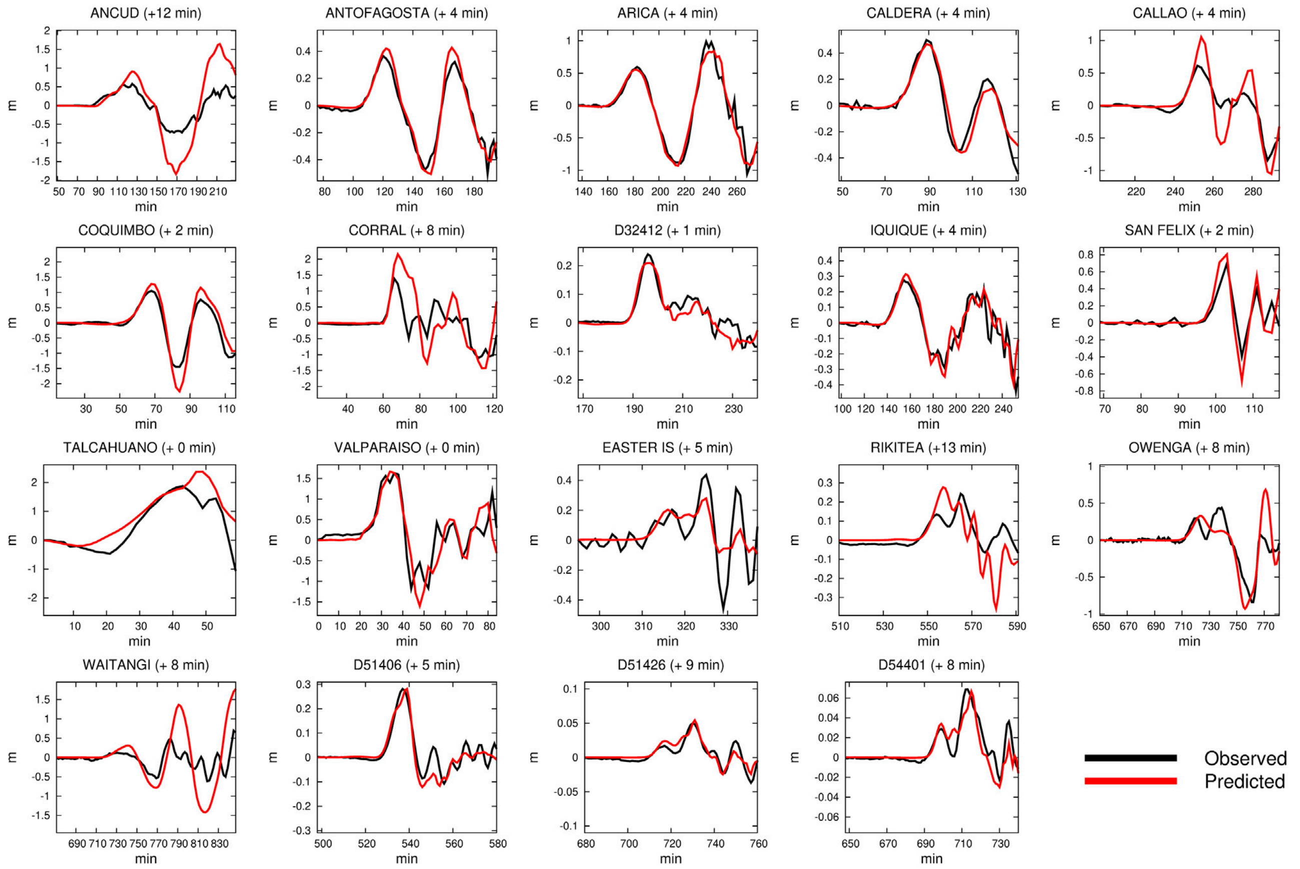

FIGURE 7 | Comparison between observed (in black) and predicted (in red) tsunami waveforms for the slip distribution obtained by jointly inverting geodetic and tsunami data using OTA (**Figure 6**); the time mismatch estimated by the OTA is indicated within brackets.

of the tsunami propagation (dispersion, ocean floor elasticity, water density variation with depth) for which Yue et al. (2014) applied theoretical corrections assuming tsunami propagation along great circles.

A comparison with the slip models by Moreno et al. (2012) and Yue et al. (2014) shows that the along-strike extent of the rupture area estimated using the OTA is comparable with both the models, as well as the northern location of the main asperity; however, while reaching the trench, the shallow slip of our model is slightly lower (~10 m) than the (Yue et al. (2014), >15 m) model (**Figures 6B,C**). The difference in the maximum slip value might be ascribed to the fact that the model by Yue et al. (2014) is obtained without inverting tide-gauge data; indeed, the maximum shallow slip value (**Figure 5B**) estimated inverting geodetic and DART waveforms only [i.e., a data configuration similar to Yue et al. (2014)] is higher (~12 m) and closer to the Yue et al. (2014) value.

As anticipated in **Data and Green's functions**, to account for non-uniqueness of the solution, for each inversion we show the average slip model (obtained as a weighted mean of a subset of models featuring the lowest cost functions) instead of the best model (the one with the lowest cost function) that could represent an "extreme" best fitting case. To emphasize potentially equivalent parameter values, the analysis of the model ensemble is illustrated in the form of marginal distributions of the slip for each subfault (**Supplementary Material Figure S19**), featuring a Gaussian shape centered on the average slip value, highlighting how the slip is well resolved over the entire fault plane. This is true also for the slip distributions obtained from the joint inversion of geodetic and tsunami data without using OTA. However, comparing the marginal distributions of the two slip models (i.e., with and without OTA) we argue that the shallow slip found using OTA is not an artifact (or an outlier) of the inversion; it rather is evident that the average slip values in the northern and larger asperity show systematic behavior moving toward the shallow part of the fault. This can be observed from another point of view through the evolution of the models explored by the algorithm during the inversion (see **Movies S1, S2 in Supplementary Material**) displaying how the inversion, as the cost function decreases, converges toward a solution that features shallow slip in the model using OTA, and the slip is forced to locate deeper in the other case.

On the other hand, significant differences are evident down-dip in the southern patch of slip; specifically, the southern asperity estimated in the model proposed here, as well as the one by Moreno et al. (2012) does not reach the shallow part of the

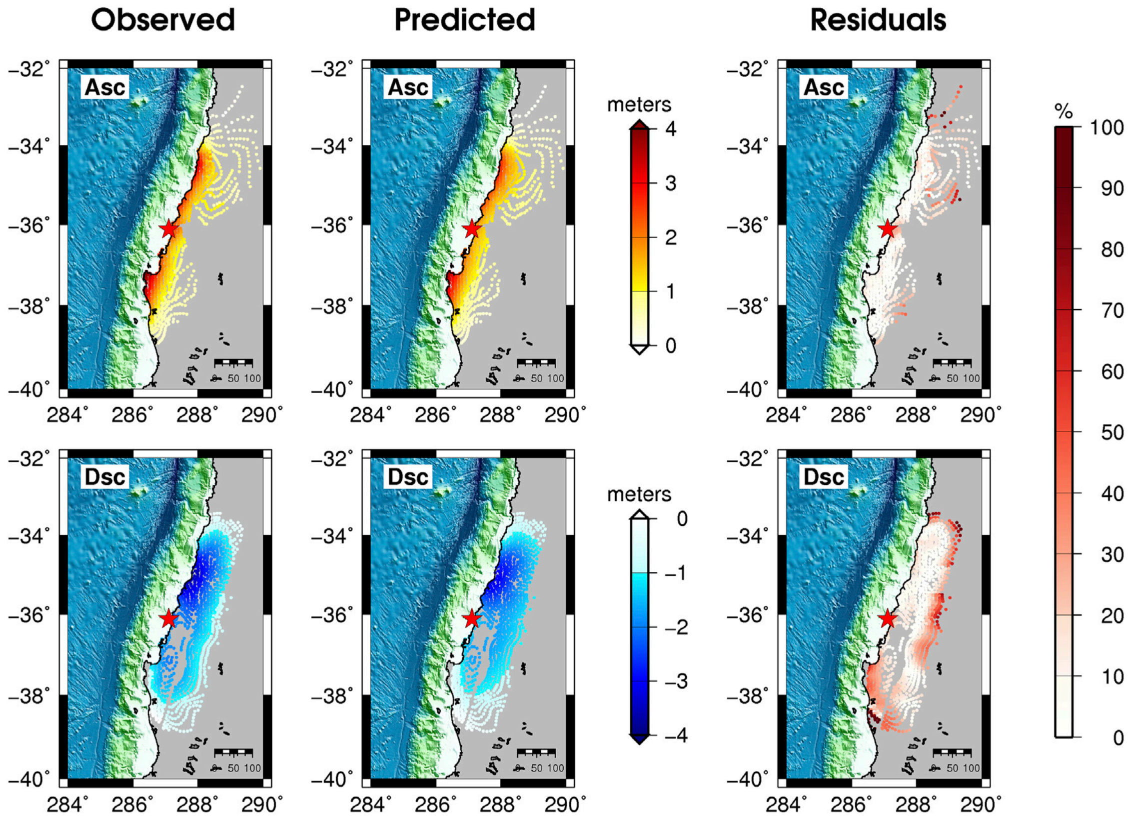

FIGURE 8 | Comparison between observed, predicted, and percentage residuals of ascending (**upper panels**) and descending (**bottom panels**) InSAR data for the slip distribution obtained by jointly inverting geodetic and tsunami data using OTA (**Figure 6**).

subduction interface, whereas the slip model proposed by Yue et al. (2014) highlights a coseismic dislocation of ~10 m close to the trench around 37°S. To address if these differences may be ascribable to the different GPS data set used by Yue et al. (2014) we perform an additional inversion incorporating these data.

Maule Earthquake-Joint Inversion (Geodetic + DARTs and Tide-gauge Data) Using OTA and a Larger GPS Data Set

Using the OTA, we jointly invert the previous data sets supplementing them with the GPS coseismic offsets used by Moreno et al., (2012) and Yue et al., (2014), whose spatial distribution is denser and might help to better constrain the slip distribution.

The resulting slip distribution (**Figure 11**; **Supplementary Table S4**) confirms both the along-strike extent of the rupture area and the bilateral rupture propagation with respect to the hypocenter. Whereas the northern asperity continues to be characterized by large slip extending to the shallow part of the subduction interface with second-order differences with respect to the model proposed in **Figure 6**, the asperity located to the south of the hypocenter is not confined close to the Arauco Peninsula, but features significant slip (~8–10 m) up to the trench. Thus, this updated slip model of the Maule earthquake is similar to the model proposed by Yue et al., (2014) (**Figure 11B**); this is consistent with the fact that, in this case, the data sets used in both models are similar (Yue et al. (2014) included teleseismic data, but did not include tide gauge data). The comparison between the observed and predicted data is satisfactory for all of the data sets (**Figures 12–14**). The seismic moment corresponding to the slip model in **Figure 11** is $M_0 = 1.76 \times 10^{22}$ Nm ($M_w = 8.8$).

DISCUSSION

This study of the 2010 Maule earthquake shows that using OTA for the tsunami waveforms inversion can affect the final slip distribution. For the 2010 Maule earthquake some prior studies indicate significant slip in the shallow region of the megathrust (Yue et al., 2014) while others do not (Lorito et al., 2011). It is important to resolve the occurrence of large shallow earthquake slip either as part of a great rupture or as distinct shallow rupturing "tsunami earthquakes" (Kanamori, 1972), as this information is valuable for tsunami hazard analyses (Kozdon and Dunham, 2014; Murphy et al., 2016; Murphy et al., 2018; Grezio et al., 2017). The physics-based corrections Yue et al. (2014) applied to the modeled tsunami waveforms directly result in prediction of the existence of coseismic shallow slip nearby the trench. This has been confirmed by direct imaging of seafloor

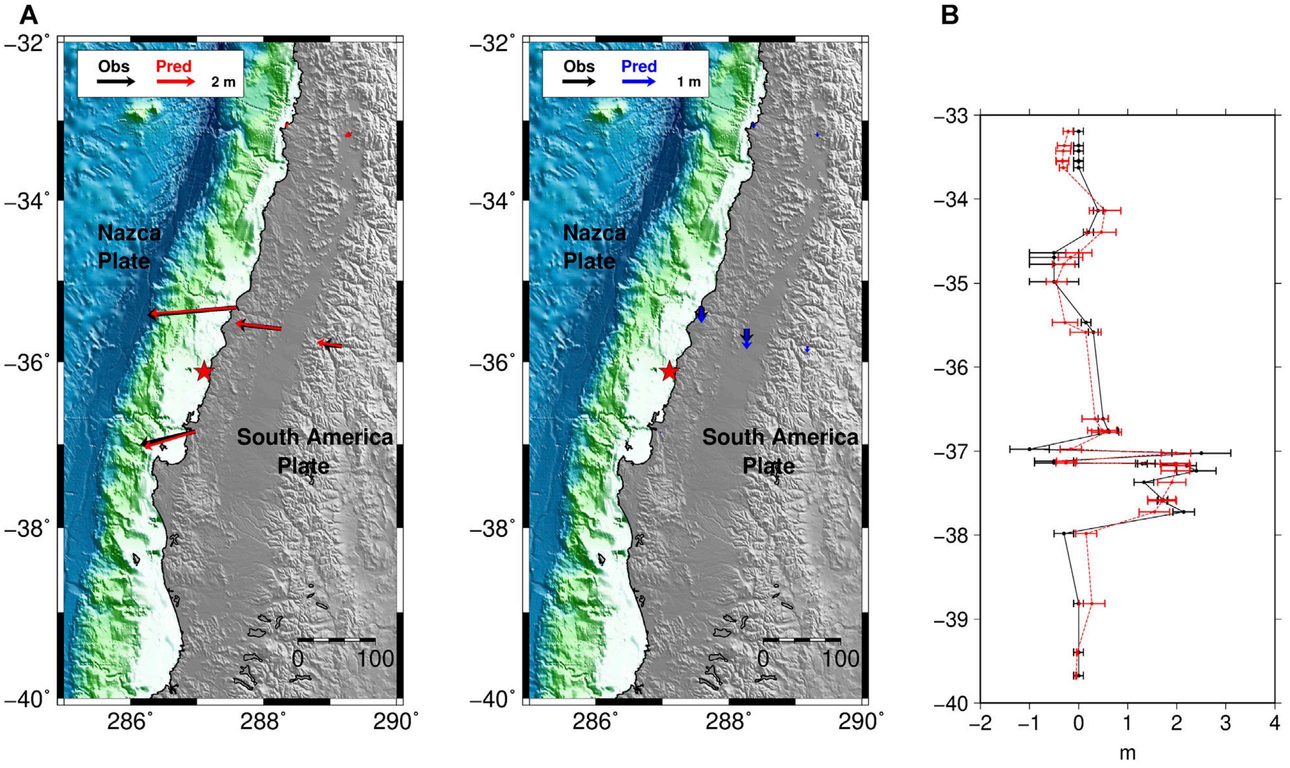

FIGURE 9 | GPS and land-level data fit for the slip model shown in **Figure 6**. Comparison between observed (in black) and predicted **(A)** GPS data (horizontal and vertical in red and blue, respectively); **(B)** observed (black) and predicted (red) land-level changes; error bars for observations are experimental uncertainties, whereas for predictions they are calculated adding ±1σ errors.

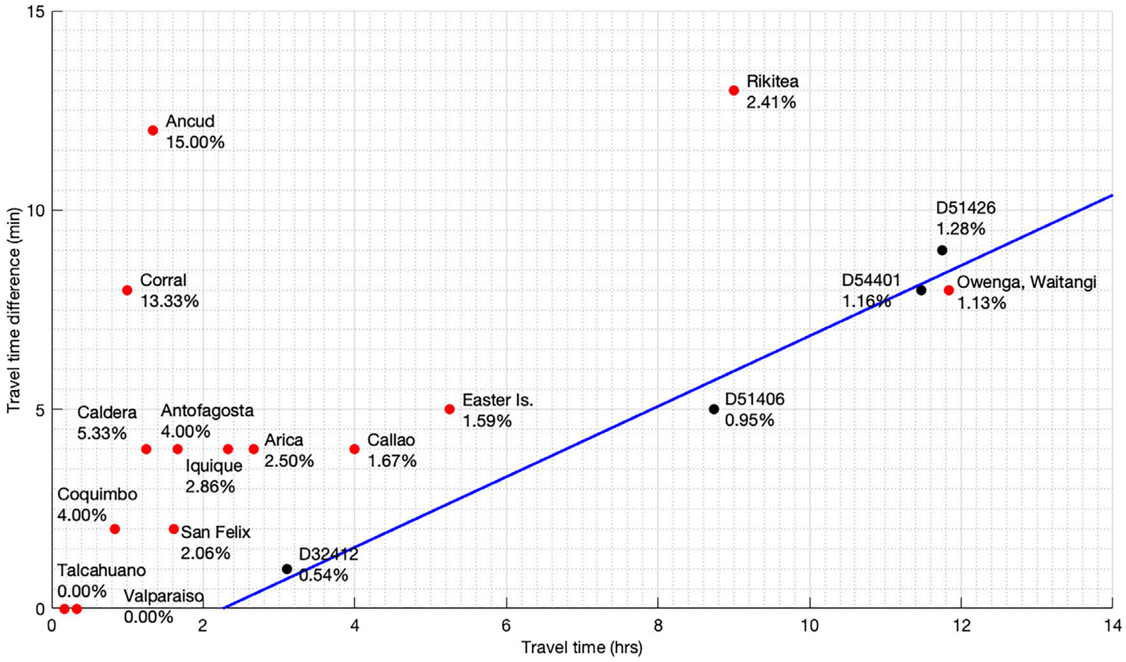

FIGURE 10 | Time-shift (absolute and percentage) estimated for DART buoys (black dots) and tide-gauges (red dots) using the OTA method in the inversion shown in **Figure 6** plotted vs. the observed arrival time. The blue line shows a systematic trend with distance for the DART data.

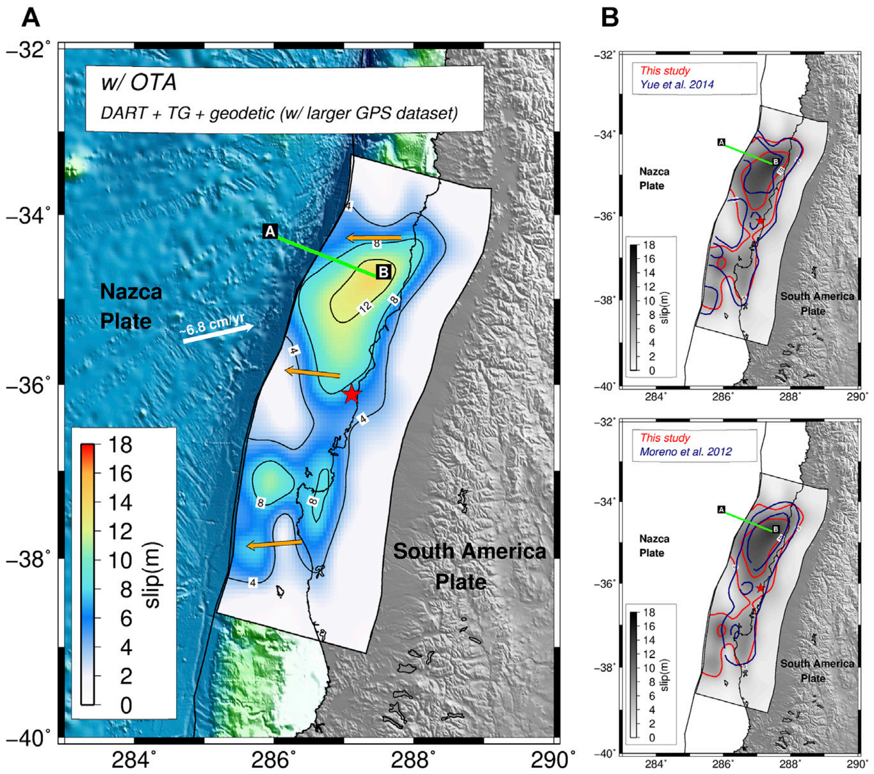

FIGURE 11 | (A) Rupture model of the 2010 Maule earthquake estimated by jointly inverting geodetic, DART, tide-gauge data, and applying OTA; the GPS data set used in this case is larger than the one shown in **Figure 9** and is the same used from (Moreno et al., 2012) and (Yue et al., 2014). Solid black lines shows the slip contour at 4 m interval; red star represents the epicenter of the Maule earthquake; orange arrows represent the average slip directions (rake); green line represents the ILOCA track. The figure also shows the comparison between the 5 m slip contour lines from the model (red line) presented in panel **(A)** and the model (blue line) by **(B)** Yue et al. (2014) and **(C)** Moreno et al. (2012).

deformation (Maksymowicz et al., 2017). Hence, it became evident that a more accurate modeling strategy for the tsunami Green's functions, which approximates the relevant physics (Tsai et al., 2013; Watada et al., 2014), should be used for slip inversions, at least in some specific cases.

Without using OTA, our slip distributions are similar to previously published coseismic rupture models that did not use any tsunami data (Delouis et al., 2010; Tong et al., 2010; Vigny et al., 2011; Moreno et al., 2012), and even more similar to those using tsunami data but without consideration of tsunami waveforms misalignments (Lorito et al., 2011). Conversely, with OTA, whereas the along-strike extent of the rupture area (**Figure 6B,C**) is still consistent with Yue et al. (2014) and Moreno et al. (2012), a significant amount of slip (~10 m) shifts trenchward in the solution; this is similar to what was shown by Yue et al. (2014) after applying physics-based corrective terms to the deep-water tsunami Green's functions (**Figure 6B**). This feature of the model is confirmed when the slip model is better constrained by a larger set of GPS data used in the inversion (**Figure 11**). The positive comparison with the slip model proposed by Yue et al. (2014) provides an encouraging confirmation that OTA works as an alternative to computing physics based corrections. More directly, the multi-beam bathymetric re-survey conducted by Maksymowicz et al. (2017) along a track named ILOCA (**Figures 1, 4–6**) measuring the vertical seafloor deformation produced by this megathrust earthquake offers an additional opportunity to benchmark the method.

Thus, we perform a forward prediction of both the vertical and horizontal components of the seafloor deformation associated with all the slip models investigated in the present study, comparing them against the observations (**Figure 15**). We also compare our results with the models by Tong et al. (2010) [hereinafter TO10], Yue et al. (2014) [YU14], and Yoshimoto et al. (2016) [YO16].

The comparisons in **Figure 15** indicate that the slip models derived with OTA reproduce the data significantly better than the models without OTA. Large slip near the trench is needed to replicate the seafloor deformation along the ILOCA track. This is found for the slip distributions obtained by jointly inverting geodetic and all tsunami data, or geodetic and DARTs; indeed, these two models show similar predictions (**Figures 5B, 6, 11**) as expected given their similar slip distributions. On the other hand for the joint OTA inversion of geodetic and tide-gauge data, the comparison with deformation along the ILOCA track becomes satisfactory only along the segment more than ~20 km from the trench. This is an indirect indication (or an a-posteriori verification) that the epistemic uncertainty of the DART data

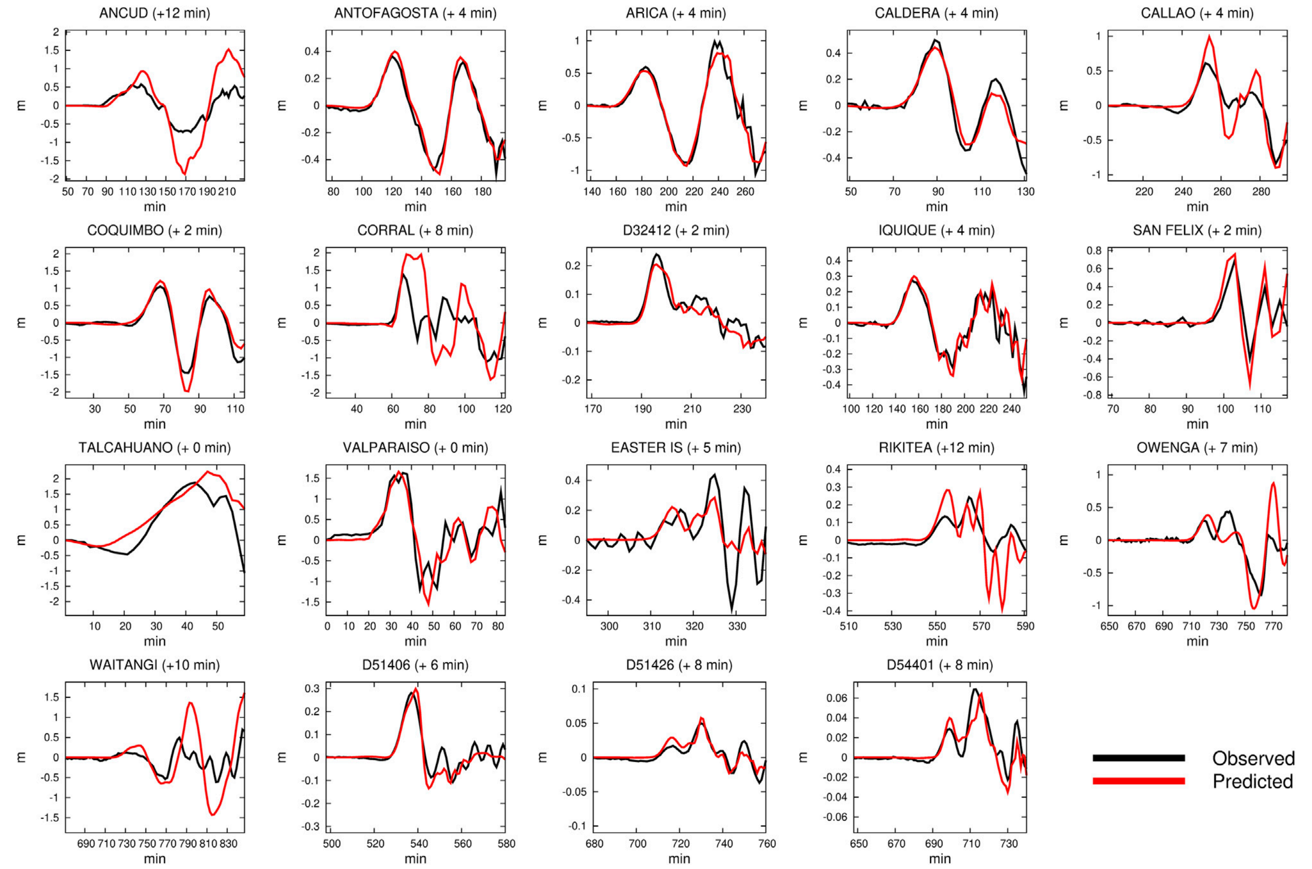

FIGURE 12 | Comparison between observed (in black) and predicted (in red) tsunami waveforms for the slip distribution obtained by jointly inverting the same GPS data set used from Moreno et al. (2012) and Yue et al. (2014), InSAR, land-leveling, and tsunami data using OTA (**Figure 11**); the time mismatch estimated by the OTA is indicated within brackets.

is less than for the tide-gauges. This is because the DART data require less-sophisticated (linear) modeling and inherently do not depend as critically on availability of high-resolution bathymetry models. This behavior motivates placing higher relative weight on the DART data in the inversion when using both data sets.

The comparison between the model with OTA and the YU14 model shows a pretty good agreement at least up to ~40 km from the trench, whereas the YO16 model predicts a vertical deformation closer to the lower limit of the error bars. The difference in the maximum shallow slip in our and YU14 models might be responsible for the under- and over-estimation of the vertical deformation measured landward around 10 km from the trench, respectively; however, both the predictions are well within the error bars. We also note that none of the models reproduce the 10 + m vertical deformation at the trench; several reasons can explain this discrepancy. The rupture models may not fully capture slip right at the trench. Actually, these slip models have too coarse of resolution for capturing the narrow peak (e.g., YU14 model has a peak which is slightly displaced landward and it is also broader but smaller). Another explanation might be related to the near trench displacement not being captured by instantaneous and elastic deformation of homogeneous crust. Also the errors associated to the data, may be larger than estimated, or a combination of some of these factors. However, the more reasonable explanation appears to be related to the errors associated to the data being larger than estimated. Indeed, as discussed by Maksymowicz et al. (2017), the larger standard deviation of the data in peak slip zone prevents an exact interpretation of the deformation in that part of the ILOCA segment. A strong bathymetric gradient close to the trench can increase the noise of the swath bathymetry data and hence be the cause of the larger error in the estimated deformation. The discrepancy with the prediction by YU14 increases landward (i.e., toward point B in **Figure 15**), with our OTA prediction remaining within or very close to the error bars, whereas the YO16 model fits very well the deformation in the eastern ~50 km of the segment. On the other hand, the deformation predicted by the models not using OTA do not match the vertical deformation in the trench region, similar to forward predictions for a model like TO10 based on only geodetic data. Otherwise, all models, with the possible exception of YU14, perform reasonably well landward along this profile. Measured horizontal seafloor deformation is characterized by larger uncertainty than vertical deformation (Maksymowicz et al., 2017). The comparison of the models with the horizontal

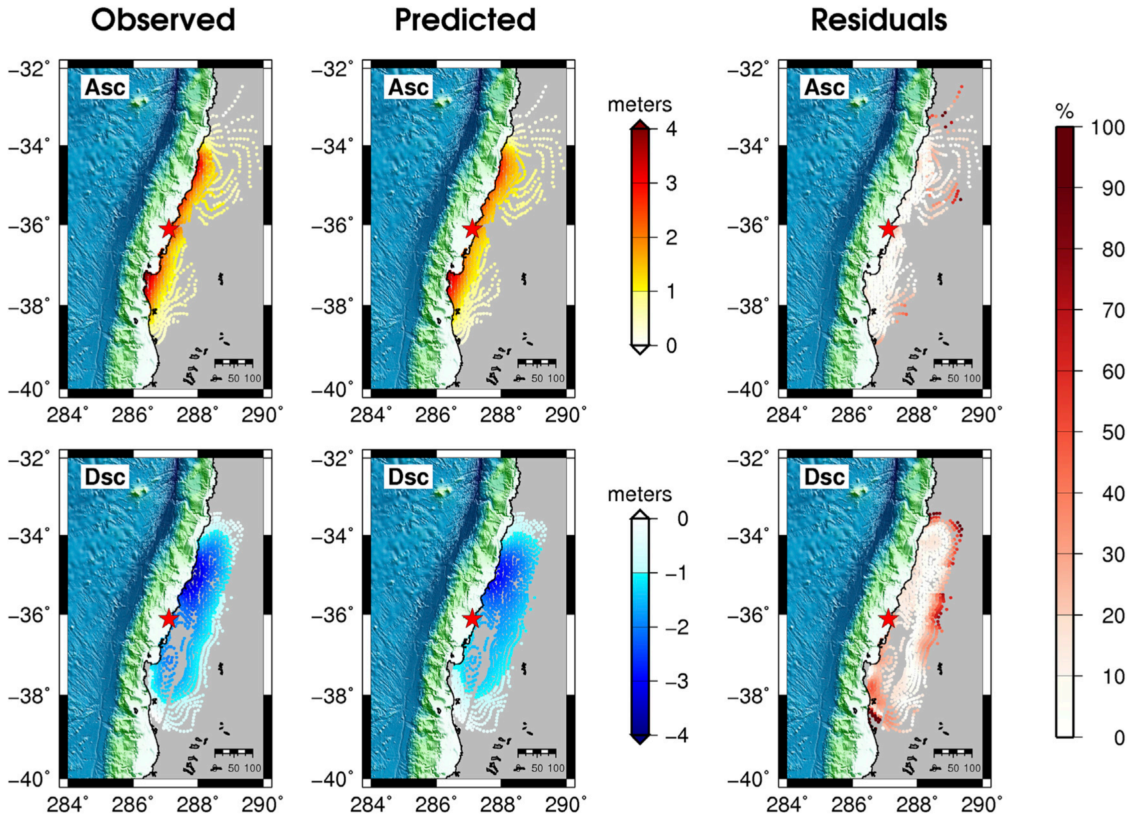

FIGURE 13 | Comparison between observed, predicted, and percentage residuals of ascending (**upper panels**) and descending (**bottom panels**) InSAR data for the slip distribution shown in **Figure 11**.

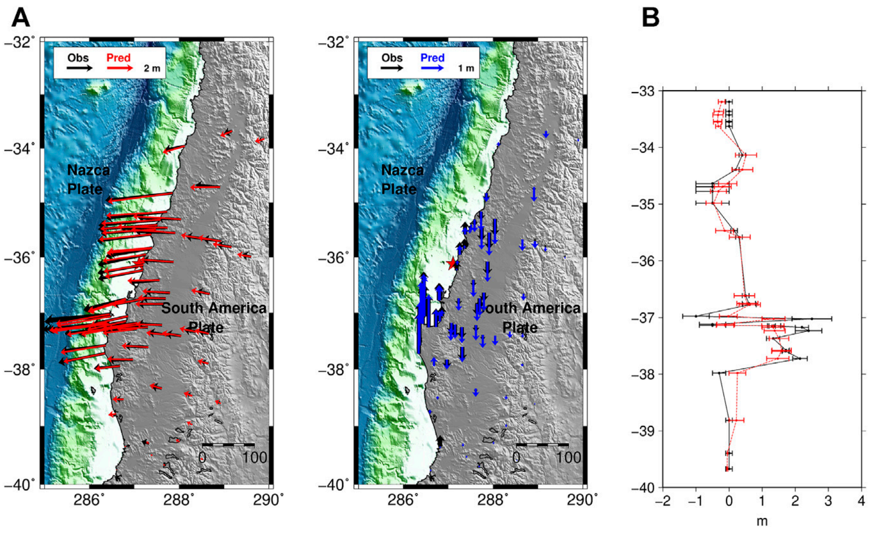

FIGURE 14 | GPS and land-level data fit for the slip model shown in **Figure 11**. Comparison between observed (in black) and predicted **(A)** GPS data (horizontal and vertical in red and blue, respectively); **(B)** observed (black) and predicted (red) land-level changes; error bars for observations are experimental uncertainties, whereas for predictions they are calculated adding ±1σ errors.

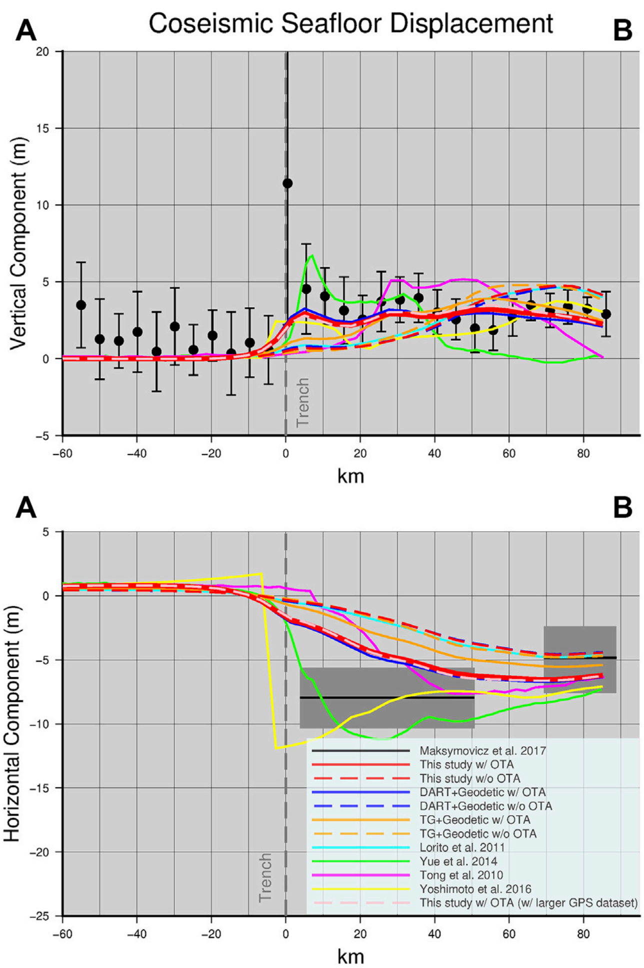

FIGURE 15 | Comparison between observed (black) and predicted **(A)** vertical and **(B)** horizontal seafloor deformation along the ILOCA track; in **(A)** error bars indicate the standard deviation, whereas in **(B)** the approximated error bars are in grey. In both panels, predicted seafloor deformations are shown for the slip distributions obtained for all cases investigated in this study (with and without OTA along with predictions for the Yue et al. (2014, green), Tong et al. (2010, magenta), and Yoshimoto et al. (2016, yellow) models. Dashed grey vertical line in both the panels indicates the trench location along the ILOCA segment.

deformation in **Figure 15** nevertheless suggests a slightly higher consistency of OTA models with the direct deformation measurements than for the models obtained without using OTA.

The present study shows that for this earthquake and using this data set, the OTA method allows retrieval of a slip distribution consistent with both the model proposed by Yue et al. (2014), which applied physics based corrections to DART calculations and independently measured seafloor deformation. The OTA method can be applied if the Green's functions are computed by either the most sophisticated methods that account for all known propagation effects (e.g., Ho et al., 2019) or by simplified procedures that give good waveshapes, but inaccurate travel times. There will always be errors in the model predictions (we cannot reproduce the Earth effects perfectly with any model), and there may be clock errors. OTA will adjust the time misalignments to avoid bias of the solution for the known and unknown limitations of the Green's functions for the time alignment. As only time shifts are involved, inadequacies of the Green's functions for predicting the waveshapes, particularly for tide-gauge recordings sensitive to detailed coastal bathymetry, are not accounted for by OTA. Only by improving the bathymetry models can those waveshape predictions be improved. But, the OTA method reduces the predicted arrival time errors for the first cycles of the tide gauge data, suppressing first-order bias in the inversions.

Of course, the epistemic uncertainty could still be reduced further with improved numerical modeling. Indeed, some modeling limitations might result from not using a more physically complete tsunami numerical model that, in general, would be preferable (Yamazaki et al., 2011; Allgeyer and Cummins, 2014) or more accurate modeling approaches for the tsunami generation (Kajiura, 1963; Nosov and Kolesov, 2011); however, our findings show that OTA approach works well given less complete computation of the tsunami Green's functions. Additionally, the absolute slip estimates could be slightly affected by neglecting in the tsunami Green's functions the contribution of the seafloor horizontal motion to the vertical uplift (Bletery et al., 2015) or by using elastically homogeneous materials instead of heterogeneous medium (Romano et al., 2014). The OTA method is used during the inversion to remove from the modeled tsunami signals any time-mismatch whose origin is unknown; once the tsunami waveforms are aligned with the observed signals then the inversion algorithm searches for the slip pattern that best fits amplitude and period of the tsunami waves. We emphasize that the OTA does not improve specific waveform shape mismatches such as the initial reverse polarity phase at distant DARTs (Watada et al., 2014) or arising from inadequate coastal bathymetry models which might change details of the slip distribution; however, these are commonly second order effects not projecting into the general rupture pattern.

Thus, when complete modeling of the tsunami wavefield (e.g. including high-resolution bathymetry, dispersion, the Earth's elasticity, etc.) is not feasible or is computationally excessively demanding, the OTA method proves very effective for tsunami data (DARTs and/or tide-gauge) inversion. We observe that without using OTA a bias is introduced in the slip distribution that for the specific case of the Maule earthquake causes the slip to be artificially confined deeper. The resolution tests for the specific configuration of tsunami sensors demonstrate that DARTs and tide-gauges have comparable resolving power, despite the former being very limited in number; but the results of inversions for the Maule event indicate that DARTs have higher spatial sensitivity for mapping the coseismic slip. Thus, in principle, DART data are preferable to the tide-gauge data or at least deserve to be weighted more in the inversion. However, even if with a lower weight, the results here indicate that the tide-gauges data should not be excluded. If they are the only tsunami sensors available for studying a tsunamigenic event, they can be reliably inverted as long as one uses OTA to mitigate bias from incorrect time alignment (Ho et al., 2019). The experiments carried out, described, and discussed in the present study are summarized and represented also in the form of a flowchart in **Supplementary Material Figure S20**.

CONCLUSION

We reanalyze the 2010 Maule earthquake by jointly inverting geodetic (GPS, InSAR, land-level) and tsunami (DART, tide-gauge) data by incorporating the optimal time alignment (OTA) method in the inversion. This allows the estimation of the earthquake slip distribution taking into account, in an automatic and non-subjective way, the time mismatch between observed and predicted tsunami waveforms. The Maule earthquake offered an opportunity to benchmark the OTA method. The resulting rupture pattern confirms bilateral rupture propagation, including a significant amount of slip (~10 m) near the trench within the northern slip patch, as previously indicated by (theoretical phase-corrected) DART data inversions. The presence of significant slip in the shallower portion of the subduction interface is supported by a comparison between seafloor deformation predicted for the OTA joint inversion estimated slip distribution and directly observed deformation for a repeated bathymetric survey off the Maule region. Finally, the inversion results show that DARTs outperform tide-gauges in estimating the slip distribution of a tsunamigenic event, giving an objective basis for the relative weights to be assigned in this type of joint inversion using the two data types.

DATA AVAILABILITY STATEMENT

The original contributions presented in the study are included in the article/**Supplementary Material**, further inquiries can be directed to the corresponding author.

AUTHOR CONTRIBUTIONS

FR was involved in all of the phases of this study. SL and TL contributed to design the Experiment, discuss and interpret the results, and to writing the manuscript. AP contributed to design the Experiment, discuss and interpret the results. MV, SM, and RT contributed to the tsunami data analysis and to discuss the results. All authors reviewed the final manuscript.

FUNDING

This work has been partially funded by EC project ASTARTE - Assessment, STrategy and Risk Reduction for Tsunamis in Europe. Grant 603839, 7th FP (ENV.2013.6.4-3 ENV.2013.6.4-3) and the Italian Flagship Project RITMARE. TL's earthquake research is supported by U.S. National Science Foundation grant EAR1802364.

ACKNOWLEDGMENTS

We wish to thank the Intergovernmental Oceanographic Commission of UNESCO (IOC) (http://www.ioc-sealevelmonitoring.org/), the University of Hawaii sea level center (https://uhslc.soest.hawaii.edu), and the National Oceanic and Atmospheric Administration (NOAA, http://www.ndbc.noaa.gov/dart.shtml) for providing tsunami data; the Japan Aerospace Exploration Agency (http://global.jaxa.jp/) for providing the ALOS-PALSAR data; the International Global Navigation Satellite Systems Service and the French Centre National de la Recherche Scientifique - Institut National des Sciences de l'Univers (INSU, France, http://igscb.jpl.nasa.gov/) for providing GPS data (https://gpscope.dt.insu.cnrs.fr/). Figures in the main text and Supporting Information made use of GMT (https://www.generic-mapping-tools.org) and MATLAB (www.mathworks.com) software. We thank three anonymous reviewers for their valuable comments and suggestions.

SUPPLEMENTARY MATERIAL

The Supplementary Material for this article can be found online at: https://www.frontiersin.org/articles/10.3389/feart.2020.585429/full#supplementary-material.

REFERENCES

Allgeyer, S., and Cummins, P. (2014). Numerical tsunami simulation including elastic loading and seawater density stratification. *Geophys. Res. Lett.* 41, 2368–2375. doi:10.1002/2014GL059348

Bletery, Q., Sladen, A., Delouis, B., and Mattéo, L. (2015). Quantification of tsunami bathymetry effect on finite Fault Slip inversion. *Pure Appl. Geophys.* 172, 3655–3670. doi:10.1007/s00024-015-1113-y

Delouis, B., Nocquet, J.-M., and Vallée, M. (2010). Slip distribution of the February 27, 2010 Mw = 8.8 Maule Earthquake, central Chile, from static and high-rate GPS, InSAR, and broadband teleseismic data. *Geophys. Res. Lett.* 37, 235. doi:10.1029/2010GL043899

Farías, M., Vargas, G., Tassara, A., Carretier, S., Baize, S., Melnick, D., et al. (2010). Land-level changes produced by the Mw 8.8 2010 Chilean earthquake. *Science.* 329, 916. doi:10.1126/science.1192094

Fritz, H. M., Petroff, C. M., Catalán, P. A., Cienfuegos, R., Winckler, P., Kalligeris, N., et al. (2011). Field survey of the 27 February 2010 Chile tsunami. *Pure Appl. Geophys.* 168, 1989–2010. doi:10.1007/s00024-011-0283-5

Fujii, Y., and Satake, K. (2013). Slip distribution and seismic moment of the 2010 and 1960 Chilean earthquakes inferred from tsunami waveforms and coastal geodetic data. *Pure Appl. Geophys.* 170, 1493–1509. doi:10.1007/s00024-012-0524-2

Fujii, Y., and Satake, K. (2006). Source of the July 2006 West Java tsunami estimated from tide gauge records. *Geophys. Res. Lett.* 33, 569. doi:10.1029/2006GL028049

Giraud, J., Pakyuz-Charrier, E., Ogarko, V., Jessell, M., Lindsay, M., and Martin, R. (2018). Impact of uncertain geology in constrained geophysical inversion. *ASEG Extend. Abstr.* 2018, 1–6. doi:10.1071/aseg2018abm1_2f

Grezio, A., Babeyko, A., Baptista, M. A., Behrens, J., Costa, A., Davies, G., et al. (2017). Probabilistic tsunami hazard analysis: multiple sources and global applications. *Rev. Geophys.* 55, 1158–1198. doi:10.1002/2017RG000579

Hauksson, E., and Shearer, P. (2005). Southern California hypocenter relocation with waveform cross-correlation, Part 1: results using the double-difference method. *Bull. Seismol. Soc. Am.* 95, 896–903. doi:10.1785/0120040167

Hayes, G. P., Bergman, E., Johnson, K. L., Benz, H. M., Brown, L., and Meltzer, A. S. (2013). Seismotectonic framework of the 2010 February 27 Mw 8.8 Maule, Chile earthquake sequence. *Geophys. J. Int.* 195, 1034–1051. doi:10.1093/gji/ggt238

Ho, T.-C., Satake, K., Watada, S., and Fujii, Y. (2019). Source estimate for the 1960 Chile earthquake from joint inversion of geodetic and transoceanic tsunami data. *J. Geophys. Res. Solid Earth.* 124, 2812–2828. doi:10.1029/2018JB016996

Kajiura, K. (1963). The leading wave of a tsunami. *Bull. Earthq. Res. Inst. Univ. Tokyo.* 41, 535–571.

Kanamori, H. (1972). Mechanism of tsunami earthquakes. *Phys. Earth Planet. Int.* 6, 346–359. doi:10.1016/0031-9201(72)90058-1

Koper, K. D., Hutko, A. R., Lay, T., and Sufri, O. (2012). Imaging short-period seismic radiation from the 27 February 2010 Chile (MW 8.8) earthquake by back-projection of P, PP, and PKIKP waves. *J. Geophys. Res.: Solid Earth.* 117, 289. doi:10.1029/2011JB008576

Kozdon, J. E., and Dunham, E. M. (2014). Constraining shallow slip and tsunami excitation in megathrust ruptures using seismic and ocean acoustic waves recorded on ocean-bottom sensor networks. *Earth Planet Sci. Lett.* 396, 56–65. doi:10.1016/j.epsl.2014.04.001

Lay, T. (2018). A review of the rupture characteristics of the 2011 Tohoku-oki Mw 9.1 earthquake. *Tectonophysics.* 733, 4–36. doi:10.1016/j.tecto.2017.09.022

Lay, T., Ammon, C. J., Kanamori, H., Koper, K. D., Sufri, O., and Hutko, A. R. (2010). Teleseismic inversion for rupture process of the 27 February 2010 Chile (Mw 8.8) earthquake. *Geophys. Res. Lett.* 37, 568. doi:10.1029/2010GL043379

Lin, Y. N., Sladen, A., Ortega-Culaciati, F., Simons, M., Avouac, J.-P., Fielding, E. J., et al. (2013). Coseismic and postseismic slip associated with the 2010 Maule earthquake, Chile: characterizing the Arauco Peninsula barrier effect. *J. Geophys. Res.: Solid Earth.* 118, 3142–3159. doi:10.1002/jgrb.50207

Liu, P. L. F., Woo, S. B., and Cho, Y. S. (1998). *Computer programs, for tsunami propagation and inundation, Technical report*. Cornell University.

Lorito, S., Romano, F., Atzori, S., Tong, X., Avallone, A., McCloskey, J., et al. (2011). Limited overlap between the seismic gap and coseismic slip of the great 2010 Chile earthquake. *Nat. Geosci.* 4, 173–177. doi:10.1038/ngeo1073

Lorito, S., Romano, F., and Lay, T. (2016). "Tsunamigenic major and great earthquakes (2004–2013): source processes inverted from seismic, geodetic, and sea-level data," in *Encyclopedia of Complexity and systems science*. Editor R. A. Meyers (Berlin, Heidelberg: Springer), 1–52. doi:10.1007/978-3-642-27737-5_641-1

Maksymowicz, A., Chadwell, C. D., Ruiz, J., Tréhu, A. M., Contreras-Reyes, E., Weinrebe, W., et al. (2017). Coseismic seafloor deformation in the trench region during the Mw8.8 Maule megathrust earthquake. *Sci. Rep.* 7, 45918. doi:10.1038/srep45918

Moreno, M., Melnick, D., Rosenau, M., Baez, J., Klotz, J., Oncken, O., et al. (2012). Toward understanding tectonic control on the Mw 8.8 2010 Maule Chile earthquake. *Earth Planet Sci. Lett.* 321 (322), 152–165. doi:10.1016/j.epsl.2012.01.006

Murphy, S., Di Toro, G., Romano, F., Scala, A., Lorito, S., Spagnuolo, E., et al. (2018). Tsunamigenic earthquake simulations using experimentally derived friction laws. *Earth Planet Sci. Lett.* 486, 155–165. doi:10.1016/j.epsl.2018.01.011

Murphy, S., Scala, A., Herrero, A., Lorito, S., Festa, G., Trasatti, E., et al. (2016). Shallow slip amplification and enhanced tsunami hazard unravelled by dynamic simulations of mega-thrust earthquakes. *Sci. Rep.* 6, 35007. doi:10.1038/srep35007

Nosov, M. A., and Kolesov, S. V. (2011). Optimal initial conditions for simulation of seismotectonic tsunamis. *Pure Appl. Geophys.* 168, 1223–1237. doi:10.1007/s00024-010-0226-6

Okada, Y. (1992). Internal deformation due to shear and tensile faults in a half-space. *Bull. Seismol. Soc. Am.* 82, 1018–1040.

Piatanesi, A., and Lorito, S. (2007). Rupture process of the 2004 sumatra–Andaman earthquake from tsunami waveform inversion. *Bull. Seismol. Soc. Am.* 97, S223–S231. doi:10.1785/0120050627

Pollitz, F. F., Brooks, B., Tong, X., Bevis, M. G., Foster, J. H., Bürgmann, R., et al. (2011). Coseismic slip distribution of the February 27, 2010 Mw 8.8 Maule, Chile earthquake. *Geophys. Res. Lett.* 38, 735. doi:10.1029/2011GL047065

Romano, F., Lorito, S., Piatanesi, A., and Lay, T. (2020). "Fifteen years of (major to great) tsunamigenic earthquakes" in *Reference module in earth systems and environmental sciences*. New York: Elsevier. doi:10.1016/B978-0-12-409548-9.11767-1

Romano, F., Piatanesi, A., Lorito, S., and Hirata, K. (2010). Slip distribution of the 2003 Tokachi-oki Mw 8.1 earthquake from joint inversion of tsunami waveforms and geodetic data. *J. Geophys. Res. Solid Earth.* 115, 648. doi:10.1029/2009JB006665

Romano, F., Piatanesi, A., Lorito, S., Tolomei, C., Atzori, S., and Murphy, S. (2016). Optimal time alignment of tide-gauge tsunami waveforms in nonlinear inversions: application to the 2015 Illapel (Chile) earthquake. *Geophys. Res. Lett.* 43 (11), 226–311. doi:10.1002/2016GL071310

Romano, F., Trasatti, E., Lorito, S., Piromallo, C., Piatanesi, A., Ito, Y., et al. (2014). Structural control on the Tohoku earthquake rupture process investigated by 3D FEM, tsunami and geodetic data. *Sci. Rep.* 4, 5631. doi:10.1038/srep05631

Satake, K. (1995). Linear and nonlinear computations of the 1992 Nicaragua earthquake tsunami. *PAGEOPH.* 144, 455–470. doi:10.1007/BF00874378

Sen, M. K., and Stoffa, P. L. (2013). *Global optimization methods in geophysical inversion*. Cambridge: Cambridge University Press. doi:10.1017/CBO9780511997570

Tong, X., Sandwell, D., Luttrell, K., Brooks, B., Bevis, M., Shimada, M., et al. (2010). The 2010 Maule, Chile earthquake: downdip rupture limit revealed by space geodesy. *Geophys. Res. Lett.* 37, 235. doi:10.1029/2010GL045805

Tsai, V. C., Ampuero, J.-P., Kanamori, H., and Stevenson, D. J. (2013). Estimating the effect of Earth elasticity and variable water density on tsunami speeds. *Geophys. Res. Lett.* 40, 492–496. doi:10.1002/grl.50147

Vigny, C., Socquet, A., Peyrat, S., Ruegg, J.-C., Métois, M., Madariaga, R., et al. (2011). The 2010 Mw 8.8 Maule megathrust earthquake of Central Chile, monitored by GPS. *Science.* 332, 1417–1421. doi:10.1126/science.1204132

Watada, S., Kusumoto, S., and Satake, K. (2014). Traveltime delay and initial phase reversal of distant tsunamis coupled with the self-gravitating elastic Earth. *J. Geophys. Res. Solid Earth.* 119, 4287–4310. doi:10.1002/2013JB010841

Yamazaki, Y., Cheung, K. F., and Kowalik, Z. (2011). Depth-integrated, non-hydrostatic model with grid nesting for tsunami generation, propagation, and run-up. *Int. J. Numer. Methods Fluid.* 67, 2081–2107. doi:10.1002/fld.2485

Yoshimoto, M., Watada, S., Fujii, Y., and Satake, K. (2016). Source estimate and tsunami forecast from far-field deep-ocean tsunami waveforms—the 27 February 2010 Mw 8.8 Maule earthquake. *Geophys. Res. Lett.* 43, 659–665. doi:10.1002/2015GL067181

Yue, H., Lay, T., Rivera, L., An, C., Vigny, C., Tong, X., et al. (2014). Localized fault slip to the trench in the 2010 Maule, Chile Mw = 8.8 earthquake from joint inversion of high-rate GPS, teleseismic body waves, InSAR, campaign GPS, and tsunami observations. *J. Geophys. Res. Solid Earth.* 119, 7786–7804. doi:10.1002/2014JB011340

Zhang, H., and Thurber, C. H. (2003). Double-difference tomography: the method and its application to the Hayward fault, California. *Bull. Seismol. Soc. Am.* 93, 1875–1889. doi:10.1785/0120020190

Conflict of Interest: The authors declare that the research was conducted in the absence of any commercial or financial relationships that could be construed as a potential conflict of interest.

frontiers
in Earth Science

ORIGINAL RESEARCH
published: 18 January 2021
doi: 10.3389/feart.2020.594176

Deformation Pattern of the Northern Sector of the Malta Escarpment (Offshore SE Sicily, Italy): Fault Dimension, Slip Prediction, and Seismotectonic Implications

Salvatore Gambino[1], Giovanni Barreca[1,2], Felix Gross[3,4], Carmelo Monaco[1,2,5], Sebastian Krastel[3] and Marc-André Gutscher[6]*

[1]Department of Biological, Geological and Environment Sciences, University of Catania, Catania, Italy, [2]CRUST—Interuniversity Center for 3D Seismotectonics with Territorial Applications, Chieti, Italy, [3]Institute of Geosciences, Kiel University, Kiel, Germany, [4]Center for Ocean and Society, Kiel University, Germany, Kiel, [5]Istituto Nazionale di Geofisica e Vulcanologia, Osservatorio Etneo, Catania, Italy, [6]Laboratoire Géosciences Ocean, UMR6538 CNRS/University of Brest, Plouzané, France

Marine seismic reflection data coupled with on-land structural measurements improve our knowledge about the active deformation pattern of the northern sector of the Malta Escarpment, a bathymetric and structural discontinuity in the near-offshore of Eastern Sicily. As favourably oriented to be reactivated within the Neogene Africa–Europe convergence, it is believed that the Malta Escarpment has a significant role in the recent seismotectonic framework of the Western Ionian Basin and the Hyblean foreland domain of SE Sicily, where some of the largest and most destructive Mediterranean earthquakes are located according to available historical catalogs. Offshore seismic data along with bathymetric grids illuminate the shallow subseafloor setting and allow more accurate mapping of the seafloor expression of previously identified faults in the area. The seismic interpretation and the near-fault sediment pattern analysis provide constraints on fault 3D geometries as well as on their through-time tectonic activity, suggesting also that part of the observed deformation may have been caused by nontectonic processes. Identified faults form currently an E-dipping, roughly N–S trending, and 60 km-long extensional belt deforming the seafloor with a significant displacement amount in the Ionian offshore between Catania and Siracusa. 3-dimensional parameters of faults were then used to derive expected magnitudes and their reactivation propensity. Empirical scaling relationships and forward methods point to a high seismic potential for the detected fault as well as predict the fault slip behavior according to the field-derived differential stress. This combined analysis along with faults displacement measurements pointed out how the longest and most continuous fault could be capable of generating M > 7 seismic events, putting forward strong seismotectonic implications for the adjacent and densely populated Hyblean Plateau. The expected magnitude and the estimated recurrence time interval are compatible with those inferred for large historical earthquakes in the area even if other offshore seismic sources cannot be ruled out.

Keywords: seismic potential, fault slip prediction, 3D data modeling, recent/active tectonics, field deformation pattern, offshore seismic investigation, malta escarpment

OPEN ACCESS

Edited by:
Sebastiano D'Amico,
University of Malta, Malta

Reviewed by:
Andrea Billi,
National Research Council (CNR), Italy
Mario Mattia,
National Institute of Geophysics and Volcanology (INGV), Italy
Francesco Muto,
University of Calabria, Italy

****Correspondence:***
Giovanni Barreca
g.barreca@unict.it

Specialty section:
This article was submitted to Structural Geology and Tectonics, a section of the journal Frontiers in Earth Science

Received: *12 August 2020*
Accepted: *16 November 2020*
Published: *18 January 2021*

Citation:
Gambino S, Barreca G, Gross F, Monaco C, Krastel S and Gutscher M-A (2021) Deformation Pattern of the Northern Sector of the Malta Escarpment (Offshore SE Sicily, Italy): Fault Dimension, Slip Prediction, and Seismotectonic Implications. Front. Earth Sci. 8:594176. doi: 10.3389/feart.2020.594176

INTRODUCTION

The Malta Escarpment in the Western Ionian Basin (Southern Italy, **Figure 1**) is a 300 km long structural and bathymetric discontinuity inherited from the Permian–Triassic paleotectonic setting (Scandone et al., 1981; Fabbri et al., 1982; Casero et al., 1984) separating at that time two sectors of the African plate with different crustal thickness/rheology: the thinned/oceanic Ionian Basin to the east and the Hyblean continental "promontory" to the west. More recently, this inherited discontinuity has been partly reactivated in the frame of the Nubia–Eurasia convergence dynamics and forms an impressive NNW–SSE trending submarine fault-scarp in the near-offshore of the densely populated SE Sicily. Although debated, several studies have considered this tectonic structure as a potential source for major historical earthquakes and tsunamis in Eastern Sicily in historical times (Piatanesi and Tinti, 1998; Bianca et al., 1999; Azzaro and Barbano, 2000; Argnani and Bonazzi, 2005; Argnani et al., 2012). For this reason, it is considered a key feature for the seismotectonics of SE Sicily and the Western Ionian Basin. Based on macroseismic data and numerical modeling (Mulargia et al., 1985; Barbano and Rigano, 2001; Sirovich and Pettenati, 2001; DISS working group,

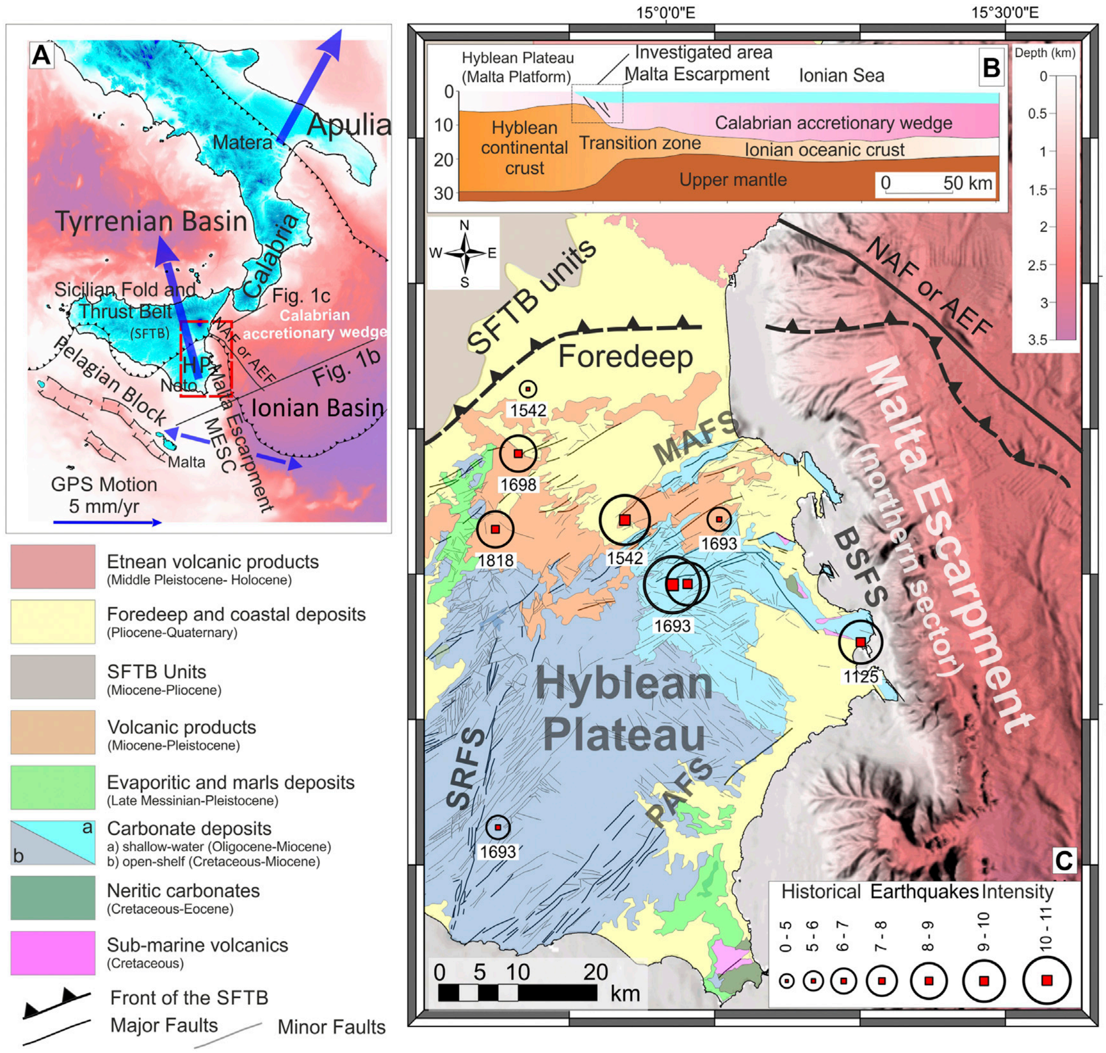

FIGURE 1 | (A) The Malta Escarpment framed in the structural setting of the central Mediterranean region. Large blue arrows indicate diverging geodetic velocities (see Ward 1994; Mastrolembo et al., 2014; D'Agostino and Selvaggi, 2004; Grenerczy et al., 2005; Palano et al., 2012) measured in the lower plate (Hyblean Plateau and Apulia Block) of the collisional system. The diverging motion resolves a resultant WNW–ESE extension along the E-Sicily/Western Ionian Basin domain (small blue arrows) where the inherited NNW–SSE trending Malta Escarpment occurs. **(B)** Structurally, the investigated area places at the shallow portion of an ancient (Permo–Triassic) ocean–continent transition domain where the Malta Escarpment is widely considered to be a Mesozoic passive margin related either to E-W spreading of an Ionian oceanic ridge (see Catalano et al., 2001), or as has been recently suggested a transform margin, related to NE-SW extension (Gallais et al., 2011; Dellong et al., 2018). **(C)** Structural setting of the Malta Escarpment footwall block, the SE Sicily. Black circles indicate the epicentres of the most energetic historical earthquakes occurred in the area. Acronyms are as follows: SRFS, Scicli–Ragusa Faults System; PAFS, Pozzallo–Avola Faults System; MAFS, Monterosso–Agnone Faults System; BSFS, Brucoli–Siracusa Faults Systems; NAF of AEF, North Alfeo Fault or Alfeo Etna Fault (Gutscher et al., 2016; Polonia et al., 2016).

2018) and according to CPTI15 reference catalog (Rovida et al., 2016), epicentres of most historical events (e.g., February 4, 1169, and January 11, 1693, events, among the most destructive) have been positioned in the footwall of this tectonic feature. Whatever the source, Southeastern Sicily, forming the footwall block of the Malta Escarpment, is one of the most seismically active areas in Europe having experienced many destructive earthquakes (M > 5.5) and associated tsunamis (Boschi et al., 1995; Tinti et al., 2001; Tinti et al., 2004; Jenny et al., 2006).

Despite the many authors mentioned above, identifying the Malta Escarpment as the most likely fault system as having produced most of the historical and recent earthquakes, evidence of recent/active tectonics has so far remained elusive. This is due to the absence or scant evidence of faulted Quaternary sediments on-land and to the unavailability of offshore data capable of adequately imaging the shallow subseafloor environment, where the youngest sediments occur. Accordingly, the seismic potential of the Malta Escarpment along with its structural architecture, fault dimension, and kinematics, as well as deformation rate, remains poorly understood. In this study, we present a detailed investigation of the structural architecture of the northernmost sector of the Malta Escarpment by using marine geophysical data with unprecedented resolution, field constraints, and data modeling. Interpretation of 2D seismic reflection profiles provides further constraints on the tectonic setting of the investigated area allowing for the classification of the activity and the geometric parameters of the detected faults. All available 2D seismic data were analyzed to build-up a consistent 2½D model of the fault planes. Reconstructed fault surfaces combined with stress orientations coming from field investigations performed alongshore Southeastern Sicily allow us to evaluate their seismic potential by assessing the likelihood of their reactivation.

GEOLOGICAL SETTING

The Malta Escarpment (hereinafter MESC) is a steep, E-facing submarine slope with a total bathymetric drop of more than 3,000 m (**Figure 1A**). Structurally, it marks the ocean–continent transition zone as its separates two sectors of the African margin with different lithospheric thicknesses: the thinned (oceanic) Ionian Basin to the east and the Hyblean continental promontory to the west (Dellong et al., 2018, **Figure 1B**). This transition zone is a remnant of a paleotectonic setting related to the Permo–Triassic opening of the Neo-Tethys (Şengör, 1979) and to the subsequent Jurassic–Cretaceous spreading stage (Ben-Avraham and Grasso, 1991; Catalano et al., 2001; Gallais et al., 2011; Dellong et al., 2018). Successively, this passive paleomargin has been reactivated during the Neogene convergence between Africa and Eurasia plates as it is oriented transversally (NNW–SSE) to the roughly E–W trending of the advancing front of the resulting collisional system (**Figure 1A**). The progressive foreland-ward migration of the collisional system involved the ocean–continent preorogenic configuration leading to the shaping of the Sicilian fold and thrust belt (SFTB in **Figure 1A**) to the west and the Calabrian accretionary wedge to the east (**Figure 1A**). In this context, the impingement of the collisional front against the MESC paleotopography probably allowed the passive margin to be reactivated by oblique extension during the Plio–Quaternary (Scandone et al., 1981; Fabbri et al., 1982; Casero et al., 1984; Bianca et al., 1999; Palano et al., 2012). The footwall block of the MESC is locally known as the Hyblean Plateau (**Figure 1C**), and it represents the emergent of a larger foreland domain, the Pelagian Block (Burollet et al., 1978; Ben-Avraham and Grasso, 1991, **Figure 1A**), a 25–30 km thick continental crustal compartment of the African margin. The Hyblean Plateau sedimentary covers consist of 10 km-thick, Meso–Cenozoic open-shelf to shallow-water carbonate sequences, hosting several intercalations of volcanic products (Patacca et al., 1979; Bianchi et al., 1987; Grasso et al., 2004). The Quaternary top sequences are widespread all over the plateau edges on the coastal domains where they are generally preserved within fault-bounded structural depressions (Grasso and Lentini, 1982, **Figure 1C**).

Structurally, the Hyblean Plateau consists of a rigid, highly fractured crustal intender delimited by the front of the Sicilian Fold and Thrust Belt to the north–west and by the MESC to the east (**Figure 1C**). This structural pattern, strongly influenced by inherited Mesozoic structures (Grasso and Reuther, 1988; Henriquet et al., 2019) is dominated by major structural features and associated minor structures pervasively deforming the plateau. The NW and SE margins are controlled by large, NE–SW trending normal fault systems (Monterosso–Agnone and Pozzallo–Avola fault systems, respectively, see Cultrera et al., 2015, **Figure 1C**) which have been associated with flexural bulging processes (Pedley and Grasso, 1992; Cogan et al., 1989; Billi et al., 2006). To the west, the Hyblean Plateau is sliced by a roughly N–S-oriented strike-slip fault belt known as the Scicli–Ragusa fault system (Ghisetti and Vezzani, 1980; Grasso and Reuther, 1988). The eastern margin is structurally controlled by an NNW–SSE, E-dipping extensional fault system (Brucoli–Siracusa fault system, **Figure 1C**) encompassing the MESC and its associated on-land structures. Here, Plio–Quaternary tectonic activity is testified by the occurrence of syntectonic sediments within extensional basins mainly occurring on the footwall of MESC, whereas in the hanging wall, located offshore, Quaternary deformation was imaged through deep-penetrating but low-resolution seismic lines (Bianca et al., 1999; Adam et al., 2000; Argnani and Bonazzi, 2002; Argnani and Bonazzi, 2005). More recently, some authors framed the MESC in the Ionian subduction dynamics, interpreting it as the upper crustal expression of a deep-seated lateral tear in the Ionian lithosphere (Subduction Transform Edge Propagator—STEP fault, see Argnani and Bonazzi, 2005; Govers and Wortel, 2005; Polonia et al., 2012; Argnani et al., 2013). However, since STEP fault propagation typically produces alongside vertical-axis structural rotations (see Govers and Wortel, 2005; Barreca et al., 2016), the adjacent paleomagnetically unrotated Hyblean Plateau (Grasso et al., 1983; Cifelli et al., 2004) doesn't support a STEP behavior for the MESC. Late Quaternary sense of motion along the MESC is also still debated primarily due to the impossibility of measuring African plate movements in the offshore and also due to the lack of clear temporal and kinematic constraints on-land. Based on

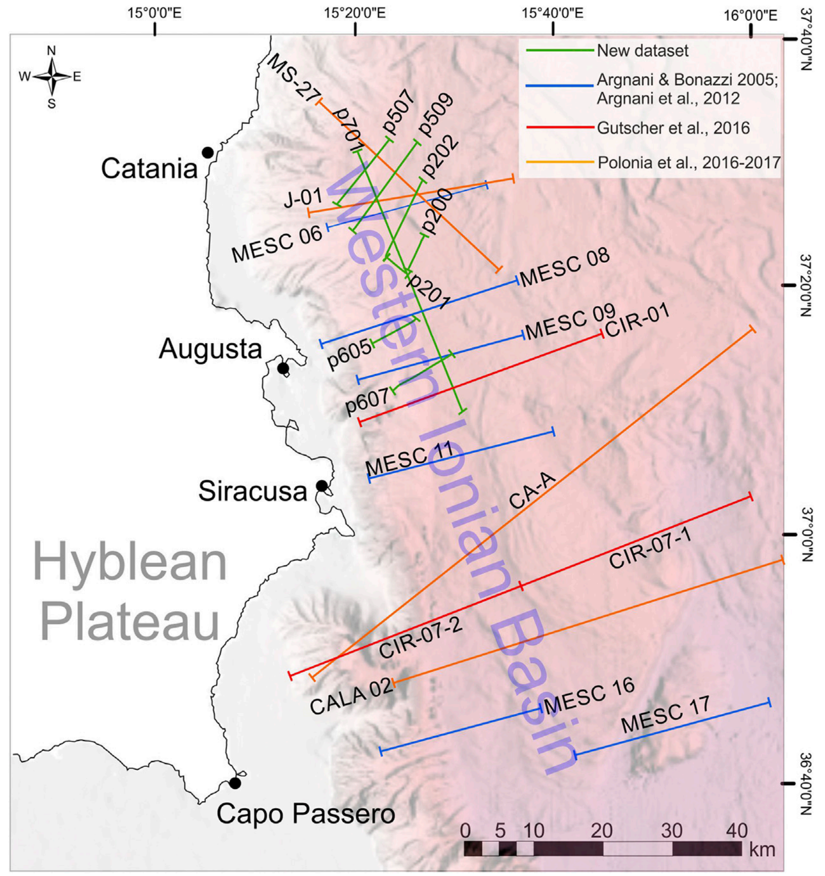

FIGURE 2 | Location of the interpreted seismic dataset in the offshore of SE Sicily. The dataset includes new seismic profiles (green lines) and previously published geophysical data.

neotectonic observations, Adam et al. (2000) suggested that onshore structures related to the MESC fault system are characterized by left-lateral kinematics. Although doubtful, this assertion appears to be consistent with seismological data (Amato et al., 1995; Musumeci et al., 2014). On the contrary, regional-scale geodynamic interpretations (e.g., Doglioni et al., 2001) and seismological (Presti et al., 2013) and geodetic data (Palano et al., 2012) suggest a right-lateral component of motion for the considered fault system. Diverging GPS vectors measured on the lower plate (including the Hyblean and Adria blocks, see Ward 1994; Mastrolembo et al., 2014; D'Agostino and Selvaggi, 2004; Grenerczy et al., 2005) indicates the latter as a crustal domain extending according to the resultant ESE–WNW-oriented vector (**Figure 1A**). In this geodynamic frame, the NNW–SSE trending MESC should have been reactivated with an oblique (right-lateral transtensional) component of deformation.

DATA AND METHODS

The analyzed data primarily consist of seismic reflection lines recorded during various marine geophysical cruises performed in the Western Ionian Basin (**Figure 2**). Interpreted seismic data consist of high-resolution seismic profiles sounded in the frame of the CIRCEE-HR project (R/V le Suroît, October 2013, see also Gutscher et al., 2016) and Poseidon expedition POS496 (R/V Meteor, March–April 2016, see also Krastel, 2016). The CIRCEE-HR seismic data were acquired using a 450 m long, 72 channel Sercel seismic streamer with an average geophone spacing of 6.25 m. The seismic source was a six mini-GI airgun array with a total volume of 111 cubic inches fired at a cadence of once every 6 s, for an average shot spacing of 16 m and a 24-fold coverage for each common midpoint. Quality control of the seismic data, including processing of the navigation files (shot position and streamer geometry), was performed with the SISPEED software (Ifremer). The seismic data were subsequently bandpass filtered (70–425 Hz), stacked, and time migrated (water velocity of 1500 m/s), using the Seismic Unix software package. During cruise POS496, an 80-channel digital solid-state Geometrics GeoEel streamer with a group interval of 1.5625 m was used for seismic acquisition. A Sercel Mini GI-Gun seismic source, with a total volume of 0.4 L, was shot in a harmonic mode. The shot interval was set to 6 s, resulting in a shot distance of ~12 m at a ship's speed of four knots. The seismic profiles were processed by using the commercial software package Schlumberger Vista Seismic Processing. The processing workflow includes bandpass filtering with corner frequencies of 40/80/600/1000 Hz, despiking, debias filtering, CMP binning, and normal-move-out (NMO) correction. All data were time migrated by using the software's finite difference migration. Due to the relatively short streamer and the high water depths, no dedicated velocity analysis could be applied during NMO correction and migration. Hence, a constant velocity of 1500 m/s was applied. Moreover, other published seismic dataset (Argnani and Bonazzi, 2002; Argnani and Bonazzi, 2005; Argnani et al., 2012; Polonia et al., 2016; Polonia et al., 2017) and high-resolution bathymetry (Gutscher et al., 2016; Gutscher et al., 2017) were considered to better constraint the spatial extension of faults at the seafloor and their in-depth geometry.

Only the most representative seismic lines will be described in detail in this article (see *Deformation Pattern and Fault Activity*), whereas basic line drawing of the POS496 dataset (TWT) and of the entire time to depth-converted seismic dataset (including published seismic lines) can be found in the Supplementary Material (**Supplementary Figures 1 and 2**). To obtain geometric realistic parameters of the faults, seismic profiles (**Supplementary Figure 3A**) were time/depth converted by assigning average acoustic velocity to the two-way travel time sequence thickness (see *Seismic Stratigraphy*). The adopted acoustic velocity model was achieved from previous studies in the area (Gallais et al., 2011; Gross et al., 2016; Kokinou et al., 2013; Le Meur, 1997; Maeasano et al., 2017), and it is reported in **Supplementary Table 1**. Once time/depth converted, 2D linear features (fault traces and top/base reflectors) picked all along the seismic dataset (**Supplementary Figure 3B**) were modeled as 2½D features using common interpolation methods (e.g., kriging and IDW, **Supplementary Figure 3C**) operated into the Move 2019.1 geomodelling software package (Petex Ltd.). Bathymetric fault expression allowed us to further constrain the along-strike fault geometry (see **Supplementary Material**).

The local stress field orientation was derived by structural measurements performed on-land in the adjacent coastal sector. Structural data consist of mesofaults and fracture planes attitude and kinematic indicators mainly collected along the outcropping Miocene carbonate and Quaternary top sequences (see **Supplementary Table 2**). Even if the weak lithology (coarse sandstones, gravels, etc.) of Quaternary deposits does not usually favor the development or preservation of kinematic indicators, movement directions along faults planes have been obtained by tectogrooves, Riedel fractures, and rare slickenlines. All data were digitally stored on field by using Field Move Mobile App and finally analyzed and plotted using the FaultKin eight software (Allmendinger et al., 2012; Cardozo and Allmendinger, 2013) by adopting Schmidt's lower hemisphere projection.

Obtained stress field orientation was compared to other data concerning the modern deformation field at local and regional scales and finally applied on the 2½ D modeled fault surfaces to predict their tendency to the tectonic reactivation.

OFFSHORE GEOPHYSICAL DATA

Seismic Stratigraphy

Interpretation of seismic profiles allowed us to recognize four main seismic units based on i) their seismic features (e.g., amplitude, lateral continuity, and frequency of internal reflectors), ii) bounding discontinuities, and iii) strata architecture. Accordingly, basin-fill seismostratigraphic units were distinguished and labeled from older to younger as pre-MES, MES, and PQ, and the latter was furtherly subdivided into the subunits PQ_1 and PQ_2 (**Figure 3A**). The units are generally confined between well-defined discontinuities that have been interpreted as angular and/or erosional unconformities (S1, S2, and S3 in **Figure 3A**).

The pre-MES (acoustic basement) consists of a chaotic, locally transparent unit occasionally characterized by isolated and highly reflective bodies (**Figure 3B**). To the west, the seismic unit is truncated upward by an erosive surface (S1 in **Figure 3A**), a paleoslope above in which the younger units unconformably deposited, generally with on-lap and/or off-lap geometries (**Figure 3B**). The overlying MES unit is characterized by low- to medium-amplitude reflectors with medium frequency and locally subparallel geometry (**Figure 3B**). The unit is limited upwards by the S2 discontinuity (**Figure 3A**) that consists of an irregular erosive surface above which the overlying units often rest in paraconformity (**Figure 3B**). The PQ_1 unit consists of a variable in thickness alternance of low- to high-amplitude, low-medium frequency, subparallel or occasionally cross-stratified continuous reflectors (**Figure 3B**). Toward the west, along the MESC slope, the PQ_1 unit on-laps directly on the pre-MES unit, while upwards, it is delimited by the S3 discontinuity that is locally represented by an undulated erosive truncation. Close to the fault planes, the unit includes wedge-shaped seismic bodies with chaotic facies thinning away from the faults (**Figure 3C**). To the bottom, the PQ_1 unit is locally floored by a semitransparent seismic unit (subunit PQ_1a in **Figure 3A**) that, although discontinuously, was detected in most of seismic lines, where generally, it occurs within structural depressions or paleochannels (**Figure 3D**). The overlying PQ_2 unit is characterized by high-frequency, laterally continuous, parallel, and high-amplitude reflectors (**Figure 3B**). Locally, the PQ_2 unit on-laps against or down-laps on the older PQ_1 unit, and it is limited upwards by the seafloor.

In the absence of drill-hole data from the sediment section, we provide a basic lithological interpretation of the detected seismic units by following the available literature and by comparing the marine geophysical data with the on-land geology. The pre-MES unit is not well highlighted by the seismic signal, but locally its seismic features are consistent with carbonate-type sequences, a lithology widely outcropping on-land. Accordingly, the pre-MES unit has been interpreted as a Cenozoic sediment package that includes mainly limestone and marls, locally pierced by volcanic and/or mud intrusions forming sometimes cone-shaped seamounts at the seafloor (**Figure 3A**) (see also Scandone et al., 1981; Catalano et al., 2001; Barreca, 2014). According to its seismic characters (high reflectivity of the top reflector) and to the abundant literature concerning similar deposits occurring all around the Mediterranean basin (Lofi et al., 2011; Micallef et al., 2019 and references therein), the MES unit has been interpreted as Messinian in age deposits (mainly gypsum and evaporitic carbonate). The overlying Unit PQ_1 is interpreted as a part of the Pliocene succession since it correlates with the subunits "PQb"

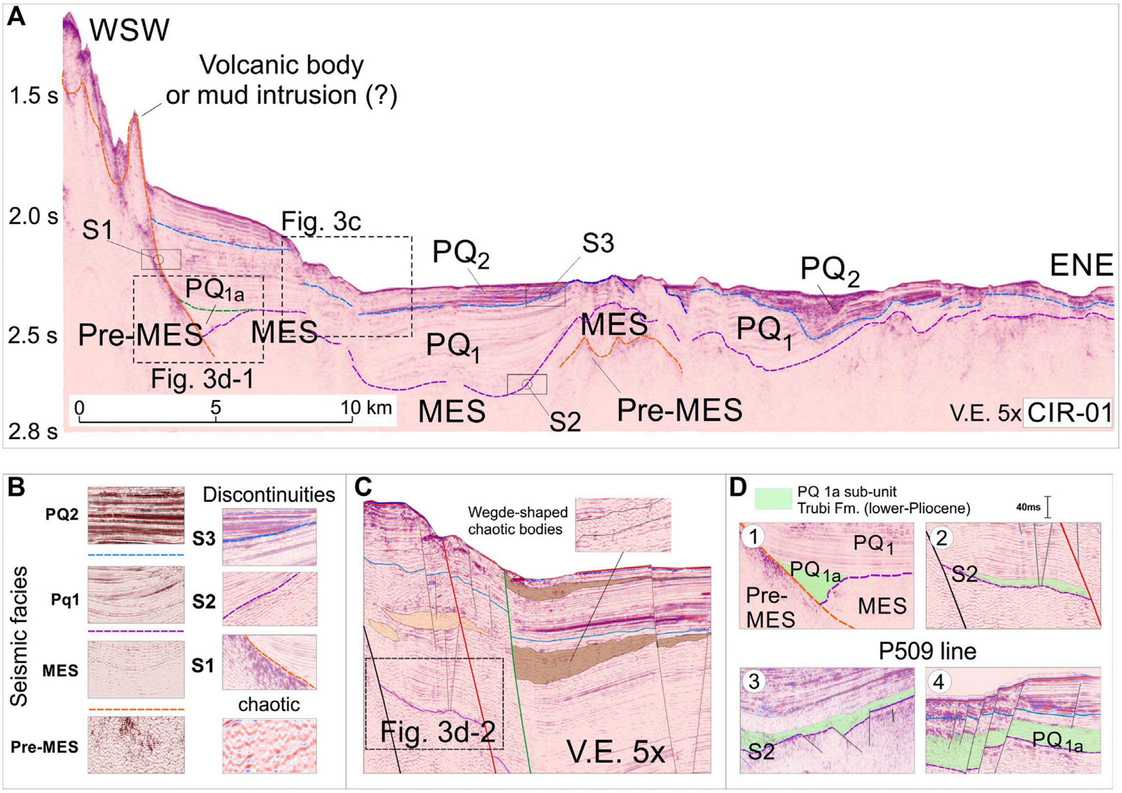

FIGURE 3 | (A) Seismostratigraphic analysis performed over the representative CIR-01 line displaying the recognized seismic facies/units and bounding discontinuities **(B)**. **(C)** In the upper part of the Pliocene section and within the Pleistocene succession, wedge-shaped chaotic bodies occur supporting syntectonic sedimentation during the considered time interval. **(D)** The base of Pliocene section is occasionally and discontinuously floored by a semitransparent seismic unit (PQ1a) interpreted as a Zanclean in age Trubi Fm.

and "PQc" described by Camerlenghi et al. (2019) and partly with the "Unit one" of Micallef et al. (2018). The basal portion of this unit is locally characterized by the occurrence of a semitransparent body ($PQ_{1}a$ in **Figure 3D**) that for its stratigraphic position is interpreted as the Zanclean in age Trubi formation (Butler et al., 2015). The seismic character of the PQ_2 unit suggests that it consists of a well-layered alternance of marly–arenaceous succession. Accordingly, PQ_2 unit can be interpreted as part of the Pleistocene sequence since it correlates for stratigraphic position and lithology with the distal part of the Panchina formation, outcropping on-land and characterized by Middle-Late Pleistocene sands and biocalcarenites (Servizio Geologico d'Italia, 2011). Moreover, it correlates with the PQa unit of Camerlenghi et al. (2019), whose basal erosional surface has been dated at 650 ka from DSDP site 374 cores (Hsü et al., 1978).

Deformation Pattern and Fault Activity

Displaced reflectors observed throughout the entire seismic dataset (**Supplementary Figure 1B**) and the analysis of the available bathymetric data (i.e., Gutscher et al., 2017 and Emodnet database) have allowed depicting the tectonic pattern that characterizes the northernmost sector of the Malta Escarpment. The recognized tectonic structures form an array of sea-dipping, NNW–SSE trending, dip-slip faults extending offshore from Catania (in the north) to Siracusa (in the south) for a total length exceeding 60 km (**Figures 4** e-f). Within the system, three major faults segments (F1, F2, and F3 in **Figure 4A**) and minor faults (F4 and F5) have been structurally and geometrically characterized following their offsets in seismic lines and their bathymetric expression (see **Supplementary Material**). The F1 fault segment is the westernmost tectonic structure of the system and consists of an E-dipping, roughly N–S trending, 45 km-long, dip-slip fault. Following the seafloor expression, the F1 fault terminates against the NAF (North Alfeo Fault of Gutscher et al., 2016 or Alfeo–Etna Fault of Polonia et al., 2016, see **Figures 1A,C** for location) as suggested by cross-cutting relations. To the south, F1 merges to F3, the longest fault of the system. The fault has propagated throughout the illuminated subseafloor setting and has displaced the detected seismostratigraphic units with variable offsets (**Figure 4B**). According to the adopted time/depth conversion model (see **Supplementary Table 1** and *Offshore Geophysical Data*), F1 has displaced the base of the PQ_1 (S2 surface) and PQ_2 (S3 surface) units up to 460 and 260 m, respectively. Displacement has propagated up to the seafloor producing in average a vertical offset of about 70 m with a maximum value (about 150 m) along the MESC09 line. The F2 fault segment occurs about 2 km east of

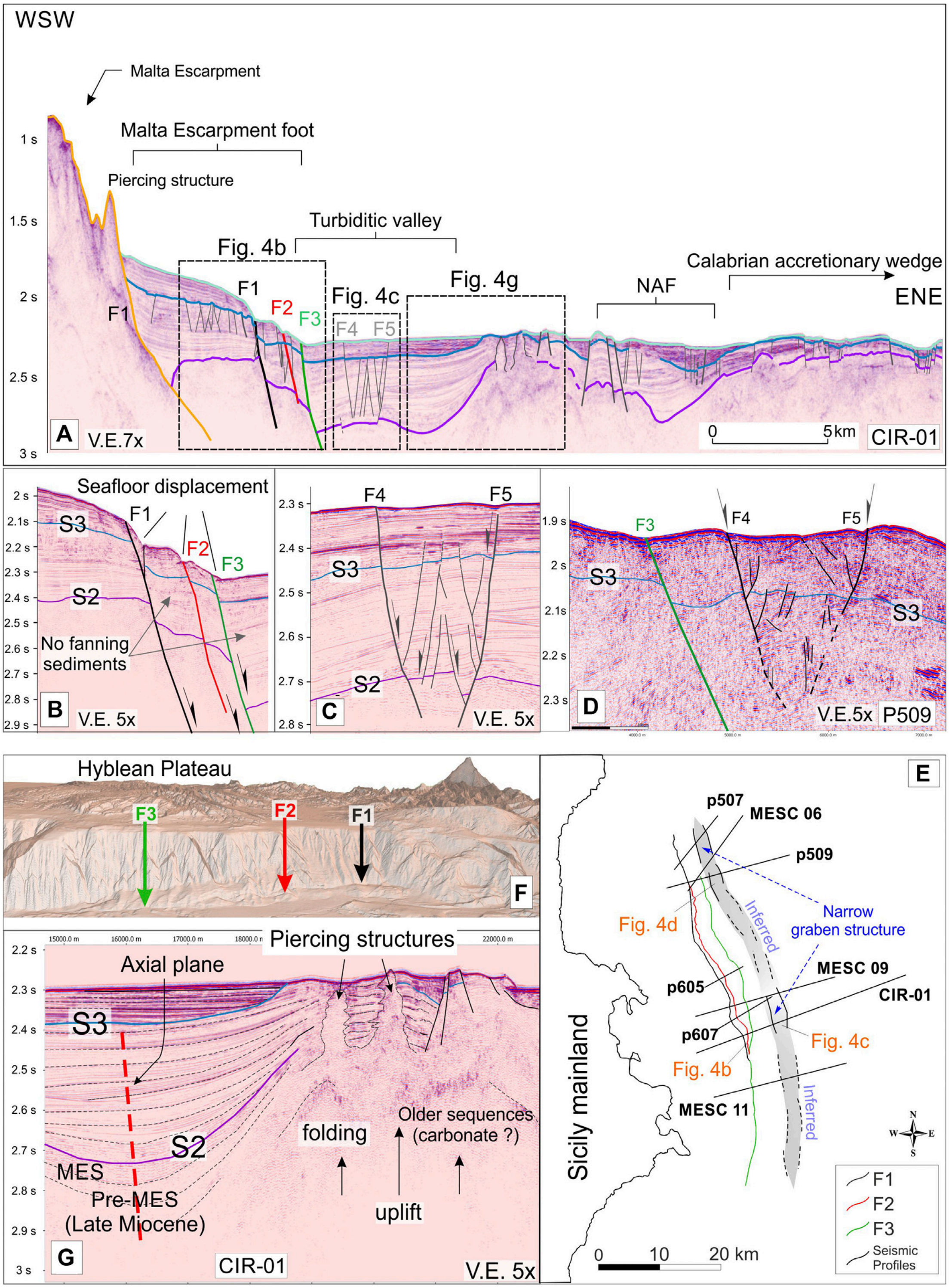

FIGURE 4 | (A) 3D perspective view of the interpreted seismic dataset. **(B)** Structural interpretation performed over the CIR-01 line showing the tectonic features occurring in the area. **(C)** Extensional E-dipping fault system deforming the foot of the Malta Escarpment and narrow graben structure propagating through the turbiditic valley recognized along the CIR-01 **(D)** and P509 **(E)** seismic lines. Structural interpretation on the whole seismic dataset (see **Supplementary Figure 2**) allows to map accurately faults in the E-Sicily offshore **(F)** also following their bathymetric expression **(G)**. **(H)** Folded and diapirically pierced structure occurring in the western portion of the CIR-01 line and sediment pattern on its western limb.

F1 and consists of an E-dipping, NNW-oriented, 34 km-long fault structure. To the north, F2 converges toward F1, whereas to the south toward F3 (**Figure 4E**). This array suggests F2 as a subordinated splay fault. Fault activity has produced in average displacement in the S2 surface (MES top reflector) of about 150 m and in the S3 surface (PQ1 top reflector) of about 65 m, whereas seafloor appears to be displaced in average of about 30 m (**Figure 4B**). The F3 fault segment is the easternmost structure of the system controlling the foot of the MESC. The structure consists of an E-dipping, NNW trending fault with a total length of about 57 km. It has deformed the whole illuminated seismostratigraphic succession, displacing in average the S2 and S3 discontinuities of about 150 and 47 m, respectively (**Figures 4B,D**). Further east, a narrow (about 3.5 km wide) graben structure deforms the abyssal plain occupied by a 7 km-wide, N–S-oriented, sedimentary basin (turbidic valley of Gutscher et al., 2016, see **Figure 4A**). The graben structure roughly extends from the CIR-01 line, in the South (see **Figure 2** for location), to the Catania offshore, in the north, whereas its continuation further south has been only inferred because of lack of good quality seismic lines (see **Figure 4E**). It is bounded by opposite-dipping normal faults (F4 and F5 in **Figure 4A**), both characterized by a moderate offset gradually increasing with depth (**Figures 4C–D**). Diffuse minor splays associated with the major bounding faults internally deform the down-faulted block. The interpreted seismic dataset (see **Supplementary Figures 1 and 2**) revealed the continuity of the detected faults all along the offshore E Sicily, allowing to map accurately their spatial distribution (**Figure 4E**) and to follow their bathymetric expression at the seafloor (**Figure 4F**).

It is worth noting that a prominent structural culmination occurs to the east of the analyzed fault system, bounding the turbiditic valley (the uplifted area of Argnani and Bonazzi, 2005). It consists of ~10 km-wide folded sectors interpreted as a positive flower structure related to the recent activity of the North Alfeo Fault System by Gutscher et al. (2016) or as a forced fold related to the upraise of a mantle-derived serpentinite diapirs by Polonia et al. (2017). Seismostratigraphy and growth geometry on the limbs of the folded structure suggests that it was active from the Late Miocene up to the Late Pliocene before being eroded on its top (S3 discontinuity), sealed by Pleistocene sediments, and it was finally pierced by some diapiric structures (**Figure 4G**). Accordingly, the time-growing of the folds indicates that they cannot be related to the recent activity of the North Alfeo Fault nor (as proposed by Argnani and Bonazzi, 2002; Argnani and Bonazzi, 2005) to the tectonic shortening of the deformation front of the Calabrian accretionary wedge since it was located far away (>100 km) to the NW during the Late Miocene–Pliocene. In this frame, most of the diverging pattern of the upper Miocene–Pliocene strata is interpreted as related to the time-growing uplifting of the fold system rather than to the Quaternary activity of North Alfeo and/or MESC faults, accounting thereby for a more recent onset of the extensional deformation in the area. The occurrence of some wedge-shaped, chaotic seismic bodies thinning away from the faults mainly within the PQ_2 unit (see *Seismic Stratigraphy* and **Figure 3C**) along with the very slight sediment thickening observed close to the F1, F2, and F3 faults in the older sections (**Figure 4B**) support, in fact, the initiation of extensional tectonic activity around the Early Pleistocene. During this period, slight fanning strata and the nondevelopment of a typical sedimentary wedge opening toward the faults should be charged to the consistent rate of sedimentation (about 0.4 mm/yr) characterizing the Pliocene section that was higher than the tectonic rate of the three extensional faults (<0.1 mm/yr, see *Deformation Pattern and Fault Activity*).

Fault Displacement Analysis and Deformation Rate

With the aim of estimating the deformation rate of tectonic structures characterizing the MESC, a fault displacement analysis was performed on the time/depth-converted seismic dataset (see **Supplementary Figure 2**). The displacement produced by the activity of the main detected faults (F1, F2, and F3) was measured considering the vertical component (throw) and using fault-displaced reference timelines (S2, S3, and S4-seafloor, see **Supplementary Table 3**). Throws measured along each fault for the S2 (top-MES), S3 (top-PQ1), and the seafloor describe in general an along-strike variable pattern with displacements decreasing from the fault center to the tips (**Figure 5**). Longitudinal trends for F1 and F2 faults define a double bell-shaped pattern for the three displaced timelines with relative maxima of throw (about 460 and 300 m, respectively) recorded by the older F1-displaced S2 surface, whereas the younger S3 is less deformed by the same fault as it reaches the maximum offset of about 260 m (**Figures 5A,B**). By contrast, longitudinal throw trend of the F3 structure outlines a double bell-shaped pattern only for the older S2 surface, whereas S3 and the seafloor timelines (S4) tend to assume an irregular pattern resembling a single bell-shaped throw curve (**Figure 5B**). Displacement of the seafloor was analyzed to evaluate the recent deformation history of the detected faults even if a large uncertainty could affect offset estimation, related to the erosive or depositional nature of the seafloor. Nonetheless, the along-strike trend of the seafloor throw produced by the considered faults displays different patterns varying from a double bell-shaped curve for the F1 structure (**Figure 5A**) to a single bell-shaped curve for the F2 and F3 structures (**Figure 5C**). The recent and combined activity of the faults has produced a cumulative offset at the seafloor of ~210 m.

Based on the vertical and along-dip offsets measured on the displaced S2 (top-MES), S3 (top-PQ_1), and on the seafloor (S4) reference timelines and considering time intervals for the fault-deformed sections PQ1 (Pliocene, 2.75 Myr), PQ2 (Middle-Upper Pleistocene, 0.63 Myr, see *Seismic Stratigraphy*), and ~Holocene (0.0117 Myr), the long- and short-term throw (T_r) and propagation rates (P_r) for the three main faults have been estimated (**Figures 5E,F,G**). Accordingly, measured vertical (T_r) and along-dip (P_r) displacement components were restored at the considered time interval by removing from the cumulated older offsets the contribution of the younger fault movement. During the Pliocene, faults slipped simultaneously but with different rates according to the measured two-component of movement, in average higher for the F1 (T_R ~ 0.05 mm/yr and P_R ~ 0.09 mm/yr) and lower for the F2 (T_R ~0.04 mm/yr and P_R~

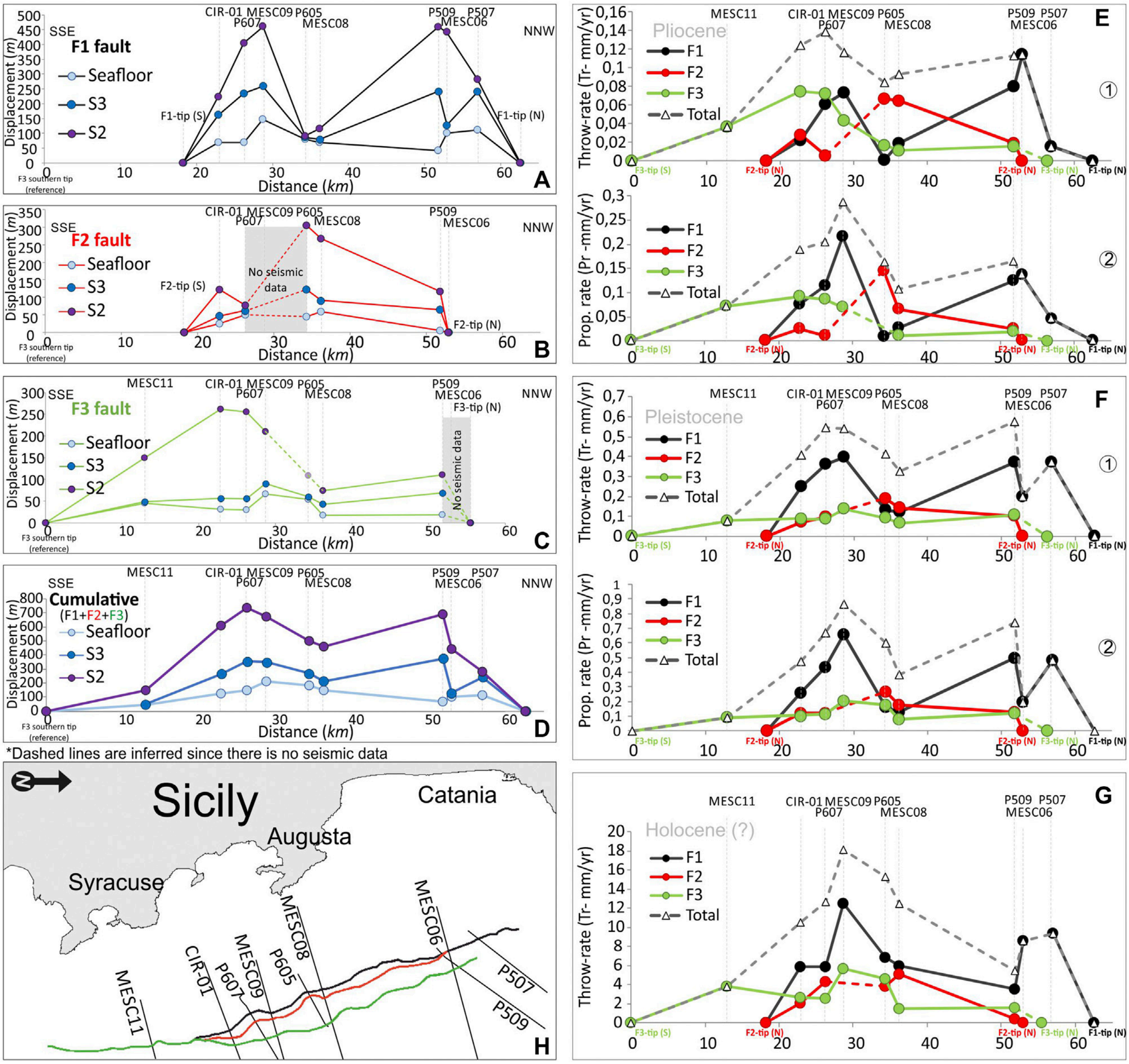

FIGURE 5 | Vertical displacement (throw) analysis performed for the F1 **(A)**, F2 **(B)**, and F3 **(C)** extensional structures based on the fault-displaced reference timelines (S2, S3, and seafloor S4). Amount of vertical and along-dip displacements for each fault allows to calculate their throw and propagation rate for the Pliocene **(D)**, Pleistocene **(E)**, and Holocene **(F)** time intervals.

0.05 mm/yr) and F3 (T_R~ 0.04 mm/yr and P_R ~0.06 mm/yr), respectively (**Figures 5E1–2** and **Supplementary Table 4**). Since the Middle Pleistocene, faults accelerated slipping at a higher rate compared to the Pliocene. During this time interval, the F1 still slipped faster (in average T_R~ 0.27 and P_R~0.4 mm/yr) than the F2 (in average T_R~ 0.12 and P_R~0.16 mm/yr) and F3 (in average T_R~ 0.04 and P_R~ 0.12 mm/yr), respectively (**Figure 5F**). In this stage, the segmented F1 and F2 evolved (fault linkage) in well-defined structures. The poorly constrained Holocene deformation pointed out a further acceleration of the faults during this time interval even if, as stated above, large uncertainties (erosion, slope instability, etc.) could affect bathymetric throw measurements. T_R for F1 and F2 reaches in average the value of ~7.3 and 3.1 mm/yr, respectively, whereas about 3.2 mm/yr has been calculated for the F3 structure (**Figure 5G**). The high throw rate value calculated for the F1 suggests that this value could be amplified by a nontectonic component. Conversely, throw rates for F2 and F3 are consistent with tectonic deformation and coherent with the return periods for large earthquakes in the area (see *Discussion*).

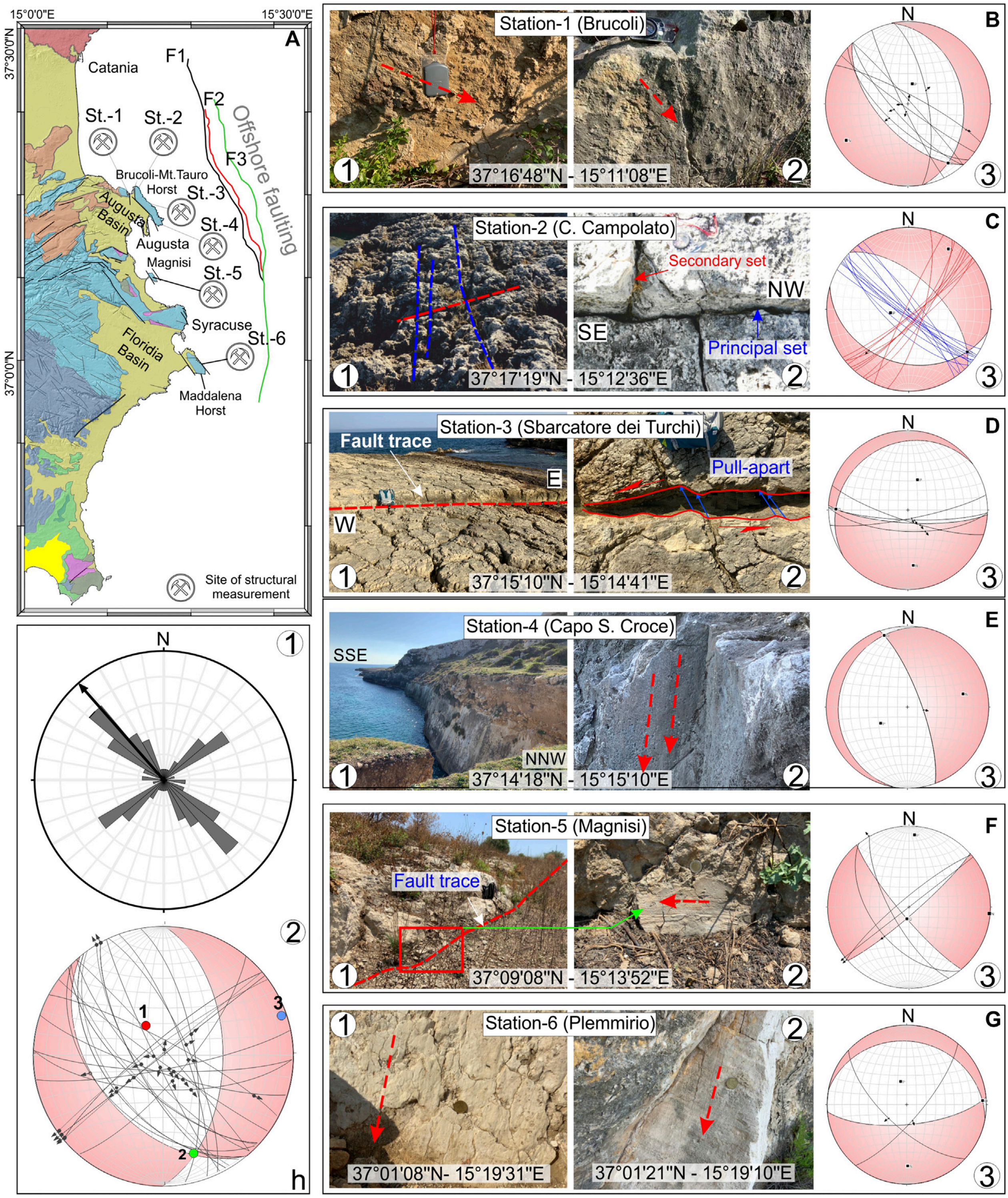

FIGURE 6 | (A) Location of the sites of structural measurements performed along the footwall block of the Malta Escarpment (SE Sicily coastal domain, see **Figure 1B** for the geology on-land) and collected fault planes and kinematic indicators **(B–G)**. Diagrams on the right panels (Schmidt lower hemisphere) show faults plane attitude and movement on the respective hanging walls (black arrows) and calculated pseudofocal mechanisms. h-1) Rose diagram of the whole mesostructural dataset showing the faults having a dominant strike in the range N130–140E. h-2) Stress field derived from slip-data inversion highlighting the area as deformed under a slightly transtensional tectonic regime characterized by a ~70° plunging, NNW–SSE trending σmax.

ON-LAND STRUCTURAL DATA

To derive the orientation of the local stress field, geostructural data were collected in six key sites along the Hyblean coastal domain, between the cities of Augusta and Syracuse, on the footwall block of the offshore faults that were analyzed (**Figure 6A**). According to available geological maps (Carbone et al., 1984; Carbone et al., 1986; Servizio Geologico d'Italia, 2011), in this area Lower-Middle Miocene carbonates mostly outcrop, unconformably covered by a regressive Quaternary sequence made up of marly-clays, sands, and calcarenites. The investigated sector has been deformed by an array of NNW–SSE trending and dip-slip/oblique faults (**Figure 6A**) whose activity has produced horst (i.e., Brucoli–Mt. Tauro, Magnisi, and Maddalena) and graben (i.e., Augusta and Floridia Basins) structural associations whose bounding structures are roughly coaxial to the faults detected in the offshore (see *Deformation Pattern and Fault Activity* and **Figure 6A** for location).

Faults and Fractures

Along the Brucoli–Mt. Tauro horst structure, in the North (**Figure 6A**), Miocene and Quaternary deposits have been mainly deformed by oblique faults systems and associated fracturing. In the Brucoli area (Station-1, **Figure 6A**), mesostructures mostly consist of subvertical (70–80° dipping) NNW–SSE and NW–SE trending fault segments. Kinematic indicators (slickenlines and rare tectogrooves, see **Figure 6B**), suggest oblique right-lateral and dip-slip movement and a rare left-lateral component on the NNW–SSE and NW–SE-oriented fault planes, respectively (see diagram in **Figure 6B**). At the Capo Campolato locality, in the northern termination of the Mt. Tauro–Brucoli structural culmination (station-2, **Figure 6A**), outcropping carbonates are pervasively deformed by a system of extensional cross-joints (**Figure 6C**). The system is arranged in a ladder-like geometry with a more continuous and principal joint-set-oriented NW–SE and a secondary one oriented orthogonally according to the NE–SW direction (see diagram in **Figure 6C**). At Sbarcatore dei Turchi (station-3, **Figure 6A**), a system of south-dipping, roughly E–W striking fault planes has been measured (**Figures 6D–L**). Sense of movement on fault planes was derived by dislocated geological markers exposed on both sides of the structures. The reconstructed vertical and lateral component of movement (resulting slip-vector plunging toward the SE at 60–80°) and alongside pull-apart basins (**Figure 6D**) suggest oblique, left-lateral kinematics for the detected fault planes (see diagram in **Figure 6D**). At Capo S. Croce locality (station-4, **Figure 6A**) in the southernmost termination of the Mt. Tauro–Brucoli horst, structural measurements were performed on the eastern border fault. The structure is well exposed along the coastline where it forms a subvertical sea cliff (**Figures 6E–L**) and consists of an ENE-dipping, NNW–SSE trending fault. Slickensides on fault plane dipping at 70° toward the N65E direction (**Figures 6E-2**) indicate an extensional dip-slip sense of movement according to an ENE trending extension (see diagram in **Figure 6E-3**). Further south, data were collected along the Magnisi Peninsula (station-5, **Figure 6A), a** narrow carbonate horst bounded by NNW–SSE trending faults (**Figure 6F**). Slickensides on mesostructures planes were collected on the landward side of the peninsula where strike-slip faults with related pull-apart basins and associated fractures occur (**Figure 6F**). The few kinematic indicators suggest a right-lateral sense of movement for the detected faults (see diagram in **Figure 6F**). Some data have also been collected along the Maddalena horst south of Syracuse (station-6, **Figure 6A**) which consists of NW–SE and NE–SW trending oblique right-lateral transtensional mesofaults (**Figure 6G**).

Stress Field

The paleostress tensors for the onland faults were derived by using directional statistics (e.g., Linked Bingham Analysis, Bingham, 1974) that is based primarily on the slip-data inversion of fault planes exhibiting clear kinematic indicators. Extensional joints pattern measured at the station two were included, considering that, in a ladder-like joint arrangement, the orientation of the principal joints-set (the more continuous, **Figure 6C**) coincide with that of the maximum stress axis (Bai and Pollard, 2000; Bai et al., 2002). Data analysis revealed that the on-land area has been deformed by an array of slightly (right-lateral) oblique faults oriented in a prevailing NNW–SSE direction (18.75% between N131 and 140E, see rose diagram in **Figure 6H**) developed under a stress field characterized by a 70° plunging, nearly N–S-oriented (N330E) σ max and by a subhorizontal, about E–W oriented σmin (**Figure 6H**). Slip-data inversion also provides a pseudofocal mechanism which is characterized by a P-axis plunging toward N332E at about 70° and by a subhorizontal T-axis-oriented N70E (**Figure 6H**). Although field measurements and slip-data inversion point to the on-land faults being deformed under a slight transtensional tectonics regime, the propagation of the tectonic structures through the Quaternary sequences remains doubtful; accordingly, the age of last deformation events is not fully determinable. Despite this, the comparison of our results with other published data concerning stress tensors at local and regional scales suggests that the derived stress field is compatible with the recent kinematic of SE Sicily. In fact, computed ENE–WSW trending $\sigma_{\min}$ is roughly consistent with i) the regional NE–SW to WNW–ESE extension derived from inversion of slickensides data on fault planes (Adam et al., 2000; Monaco and Tortorici, 2000; De Guidi et al., 2013), ii) geodetic data (D'Agostino and Selvaggi, 2004; Mattia et al., 2012; Palano et al., 2012), and iii) the local ENE–WSW trending minimum stress resulting from boreholes breakout data analysis in the eastern sector of the Hyblean Plateau (Ragg et al., 1999; Montone et al., 2012).

FAULT MODELING AND SEISMOTECTONIC POTENTIAL

Structural interpretation and interpolation of 2D seismic profiles and time/depth conversion of seismic dataset along with faults bathymetric expression (see *Deformation Pattern and Fault Activity* and **Supplementary Table 1** for adopted velocity model) allowed us to build up a simplified but consistent

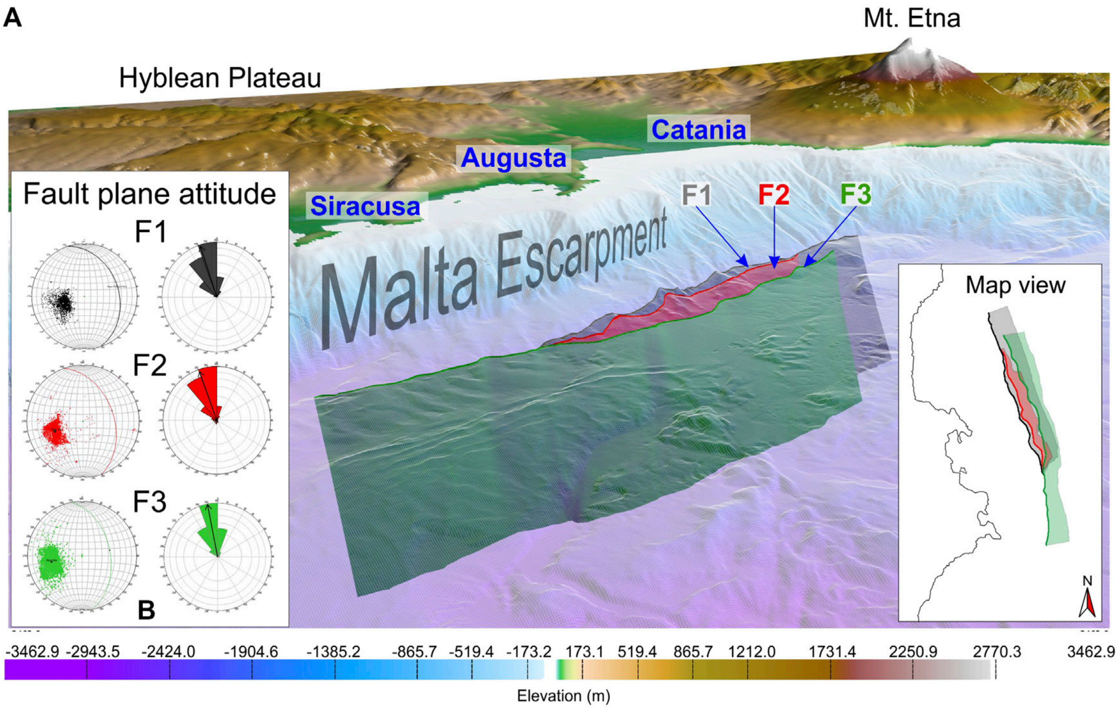

FIGURE 7 | (A) 2½D fault surfaces (perspective view from the SE) modeled according to reference lines (fault traces) picked along the seismic dataset (see **Supplementary Figure 1** for the workflow) and related attitude in the 3D environment **(B)**.

TABLE 1 | Geometric parameters derived from the 2½D data modeling and expected magnitudes from empirical-scaling relationships (Wells and Coppersmith, 1994; Leonard, 2010). Note that, according to fault segmentation inferred from the fault displacement analysis (see *Fault Displacement Analysis and Deformation Rate*), seismic potential for F1 and F2 faults may be overestimated.

Geometric parameters		**F1**			**F2**			**F3**	
Mean strike		**N345E**			**N340E**			**N352E**	
Mean dip (°)		**36**			**46**			**49**	
Length (km)		**44.44**			**33.72**			**56.46**	
Fault depth range and width (m)	min	Width*	Max*	min	Width*	Max*	min	Width*	Max*
	−1,813	**4,337**	−6,150.5	−1908	**3,322**	−5,230	−1854	**5,275**	−7,129
Area (km^2)*		276.92			98.65			334.05	
					Expected magnitude, Wells and Coppermisth (1994)				
	min	*mean*	*max*	*min*	*mean*	*max*	*min*	*mean*	*max*
M based on surface rupture length (SRL)	6.27	**7.03**	7.80	6.14	**6.88**	7.61	6.38	**7.17**	7.97
M based on rupture area (RA)*	5.95	**6.42**	6.90	5.53	**5.96**	6.39	6.02	**6.50**	6.99
M based on downdip rupture width (RW)*	6.27	**7.04**	7.81	6.15	**6.89**	7.63	6.38	**7.17**	7.97
					(*) underestimated				
					Expected magnitude, Leonard (2010)				
M based on surface rupture length (SRL)		**6.99**			**6.79**			**7.16**	
M based on rupture area (RA)*		**6.44**			**5.99**			**6.5**	
% difference WC94-L10 on SRL		**0.54**			**1.23**			**0.09**	
% difference WC94-L10 on RA		**0.32**			**0.5**			**0.3**	

2½D model of the faults occurring in the study area (**Figure 7A**, see also **Supplementary Figure 3** for the workflow). Although depth-limited, due to the penetration of the seismic signal in the subseafloor, the model provides an estimate of the geometric parameters (i.e., length, width, dipping, and strike, see **Figure 7B** and **Table 1**) for the shallow portion of the investigated faults. According to the reconstructed model and to the fault displacement analysis, the F1 consists of a roughly 45 km-long, two-branched structure-oriented N345E with a fault plane dipping toward the ENE at about 45°. The F2 is a N340E trending two-branched structure, about 35 km-long dipping at 50° toward the ENE. Finally, F3 is a continuous,

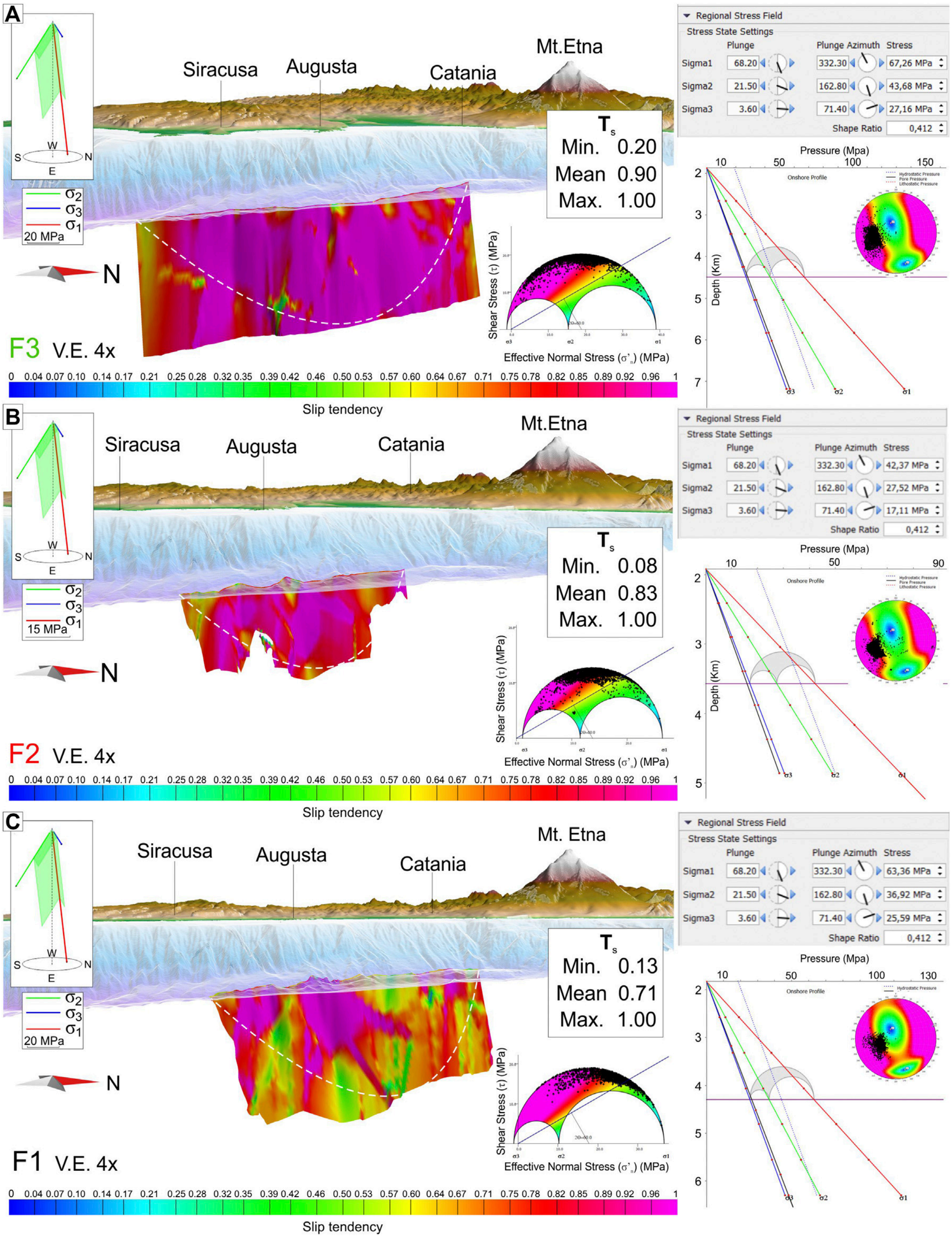

Regional Stress Field

Stress State Settings

	Plunge	Plunge Azimuth	Stress
Sigma1	68.20	332.30	67,26 MPa
Sigma2	21.50	162.80	43,68 MPa
Sigma3	3.60	71.40	27,16 MPa
		Shape Ratio	0,412

Regional Stress Field

Stress State Settings

	Plunge	Plunge Azimuth	Stress
Sigma1	68.20	332.30	42,37 MPa
Sigma2	21.50	162.80	27,52 MPa
Sigma3	3.60	71.40	17,11 MPa
		Shape Ratio	0,412

Regional Stress Field

Stress State Settings

	Plunge	Plunge Azimuth	Stress
Sigma1	68.20	332.30	63,36 MPa
Sigma2	21.50	162.80	36,92 MPa
Sigma3	3.60	71.40	25,59 MPa
		Shape Ratio	0,412

FIGURE 8 | Slip tendency analysis performed on the 2½D modeled fault surfaces **(A–C)** and based on the remotely applied stress field orientation. Stress parameters and related pressure profiles are showed in the right panels. Color overlaid on the fault surfaces indicates the propensity (blue = low and red = high) of faults to be reactivated according to the considered stress field. Dashed line indicates the possible fault planes boundaries.

roughly 60 km-long fault with a N352E-oriented fault plane dipping toward the east at 55° (see pole/attitude diagrams in **Figure 7B** and **Table 1**). Derived fault geometric parameters were then used as input data to estimate the maximum expected earthquake magnitude for each fault assuming a reactivation where there is a seismic slip along their entire length. Based on the surface rupture length (SRL) and the underestimated rupture area (RA) and considering fault segmentation (i.e., for F1 and F2, see **section 4.3**), empirical scaling relationships (Wells and Coppersmith, 1994; Leonard, 2010) put forward a high seismic potential for the most continuous F3 faults capable of generating events exceeding magnitude 7 (see also Trippetta et al., 2019). (**Table 1**). Even if fault reactivation depends on several parameters such us surface frictional characteristics, fault cohesion, shear normal stresses on the fault plane, and fluid pressure, potential reactivation of faults has been here evaluated through a slip tendency analysis (Morris et al., 1996), which defines the propensity of a surface to undergo slip when a stress is applied. Slip tendency (T_s) is based on Amonton's law which governs the slip of a cohesionless plane and is expressed by the shear/normal stress ratio acting on the surface (Morris et al., 1996). The formulation is

$$Ts = \tau/\sigma' \mathrm{n},$$

where τ is the shear stress and σ'_n is the effective normal stress (i.e., the normal stress minus fluid pressure) acting on the plane. Following the assumptions proposed in the Wallace–Bott hypothesis (Wallace, 1951; Bott, 1959) and using the stress analysis tools of Move 2019.1 software (Petex Ltd.), stress field tensors orientation derived from slip-data inversion (see *Stress Field*) were remotely applied to the modeled fault surfaces (**Figure 7**). Considering an average density of 2,600 and 1050 kg/m^3 for the overburden rocks and seawater, respectively, and approximating the maximum stress (σ_1) to the lithostatic load, a confining stress is resolved at a mean depth in the medium around each fault (see applied stress and relative pressure profiles for each fault in **Figure 8** right panels and in **Table 2**). Slip tendency computation (T_s in **Figure 8**) found that the F3 as the fault structure most prone to be reactivated along its entire length with the highest average T_s value (0.90) homogeneously distributed along the fault plane (**Figure 8A**). F2 also exhibits a high mean T_s value of 0.83 with a maxima (T_s = 1) reached mainly on the southern portion of the fault plane (**Figure 8B**). Conversely, F1 shows the lowest average T_s value (0.71) with a maxima (T_s = 1) occurring over limited and shallow portions of the fault plane mainly off Siracusa and Augusta (**Figure 8C**). Additionally, the fault displacement analysis (see *Fault Displacement Analysis and Deformation Rate*) suggests segmentation of the F1 and F2 faults (i.e., the double bell-shaped displacement pattern, see **Figure 5C**), suggesting these structures have grown following a segment linkage pattern. Accordingly, a lower seismic potential should therefore be applied to these tectonic structures. Conversely, fault displacement analysis revealed that the F3 fault structure has grown in a radial way since at least the Pleistocene whereby its seismic potential has likely not been overestimated.

TABLE 2 | Deviatoric stress applied to the modeled fault surfaces and considered elastic parameters of the medium.

Fault	σ1			σ2			σ3			Pore pressure (Mpa)	Cohesion (Mpa)	Friction angle (°)	Young's modulus (Mpa)	Poisson's ratio	Friction coeff.
	Magnitude (Mpa)	Azimuth (°)	Dip (°)	Magnitude (Mpa)	Azimuth (°)	Dip (°)	Magnitude (Mpa)	Azimuth (°)	Dip (°)						
F1	63.4	332.3	68.2	36.9	162.8	21.5	25.6	71.4	3.6	26.7	0	30	27,000	0.25	0.58
F2	42.4	332.3	68.2	27.5	162.8	21.5	17.1	71.4	3.6	16	0	30			
F3	67.3	332.3	68.2	43.7	162.8	21.5	27.2	71.4	3.6	28.3	0	30			

DISCUSSION

Structural interpretation of seismic reflection data on the Ionian Sea offshore of SE Sicily, field measurements, and 2½D data modeling provide further information on the tectonic pattern and deformation rates affecting the northernmost sector of the Malta Escarpment since the Pliocene times. Seismic data illuminates, with good resolution, the shallowest portion of some of the tectonic structures previously mapped in the area (e.g., Bianca et al., 1999; Argnani and Bonazzi, 2002; Argnani and Bonazzi, 2005; Argnani et al., 2012; Polonia et al., 2012; Gutscher et al., 2016, Maesano et al., 2020) providing an opportunity to better characterize their dimension and through-time tectonic activity. These data reveal that deformation in the Ionian Sea offshore of SE Sicily is accommodated by a nearly N–S trending fault belt that is composed of three main, E-dipping, and slightly oblique (right-lateral) fault segments (F1, F2, and F3 in **Figure 4**). Seismostratigraphic pattern analysis within the recognized seismic units was performed to achieve information on fault activity. However, the growth of the fold and thrust system located to the east of the investigated faults and the thickening of late Miocene–Pliocene sediment on its flanks (**Figure 4H**) has posed significant issues in discerning inception of the extensional phase in the area. Dipping toward the culmination of the axial plane of the fold deforming the late Miocene–Pliocene sediment wedge in the turbiditic valley (see **Figure 4H**) allows excluding that fanning and folding of the strata could be generated by a sedimentary draping process. Accordingly, even though the geometry of the sedimentary wedge could be associated with the Quaternary activity of the extensional faulting to the west, we attribute the growth strata pattern of Upper Miocene–Pliocene sediments mostly to the trough-time uplift of folded system. This interpretation accounts for a possible more recent onset of the extensional deformation reactivation of the northernmost sector of the Malta Escarpment.

Fault deformation rates point out the investigated area as a slow-rate extensional domain where fault activity was modulated through time. The longitudinal fault-throw trend and the through-time deformation rate provide further information on the inception of extensional tectonics in the area and on the growing mode of the faults. According to the along fault strain localization over time, the very low deformation rate affecting the faults during the Pliocene strongly confirms the onset of extensional deformation since that time (see *Seismic Stratigraphy*), hence simultaneously to the growing of the folded system eastwards (see above). The observed bell-shaped pattern on the longitudinal fault-throw trend reveals that F1 and F2 faults have grown discontinuously in the Pliocene and suggest that they are probably segmented into two branches (**Figures 5E–F**). Consequently, each of these faults appears to have grown in the near-surface mainly by segment linkage rather than in a radial way (see Cartwright et al., 1995 for further explanation) even if no overlapping setting and relay ramps have been resolved at the seafloor where their vertical offset decreases considerably. Fault segmentation pattern seems also to have characterized the F3 fault activity only during the Pliocene, whereas since the Pleistocene, this fault has grown in a radial way working as a continuous structure (**Figures 5E–F**). The increasing dip of the faults from west to east (36°, 46°, and 49°, respectively, for F1, F2, and F3, see **Table 1**) would suggest a rotational (simple shear) dominostyle deformation context where block-bounding faults, as the effect of rotation, become progressively unfavourably oriented to the maximum stress axis and new high-angle faults form. However, the simultaneous activity observed with the fault displacement analysis (see *Deformation Pattern and Fault Activity*) leads to interpret such faults as merging down-dip into a single tectonic structure even if depth penetration of seismic data does not resolve its deeper trajectory. Detected faults should be therefore thought of as low hierarchical-order splay structures through which the strain accumulated by the deeper and larger tectonic structure is partitioned at a shallow crustal level. Strain partitioning in the upper crust appears to be supported by the along-strike trend of displacements and throw rates (**Figure 5**).

By comparing the depicted tectonic pattern with other structural settings concerning passive margin worldwide (e.g., along the Pará-Maranhão Basin in the Brazilian equatorial margin, see Matos, 2000) and considering i) the long-lived (late Miocene–Pliocene) grown of the folds system, ii) its inferred simultaneous activity, during the Pliocene, with the extensional faults, iii) the high-rate of extensional deformation during the Holocene (in average about 5 mm/yr for the F1 and F2 structures, see **Figure 5G**) and iv) the low-angle and down-dip converging geometry of the F1, F2, and F3 faults, part of the observed deformations should be also charged to large-scale slope instability. According to this last hypothesis, both faults to the west and the fold to the east may have been initially nucleated by gravitational forces in a deep-seated gravitational slope deformation context. Later, in Quaternary times, a tectonic component of deformation probably prevailed as testified by the occurrence on the MESC footwall block (SE Sicily coastal domain) of a flight of out-of-water, Middle-Late Pleistocene marine terraces (Bianca et al., 1999), by oblique deformation on-land, and by the quite rectilinear fault traces at the seafloor. In this perspective, previous extensional faults related to the deep-seated gravitational slope deformation were obliquely reactivated since the Middle Pleistocene according to the E–W trending extensional kinematics resulting from regional-scale diverging motion affecting the lower plate of the collisional system (see **Figure 1A**).

Seismotectonic Implications

Whatever the process by which the normal faults were generated, earthquakes occurring in the area reveal that a seismogenic stress is anyway accumulating in the Western Ionian Basin at crustal level (see Musumeci et al., 2014). In this frame, considering that splays fall into an area, the SE Sicily, hit by large historical earthquakes (e.g., January 11, 1693, event with M = 7.4, Rovida et al., 2016), we estimated their seismic potential using empirical scaling relationships (Wells and Coppersmith, 1994; Leonard, 2010) and slip tendency analysis (Morris et al., 1996). Our combined analysis puts forward that the splays could be capable of generating high-energetic seismic events (see **Table 2**) and, among them, the longest and most continuous F3 fault could

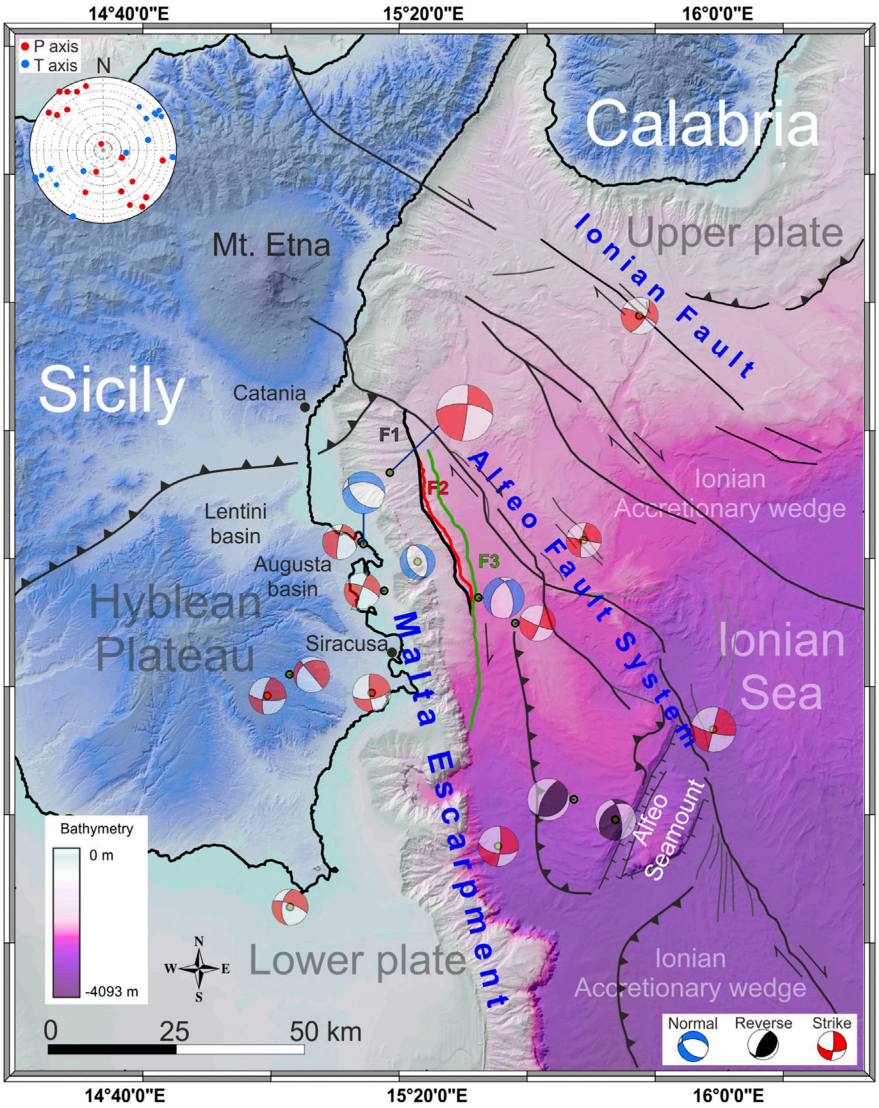

FIGURE 9 | Mapped faults (F1, F2, and F3) framed in the larger tectonic framework of the Western Ionian Basin. Alfeo Fault system and Ionian Fault are from Gutscher et al. (2016) and Polonia et al. (2016). Available focal solutions of M > 3.5 earthquakes (Pondrelli, 2002; Scarfi et al., 2013; Musumeci et al., 2014; Scarfi et al., 2016) and PT axes computation (see diagram in the top-left) support transtensional deformation in the studied area.

be the most prone structure to reactivation along its entire length which could therefore produce an earthquake exceeding magnitude 7. According to the empirical fault-scaling relationships (Wells and Coppersmith, 1994; Leonard, 2010), a 7.17 magnitude event expected for the F3 (see **Table 2**) would produce a maximum displacement (MD) of about 3 m or an average displacement (AD) of about 1.2 m. Assuming that the F3 seafloor scarp is the result of cumulative coseismic slips, the number of seismic events with M = 7.17 needed to produce such fault-scarp has been tentatively estimated by dividing the fault-scarp height for the coseismic displacement expected for 7.17 magnitude earthquakes (see **Table 2**). Furthermore, by dividing the age inferred for the S4 boundary (the seafloor) for the obtained number of seismic events (about 22 events considering the max throw/MD or about 25 seismic events considering the mean throw/AD), a return period for large earthquakes (M > 7) can be estimated over the considered time interval. On this basis, given the height of the F3 fault-scarp at the seafloor (mean and max throw of 66 and 29 m, respectively, see **Figure 5C** and **Supplementary Table 3B**) and the inferred age for S4 (11.7 ka), the return periods of 470 years (considering the mean throw and the average expected displacement) and 537 years (considering the maximum throw and the maximum expected displacement), have therefore been estimated. It is worth to note that our estimation is quite close to the return periods provided by previous authors (e.g., Barbano et al., 2001; Bianca et al., 1999) for the studied area. Based on the inferred macroseismic intensity for historical earthquakes that have occurred in the Hyblean Plateau, Barbano et al. (2001) estimated indeed return periods of about 475 years for events with intensity IX-X and 644 years for events with intensity X, even though the latter is associated with an extremely high error. Expected magnitudes and the estimated recurrence time interval are compatible with those inferred for large historical earthquakes in the area (e.g., the 1693 and 1169 events, see Barbano, 1985; Boschi et al., 1995; Rovida et al., 2016), suggesting the F3 fault the potentially causative faults from which destructive seismic events generated. This assertion appears to be supported for instance by the intensity contours of the 1693 event macroseismic field (see Barbano, 1985), suggesting an offshore seismic source since they are open to the Ionian Sea. The mismatch between the NNW orientation of the studied faults and the NE–SW trending of the macroseismic high-intensity contours should be explained by considering site effects according to which damages may have concentrated on-shore in areas where soft sediments outcrop (i.e., in the Augusta and Lentini basins, see **Figure 1C** and **Figure 9**). Furthermore, the prevailing dip-slip kinematic of the studied faults is in favor of producing tsunamis by coseismic seafloor displacement even if slope failure triggered by seismic shacking cannot be ruled out along the steep, 3,000 m high bathymetric drops of the Malta Escarpment (see Billi et al., 2010).

CONCLUSION

Seismic data interpretation from the offshore SE Sicily along with fault-applied empirical scaling relationships and forward methods allow is to achieve additional information on the structural pattern and seimotectonics of the northernmost branch of the Malta Escarpment. Primary findings are summarized as follows:

- The northernmost branch of the Malta Escarpment has been deformed recently according to E–W tectonic extension, and this kinematics appears to affect mainly the lower plate of the collisional system, whereas eastwards of the studied area, strike-slip deformation prevails within the Ionian accretionary wedge in the tectonically overlaying upper plate (see **Figure 9**).
- The occurrence of extension and contraction at the same structural level (see *Deformation Pattern and Fault Activity*) suggests that, during the Pliocene, faulting and folding may have been nucleated in response to the same process. By similarity with the structural settings observed along other passive margins worldwide, this process is inferred to be a large-scale slope instability.
- Seafloor fault scarps suggest active deformation in the area even if further investigations are needed to better understand the deformation context (i.e., tectonic, gravitative or both) and the related seismotectonic implications.
- Derived fault dimensions (e.g., for F3) and recurrence time interval are compatible with the magnitudes and return period estimated for large historical earthquakes in the area (e.g., the 1693 and 1169 events) although other seismic sources such as the 80 km-long North Alfeo Fault (Gutscher et al., 2016 and **Figure 9** for location) must be considered as well in the seismotectonic framework of the Western Ionian Basin (see Gutscher et al., 2006).

Finally, our data provide additional information to consider reactivation of the Malta Escarpment as one of the potentially causative processes from which destructive seismic events in the area nucleated (see also Bianca et al., 1999; Azzaro and Barbano, 2000; Argnani and Bonazzi, 2005; Argnani et al., 2012). Assuming a prevailing tectonic component of deformation during the Quaternary, our data could provide useful information to improve databases concerning potential seismogenic sources in Italy (e.g., DISS or ITHACA) and contribute to a better assessment of the seismic hazard in the densely populated SE Sicily.

DATA AVAILABILITY STATEMENT

The original contributions presented in the study are included in the article/**Supplementary Material**, further inquiries can be directed to the corresponding author.

AUTHOR CONTRIBUTIONS

GB: work planning, conceptualization, seismic data interpretation, data analysis and interpretation of results, review of the literature data, geodynamics consideration, figures preparation, writing the final version of the manuscript, supervision, funding acquisition. SG: seismic data interpretation, field data measurement/elaboration, 3D modeling, stress-field and slip tendency computation, writing initial draft of the manuscript, draft figures preparation. FG and SK: POS496 seismic data acquisition and processing, critical reading of the manuscript. M-AG: planned the CIRCEE marine geophysical survey, seismic data acquisition, critical reading of the manuscript. CM: geodynamic considerations, review of the literature data, critical reading of the manuscript, funding acquisition, supervision.

FUNDING

This work benefits from funding from the University of Catania in the frame of the project “Multidisciplinary analysis of the deformation around active tectonic structures” (responsible GB) and partly from the MUSE 4D project—Overtime tectonic, dynamic and rheologic control on destructive multiple seismic events-Special Italian Faults and Earthquakes: from real 4D cases to models in the frame of PRIN 2017.

ACKNOWLEDGMENTS

The bathymetric data were extracted from Gutscher et al. (2017) and from EMODnet open dataset (http://www.emodnet-bathymetry.eu/).

Digital topographic data are from the Japan Aerospace Exploration Agency (https://www.eorc.jaxa.jp). The authors also acknowledge the use of MOVE Software Suite granted by Petroleum Experts Limited (www.petex.com). This work is part of the S. Gambino Ph.D.' research project at the University of Catania. Bernard Mercier de Lepinay (GeoAzur, Université de Nice/CNRS), is also acknowledged for the CIRCEE-HR seismic data processing. The reviewers and the Editor are kindly acknowledged for their constructive comments and suggestions which improved the quality of the manuscript.

SUPPLEMENTARY MATERIAL

The Supplementary Material for this article can be found online at: https://www.frontiersin.org/articles/10.3389/feart.2020.594176/full#supplementary-material.

REFERENCES

Adam, J., Reuther, C.-D., Grasso, M., and Torelli, L. (2000). Active fault kinematics and crustal stresses along the Ionian margin of southeastern Sicily. *Tectonophysics* 326, 217–239. doi:10.1016/S0040-1951(00)00141-4

Allmendinger, R. W., Cardozo, N., and Fisher, D. (2012). *Structural geology algorithms: vectors and tensors in structural geology* Cambridge, England: Cambridge University Press.

Amato, A., Azzara, R., Basili, A., Chiarabba, C., Cocco, M., Di Bona, M., et al. (1995). Main shock and aftershocks of the December 13, 1990 Eastern Sicily earthquake. *Ann. Geophys.* 38 (2), 255–266. doi:10.4401/ag-4122

Argnani, A., Armigliato, A., Pagnoni, G., Zaniboni, F., Tinti, S., and Bonazzi, C. (2012). Active tectonics along the submarine slope of south-eastern sicily and the source of the 11 january 1693 earthquake and tsunami. *Nat. Hazards Earth Syst. Sci.* 12 (5), 1311–1319. doi:10.5194/nhess-12-1311-2012

Argnani, A., and Bonazzi, C. (2005). Malta Escarpment fault zone offshore eastern Sicily: Pliocene-Quaternary tectonic evolution based on new multichannel seismic data. *Tectonics* 24, TC4009. doi:10.1029/2004TC001656

Argnani, A., and Bonazzi, C. (2002). Tectonics of eastern Sicily offshore: preliminary results from the MESC 2001 marine seismic cruise. *Boll. Geofis. Teor. Appl.* 43 (3–4), 177–193.

Argnani, A., Mazzarini, F., Bonazzi, C., Bisson, M., and Isola, I. (2013). The deformation offshore of Mount Etna as imaged by multichannel seismic reflection profiles. *J. Volcanol. Geotherm. Res.* 251, 50–64. doi:10.1016/j.jvolgeores.2012.04.016

A. Rovida, M. Locati, R. Camassi, B. Lolli, and P. Gasperini (2016). *CPTI15, the 2015 version of the parametric catalogue of Italian earthquakes* Rome, Italy: Istituto Nazionale di Geofisica e Vulcanologia.

Azzaro, R., and Barbano, M. S. (2000). Analysis of the seismicity of southeastern Sicily: a proposed tectonic interpretation. *Ann. Geofisc.* 43 (1), 171–188. doi:10.4401/ag-3628

Bai, T., Maerten, L., Gross, M. R., and Aydin, A. (2002). Orthogonal cross joints: do they imply a regional stress rotation? *J. Struct. Geol.* 24, 77–88. doi:10.1016/S0191-8141(01)00050-5

Bai, T., and Pollard, D. D. (2000). Fracture spacing in layered rocks: a new explanation based on the stress transition. *J. Struct. Geol.* 22, 43–57. doi:10.1016/S0191-8141(99)00137-6

Barbano, M. S., Rigano, R., Cosentino, M., and Lombardo, G. (2001). Seismic history and hazard in some localities of south-eastern Sicily. *Boll. Geofis. Teor. Appl.* 42 (1–2), 107–120.

Barbano, M. S., and Rigano, R. (2001). Earthquake sources and seismic hazard in south-eastern Sicily. *Ann. Geophys.* 44, 723–738. doi:10.4401/ag-3570

Barbano, M. S. (1985). "The val di Noto earthquake of january 11, 1693," in *Atlas of isoseismal maps of Italian earthquakes, CNR-PFG, quad* Bologna: Consiglio nazionale delle ricerche, Vol. 2A, 48–49.

Barreca, G. (2014). Geological and geophysical evidences for mud diapirism in south-eastern Sicily (Italy) and geodynamic implications. *J. Geodyn.* 82, 168–177. doi:10.1016/j.jog.2014.02.003

Barreca, G., Scarfì, L., Cannavò, F., Koulakov, I., and Monaco, C. (2016). New structural and seismological evidence and interpretation of a lithospheric-scale shear zone at the southern edge of the Ionian subduction system (centraleastern Sicily, Italy). *Tectonics* 35, 1489–1505. doi:10.1002/2015tc004057

Ben-Avraham, Z., and Grasso, M. (1991). Crustal structure variations and transcurrent faulting at the eastern and western margins of the eastern Mediterranean. *Tectonophysics* 75, 269–277. doi:10.1016/0040-1951(91)90326-N

Bianca, M., Monaco, C., Tortorici, L., and Cernobori, L. (1999). Quaternary normal faulting in southeastern Sicily (Italy): a seismic source for the 1693 large earthquake. *Geophys. J. Int.* 139, 370–394. doi:10.1046/j.1365-246x.1999.00942.x

Bianchi, F., Carbone, S., Grasso, M., Invernizzi, G., Lentini, F., LongarettiMerlini, G. S., et al. (1987). Sicilia orientale: profilo geologico Nebrodi-Iblei. *Mem. Soc. Geol. It.* 38, 429–458.

Billi, A., Minelli, L., Orecchio, B., and Presti, D. (2010). Constraints to the cause of three historical tsunamis (1908, 1783, and 1693) in the messina straits region, Sicily, Southern Italy. *Seismol Res. Lett.* 81 (6), 907–915. doi:10.1785/gssrl.81.6.907

Billi, A., Porreca, M., Faccenna, C., and Mattei, M. (2006). Magnetic and structural constraints for the noncylindrical evolution of a continental forebulge (Hyblea, Italy). *Tectonics* 25, TC3011. doi:10.1029/2005TC001800

Bingham, C. (1974). An antipodally symmetric distribution on the sphere. *Ann. Stat.* 2 (6), 1201–1225.

Bott, M. H. P. (1959). The mechanics of oblique slip faulting. *Geol. Mag.* 96, 109–117.

Burollet, P. F., Mugniot, G. M., and Sweeney, P. (1978). "The geology of the pelagian block: the margins and basins of southern Tunisia and tripolitania," in *The Ocean basins and margins 4 B* Editors Nairn, A. E. M., and Stehli, F. G. (New York, NY: Plenum Press), 331–339.

Boschi, E., Ferrari, G., Gasperini, P., Guidoboni, E., Smriglio, G., and Valensise, G. (1995). Catalogo dei Forti Terremoti in Italia dal 461 a.c, al 1980. Roma, Italy: Istituto Nazionale di Geofisica, S.G.A.

Butler, R. W. H., Maniscalco, R., Sturiale, G., and Grasso, M. (2015). Stratigraphic variations control deformation patterns in evaporite basins: Messinian examples, onshore and offshore Sicily (Italy). *J. Geol. Soc.* 172, 113–124. doi:10.1144/jgs2014-024

Camerlenghi, A., Del Ben, A., Hubscher, C., Forlin, E., Geletti, R., Brancatelli, G., et al. (2019). Seismic markers of the Messinian salinity crisis in the deep Ionian Basin. *Basin Res.* 32, 716–738. doi:10.1111/bre.12392

Carbone, S., Grasso, M., and Lentini, F. (1986). *Carta geologica del settore nord-orientale ibleo (Sicilia S.E.), scala 1:50.000* Firenze: SELCA.

Carbone, S., Grasso, M., and Lentini, F. (1984). *Carta geologica della Sicilia sud-orientale, scala 1:100.000* Firenze: SELCA.

Cardozo, N., and Allmendinger, R. W. (2013). Spherical projections with OSXStereonet. *Comput. Geosci.* 51, 193–205. doi:10.1016/j.cageo.2012.07.021

Cartwright, J. A., Trudgill, B. D., and Mansfield, C. S. (1995). Fault growth by segment linkage: an explanation for scatter in maximum displacement and trace length data from the Canyonlands Grabens of SE Utah. *J. Struct. Geol.* 17 (9), 1319–1326. doi:10.1016/0191-8141(95)00033-A

Casero, P., Cita, M. B., Croce, M., and De Micheli, A. (1984). Tentativo di interpretazione evolutiva della Scarpata di Malta basata sui dati geologici e geofisici. *Mem. Soc. Geol. It.* 27, 233–254.

Catalano, R., Doglioni, C., and Merlini, S. (2001). On the mesozoic ionian basin. *Geophys. J. Int.* 144, 49–64. doi:10.1046/j.0956-540X.2000.01287.x

Cifelli, F., Rossetti, F., Mattei, M., Hirt, A. M., Funiciello, R., and Tortorici, L. (2004). An AMS, structural and paleomagnetic study of quaternary deformation in eastern Sicily. *J. Struct. Geol.* 26, 29–46. doi:10.1016/S0191-8141(03)00092-0

Cogan, J., Rigo, L., Grasso, M., and Lerche, I. (1989). Flexural tectonics of southeastern sicily. *J. Geodyn.* 11 (3), 189–241. doi:10.1016/0264-3707(89)90007-0

Cultrera, F., Barreca, G., Scarfì, L., and Monaco, C. (2015). Fault reactivation by stress pattern reorganization in the Hyblean foreland domain of SE Sicily (Italy) and seismotectonic implications. *Tectonophysics* 661, 215–228. doi:10.1016/j.tecto.2015.08.043

De Guidi, G., Caputo, R., and Scudero, S. (2013). Regional and local stress field orientation inferred from quantitative analyses of extension joints: case study from southern Italy. *Tectonics* 32, 1–13. doi:10.1002/tect.20017

Dellong, D., Klingelhoefer, F., Kopp, H., Graindorge, D., Margheriti, L., Moretti, M., et al. (2018). Crustal structure of the Ionian basin and eastern Sicily margin: results from a wide-angle seismic survey. *J. Geophys. Res. Solid Earth* 123, 2090–2114. doi:10.1002/2017JB015312

DISS Working Group (2018). Database of Individual Seismogenic Sources (DISS), Version 3.2.1: a compilation of potential sources for earthquakes larger than M 5.5 in Italy and surrounding areas. Available at: http://diss.rm.ingv.it/diss/ (Accessed December 3, 2018).

Doglioni, C., Innocenti, F., and Mariotti, G. (2001). Why Mt Etna? *Terra. Nova* 13 (1), 25–31. doi:10.1046/j.1365-3121.2001.00301.x

D'Agostino, N., and Selvaggi, G. (2004). Crustal motion along the eurasia-nubia plate boundary in the calabrian arc and sicily and active extension in the messina straits from GPS measurements. *J. Geophys. Res.* 109, B11402. doi:10.1029/2004JB002998

Fabbri, A., Rossi, S., Sartori, R., and Barone, A. (1982). Evoluzione neogenica dei margini marini dell'Arco Calabro-Peloritano: implicazioni geodinamiche. *Mem. Soc. Geol. It.* 24, 357–366.

Gallais, F., Gutscher, M.-A., Graindorge, D., Chamot-Rooke, N., and Klaeschen, D. (2011). A Miocene tectonic inversion in the Ionian Sea (central Mediterranean): evidence from multichannel seismic data. *J. Geophys. Res.* 116, B12108. doi:10.1029/2011JB008505

Ghisetti, F., and Vezzani, L. (1980). The structural features of the Hyblean Plateau and the Mount Judica area (south-eastern Sicily): a microtectonic contribution to the deformational history of the Calabrian arc. *Boll. Soc. Geol. Ital.* 99, 55–102.

Govers, R., and Wortel, M. J. R. (2005). Lithosphere tearing at STEP faults: response to edges of subduction zones. *Earth Planet Sci. Lett.* 236 (1–2), 505–523. doi:10.1016/j.epsl.2005.03.022

Grasso, M., Lentini, F., Nairn, A. E. M., and Vigliotti, M. (1983). A geological and paleomagnetic study of the Hyblean volcanic rocks. *Tectonophysics* 98 (3-4), 271–295. doi:10.1016/0040-1951(83)90298-6

Grasso, M., and Lentini, F. (1982). Sedimentary and tectonic evolution of the eastern Hyblean Plateau (South-eastern Sicily) during late cretaceous to quaternary time. *Palaeogeogr. Palaeoclimatol. Palaeoecol.* 39, 261–280. doi:10.1016/0031-0182(82)90025-6

Grasso, M., Pedley, H. M., Behncke, B., Maniscalco, R., and Sturiale, G. (2004). "Integrated the neogene-frontiers quaternary sedimentation and volcanism in the northern Hyblean Plateau (sicily)," in *Mapping geology in Italy* Editors G. Pasquarè and C. Venturini (Roma, IT: APAT), 159–166.

Grasso, M., and Reuther, C. D. (1988). The western margin of the Hyblean Plateau: a neotectonic transform system on the SE Sicilian foreland. *Ann. Tect.* 2, 107–120.

Grenerczy, G., Sella, G., Stein, S., and Kenyeres, A. (2005). Tectonic implications of the GPS velocity field in the northern Adriatic region. *Geophys. Res. Lett.* 32, L16311. doi:10.1029/2005GL022947

Gross, F., Krastel, S., Geersen, J., Hinrich, B. J., Ridente, D., Chiocci, F. L., et al. (2016). The limits of seaward spreading and slope instability at the continental margin offshore Mt. Etna, imaged by high-resolution 2D seismic data. *Tectonophysics* 667, 63–76. doi:10.10164/j.tecto.2015.11.011

Gutscher, M.-A., Dominguez, S., Mercier de Lepinay, B., Pinheiro, L., Gallais, F., Babonneau, N., et al. (2016). Tectonic expression of an active slab tear from high-resolution seismic and bathymetric data offshore Sicily (Ionian Sea). *Tectonics* 35, 39–54. doi:10.1002/2015TC003898

Gutscher, M.-A., Kopp, H., Krastel, S., Bohrmann, G., Garlan, T., Zaragosi, S., et al. (2017). Active tectonics of the Calabrian subduction revealed by new multi-beam bathymetric data and high-resolution seismic profiles in the Ionian Sea (Central Mediterranean). *Earth Planet Sci. Lett.* 461, 61–72. doi:10.1016/j.epsl.2016.12.020

Gutscher, M.-A., Roger, J., Baptista, M. A., Miranda, J. M., and Tinti, S. (2006). The source of the 1693 Catania earthquake and tsunami (Southern Italy): new evidence from tsunami modeling of a locked subduction fault plane. *Geophys. Res. Lett.* 33, L08309. doi:10.1029/2005GL025442

Henriquet, M., Dominguez, S., Barreca, G., Malavieille, J., Cadio, C., and Monaco, C. (2019). Deep origin of the dome-shaped Hyblean Plateau, southeastern sicily: a new tectono-magmatic model. *Tectonics* 38 (12), 4488–4515. doi:10.1029/2019TC005548

Hsü, K. J., Montadert, L., Bernoulli, D., Bizon, G., Cita, M., Erickson, A., et al. (1978). "Site 374: messina abyssal plain part 1," in *Initial reports of the deep-sea drilling project* Washington, DC: U.S. Government Printing Office, Vol. 42.

Jenny, S., Goes, S., Giardini, D., and Kahle, H.-G. (2006). Seismic potential of southern Italy. *Tectonophysics* 415, 81–101. doi:10.1016/j.tecto.2005.12.003

Kokinou, E., Vafidis, A., Loucogiannakis, M., and Louis, I. (2013). Deep seismic imaging and velocity estimation in Ionian Sea. *J. Balkan Geophys. Soc.* 6 (2), 100–116.

Krastel, S. (2016). "Short cruise report: MAGOMET—offshore flank movement of mount Etna and associated landslide hazard in the Ionian Sea (mediterranean sea)," in RV POSEIDON-CRUISE POS496, Malaga, Catania, March 24–April 4, 2016 (Christian-Albrechts-Universität zu Kiel, Institute of Geosciences), 8.

Le Meur, D. (1997). *Etude géophysique de la structure profonde et de la tectonique active de la partie occidentale de la Ride Méditerranéenne* [Ph.D. thesis]. Paris (FR): University of Paris XI.

Leonard, M. (2010). Earthquake fault scaling: self-consistent relating of rupture length, width, average displacement, and moment release. *Bull. Seismol. Soc. Am.* 100 (5A), 1971–1988. doi:10.1785/0120090189

Lofi, J., Deverchère, J., Gaullier, V., Gillet, H., Gorini, C., Guennoc, P., et al. (2011). Seismic atlas of the messinian salinity crisis markers in the mediterranean and black seas. *Mém. Soc. Géol. CCGM* 179, 1–72.

Maesano, F. E., Tiberti, M. M., and Basili, R. (2020). Deformation and fault propagation at the lateral termination of a subduction zone: the alfeo Fault system in the calabrian arc, southern Italy. *Front. Earth Sci.* 8, 107. doi:10.3389/feart.2020.00107

Maesano, F. E., Tiberti, M. M., and Basili, R. (2017). The Calabrian Arc: three-dimensional modelling of the subduction interface. *Sci. Rep.* 7, 8887. doi:10.1038/s41598-017-09074-8

Mastrolembo, V. B., Serpelloni, E., Argnani, A., Bonforte, A., Bürgmann, R., Anzidei, M. P., et al. (2014). Fast geodetic strain-rates in eastern sicily (southern Italy): new insights into block tectonics and seismic potential in the area of the great 1693 earthquake. *Earth Planet Sci. Lett.* 404, 77–88. doi:10.1016/j.epsl.2014.07.025

Matos, R. M. D. (2000). "Tectonic evolution of the equatorial south atlantic," in *The Brazilian and west African equatorial margins comprise America in, Atlantic rifts and continental margins* Editors W. Mohriak and M. Taiwani (Hoboken, NJ: Wiley), 115, 331–354.

Mattia, M., Bruno, V., Cannavò, F., and Palano, M. (2012). Evidences of a contractional pattern along the northern rim of the Hyblean Plateau (sicily, Italy) from GPS data. *Geol. Acta* 10 (1), 63–70. doi:10.1344/105.000001705

Micallef, A., Camerlenghi, A., Garcia-Castellanos, D., Cunarro Otero, D., Gutscher, M.-A., Barreca, G., et al. (2018). Evidence of the zanclean megaflood in the eastern Mediterranean basin. *Sci. Rep.* 8 (1), 1078. doi:10.1038/s41598-018-19446-3

Micallef, A., Camerlenghi, A., Georgiopoulou, A., Garcia-Castellanos, D., Gutscher, M.-A., Lo Iacono, C., et al. (2019). Geomorphic evolution of the Malta Escarpment and implications for the Messinian evaporative drawdown in the eastern Mediterranean Sea. *Geomorphology* 327, 264–283. doi:10.1016/j.geomorph.2018.11.012

Monaco, C., and Tortorici, L. (2000). Active faulting in the Calabrian arc and eastern Sicily. *J. Geodyn.* 29 (3–5), 407–424. doi:10.1016/S0264-3707(99)00052-6

Montone, P., Mariucci, M. T., and Pierdominici, S. (2012). The Italian present-day stress map. *Geophys. J. Int.* 189 (2), 705–716. doi:10.1111/j.1365-246X.2012.05391.x

Morris, A., Ferrill, D. A., and Henderson, D. B. (1996). Slip-tendency analysis and fault reactivation. *Geology* 24, 275–278. doi:10.1130/0091-7613(1996)024<0275:STAAFR>2.3.CO;2

Mulargia, F., Broccio, F., Achilli, V., and Baldi, P. (1985). Evaluation of a seismic quiescence pattern in southeastern Sicily. *Tectonophysics* 116, 335–364. doi:10.1016/0040-1951(85)90214-8

Musumeci, C., Scarfì, L., Palano, M., and Patanè, D. (2014). Foreland segmentation along an active convergent margin: new constraints in southeastern Sicily (Italy) from seismic and geodetic observations. *Tectonophysics* 630, 137–149. doi:10.1016/j.tecto.2014.05.017

Palano, M., Ferranti, L., Monaco, C., Mattia, M., Aloisi, M., Bruno, V., et al. (2012). GPS velocity and strain fields in Sicily and southern Calabria, Italy: updated geodetic constraints on tectonic block interaction in the central Mediterranean. *J. Geophys. Res.* 117, B07401. doi:10.1029/2012JB009254

Patacca, E., Scandone, P., Giunta, G., and Liguori, V. (1979). Mesozoic paleotectonic evolution of the Ragusa zone (southern Sicily). *Geol. Rom.* 18, 331–369.

Pedley, M., and Grasso, M. (1992). Miocene syntectonic sedimentation along the western margins of the Hyblean-Malta platform: a guide to plate margin processes in the central Mediterranean. *J. Geodyn.* 15 (1–2), 19–37. doi:10.1016/0264-3707(92)90004-C

Piatanesi, A., and Tinti, S. (1998). A revision of the 1693 eastern Sicily earthquake and tsunami. *J. Geophys. Res. Solid Earth* 103 (B2), 2749–2758. doi:10.1029/97JB03403

Polonia, A., Torelli, L., Artoni, A., Carlini, M., Faccenna, C., Ferranti, L., et al. (2016). The Ionian and Alfeo-Etna fault zones: new segments of an evolving plate boundary in the central Mediterranean Sea? *Tectonophysics* 675, 69–90. doi:10.1016/j.tecto.2016.03.016

Polonia, A., Torelli, L., Gasperini, L., Cocchi, L., Muccini, F., Bonatti, E., et al. (2017). Lower plate serpentinite diapirism in the Calabrian Arc subduction complex. *Nat. Commun.* 8, 2172. doi:10.1038/s41467-017-02273-x

Polonia, A., Torelli, L., Gasperini, L., and Mussoni, P. (2012). Active faults and historical earthquakes in the messina straits area (Ionian Sea). *Nat. Hazards Earth Syst. Sci.* 12, 2311–2328. doi:10.5194/nhess-12-2311-2012

Pondrelli, S.[Dataset] (2002). European-mediterranean regional centroid-moment tensors catalog (RCMT). (INGV) Istituto Nazionale di Geofisica e Vulcanologia. Available at: https://doi.org/10.13127/rcmt/euromed (Accessed 2002).

Presti, D., Billi, A., Orecchio, B., Totaro, C., Faccenna, C., and Neri, G. (2013). Earthquake focal mechanisms, seismogenic stress, and seismotectonics of the Calabrian Arc, Italy. *Tectonophysics* 602 153–175. doi:10.1016/j.tecto.2013.01.030

Ragg, S., Grasso, M., and Müller, B. (1999). Patterns of tectonic stress in Sicily from borehole breakout observations and finite element modeling. *Tectonics* 18 (4), 669–685. doi:10.1029/1999TC900010

Scandone, P., Patacca, E., Radoicic, R., Ryan, W. B. F., Cita, M. B., Rawson, M., et al. (1981). Mesozoic and cenozoic rocks from Malta escarpment (Central Mediterranean). *AAPG Bull.* 65 (7), 1299–1319. doi:10.1306/03B5949F-16D1-11D7-8645000102C1865D

Scarfì, L., Barberi, G., Musumeci, C., and Patanè, D. (2016). Seismotectonics of northeastern Sicily and Southern Calabria (Italy): new constraints on the tectonic structures featuring in a crucial sector for the Central Mediterranean geodynamics. *Tectonics* 35, 812–832. doi:10.1002/2015TC00402

Scarfì, L., Messina, A., and Cassisi, C. (2013). Sicily and Southern Calabria focal mechanism database: a valuable tool for the local and regional stress field determination. *Ann. Geophys.* 56, 6109. doi:10.4401/ag-6109

Şengör, A. M. C. (1979). Mid-mesozoic closure of permo-triassic tethys and its implications. *Nature* 279, 590–593. doi:10.1038/279590a0

Servizio Geologico d'Italia (2011). Foglio 641 Augusta della Carta Geologica d'Italia alla scala 1:50.000. Coordinatore scientifico Carbone S. Direttore dei rilevamenti Lentini F. Note illustrative a cura di Carbone S. (ISPRA). 247.

Sirovich, L., and Pettenati, F. (2001). Test of source-parameter inversion of the intensities of a 54,000-death shock of the seventeenth century in southeastern Sicily. *Bull. Seismol. Soc. Am.* 91, 792–811.

Tinti, S., Armigliato, A., and Bortolucci, E. (2001). Contribution of tsunami data analysis to constrain the seismic source: the case of the 1693 eastern Sicily earthquake. *J. Seismol.* 5 (1), 41–61. doi:10.1023/A:1009817601760

Tinti, S., Maramai, A., and Graziani, L. (2004). The new catalogue of Italian tsunamis. *Nat. Hazards* 33, 439–465. doi:10.1023/B:NHAZ.0000048469.51059.65

Trippetta, F., Petricca, P., Billi, A., Collettini, C., Cuffaro, M., Lombardi, A. M., et al. (2019). From mapped faults to fault-length earthquake magnitude (FLEM): a test on Italy with methodological implications. *Solid Earth* 10, 1555–1579. doi:10.5194/se-10-1555-2019

Wallace, R. E. (1951). Geometry of shearing stress and relation to faulting. *J. Geol.* 59, 118–130. doi:10.1086/625831

Ward, S. (1994). Constraints on the seismotectonics of the central mediterranean from very long baseline interferometry. *Geophys. J. Int.* 117, 441–452. doi:10.1111/j.1365-246X.1994.tb03943.x

Wells, D. L., and Coppersmith, K. J. (1994). New empirical relationships among magnitude, rupture length, rupture width, rupture area, and surface displacement. *Bull. Seismol. Soc. Am.* 84 (4), 974–1002.

Conflict of Interest: The authors declare that the research was conducted in the absence of any commercial or financial relationships that could be construed as a potential conflict of interest.

frontiers in Earth Science

ORIGINAL RESEARCH
published: 20 January 2021
doi: 10.3389/feart.2020.608063

Fault Pattern and Seismotectonic Style of the Campania – Lucania 1980 Earthquake (M_w 6.9, Southern Italy): New Multidisciplinary Constraints

S. Bello[1,2]*, R. de Nardis[1,2]*, R. Scarpa[2,3], F. Brozzetti[1,2], D. Cirillo[1,2], F. Ferrarini[1,2], B. di Lieto[4], R. J. Arrowsmith[5] and G. Lavecchia[1,2]

[1]DiSPUTer, University "G. d' Annunzio" Chieti-Pescara, Chieti, Italy, [2]Centro InteRUniversitario per l'analisi Sismotettonica Tridimensionale (CRUST), Chieti, Italy, [3]Dipartimento di Fisica Università "E.R. Caianiello", Salerno, Italy, [4]Osservatorio Vesuviano, INGV, Napoli, Italy, [5]School of Earth and Space Exploration, Arizona State University, Tempe, AZ, United States

Edited by:
Ioannis Kassaras,
National and Kapodistrian University of Athens, Greece

Reviewed by:
Alessandro Maria Michetti,
University of Insubria, Italy
Erhan Altunel,
Eskisehir Osmangazi University, Turkey

***Correspondence:**
S. Bello
simone.bello@unich.it
R. de Nardis
rita.denardis@unich.it

Specialty section:
This article was submitted to Structural Geology and Tectonics, a section of the journal Frontiers in Earth Science.

Received: 18 September 2020
Accepted: 25 November 2020
Published: 20 January 2021

Citation:
Bello S, de Nardis R, Scarpa R, Brozzetti F, Cirillo D, Ferrarini F, di Lieto B, Arrowsmith RJ and Lavecchia G (2021) Fault Pattern and Seismotectonic Style of the Campania – Lucania 1980 Earthquake (M_w 6.9, Southern Italy): New Multidisciplinary Constraints. Front. Earth Sci. 8:608063. doi: 10.3389/feart.2020.608063

New fault trace mapping and structural survey of the active faults outcropping within the epicentral area of the Campania-Lucania 1980 normal fault earthquake (M_w 6.9) are integrated with a revision of pre-existing earthquake data and with an updated interpretation of the CROP-04 near-vertical seismic profile to reconstruct the surface and depth geometry, the kinematics and stress tensor of the seismogenic fault pattern. Three main fault alignments, organized in high-angle en-echelon segments of several kilometers in length, are identified and characterized. The inner and intermediate ones, i.e. Inner Irpinia (InIF) and Irpinia Faults (IF), dip eastward; the outer Antithetic Fault (AFA) dips westward. Both the InIF and the IF strike NW-SE along the northern and central segments and rotate to W-E along the southern segments for at least 16 km. We provide evidence of surface coseismic faulting (up to 1 m) not recognized before along the E-W segments and document coseismic ruptures with maximum vertical displacement up to ~1 m where already surveyed from other investigators 40 years ago. Fault/slip data from surface data and a new compilation of focal mechanisms (1980 – 2018) were used for strain and stress analyses to show a coherent NNE-directed least principal stress over time and at different crustal depths, with a crustal-scale deviation from the classic SW-NE tensional direction across the Apennines of Italy. The continuation at depth of the outcropping faults is analyzed along the trace of the CROP-04 profile and with available hypocentral distributions. Integrating all information, a 3D seismotectonic model, extrapolated to the base of the seismogenic layer, is built. It outlines a graben-like structure with a southern E-W bend developed at depth shallower than 10–12 km, at the hanging wall of an extensional NE- to E-dipping extensional basal detachment. In our interpretation, such a configuration implies a control in the stress transfer during the 1980 earthquake ruptures and provides a new interpretation of the second sub-event, occurred at 20 s. Our reconstruction suggests that the latter ruptured a hanging wall NNE-dipping splay of the E-W striking main fault segment and possibly also an antithetic SSW-dipping splay, in two in-sequence episodes.

Keywords: Italy, active faulting, structural geology, kinematic analysis, seismotectonics, stress inversion, 3D fault model, Irpinia 1980 earthquake

INTRODUCTION

Moderate-to-large intra-continental extensional seismic sequences (M_w 6.5–7) occurring in regions with well-exposed Quaternary faults are unusual. They are precious for two scientific reasons: to understand the faulting processes controlling the earthquake rupture and propagation from depth to surface and to reconstruct and model fault pattern for hazard purposes.

In the Mediterranean area, large extensional instrumental earthquakes (M ≥ 6.5) are mainly concentrated along the Apennines of Italy and in the Hellenides of Greece (**Figure 1A**). Since 1980, destructive events were those of Campania-Lucania 1980 (M_w 6.9, Bernard and Zollo, 1989), Corinth 1981 (M_s 6.7, Jackson et al., 1982; Kim et al., 1984), and Central Italy 2016 (M_w 6.5, Lavecchia et al., 2016; Civico et al., 2018; Villani et al., 2018; Brozzetti et al., 2019).

When focusing on Italian cases, we observe that the Central Italy 2016 seismic sequence (CISS-2016) released in three months three neighboring major events with M_w between 6.0 and 6.5, activating as a whole a ~60 km-long SW-dipping extensional fault alignment and releasing a cumulate magnitude of M_w ~6.8 (Lavecchia et al., 2016; Menichetti et al., 2016; Porreca et al., 2020; Brozzetti et al., 2019; Brozzetti et al., 2020).

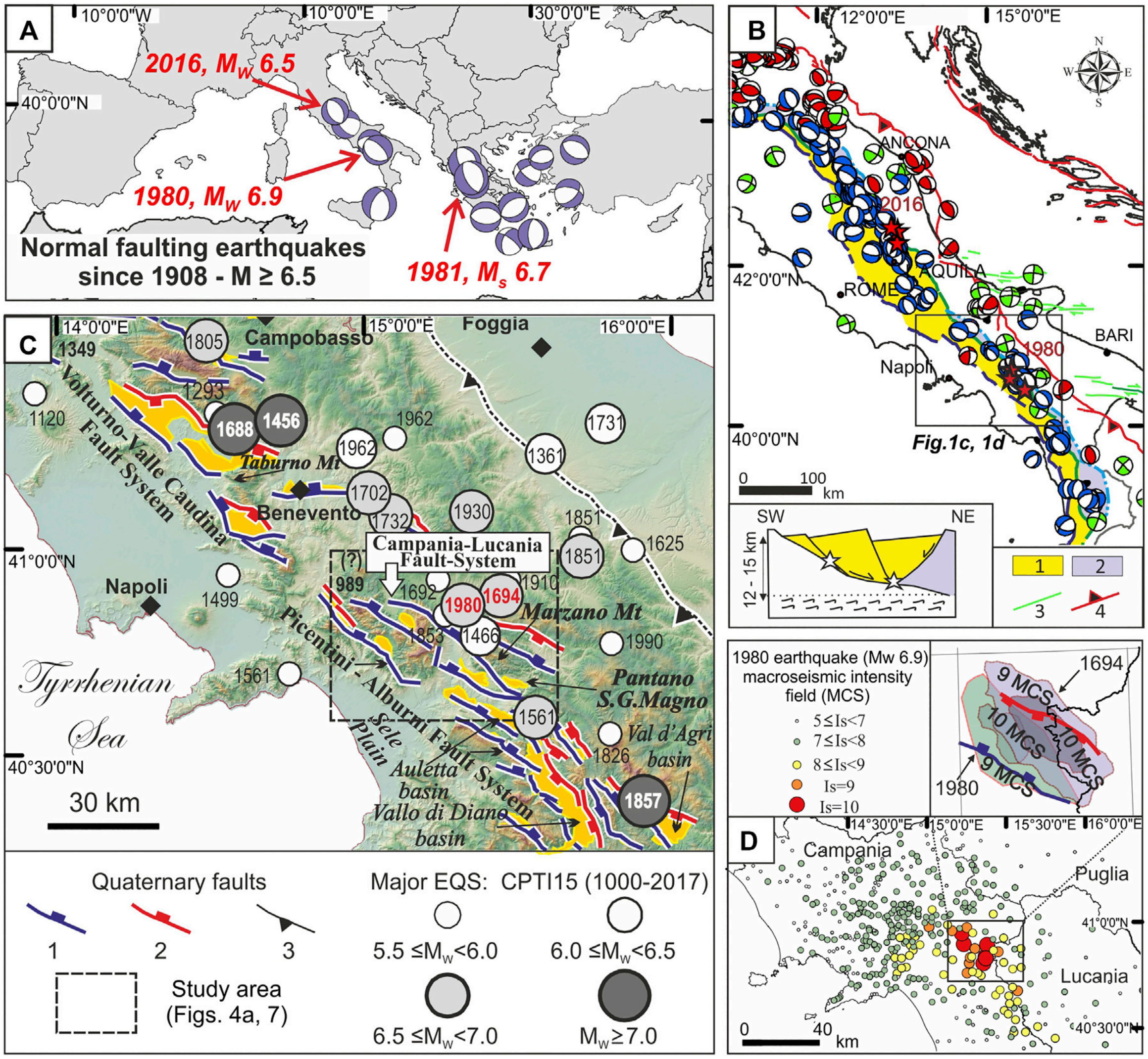

FIGURE 1 | The Campania-Lucania 1980 earthquake in the Mediterranean seismotectonic context. **(A)** Mediterranean normal faulting earthquakes with M ≥ 6.5 since 1908 derived from the World Stress Map database (Heidbach et al., 2018). **(B)** The Italian earthquake focal mechanisms (M_W ≥ 4.0) from 1908 to 2015 (Montone and Mariucci, 2016); red stars represent the mainshocks of 2016/2017 Central Italy and 1980 Campania-Lucania seismic sequences. The background colors indicate the extensional seismotectonic provinces as in Lavecchia et al., 2021: Key: 1 = Extensional seismogenic province; 2 = Deep extensional seismogenic province; 3 = right-lateral strike-slip faults within the Adriatic foreland; 4 = Active outer thrust system; The sketch in the lower left corner represents the simplified model of the Apennine extensional system as in Lavecchia et al., 2011. **(C)** Active faults in Southern Italy (after Adinolfi et al., 2015) with major historical and instrumental earthquakes from Parametric Catalogue of Italian Earthquakes, CPTI15 v2.0 (Rovida et al., 2019). Key: 1, east-dipping normal faults; 2, west-dipping normal faults; 3 thrust faults. **(D)** 1980 earthquake macroseismic field from the Italian Macroseismic database DBMI15 v2.0 (Locati et al., 2019). The inset in the right upper corner represents the contour of IX and X MCS intensity of the 1694 and 1980 earthquakes.

Conversely, the Campania-Lucania earthquake of November 23, 1980 (also Irpinia earthquake, hereinafter referred to as 1980-EQ), released a similar total magnitude (M_w 6.9) in a time span of about 1 min (Bernard and Zollo, 1989). It had multiple sub-events that activated in sequence three distinct neighboring fault segments, also with opposite dips (east- and west-dipping) (Westaway and Jackson, 1987; Bernard and Zollo, 1989). Surface displacements with peaks slightly exceeding 1 m were documented along the fault trace (Pantosti and Valensise, 1990; Galli and Peronace, 2014).

Surface ruptures, aftershock distributions and kinematics of both 1980-EQ and CISS-2016 are well consistent with the activation of normal and normal-to-oblique intra-Apennine Quaternary faults at upper crustal-depths (Valensise and Pantosti, 2001; Basili et al., 2008; DISS Working Group, 2018). The kinematics characterizing either the active normal faults or the focal mechanisms of all the instrumental $M_w \geq 5.5$ earthquakes that occurred along the intra-Apennine extensional belt are consistent with a NE-SW minimum horizontal stress axis (Pantosti and Valensise, 1990; Brozzetti and Lavecchia, 1994; Pondrelli et al., 2006; Brozzetti et al., 2009a; Ferrarini et al., 2015).

The 1980-EQ was the most destructive Italian earthquake of the last 40 years, but it occurred almost in early instrumental times and in spite of large efforts in the literature its seismotectonic and seismogenic interpretation is still questioned, starting from the size, the attitude, the dip-angle and the depth of the involved fault segments.

CISS-2016 taught us that extensive and detailed use of geometric and kinematic fault data, covering a time span from Late Pliocene to present, can help to identify the segmentation pattern that controls the seismogenic stress release (Lavecchia et al., 2016; Livio et al., 2016; Wilkinson et al., 2017; Brozzetti et al., 2019; Porreca et al., 2020). Therefore, in this paper, in the light of lessons learned from CISS-2016, we attempt a thorough seismotectonic revision of the 1980-EQ with the main aim to improve our understanding of earthquake-fault association and seismogenic scenarios in Italy.

In this paper, after an overview of the geological and seismological background of the 1980-EQ, we:

(1) Update the geometry and kinematics of the Quaternary extensional fault pattern within the epicentral area through detailed structural mapping and construction of a new digital fault-slip database (**Supplementary Tables S1, S2 and Data Sheet S1**) and compare the present state of the coseismic rupture pattern with that developed within few years from the event (Pantosti and Valensise, 1990).
(2) Revise and partially update seismological data from the literature (hypocentral distributions and focal mechanisms of three major 1980-EQ sub-events, of the aftershock sequence and of the recent background seismicity (**Supplementary Tables S3–S5**).
(3) Perform independent stress inversion of geological and seismological data to evaluate the present and Quaternary stress tensor and compare them over time.
(4) Reconstruct the depth geometry of the outcropping fault pattern, down to the base of the seismogenic layer, along the trace of the CROP-04 seismic profile, which strikes across the 1980-EQ source area.
(5) Build a 3D fault model of the 1980-EQ seismogenic faults by integrating all the newly acquired and the revised multi-source information.
(6) Advance a new seismotectonic hypothesis concerning the fault segmentation control on the 1980-EQ sub-events propagation.

BACKGROUND

Seismotectonic Setting

The 1980-EQ is located within the Campania-Lucania sector of the intra-Apennine Extensional Province (**Figures 1B,C**). This Province is manifest along the entire length of peninsular Italy (Lavecchia et al., 2011; Lavecchia et al., 2021 and references therein). It consists of moderate to high-angle (>45°) westward and eastward-dipping normal faults, Quaternary and Late Quaternary in age (Martini et al., 2001; Brozzetti, 2011). At depth, these faults detach along low-angle east-dipping discontinuities (**Figure 1B**) interpretable as regional low-angle normal faults (LANFs) highlighted by seismic lines and background seismicity rock volumes (Boncio et al., 2000; Barchi et al., 2007; Brozzetti et al., 2009b; Mirabella et al., 2011; Di Naccio et al., 2013; Lavecchia et al., 2017). Recent works suggest active asymmetrical extension driven by east-dipping LANFs which would represent the basal detachment of the high-angle seismogenic fault bounding the seismically deforming upper crust for the Campania-Lucania and northern Calabria arcs (Brozzetti, 2011; Brozzetti et al., 2017a; Brozzetti et al., 2017b).

The Extensional Province dislocates pre-existing Late-Miocene Early-Pliocene compressional structures (Lavecchia, 1988) on the west. On the east, it is parallel to an active and seismogenic eastward verging coaxial contractional belt (Lavecchia et al., 1994) also revealed from focal mechanisms (**Figure 1B**). In a even more external position, near-vertical E-W-striking faults confined within the Adriatic foreland are also known (**Figure 1B**).

Within the Campania-Lucania sector of the Intra-Apennine extensional belt (area of **Figure 1C**), the deformation is accommodated by distributed faults, east-to west-dipping with low to moderate slip rates (0.2–2 mm/yr; Galli and Bosi, 2003; Galli et al., 2006; Papanikolaou and Roberts, 2007; Ferranti et al., 2014; Sgambato et al., 2020). These structures are mainly developed in the hanging wall of a regional east-dipping system, whose inner outcropping master faults can be traced from the Volturno-Valle Caudina Fault System to the Alburni-Picentini Fault System (Brozzetti, 2011). The associated hanging wall basins are asymmetric, filled by syntectonic continental deposits and characterized by south-westward thickening, tilted beds. They well document extensional activity in the time interval from the Early Pleistocene to the Holocene (Abate et al., 1998; Ascione et al., 2003; Giano and Martino, 2003; Brozzetti and Salvatore, 2006; Martino, 2007). Activity predating the Early Pleistocene is indicated in some key areas (Auletta and Vallo di Diano basins) by seismic reflection profiles (Barchi et al., 2007; Amicucci et al., 2008).

Ongoing extensional activity of the area is testified by geodetic data (2–5 mm/y, Devoti et al., 2011; D'Agostino, 2014; Ferranti et al., 2014) and diffuse seismicity. Focal mechanisms testify an upper crustal (<12–15 km) stress state with SW-NE minimum horizontal axis. The pure-normal and normal-oblique kinematics focal mechanisms show a dominant SW–NE extensional regime, compatible with the attitude of the known active faults (Cello et al., 2003; Maschio et al., 2005; Brozzetti et al., 2009b).

Since the 1980-EQ, diffuse background seismicity with a few small-to-moderate events ($M_w < 5.0$) have been recorded (De Matteis et al., 2012; Stabile et al., 2012; Amoroso et al., 2014; De Landro et al., 2015; Vassallo et al., 2016). Destructive earthquakes have occurred historically (**Figure 1C**; Porfido et al., 2002; Rovida et al., 2019). In particular, there is knowledge of three events ($M_w \geq 7.0$, Io XI MCS) among the strongest of the Italian territory (1456 M_w 7.2; 1688, M_w 7.1; 1857, M_w 7.2) plus seven moderate-large events ($6.5 \leq M_w < 7.0$ with macroseismic intensity up to X-XI MCS). In the study area (**Figure 1C**) the Italian Parametric Catalogue (CPTI15v.2, Rovida et al., 2019) reports other six events with equivalent magnitude greater than M 5.5 occurred from the second half of 1400 to date (1466, 1561, 1692, 1694, 1853, and 1910). Furthermore, archaeoseismic evidence highlights two destructive earthquakes occurred in the second half of the first century and in 989–990 AD (Blumetti et al., 2002; Galli and Peronace, 2014; Galli, 2020).

The Campania-Lucania 1980 Earthquake (1980-EQ)

On the 23rd of November (18:34 UTC) 1980, a sector of the Campania Lucania Fault System (hereinafter referred to as CLFS) broke in a M_w 6.9 destructive earthquake (Westaway, 1993) that produced widespread damage, razed to the ground six villages (X MCS) and caused ~3,000 casualties (red circles in **Figure 1D**). The 1980-EQ was not preceded by significant events (Martini and Scarpa, 1983), but only by swarms of microearthquakes along the boundaries of the current rupture (Del Pezzo et al., 1983) observed with a local seismic network by Cagnetti et al. (1981). It was followed by several hundred earthquakes, with four major aftershocks ($M \geq 5.0$) occurred on the 24th and 25th November, on the 16th of January, 1981, and on the 3rd of December 1980 (Pantosti and Valensise, 1990). A temporary network was operating from the 1st to the 15th of December and many authors analyzed the aftershock relocations, focal mechanisms, and velocity models (Deschamps and King, 1984; Westaway and Jackson, 1987; Bernard and Zollo, 1989; Pantosti and Valensise, 1990; Amato and Selvaggi, 1993; Amoruso et al., 2011).

Significant surface fractures were generated by the 1980-EQ. The papers published immediately after the earthquake ascribed them to gravitational phenomena or landslide with tectonic origin (Bollettinari and Panizza, 1981; Cantalamessa et al., 1981; Carmignani et al., 1981; Ortolani and Torre, 1981). Only some years later, they were recognized as primary coseismic ruptures in some still pivotal papers. Westaway and Jackson (1987) reported on 20 km-long primary coseismic faulting. Pantosti and Valensise (1990) and Pantosti and Valensise (1993) described 38 km of coseismic ruptures. Subsequently, Blumetti et al. (2002) presented new field data and demonstrated the importance of an antithetic west-dipping system. Galli and Peronace (2014) reviewed the effects of the surface faulting through a structural and topographic survey along a 43-km-long fault.

Sub-events of the 1980-EQ

The 1980-EQ was a complex normal faulting event characterized by multiple ruptures. It consisted of three sub-events (**Figure 2A**) occurring within 1 min (0 , ~20 and ~40 s), and of several rupture episodes (2–12) within the first 20 s (Westaway and Jackson, 1987; Bernard and Zollo, 1989; Pantosti and Valensise, 1990; Vaccari et al., 1990; Westaway, 1993). The 1980-EQ released a total seismic moment between (1.4–3.0 E+19 Nm) corresponding to a cumulate magnitude moment between M_w 6.7 and 6.9. The magnitude attributed to the three sub-events ranges from M_w 6.7 to 6.8 for sub-event 1, from M_w 6.3 to 6.4 for sub-event 2 and from M_w 6.2 to 6.3 for sub-event 3 (**Supplementary Tables S3, S5**). The location of three sub-events are ambiguous due to the backswing of earlier arrivals, but focal mechanisms are coherent with prevailingly normal kinematics (Giardini et al., 1993). A summary of available data is here given in **Supplementary Tables S3, S5**.

Sub-event 1 was located from most of investigators to the eastern flank of Marzano Mt., with epicentral solutions clustered within ~3 km (blue dots, n° = 1–7, **Figure 2A**). Substantially different seismic locations were given by the seismological agencies (e.g., NEIC, NEIS, ISC, ING; dark blue dots n° = 8–12 in **Figure 2A**) and by Westaway (1993) (**Figure 2A**, **Supplementary Table S3**, n°14). Conversely, there is a good agreement for the fault planes (**Supplementary Table S4**), that show an average dip angle of 60° (±15°) and a N45°E (±15°) dip direction.

The epicentral locations and seismogenic fault planes of sub-events 2 and 3 are more dispersed. The solutions of sub-event 2, as located by Westaway and Jackson (1987) and by Bernard and Zollo (1989) (red dots, n° = 1–2 in **Figure 2A**), are about 20 km away each other.

Even if with dispersed epicentral locations, sub-event 3 is almost unanimously attributed to the west-dipping high-angle (70–80°) antithetic normal fault system, although assuming different fault strikes as shown in the stereonet of **Figure 2A** (156°, Westaway and Jackson, 1987 and 115° Pingue and De Natale, 1993). The most recent location of sub-event 3 was proposed by Amoruso et al., (2011) (the southernmost location of this sub-event, green dot n° 3 in **Figure 2A**).

Source Models

Various source models have been proposed for the 1980-EQ. The main ones, associated to the three sub-events, are summarized in

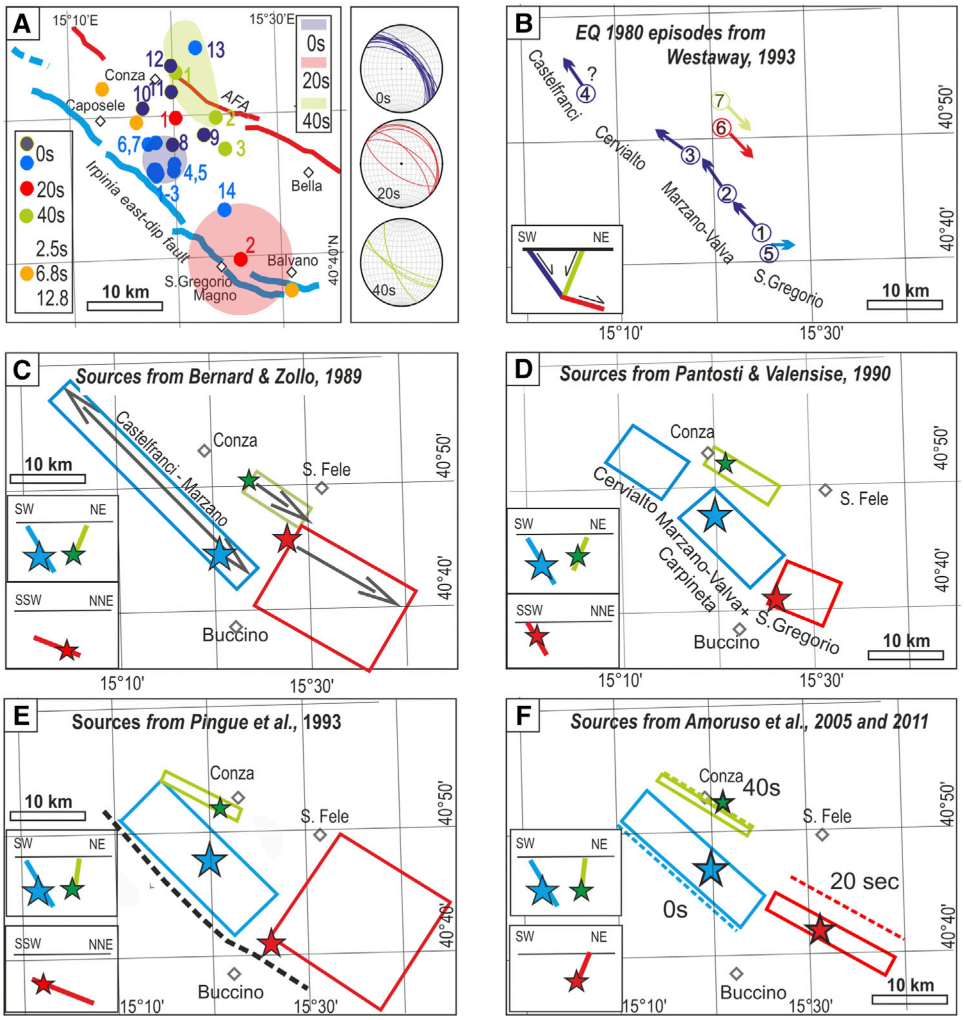

FIGURE 2 | Epicentral locations and source models of the 1980 Campania-Lucania earthquake from the literature. **(A)** Summary of epicentral location proposed by different investigators for the sub-event 1 (blue circles), sub-event 2 (red circles), sub-event 3 (green circles). The respective table with references is given in the supplementary material (**Supplementary Table S3**). The orange circles are other seismic episodes occurred at 2.5, 6.8, and 12 s from the sub-event 1 as in Westaway and Jackson (1987). The colored areas represent the seismic location uncertainty as in Bernard and Zollo, 1989. Summary of preferential fault plane solutions proposed in literature for sub-events 1–3 (**Supplementary Table S4**). **(B–F)** The geometry of the main seismogenic sources of the three events representing a complex rupture mechanism occurred within 1 min of the onset of the main event (0, 20, 40 s) proposed by different investigators (Westaway and Jackson 1987; Bernard and Zollo 1989; Pantosti and Valensise 1990; Pingue and De Natale, 1993; Westaway, 1993; Troise et al., 1998; Dalla Via et al., 2003; Amoruso et al., 2005; Amoruso et al., 2011) Blue boxes refer to the first event (0 s), red boxes to the second (20 s) and the green boxes to the third one (40 s). The inset inside each panel is the schematic cross section of the proposed model.

Figure 2. Sub-event 1 is unanimously associated to the NE-dipping fault along the eastern flank of the Cervialto and Marzano Mts, although different names are given to this structure (Scarpa and Slejko, 1982; Brüstle and Müller, 1983; Del Pezzo et al., 1983; Deschamps and King, 1983; Westaway and Jackson, 1987; Pantosti and Valensise, 1990; Giardini et al., 1996; Amoruso et al., 2011).

Westaway and Jackson (1987) and Westaway (1993) proposed that it involved all the NE-dipping fault alignment from Castelfranci to S. Gregorio, for an along strike extent of ~70 km and with 4-5 rupture episodes (numbered circles in **Figure 2B**).

Bernard and Zollo (1989), based on a re-evaluation of teleseismic, strong motion and leveling data, associated sub-event 1 to a multiple fracture from Castelfranci to Marzano, excluding the activation of the San Gregorio fault segment (**Figure 2C**).

Pantosti and Valensise (1990) considered for sub-event 1 a more conservative along-strike extent (~40 km in length). Based on a geological approach, they associated the 0 s earthquake exclusively to the Marzano and Cervialto faults, because they did not find any surface faulting evidences north of Cervialto Mt. (**Figure 2D**).

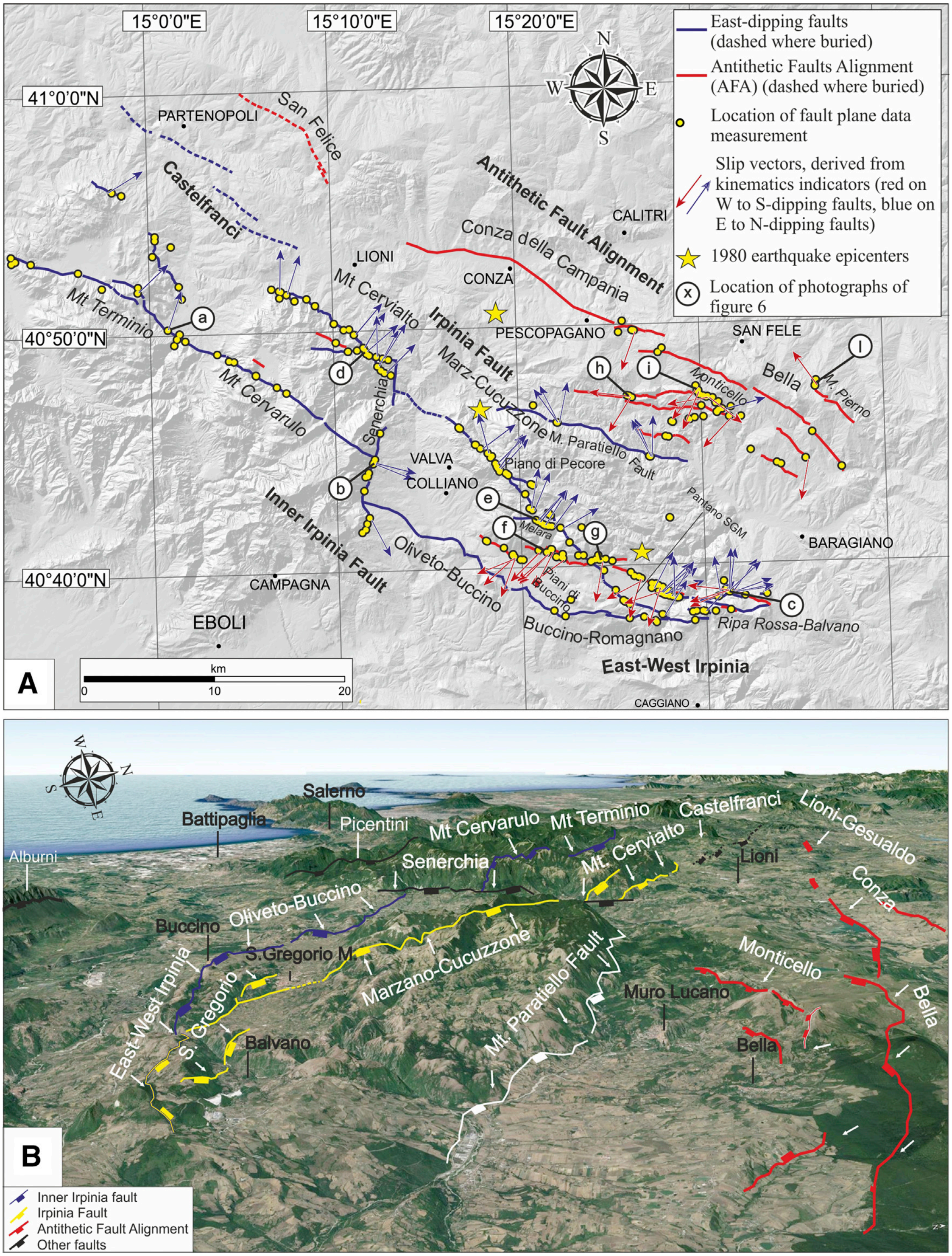

FIGURE 3 | (A) Summary map of the reconstructed tectonic structures and of the acquired data in the Campania-Lucania 1980 earthquake epicentral area. Arrows show the slip vectors derived from kinematic indicators and reported together with the structural data of the fault planes in the stereoplots of **Figure 4**. Yellow circles represent the location of the structural data summarized in stereoplots of **Figure 4** and listed in **Supplementary Table S1**. Letters in white circles refer to photographs of **Figure 6. (B)** Panoramic view looking WNW of the entire study area. The fault alignments are shown in their subdivision into segments.

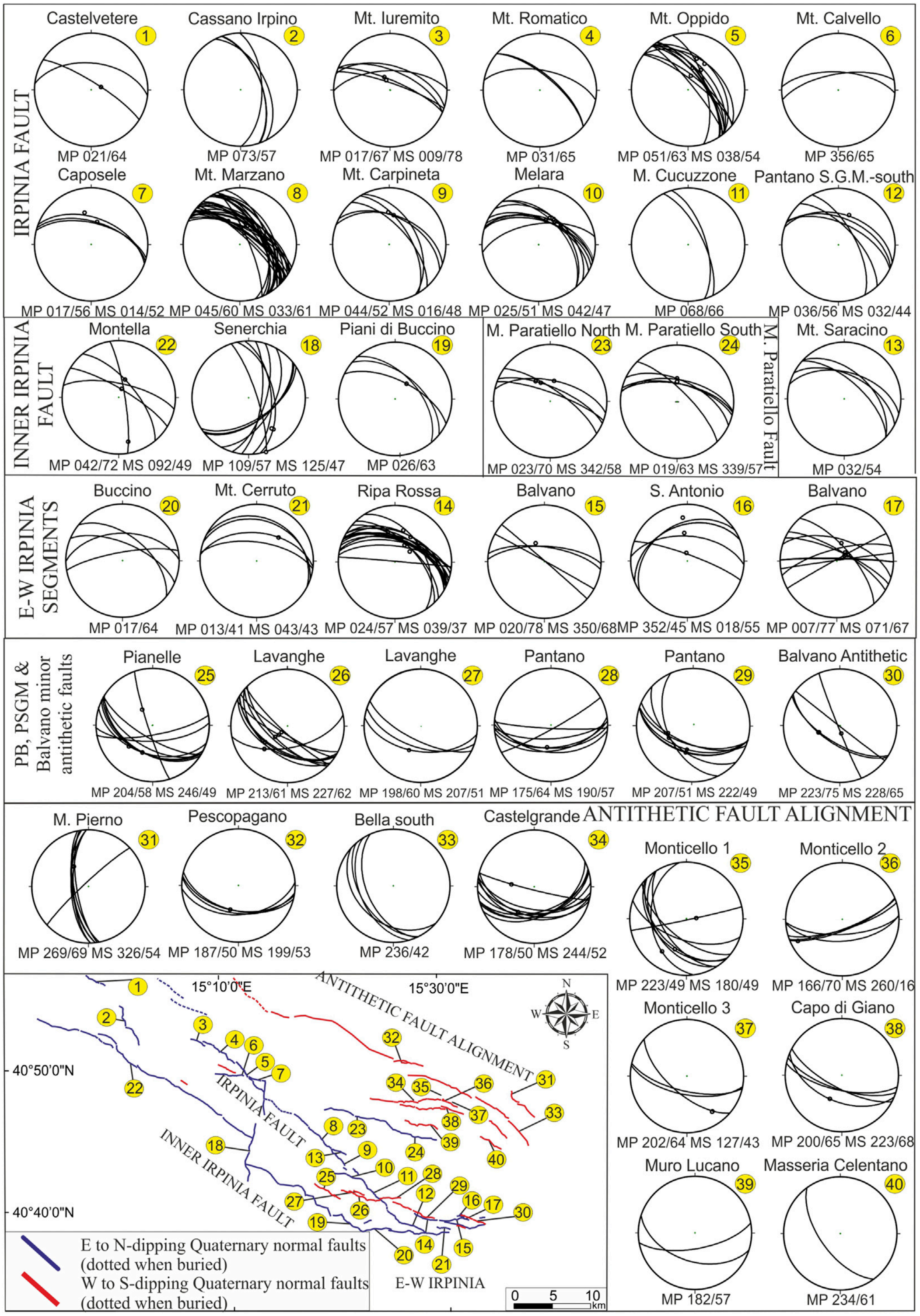

FIGURE 4 | Structural analysis carried out on the Quaternary normal faults outcropping in the Campania–Lucania 1980 earthquake epicentral area. Stereoplots of survey sites (SS) depicting normal faults (great circles) and striated normal faults (great circles with small black circles) are grouped by the fault or fault-alignment on which the data were acquired. Only normal or normal-oblique senses of slip were observed. The map (lower left) shows, as small yellow circles, the location of the SS that consist either of structurally homogeneous outcrops, or group of close outcrops. Sites are numbered from north to south for each of the reconstructed structures.

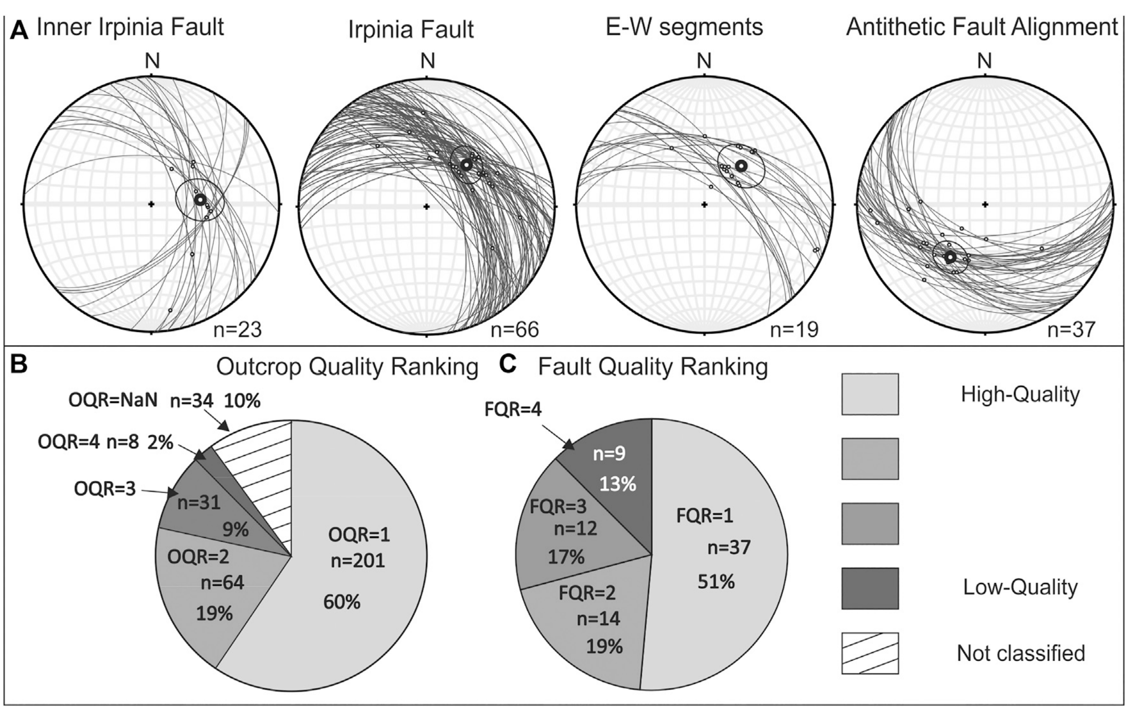

FIGURE 5 | Summary of structural data and quality parameters. **(A)** Faut/slip data (fault planes and slip vectors from slickenlines) summarized for the main faults reconstructed in this paper. The mean slip vectors are reported for each fault with the bold black circles; error calculated are reported with the thin black circles around the mean slip vectors. **(B)** Distribution of the measurements by the assigned four-class Outcrop Quality Rankings (OQR) (see also **Supplementary Table S1**). **(C)** Distribution of the mapped faults divided on the basis of the four-class Fault Quality Rankings (FQR) assigned (see also **Supplementary Table S2** where FQR are reported close to the fault name).

Based on leveling data, other authors (Pingue et al., 1993; Troise et al., 1998; Dalla Via et al., 2003; Amoruso et al., 2005) indicated a rupture length (25 km) for the sub-event 1, even if the northern termination of the fault is not well constrained by such data (**Figure 2E**).

Sub-event 2 is located by Westaway and Jackson (1987) NE of Marzano Mt. and is attributed to the down-dip low-angle continuation of the high-angle NE-dipping Marzano fault. Several other authors (Bernard and Zollo, 1989; Pingue et al., 1993; Westaway, 1993; Troise et al., 1998; Dalla Via et al., 2003; Lancieri and Zollo, 2009) associated sub-event 2 as well to a low-angle normal fault, but located it at the base of the brittle layer along the down dip prosecution of the NNE-dipping outcropping of San Gregorio fault (inset in **Figures 2C,E**).

Pantosti and Valensise (1990) associated sub-event 2 with a high-angle normal fault belonging to the San Gregorio segment along the southward continuation of the Marzano fault (inset in **Figure 2D**). Amoruso et al. (2005), based on leveling data and aftershock distribution, detected, as a possible causative fault of the 20 s event, a SW-dipping high-angle normal fault, antithetic to the S. Gregorio one (inset in **Figure 2F**), which possibly reactivated a high-angle thrust fault located at the eastern edge of the Apulian belt (Improta et al., 2014).

Sub-event 3 is mostly attributed to the SW-dipping high-angle normal fault system antithetic to the Marzano Mt., possibly reactivating pre-existing Pliocene thrust structures (Amato and Selvaggi, 1993). The source is given in correspondence of the Conza fault or several kilometers southward (Westaway and Jackson 1987; Bernard and Zollo, 1989). Pingue and De Natale (1993), based on leveling data, proposed a 120°-striking and 80° SW-dipping fault. A very different hypothesis was advanced by Crosson et al. (1986), that associated sub-event 3 to a NE-trending fault orthogonal to the main Cervialto-Marzano alignment.

STRUCTURAL-GEOLOGICAL DATA AND ANALYSIS

An extensive set of observations were made during four field campaigns from 2017 to 2019. We carried out the fieldwork over an area of ~2400 km^2, primarily aimed at acquiring long-term and coseismic fault/slip data and at mapping the fault trace using a tablet computer on which the Petroleum Experts Fieldmove software was installed. We integrated the new data with geological maps from Servizio Geologico d'Italia (Servizio Geologico d'Italia, 1969; Servizio Geologico d'Italia, 1970a; Servizio Geologico d'Italia, 1970b; Servizio Geologico d'Italia, 1970c), scale 1:100.000, producing an original structural-geological map of the CLFS across the epicentral zone of the 1980-EQ (**Figure 3**; **Supplementary Figure S1**) and surrounding areas.

On a whole, we acquired ~350 data points (**Figure 3**), grouped in 40 survey sites (hereinafter referred to as SS) and we plotted the

TABLE 1 | Pseudo-focal mechanisms parameters. Lat N and Long E are representative location as they refer to an average location of a number of neighboring data points at different outcrop sites; N = number of fault slip/data used for the pseudo focal mechanism computation. Attitude is in strike/dip and rake is in Aki-Richards format; T axis (trend/plunge) have been computed applying the dihedron angle method to fault populations (Angelier and Mechler, 1977).

Main fault	Fault section or minor fault	SS n	Mean strike [deg. RHR]	Dip direction	Mean dip angle [deg.]	Lat N	Long E	N	Attitude [deg.]	Rake	T-trend	T-plunge
Irpina fault	Mt. Iuremito	3	300	NE	63	40°51′46.97″	15°7′9.65″	4	291/78.2	−87	018.8	33.2
	Mt. Oppido	5				40°49′13.31″	15°11′41.40″	10	316.4/54.4	−85	043.1	09.2
	Caposele	7				40°48′52.02″	15°12′46.9″	4	290.1/52.7	−86	017	07.7
	Mt. Marzano	8	315	NE	58	40°44′35.8″	15°18′30″	10	307/62.1	−88	035.4	17.1
	Mt. Carpineta	9				40°42′47.53″	15°20′33.7″	4	293.6/48.2	−85	019.9	03.1
	Melara	10				40°41′51.85″	15°21′8″	10	299.3/48.4	−99	035.7	03
	Pantano SGM	12				40°38′18.94″	15°26′37.9″	2	122/45.9	−80	205.1	00.5
	Ripa rossa	14	265	N	55	40°38′43.36″	15°27′59.45″	14	304.2/54.3	−92	035.8	09.3
	Balvano	15				40°38′38.75″	15°38′38.75″	2	278/69	−90	002.9	23.7
	Sant'Antonio	16				40°38′59.75″	15°31′1.95″	6	273.3/55	−90	000.5	10
	Sant'Antonio	17				40°38′42.75″	15°31′32.95″	14	287/74	−110	032.4	26.4
	Mt. Cerruto	21				40°38′5.44″	15°29′28.99″	2	276.1/49.2	−116	024.2	01.1
Mt. Paratiello	Mt. Paratiello north	23	280	NNE	67	40°45′9.58″	15°21′49.72″	6	288.8/67.2	−91	04.9	20.1
	Mt. Paratiello south	24				40°44′33.57″	15°27′1.58″	8	284.6/62.6	−93	001.6	15.8
Inner irpinia fault	Montella	22	300	NNE	72	40°50′3.73″	15°0′58.03″	2	301/77.7	−87	028.6	32.6
	Pianelle	25	104	SSW	60	40°40′58.89″	15°18′51.57″	6	121.6/47.9	−100	218.5	02.5
	Lavanghe	26				40°40′28.83″	15°21′47.62″	10	115.6/64.5	−98	211.5	19.1
	Lavanghe	27				40°40′45.80″	15°21′46.65″	2	097.9/52.8	−102	196.4	07.1
	Pantano antithetic	28				40°40′17.82″	15°25′12.24″	2	086.1/57.4	−98	181.5	12.1
	Pantano antithetic	29				40°38′55.14″	15°27′49.91″	8	125.1/50	−94	217.6	05
	Balvano antithetic	30				40°38′33.09″	15°32′36.94″	6	132.3/69.5	−96	227	24.2
Antithetic fault alignment	Pescopagano	32	110	SW	51	40°49′52.45″	15°26′6.02″	2	100/53.2	−95	193.9	08
	Castelgrande	34	123	SSW	60	40°47′7.27″	15°27′11.47″	4	107.6/64	−115	215.3	15.5
	Monticello Mt.	35				40°47′18.28″	15°29′47.18″	4	302.7/55.2	−108	045.2	08.6
	Monticello Mt.	36				40°47′3.65″	15°30′2.27″	2	350.1/73.9	−223	039.4	04
	Capo di Giano	37				40°46′34.29″	15°30′8.83″	2	108.1/69.4	−99	205.1	23.9
	Monticello Mt.	38				40°46′58.53″	15°30′39.91″	4	102.1/65.4	−49	163.7	10.9

fault/striae measurements in stereoplots using the FaultKin7 software (Allmendinger et al., 2012; **Figure 4**). To our dataset we added ~50 more observations from other authors (Brozzetti, 2011; Ascione et al., 2013; Galli and Peronace, 2014). We provide the dataset of georeferenced structural-geological observations and measurements as an Excel file to facilitate further use (**Supplementary Table S1**).

To provide an immediate view of the data distribution on the three main faults (detailed in the next section), we plotted them on four stereoplots (**Figure 5A**).

We analyzed the measured fault planes containing kinematic indicators using both the FaultKin7 and Stereonet software (Allmendinger et al., 2012). From this analysis we obtained the pseudo-focal mechanism for groups of fault/slip data belonging to or neighboring of a single SS (**Supplementary Figure S2**). In **Table 1**, we report the deformation parameters expressed as fault attitude, rake, and deformation axes of the pseudo-focal mechanisms with a representative location (Lat and Long).

For quality control, we assigned each of the structural-geological data with a quality parameter called Outcrop

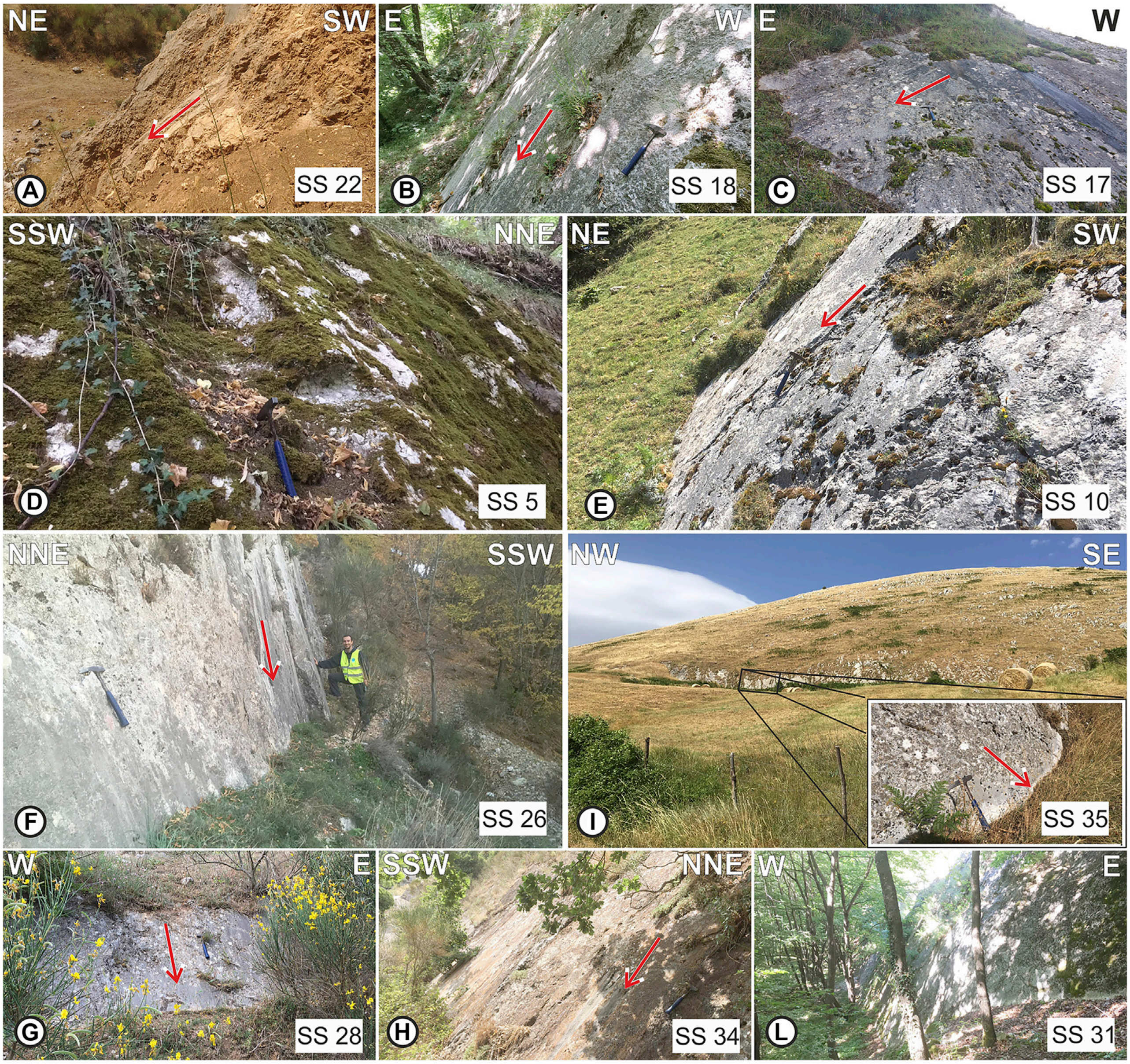

FIGURE 6 | Outcrop views of the Quaternary normal faults mapped in the study area (locations in **Figure 3** as small white circles) **(A,B)** refer to InIF; **(C)** to the E-W Irpinia; **(D,E)** to IF; **(F,G)** to minor antithetic structures in the PB and PSGM basins; **(H,I,L)** refer to AFA. Red arrows indicate the sense of slip given by the slickenlines measured on the fault plane. On each picture the number of the SS located in **Figure 6** is also indicated.

Quality Ranking (OQR). We assigned the OQRs during the field campaigns describing the degree of preservation and therefore the level of reliability of the outcrop on which the data was acquired. OQR is ascending (one is best). Out of the ~330 measurements, we assigned OQR = 1 to the 60% of them, OQR = 2 to the 19%, OQR = 3 to the –9% and OQR = 4 to the 2%. (**Figure 5B**). 10% of the outcrops were not rated. Looking at the overall data, we find a direct proportionality between the rock type and the OQR; measurements acquired on limestone or on indurated rock types obtained a higher OQR. The high percentage of OQR = 1 is in fact due to the presence, in this area of the southern Apennines, of formations belonging to the Apennine Carbonate Platform (Late Triassic - Middle Miocene), (**Supplementary Figure S1 and Table S1**).

To facilitate the use of the collected data and to increase quality control, we produced and provide a collection of the most significant sites' pictures to illustrate the landscapes, outcrops and features of the whole area (**Supplementary Data Sheet S1**). We produced the photographic documentation with one, two or three pictures on the ~60% of the outcrops. Each of the picture is uniquely identified with an ID number (photographic documentation ID in **Supplementary Table S1 and Data**

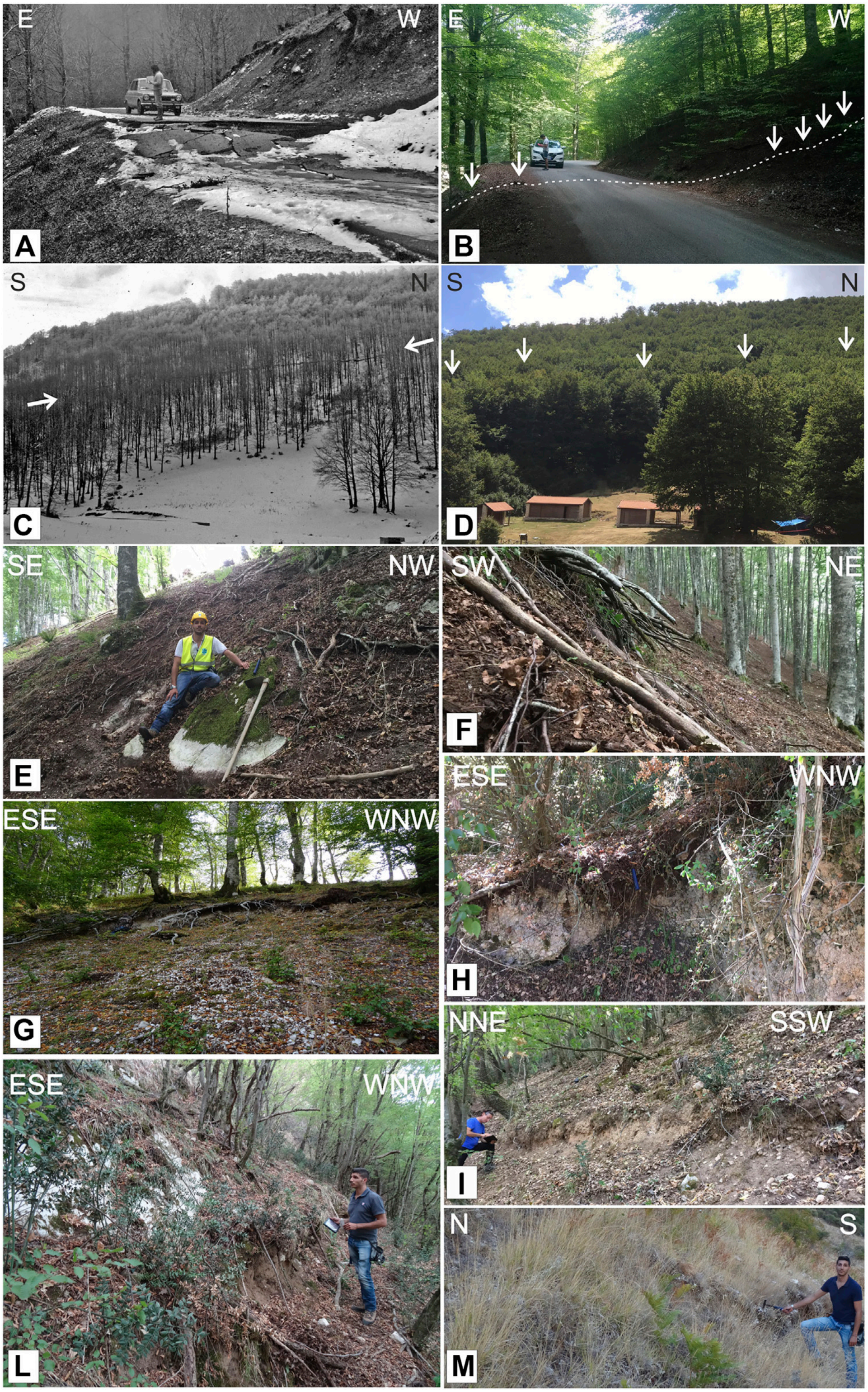

FIGURE 7 | Coseismic rupture evidence along the IF and AFA. Location in **Figure 8A**. **(A)** The road that coast the Piano di Pecore on Marzano Mt. with surface faulting of about 1 meter. **(B)** The restoration of the road surface has erased the trace along the road of the coseismic rupture, but the latter remains evident at its edges (black arrows). **(C)** Coseismic rupture along the Marzano Mt. slope in January 1981. **(D)** Panoramic view of the fault escarpment that highlights the shadow that the trees on the hanging wall expose on the trees on the footwall due to the coseismic ruptures (white arrows). **(A and C)** are photographs of I. Sgrosso published by Galli and Peronace, 2014 and **(B, D)** are photographs taken in the same places 40 years later during our field campaigns. **(E)** CoRs with the bedrock fault plane outcropping (Marzano Mt.). **(F)** Roots cut by the 1980 ruptures along the Marzano Mt. slope (details in the text). **(G)** CoRs affecting the slope close to the Melara locality (Melara fault section). **(H)** CoRs in the breccias at the southern edge of the PSGM basin (PSGM fault segment). **(I, L)** CoRs along the Ripa Rossa–Balvano segment affecting the slope debris at the base of the bedrock, or by fracture in soils and colluvium (details in the text), with vertical separations up to 1 m. **(M)** Rupture in the slope deposits with ~20 cm offset along the slope of Monticello Mt.

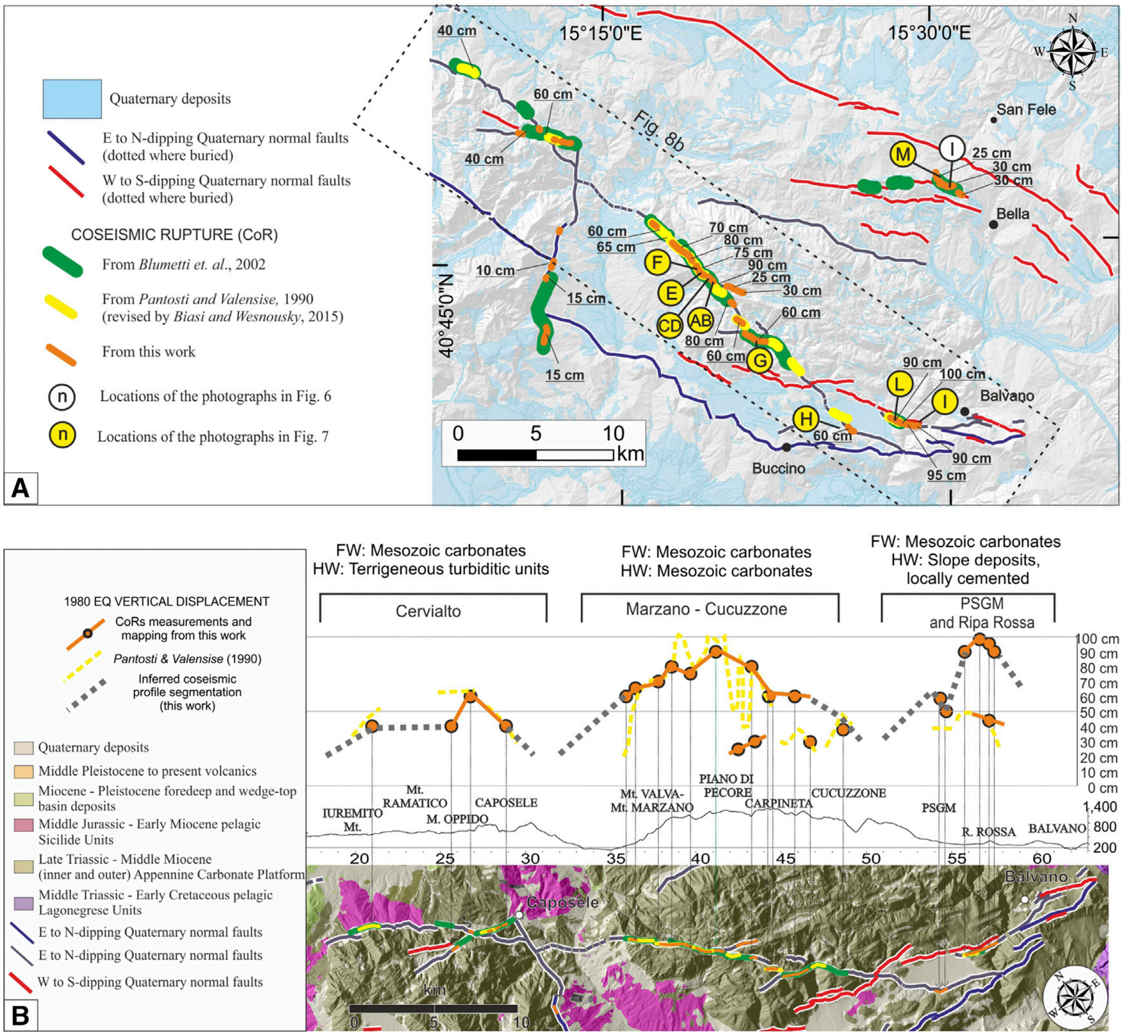

FIGURE 8 | Representation and analysis of 1980 coseismic data **(A)** Schematic structural map of the study area on which the Quaternary deposits are represented in light-blue on a 10 m resolution DEM. Along the traces of the main faults, the vertical displacement (in centimeters) of the CoRs measured during our fieldwork are reported. The extent along the strike of the CoRs is represented through colored ribbons according to the authors who mapped them (explained in the legend). Yellow circles are the locations of the photographs of **Figure 7**. **(B)** The graphics is a comparison between CoRs mapped in this work (orange lines and circles) and CoRs mapped by Pantosti and Valensise (1990) (yellow dashed lines) reported in map view through the topographic profile on the trace of IF. A schematic summary of the geologic contacts between the hanging wall and the footwall of the CoRs along the different segments is reported.

Sheet S1). We also show some examples of representative fault planes outcropping in the 1980-EQ epicentral area in **Figure 6**.

We also focused attention on evidence of coseismic slip associated with the 1980-EQ. We paid attention to those structures along which previous authors documented the 1980 earthquake primary coseismic ruptures (hereinafter referred to as CoRs), but we also identified some new evidence of coseismic slip which is significant for the seismotectonic interpretation of the system. After forty years, the CoRs are excellently preserved as it can be appreciated in **Figure 7**. Both the CoRs traces from previous papers (Pantosti and Valensise, 1990; Blumetti et al., 2002) and the new ones observed, are shown on the map of **Figure 8A**. A schematic summary of the geologic contacts between the hanging wall and the footwall of the CoRs is also reported.

Fault Segmentation Pattern

The field mapping and the structural dataset allowed us to highlight a complex Quaternary structural setting and segmentation pattern across the CLFS (**Figure 3A**; **Supplementary Figure S1**). Three main fault strands were mapped; they are here referred to as Inner Irpinia Fault (InIF) and Irpinia Fault (IF), eastward-dipping, and as Antithetic Fault Alignment (AFA), westward-dipping. Each of them, which have along-strike lengths in the order of several tens of km, represents a first-order structure, organized in second-order segments (few tens of km) and third-order sections (some km). The hierarchical order was defined at the 100.000 mapping scale and was based on the segmentation pattern of the fault traces derived from the distribution and size of structural-geometric features and complexities and locally integrated with 1980 coseismic displacement observations from the literature (e.g., Boncio et al., 2004; Manighetti et al., 2005; Christophersen et al., 2015) and from this paper.

The three first-order main faults, with lengths of 50–60 km, may be considered as individual and potentially seismogenic master faults. They would be substantially continuous at seismogenic depths (10–12 km) even if segmented at the surface and capable of releasing large-magnitude multi-rupture normal fault earthquakes, such as the 1980-EQ.

The second-order faults, here referred to as segments, span over a relatively broad range of lengths (10–30 km); they are separated from each other by a few kilometric size structural or geometrical complexities such as fault gaps, sharp bends, intersections with cross structures and transfer faults. The segments, in turn, may be continuous along strike or envelope interconnected sections. The here identified sections have length varying between 3 and 10 km; they are not necessarily continuous along strike, but often arranged at the surface in closely spaced structures of minor hierarchical order, separated by hundreds of meter complexities.

Detailed information concerning the identified fault segments and sections, including location, length, strike, dip-angle and rake were determined and are made available in **Supplementary Table S2**. In addition to the segments and sections, we have also parameterized all minor faults or splays by dividing them in their position with respect to the main fault to which they belong (i.e., hanging wall, footwall, synthetic or antithetic).

We assigned to each fault section or splay a Fault Quality Ranking (FQR) between 1 and 4 (1 is best) based on the reliability of surface constraints. A fault well constrained by a considerable number of new or bibliographic structural data, with the presence of significant geomorphological evidence (e.g., triangular facets) received a FQR = 1. On the contrary, a fault not very defined at the surface by structural data, with scarce geomorphological evidence was considered model-driven and received a FQR = 4. On a total of 72 mapped sections and splays, we assigned a FQR = 1 to the 51% of them, a FQR = 2 to the 19%, a FQR = 3 to the 17% and a FQR = 4 to the 13% (**Figure 5B**). We reported the FQRs in **Supplementary Table S2** close to the name of the fault.

We provide the mapped faults as a shapefile (**Supplementary Data Sheet S2**) and a full-page map with all the mapped faults and their names (segments, sections and minor faults; **Supplementary Figure S3**).

Detailed Fault Description

Inner Irpinia Fault

InIF is the westernmost main fault (~55 km-long) of the study area. The measures are variable within a fairly wide range of strikes because the fault is made up of well-identified segments with sudden changes of directions (**Figures 4**, **5A**). It is composed of four normal fault segments (from north to south they are referred to as Mt. Terminio, Mt. Cervarulo, Oliveto-Buccino and Buccino-Romagnano; **Figure 3**; **Supplementary Data Sheet S2**).

The Mt. Terminio segment is a NE-dipping segment extending for ~22 km. The segment develops within the rock types belonging to the Apennine Carbonate Platform (**Supplementary Figure S1**). We divided this segment in three sections (**Supplementary Data Sheet S2**). In the central one, for nearly 2-3 km, it causes the tectonic contact between the carbonate platform and the Sicilian pelagic units (**Supplementary Figure S1**). The envelope of these three sections was described and identified as “Volturara Fault” in Papanikolaou and Roberts (2007) and similarly interpreted in Faure Walker et al. (2012) and in Sgambato et al. (2020).

Due to the dense vegetation and the diffuse soil coverage, we observed only a few striated fault planes in the field (SS 22-**Figures 4**, **6A**), showing dip-slip. The fault segment defines several small intermontane basins filled with Quaternary sediments and bordered by slope breaks (**Figure 8A**; **Supplementary Figure S1**).

The Mt. Cervarulo segment strikes ~ N300 for ~14 km. It develops within the rock types belonging to the carbonate platform. It has been divided into two sections, the Mt. Cervarulo North and South, extended ~9 and ~5 km, respectively. Like the Mt. Terminio segment, several along-strike elongated basins are spread along its trace (**Supplementary Figure S1**).

A ~ N-S striking transfer fault, named Senerchia, extending for ~9 km, separates the two northern segments on the InIF from the southern ones. The fault causes the tectonic contact between the carbonate platform and the Sicilian pelagic units for its entire extent. Along this structure, numerous fault planes have been measured (**Figure 6B**; stereoplot 18, **Figure 4**). The calculated rakes for this fault range between −70° and −140° (**Supplementary Table S1**). The measurements made along this transfer fault, which is here considered part of the InIF, are evident in **Figure 5A**. The fault shows some evidence of coseismic displacement associated with the 1980-EQ (Blumetti et al., 2002; this paper). CoRs are on calcareous bedrock with vertical displacement of a few cm, along a road located east of the village of Senerchia.

The southern portion of InIF is composed of two segments divided by a sudden strike variation. The Oliveto-Buccino segment is a NE-dipping fault further divided based on minor strike variations into four sections. The extent and continuity of the fault are poorly constrained, due to the non-conservative lithology of the displaced units (**Supplementary Figure S1**) and to the abundant alluvial and slope debris cover. Nevertheless, the integration of field data with photo-geological interpretation, locally integrated with the visual analysis of morphostructural elements, led us to map for ~20 km-along-strike. Where exposed, it dips north-westward at a high-angle of 60–65° and shows dip-slip sense of motion (SS 19 **Figure 4**).

With the Buccino-Romagnano segment, InIF turns to an E-W direction. It stretches for ~9 km with local deviations in strike to WNW-ESE bordering the Piani di Buccino basin. The structural data measured along this segment are synthesized in the stereoplots of the SS 20–21 (**Figure 4**). We located the tip of the InIF at the intersection with the IF, described below.

The northern side of the Piani di Buccino are bordered by a left-handed arranged en-echelon pattern of minor faults here considered to be antithetic at the footwall of InIF (**Supplementary Table S2**). As for InIF, a clear change in strike is observed from NW-SE to ~ E-W. This alignment develops for ~17 km along-strike and contributes together with the whole east-dip system to the setting of the two intramountain continental basins (i.e., Piani di Buccino and Pantano di San Gregorio Magno, hereinafter referred to as PB and PSGM). The origin of these lacustrine basins, separated by a bedrock threshold and filled with quaternary deposits, occurred during the Middle Pleistocene (Ascione et al., 2013). We report the measurements of striated fault planes acquired on this alignment in the stereoplots SS25 to SS30 (**Figure 4**) and photographs in **Figures 6F, 6G**. The structural analysis shows mostly dip-slip (**Figures 6F, 6G**) and a slightly normal-left sense of motion in a few outcrops (SS29 in **Figure 4**).

Irpinia Fault

The IF is a largely exposed normal fault, widely described for large part of its extent in previous works (Pantosti and Valensise, 1990; Galli and Peronace, 2014, among others). It strikes in an average N125 E direction and develops for a total length of ~55 km along-strike, with an average dip of 65° to the NE. It consists of three segments elongated in the Apennine direction (i.e., Mt. Cervialto, Marzano-Cucuzzone and PSGM segments, **Supplementary Figure S3**) and of a southernmost segment bent in the E-W direction (i.e., Ripa Rossa-Balvano) (**Figures 3**, **5A**). The three NW striking structures extend along-strike for ~13 km, ~23 and 10 km respectively and are arranged in a right-handed en-echelon pattern.

The Mt. Cervialto segment consists of five en-echelon sections, each with a length between 2 and 3 km. The segment marks the contact between the Apennine carbonates at the footwall and terrigenous turbiditic units at the hanging wall (**Supplementary Figure S1**). Structural data acquired (**Figures 4**, **5A**) show a purely dip-slip or slightly normal-left kinematic (**Table 1**; **Supplementary Table S1**). The average rake is −86°. Along this segment, near the village of Caposele, we measured CoRs with variable vertical displacements between 40 and 60 cm on bedrock (**Figure 8**). This segment is separated from the southern one by the pre-existing N-S discontinuity, coinciding with the Senerchia fault (described above).

The Marzano-Cucuzzone segment is composed of five sections each slightly bending in the southern portion from a NW-SE strike to a NNW-SSE (**Figures 3**, **5A**); their length ranging between 3 and 5 km. The segment puts in contact two different portions of the same carbonates platform succession (**Supplementary Figure S1**). Nevertheless, it bounds westward several small intramountain basins such as the Piano di Pecore or Melara plains, filled with colluvial deposits. Data acquired along this segment show a dip-slip to slightly normal-left sense of motion (stereoplots 8 to 11, **Figures 4**, **5A**, **6E** and **Supplementary Data Sheet S1**) with an average rake of −88°. Slickenlines measured display a plunge toward N035° along fault planes dipping ~65° toward N045°. On the Marzano section we measured CoRs with a peak of ~90 cm (**Figures 7E**, **7F**, **8**; **Supplementary Data Sheet S1**). The 1980-EQ CoRs truncated the roots of the trees that remained suspended on the footwall of the ruptures (**Figures 7E–G, 7L**). Along the Melara section, we observed CoRs with vertical displacements ranging from 40 to 60 cm (**Figures 7G**, **8**).

TABLE 2 | Seismological and Geological stress tensor parameters showed in **Figure 10E** for the Irpinia fault systems. σ_1, σ_2, σ_3 = principal stress axes; Φ = stress ratio = $(\sigma_2-\sigma_3)/(\sigma_1-\sigma_3)$; QR = quality ranking: AQRw as in Sperner et al. (2003) and A-QRfm as in Heidbach et al. (2010).

Dataset	σ_1	±1σ	σ_2	±1σ	σ_3	±1σ	R*	±1σ	QR
FM2	79/216	16.0	04//325	14.5	10/056	13.0	0.4	0.1	A
FM1	75/186	19.5	07/301	22.9	14/032	18.9	0.6	0.2	A
PFM	83/235	17.5	03/121	17.5	07/031	15	0.3	0.2	B

The southernmost segment with NW-SW direction is the PSGM. The SGM Gap separates this segment from the Marzano-Cucuzzone segment. It is composed of two sections NE- and NNE-dipping with lengths of ~2 and ~4 km respectively (**Figure 3**; **Supplementary Table S2**). The fault can be observed outcropping on the western edge of the PSGM basin. The data acquired (stereoplot SS12 in **Figure 4**) show the strike variation of the two sections and dip-slip kinematics (slightly left-normal) with an average rake of -80° and a plunge of the slickenlines toward N030°. We measured CoRs of ~60 cm (**Figures 7F**, **8**). Also within the PSGM basin fill, important CoRs formed. Although these are no longer visible in outcrop due to widespread agriculture in the plain, some photographs taken just after the earthquake document their presence (e.g., Galli, 2010).

The E-W striking segment of the IF (Ripa Rossa-Balvano), is arranged in a left en-echelon pattern with respect to the PSGM segment. It is composed of two sections (Ripa Rossa and Balvano) with good exposures of fault planes both along the northern slope of the Ripa Rossa Ridge and along the east side of Balvano village (**Figures 6C, 7H, 7L**). In these outcrops, the fault cuts the Late Pleistocene-Holocene slope debris (Servizio Geologico d'Italia, 1969). The observed sense of motion is dip-slip along the westernmost fault planes (SS14 and SS15 in **Figure 4**) and normal-oblique along the easternmost ones (SS16, SS17). This ~ N-dipping fault extends for ~10 km along the Campania-Lucania border. The attitude of the kinematic indicators observed on the fault planes shows a slight left-lateral component (average rake of −80°) (**Figures 5A**, **6C**). CoRs with vertical displacement up to ~90 cm were measured halfway up the slope of the Ripa Rossa Ridge, spreading over the slope deposits locally cemented and ending up on carbonate platform bedrock fault planes (**Figures 7I, 7L**, **8**). We present pictures of the CoRs here observed in the photographic documentation of **Supplementary Data Sheet S1**. In an antithetic position with respect to the Balvano section, we measured fault planes considered to be part of the minor faults that border the PB and PSGM basins, antithetic to the InIF and described above (SS25 to SS30 in **Figure 4**). Further minor faults have been mapped in this area (few km lengths). The structural data show normal-to-slightly right-normal sense of motion (**Table 2**; **Supplementary Tables S1, S2; Supplementary Data Sheet S1, S2**).

Antithetic Fault Alignment

The AFA is a SW- to SSW-dipping alignment of faults antithetic to IF and InIF. The three segments branch off parallel to the IF for over 60 km (**Supplementary Figure**

S3). The northernmost one (San Felice) extends for ~10 km and is divided in two ~5 km-long sections. Its norhern portion affects the Middle Triassic-Early Cretaceous pelagic Lagonegrese Units and partially the Middle Miocene Carbonate Platform units (**Supplementary Figure S1**). Due to the weakness of the outcropping units, they are poorly detectable in the field and are mainly defined through geophysical and seismological data. The central segment, known as "Conza" (DISS Working Group, 2018) extends for ~22 km and is composed of three sections. The two northern sections, as the San Felice segment, are buried. The southernmost section (Pescopagano) crops out, and the data show a normal to slightly-right-normal sense of motion, with fault planes S-to-SSW-dipping of ~55° and slickenlines plunging ~ N210°.

The Bella segment is a ~20 km-long normal fault with a ~N120 strike SW-dipping of ~60° (SS 33 in **Figure 4**). This segment is composed of three sections, Bella North, Central and South, ~9, 5 and 4 km-long respectively. It presents several splays both at its hanging wall and footwall (**Supplementary Table S2 and Data Sheet S2**). Data in SS31 (**Figure 4**) refer to the synthetic minor fault at its footwall whereas SS34 to SS40 refer to splays and minor faults within the Bella (central) hanging wall. In this position are located the synthetic Pescopagano and Monticello splays, that overall are ~18 km-long. They extend in E-W direction from the village of Castelgrande to Monticello and in NW-SE direction from Monticello mount to the locality of Baragiano (**Supplementary Figure S3**). The change in direction of the structure (NW-SE to E-W) is shown in SS35–38 of **Figure 4**. The outcrops are characterized by well-preserved planes showing ~ N190/200°-trending normal slickenlines (**Figure 6I,H**) with a rake of ~ −110°. Along the Monticello splay it is possible to observe at the base of the fault planes a white free-face of ~20 cm (**Figure 6I**) some tens of meters-long. In the same locality, a rupture in the slope deposits with ~20 cm offset is visible for some hundred meters (**Supplementary Data Sheet S1**).

Other Faults

In the northernmost sector we reconstructed a normal fault (i.e., Castelfranci), consisting of four sections of variable length between 3 and 6 km, through photo-geological interpretation, integrated with the analysis of morphostructural elements. Nevertheless, the fault was identified by Westaway (1993) because of a dense NNW-SSE elongate cluster of seismicity developed between the localities of Partenepoli and Nusco, documenting then the northward propagation of the rupture of the 1980-EQ for ~10 km.

Between the IF and the AFA, close to the village of Muro Lucano, a NE-dipping fault, Mt. Paratiello, crops out (Brozzetti and Salvatore, 2006; Brozzetti, 2011). The recent activity of this fault is suggested by the deformation, within its damage zone, of recent debris, possibly Late Pleistocene–Holocene in age, as suggested by the lack of sensible cementation and by the presence of dark brown paleosol lenses. The fault planes dip ~065° toward NNE and display slickenlines ~ N020°-plunging (SS23 and SS24 in **Figure 4**). Along this fault two generations of slickenlines show respectively transtensional and normal sense of motion. The latter is reasonably associated with Quaternary extension, whereas the former might be related to a previous strike-slip faulting phase which would have occurred during the Late Pliocene–very Early Pleistocene (Brozzetti, 2011 and references therein).

SEISMOLOGICAL DATA AND ANALYSIS

A comparison between the seismicity pattern observed during the 1980-EQ seismic sequence and the recent seismic activity is useful to understand the reliability of early instrumentals data and to better discuss their association with the seismogenic faults. To this aim, we performed a comprehensive review, collected and analyzed seismological data available in the literature from 1980 to 2018.

We have analyzed the aftershock distribution in the time interval from 01/12/1980–15/12/1980 relocated by Amoruso et al. (2011) with a 3D velocity model. The dataset consisted of 629 earthquakes (1.0 ≤ M_L≤ 4.0) and represents the most recent revision of the 1980-EQ aftershocks.

The overall aftershock distribution was analyzed by mean Kernel Density Estimation (KDE). The aftershocks show that the epicentral area extended for a length of ~60 km in the NW-SE direction and its largely confined between the east-dipping IF and the antithetic west-dipping fault zone. Along strike, it is possible to identify four major epicentral clusters, mainly positioned in the center of the graben. The contours define the three seismic gap zones (Nusco, Sele and San Gregorio gaps in **Figure 9A**) well known in the literature (Westaway and Jackson, 1987; Bernard and Zollo, 1989; Pantosti and Valensise, 1990). It is also noteworthy that part of seismicity can be also associated with the InIF. Northward, the aftershock area reaches the Castelfranci segment, whereas earthquake data are missing in the southern sector. This configuration was conditioned by the seismic station distribution more concentrated to the northern sector as demonstrated by Bernard and Zollo (1989). We do not exclude the occurrence of aftershocks associated with the southern sector of the Irpinia and East-West Irpinia faults.

Background Seismicity

This seismicity of the Campania-Lucania area is monitored by the Italian Seismic Network and by a local network (Irpinia Seismic Network, ISNet, Iannaccone et al., 2010). The large amount of available data has allowed refinement of the velocity models and constrain the seismicity distribution and focal mechanisms (De Matteis et al., 2012; Stabile et al., 2012; Amoroso et al., 2014; De Landro et al., 2015; Vassallo et al., 2016; Adinolfi et al., 2019). The area is mainly characterized by low-to-moderate recurrent seismicity (M_L ≤ 3.0) at upper crustal depths and defined as background seismicity by De Matteis et al., 2012. The only significant event, after the 1980-EQ, occurred on April 3, 1996 (M_w 5.1) in the southern IF sector. Its instrumental epicentre is within the seismic gap of the two fault segments associated with the 0 and 20 s sub-events (Cocco et al., 1999).

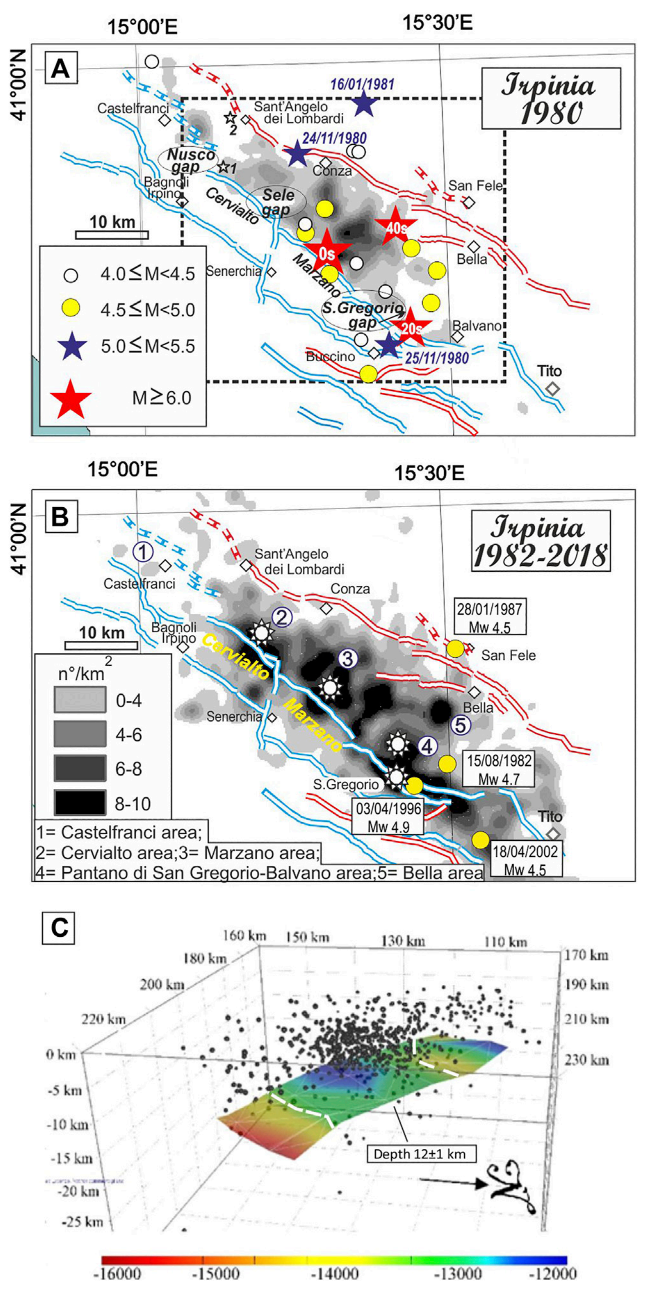

FIGURE 9 | Instrumental seismicity of the study area from 1980 to 2018. **(A)** Seismicity distribution of the Irpinia 1980 seismic sequence (M_w 6.9, Io X MCS) from November 23, 1980 to December 31, 1981. The main events epicentres (red stars) are from Amoruso et al., (2005) and Amoruso et al., 2011, the other significant events are from Montone and Mariucci 2016, Italian CMT (Pondrelli et al., 2006) and some unpublished data. The density contour lines (number of earthquakes per square kilometer) are referred to the aftershocks ($1.0 \leq M_L \leq 4.0$) occurred from the first to the 15th December of 1980 and relocated by Amoruso et al., (2011). The two small white stars, 1 and 2, are the epicenters of the Nusco (April 15, 2020, ML 3.3) and Rocca San Felice (July 6, 2020, M_L 2.7) recent small events, respectively. **(B)** Seismicity distribution from 1982 to 2018 obtained compiling the Italian Seismic Catalogue CSI (Castello et al., 2006) and all the events ($0.3 \leq M_L \leq 5.1$) listed in the Italian Seismological Instrumental and Parametric database (ISIDe, working group 2016). The white stars represent the seismicity cluster as in reported in Stabile et al., 2012. **(C)** Base of the seismogenic layer computed for the study area and used for the source model reconstruction, obtained with De Landro et al., 2015 relocated seismicity. The white line represents the reliable curve.

We analyzed the instrumental seismicity, from 1982 to 2018, available from Italian catalogs (Castello et al., 2006, CSI 1.1, 1981–2002; Italian Seismological Instrumental and Parametric database, 2003–2018; **Figure 9**). We also used the 2005–2011 3D relocated seismicity by De Landro et al. (2015) and the revised seismic bulletin by Chiarabba et al. (2015). The epicentral density contours of seismicity, derived from Italian catalogs (**Figure 9B**), shows that the 1980-EQ area still displays significant seismic activity along Cervialto (n°2) and Marzano (n°3), with exclusion of the northernmost Castelfranci area (n°1). The density contour also shows that the background seismicity is not only concentrated along the Apennine chain axis, in between the east- and west-dipping seismogenic faults, but enlarged southward along San Gregorio Magno sector (n°4), eastward close to Bella village (n°5), and westward indicating activity also associated to the Inner Irpinia fault. Just recently (April 15, 2020), an M_L 3.3 event occurred, 3 km SE of Nusco at a depth of 12 km, apparently activating InIF at depth, with extensional sense of motion (**Figure 9A**). Furthermore, a small extensional sequence (M 2.7) occurred at Rocca San Felice, from July 4-6, 2020. Earthquake locations from local networks (Festa et al., 2020), show a small high-angle (~60°) SE-dipping hypocentral volume at depths of 11–12 km, possibly activating the Castefranci fault.

We also computed density contours of the seismic activity for the three datasets, above mentioned, in order to verify the stability and the persistence of the seismicity clusters. The corresponding maps are given in **Supplementary Figure S4**. The results of spatial clusters of **Figure 9B** are in agreement with what has been observed, at smaller scale, by Stabile et al. (2012), who showed that earthquakes are prevalently clustered around specific areas, probably asperities of the IF, and the seismicity is typically released in swarm-like seismic sequences (white stars in **Figure 9B**) (De Matteis et al., 2012; Stabile et al., 2012).

Base of the Seismogenic Layer

In order to study the depth distribution of seismicity, we considered only the best relocated seismic catalogs: the 3D relocated aftershocks by Amoruso et al. (2011), the 3D relocated background seismicity by De Landro et al. (2015), and the relocated events by Chiarabba and Gori (2016) (hereinafter referred to as DD1, DD2, DD3). Starting from these three datasets, we computed a 3D seismogenic layer as part of the 1980-EQ 3D fault model reconstruction following the approach proposed in Ferrarini et al. (2017) and Castaldo et al. (2018) (**Figure 9**; **Supplementary Figure S5**). Specifically, the base of seismogenic thickness was computed starting on a regular grid chosen performing preliminary tests to find the optimal grid-space configuration respect to the earthquake distribution. The events, falling into the adjacent parallelepipeds (10 × 10 km of base) centered on the grid nodes, were selected and used to compute the cumulative frequency vs. depth. The evaluation was performed detecting the layer that releases the 90% of events at each node. The 3D reconstruction was carried out by interpolating the results with the Delaunay triangulation method (Okabe et al., 1992). This procedure was independently repeated for DD1, DD2 and DD3. To define the base of the seismogenic layer, we consider reliable the grid

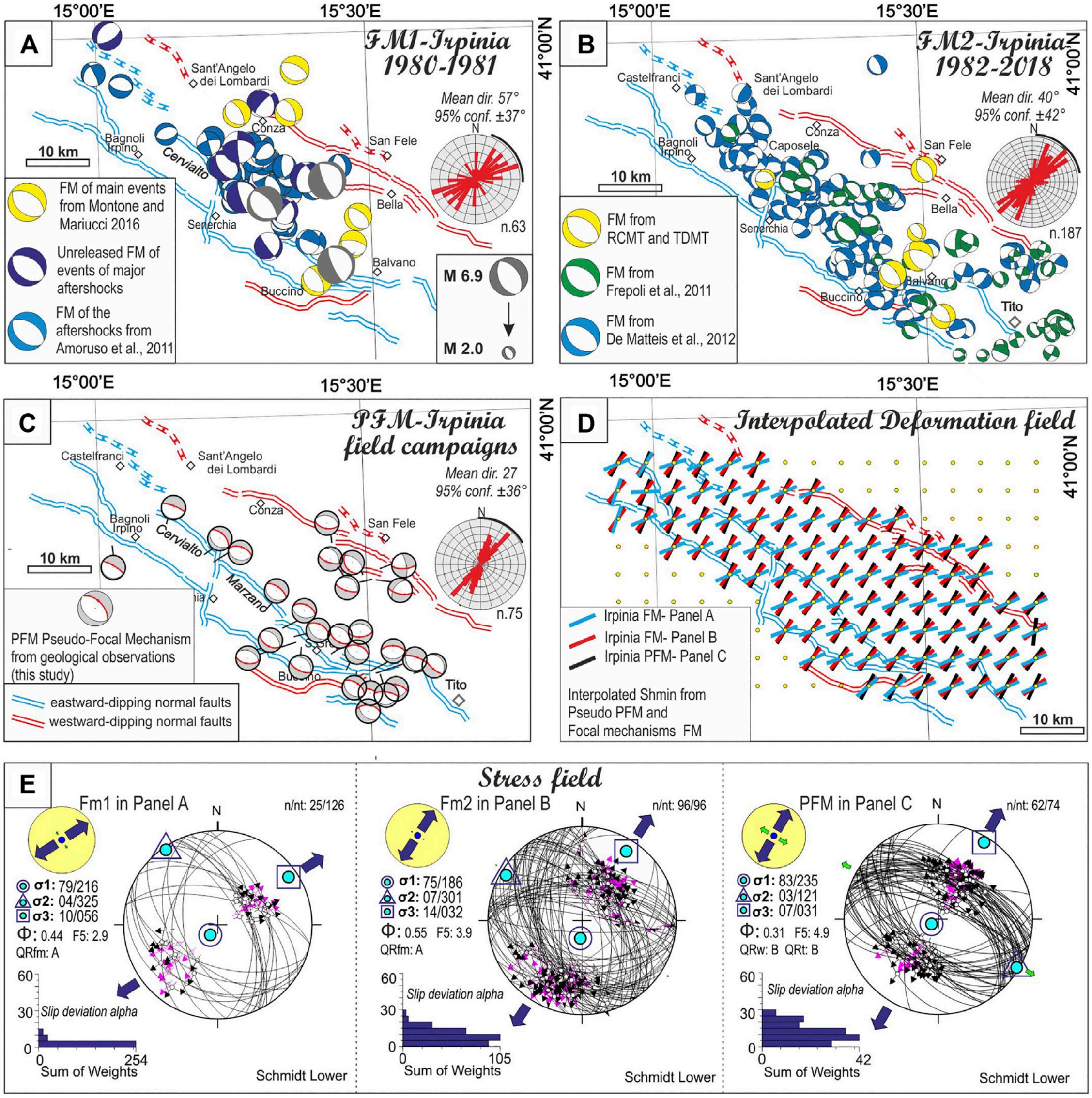

FIGURE 10 | Deformation and stress field of the study area. **(A)** Focal mechanisms distribution of 1980-EQ seismic sequence. The beach-balls of the main event are from Westaway and Jackson (1987), the major aftershocks ($M_w > 5.0$) from Italian CMT, and the aftershocks from Amoruso et al., 2011. The blue ones refer to **Supplementary Data Sheet S3**. **(B)** Focal mechanisms distribution from 1982 to 2018. Focal mechanisms solutions of the more energetic events ($M_w \geq 4.0$) are from the Italian CMT and Time Domain Moment Tensor catalog (Scognamiglio et al., 2006), the others are from detailed papers (Frepoli et al., 2011; De Matteis et al., 2012). **(C)** Pseudo focal mechanisms computed with geological structural data. **(D)** Deformation pattern from data in **Panel A–C** opportunely selected for quality. The colored axes represent the results of the interpolated sh_{min} computed following the approach of Carafa and Barba (2013). **(E)** Stress inversion of the fault plane solutions given in **panel A, B** and of Pseudo focal mechanisms obtained with geological fault/slip data. The followed inversion procedure as in Delvaux and Sperner (2003). The histograms represent the corresponding misfit angles vs. the number of data points; nt = total number of data; n = number of successfully inverted data; σ1, σ2, σ3 = principal stress axes; φ = stress ratio = $(\sigma_2-\sigma_3)/(\sigma_1-\sigma_3)$; the quality ranking factors (QR) and the stress inversion parameters with associated uncertainties are listed in **Table 2**.

nodes containing at least 15 earthquakes (dashed line in **Figure 9C**). The results and the comparison are showed in **Figure 9C** and **Supplementary Figure S5**.

DD1, DD2, and DD3 depict a pattern of seismicity contained in a well-defined volume confined between the east and west-dipping fault alignments. The base computed with the three datasets is well defined at depth of ~12–13 km with an average maximum vertical error of ~1 km (**Supplementary Figure S5**).

DEFORMATION AND THE EVOLVING STRESS FIELD

Focal Mechanism Dataset Compilation

To determine the Quaternary and present deformation and stress field in the 1980-EQ area, we used seismological and geological data. We subdivided the available seismological data in two datasets taking into consideration the diverse quality of modern observations with respect to the ones of the eighties

(**Figures 10A, 10B**). The first dataset consists of a compilation of 63 focal solutions ($2.5 \le M \le 6.9$) spanning from November 23, 1980 to December 31, 1981. It is composed by focal mechanisms (FM) of the 0 , 20 , and 40 s events (Westaway and Jackson, 1987), the major earthquakes ($M_w \ge 5.0$) (Montone and Mariucci, 2016), 10 unpublished focal mechanisms (computed with the first polarities of the teleseismic data, **Supplementary Data Sheet S3**) and the aftershocks of the seismic sequence relocated by Amoruso et al. (2011). The latter provides the most complete set of solutions that have been derived to date from the data related to the 1980-EQ (**Figure 10A**). The second data set is composed by 187 (**Figure 10B**) focal mechanisms of earthquakes occurred from 1982 to 2018 mainly derived from microseismicity $2.0 \le M_L \le 4.0$ (Frepoli et al., 2011; De Matteis et al., 2012) and from the Italian CMT and TDMT catalogs, $4.0 \le M_w \le 5.4$ (Pondrelli et al., 2006; Scognamiglio et al., 2006).

The geological dataset is composed by pseudo-focal mechanisms (PFM) (**Figure 10C**) computed from fault/slip data of this study (**Figures 4**, **10C**; **Supplementary Figure S2 and Table 1**). The three datasets show prevalent normal-to-normal-oblique sense of slip with a scattered (~± 40°) T axes distribution around mean values of 57°, 40°, and 27° respectively (**Figure 10**). We explored this discrepant T-axis attitude and evaluated the strain and stress field pattern. Whenever possible, we first performed a preliminary quality analyses for FM computed with the polarities. The available focal mechanisms were selected based on the two quality factors (Q) of the FPFIT code, decreasing from A to C, which are the degree of polarity misfit (Qp) and the range of uncertainties of strike, dip and rake (Qf). The selected solutions have quality A–A, A–B, B–A and B–B and a threshold magnitude $M_L \ge 2.5$. The selected datasets are composed of 63, 96, and 74 focal and pseudo focal mechanisms (**Figure 10E**, Fm1, Fm2 and PFM).

Strain Field and Stress Inversion

In order to analyze the map variation of the strain field, we computed the minimum horizontal stress (Sh_{min}) from the focal and pseudo focal mechanisms related to the three datasets described above. We built a regular grid comprising the east- and west-dipping active faults and evaluated the variation of Sh_{min} at each node. For the interpolation we followed the approach proposed by Carafa and Barba (2013) to calculate the SH_{max} that considers the uneven sampling of FM data and the correlation of stress orientation with distance. We observe small differences between the deformation field derived by focal solutions (1982–2018) and the ones obtained from geological data (mean ~14° ± 5°) (black and red deformation axes in **Figure 10D**); such differences represent the average Sh_{min} changes from surface to depth, in fact the highest differences between these two datasets are observed for grid nodes positioned in the center of the graben, in between the east- and west-dipping normal fault alignments. On the contrary, large differences (mean ~38° ± 9°) are obtained comparing the Sh_{min} map distribution from 1980 seismic sequence and the other two datasets in most points of the grid. The deformation field can be considered homogeneous because of large or significant variation of Sh_{min} along the study area are not observed for all datasets.

This difference between the 1980 dataset and recent FM are also evident comparing the stress tensors. In fact, to compute and analyze the seismogenic stress tensor of the study area we independently inverted the three datasets following the procedure proposed in Delvaux and Sperner (2003) and the methodological approach as in Ferrarini et al. (2015). The orientation of the three principal axes of the stress (σ1, σ2, σ3) and the stress ratio $\Phi = (\sigma2 - \sigma3)/(\sigma1 - \sigma3)$ are considered as model parameters.

All theinversions highlight a normal faulting stress regime with a nearly horizontal, NNE–SSW to NE-SW trending σ3-axis (10/056, 10/032, 07/031) and a subvertical σ1-axis attitude (79/216, 75/186, 83/235); the shape factor, equal to 0.44, 0.55, 0.31 respectively, indicates a near triaxial tensor in the case of inversion obtained with FM. The stress orientations solutions fall in the quality rank QRfm = A, QRfm = A and QRw = B as shown in **Figure 10E** and summarized in **Table 2** (quality factor as in Sperner et al. (2003) and Heidbach et al. (2010)). We can observe that the inversion of the 1980-EQ seismological dataset (63 focal mechanisms, nt = 126 nodal planes) shows a 056 trending σ3-axis rotated of ~30° respect to the ones obtained with the other two datasets that show a coaxial attitude (032 and 031). It is worth noting that, notwithstanding the resulting stress tensor is of A-quality, a large percentage of total data was rejected. This is due to the high heterogeneity of the resulting senses of motion retrieved by the aftershock focal mechanisms as highlighted in Deschamps and King (1984), Westaway and Jackson (1987), and by Pasquale et al. (2009). In contrast, the results of second and third formal inversion show that most of the data are consistent with the computed stress tensor being 100% and 84% considered in the inversion (n/nt, **Figure 10E**).

FAULT MODEL BUILDING

Depth Geometry and 1980-EQ/fault Association Along the CROP-04 Seismic Profile

The epicentral area of the 1980-EQ is cross-cut by the CROP-04 near-vertical seismic line (Cippitelli, 2007; Patacca and Scandone, 2007; Scrocca et al., 2007) that runs SW-NE perpendicular to the average axial extensional trend (**Figure 11**).

To define the downdip geometry of the CLFS involved in the 1980-EQ, we updated the Brozzetti's (2011) interpretation of the central part of the profile by integrating it with our geological data along the trace of the Alburni–San Fele transect (**Figure 11A**). Beneath the 1980-EQ epicentral area, we have an upper crust sedimentary pile of ~10 km. Such a pile lies above a thin low-velocity clastic layer (e.g., sedimentary basement) transitional to the underlying metamorphic basement (Improta et al., 2000; Patacca and Scandone, 2007; Steckler et al., 2008; Di Luzio et al., 2009; Brozzetti, 2011; Ascione et al., 2013).

The two main faults involved in the 1980-EQ (IF and AFA) are recognized in the sections of **Figures 11C, 11D**. They belong to a broader extensional system, which from west to east, consists of

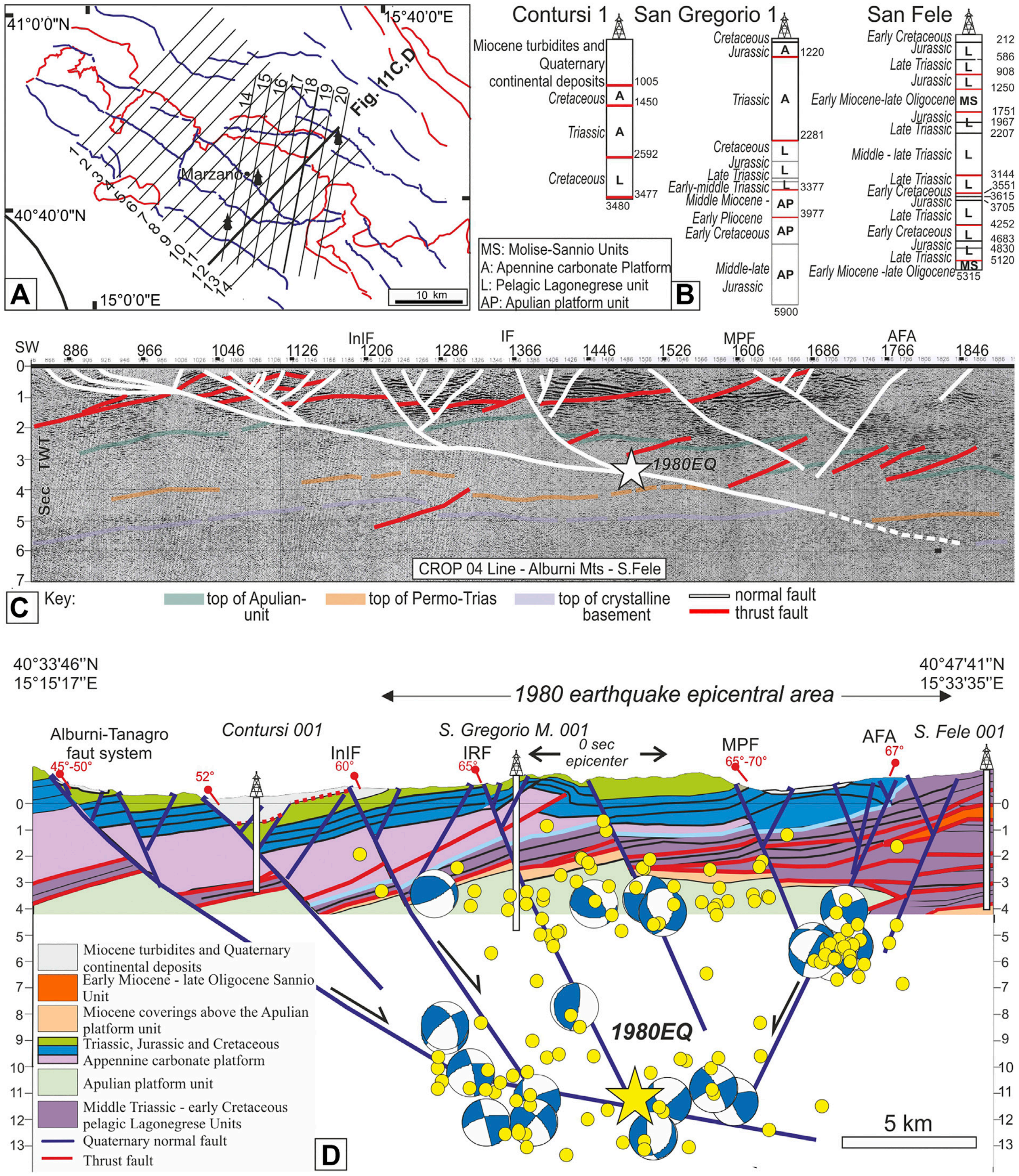

FIGURE 11 | Depth interpretation of the outcropping 1980-EQ faut pattern along the trace of the CROP-04 near vertical seismic profile. **(A)** Location map with the trace of the CROP-04 line; the serial transects used to build the 3D faut model of **Figure 12** are reported. **(B)** Contursi, San Gregorio Magno 001 and San Fele wells stratigraphy. **(C)** Interpretation of the CROP-04 profile, along the Tanagro–S. Fele transect (from Brozzetti, 2011). **(D)** Geological cross-section along the CROP-04 line, oil wells, seismicity (yellow circle from De Landro et al., 2015) and focal mechanisms from De Matteis et al., 2012 (semi-width 5 km).

four well distinct east-dipping faults (Alburni-Tanagro (ATf), the Picentini, InIF and IF) with dips ranging from 45° to 65°. The ATf represents the break-away fault of the overall system, which develops above the east-deepening detachment layer. The ATf reflector can be recognized at 2.5s-depths (5–6 km) below the PB basin at the hanging wall of the IF and in some continuous

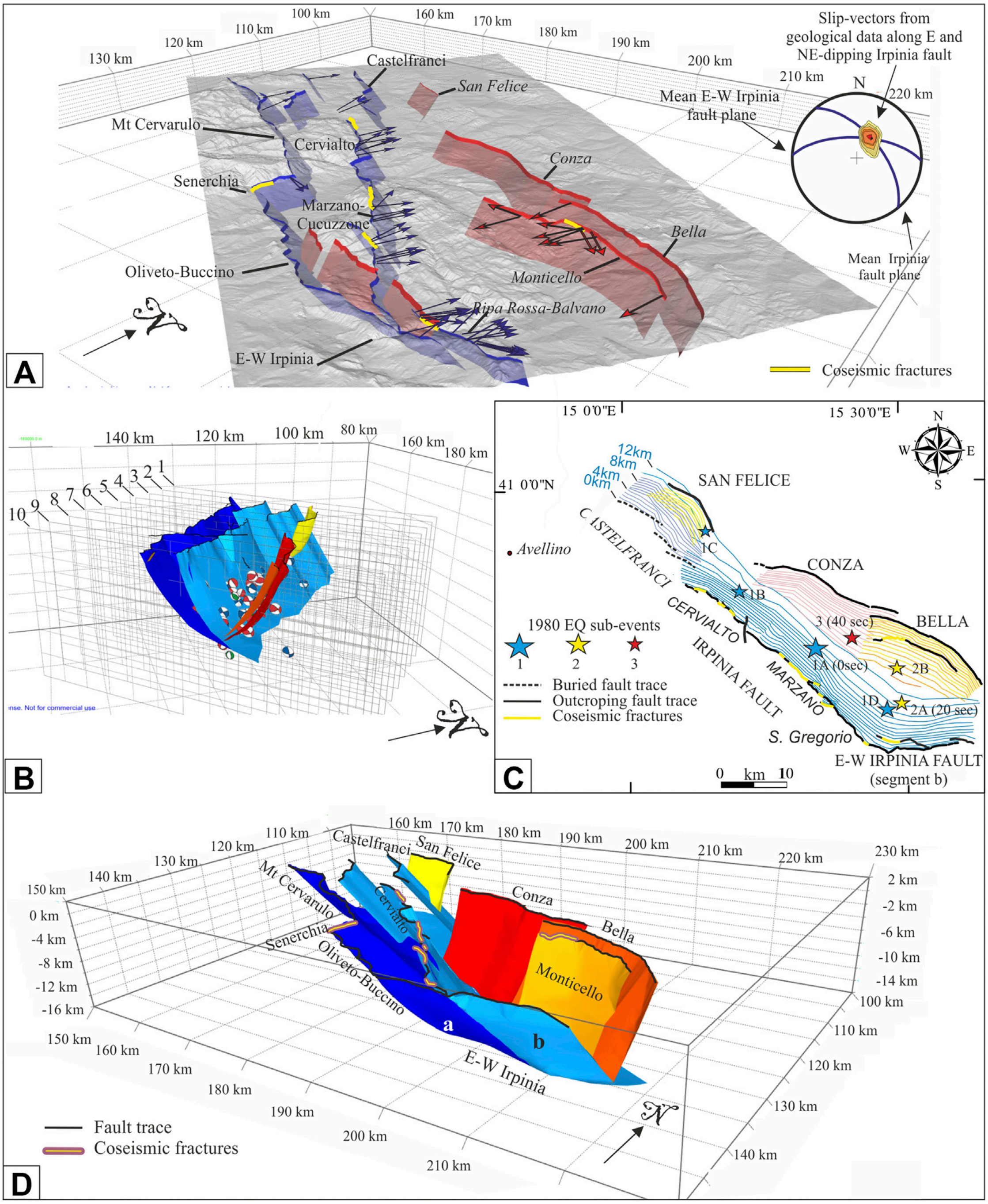

FIGURE 12 | 3D model building and seismotectonic interpretation of 1980-EQ. **(A)** Fault "Ribbons" i.e., extrapolation in depth for 3 km of the fault traces with the dip-angle acquired during the field work (**Figure 3A**; **Supplementary Data Sheet S2; Supplementary Tables S1, S2**); the fault slip vectors are also reported as blue and red arrows projected on the surface. The model is represented on a 10 m DEM; the coseismic ruptures (yellow lines) are from this paper and from Pantosti and Valensise (1990). **(B)** Serial hypocentral and focal mechanisms cross-sections used to build the 3D surface along the ribbon down dip extrapolation (data from De Landro, et al. (2015) and De Matteis et al. (2012)). **(C)** Depth contour lines of the reconstructed fault surfaces with location of the epicenters of the sub-events and episodes of 1980-EQ. **(D)** 3D fault model of the Inner Irpinia Fault and Irpinia Fault (e.g., Cervialto, Marzano and San Gregorio) with their common southern E-W segment plus the Antithetic Fault Alignment.

packages of low-angle east-dipping reflectors detectable below San Gregorio Magno and Muro Lucano (at depth of 3–4 s) and between the Muro Lucano basin and San Fele (at depth of 4–5.5 s). There is evidence of a regional low-angle reflector, which dips undisturbed eastward and is not displaced by other high-angle normal faults.

Along the seismic profile, there is evidence of the Marzano-Carpineta fault. This implies that such a fault has cumulated enough vertical slip to be clearly resolved by seismic reflection profile.

To assess the spatial association at depth between the major 1980-EQ sub-event and its seismogenic fault (Marzano fault), we projected, along the CROP-04 section in **Figure 11C**, the epicentre of sub-event 1 with its range of variability (**Figure 2A**). We assumed for the Marzano fault, an average planar geometry with an average dip of 60° which fit both surface data (65°) and focal mechanisms solutions (50°–70°) (**Supplementary Table S4**).

Such a geometry is also supported by well data. At a depth of ~3 km, the Marzano-Carpineta segment (IF) is drilled by the San Gregorio Magno 1 well (Patacca and Scandone, 2007) (**Figures 11B, 11C**). The fault is revealed by the sharp contact between the Scisti Silicei formation and the Monte Facito formation with elision of the Calcari con Selce formation. The well projection on the CROP-04 trace (**Figure 11C**) falls at a horizontal distance of ~1200 m from the IF trace. When corrected with topography, this fit with a planar dip of ~65° for the upper portion of IF.

The hypocentre of sub-event 1 intercepts the IF close to the intersection with the basal detachment at a depth corresponding to ~3.7 s. Assuming the overall sedimentary pile has an average velocity of 5.5 km/s, the Marzano-Carpineta segment of IF is encountered at a depth of ~11 km. The depth may vary from 10 to 12 km when assuming slightly different an average dip angles (±10°) and/or average velocities (5.5–6 km/s). The major reflectors drawn within the seismic line (**Figure 11C**) and the hypocenter seems to lie at the bottom of the Apulia platform carbonates, possibly within the Triassic Anhydrite layer (**Figure 11C**).

The here reconstructed hypocentral depth is not different from others proposed in the literature based on geological and geophysical data (~8 km by Ascione et al., 2013, ~9 km by Brozzetti (2011), ~10 km by Improta et al. (2010). It is also consistent with the depth of 10–12 km calculated from seismological data by Westaway and Jackson (1987); Westaway (1993) and with ground effects described by Porfido et al., 2002 for large earthquakes in this portion of the southern Apennines. Conversely, it is much shallower than the hypocentral depth of 16–18 km given by Del Pezzo et al. (1983), Gasparini et al. (1985), and Amoruso et al. (2011).

To compare the reconstructed fault geometry with the depth distribution of the background seismicity in **Figure 11C**, we have projected along the trace of the section, a selection of good quality hypocentral locations and focal mechanisms (de Matteis et al., 2012; De Landro et al., 2015), assuming a semi-width of 5 km. A rather good geometric fit may be observed between the distribution of seismic events and the fault geometries independently reconstructed. The focal mechanisms preferentially focus on IF and on the underlying detachment and highlight the involvement of the InIF and the antithetic west-dipping system.

Geometric Fault Model

In order to build a 3D representation of the active fault segments involved in the 1980-EQ, we integrate available geological and seismological data, at the light of the structural style interpreted along the trace of the CROP-04 profile. We follow the methodological approach classically adopted by the Community Fault Model of Southern California (Nicholson et al., 2014; Nicholson et al., 2015; Plesch et al., 2014) and already applied to some other Italian cases (Lavecchia et al., 2017; Castaldo et al., 2018).

We paid particular attention to the role of the uncertainties and subjectivity in depicting the active fault segments and the fault-earthquake association. In order to properly address this issue we considered OQR and FQR (Bello et al., 2021) and the seismological formal errors derived from our analyses (*Seismological Data and Analysis*; **Supplementary Figure S5; Supplementary Tables S1, S2**). Specifically, the two quality factors used to constrain the faults at the surface together with the high-sampling step (as recently suggested by Sgambato et al., 2020) helped reducing the subjectivity in the interpretation (e.g., Bond et al., 2007; Bond et al., 2011; Hester, 2012; Salisbury et al., 2015). With our approach it is possible to discern and further select the objective and subjective parts of our final model.

The reconstruction was performed using the Move suite software (by PetEx Ltd., version 2019.1) and is articulated in three steps:

(1) Fault traces extrusion to shallow depths (ribbons in **Figure 12A**).

The detailed Quaternary fault traces (**Figure 3**; **Supplementary Figure S3**), specifically the Inner Irpinia (InIF), Irpinia Faults (IF) and the Antithetic Fault Alignment (AFA), together with the Monticello Splay and the minor faults antithetic to InIF, are extruded along dip to a common depth of 3 km beneath sea level, with different degrees of approximation. In most cases, the depth extrapolation is constrained with dip-angle data (**Supplementary Table S2**); whereas, if the latter are not available, it is extruded from the surface trace at a fixed dip (60°). Up-dip, the fault ribbons are bounded by topographic digital elevation model data (10 m-resolution); laterally, they may slightly overlap or terminate into another. Horizontal shear stress direction derived from fault-slip data (**Figures 4**, **5**; **Supplementary Table S1**) and associated to the various ribbons are projected in **Figure 12A**.

(2) Construction of interpretative section-view fault traces along serial hypocentral transects.

14 transects are built in direction N45° and ten in direction N10° (**Figure 11A**). Along each transect we projected all the intersected ribbon and available good-quality earthquake data assuming a semi-width of 1.25 km (de Matteis et al., 2012; Stabile et al., 2012; De Landro et al., 2015). The fault traces are drawn by connecting each ribbon with hypocentral distributions and preferential fault planes from focal mechanisms, down to the base of the seismogenic layer (as in **Figure 12B**). The fault geometry reconstructed along the CROP-04 profile (**Figure 11**) which, corresponding to transect number 12, was adopted as reference structural style for the neighboring transects.

(3) 3D Delaunay triangulation-based interpolation of data from steps 1-2.

Based on the obtained geometric accuracy, we assign to each fault representation a quality factor, adopting five quality ranking factors (R) as in Castaldo et al. (2018). At shallow depth (<3 km), the reconstructed surfaces are well-constrained and highly detailed based on the data acquired in this paper (**Supplementary Tables S1, S2**). The interpretation at depth is more schematic and partially suffers of the inconsistency between the velocity model from the seismic line (e.g., CROP) and from earthquake data. In fact, the latter appear to be systematically deeper with a vertical difference in the order of 2 km between the two. Nevertheless, in our opinion, the position and mutual relations among the various faults appears rather constrained (R2 to R3).

The final 3D-model is represented in **Figure 12**, in both 3D and 2D view. It consists of the major fault segments involved in the 1980-EQ, that are the east-dipping Irpinia Fault and its Antithetic Fault Alignment, together with the synthetic Ripa Rossa-Balvano Splay and the Monticello splay.

RESULTS AND DISCUSSION

Structural Style and Timing of the Extensional Fault System

The structural analysis performed in the 1980-EQ epicentral area (**Figures 4**, **5**; **Table 1**; **Supplementary Table S1; Data Sheet S1**), together with the building of a new fault map (**Figure 3**; **Supplementary Figure S3; Supplementary Table S2; Supplementary Data Sheet S2**) and local *focus* on coseismic evidence (**Figures 7**, **8**), pointed out the presence of a more complex Quaternary extensional system than previously known. Both the IF and the InIF trend NW-SE in their northern and central segments and are characterized by a sharp bend to E-W along their southernmost segment (Buccino-Romagnano section along the InIF and Mt. Ruga section along the IF, **Supplementary Figure S3**). The E-W bend is not a subordinate feature, having an overall extent of ~15 km, also including the NNE-dipping Ripa Rossa-Balvano hanging wall synthetic splay. Such a splay, here recognized for an overall length of ~13 km, shows evidence of coseismic deformation, with a vertical displacement up to 1 m in the Ripa Rossa locality. As well, the Monticello SSW-dipping antithetic splay also shows evidence of coseismic displacement with a preserved vertical separation of 10–20 cm.

Locally the IF and the InIF show other minor bends in the E-W direction, possibly reactivating pre-existing strike-slip discontinuities, but such bends do not substantially modify the geometry and trend of the overall fault system. A more evident N-S transfer zone, as well possibly corresponding to a pre-existing discontinuity of the compressional phase, has been recognized between the villages of Senerchia and Calabritto. It propagates across both the IF and the InIF, subdividing them into a northern and a southern NW-SE segments. Evidence of coseismic displacement associated to the 1980-EQ are evident along the Senerchia section (**Figure 3**). The Calabritto section bounds to the south the NW-SE-striking Marzano-Cucuzzone segment and delimits northward the Sele gap. Such a structural complexity may have controlled the deformation partitioning during the 1980-EQ.

The main IF fault segments (Cervialto, Marzano-Cucuzzone, San Gregorio) were already well known in the literature, nevertheless the presence of the southern bend and, in general, the role of the InIF was underestimated. The along strike extent of the faults mapped in this work is sensibly greater than what was considered in previous work, with evident implications for seismic hazard. If we compare the IF with the corresponding segment in the DISS database (DISS Working Group, 2018), we measure a length of ~50/55 km in the first case and of ~40 km in the second. Furthermore, the InIF is partially present in a few papers for its northern segment (i.e., Volturara Fault; Papanikolaou and Roberts, 2007; Faure Walker et al., 2012; Sgambato et al., 2020) but entirely absent from the DISS database.

An important role in the understanding of this system is also played by the minor structures mapped throughout the area (**Supplementary Table S2**). In particular, the alignment of minor faults in the PB and PSGM (**Figure 3**) can be interpreted as a system initially antithetic to the InIF and subsequently cut and partially reactivated by the IF in the gradual eastward migration of the normal faulting. As for InIF and IF, these faults substantial bend from NW-SE-direction in the northern portions to ~ E-W in the south. A Quaternary age of the extensional faults involved in the 1980-EQ, is also supported by the San Gregorio Magno well which shows a stratigraphic gap of some hundreds of meters, when drilling the IF (**Figure 11**), as well as by the clear evidence of extensional displacement of some of the stratigraphic records across the CROP-04 seismic line (**Figure 11**). The IF shear zone appears well visible as well as its low-angle basal detachment. Such a good resolution, together with the significant offset, implies a longer record of deformation.

A kinematic novelty in the interpretation of the fault system comes from the observation that whereas the prevailing dip-direction of the various fault segments and sections may variate from NNW to NE (**Figures 4**, **5A**), all planes show a prevailing and common NNE trending slip vector. Such a common shear direction evidently represents a kinematic compatibility of the overall system, which may have therefore moved at the same time instantaneously along differently oriented segments. In particular, the E-W striking segments suggest a slight right-lateral component, which makes the movements on this structure to remain consistent with the kinematics of the entire system and avoiding that the breakdown propagation would stop in the area of direction change during the 1980 coseismic faulting (**Figures 5A**, **6C**, **10D**).

The age of the onset of the extensional tectonics in the southern Apennines and, specifically, in the Irpinia area is controversial in the literature. Some authors (e.g., Cinque et al., 1993) based on regional morphotectonic evidence of a regional uplift, consider the beginning of the extensional activity only since Middle-Pleistocene times (last 700 kyr). As well, a beginning of the fault activity in the Middle-Pleistocene is suggested by radiometric age of the PSGM basin basal layers of the syn-tectonic deposits in Ascione et al., 2013. Another position is taken by Pierdominici et al. (2011), envisaging a fully linked fault zone, organized in interacting segments, for more than 50 km.

The high degree of fault interaction and multi-scale linkage evident in our maps (**Figure 3**; **Supplementary Figure S3**) better support this latter interpretation. Furthermore, the age of the syntectonic extensional basin deposits along the trace of the CROP-04 section, from the Alburni ridge to the west to the Muro Lucano area to the east, indicate an onset of the extension at least since the beginning of Quaternary (last 2.5 Myr) or even Late Pliocene times.

Surface-Depth Connection and Stress Field

According to our interpretation the IF, the InIF and the AFA are part of a more complex asymmetric system of eastward-dipping listric faults that detach on an eastward-dipping extensional basal detachment (**Figure 11**). This configuration does not exclude that even the W-dipping structures play a crucial role in the deformation of the area.

Such a prevailing top-to-east sense of shear interpretation differs from others in the literature, which either do not represent the normal faults at all (Patacca et al., 2000; Patacca and Scandone, 2007) or represent them schematically as high-angle west-dipping normal faults, dissecting the compressional ones and/or locally reactivating them (Scrocca et al., 2007; Improta et al., 2014), or still assumes that all major normal faults dip to the west and detach along a regional westward-dipping thrust (Cippitelli, 2007).

Previous authors pointed out a mismatch in the attitude of the Quaternary faults outcropping in the 1980-EQ epicentral area (typically WNW-ESE in their reconstruction) and of the underlying deep faults as unraveled by focal mechanism analysis (Ascione et al., 2013). The decoupling could be related to the presence of the clay-rich melange zone interposed at a depth of 4–6 km between the foreland Apulia platform carbonates and the overlying eastward-verging allochthonous units (Amoroso et al., 2017).

The hypothesis of a decoupling may be definitively excluded from our data in this paper, for three main reasons:

(1) Prevailing structural trends all over the area are NW-SE oriented with local N-S and E-W deflections, both at shallow and seismogenic depths (**Figures 3**, **12**; **Supplementary Table S2**).
(2) The CROP-04 profile shows deeply rooted Quaternary normal faults dissecting pre-existing compressional structures and connecting surface and depth levels, as already accepted in most of the literature (Scrocca et al., 2005; Cippitelli, 2007; Brozzetti, 2011; Pierdominici et al., 2011).
(3) The stress field inverted from both the Campania-Lucania outcropping faults and from the background seismicity (1982–2018. M_w 2.0–5.1), are strictly coaxial and all coherent with a SSW-NNE oriented least principal stress (**Figure 10**). A corresponding minimum principal stress axis (N20° ± 4°) is also indicated by stress *in situ* data along the San Gregorio well (Pierdominici et al., 2011).

The discrepancy shown by the stress parameters computed for the 1980-EQ, which indicate an average SW-NE σ3 axis (**Figure 10**), may be reasonably attributed to the relatively low quality of the available aftershock focal mechanisms. In effect, often in the literature, the upper crust regional stress trend in the southern Apennines is given as Sh_{min} in direction N44° ± 20° (Pierdominici et al., 2011).

Given that the geological and seismological data we present here cover a large area (~2400 km^2), we wonder if an homogeneous NNE Sh_{min} axis indicated since Quaternary times, represents a local or a regional stress deviation, in any case over time. Certainly, within the boundary of the study area, it does nor represent a local variation due to differently oriented active faults, neither represents a multi-stage deformation pattern. At the moment, we do not have detailed data to evaluate its configuration. It is evident that the implication in assuming a Sh_{min} ~ N30°E may imply significant variation for any stress analysis across the 1980-EQ involved area.

1980-EQ Sub-events/Fault Association

The analysis performed in this paper allow us to contribute to the discussion on the fault sources of the 1980-EQ sub-events, constraining and parameterizing the hypocentral location of sub-event 1 and proposing a new lecture key for sub-event 2.

Regarding the hypocentral structural location of the sub-event 1, Improta et al. (2010) and Ascione et al. (2013) localize it within the crystalline basement of the Apulia carbonate platform, at a depth of 10–11 km, beneath the low velocity basal clastic, within a CO2 pressurized reservoir.

In our reconstruction, the 0 s hypocentre is located at a depth of 11 ± 1 km, at the intersection between the high-angle IF and the east-dipping basal detachment. It lies within the Triassic Anhydrite layer at the bottom of an eastward overthrusted slice of the Apulia platform (**Figure 11**). The Anidriti di Burano fm, consisting of alternance of evaporite and dolostone layers, is especially capable of triggering earthquakes (De Paola et al., 2008; Trippetta et al., 2010; Porreca et al., 2018), due to the tendency of localize the deformation along thin anhydrite and dolomites shear zones, in such way promoting a transition from velocity strengthening to velocity weakening behavior (Scuderi et al., 2013).

At the light of our data, we consider suitable two alternative solutions as the most likely fault source for sub-event 2:

(1) The western border fault of PSGM, NE-dipping in the northern sector and NNE in the southern one, for a total along-strike length of ~6 km, an average dip-angle of 65°, a width of 12 km, a coseismic displacement of 60 cm. The fault trace is not linear, but it shows an along strike bent. The intersection line between the two differently striking fault sections plunges 60° NNE-ward and would represent the slip vector of sub-event 2 (**Figure 12**). As matter of fact, this solution has been proposed by Pantosti and Valensise (1993).
(2) The NNE-dipping Ripa Rossa-Balvano segment of the Irpinia E-W, with a total along-strike length of ~13 km, an average dip-angle of 60°, a coseismic displacement of 90/100 cm along the Ripa Rossa slope (**Figures 7**, **8** and

Supplementary Data Sheet S1). In such a case, the PSGM fault would have been reactivated by the last episode (14 s) of sub-event 1 (Westaway, 1993). We advance the hypothesis that sub-event 2 may have also activated the SSW-dipping Monticello splay, in front of Ripa-Rossa Balvano, which also shows evidence of coseismic rupture with vertical displacement up to 20 cm. As a matter of fact, our Monticello source geographically corresponds with the SW-dipping 20 s source modeled by Amoruso et al. (2005) and Amoruso et al., 2011 (**Figure 2D**). Also considering that equally convincing seismologic and geodetic modeling by the same authors (Amoruso et al., 2005; Amoruso et al., 2011) point to a NE-dipping source for sub-event 2 (**Figure 2**), we advance the hypothesis that effectively the sub-event 2, such as sub-event 1, was more complex and characterized by initial displacement on a NE-dipping structure (either San Gregorio or Ripa-Rossa Balvano segments) which might have triggered further displacement on its antithetic structure.

In summary, in our interpretation, the CLFS involved in the 1980-EQ consists of high-angle E-dipping normal fault detaching at depths of ~11 km along a low-angle detachment synthetic and of SW to SSW-dipping antithetic structures. The here built 3D model highlights a NW-SE graben-like structure with a significant E-W bent in the southern portion. Following Westaway (1993), we consider that the first sub-event almost entirely activated the NE-dipping border fault of the graben, with shearing moving with time from the Marzano-Cucuzzone segment northward toward the Castelfranci fault and, soon after, southward toward the PSGM fault. The second event was controlled by the southern E-W bend, with activation of a significant E-dipping segment and of its near parallel antithetic Monticello splay. With the third sub-event the deformation was triggered further north on the antithetic SW-dipping Conza fault. In such interpretation the eastward-deepening basal detachment, also characterized by the southern E-W bend, plays a significant geometric-kinematic role in controlling the enucleation of its hanging wall structures, but it has not been activated by energetic earthquake release.

CONCLUSIONS

A full synthesis of multi-source data in a 3D frame allows for a better geometric-kinematic reconstruction of the 1980-EQ and associated fault system. The newly acquired structural-geologic data and their geometric and kinematic elaborations, together with a synthesis of seismological data, are here provided, for future applications (**Supplementary Figure S3; Tables S1–S3; Data Sheet S1, S2**).

The main results are summarized as follows:

(1) The NW-SE striking CLFS is characterized in its southern portion by a sharp E-W bend, which has controlled the nucleation of the second 1980-EQ sub-event. This particular arrangement, which also characterizes the InIF, might also control the stress transfer in the area with eastward migration of the seismogenic extensional front toward the Val d'Agri basin, rather than along strike in correspondence of the Vallo di Diano basin, in the past activated by one of the two sub-events of the 1857 earthquake (M_w 7.1, Io XI MCS). In other words, the E-W Irpinia segment may represent the existence of an Earthquake Gate (EGA, sensu Oskin et al., 2015), exerting a control on the southward IF propagation. Possibly, during the 1980-EQ such a gate was closed. The 20 s event, after a first rupture episode on the NNE-dipping IF segment, turned northward activating the antithetic SSW-dipping Monticello splay. After that, the deformation continued northward activating the SW-dipping partially blind Conza structure.

(2) The E-W fault bend, north-dipping along IF and S-dipping along AFA, runs parallel to the E-W S-dipping lateral ramp of the Early/Late Pliocene Ofanto thrust front (**Supplementary Figure S1**). Both structures represent a deviation from the classic NW-SE extensional and compressional trends. We advance the hypothesis that the E-W striking N-dipping segments of the IF and the InIF, although not reactivating any pre-existing thrust structure, are controlled in their structural trends by the pre-existing compressional Ofanto structures. Otherwise, both might be controlled by pre-existing E-W crust-scale discontinuities. As a matter of fact, heat flow data and shear waves pattern highlight such a configuration (Vassallo et al., 2016).

(3) The extensional deformation is associated with a NNE-SSW directed least principal stress, with a crust-scale deviation from the classic SW-NE tensional direction across the Apennines of Italy. All stress analyses to be performed in the area must take into consideration such a result.

(4) A potentially seismogenic structure, of the same geometric significance of the Irpinia Fault, is identified in the Inner Irpinia Fault. Such a structure with a total along-strike extent of ~55 km is not highlighted in the DISS database but brighten by background seismicity and subordinately activated during the 1980-EQ. It should be considered in the elaboration of seismic hazard scenarios.

(5) The 1980-EQ has involved in the sub-event 1 rupture process also the independent Castelfranci fault segment, located north-eastward of the Irpinia main fault (**Figure 12C**). Such a structure has remained substantially silent during the last forty years (**Figure 9**), but just very recently it has been activated by the small normal fault E-dipping San Felice sequence (Festa et al., 2020). In our reconstruction, it does not represent the northern termination of the IF, but rather the southern tip of an independent potentially seismogenic structure which might be capable of releasing strong earthquakes.

The partitioning of the 1980-EQ in three distinct sub-events within the time lapse of 40 s reminds us of the partitioning in three events of the CISS-2016, occurred in a time lapse of nearly two months (24 August, 26 October and 30 October). In both cases, a cumulate magnitude equal to about ~M_w 6.9, activated a complex interconnected pattern of fault segments at depth connected and detaching along a regional east-deepening master fault.

DATA AVAILABILITY STATEMENT

The original contributions presented in the study are included in the article/**Supplementary Material**, further inquiries can be directed to the corresponding authors.

ETHICS STATEMENT

Written informed consent was obtained from the individual(s) for the publication of any potentially identifiable images or data included in this article.

AUTHOR CONTRIBUTIONS

SB worked in field and collected the structural data. FB and DC contributed to the fieldwork and in geological discussion. SB, FF, and GL processed and analyzed the geological data. RdN and GL took care of the methodological approach. RdN led the review, analyses and processing of the seismological data. RS and BdL provided support in analyzing and interpreting seismological data. DC, SB, and GL realized the 3D model with the Move suite software. SB, RdN, and GL wrote the manuscript and prepared maps, graphs, and tables. RdN, GL, FB, RS, and RA supervised the work and involved in the review and editing of the manuscript. All authors contributed to the article and approved the submitted version.

FUNDING

This research was supported by DiSPUTer Department funds (Resp. Rita de Nardis), by PRIN 2017 (2017KT2MKE) funds from the Italian Ministry of Education, University and Research (P.I. Giusy Lavecchia), and by funds from the School of Advanced Studies G. d'Annunzio at University of Chieti-Pescara (Italy) to the "Earthquake and Environmental Hazards" Ph.D. Course.

ACKNOWLEDGMENTS

We acknowledge Grazia De Landro for providing the high-precision seismological data and Luigi Ferranti for the fruitful discussion. We acknowledge PetEx that provided the Move 2019.1 suite software license. We also thank the editor and the two reviewers for costructive comments.

SUPPLEMENTARY MATERIAL

The Supplementary Material for this article can be found online at: https://www.frontiersin.org/articles/10.3389/feart.2020.608063/full#supplementary-material.

REFERENCES

Abate, D., De Pippo, T., Massaro, E., and Pennetta, M. (1998). Evoluzione morfologica tardo-quaternaria della valle caudina (benevento, Italia). *Quaternario* 11 (2), 255–264.

Adinolfi, G. M., De Matteis, R., Orefice, A., Festa, G., Zollo, A., de Nardis, R., et al. (2015). The September 27, 2012, ML 4.1, Benevento earthquake: a case of strike-slip faulting in Southern Apennines (Italy). *Tectonophysics* 600, 35–46.

Allmendinger, R., Cardozo, N., and Fisher, D. (2012). *Structural geology algorithms: vectors and tensors*. Cambridge: Cambridge University Press.

Amato, A., and Selvaggi, G. (1993). Aftershock location and P-velocity structure in the epicentral region of the 1980 Irpinia earthquake. *Ann. Geofisc* 36, 3–15

Amicucci, L., Barchi, M. R., Montone, P., and Rubiliani, N. (2008). The vallo di diano and auletta extensional basins in the southern apennines (Italy): a simple model for a complex setting. *Terra. Nova* 20, 475–482. doi:10.1111/j.1365-3121.2008.00841.x

Amoroso, O., Ascione, A., Mazzoli, S., Virieux, J., and Zollo, A. (2014). Seismic imaging of a fluid storage in the actively extending apennine mountain belt, southern italy. *Geophys. Res. Lett* 41, 3802–4380. doi:10.1002/2014GL060070

Amoroso, O., Russo, G., De Landro, G., Zollo, A., Garambois, S., Mazzoli, S., et al. (2017). From velocity and attenuation tomography to rock physical modeling: inferences on fluid-driven earthquake processes at the irpinia fault system in southern italy. *Geophys. Res. Lett* 44, 6752–6760. doi:10.1002/2016GL072346

Amoruso, A., Crescentini, L., and Scarpa, R. (2005). Faulting geometry for the complex 1980 campania-lucania earthquake from levelling data. *Geophys. J. Int* 162, 156–168. doi:10.1111/j.1365-246X.2005.02652.x

Amoruso, A., Crescentini, L., Di Lieto, B., and Scarpa, R. (2011). Faulting mechanism of the campania–lucania 1980 earthquake, Italy, from high-resolution, 3D velocity structure, aftershock relocation, fault-plane solutions, and post-seismic deformation modeling. *Ann. Geophys* 54, 806–821. doi:10.4401/ag-4984

Angelier, J., and Mechler, P. (1977). Sur une méthode graphique de recherche des contraintes principales également utilisable en tectonique et en séismologie: La méthode des diédres droits. *Bulletin de la Société géologique de France* 19, 1309–1318. doi:10.2113/gssgfbull.S7-XIX.6.1309

Ascione, A., Cinque, A., Improta, L., and Villani, F. (2003). Late quaternary faulting within the southern apennines seismic belt: new data from Mt. Marzano area (southern Italy). *Quat. Int* 101–102, 27–41. doi:10.1016/S1040-6182(02)00127-1

Ascione, A., Mazzoli, S., Petrosino, P., and Valente, E. (2013). A decoupled kinematic model for active normal faults: insights from the 1980, MS = 6.9 Irpinia earthquake, southern italy. *GSA Bull* 125, 1239–1259. doi:10.1130/B30814.1

Barchi, M., Amato, A., Cippitelli, G., Merlini, S., and Montone, P. (2007). Extensional tectonics and seismicity in the axial zone of the southern apennines. *Boll. Soc. Geol. It (Ital.J.Geosci.)* 7, 47–56.

Basili, R., Valensise, G., Vannoli, P., Burrato, P., Fracassi, U., Mariano, S., et al. (2008). The database of individual seismogenic sources (DISS), version 3: summarizing 20 years of research on italy's earthquake geology. *Tectonophysics* 453, 20–43. doi:10.1016/j.tecto.2007.04.014

Bello, S., Scott, C. P., Ferrarini, F., Brozzetti, F., Scott, T., Cirillo, D., et al. (2021). *High-resolution surface faulting from the 1983 Idaho Lost River Fault Mw 6.9 earthquake and previous events*. Sci. Data.

Bernard, P., and Zollo, A. (1989). The irpinia (Italy) 1980 earthquake: detailed analysis of a complex normal faulting. *J. Geophys. Res* 94, 1631–1647. doi:10.1029/jb094ib02p01631

Biasi, G. P., and Wesnousky, S. G. (2015). Steps and gaps in ground ruptures: empirical bounds on rupture propagation. *Bull. Seismol. Soc. Am* 106 (3), 1110–1124. doi:10.1785/0120150175

Blumetti, A. M., Esposito, E., Ferreli, L., Michetti, A. M., Porfido, S., Serva, L., et al. (2002). New data and the reinterpretation of the november 23, 1980, M 6.9, irpinia-lucania earthquake (Southern Apennine) coseismic surface effects. *Spec. Issue Studi Geologici Camerti* 2, 19–27.

Bollettinari, G., and Panizza, M. (1981). Una "faglia di superficie" presso San gregorio magno in occasione del sisma del 23/11/1980 in irpinia. *Rend. Soc. Geol. Ital* 4, 135–136.

Boncio, P., Brozzetti, F., and Lavecchia, G. (2000). Architecture and seismotectonics of a regional low-angle normal fault zone in central ltaly. *Tectonics* 19, 1038–1055. doi:10.1029/2000tc900023

Boncio, P., Lavecchia, G., and Pace, B. (2004). Defining a model of 3D seismogenic sources for seismic hazard assessment applications: the case of central apennines (Italy). *J. Seismol* 8, 407–425. doi:10.1023/b:jose.0000038449.78801.05

Bond, C. E., Gibbs, A. D., Shipton, Z. K., and Jones, S. (2007). What do you think this is? "Conceptual uncertainty" in geoscience interpretation. *GSA Today* 17 (11), 4–10. doi:10.1130/GSAT01711A.1

Bond, C. E., Philo, C., and Shipton, Z. K. (2011). When there isn't a right answer: interpretation and reasoning, key skills for twenty-first century geoscience. *Int. J. Sci. Educ* 33 (5), 629–652. doi:10.1080/09500691003660364

Boschi, E., Mulargia, F., Mantovani, E., Bonafede, M., Dziewonski, A. M., and Woodhouse, J. H. (1981). The Irpinia earthquake of november 23, 1980. *Abstracts Eos Trans. AGU* 6, 330.

Brozzetti, F., Lavecchia, G., Mancini, G., Milana, G., and Cardinali, M. (2009a). Analysis of the 9 September 1998 M_w 5.6 mercure earthquake sequence (southern Apennines, Italy): a multidisciplinary approach. *Tectonophysics* 476, 210–225. doi:10.1016/j.tecto.2008.12.007

Brozzetti, F., Boncio, P., Lavecchia, G., and Pace, B. (2009b). Present activity and seismogenic potential of a low-angle normal fault system (Città di Castello, Italy): constraints from surface geology, seismic reflection data and seismicity. *Tectonophysics* 463, 31–46. doi:10.1016/j.tecto.2008.09.023

Brozzetti, F., Cirillo, D., de Nardis, R., Cardinali, M., Lavecchia, G., Orecchio, B., et al. (2017a). Newly identified active faults in the Pollino seismic gap, southern Italy, and their seismotectonic significance. *J. Struct. Geol* 94, 13–31. doi:10.1016/j.jsg.2016.10.005

Brozzetti, F., Cirillo, D., Liberi, F., Piluso, E., Faraca, E., de Nardis, R., et al. (2017b). Structural style of quaternary extension in the crati valley (calabrian arc): evidence in support of an east-dipping detachment fault. *Ital. J. Geosci* 136, 434–453. doi:10.3301/IJG.2017.11

Brozzetti, F., Boncio, P., Cirillo, D., Ferrarini, F., de Nardis, R., Testa, A., et al. (2019). High-resolution eldmapping and analysis of the August–October 2016 coseismic surface faulting(central Italy earthquakes): slip distri-bution, parameterization, and comparison with global earthquakes. *Tectonics* 38, 417–439. doi:10.1029/2018TC005305

Brozzetti, F., and Lavecchia, G. (1994). Seismicity and related extensional stress field: the case of the norcia seismic zone (Central Italy). *Annales Tectonicæ* 8, 36–57.

Brozzetti, F., Mondini, A. C., Pauselli, C., Mancinelli, P., Cirillo, D., Guzzetti, F., et al. (2020). Mainshock anticipated by intra-sequence ground deformations: insights from multiscale field and SAR Interferometric measurements. *Geosciences* 10, 186. doi:10.3390/geosciences10050186

Brozzetti, F., and Salvatore, A. (2006). La distensione nell'appennino campano-lucano: nuovi dati sui bacini in tramontani della valle del tanagro, di S. gregorio magno e di muro lucano. *Rend. Soc. Geol. Ital* 2, 98–100

Brozzetti, F. (2011). The campania-lucania extensional fault system, southern italy: a suggestion for a uniform model of active extension in the italian apennines. *Tectonics* 30, TC5009. doi:10.1029/2010TC002794

Brüstle, W., and Müller, G. (1983). Moment and duration of shallow earthquakes from Love-wave modelling for regional distances. *Phys. Earth Planet In* 32, 312–324. doi:10.1016/0031-9201(83)90031-6

Cagnetti, V., Caiaffa, E., Capocecera, P., Cervellati, R., and Cochi, C. (1981). *Attività sismica dell'area irpina rilevata con la rete sismometrica del CNEN nel periodo Febbraio 1979-Novembre 1980Tech. Rept*. Rome, Italy: CNEN-ENEL.

Cantalamessa, G., Dramis, F., Pambianchi, G., Romano, A., Santoni, A. M., and Tonnetti, G. (1981). Fenomeni franosi connessi con attività sismica nell'area compresa tra S. *Giorgio La Molara e Bisaccia. Rend. Soc. Geol. It* 4, 467–469.

Carafa, M., and Barba, S. (2013). The stress field in europe: optimal orientations with confidence limits. *Geophys. J. Int* 193, 531–548. doi:10.1093/gji/ggt024

Carmignani, L., Cello, G., Cerrina Peroni, A., Funiciello, R., Kalin, O., Mecchieri, M., et al. (1981). Analisi del campo di fratturazione superficiale indotta dal terremoto campano-lucano del 23/11/1980. *Rend. Soc. Geol. It* 4, 451–465.

Castaldo, R., de Nardis, R., De Novellis, V., Ferrarini, F., Lanari, R., Lavecchia, G., et al. (2018). Coseismic stress and strain field changes investigation through 3-D Finite Element modeling of DInSAR and GPS measurements and geological/seismological data: the l'aquila (Italy) 2009 earthquake case study. *J. Geophys. Res. Solid Earth* 123, 4193–4222. doi:10.1002/2017JB014453

Castello, B., Selvaggi, G., Chiarabba, C., and Amato, A. (2006). *CSI Catalogo della sismicità italiana 1981-2002, versione 1.1*. Roma: INGV-CNT.

Cello, G., Tondi, E., Micarelli, L., and Mattioni, L. (2003). Active tectonics and earthquake sources in the epicentral area of the 1857 Basilicata earthquake (southern Italy). *J. Geodyn* 36, 37–50. doi:10.1016/S0264-3707(03)00037-1

Chiarabba, C., De Gori, P., and Mele, F. M. (2015). Recent seismicity of Italy: active tectonics of the central Mediterranean region and seismicity rate changes after the Mw 6.3 l'aquila earthquake. *Tectonophysics* 638, 82–93. doi:10.1016/j.tecto.2014.10.016

Chiarabba, C., and De Gori, P. (2016). The seismogenic thickness in Italy: constraints on potential magnitude and seismic hazard. *Terra. Nova* 28, 402–408. doi:10.1111/ter.12233

Christophersen, A., Litchfield, N., Berryman, K., Thomas, R., Basili, R., Wallace, L., et al. (2015). Development of the global earthquake model's neotectonic fault database. *Nat. Hazards* 79, 111–135. doi:10.1007/s11069-015-1831-6

Cinque, A., Patacca, E., Scandone, P., and Tozzi, M. (1993). Quaternary kinematic evolution of the southern apennines. relationship between surface geological features and lithospheric structures. *Ann. Geofisc* 36, 249–260. doi:10.4401/ag-4283

Cippitelli, G. (2007). The CROP-04 seismic profile. Interpretation and structural setting of the Agropoli–Barletta Geotraverse. *Boll. Soc. Geo. It* 7, 267–281.

Civico, R., Pucci, S., Villani, F., Pizzimenti, L., De Martini, P. M., Nappi, R., et al. (2018). Surface ruptures following the 30 October 2016 M_w 6.5 norcia earthquake, central Italy. *J. Maps* 14, 151–160. doi:10.1080/17445647.2018.1441756

Cocco, M., Chiarabba, C., Di Bona, M., Selvaggi, G., Margheriti, L., Frepoli, A., et al. (1999). The April 1996 Irpinia seismic sequence: evidence for fault interaction. *J. Seismol* 3, 105–117.

Crosson, R. S., Martini, M., Scarpa, R., and Key, S. C. (1986). The southern Italy earthquake of 23 November 1980: an unusual pattern of faulting. *Bull. Seismol. Soc. Am* 76, 381–394.

Dalla Via, G., De Natale, G., Troise, C., Pingue, F., Obrizzo, F., Riva, R., et al. (2003). First evidence of post-seismic deformation in the central mediterranean: crustal visco-elastic relaxation in the area of the 1980 Irpinia Earthquake (Southern Italy). *Geophys. J. Int* 154, F9–F14. doi:10.1046/j.1365-246X.2003.02031.x

De Landro, G., Amoroso, O., Stabile, T. A., Matrullo, E., Lomax, A., and Zollo, A. (2015). High-precision differential earthquake location in 3-D models: evidence for a rheological barrier controlling the microseismicity at the Irpinia fault zone in southern apennines. *Geophys. J. Int* 203, 1821–1831. doi:10.1093/gji/ggv397

De Matteis, R., Matrullo, E., Rivera, L., Stabile, A. T., Pasquale, G., and Zollo, A. (2012). Fault delineation and regional stress direction from the analysis of background microseismicity in the southern apennines, italy. *Bull. Seismol. Soc. Am* 102, 1899–1907. doi:10.1785/0120110225

De Paola, N., Collettini, C., Faulkner, D. R., and Trippetta, F. (2008). Fault zone architecture and deformation processes within evaporitic rocks in the upper crust. *Tectonics* 27, TC4017. doi:10.1029/2007TC002230

Del Pezzo, E., Iannacone, G., Martini, M., and Scarpa, R. (1983). The 23 november 1980 southern Italy earthquake. *Bull. Seismol. Soc. Am* 73, 187–200

Delvaux, D., and Sperner, B. (2003). New aspects of tectonic stress inversion with reference to the TENSOR program. *Geol. Soc. Spec. Publ* 212, 75–100. doi:10.1144/gsl.sp.2003.212.01.06

Deschamps, A., and King, G. C. P. (1984). Aftershocks of the campania-lucania (Italy) earthquake of 23 november 1980. *Bull. Seismol. Soc. Am* 74, 2483–2517

Deschamps, A., and King, G. C. P. (1983). The campania-lucania (southern Italy) earthquake of 23 november 1980. *Earth Planet Sci. Lett* 62, 296–304. doi:10.1016/0012-821X(83)90092-4

Devoti, R., Esposito, A., Pietrantonio, G., Pisani, A. R., and Riguzzi, F. (2011). Evidence of large-scale deformation patterns from GPS data in the italian subduction boundary. *Earth Planet Sci. Lett* 311, 230–241. doi:10.1016/j.epsl.2011.09.034

Di Luzio, E., Mele, G., Tiberti, M. M., Cavinato, G. P., and Parotto, M. (2009). Moho deepening and shallow upper crustal delamination beneath the central apennines. *Earth Planet Sci. Lett* 280, 1–12. doi:10.1016/j.epsl.2008.09.018

Di Naccio, D., Boncio, P., Brozzetti, F., Pazzaglia, F. J., and Lavecchia, G. (2013). Morphotectonic analysis of the lunigiana and garfagnana grabens (northern apennines, italy): implications for active normal faulting. *Geomorphology* 201, 293–311. doi:10.1016/j.geomorph.2013.07.003

DISS Working Group (2018). Database of individual seismogenic sources (DISS), version 3.2.1: a compilation of potential sources for earthquakes larger than M 5.5 in italy and surrounding areas istituto nazionale di geofisica e vulcanologia. Available at: http://diss.rm.ingv.it/diss/ (Accessed June, 2020).

D'Agostino, N. (2014). Complete seismic release of tectonic strain and earthquake recurrence in the apennines (italy). *Geophys. Res. Lett* 41, 1155–1162. doi:10.1002/2014GL059230

Ekström, G., Dziewonski, A. M., and Woodhouse, J. H. (1987). Centroid-moment tensor solutions for the 51 IASPEI selected earthquakes, 1980–1984. *Phys. Earth Planet. In* 47, 62–66. doi:10.1016/0031-9201(87)90067-7

Faure Walker, J. P., Roberts, G. P., Cowie, P. A., Papanikolaou, I., Michetti, A. M., Sammonds, P., et al. (2012). Relationship between topography, rates of extension and mantle dynamics in the actively-extending italian apennines. *Earth Planet Sci. Lett* 325–326, 76–84. doi:10.1016/j.epsl.2012.01.028

Ferranti, L., Palano, M., Cannavò, F., Mazzella, M. E., Oldow, J. S., Gueguen, E., et al. (2014). Rates of geodetic deformation across active faults in southern italy. *Tectonophysics* 621, 101–122. doi:10.1016/j.tecto.2014.02.007

Ferrarini, F., Lavecchia, G., de Nardis, R., and Brozzetti, F. (2015). fault geometry and active stress from earthquakes and field geology data analysis: the colfiorito 1997 and l'aquila 2009 cases (Central Italy). *Pure Appl. Geophys* 9, 1079–1103. doi:10.1007/s00024-014-0931-7

Ferrarini, F., Boncio, P., de Nardis, R., Pappone, G., Cesarano, M., Aucelli, P. P. C., et al. (2017). Segmentation pattern and structural complexities in seismogenic extensional settings: the north matese fault system (Central Italy). *J. Struct. Geol* 95, 93–112. doi:10.1016/j.jsg.2016.11.006

Festa, G., Adinolfi, G. M., Caruso, A., Colombelli, S., De Landro, G., Elia, L., et al. (2011). Rocca San Felice Seismic Sequence, Southern Apennines, Italy 04-06/07/2020, Special Report, Irpinia Near Fault Observatory. Available at: http://isnet.unina.it/.

Frepoli, A., Maggi, C., Cimini, G. B., Marchetti, A., and Chiappini, M. (2011). Seismotectonic of Southern Apennines from recent passive seismic experiments. *J. Geodyn* 51, 110–124.

Galli, P., and Bosi, V. (2003). "Analisi paleosismologiche lungo la faglia di caggiano (Monti della Maddalena, SA)," in Abstracts of the 22th congress of the national group of solid earth geophysics, Roma, November 18–20, 2003.

Galli, P., Bosi, V., Piscitelli, S., Giocoli, A., and Scionti, V. (2006). Late Holocene earthquakes in southern apennine: paleoseismology of the caggiano fault. *Int. J. Earth Sci* 95, 855–870. doi:10.1007/s00531-005-0066-2

Galli, P. (2010). "La storia sismica di conza," in *Conza storia arte fede*. Editor E. Ricciardi (Calitri, Italy: Grafiche Pannisco), 23–70.

Galli, P., and Peronace, E. (2014). New paleoseismic data from the irpinia fault. a different seismogenic perspective for the southern apennines. *Earth Sci. Rev* 136, 175–201. doi:10.1016/j.earscirev.2014.05.013

Galli, P. (2020). Roman to middle age earthquakes sourced by the 1980 Irpinia fault: historical, archaeoseismological, and paleoseismological hints. *Geosciences* 10, 286. doi:10.3390/geosciences10080286

Gasparini, C., Iannacone, G., Scandone, P., and Scarpa, R. (1982). Seismotectonics of the calabriain arc. *Tectonophysics* 84, 267–286

Gasparini, C., Iannaccone, G., and Scarpa, R. (1985). Fault-plane solutions and seismicity of the Italian peninsula. *Tectonophysics* 117, 59–78. doi:10.1016/0040-1951(85)90236-7

Giano, S. I., and Martino, C. (2003). Assetto morfotettonico e morfostratigrafico di alcuni depositi continentali pleistocenici del bacino del pergola–melandro (Appennino Lucano). *Quaternario* 16 (2), 289–297.

Giardini, D. (1993). Teleseismic observation of the november 23 1980, irpinia earthquake. *Ann. Geofisc* 00, 17–25

Giardini, D., Basili, A., and Boschi, E. (1996). Applying the relative hypocentre location approach: where was the 1980 november 23 irpinia earthquake?. *Geophys. J. Int* 127, 605–615.

Heidbach, O., Tingay, M., Barth, A., Reinecker, J., Kurfeß, D., and Müller, B. (2010). Global crustal stress pattern based on the world stress map database release 2008. *Tectonophysics* 482, 3–15. doi:10.1016/0031-9201(87)90067-7

Heidbach, O., Rajabi, M., Cui, X., Fuchs, K., Müller, B., Reinecker, J., et al. (2018). The World Stress Map database release 2016: crustal stress pattern across scales. *Tectonophysics* 744, 484–498. doi:10.1016/j.tecto.2018.07.007

Hester, P. (2012). Epistemic uncertainty analysis: an approach using expert judgement and evidential credibility. *Int. J. Qual. Stat. Reliab* 2012, 617481. doi:10.1155/2012/617481

Iannaccone, G., Zollo, A., Elia, L., Convertito, V., Satriano, C., Martino, C., et al. (2010). A prototype system for earthquake early-warning and alert management in southern italy. *Bull. Earthq. Eng* 8, 1105–1129. doi:10.1007/s10518-009-9131-8

Improta, L., Iannaccone, G., Capuano, P., Zollo, A., and Scandone, P. (2000). Inferences on the upper crustal structure of southern apennines (Italy) from seismic refraction investigations and subsurface data. *Tectonophysics* 317, 273–298. doi:10.1016/S0040-1951(99)00267-X

Improta, L., Ferranti, L., De Martini, P. M., Piscitelli, S., Bruno, P. P., Burrato, P., et al. (2010). Detecting young, slow-slipping active faults by geologic and multidisciplinary high-resolution geophysical investigations: a case study from the apennine seismic belt. *Italy. J. Geophys. Res* 115, B11307. doi:10.1029/2010JB000871

Improta, L., De Gori, P., and Chiarabba, C. (2014). New insights into crustal structure, cenozoic magmatism, CO2 degassing, and seismogenesis in the southern apennines and irpinia region from local earthquake tomography. *J. Geophys. Res. Solid Earth* 119, 8283–8311. doi:10.1002/2013JB010890

Jackson, J. A., Gagnepain, J., Houseman, G., King, G. C. P., Papadimitriou, P., Soufleris, C., et al. (1982). Seismicity, normal faulting, and the geomorphological development of the gulf of corinth (Greece): the corinth earthquakes of february and march 1981. *Earth Planet Sci. Lett* 57, 377–397. doi:10.1016/0012-821X(82)90158-3

Kanamori, H., and Given, J. W. (1982). Use of long-period surface waves for rapid determination of earthquake source parameters 2. preliminary determination of source mechanisms of large earthquakes ($M_S \geq 6.5$) in 1980. *Phys. Earth Planet. In* 30, 260–268. doi:10.1016/0031-9201(82)90112-1

Kim, W. Y., Kulhánek, O., and Meyer, K. (1984). Source processes of the 1981 gulf of corinth earthquake sequence from body-wave analysis. *Bull. Seismol. Soc. Am* 74, 459–477.

Lancieri, M., and Zollo, A. (2009). Simulated shaking maps for the 1980 Irpinia earthquake, Ms 6.9: insights on the observed damage distribution. *Soil Dynam. Earthq. Eng* 29, 1208–1219. doi:10.1016/j.soildyn.2009.01.007

Lavecchia, G. (1988). The tyrrhenian-apennines system: structural setting and seismotectogenesis. *Tectonophysics* 147, 263–296. doi:10.1016/0040-1951(88)90190-4

Lavecchia, G., Boncio, P., Brozzetti, F., De Nardis, R., Di Naccio, D., Ferrarini, F., et al. (2011). The April 2009 L'Aquila (central Italy) seismic sequence (Mw 6.3): a preliminary seismotectonic picture. *Recent Prog. Earthquake Geol* 2011, 1–17.

Lavecchia, G., Brozzetti, F., Barchi, M., Menichetti, M., and Keller, J. V. A. (1994). Seismotectonic zoning in east-central Italy deduced from an analysis of the neogene to present deformations and related stress fields. *Geol. Soc. Am. Bull* 106, 1170–1120. doi:10.1130/0016

Lavecchia, G., Castaldo, R., de Nardis, R., De Novellis, V., Ferrarini, F., Pepe, S., et al. (2016). Ground deformation and source geometry of the 24 August 2016 amatrice earthquake (Central Italy) investigated through analytical and numerical modeling of DInSAR measurements and structural-geological data. *Geophys. Res. Lett* 43, 12,389–12,398. doi:10.1002/2016GL071723

Lavecchia, G., Adinolfi, G. M., de Nardis, R., Ferrarini, F., Cirillo, D., Brozzetti, F., et al. (2017). Multidisciplinary inferences on a newly recognized active east-dipping extensional system in central italy. *Terra. Nova* 29, 77–89. doi:10.1111/ter.12251

Lavecchia, G., de Nardis, R., Ferrarini, F., Cirillo, D., Bello, S., and Brozzetti, F. (2021). "Regional seismotectonic zonation of hydrocarbon fields in active thrust belts: a case study from Italy," in *Building knowledge for geohazard assessment and management in the caucasus and other orogenic regions*. Editors F. L. Bonali, F. Pasquaré Mariotto, and N. Tsereteli (the Netherlands: Springer). doi:10.1007/978-94-024-2046-3

Livio, F., Michetti, A. M., Vittori, E., Gregory, L., Wedmore, L., Piccardi, L., et al. (2016). Surface faulting during the august 24, 2016, central italy earthquake (M_w 6.0): preliminary results. *Ann. Geophys* [Epub ahead of print]. doi:10.4401/ag-7197

Locati, M., Camassi, R., Rovida, A., Ercolani, E., Bernardini, F., Castelli, V., et al. (2019). *Database macrosismico italiano (DBMI15), versione 2.0*: Istituto Nazionale di Geofisica e Vulcanologia (INGV). doi:10.13127/DBMI/DBMI15.2

Manighetti, I., Campillo, M., Sammis, C., Mai, P. M., and King, G. (2005). Evidence for self-similar, triangular slip distributions on earthquakes: implications for earthquake and fault mechanics. *J. Geophys. Res* 110, B05302. doi:10.1029/2004JB003174

Martini, I. P., Sagri, M., and Colella, A. (2001). "Neogene quaternary basins of the inner apennines and calabrian arc," in *Anatomy of an orogen, the Apennines and adjacent mediterranean basins*. Editors G. B. Vai and I. P. Martini (Dordrecht, The Netherlands: Kluwer Acad.), 375–400.

Martini, M., and Scarpa, R. (1983). "Earthquakes in Italy in the last century," in *Earthquakes, Observation, Theory and Interpretation. North Holland, Amsterdam*, 479–492.

Martino, C. (2007). Stima dei tassi di scorrimento delle faglie ed evoluzione tettonica quaternaria della valle del melandro (appennino campano-lucano). *Boll. Soc. Geol. Ital* 126 (1), 37–53.

Maschio, L., Ferranti, L., and Burrato, P. (2005). Active extension in val d'agri area, southern apennines, italy: implications for the geometry of the seismogenic belt. *Geophys. J. Int* 162, 591–609. doi:10.1111/j.1365-246X.2005.02597.x

Menichetti, M., Piacentini, D., De Donatis, M., Roccheggiani, M., Tamburini, A., and Tirincanti, E. (2016). "Virtual outcrop and 3D structural analysis of monte vettore extensional active faults," in Abstract of the 35th congress of the national group of solid earth geophysics, Lecce, Italy, November 22–24 2019.

Mirabella, F., Brozzetti, F., Lupattelli, A., and Barchi, M. R. (2011). Tectonic evolution of a low-angle extensional fault system from restored cross-sections in the northern apennines (Italy). *Tectonics* 30, TC6002. doi:10.1029/2011TC002890

Montone, P., and Mariucci, M. T. (2016). The new release of the Italian contemporary stress map. *Geophys. J. Int* 205, 1525–1531. doi:10.1093/gji/ggw100

Nakanishi, I., and Kanamori, H. (1984). Source mechanisms of twenty-six large, shallow earthquake ($MS \geqq 6.5$) during 1980 from P-wave first motion and long-period rayleigh wave data. *Bull. Seismol. Soc. Am* 74, 805–818.

Nicholson, C., Plesch, A., Sorlien, C. C., Shaw, J. H., and Hauksson, E. (2015). "The SCEC community fault model version 5.0: an updated and expanded 3D fault set for southern california," in 2015 pacific section AAPG joint meeting program (Oxnard, CA), Vol. 77, September 12–16.

Nicholson, G., Plesch, A., Sorlion, C. C., Shaw, J. H., and Hauksson, E. (2014). The SCEC 3D community fault model (CFM-v5): an updated and expanded fault set of oblique crustal deformation and complex fault interaction for southern california. *Eos Trans. Am. Geophys. Union* 95 (52). Abstract T31B-4584

Okabe, A., Boots, B., and Sugihara, K. (1992). *Spatial tessellation concept and applications of voronoi diagrams*. New York: John Wiley & Sons, 532.

Ortolani, F., and Torre, M. (1981). Guida all'escursione nell'area interessata dal terremoto del 23/11/1980. *Rend. Soc. Geol. It* 4, 173–214.

Oskin, M., Elliot, A., Benchum, D., Liu-Zeng, J., Liu, Z., Shao, Y., et al. (2015). Earthquake gates: linking ruptures length to geologically constrained dynamics of fault complexity, with examples from the altyn tagh and san andreas faults. *Abstr. Progr. Geol. Soc. Am* 47, 35.

Pantosti, D., and Valensise, G. (1990). Faulting mechanism and complexity of the november 23, 1980, campania-lucania earthquake, inferred from surface observation. *J. Geophys. Res* 95, 15319. doi:10.1029/jb095ib10p15319

Pantosti, D., and Valensise, G. (1993). Source geometry and long term behavior of the 1980, Irpinia earthquake fault based on field geologic observations. *Ann. Geofisc* 36, 41–49. doi:10.4401/ag-4299

Papanikolaou, I. D., and Roberts, G. P. (2007). Geometry, kinematics and deformation rates along the active normal fault system in the southern Apennines: implications for fault growth. *J. Struct. Geol* 29, 166–188. doi:10.1016/j.jsg.2006.07.009

Pasquale, G., De Matteis, R., Romeo, A., and Maresca, R. (2009). Earthquake focal mechanisms and stress inversion in the irpinia region (southern Italy). *J. Seismol* 13, 107–124. doi:10.1007/s10950-008-9119-x

Patacca, E., and Scandone, P. (2007). Geological interpretation of the CROP-04 seismic line (southern Apennines, Italy). results of the CROP project sub-project CROP-04 southern apennines (Italy). bollettino della società geologica italiana. *Ital. J. Geosci. Spec. Issue* 7, 297–315.

Patacca, E., Scandone, P., and Tozzi, M. (2000). Il profilo CROP-04. *Protecta* 10-12, 49–52.

Pierdominici, S., Mariucci, M. T., and Montone, P. (2011). A study to constrain the geometry of an active fault in southern italy through borehole breakouts and downhole logs. *J. Geodyn* 52, 279–289. doi:10.1016/j.jog.2011.02.006

Pingue, F., De Natale, G., and Briole, P. (1993). Modelling of the 1980 Irpinia earthquake source: constraints from geodetic data. *Ann. Geofisc* 36, 27–40. doi:10.4401/ag-4296

Pingue, F., and De Natale, G. (1993). Fault mechanism of the 40 seconds subevent of the 1980 irpinia (southern Italy) earthquake from levelling data. *Geophys. Res. Lett* 20, 911–914. doi:10.1029/92GL02823

Plesch, A., Shaw, J. H., and Jordan, T. H. (2014). "Stochastic descriptions of basin velocity structure from analyses of sonic logs and the SCEC community velocity model (CVM-H)," in Presentation at 2014 SSA annual meeting, Palm Springs, CA, September 6–10.

Pondrelli, S., Salimbeni, S., Ekström, G., and Morelli, A. (2006). The Italian CMT dataset from 1977 to the present. *Phys. Earth Planet. In* 159, 286–303. doi:10.1016/j.pepi.2006.07.008

Porfido, S., Esposito, E., Vittori, E., Tranfaglia, G., Michetti, A. M., Blumetti, M., et al. (2002). Areal distribution of ground effects induced by strong earthquakes in the Southern Apennines (Italy). *Surv. Geophys* 23 (6), 529–562. doi:10.1023/A:1021278811749

Porreca, M., Fabbrizzi, A., Azzaro, S., Pucci, S., Del Rio, L., Pierantoni, P. P., et al. (2020). 3D geological reconstruction of the M. Vettore seismogenic fault system (Central Apennines, Italy): cross-cutting relationship with the M. Sibillini thrust. *J. Struct. Geol* 131, 103938. doi:10.1016/j.jsg.2019.103938

Porreca, M., Minelli, G., Ercoli, M., Brobia, A., Mancinelli, P., Cruciani, F., et al. (2018). Seismic reflection profiles and subsurface geology of the area interested by the 2016–2017 earthquake sequence (Central Italy). *Tectonics* 37, 1116–1137. doi:10.1002/2017TC004915

Rovida, A., Locati, M., Camassi, R., Lolli, B., and Gasperini, P. (2019). *Catalogo Parametrico dei Terremoti Italiani (CPTI15), versione 2.0*. Istituto Nazionale di Geofisica e Vulcanologia (INGV). doi:10.13127/CPTI/CPTI15.2

Salisbury, J. B., Haddad, D. E., Rockwell, T., Arrowsmith, J. R., Madugo, C., Zielke, O., et al. (2015). Validation of meter-scale surface faulting offset measurements from high-resolution topographic data. *Geosphere* 11, 1884–1901. doi:10.1130/GES01197.1

Scarpa, R., and Slejko, D. (1982). *Some analyses of seismological data Southern Italy November 23, 1980 earthquake*. Rome: The Italian Geodynamics Project of CNR, Publ., Vol. 503.

Scognamiglio, L., Tinti, E., and Quintiliani, M. (2006). *Time Domain moment tensor [data set]*: Istituto Nazionale di Geofisica e Vulcanologia (INGV). doi:10.13127/TDMT

Scrocca, D., Carminati, E., and Doglioni, C. (2005). Deep structure of the southern apennines, italy: thin-skinned or thick-skinned?. *Tectonics* 24, TC3005. doi:10.1029/2004TC001634

Scrocca, D., Carminati, E., Doglioni, C., and Marcantoni, D. (2007). "Slab retreat and active shortening along the central-northern apennines"," in *Thrust belts and foreland basins: from fold kinematics to hydrocarbon systems*. Editors O. Locambe, J. Lavè, F. Roure, and J. Vergés (Berlin, Heidelberg: Springer), 471–487. doi:10.1007/978-3-540-69426-7

Scuderi, M. M., Niemeijer, A. R., Collettini, C., and Marone, C. (2013). Frictional properties and slip stability of active faults within carbonate–evaporite sequences: the role of dolomite and anhydrite. *Earth Planet Sci. Lett* 369-370, 220–232. doi:10.1016/j.epsl.2013.03.024

Servizio Geologico d'Italia (1970a). *Foglio 186 (S. Angelo dei Lombardi) della Carta 1:100.000 dell'I.* Roma: G.M.

Servizio Geologico d'Italia (1970b). *Foglio 187 (melfi) della Carta 1:100.000 dell'I.* Roma: G.M.

Servizio Geologico d'Italia (1970c). *Foglio 198 (eboli) della Carta 1:100.000 dell'I.* Roma: G.M.

Servizio Geologico d'Italia (1969). *Foglio 199 (potenza) della Carta 1:100.000 dell'I.* Roma: G.M.

Sgambato, C., Walker, J. P. F., and Roberts, G. P. (2020). Uncertainty in strain-rate from field measurements of the geometry, rates and kinematics of active normal faults: implications for seismic hazard assessment. *J. Struct. Geol* 131, 103934. doi:10.1016/j.jsg.2019.103934

Sperner, B., Müller, B., Heidbach, O., Delvaux, D., Reinecker, J., and Fuchs, K. (2003). Tectonic stress in the earth's crust: advances in the world stress map project. *Geol. Soc. London Spec. Publ* 212, 101–116. doi:10.1144/GSL.SP.2003.212.01.07

Stabile, T. A., Satriano, C., Orefice, A., Festa, G., and Zollo, A. (2012). Anatomy of a microearthquake sequence on an active normal fault. *Sci. Rep* 2, 410. doi:10.1038/srep00410

Steckler, M. S., Agostinetti, N. P., Wilson, C. K., Roselli, P., Seeber, L., Amato, A., et al. (2008). Crustal structure in the southern apennines from teleseismic receiver functions. *Geology* 36, 155–158. doi:10.1130/G24065A.1

Trippetta, F., Collettini, C., Vinciguerra, S., and Meredith, P. G. (2010). Laboratory measurements of the physical properties of triassic Evaporites from central italy and correlation with geophysical data. *Tecnophysics* 492, 121–132. doi:10.1016/j.tecto.2010.06.001

Troise, C., De Natale, G., Pingue, F., and Petrazzuoli, S. M. (1998). Evidence for static stress interaction among earthquakes in the south–central apennines (Italy). *Geophys. J. Int* 134, 809–817. doi:10.1046/j.1365-246x.1998.00610.x

Vaccari, F., Suhadolc, P., and Panza, G. F. (1990). Irpinia, Italy, 1980 earthquake: waveform modelling of strong motion data. *Geophys. J. Int* 101, 631–647. doi:10.1111/j.1365-246x.1990.tb05575.x

Valensise, G. (1993). Summary of contributions on the 23 november 1980, Irpinia earthquake. *Ann. Geofisc* 00, 345–351.

Valensise, G., and Pantosti, D. (2001). The investigation of potential earthquake sources in peninsular Italy: a review. *J. Seismol* 5, 287–306. doi:10.1023/A:1011463223440

Vassallo, M., Festa, G., Bobbio, A., and Serra, M. (2016). Low shear velocity in a normal fault system imaged by ambient noise cross correlation: the case of the Irpinia fault zone, Southern Italy. *J. Geophys. Res. Solid Earth* 121, 4290–4305. doi:10.1002/2015JB012410

Villani, F., Pucci, S., Civico, R., De Martini, P. M., Cinti, F. R., and Pantosti, D. (2018). Surface faulting of the 30 October 2016 M_w 6.5 central Italy earthquake: detailed analysis of a complex coseismic rupture. *Tectonics* 37, 3378–3410. doi:10.1029/2018TC005175

Westaway, R. (1993). Fault rupture geometry for the 1980 Irpinia earthquake: a working hypothesis. *Ann. Geofisc* 36, 51–69.

Westaway, R., and Jackson, J. (1987). The earthquake of 1980 november 23 in campania-basilicata (southern Italy). *Geophys. J. Roy. Astron. Soc* 90, 375–443.

Wilkinson, M. W., McCaffrey, K. J. W., Jones, R. R., Roberts, G. P., Holdsworth, R. E., Gregory, L. C., et al. (2017). Near-field fault slip of the 2016 Vettore M. *Sci. Rep* 7, 4612. doi:10.1038/s41598-017-04917-w10.1038/s41598-017-04917-w

Conflict of Interest: The authors declare that the research was conducted in the absence of any commercial or financial relationships that could be construed as a potential conflict of interest.

frontiers
in Earth Science

ORIGINAL RESEARCH
published: 15 February 2021
doi: 10.3389/feart.2020.581396

Megathrust Slip Behavior for Great Earthquakes Along the Sumatra-Andaman Subduction Zone Mapped From Satellite GOCE Gravity Field Derivatives

Orlando Álvarez[1,2], Stefanie Pechuan Canet[2], Mario Gimenez[1,2] and Andrés Folguera[3]*

[1]Instituto Geofísico y Sismológico Ing. Volponi, FCEFyN, Universidad Nacional de San Juan, San Juan, Argentina, [2]Consejo Nacional de Investigaciones Científicas y Técnicas, Buenos Aires, Argentina, [3]IDEAN – Instituto de Estudios Andinos "Don Pablo Groeber", Departamento de Cs. Geológicas, FCEN, Universidad de Buenos Aires, Buenos Aires, Argentina

During the last two decades, space geodesy allowed mapping accurately rupture areas, slip distribution, and seismic coupling by obtaining refined inversion models and greatly improving the study of great megathrust earthquakes. A better understanding of these phenomena involving large areas of hundreds of square kilometers came from the last gravity satellite mission that allowed detecting mass transfer through the Earth interior. In this work, we performed direct modeling of satellite GOCE (Gravity Field and Steady-State Ocean Circulation Explorer) derived gravity gradients up to degree/order N = 200 of the harmonic expansion and then corrected this by the effect of topography. Cutting off the model up to this degree/order allows inferring mass heterogeneities located at an approximate depth of 31 km, just along the plate interface where most (but not all) significant slip occurs. Then, we compared the vertical gravity gradient to well-constrained coseismic slip models for three of the last major earthquakes along the Sunda interface. We analyzed seismic rupture behavior for recent and for historical earthquakes along this subduction margin and the relationship of the degree of interseismic coupling using the gravity signal. From this, we found that strong slip patches occurred along minima gravity gradient lobes and that the maximum vertical displacements were related quantitatively to the gravity-derived signal. The degree of interseismic coupling also presents a good correspondence to the vertical gravity gradient, showing an inverse relationship, with low degrees of coupling over regions of relatively higher density. This along-strike segmentation of the gravity signal agrees with the along-strike seismic segmentation observed from recent and historical earthquakes. The thermally controlled down-dip ending of the locked fault zone along central Sumatra also presented an inverse relationship with the density structure along the forearc inferred using our modeling. From this work, we inferred different mass heterogeneities related to persistent tectonic features along the megathrust and along the marine forearc, which may control strain accumulation and release along the megathrust. Combining these data with geodetical and seismological data could possibly delimit and monitor areas with a higher potential seismic hazard around the world.

Keywords: great earthquake rupture process, megathrust earthquakes, Gravity Field and Steady-State Ocean Circulation Explorer satellite data, seismic hazard, subduction zone, Sumatra-Andaman earthquake, Sunda arc subduction zone, coseismic slip distribution

Edited by:
Debora Presti,
University of Messina, Italy

Reviewed by:
Gianluca Vignaroli,
University of Bologna, Italy
Sebastiano D'Amico,
University of Malta, Malta

****Correspondence:***
Orlando Álvarez
orlando_a_p@yahoo.com.ar

Specialty section:
This article was submitted to
Structural Geology and Tectonics,
a section of the journal
Frontiers in Earth Science

Received: *09 July 2020*
Accepted: *10 December 2020*
Published: *15 February 2021*

Citation:
Álvarez O, Pechuan Canet S,
Gimenez M and Folguera A (2021)
Megathrust Slip Behavior for
Great Earthquakes Along the Sumatra-
Andaman Subduction Zone Mapped
From Satellite GOCE Gravity
Field Derivatives.
Front. Earth Sci. 8:581396.
doi: 10.3389/feart.2020.581396

INTRODUCTION

Numerous major to great earthquakes had affected the Sunda subduction system in the past, with some giant events in the last decades from Southern Sumatra to the Andaman Islands. This region is characterized by lateral variations of the convergence rate and obliquity that occur gradually (Chlieh et al., 2008) as the Indo and Australian plates are thrust beneath the Sunda plate. This work divided this subduction zone into four main segments according to the historical earthquakes that affected the margin. Along the Northern section occurred the great Mw = 9.15 2004 Sumatra-Andaman earthquake, one of the four largest earthquakes recorded in instrumental times and the largest of the last 40 years (Lay et al., 2005; Stein and Okal, 2005; Klingelhoefer et al., 2010). This segment ranges from the Simeulue Is. located at 2.5° N to the Andaman Is. to the North (**Figures 1**, **2**). The Nias segment is located between Simeulue Is. and the Batu Islands; this central segment broke during the Mw = 8.6 2005 event (Briggs et al., 2006; Hsu et al., 2006; Konca et al., 2007) and previously in 1861 (~Mw 8.5, Newcomb and McCann, 1987). To the South of this area, the central Sumatra margin beneath the Mentawai Islands (**Figures 1**, **2**) had many major earthquakes in the past (**Figures 1–3**), e.g., in 1797 (Mw = 8.78.9), 1833 (Mw = 8.9–9.1), and 1861 (Newcomb and McCann, 1987; Zachariasen et al., 1999; Sieh et al., 2004; Natawidjaja et al., 2006) and even recently in 2007 with a Mw = 8.4. The last segment is located to the South of Enggano Is. Only moderate earthquakes have been reported, such as the 2000 Mw = 7.9 Enggano Is. earthquake (Abercrombie et al., 2003).

Different hypotheses have been proposed about the variables governing heterogeneous seismic behavior along the megathrust (e.g., thermal structure, subducting sediments and high oceanic features, and the forearc structure's variable weight). These proposals were tested and studied through different methods and databases without any general conclusive result, leaving numerous open questions. One of them is the degree of interaction between the forearc density structure along the megathrust and seismic rupture behavior. From the early works of Song and Simons (2003) and Wells et al. (2003), it is expected that strong negative gravity anomalies between the coast and the trench correlate geographically to maximum coseismic slip for giant earthquakes.

The last authors proposed that large coseismic slip is associated with forearc gravity lows related to active basins and enhanced subduction erosion. Later, Llenos and Mc Guire (2007) related negative gravity variations to high-shear traction on the interplate thrust, associated with an increase in the effective coefficient of friction. The different variables governing this relationship have been proposed; e.g., changes of vertical stress loading due to forearc density structure produce lateral variations of shear strength, as stated by other authors (e.g., Sobiesak et al., 2007; Tassara 2010; among others).

Gravity modeling has proven to be useful for mapping the structure, geometry, and seismic segmentation of the interplate megathrust (e.g., Llenos and Mc Guire, 2007; Sobiesiak et al., 2007; Tassara, 2010; Alvarez et al., 2014; Alvarez et al., 2019a) and also for observing mass variations inside the Earth after great earthquakes. The Sumatra-Andaman earthquake has become one of the most studied from satellite gravimetry, particularly from the GRACE (Gravity Recovery and Climate Experiment) mission. Coseismic and postseismic gravity changes detected from this mission allowed for detecting deformation and a crustal dilatation resulting from this earthquake (e.g., Han et al., 2006; Chen et al., 2007; Panet et al., 2007).

We explore the seismic structure along the Sunda subduction zone from the GO_CONS_GCF_2_DIR_R6 satellite GOCE (Gravity Field and Steady-State Ocean Circulation Explorer) derived model (Bruinsma et al., 2014), as we made previously for the South American subduction margin (see Alvarez et al., 2019a and references therein). Then we compare the vertical gravity gradient to coseismic slip models for recent earthquakes, rupture areas for historical earthquakes, and the degree of interseismic coupling and the thermal structure along a portion of this margin.

MAPPING ASPERITIES ALONG THE MEGATHRUST FROM THE VERTICAL GRAVITY GRADIENT (TZZ)

Despite the numerous studies carried out based on the mass changes detected by satellite gravimetry, the behavior of the rupture during the earthquake based on satellite-derived gradient data had not been addressed until the recent works of Alvarez et al. (2019a) and Alvarez et al. (2019b) and references therein. Following the pioneering works from Song and Simons (2003) and Wells et al. (2003), we found that minimum lobes in the negative vertical gravity gradient Tzz (the second vertical derivative of the anomalous potential) from GOCE present an inverse relationship with maximum slip areas during great megathrust earthquakes. This quantity (Tzz) offers a better spatial resolution than the gravity anomaly for mapping shallower mass anomalies (e.g., Li, 2001; Braitenberg et al., 2011; Alvarez et al., 2012).

In a recent review, Alvarez et al. (2019a) and references therein highlighted this relationship, mapping asperities and barriers (Lay et al., 1982), and showing how the gravity signal could also explain the directivity effect for some of these events (seismic asperities are interpreted as the site where the maximum seismic moment is released during large interplate earthquakes). They also proposed that the density structure (derived from GOCE satellite data at long wavelengths) affects the forearc region's seismic behavior, mainly for these large-magnitude events.

Other works (e.g., Hicks et al., 2014) pointed out a moderate positive correlation between gravity and seismic velocity Vp from a seismic tomography in the lower forearc for the 2010 Maule earthquake. This relationship was also observed by Alvarez et al. (2019a) using GOCE derived vertical gradient (Tzz) at a spatial resolution of 80 km, corresponding to the maximum degree and order of the spherical harmonic expansion N = 250 and with Z = 25 km. In previous work, Sobiesak et al. (2007) found along the Northern Chilean margin that seismic b-value was correlated with geologic structures mapped by isostatic residual gravity anomalies. Now, we explore these relationships along the Sunda subduction zone, one of the regions of most significant interest on a global scale for the study of great megathrust earthquakes.

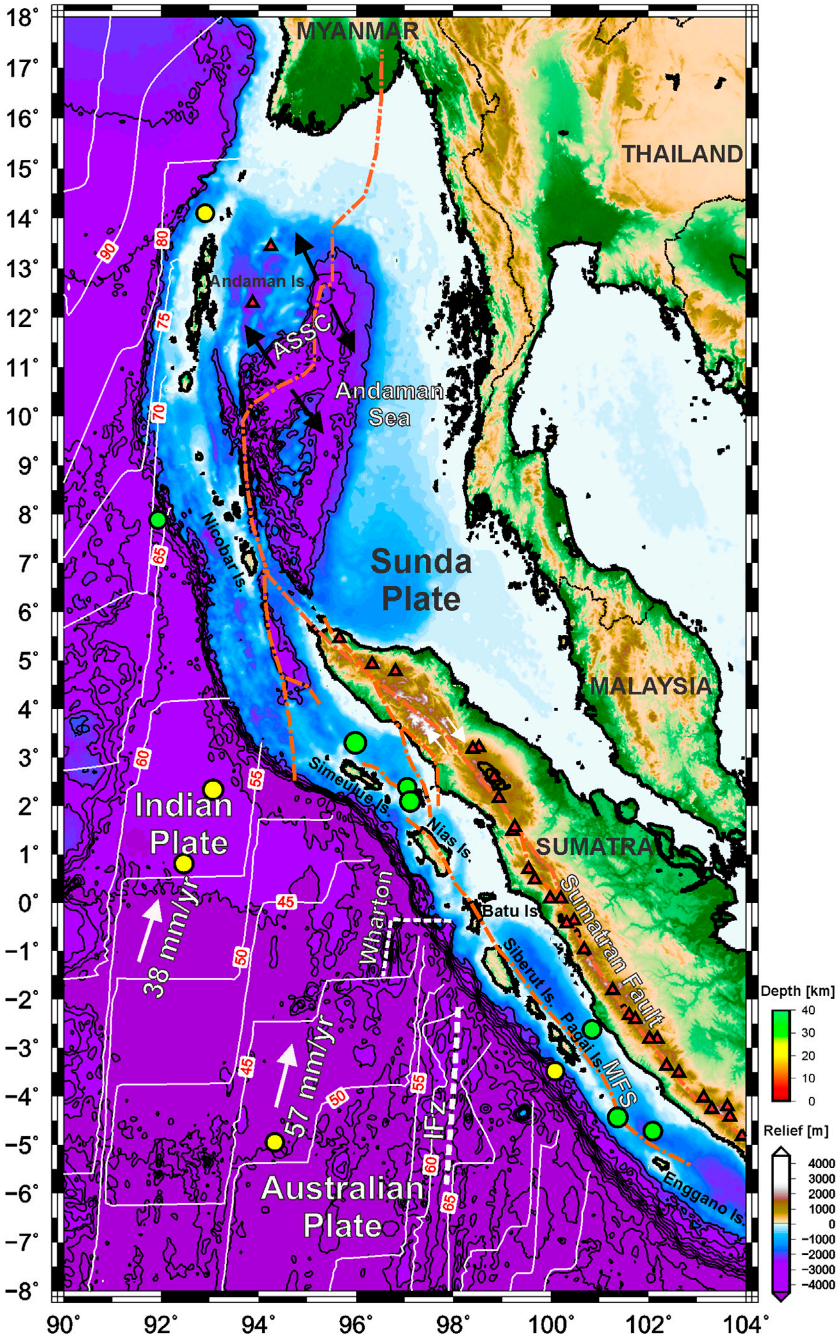

FIGURE 1 | Relief map of the Australian, Indian, and Sunda plates from ETOPO1 (Amante and Eakins, 2009) with main bathymetric features. Orange dot and dashed line indicate the main faults as the Sumatran, Andaman, and Mentawi fault system (MFS). In this region, the Indian plate subducts obliquely beneath the Eurasian plate along the Sunda subduction zone at an approximate rate convergence of 39 mm/yr Chlieh et al. (2008). White arrows in the Andaman Sea indicate the Andaman Sea Spreading Center (ASSC). Plates rate convergence is from Chlieh et al. (2008), plate ages (white solid lines) are from Müller et al. (2008), red triangles indicate the volcanic arc (Siebert and Simkin, 2002), and white dashed lines indicate the Wharton fossil ridge and the investigator fracture zone (Fz). Circles indicate earthquakes with Mw > 7.5 from 2000 A.D (from USGS); the upper color bar indicates earthquake depth.

METHODOLOGY

Satellite Data and Gravity Derivatives

For calculation of the gravity derivatives, we used the satellite GOCE static model GO_CONS_GCF_2_DIR_R6 (Bruinsma et al., 2014), which is a full combination of data from GOCE-SGG (Satellite Gravity Gradiometer), GOCE-SST (Satellite-to-Satellite Tracking), GRACE (Gravity Recovery and Climatic Experiment), and LAGEOS (Laser GEOdynamics Satellite). The disturbing potential (T) is derived by subtracting the reference ellipsoid's

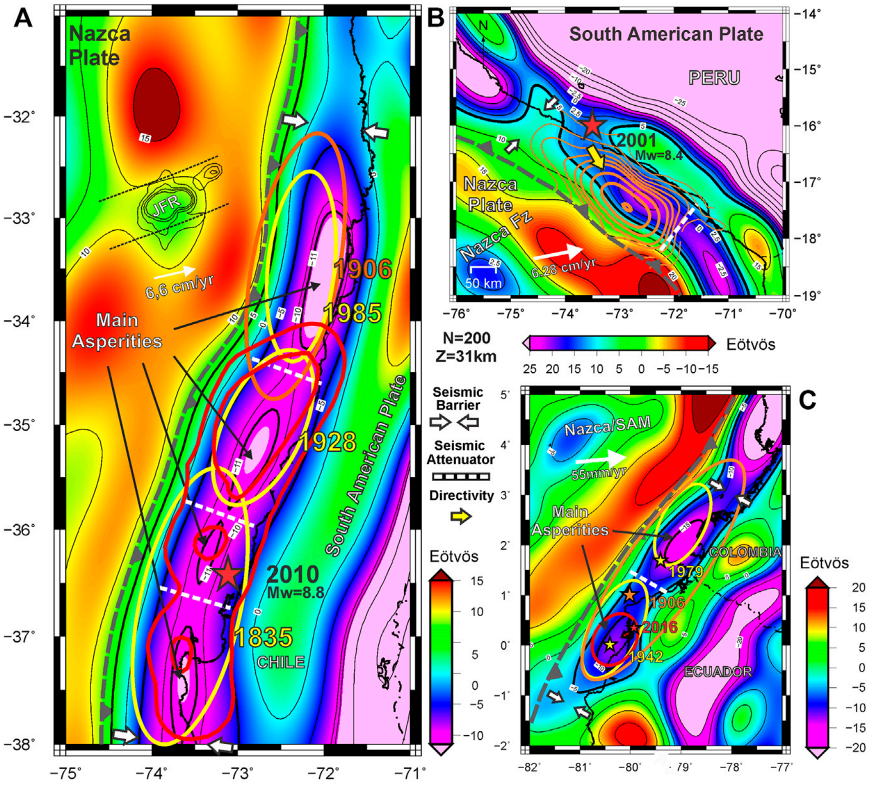

FIGURE 2 | Topography corrected vertical gravity gradient obtained from GOCE satellite-only model GO_CONS_GCF_2_DIR_R5 (Bruinsma et al., 2013) up to N = 200. **(A)** Slip distribution (red solid line) for the Mw = 8.8 2010 Maule earthquake (Moreno et al., 2012), the −5 Eötvös contour (thick black line) roughly coincides with the seismogenic zone along the forearc. The −10 Eötvös contour coincides with the location of maximum slip lobes. Solid white arrows indicate a narrowing of the Tzz minima contours, which corresponds to main slip limits along strike (Alvarez et al., 2014; Alvarez et al., 2019b). Nazca-South American plates convergence (black arrow) is from DeMets et al. (2010). **(B)** Slip distribution for the Mw = 8.4 2001 Arequipa earthquake (Chlieh et al., 2011). The +5 Eötvös contour (thick black line) depicts higher densities to the NW and SE of the epicenter along the forearc (Alvarez et al., 2015; Alvarez et al., 2019a). A low Tzz anomaly to the SSE of the epicenter connects to the maximum slip, following the rupture propagation in the Southward direction (blank white arrow). Nazca-South American plates convergence (white arrow) is from Kendrick et al. (2003). **(C)** Historical ruptures along the Ecuador-Colombia margin (Alvarez et al., 2017b; Alvarez et al., 2019b). Red star indicates the epicenter's location and the Perú-Chilean trench is indicated with a gray dashed line.

normal potential field (WGS84) from the observed potential. We calculated the disturbing potential by direct modeling from the spherical harmonic coefficients (Janak and Sprlak, 2006) of the GOCE mentioned above model. Then the vertical gravity gradient (***Tzz***) was obtained on a regular grid of 0.05° grid cell size as the second radial derivative of T (Rummel et al., 2011):

$$T_{zz} = \frac{\partial^2 T}{\partial r^2}\left[1\ \textbf{Eötvös} = 10^{-4}\frac{\boldsymbol{mGal}}{\boldsymbol{m}}\right] \qquad (1)$$

Tzz is expressed in Eötvös and represents a better theoretical resolution than the gravity vector itself for detecting crustal density variations (Li, 2001) (mainly shallower structures with high-density contrast), allowing determination of the edges of anomalous masses with better detail and accuracy. The gravity disturbance presents a spread signal highlighting deeper sources (Braitenberg et al., 2011; Alvarez et al., 2012).

Topographic Correction

To remove the correlation of the satellite-derived gravity signal with topographic masses, Tzz was reduced by the topographic effect. This correction allows highlighting the different (and unknown) density contrasts within the crust.

The topographic contribution calculation requires discretization of a digital elevation model (ETOPO1, Amante and Eakins, 2009) using spherical prisms of constant density (Grombein et al., 2013). Using a spherical approximation, the Earth's curvature was taken into account, avoiding considerable errors over the large study region. Then, the effect generated by the topographic masses on the gravity field and over its derivatives was calculated following Newton's law of universal gravitation.

We performed the topography contribution calculation to ***Tzz*** using the Tesseroids Phyton package from Uieda et al. (2016). Densities used are mean standard values of 2,670 kg/m^3 for masses above sea level and 1,030 kg/cm^3 for seawater. The calculation height selected is of 3,000 m to ensure that all values are above the topography. Before satellite data reduction, the topographic effect contribution was filtered using a 4th order Butterworth filter at 133 km wavelength to compare to satellite data at similar wavelengths.

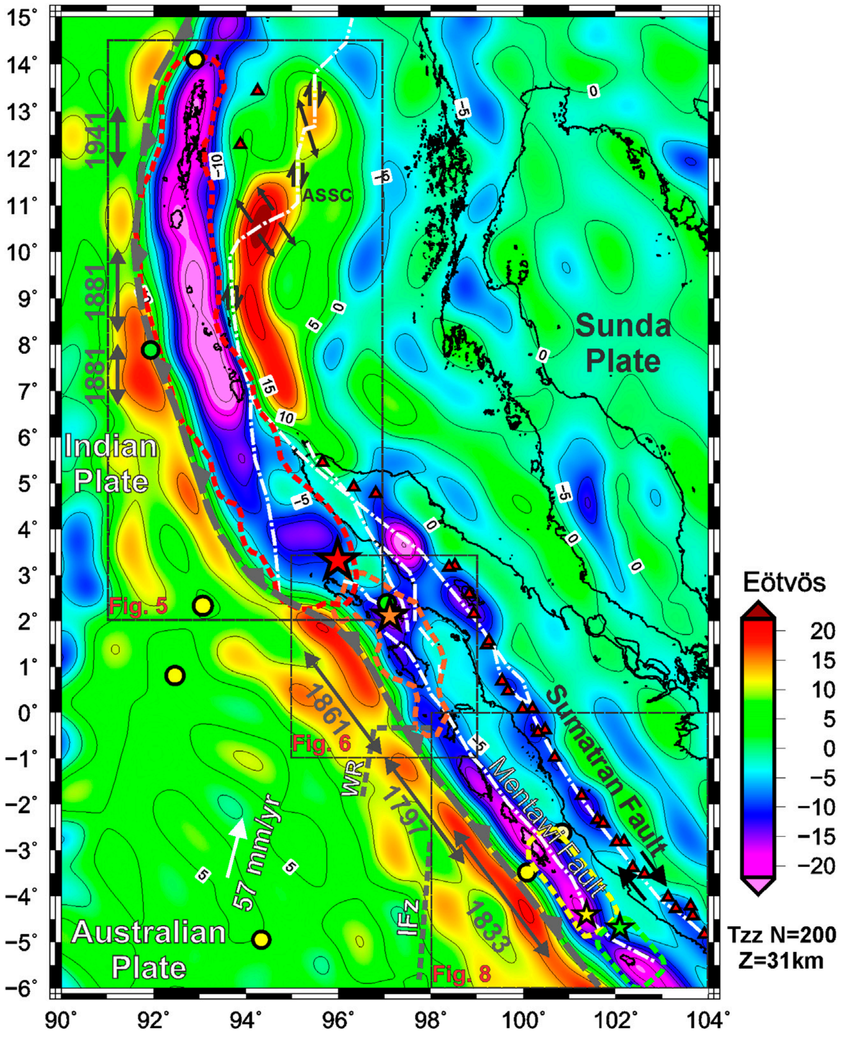

FIGURE 3 | Topography corrected vertical gravity gradient (Tzz) obtained from GOCE model GO_CONS_GCF_2_DIR_R6 up to N = 200 (Bruinsma et al., 2014). The forebulge presents a high gravity gradient signal while lower to negative values are observed along the outer forearc, to the Northwest is clearly depicted the Andaman Sea Spreading Center (ASSC). Historical great earthquakes are indicated with gray double-arrows. The dimensions of the approximate rupture areas for four of the last great earthquakes along the Sumatra-Andaman margin are indicated with dashed lines. Stars indicate epicenter location of the Mw = 9.15 2004 Sumatra-Andaman earthquake (yellow), the Mw = 8.6 2005 Nias–Simeulue earthquake (orange), the Mw = 7.9 2007 Kepulauan-Mentawai earthquake (red), and the Mw = 7.9 2000 Southern Sumatra earthquake (green). Rectangles indicate the location of **Figures 5**, **6**, and **8**. IFz: investigator fracture zone, WR: Wharton ridge.

Tzz Harmonic Decomposition From Spherical Coefficients

In previous works, we found that, by limiting the harmonic expansion to degree and order N = 200, we reached an exploration depth of approximately 30 km. At this exploring depth, where the shallow portion of the plate interface (megathrust) is located, we found the best correlation between slip distribution and Tzz.

The harmonic decomposition from spherical coefficients is based on Featherstone (1997), who performed a spectral analysis of the geoid and gravity anomalies and found that limiting the degree/order allows decomposition of the gravimetric signal as causative mass depth increases. By deriving a similar equation (**Eq. 2**) (see Alvarez et al., 2017a and references therein) the depth (Z_l) of a causative mass was related to a determined degree of the spherical harmonic expansion (N) for the Tzz:

TABLE 1 | Approximated depth (Z_l) of a causative mass for a determined degree of the spherical harmonic expansion for **Tzz** and corresponding spatial resolution (Alvarez et al., 2017a).

Degree/Order *N*	**Spatial resolution $\lambda/2 = \pi R/N_{max}$ [Km]**	**Z_l[Km] *for Tzz* (H_c = 3 km)**
300	67	21
250	80	25
200	100	31
150	133	41
100	200	61

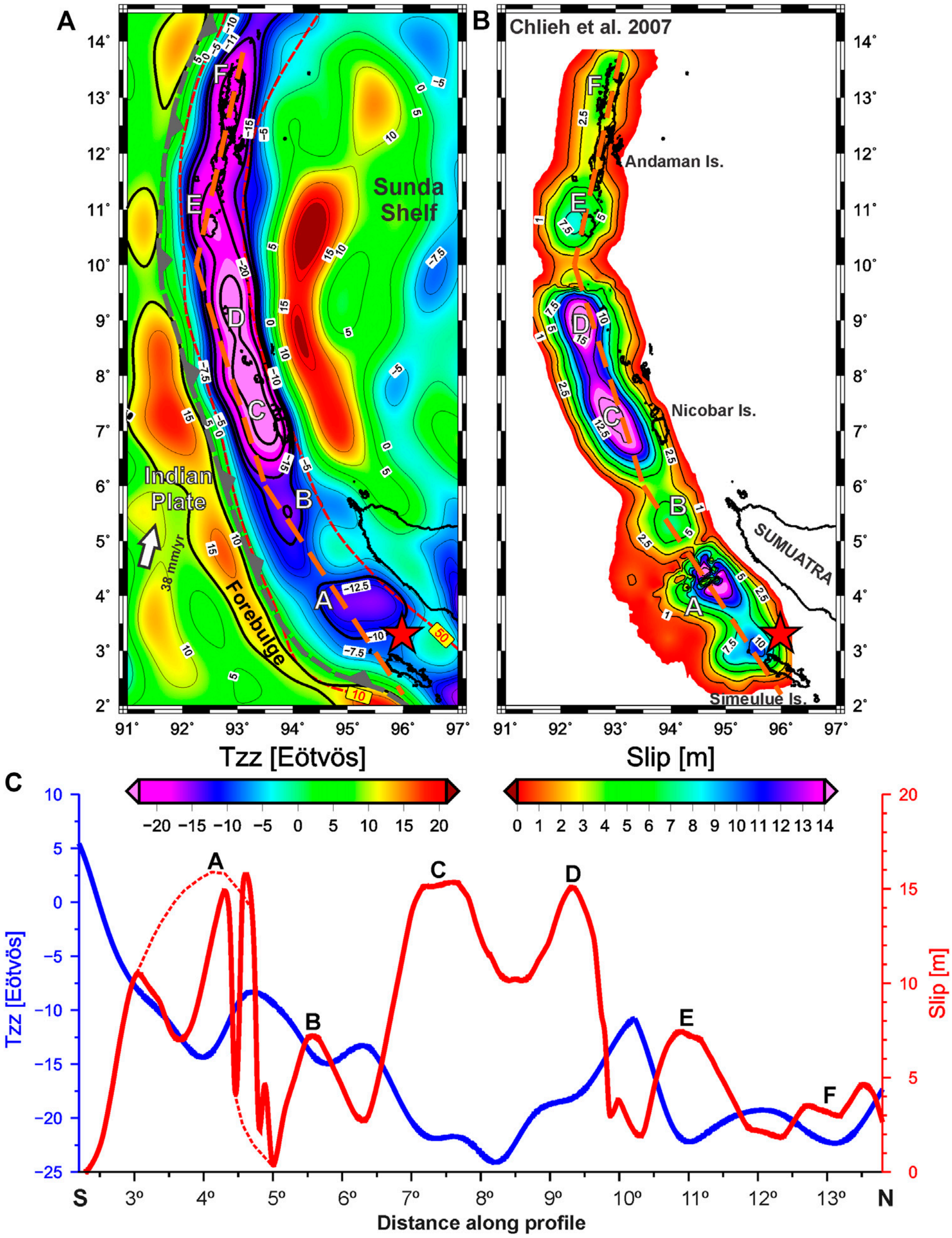

FIGURE 4 | (A) Topography corrected vertical gravity gradient (Tzz) obtained from GOCE model GO_CONS_GCF_2_DIR_R6 up to N = 200 (Bruinsma et al., 2014). Slab depths of 10 km and 50 km from Slab 2.0 of Hayes (2018) are plotted with red dashed lines. **(B)** Slip model for the Mw = 9.15 2004 Sumatra-Andaman earthquake (Chlieh et al., 2007). **(C)** Latitudinal profile along the Tzz signal (blue) and along the slip model (red), letters indicate the location of asperities where slip is enhanced. Note that maximum slip coincides with minimum Tzz and vice versa. The red dashed line indicates a "high-wavelength" component of the slip. Letters A to F indicate the location of different seismic asperities where a high amount of energy and minor short-period seismic radiation were released.

$$Z_l = \frac{(R_E + H_c)(N-1)}{(N+2)(N+1)}, \qquad (2)$$

where, for an Earth's radius R_E of approximately 6,371 km, ***Tzz*** calculation height H_C of 3,000 m, and a degree/order of the harmonic expansion N = 200, we obtained an exploration depth of approximately 31 km. **Table 1** shows the depth Z_l and corresponding spatial resolution for different degrees/orders of the harmonic expansion. Higher orders are associated with shallower sources (low Z_l), while low orders are related to deeper mass anomalies (higher Z_l).

RESULTS AND DISCUSSION

From the early 2000 A.D., more than ten earthquakes with Mw > 7.5 affected the Sumatra-Andaman margin, four of them with Mw > 8

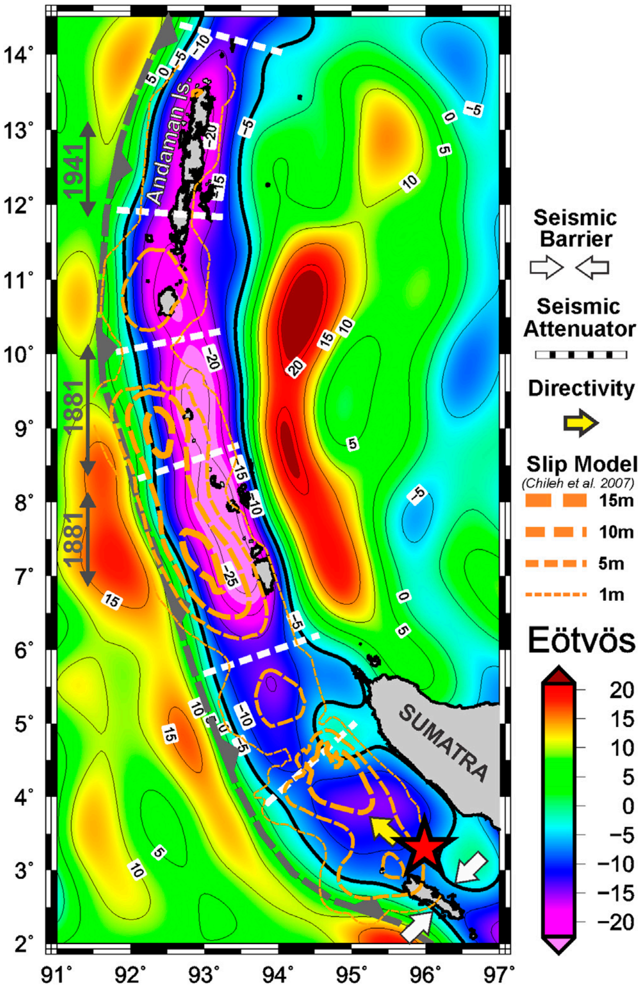

FIGURE 5 | Slip model for the Mw = 9.15 2004 Sumatra-Andaman earthquake (Chlieh et al., 2007) superimposed to the topography corrected Vertical Gravity Gradient (Tzz) obtained from GOCE model GO_CONS_GCF_2_DIR_R6 up to N = 200 (Bruinsma et al., 2014). The dashed white line indicates the location of regions that behaved as seismic energy attenuators; white arrows indicate the existence of a seismic barrier that arrested rupture propagation. Historical great earthquakes are indicated with gray double-arrows.

(two offshore in the region of the Indian Ocean) and one of the four Mw > 9.0 registered. Some of these events have been extensively studied and accurately modeled from different datasets with widely distributed seismic and GPS networks along the margin and with sea bottom sensors resulting in well-constrained slip models (e.g., Abercrombie et al., 2003; Briggs et al., 2006; Chlieh et al., 2007; Konca et al., 2007; Konca et al., 2008). Some works also found meaningful mass redistribution from gravity changes detected by the GRACE satellite (Han et al., 2006; Chen et al., 2007; Panet et al., 2007). In this work, we analyze the rupture propagation pattern for some of these events and its relation with the distribution of crustal mass heterogeneities from satellite GOCE derived data.

At first glance over the gradient signal (**Figure 2**), we can highlight the positive effect of the Australian and Indian oceanic plates, which is enhanced at the forebulge (outer rise), reaching more than +10 Eötvös. Between 0° and 2.5° N it is important to highlight an anomalous region where the positive expression of the forebulge presents an abnormal behavior compared to other regions along the margin (i.e., presents an inflection toward the Simeulue and Nias Islands). In this region, Franke et al. (2008) observed (based on marine geophysical data acquired offshore Simeulue in 2006) that the top of the oceanic crust presents a significant deepening toward the SE and suggested that the segmentation of the margin at this latitude is caused by a ridge currently undergoing subduction.

To the South of this (**Figures 2**, **4**), the high positive signal along the forebulge is segmented at the collision points of the Wharton fossil ridge and at the investigator Fz. Relatively higher values in Tzz lobes (>+15 Eötvös) are observed along the outer rise, not only offshore Simeulue and Nias Islands but at the offshore of Batu, Siberut, and Pagai Islands (Mentawi Is.). Henstock et al. (2016) had already identified different regions of positive residual gravity, namely, 1° offshore Nias beneath the accretionary prism (that corresponds to an area of active uplift: Cook et al., 2014); 2° offshore the Batu Islands (reported as a series of positive residuals immediately adjacent to the location of the extinct WFR: Liu et al., 1983); and 3° offshore Siberut (where positive residuals were found aligned with fracture zones in the subducting plate).

Another first-order gravity signature is observed (**Figures 2**, **5**) at the Andaman Sea Spreading Center (ASSC) where two highly positive lobes (with more than +20 Eötvös) indicate a shallower mantle over the divergent plate boundary. Along the trench, the high forebulge gravity rapidly decreases, representing the deepening of the slab, to a negative gradient signal beneath the forearc.

The negative gravity gradient signal along the marine forearc (or between the trench and the coastline along Sumatra) may be in response to lower density material along the accretionary wedge, the deep-sea terrace, marginal basins, and high sediment thickness along the trench, which cannot be differentiated at this spatial resolution without other constraints. This low gravity signal appears to be segmented along strike (**Figure 2**), with lower values to the North of the Nicobar Is. (<−25 Eötvös), intermediate values between 6° N and −1° S (−5 to −15 Eötvös), and low values in the region of Mentawi Islands to the South (−20 Eötvös approximately). An across-strike segmentation is observed to the North and South of the Mw = 9.15 2004 earthquake and the NE of the Mentawi fault zone (**Figures 4–6**).

Along the Southern region (**Figures 2**, **6**), the Mentawi fault zone (MFZ, Diament et al., 1992) can be mapped lying to the East of the outer arc ridge (along the center of the marine forearc) and can be mapped to the North up to the Nias Island where it intersects with other faults that can be tracked following the Tzz contours. Inland, the right-lateral Sumatran Fault System can be observed following Tzz minima over the active volcanic arc.

Along the Sumatra-Andaman region, historical and recent earthquake ruptures coincide with the along-strike segmentation of the gradient signal over the marine forearc (**Figure 2**), as observed in previous works along the South American active

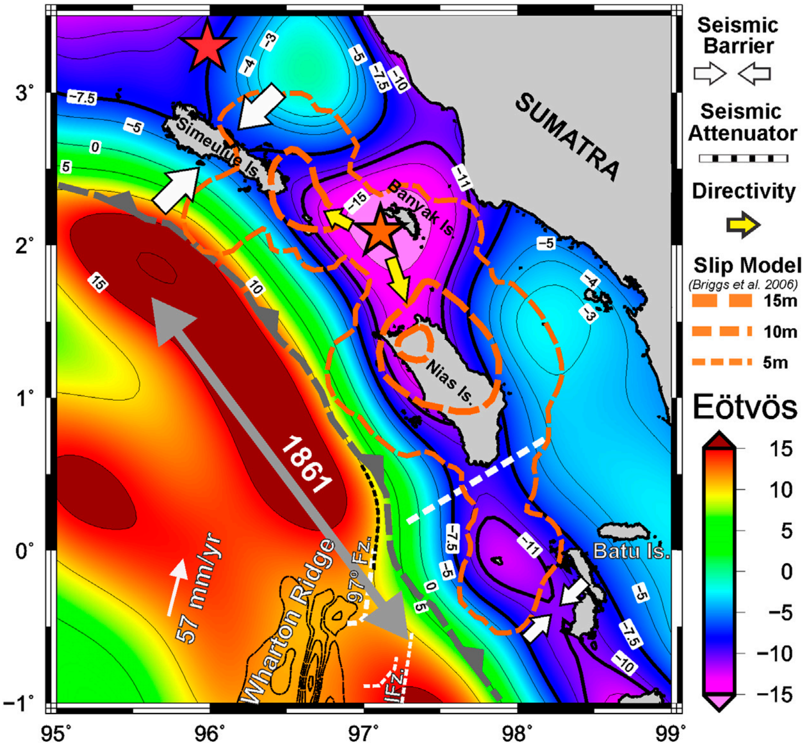

FIGURE 6 | Slip model (dashed orange contours) for the Mw = 8.6 2005 Simeulue-Nias earthquake (Briggs et al., 2006) superimposed to the topography corrected vertical gravity gradient (Tzz) obtained from GOCE model GO_CONS_GCF_2_DIR_R6 up to N = 200 (Bruinsma et al., 2014). The dashed white line indicates the location of regions that behaved as seismic energy attenuators; white arrows indicate the existence of a seismic barrier that arrested rupture propagation. The great historical earthquake of 1861 is indicated with gray double-arrows (Newcomb and McCann, 1987).

margin (Alvarez et al., 2019a). In the next section, we will compare results derived from satellite GOCE with the slip models of the Mw = 9.15 2004 Sumatra-Andaman earthquake, the Mw = 8.6 2005 Nias–Simeulue earthquake, the Mw = 7.9 2007 Kepulauan-Mentawai earthquake, and the Mw = 7.9 2000 Southern Sumatra earthquake (**Figure 2**).

The Mw = 9.15 2004 Sumatra-Andaman Earthquake

On December 26, 2004, the NW Sumatra margin was affected by a giant earthquake that initiated to the North of the Simeulue Island (**Figures 1**, **7**) at an approximate depth of 30 km with an estimated magnitude of Mw ~ 9.15 (Ammon et al., 2005; Lay et al., 2005; Vigny et al., 2005; Chlieh et al., 2007). Rupture extended along the trench from Northern Sumatra to the Andaman Islands; different slip models showed three distinct peaks, reaching up to approximately 20 m, at about 4° N, 7° N, and 9° N (Bilham et al., 2005; Chlieh et al., 2007; Dewey et al., 2007). The seismic rupture was the longest ever recorded (~515 s), making it difficult to constrain some seismic characteristics using seismological methods. The coseismic slip model from Chlieh et al. (2007), derived from geodetic observations, conciliates the spatial distribution of slip along ~1,500 km (and width of ~150 km) with the total released moment of 6.7–7.0 × 1,022 Nm, being one of the most robust, reliable, and better constrained for this earthquake. This model is roughly similar to that estimated from seismological data by Ammon et al. (2005), consistent with the latitudinal seismic moment released and T-waves from Guilbert et al. (2005) and with body waves from Ni et al. (2005).

Earthquake Rupture Behavior From Tzz

The topography corrected vertical gravity gradient calculated up to N = 200 (**Figure 8A**) in the region of the Sumatra-Andaman earthquake presents a first-order anticorrelation with the rupture model of Chlieh et al. (2007) (**Figure 8B**) along the marine forearc. The along-strike segmentation of Tzz (relative maxima) coincides with minimum vertical displacements, while maximum slip patches (A to F) agree with relative minima Tzz (**Figure 8C**). The slip model shows high-frequency components close to the epicenter that cannot be solved by the long-wavelength characteristic of the GOCE signal. Despite this, assuming a “higher wavelength” trend for slip distribution (dashed line in **Figure 8A**), the relationship above explained is maintained (high slip over low Tzz). When superimposing the slip model to the Tzz (**Figure 5**), a slight lateral shift is observed between both quantities. This is interpreted as the positive effect of the subducting plate over the gradient signal masking the low Tzz

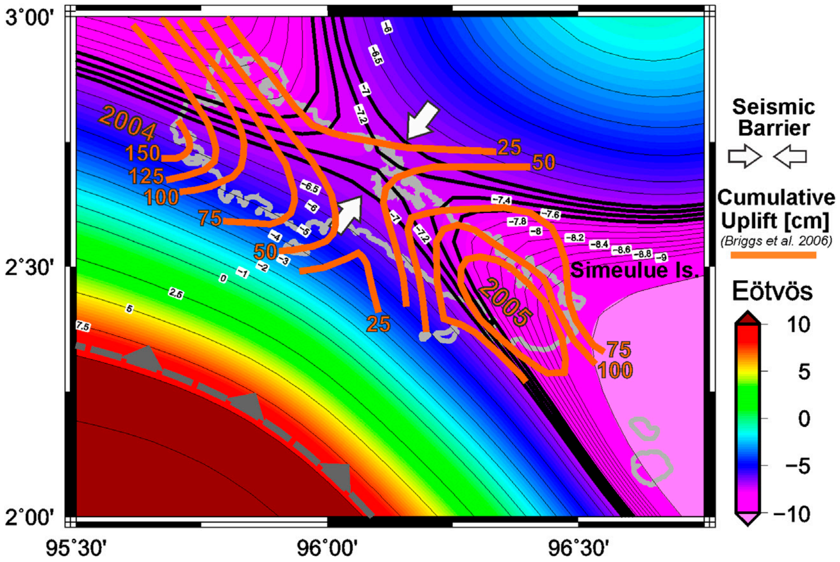

FIGURE 7 | Cumulative uplift (solid orange contours) from Briggs et al. (2006), recorded after the 2004 Sumatra-Andaman and the 2005 Simeulue-Nias earthquakes, superimposed to the topography corrected vertical gravity gradient (Tzz) obtained from GOCE model GO_CONS_GCF_2_DIR_R6 up to N = 200 (Bruinsma et al., 2014). White arrows indicate the existence of a seismic barrier that arrested rupture propagation. Note the saddle structure of the cumulative uplift (in cm) that seems to replicate the gravimetric structure, coinciding the minimum in the center of the Island with the local maxima in Tzz interpreted as a seismic barrier to rupture propagation.

trend observed along the marine forearc. From the next subsection onwards, we will make a detailed analysis of the above explained.

Northern Directivity

The Sumatra-Andaman earthquake was initiated at ~3° N with an initially rapid rupture followed by an important slip propagating in the Northward direction to the Andaman Islands at decreasing speed, with little or no slip to South of the epicenter (Banerjee et al., 2005; Lay et al., 2005; Chlieh et al., 2007). The strong unilateral rupture in one preferential direction is known as directivity and has been observed for many great earthquakes (McGuire et al., 2002), including the Mw = 9.6 1960 Valdivia earthquake.

The epicenter for the Sumatra-Andaman earthquake nucleated close to a relatively higher Tzz anomaly (**Figure 5**), in a region where the Tzz signal shows a narrowing to the South of the epicenter (white arrows in **Figure 5**) over the Simeulue Island. On the contrary, to the NE of the epicenter is observed a relative lower gradient signal where the first maxima slip patch occurred. Further North, in the vicinity of the Nicobar Islands the minima Tzz obtained along this portion of the Sunda margin are located, where maximum slip patches occurred, both in size and in amplitude. The low Tzz trend bounded by the −5 Eötvös (thick black contour in **Figure 5**), connecting the hypocenter location (30 km) to the maximum slip patches in the North, could be indicative of first-order structural or compositional characteristics that favored directivity in this direction. This behavior was also observed by means of Tzz for the 1960 Mw = 9.6 Valdivia (Alvarez et al., 2014), 2001 Mw = 8.4 Arequipa, and 2014 Mw = 8.2 Illapel earthquakes (Alvarez et al., 2014; Alvarez et al., 2015; Alvarez et al., 2019a).

Asperities Identification From Tzz

As explained in **section 4.1**, the latitudinal variation of geodetic moment from Chlieh et al. (2007) shows three distinct peaks, at about 4° N, 7° N, and 9° N. These peaks (A, C, and D in **Figure 8B**) coincide with the latitudinal variation of the energy radiated by T-waves from Guilbert et al. (2005) and are also consistent with the three distinct bursts of energy of high-frequency diffracted body waves as observed by Ni et al. (2005). These heterogeneities along the interplate megathrust that concentrate high seismic moment release and slip and a high-stress drop are known as asperities, as proposed in the model of Lay and Kanamori (1981) and Lay et al. (1982) and more recently in Lay et al. (2012).

Particularly, the region along the central portion of the megathrust where large earthquakes and high slip occur is named domain B in the model above mentioned. The along-strike segmentation of the vertical gravity gradient (**Figure 8**) shows different lobes of minimum negative values in agreement with those regions of minor short-period seismic radiation described as large and relatively uniform regions with unstable sliding frictional properties. Quantitatively, the region between 6.5° and 10° N (**Figure 8C**) where a high amount of energy (with more than +15 m of slip) was released coincides with the region where minimum mean negative Tzz (<−25 Eötvös) is obtained (C and D in **Figure 8A**). In general, the amount of slip at each asperity (A to F in **Figure 8**) presents a quantitative relationship (i.e., in

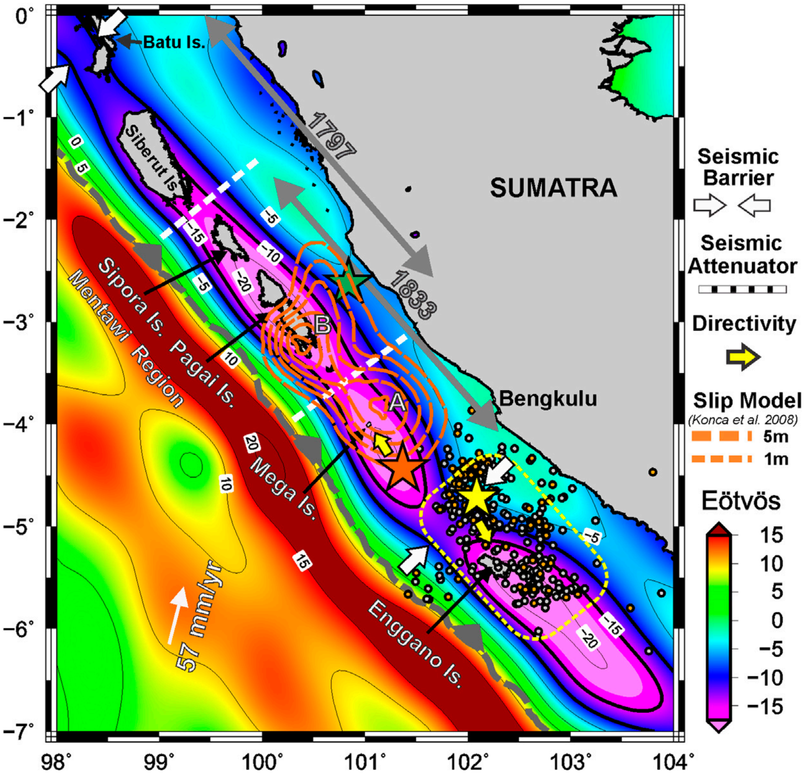

FIGURE 8 | Cumulative slip model (dashed orange contours) for the September 2007 sequence (Konca et al., 2008) superimposed to the topography corrected vertical gravity gradient (Tzz) obtained from GOCE model GO_CONS_GCF_2_DIR_R6 up to N = 200 (Bruinsma et al., 2014). Stars indicate epicenter location for each event: Mw = 8.4 (orange), Mw = 7.9 (green). The Enggano 2000 Mw = 7.9 earthquake (yellow star) ruptured to the South as indicated by the aftershock activity (orange circles are from Pan et al. (2001) and gray circles are from USGS database). The dashed yellow rectangle shows the approximate rupture area (Abercrombie et al., 2003). The dashed white line indicates the location of regions that behaved as seismic energy attenuators; white arrows indicate the existence of a seismic barrier that arrested rupture propagation. Historical great earthquakes of 1833 and 1797 are indicated with gray double-arrows (Newcomb and McCann 1987; Natawidjaja et al., 2006).

the amount of amplitude) to the amplitude of the Tzz signal (see **Figure 8C**).

Seismic Segmentation and Seismic Barrier at the Simeulue Island

Earthquake magnitude and location are controlled to a high degree by segmentation along convergent margins. These segment boundaries have been mapped along the Chilean margin based on the vertical gravity gradient (Alvarez et al., 2014) and are related to relative positive values in the Tzz (see **Figure 7**). In work mentioned above, we mapped and differentiated two kinds of segment boundaries (first-order attenuators or barriers and second-order attenuators) based on the limits of different rupture zones (recent and historical ones), the entrance of high oceanic features (e.g., seamounts, aseismic ridges, and fracture zones), and the Tzz. A second-order attenuator differs from a barrier because ruptures across them present a certain overlap, thus indicating a degree of blockage rather than a barrier to rupture propagation. The vertical gravity gradient signal shows higher relative values at the location of second-order attenuators (i.e., a gradual transition between high and low along strike). On the other hand, higher Tzz values or regions where the narrowing of the general trend of low Tzz anomaly along the outer forearc is significant, which in turn are related to the subduction of high oceanic features, were identified as first-order attenuators or barriers.

The 2004 Sumatra-Andaman earthquake terminated abruptly along a common boundary with the 2005 Nias earthquake over the Simeulue Island (**Figure 2**). In this region, the Tzz signal shows an important narrowing of the −5 Eötvös contour (white arrows in **Figure 5**), indicating the probable location of a seismic barrier. Franke et al. (2008) found a ridge on the subducting Indo-Australian oceanic crust masked by the sedimentary cover in the trench from joint modeling of wide-angle and reflection seismic data, proposing that it may exert control on margin segmentation. The ridge was interpreted in that work as a fracture zone on the subducting oceanic plate, with most likely trend NNE–SSW beneath Simeulue Island, in agreement with the trend and location observed in the Tzz signal (white arrows in **Figure 5**).

To the North of the epicenter location (between 4.5° N and 5° N), on the western side of Sumatran coast, a relative high Tzz (>−5 Eötvös) coincides with an important narrowing of the slip distribution model, indicating the existence of heterogeneity that acted as a seismic attenuator. To the North up to the Andaman Islands, each narrowing of the gradient signal (dashed white lines in **Figure 5**) indicates different second-order barriers to seismic energy, which agree with amplitude attenuation in the slip model from Chlieh et al. (2007). Historical earthquake rupture areas are comprised of these second-order barriers, as previously observed along the Southern Chilean margin (Alvarez et al., 2014).

The 2005 Nias–Simeulue Mw = 8.6 Earthquake

On March 28, 2005, the Sunda megathrust ruptured offshore Northern Sumatra, along the Simeulue-Nias segment, as a result of a Mw = 8.6 earthquake, with hypocenter location at approximately 32 km depth close to the Banyak Island (**Figure 4**). This earthquake occurred three months before the great Sumatra-Andaman earthquake in 2004, causing widespread destruction and many humans loss (about 2,000), including a moderate Tsunami. McCloskey et al. (2005) explained that this earthquake might have been a consequence of increased Coulomb failure stress induced by the Sumatra-Andaman earthquake. The rupture took place along a 400 km gap between great ruptures in 2004 and 1797 (**Figure 2**) and propagated bilaterally with two high slip patches: one to the Northwest of the epicenter beneath Simeulue Island and one Southeast beneath Nias Island, respectively (Nalbant et al., 2005; Briggs et al., 2006; Konca et al., 2007). Geodetic measurements of surface deformation (coral and CGPS data) revealed about 8 m to more than 11 m of fault slip under those islands and a notorious decrease of slip to the trench (Briggs et al., 2006).

The approximate rupture area of the Mw 8.3-8, February 5, 1861, earthquake extended from the equator to the Banyak Islands as reported by Newcomb and McCann (1987, based on field data and tsunami reports) roughly coincident with the Southern patch of the 2005 Nias earthquake.

Earthquake Rupture Behavior From Tzz

The Simeulue-Nias 2005 earthquake nucleated over a Tzz minimum (<−15 Eötvös) close to the Banyak Island and propagated bilaterally to the NW and to the S-SE (yellow arrows in **Figure 4**). In this way, the 2010 Mw = 8.8 Maule earthquake nucleated close to a minima Tzz lobe (located along the marine forearc, see **Figure 7**) and propagated bilaterally (e.g., Moreno et al., 2012). Briggs et al. (2006) proposed that the structure and division of the 2005 rupture suggest the possibility that the megathrust has a tear or kink between Simeulue and Nias Islands. Moreover, Konca et al. (2007) reported that the region between the two maximum slip patches (at the hypocentral location) appears to be coincident with a local geological disruption of the forearc (i.e., a structural break) in the vicinity of the Banyak Islands (based on Sieh and Natawidjaja, 2000, and Karig et al., 1980). The low spatial resolution of the model developed up to N = 200 hinders to infer or identify these structures. However, the minima mentioned above (<−15 Eötvös) in the topography corrected vertical gravity gradient, calculated up to N = 200, present an elongation in both directions of rupture propagation (highlighted in the −11 Eötvös contour) having a more pronounced shape (like a tear) in the Southern one (**Figure 4**). Particularly, in this direction occurred the highest slip under Nias Island. Rupture models (Briggs et al., 2006; Konka et al., 2007) indicate a smaller slip patch (~5 m) between the Nias and Batu Islands in agreement with the relative minima lobe of Tzz (<−11 Eötvös contour).

Up-Dip and Down-Dip Limits of the Seismogenic Zone

Briggs et al. (2006) reported that most of the moment (95%) was concentrated between depths of about 14–35 km, while slip values were highest at depths of about 25 km and decreased gradually both up-dip and down-dip. During the 2004 earthquake most of the slip occurred along Tzz minima stripe over the marine forearc (see the −7 Eötvös black thick contour of **Figure 4**). Joint inversion of geodetic and seismological data shows that the coseismic slip of the 2005 Simeulue-Nias earthquake decays significantly up-dip before it reaches the trench at two locations: ~0° N and ~1.5° N (Briggs et al., 2006; Konca et al., 2007). The last authors (Konca et al., 2007) explained that the rupture propagation was impeded when it reached the accretionary prism resulting in a small amount of slip toward the trench. The Tzz signal shows an important bulge penetrating inland between 0° N and 2.5° N (Tzz maxima lobe of > +15 Eötvös). This high in the gravity signal could be indicative of structural heterogeneities that acted as a barrier to seismic propagation toward the trench and consequently limiting the size of the Tsunami associated with this earthquake. As mentioned in **section 4**, in this region, a significant deepening of the top of the oceanic crust toward the SE was observed by Franke et al. (2008), suggesting that the margin's segmentation at these latitudes is related to a ridge currently undergoing subduction.

Regarding the down-dip limit of the seismogenic zone, different authors explained that seismic slip decreases landward across a strong gravity gradient generally observed along the coastline (e.g., Bassett and Watts, 2015a; Bassett and Watts, 2015b). This gravity high could be related to the landward edge of the forearc basins and deep-sea terrace (Wells et al., 2003), to the thermal structure (Grevemeyer and Tiwari, 2006; Kopp, 2013 as well as to the forearc morphology (Krabbenhoeft et al., 2010).

In this work, instead of a highly positive gradient as observed along the South American margin (see **Figure 7**), we can observe that the Tzz signal becomes more positive (−5 Eötvös contour) to the NE of the Mentawi Fz (**Figures 2**, **4**) along the center of the marine forearc (Diament et al., 1992). Simoes et al. (2004) found that at these latitudes the forearc Moho intersects with the subduction interface at a distance of 110 km from the trench and a depth of 30 km (based on bathymetry from Sandwell and Smith, 1997, seismic refraction data, Kieckhefer et al., 1980, and seismicity, Engdhal et al., 1998). Thus, the −5 Eötvös contour could be interpreted as indicative of structural heterogeneities related to the expression of the forearc Moho at this distance from the trench.

Asperities Identification From Tzz

Joint inversions of geodetic measurements and seismological data revealed that this earthquake ruptured along two main

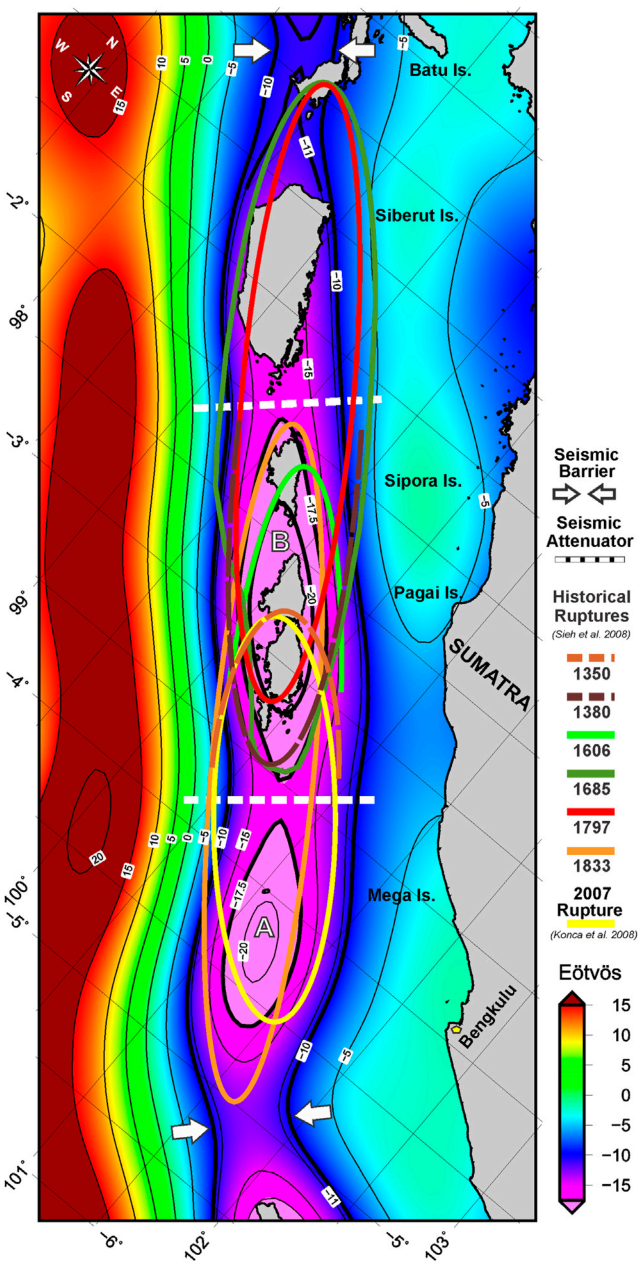

FIGURE 9 | Approximate rupture areas for recent (Konca et al., 2008) and historical earthquakes (Sieh et al., 2008) superimposed to the topography corrected vertical gravity gradient (Tzz) obtained from GOCE model GO_CONS_GCF_2_DIR_R6 up to N = 200 (Bruinsma et al., 2014). Dashed white line indicates the location of regions that behaved as seismic energy attenuators; white arrows indicate the existence of a seismic barrier that arrested rupture propagation.

asperities generating a fault slip in the order of 10 m under the Simeulue and Nias Islands, a slip deficiency around the hypocenter, and no significant slip near the trench (Briggs et al., 2006; Konca et al., 2007). Although, for this event, it is not possible to establish a clear relationship between maximum slip patches and minima Tzz lobes as that of Sumatra-Andaman (**Figure 4**), slip also occurred over minimum Tzz. The smaller patch near Southern Simeulue (of about 8 m) was "comprised" between the −7.5 Eötvös contour, whereas the most significant patch under Northern Nias (with a maximum slip of about 15 m) occurred inside the −12 Eötvös contour. For this patch, the 10 m contour of slip occurred inside the −7.5 Eötvös contour, as what occurred for the southernmost smaller patch between Nias and Batu Islands.

On April 6, 2010, a shallow thrust fault earthquake with Mw = 7.8 occurred at 2.383°N 97.048°E (31.0 km depth) to the North of the Banyak Is.; with an approximate rupture area of about 80 × 60 km that appears to have occurred within the rupture zone of the M = 8.6 earthquake of March 2005 (Hayes et al., 2017). The rupture that occurred predominantly surrounding and up-dip of the hypocenter matches the minima Tzz lobe of −15 Eötvös around the Banyak Is. (and between Simeulue and Nias Islands).

Seismic Barriers and Attenuators

Seismic segmentation along strike agrees with the Tzz signal morphology. Three segments can be identified: an important narrowing of the gradient signal at the Northern termination of the 2005 rupture (white arrows in **Figure 4**) and a narrowing of the signal to the South of the Nias Is. and others and at the latitudes of the Batu Is., coincident with the approximate Northern limit of the major 1797 earthquake.

Seismic Barrier at Simeulue Island

In Section 4.1.5, we explained that the 2004 and 2005 earthquakes terminated abruptly along a common boundary over the Simuelue Island in a region where the Tzz signal shows an important narrowing of the −5 Eötvös contour (white arrows in **Figures 4**, **5**, **9**) indicating the probable location of a seismic barrier. Briggs et al. (2006) made dense coral measurements on the coasts of Simeulue Island and found that summing uplifts from 2004 (up to ~1.5 m on the Northwestern flank) and 2005 (up to ~1.6 m on the Southeast) earthquakes reveal a 70-km-long saddle-shaped depression (orange contour lines in **Figure 9**) centered on the island (uplift at the center was only 0.5 m). As slip on the megathrust beneath central Simeulue was appreciably less than it was to the Northwest and Southeast, the last authors interpreted that the Simeulue saddle reflects a section of the megathrust that in general slips aseismically or fails in smaller earthquakes, probably this section being a barrier to trench-parallel propagation of large ruptures. It is remarkable to note that although there is a slight gap between uplift (from coral measurements) and the vertical gravity gradient, the latter reflects well the saddle structure. Gravity signal, in general, reflects structural heterogeneities mainly related to density variations, which reinforces the hypothesis of a structural cause for the 2004/2005 coincident rupture terminations as observed by Briggs et al. (2006) and Franke et al. (2008).

Southern Nias Is. Attenuator

Henstock et al. (2016) identified a 3 km basement high on the downgoing plate probably originated at the Wharton fossil ridge at the approximate location of the Southern termination of the 2005 rupture from multichannel seismic and gravity data. The last authors explained that where Wharton fossil ridge (WFR) intersects the 97° E Fz, basement shallows by ~3 km, forming a bathymetric high on the Southern (inside) corner. At these latitudes, we observed that the expression of the forearc bulge presents a landward inflection (black dashed line in **Figure 4**), with the negative Tzz contours "comprised" along the marine forearc and the slip distribution showing an attenuation at these latitudes. The former authors suggested that the basement high causes a fundamental segment boundary within the subduction zone, which behaved aseismically over the data set period and produced a locally strong plate boundary that stops large earthquake rupture. Moreover, Graindorge et al. (2008) explained that, at these latitudes, the upper plate deformation is strongly influenced by the structure of the lower plate (based on multibeam bathymetry data), which is characterized by North-South trending lineaments from the fossil Wharton spreading center.

The Seismic Barrier at the Offshore of Batu Is

Offshore of the Batu Is. an interruption of the −11 Eötvös contour is highlighted (solid black contour in **Figure 4**) at the Southern termination of the 5 m of slip contour. At these latitudes, the investigator fracture zone (IFZ) intersects the margin beneath the Batu Islands zone (offshore MW Siberut **Figure 2**), with a section of the relict WFR intersecting the margin offshore the Batu Islands (Liu et al., 1983; Henstock et al., 2016). The region that marks the Southern termination of the 2005 earthquake is limited to the Northwest by the great rupture of 1861 and to the Southeast by the giant earthquake rupture of 1797 (**Figure 2**). Briggs et al. (2006) exposed that the reasons for lateral variations in the mode of failure along this segment of the megathrust are unclear, explaining that abrupt lateral variations of temperature along the plate interface are improbable. This led them to propose either that variation in the mode of slip along strike may result from lithologic or pore pressure variations or that structural complexities in the Batu Islands patch may have inhibited thoroughgoing rupture during the 2004 and 2005 giant earthquakes. Our results reinforce the hypothesis of these authors of a structural cause for the 2005 Southern rupture termination. Deformation related to the subduction of the investigator fracture zone beneath the Batu Islands zone left is imprinted on the gravimetric signal (**Figure 4**) as observed previously along the Chilean margin for other Fz's that acted as seismic barriers to rupture propagation (e.g., the Mocha Fz. that acted as a barrier to the 2010 Maule Mw = 8.8 earthquake and for the 1960 Valdivia Mw = 9.6 earthquake).

The 2007 Mw = 8.4 South Pagai Is. Earthquake and the 2000 Mw = 7.9 Enggano Is. Earthquake at SW of Sumatra

On September 12, 2007, two earthquakes stroke off the west coast of Southern Sumatra (**Figure 6**) in the region of the Mentawi Islands (Konca et al., 2008; Lorito et al., 2008; Lubis et al., 2013). The first earthquake, with a magnitude Mw = 8.4, occurred about 130 km SW of Bengkulu and generated a tsunami of a moderate intensity (Borrero et al., 2009; Fujii and Satake, 2008). Twelve hours later, a second earthquake with Mw = 7.9 occurred near the SW Sumatra coast at the latitude of the Pagai Is. which also generated a small tsunami. Source models of the Mw = 8.4 main shock show a unilateral rupture that propagated to the Northwest of the epicenter (Konca et al., 2008; Lorito et al., 2008).

Konca et al. (2008) calculated a cumulative slip model including the Mw = 8.4 and Mw = 7.9 earthquakes and then calculated each rupture area separately (by using, conveniently as appropriate, GPS measurements, teleseismic data, Interferometric Synthetic Aperture Radar (InSAR), field measurements of coral uplift, and seismological records). The cumulative slip model shows two main slip peak areas (**Figure 6**), located on South Pagai Island with a maximum slip of 8 m and around Mega Island with 5 m local maxima. Another minor slip patch of about 2.5 m was obtained beneath Sipora Island.

Other authors (Lubis et al., 2013) found a similar coseismic slip distribution (from inversion of GPS and coral data), although with somewhat lower aptitudes. On the contrary, Lorito et al. (2008) found a maximum slip patch of 10 m (100 km long × 50 km wide), located about 100 km Northwest from the epicenter (by inversion of the tsunami waveforms). The 2007 sequence occurred in the region of the 1797 (M ~ 8.8) and 1833 (Mw ~ 9.0) historical earthquakes (Newcomb and McCann, 1987; Natawidjaja et al., 2006). Coseismic slip models showed that recent ruptures were much smaller than during those previous events, indicating that joint rupture did not cover the whole area of the 1833 event, thus anticipating that some slip has still to occur (Konca et al., 2008; Lorito et al., 2008).

On June 4, 2000, an intraslab strike-slip earthquake, known as Enggano earthquake (**Figure 6**), occurred with an estimated Mw = 7.9 at the Southern edge of the rupture area of the 1833 subduction earthquake (Pan et al., 2001; Abercrombie et al., 2003), about 110 km off the west coast of Bengkulu. The first strike-slip event (there was no tsunami reported following the earthquake) occurred at approximately 50 km depth within the subducting Australian plate and triggered a thrust subevent on the megathrust and ruptured SE away from the 1833 earthquake to the Enggano Is. where most of the losses occurred, as reported by Pan et al. (2001). Most aftershocks for this sequence were located to the SE of the main shock epicenter, coinciding with the inferred rupture area of the second subevent and extending approximately 150 km along the subduction interface (Abercrombie et al., 2003). Nerveless, the aftershocks also extend to the North of the main shock epicenter over 50 km along the first subevent's preferred fault plane, as explained by the last authors.

Earthquakes Rupture From Tzz (Directivity Effect)

The topography corrected vertical gravity gradient calculated up to N = 200 (**Figure 6**) in the region between 0° and 7° S can be separated into two regions or main lobes along the marine forearc following the −15 Eötvös contour, with a region relatively more positive between both lobes (at about 5° S). A first-order anticorrelation can be observed between the Tzz signal and recent earthquake ruptures (Abercrombie et al., 2003; Konca et al., 2008) and to historical ones (1797 and 1833). The along-strike segmentation of Tzz (relative maxima) coincides with ruptures ending (**Figures 3**, **6**), while maximum slip patches agree with relative minima Tzz. As observed in previous sections, the directivity effect can be observed when earthquakes nucleated close to a region with a relative higher Tzz signal (i.e., a narrowing in the contours) with seismic energy propagating off this attenuator/barrier to a region with a Tzz minima (e.g., <−15 Eötvös lobes). This rupture behavior was also observed by means of Tzz signal for the 1960 Valdivia, 2001 Arequipa, and 2016 Illapel earthquakes (Alvarez et al., 2014; Alvarez et al., 2019a).

Asperities Identification From Tzz

The coseismic slip of the 2007 MW 8.4 South Pagai Is. earthquake had two (Konca et al., 2008) or three major asperities (Lubis et al., 2013) to the NW of the epicenter (Lorito et al., 2008 found only a major slip patch in this direction). The first two mentioned models agree in a high slip patch close to the epicenter whose location coincides with a minima Tzz lobe (A in **Figure 6**); additionally, in Southwest of Pagai Is. the maximum slip occurred just over the minima Tzz lobe (B) in this region (between 0° to −5° S). The afterslip distribution for this earthquake after 15 months (corrected by poroelastic and viscoelastic response modeling) from Lubis et al. (2013) shows a maximum centered at the Pagai Islands to the trench, while aftershocks distribution (M > 4.0) during this time-lapse reached the South of Siberut Is. This relationship between aftershocks distribution and location of Tzz lobes contours was also observed for the 2015 Mw = 8.3 Illapel earthquake (Alvarez et al., 2017a) and for the 2016 Musine Mw = 7.8 earthquake (Alvarez et al., 2017b).

The 2007 earthquake sequence ruptured along distinct asperities (i.e., patches with a locally large slip that had remained locked in the interseismic period) but reached only a portion of the area ruptured in 1833 (Konca et al., 2008); see **Figures 3**, **6**. The last authors proposed that the 2007 sequence consisted of several separated asperities (in time and space) that really did not cooperate and that this probably was due to the action of nonpermanent barriers (i.e., areas with locally lower prestress that resulted from the occurrence of past earthquakes). They found a narrow zone beneath North Pagai Island that may have acted as a barrier in 2007 (although probably not a permanent barrier) because it had a locally lower stress level before the earthquake. The GOCE satellite-derived gravity model's high spatial resolution hinders to infer if the −20 Eötvös lobe beneath Pagai Islands is actually composed of two or more asperities separated by a barrier (probably not permanent as proposed by Konca et al., 2008).

When considering the historical ruptures from Sieh et al. (2008) we can observe (**Figure 3**) that the minima Tzz lobe of −17.5 Eötvös (B) under Sipora and Pagai Islands (between the second-order barriers/attenuators) coincides to the North with the 1,606 and 1,833 rupture areas ending, while to the South it agrees with the 1,685 and the 1,380 ruptures termination. This high wavelength lobe of minima Tzz is probably indicating the existence of a large region comprised of different main asperities. Moreover, the −20 Eötvös lobe under Pagai Is. coincides with the margin section that always broke through the successive earthquakes along the timeline, marking the Southern termination of the 1,797 earthquake. The historical rupture of 1,833 comprised both main asperities A and B (**Figure 3**), while the 1,797 and 1,685 historical earthquakes occurred along a region of relative minima Tzz from Batu Is. to the South, including the asperity delimited by the −17.5 Eötvös contour (asperity B in **Figure 3**).

Along-Strike Seismic Segmentation: Barriers and Attenuators

Along-strike seismic segmentation can be inferred from the study of repeated break of the plate interface along the timeline from historical earthquakes. The section of the Sunda megathrust between 0° and −5° S has generated almost repeated sequences of great megathrust earthquakes (**Figure 3**) approximately every two hundred years for at least the past 700 years as reported by Sieh et al. (2008), from corals records of the Mentawai Islands.

To the North, around the Batu Islands, the Tzz shows a narrowing and an interruption of the −11 Eötvös contour. This region, which marks the Southern termination of the 2005 Nias–Simeulue Mw = 8.6 earthquake (**section 4.2**) and the Northern termination of the 1,797 and the 1,685 historical earthquakes, behaved as a seismic barrier. In previous works (Alvarez et al., 2014; Alvarez et al., 2015; Alvarez et al., 2017a; Alvarez et al., 2017b; Alvarez et al., 2018; Alvarez et al., 2019a), we named these regions (where the along-strike limit for different ruptures coincides with local relative maxima in Tzz) first-order barriers. In the Southern portion of this region of the Sumatran margin, we propose the existence of another first-order barrier (white arrows in **Figures 3**, **6**) that separates the rupture of the 2007 earthquake and the historical rupture of 1833 to the North from the 2000 Enggano earthquake to the South.

The region between these two first-order barriers (delimited by important narrowing of the Tzz signal or relative maxima interposed along strike) presents a low Tzz trend between them which is also segmented by second-order barriers or attenuators (defined by minor values/amplitude of Tzz contours) that indicate the existence of different seismic asperities along strike. The second-order barriers (white dashed lines in **Figures 3**, **6**) locations mapped by beans of Tzz agree with seismic segmentation from historical ruptures (Sieh et al., 2008) along this portion of the Sunda megathrust.

What remains to be solved (probably through marine data or a global gravity model with higher spatial resolution as EIGEN-6c4) is the existence or not of a barrier that would separate the islands of Pagai North and South, indicating a heterogeneity that acted as a limit for the 2007 rupture and also to the historical one of 1,350. However, it is difficult to expect a relative higher Tzz (in a shorter wavelength signal, i.e., more resolution) located just in the middle of the minimum Tzz lobe (<−20 Eötvös) under the islands of Pagai. In this regard, Konca et al. (2008) explained that the sequence of 2007 essentially ruptured a set of asperities which did not cooperate efficiently (by triggering each other through static and dynamic interactions) because of the intervening barriers that were most likely not permanent, acting on the

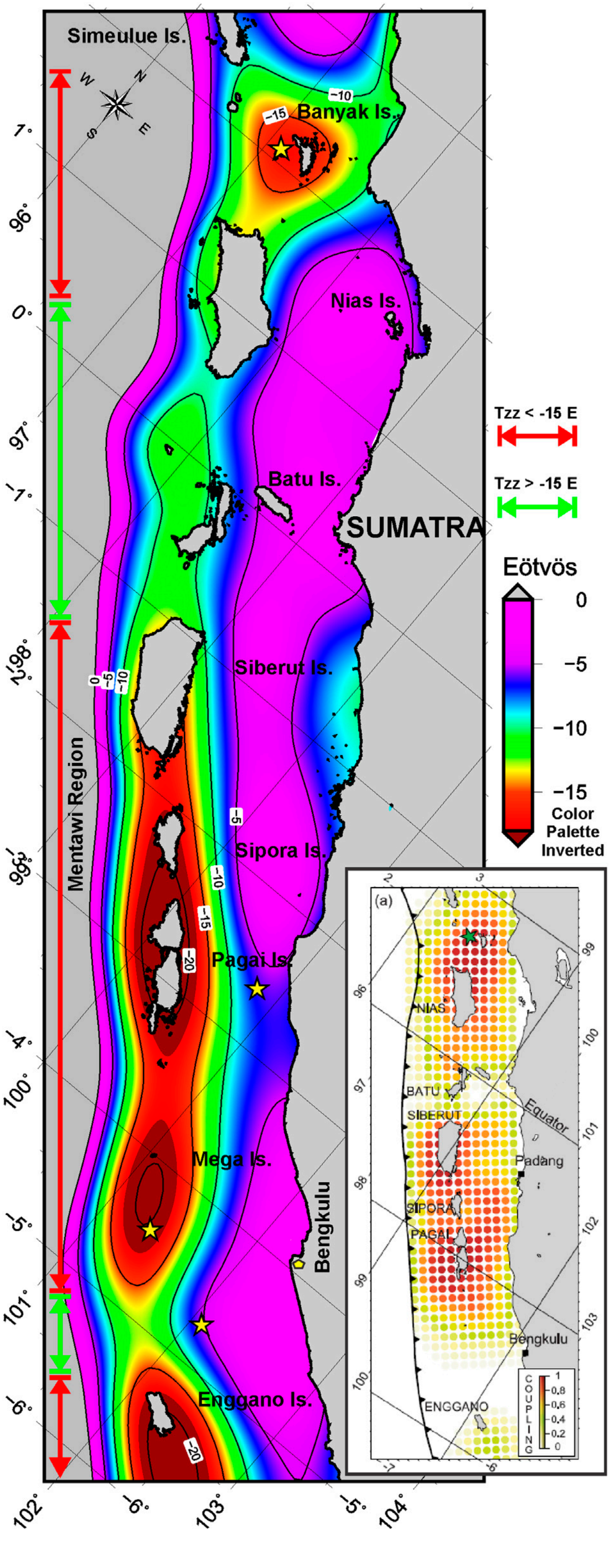

FIGURE 10 | Topography corrected vertical gravity gradient (Tzz) obtained from GOCE model GO_CONS_GCF_2_DIR_R6 up to N = 200 (Bruinsma et al., 2014) with color palette inverted. In the right lower corner is plotted the interseismic locking degree from Chlieh et al. (2008): a value of 1 corresponds to full locking while 0 corresponds to creeping at the long- *(Continued)*

coast of North Pagai more like a 'barrier' during the coseismic slip in 2007. The last authors proposed that the presence of nonpermanent barriers due to the stress distribution leftover from previous ruptures is probably the major factor introducing irregularity, as observed in dynamic fault models (Ben-Zion and Rice, 1993; Cochard and Madariaga. 1996).

The 2007 earthquake did not reach the 1833 earthquake extent (**Figures 3**, **6**), showing in its rupture behavior certain characteristics somewhat abnormal on its Northern slip patch termination. The rupture did not agree with the Tzz signal, differing from the degree of interseismic coupling from Chlieh et al. (2008). Neither the slip-predictable nor the time predictable models applied to this earthquake (Konca et al., 2008). Presumably, in this portion of the megathrust between North and South Pagai Is., instead of being permanent features, seismic asperities move from one rupture to another within the area that is locked in the interseismic period as proposed by Konca et al. (2008).

Tzz, Seismic Behavior, and Seismic Coupling

Throughout the previous sections, we have observed a correlation between the along-strike segmentation of the Tzz (by direct modeling of the Earth gravity field) and the seismic segmentation along the plate interface (considering recent and historical earthquakes). Geodetic (1991–2004) and paleogeodetic (1962–2000) measurements of interseismic deformation from Chlieh et al. (2008) revealed that the plate interface is partially or fully locked at shallower depths along the Sumatran portion of the Sunda subduction zone. Patches of high coupling, along this heterogeneous pattern of coupling from the last authors (**Figure 10**), present a high correlation with the rupture areas of large megathrust earthquakes (particularly when the locked fault zone is up to about 175 km wide). The last authors explained that these strongly coupled patches are roughly coincident with asperities that ruptured during great events, whereas the sections of narrow locking and low coupling have not produced great earthquakes (Mw > 8.0). Similar results can be found in Prawirodirdjo et al. (2010); these authors also found that coupling along the plate boundary is high throughout this region with lower coupling patches to the North of Batu Is. and around Enggano Is.

In a recent work, Metois et al. (2016) found that, for the recent Mw > 8 events over the Chilean margin (from 38° to 18° S), coseismic asperities correlate well with highly coupled segments, while low coupling zones behaved as barriers and stopped the ruptures (by analyzing interseismic coupling variations on the subduction interface based on GPS networks). From comparing the results of the last authors to our maps of Tzz along the Chilean margin, we found that relative low Tzz anomalies correlate to regions with higher slip and a high degree of coupling. On the

FIGURE 10 | term plate convergence. Note the correspondence between highly coupled segments (red) with regions of relative minima Tzz (orange-to-red) indicated with double red arrows. Regions with intermediate to close to zero coupling agree with regions of relative higher Tzz (green segments).

other hand, relative higher Tzz coincident to areas with lower coupling interposed along-strike mostly coincided with barriers to rupture propagation (Metois et al., 2016; Alvarez et al., 2014; Alvarez et al., 2017a; Alvarez et al., 2017b).

In this subsection, we will analyze the results obtained from direct modeling of the vertical gravity gradient with respect to the degree of seismic coupling from Chlieh et al. (2008) and to seismic behavior in the Sumatra region.

Banyak-Nias Strong Coupling Patch

The region comprised between the Banyak Is. and the Nias Is. to the South of it, which ruptured during the 2005 Mw = 8.7 Nias–Simeulue earthquake (**Figure 4**), coincides well with the wide patch of high coupling from Chlieh et al. (2008). This patch of high interseismic plate coupling presents a similar pattern when compared to the −10 Eötvös Tzz contour, with a maximum (of coupling) around Banyak Is. and Northern Nias Is. (−15 Eötvös), and a narrowing of Tzz in the Southern direction as what occurs with the predominantly decoupled equatorial patch.

Batu and North Enggano Low Coupling Patches

Around the Batu Is. and near the equator coupling is lower (**Figure 10**), with a narrow locked fault zone at the Northern edge of this Island (with coupling ratios close to zero at depths >35 km and a coupling ratio less than 0.6 at shallower depths, see Chlieh et al., 2008). In this area only moderate earthquakes have occurred with Mw < 8.0 (last rupture in 1935 with a magnitude 7.7), in the past few centuries (Sieh et al., 1999; Rivera et al., 2002; Natawidjaja et al., 2004; Konca et al., 2008), and none of the great historical earthquakes (**Figure 3**) ruptured significantly across this region from the South (in 1797 and 1833) or from the North (in 1861).

The Tzz (**Figure 10**) shows significant relative higher values (~5 Eötvös higher) in the region between Southern Nias Is. and Northern Siberut Is., differentiating from the regions to the North and South where the gradient is smaller and where the earthquakes of higher magnitude occurred. Chlieh et al. (2008) located a region of low interseismic coupling above the subducting investigator Fz. and a well-defined nest of seismicity within the downgoing slab (Fauzi et al., 1996; Prawirodirdjo et al., 1997). In recent works along the Chilean margin (Alvarez et al., 2014; Alvarez et al., 2017a; Alvarez et al., 2017b; Alvarez et al., 2019b), we identified these regions (where the subduction of high oceanic features intercepts the plate interface) with low coupling and high rates of low-to-moderate seismicity with seismic barriers/attenuator to seismic energy propagation by means of higher relative values of the Tzz across the margin. Nalbant et al. (2013) explained that the 1935 earthquake patch has been slipping during the past century at about half the rate at which the plate is moving and that has accumulated strains and hence stresses on the Batu Is. patch are probably low. These authors also mentioned that recent paleogeodetic studies show that the megathrust is slipping aseismically at plate convergence rate both above and below this narrow patch.

Mentawi Strong Coupling Patch

Along the Mentawi region, from Siberut Is. to the latitude of Bengkulu, Chlieh et al. (2008) found that the interplate region is under strong coupling (**Figure 10**). According to Natawidjaja et al. (2007), coupling beneath the Mentawai Is. has been high for at least the past 40 years. Great historical earthquakes with wide rupture areas as the 1797 and 1833 affected this region of the Sunda megathrust. More recently, the Southern portion was shocked by the Mw = 8.4 and Mw = 7.9 earthquakes of September 2007 as early explained in this section. In this region, we found that there is a good correspondence between low Tzz lobes and strong coupling patches, mainly under Pagai and Sipora Islands (**Figure 10**).

To the North and South of this segment, a narrowing of the locked patch and a diminishment of the coupling ratio indicating weakly coupled regions (~40% beneath the Batu Is.) correspond to the along-strike edges of the different ruptures previously analyzed. The gravity signal reflects structural and compositional heterogeneities along the megathrust, with low Tzz lobes being related to seismic asperities (Alvarez et al., 2019b), whereas interposed relative maxima are related to seismic barriers to rupture propagation (Alvarez et al., 2014). There is a high correspondence between these permanent barriers inferred from direct gravity modeling and those mapped from the modeling of interseismic strain (**Figure 10**). This agrees with the hypothesis that they are persistent segment boundary zones that influence the lateral extent of megathrust ruptures (as low coupling causes continuous strain release) that may be related to the subduction of HOF's (Chlieh et al., 2008; Konca et al., 2008). Similar results were found along the Chilean margin, where the subduction of different HOF's (aseismic ridges, seamounts, Fz's) coincides with patches of a lower degree of coupling and higher relative Tzz and that has acted as seismic barriers for the recent earthquakes and also for historical ones (Sparkes et al., 2010; Contreras-Reyes and Carrizo 2011; Alvarez et al., 2014, Alvarez et al., 2019b; Metois et al., 2016).

South Enggano Intermediate Coupling Patch

The megathrust in the area of Enggano Is. and near Bengkulu (**Figure 10**) is only slightly coupled (although from sparse GPS data in the mentioned area: see Chlieh et al., 2008) and coincides with a region of relative higher Tzz (>−15 Eötvös). This region presented in the last 15 years an intense seismic activity (Abercrombie et al., 2003) and had many major but no giant earthquakes. The most recent occurred in 2000 with an Mw = 7.9 earthquake (Abercrombie et al., 2003) and ruptured to the South where the coupling is intermediate and a low Tzz lobe is located to the South of Enggano Is (**Figure 10**). Chlieh et al. (2008) explained that the cause of the low coupling obtained to the South of Pagai Is. is enigmatic and does not appear to be related to a subducted fracture zone or the thermal structure. In this work, we propose that a plausible explanation is a rheological heterogeneity or a structural complexity along the megathrust that can be mapped by its density contrast by means of Tzz.

The Correlation Between Coupling and Tzz

As above explained in this section, Chlieh et al. (2008) found a strong correlation between historical great earthquakes and patches of the megathrust that are currently strongly coupled, suggesting that asperities are persistent features under the largest outer arc islands, caused by intrinsic local properties of the megathrust (reinforced by the fact that the pattern of coupling in the Mentawai Islands is remarkably similar before and after the two great earthquakes of December 2004 and March 2005). This is opposed to the hypothesis that the seismic moment release is generally highest beneath forearc basins proposed by (Song and Simons, 2003; Wells et al., 2003) as in this region basins are located between the Mentawi Fz and the coastal line. In this work, we found from direct modeling of GOCE satellite data (with a greatly improved resolution) that negative Tzz lobes (**Figures 3** and **6**) agree with rupture areas under the Mentawi Islands, i.e., along the accretionary wedge instead of over the basins (which are located to the East). Our results (low Tzz lobes in correspondence with highly coupled segments) agree with the proposal of Chlieh et al. (2008), who observed that the most strongly coupled patches and seismic asperities correlate with the largest outer arc islands.

Tzz and the Up/Down-Dip Limits of the Seismogenic Zone

The down-dip limit of the seismogenic zone may be controlled (in a first-order) either by the thermal structure (due to a transition to dislocation creep at high temperatures: Scholz, 1990; Hyndman and Wang, 1993; Hyndman and Peacock, 2003) or by lithological variations, as the presence of a highly serpentinized mantle wedge allows megathrust creeping (i.e., the intersection of the megathrust with the forearc Moho may coincide with the change from stick-slip to aseismic stable sliding, e.g., Reinen et al. (1991); Hyndman et al. (1997); Oleskevich et al. (1999). Different authors found that, along the Sumatran margin, the megathrust extends significantly deeper than the continental Moho (which have shallow depths 22–30 km, e.g., Kieckhefer et al. (1980) and Simoes et al., 2004), opposing the hypothesis that the Moho is the down-dip limit in this region (Chlieh et al., 2008; Klingerhoefer et al., 2010). Variations in the down-dip locking depth over this region seems to be predominantly controlled by along-strike variations in temperature, with the 350–450°C isotherms (located 210 and 250 km from the trench axis at the North of Simeulue Is., Klingerhoefer et al., 2010) and the 300–400°C isotherms (located at 210 and 250 km from the trench axis, respectively, along the Mentawi region, Chlieh et al., 2008) coincident with the down-dip limit of the seismogenic zone (**Figure 11**). The vertical gravity gradient presents a notable contrast across strike in the Mentawi region, indicating higher densities landward, coinciding the approximate location of the −5 Eötvös contour (thick black contour in **Figure 11**) with the 350°C isotherm (from Chlieh et al., 2008). The last authors observed an increase in depth of locking between the equator and 4° S consistent with the isotherms trend and with the Southward increase in convergence rate. They explained that, together, the lateral variations of these two parameters partially explain the Southward increase of the down-dip edge of the locked fault zone from the Batu Islands, where it is 35 km deep to South Pagai Island, where it reaches a depth of about 55 km. The density structure along the marine forearc obtained by direct modeling of the satellite GOCE derived gravity model is consistent with these results, with the limit of the locked fault zone (yellow dashed line in **Figure 11**) coincident with the −5 Eötvös contour, which presents an interruption between Padang and Bengkulu indicating lower densities over the marine forearc in this region were locking reaching the coastline.

Similar results were found along the South American margin, where the −5 Eötvös contour was indicated as the down-dip limit of the seismogenic zone for the Maule 2010 earthquake (Alvarez et al., 2019b) and for the Musine 2017 earthquake (Alvarez et al., 2017b). In both cases, the trend of low-density values observed along the marine forearc presented an entry under the continental forearc in correspondence with coseismic slip models for the events mentioned above (see **Figure 7**).

The Up-Dip Limit and Tsunami-Genesis From Tzz

The up-dip limit in this region has also been successfully mapped (**Figure 11**) based on the thermal modeling. Its position has been located at ∼30 ± 10 km from the trench and around the 100–150°C isotherms (which is in good agreement with the aftershocks with a shallow thrusting mechanism in this zone (Engdahl et al., 2007; Chlieh et al., 2008; Hippchen and Hyndman, 2008). The Tzz presents a high gradient positive oceanward at the approximate location of the 100°C isotherm that could be indicative of the up-dip ending of the seismogenic zone (minor to zero Tzz along the marine forearc is related to the seismogenic zone and minima Tzz lobes to seismic asperities).

A higher positive Tzz signal (>+15 Eötvös) is observed (**Figure 11**) along the outer rise along the Mentawi Islands and along the Simeulue-Nias region where the 2005 Nias–Simeulue Mw = 8.6 earthquake, the 2007 MW 8.4 South Pagai Is. Earthquake, and the 2000 Mw = 7.9 Enggano Is. earthquake occurred. These three events (even though the latter is related to an intraslab strike-slip mechanism) that present a highly positive Tzz oceanward (**Figure 11**) only presented moderate tsunamis. A similar pattern is observed for the Mw = 8.4 Arequipa 2001 earthquake (also with a > +15 Eövos Tzz oceanward) which neither presented a severe tsunami.

On the other hand, the Mw = 9.15 2004 Sumatra-Andaman earthquake that presented a tsunami of great proportions occurred in a region where the Tzz signal is lower along the forebulge (see the +10 Eötvös contour in **Figure 8**). The 2010 Mw = 8.8 Maule earthquake (which also generated a destructive tsunami) presents a similar pattern as the Tzz signal along the outer rise is limited by the +10 Eötvös contour (see **Figure 7A**). Further North, the Mw = 8.2 Illapel earthquake, which generated a moderate but destructive tsunami, occurred against an inflection of this contour of +15 Eövos over the forebulge.

If this pattern is maintained on a global scale, it would be possible to determine if the density structure around the trench area could also have some influence on tsunami-genesis. It is plausible that where there is a lower density along this region, the rupture could reach the shallow and tsunamigenic portion of the megathrust (Lay et al., 2011; Lay et al., 2012), and thus a lower

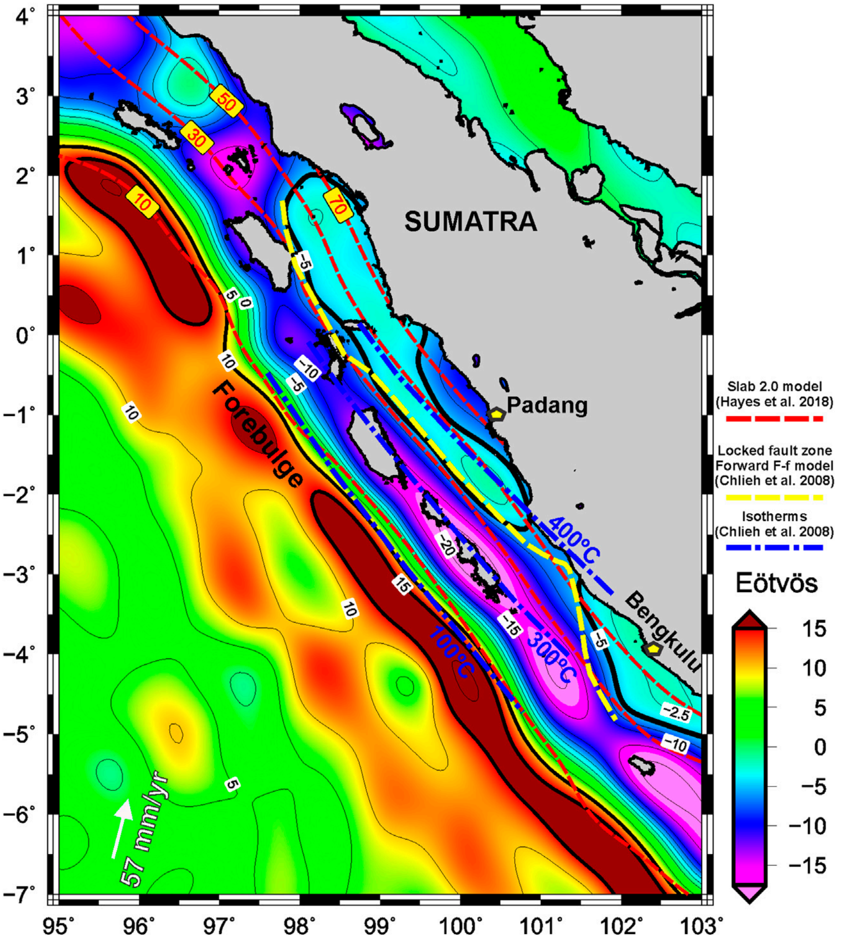

FIGURE 11 | Topography corrected vertical gravity gradient (Tzz) obtained from GOCE model GO_CONS_GCF_2_DIR_R6 up to N = 200 (Bruinsma et al., 2014). Superimposed: isotherms (blue dot and dashed line) and down-dip limit (yellow dashed line) of the locked fault zone from the forward model F-f of Chlieh et al. (2008). Slab depths from Slab 2.0 of Hayes (2018) are plotted with red dashed lines. Note the correspondence between the −5 Eötvös contour and the approximate location of the 350°C isotherm that marks the limit of the seismogenic zone in this region and with the down-dip limit of the locked zone. The up-dip limit of the seismogenic zone can be identified by the high gradient indicated by the +15 Eötvös contour.

density structure of the forebulge would facilitate greater vertical seafloor displacements.

CONCLUSION

The correspondence between strong coupled patches along the interseismic period, maxima slip patches during earthquakes occurrence, and low Tzz lobes implies that the density structure could be reflecting either structural or rheological heterogeneities (i.e., asperities) of the megathrust along the marine forearc, having a strong influence on seismic rupture behavior. Thus, by mapping regions with a general trend of low Tzz, we could infer the approximate along-strike length of the rupture (mainly for large-magnitude events due to the low spatial resolution of satellite only models) identifying seismic asperities where slip is enhanced by means of minima Tzz lobes. The heterogeneous distribution of Tzz could also be reflecting rheological changes due to slight variations in the thermal structure, particularly along the down-dip edge of the locked fault zone.

Furthermore, the along-strike seismic segmentation along the continental forearc inferred from recent and historical rupture patterns could also be characterized by means of relative higher Tzz (identified as barriers) as observed along the Chilean margin in previous works. These barriers that inhibit the lateral propagation of great earthquake ruptures agree with narrower coupling over periods of time higher than one or two hundred years. Minor lateral variations in the Tzz signal are reflecting mass heterogeneities that contributed to the lateral variations in seismic behavior. Across-strike seismic barriers could be identified in those portions of the margin where the Tzz contours are narrowed or with a relative higher Tzz (this permanently creeping barriers should favor some regularity and similarity of earthquakes).

When an earthquake nucleates close to a relatively higher Tzz rupture propagates following a directivity effect toward minima

Tzz lobes (and toward lower mean values of the Tzz signal along the margin). On the contrary, when earthquake nucleates close to a minima Tzz lobe, rupture presents a bilateral rupture propagation.

By calculating the topography corrected vertical gravity gradient up to degree/order N = 200 of the harmonic expansion (from Earth gravity field models) it could be possible to map coastal regions with a higher seismic risk along subduction margins.

DATA AVAILABILITY STATEMENT

The raw data supporting the conclusions of this article will be made available by the authors, without undue reservation.

AUTHOR CONTRIBUTIONS

OA was responsible for conceptualization, methodology, software, investigation, and writing of original draft, SC was responsible for software, investigation, and writing. MG was responsible for resources, supervision, project administration, and AF was responsible for conceptualization and writing – review and editing.

ACKNOWLEDGMENTS

The authors acknowledge the use of the GMT-mapping software of Wessel et al. (2019), to Dr. Mohamed Chlieh chlieh.geoazur@laposte.net (at the ISTerre Lab, Institut des Sciences de la Terre, Grenoble-Alpes University, France) *and colleagues* for sharing their slip model data of the Mw = 9.15 2004 Sumatra-Andaman earthquake. The authors would like to acknowledge CONICET-Argentina. Satellite GOCE models and derived data can be downloaded from the International Centre for Global Earth Models (ICGEM) http://icgem.gfz-potsdam.de/home. Topographic correction can be performed by forward modeling of gravitational fields in spherical coordinates following Uieda et.al. (2016), software freely available at Zenodo*:* doi:10.5281/zenodo.582366, http://tesseroids.leouieda.com.

REFERENCES

Abercrombie, R. E., Antolik, M., and Ekström, G. (2003). The June 2000 Mw 7.9 earthquakes south of Sumatra: deformation in the India–Australia plate. *J. Geophys. Res.* 108 (B1), ESE 6-1–ESE 6-16. doi:10.1029/2001JB000674

Alvarez, O., Folguera, A., and Gimenez, M. E. (2017b). Rupture area analysis of the Ecuador (Musine) Mw = 7.8 thrust earthquake on april 16 2016, using GOCE derived gradients. *Geod. Geodyn.* 8, 49–58. doi:10.1016/j.geog.2017.01.005

Alvarez, O., Gimenez, M. E., Braitenberg, C., and Folguera, A. (2012). GOCE satellite derived gravity and gravity gradient corrected for topographic effect in the South Central Andes region. *Geophys. J. Int.* 190 (2), 941–959. doi:10.1111/j.1365-246X.2012.05556.x

Alvarez, O., Gimenez, M., Folguera, A., Moreno Chaves, C. A., and Braitenberg, C. (2019a). Reviewing megathrust slip behavior for recent Mw > 8.0 earthquakes along the Peru-Chilean margin from satellite GOCE gravity field derivatives. *Tectonophysics* 769, 228188. doi:10.1016/j.tecto.2019.228188

Álvarez, O., Gimenez, M., Guillen, S., Tocho, C., and Folguera, A. (2018). Goce derived geoid changes before the Pisagua 2014 earthquake. *Geodesy Geodyn.* 9, 50–56. doi:10.1016/j.geog.2017.09.005

Alvarez, O., Nacif, S., Gimenez, M., Folguera, A., and Braitenberg, C. (2014). GOCE derived vertical gravity gradient delineates great earthquake rupture zones along the Chilean margin. *Tectonophysics* 622, 198–215. doi:10.1016/j.tecto.2014.03.011

Alvarez, O., Nacif, S., Spagnotto, S., Folguera, A., Gimenez, M., Chlieh, M., et al. (2015). Gradients from GOCE reveal gravity changes before Pisagua Mw=8.2 and Iquique Mw=7.7 large megathrust earthquakes. *J. S. Am. Earth Sci.* 64 (P2), 15–29. doi:10.1016/j.jsames.2015.09.014

Alvarez, O., Pechuan, S., Gimenez, M., and Folguera, A. (2019b). "Seismic structure along the South American subduction zone using satellite gravity data," in *Andean tectonics*. Editors B. K. Horton and y. Andres, and F. Capitulo (Paises Bajos: Elsevier), Vol. 1, 3–18.

Alvarez, O., Pesce, A., Gimenez, M., Folguera, A., Soler, S., and Chen, W. (2017a). Analysis of the Illapel Mw = 8.3 thrust earthquake rupture zone using GOCE derived gradients. *Pure Appl. Geophys.* 174 (1), 47–75. doi:10.1007/s00024-016-1376-y

Amante, C., and Eakins, B.W. (2009). ETOPO1, 1 Arc-Minute global relief model: procedures, data sources and analysis. NOAA technical memorandum NESDIS. National Geophysical Data Center, NOAA, Vol. 24, 19. doi:10.7289/V5C8276M

Ammon, C. J., Ji, Thio, H. K., Robinson, D., Ni, S. D., Hjorleifsdottir, V., Kanamori, H., et al. (2005). Rupture process of the 2004 Sumatra-Andaman earthquake. *Science* 308, 1133–1139. doi:10.1126/science.1112260

Banerjee, P., Pollitz, F. F., and Bürgmann, R. (2005). The size and duration of the Sumatra-Andaman earthquake from far-field static offsets. *Science* 308, 1769–1772. doi:10.1126/science.1113746

Bassett, D., and Watts, A. B. (2015a). Gravity anomalies, crustal structure, and seismicity at subduction zones: 1. Seafloor roughness and subducting relief. *Geochem. Geophys. Geosyst.* 16, 1508–1540. doi:10.1002/2014GC005684

Bassett, D., and Watts, A. B. (2015b). Gravity anomalies, crustal structure, and seismicity at subduction zones: 2. Interrelationships between fore-arc structure and seismogenic behavior. *Geochem. Geophys. Geosyst.* 16, 1541–1576. doi:10.1002/2014GC005685

Ben-Zion, Y., and Rice, J. R. (1993). Earthquake failure sequences along a cellular fault zone in a 3-dimensional elastic solid containing asperity and nonasperity regions. *J. Geophys. Res.* 98, 14109–14131. doi:10.1029/93JB01096

Bilham, R., Engdahl, R., Feldl, N., and Satyabala, S. P. (2005). Partial and complete rupture of the Indo-Andaman plate boundary 1847–2004. *Seismol Res. Lett.* 76, 299–311. doi:10.1785/gssrl.76.3.299

Borrero, J. C., Weiss, R., Okal, E. A., Hidayat, R., SurantoArcas, D., et al. (2009). The Tsunami of September 12, 2007, Bengkulu Province, Sumatra, Indonesia: post-tsunami field survey and numerical modeling. *Geophys. J. Int.* 178, 180–194. doi:10.1111/j.1365-246X.2008.04058.x

Braitenberg, C., Mariani, P., Ebbing, J., and Sprlak, M. (2011). "The enigmatic Chad lineament revisited with global gravity and gravity-gradient fields," in *The formation and evolution of Africa: a synopsis of 3.8 Ga of earth history*. Editors D. J. J. Van Hinsbergen, S. J. H. Buiter, T. H. Torsvik, C. Gaina, and S. J. Webb (London: Geological Society, London, Special Publications), 357, 329–341. doi:10.1144/SP357.18

Briggs, R. W., Sieh, K., Meltzner, A. J., Natawidjaja, D., Galetzka, J., Suwargadi, B., et al. (2006). Deformation and slip along the Sunda Megathrust in the great 2005 Nias-Simeulue earthquake. *Science* 311, 1897–1901. doi:10.1126/science.1122602

Bruinsma, S. L., Förste, C., Abrikosov, O., Lemoine, J.-M., Marty, J.-C., Mulet, S., et al. (2014). ESA's satellite-only gravity field model via the direct approach based on all GOCE data. *Geophys. Res. Lett.* 41, 7508–7514. doi:10.1002/2014GL062045

Bruinsma, S. L., Forste, C., Abrikosov, O., Marty, J. C., Rio, M. H., Mulet, S., et al. (2013). The new ESA satellite-only gravity field model via the direct approach. *Geophys. Res. Lett.* 40 (14), 3607–3612. doi:10.1002/grl.50716

Chen, J. L., Wilson, C. R., Tapley, B. D., and Grand, S. (2007). GRACE detects coseismic and postseismic deformation from the Sumatra-Andaman earthquake. *Geophys. Res. Lett.* 34, L13302. doi:10.1029/2007GL030356

Chlieh, M., Avouac, J. P., Hjorleifsdottir, V., Song, T.-R. A., Ji, C., Sieh, K., et al. (2007). Coseismic slip and afterslip of the great (Mw 9.15) Sumatra-Andaman earthquake of 2004. *Bull. Seismol. Soc. Am.* 97, S152–S173. doi:10.1785/0120050631

Chlieh, M., Avouac, J. P., Sieh, K., Natawidjaja, D. H., and Galetzka, J. (2008). Heterogeneous coupling of the Sumatran megathrust constrained by geodetic and paleogeodetic measurements. *J. Geophys. Res.* 113, B05305. doi:10.1029/2007JB004981

Chlieh, M., Perfettini, H., Tavera, H., Avouac, J., Remy, D., Nocquet, J., et al. (2011). Interseismic coupling and seismic potential along the Central Andes subduction zone. *J. Geophys. Res.* 116, B12405. doi:10.1029/2010JB008166

Cochard, A., and Madariaga, R. (1996). Complexity of seismicity due to highly ratedependent friction. *J. Geophys. Res.* 101, 25321–25336. doi:10.1029/96JB02095

Contreras-Reyes, E., and Carrizo, D. (2011). Control of high oceanic features and subduction channel on earthquake ruptures along the Chile–Peru subduction zone. *Phys. Earth Planet. In.* 186, 49–58. doi:10.1016/j.pepi.2011.03.002

Cook, B. J., Henstock, T. J., McNeill, L. C., and Bull, J. M. (2014). Controls on spatial and temporal evolution of prism faulting and relationships to plate boundary slip offshore north-central Sumatra. *J. Geophys. Res.* 119, 5594–5612. doi:10.1002/2013JB010834

DeMets, C., Gordon, R. G., and Argus, D. F. (2010). Geologically current plate motions. *Geophys. J. Int.* 181, 1–80. doi:10.1111/j.1365-246X.2009.04491.x

Dewey, J.W., Choy, G., Presgrave, B., Sipkin, S., Tarr, A.C., Benz, H., et al. (2007). Seismicity associated with the Sumatra– Andaman islands earthquake of December 26, 2004. *Bull. Seismol. Soc. Am.* 97 (1A), S25–S42. doi:10.1785/0120050626

Diament, M., Harjono, H., Karta, K., Deplus, C., Dahrin, D., Zen, M., et al. (1992). Mentawai fault zone off Sumatra: a new key to the geodynamics of western Indonesia. *Geology* 20, 259–262. doi:10.1130/0091-7613(1992)020<0259:MFZOSA>2.3.CO;2

Engdahl, E. R., Villasenor, A., DeShon, H. R., and Thurber, C. H. (2007). Teleseismic relocation and assessment of seismicity (1918–2005) in the region of the 2004 Mw 9.0 Sumatra-Andaman and 2005 Mw 8.6 Nias Island great earthquakes. *Bull. Seismol. Soc. Am.* 97, 43–61. doi:10.1785/0120050614

Engdhal, E., van der Hilst, R., and Buland, R. (1998). Global teleseismic earthquake relocation with improved travel times and procedures for depth determination. *Bull. Seismol. Soc. Am.* 88, 722–743.

FauziMcCaffrey, R., Wark, D., and SunaryoPrih Haryadi, P.Y. (1996). Lateral variation in slab orientation beneath Toba Caldera, northern Sumatra. *Geophys. Res. Lett.* 23, 443–446. doi:10.1029/96GL0038

Featherstone, W. (1997). On the use of the geoid in geophysics: a case study over the North West shelf of Australia. *Explor. Geophys.* 28 (1–2), 52–57. doi:10.1071/EG997052

Franke, D., Schnabel, M., Ladage, S., Tappin, D. R., Neben, S., Djajadihardja, Y. S., et al. (2008). The great Sumatra-Andaman earthquakes. Imaging the boundary between the ruptures of the great 2004 and 2005 earthquakes. *Earth Planet. Sci. Lett.* 269 (1–2), 118–130. doi:10.1016/j.epsl.2008.01.047

Fujii, Y., and Satake, K. (2008). Tsunami waveform inversion of the 2007 Bengkulu, southern Sumatra, earthquake. *Earth Planet Sp.* 60, 993–998. doi:10.1186/BF03352856

Graindorge, D., Klingelhoefer, F., Sibuet, J. C., McNeill, L., Henstock, T. J., Dean, S., et al. (2008). Impact of the lower plate on upper plate deformation at the NW Sumatran convergent margin from seafloor morphology. *Earth Planet. Sci. Lett.* 275, 201–210. doi:10.1016/j.epsl.2008.04.053

Grevemeyer, I., and Tiwari, V.M. (2006). Overriding plate controls spatial distribution of megathrust earthquakes in the Sunda–Andaman subduction zone. *Earth Planet. Sci. Lett.* 251, 199–208. doi:10.1016/j.epsl.2006.08.021

Grombein, T., Heck, B., and Seitz, K. (2013). Optimized formulas fors the gravitational field of a tesseroid. *J. Geod.* 87, 645–600. doi:10.1007/s00190-013-0636-1

Guilbert, J., Vergoz, J., Schissele, E., Roueff, A., and Cansi, Y. (2005). Use of hydroacoustic and seismic arrays to observe rupture propagation and source extent of the M-w 9.0 Sumatra earthquake. *Geophys. Res. Lett.* 32, L15310. doi:10.1029/2005GL022966

Han, S.C., Shum, C., Bevis, M., Ji, C., and Kuo, C. (2006). Crustal dilatation observed by GRACE after the 2004 Sumatra-Andaman. *Earthquake Shin-Chan Sci.* 313, 658–662. doi:10.1126/science.1128661

Hayes, G. (2018). Slab2 – a comprehensive subduction zone geometry model. *Science* 362, 58–61. doi:10.1126/science.aat4723

Hayes, G. P., Myers, E. K., Dewey, J. W., Briggs, R. W., Earle, P. S., Benz, H. M., et al. (2017). Tectonic summaries of magnitude 7 and greater earthquakes from 2000 to 2015: United States. *Geol. Surv. Open-File Rep. 2016–1192*, 148. doi:10.3133/ofr20161192

Henstock, T. J., McNeill, L. C., Bull, J. M., Cook, B., Gulick, S., Austin, J. A., et al. (2016). Downgoing plate topography stopped rupture in the A.D. 2005 Sumatra earthquake. *Geology* 44 (1), 71–74. doi:10.1130/G37258.1

Hicks, S. P., Rietbrock, A., Rydera, I. M. A., Lee, C. S., and Miller, M. (2014). Anatomy of a megathrust: the 2010 M8.8 Maule, Chile earthquake rupture zone imaged using seismic tomography. *Earth Planet Sci. Lett.* 405, 142–155. doi:10.1016/j.epsl.2014.08.028

Hippchen, S., and Hyndman, R.D. (2008). Thermal and structural models of the Sumatra subduction zone: implications for the megathrust seismogenic zone. *J. Geophys. Res.* 113, B12103. doi:10.1029/2008JB005698

Hsu, Y. J., Simons, M., Avouac, J. P., Sieh, K., Galetzka, J., Chlieh, M., et al. (2006). Frictional afterslip following the Mw 8.7, 2005 Nias-Simeuleu earthquake, Sumatra. *Science* 312, 1921–1926. doi:10.1126/science.1126960

Hyndman, R. D., and Peacock, S.M. (2003). Serpentinization of the forearc mantle. *Earth Planet. Sci. Lett.* 212, 417–432. doi:10.1016/S0012-821X(03)00263-2

Hyndman, R. D., and Wang, K. (1993). Thermal constraints on the zone of major thrust earthquake failure: the Cascadia Subduction Zone. *J. Geophys. Res.* 98, 2039–2060. doi:10.1029/92JB02279

Hyndman, R. D., Yamano, M., and Oleskevich, D. A. (1997). The seismogenic zone of subduction thrust faults. *Isl. Arc.* 6, 244–260. doi:10.1111/j.1440-1738.1997.tb00175.x

Janak, J., and Sprlak, M. (2006). New software for gravity field modelling using spherical Armonic. *Geod.Cartog. Hor.* 52, 1–8.

Karig, D. E., Lawrence, M. B., Moore, G. F., and Curray, J. R. (1980). Structural frame work of the fore-arc basin, NW Sumatra. *J. Geol. Soc.* 137 (1), 77–91. doi:10.1144/gsjgs.137.1.0077

Kendrick, E., Bevis, M., Smalley, R., Jr., Brooks, B., Vargas, R. B., Lauría, E., et al. (2003). The Nazca-South America Euler vector and its rate of change. *J. S. Am. Earth Sci.* 16 (2), 125–131. doi:10.1016/S0895-9811(03)00028-2

Kieckhefer, R. M., Sho, G. G., and Curray, J. R. (1980). Seismic refraction studies of the Sunda trench and forearc basin. *J. Geophys. Res.* 85, 863–889. doi:10.1029/JB085iB02p00863

Klingelhoefer, F., Gutscher, M. A., Ladage, S., Dessa, J. X., Graindorge, D., Franke, D., et al. (2010). Limits of the seismogenic zone in the epicentral region of the 26 December 2004 great Sumatra-Andaman earthquake: results from seismic refraction and wide-angle reflection surveys and thermal modeling. *J. Geophys. Res.* 115, B01304. doi:10.1029/2009JB006569

Konca, A., Avouac, J., Sladen, A., Meltzner, A. J., Sieh, K., Fang, P., et al. (2008). Partial rupture of a locked patch of the Sumatra megathrust during the 2007 earthquake sequence. *Nature* 456, 631–635. doi:10.1038/nature07572

Konca, A. O., Hjorleifsdottir, V., Song, T., Avouac, J.-P., Helmberger, D. V., Ji, C., et al. (2007). Rupture kinematics of the 2005, Mw 8.6, Nias-Simeulue earthquake from the joint inversion of seismic and geodetic data. *Bull. Seismol. Soc. Am.* 97 (1A), S307–S322. doi:10.1785/0120050632

Kopp, H. (2013). Invited review paper: the control of subduction zone structural complexity and geometry on margin segmentation and seismicity. *Tectonophysics* 589, 1–16. doi:10.1016/j.tecto.2012.12.037

Krabbenhoeft, A., Weinrebe, R. W., Kopp, H., Flueh, E. R., Ladage, S., Papenberg, C., et al. (2010). Bathymetry of the Indonesian Sunda margin relating morphological features of the upper plate slopes to the location and extent of the seismogenic zone. *Nat. Hazards Earth Syst.* 10, 1899–1911. doi:10.5194/nhess-10-1899-2010

Lay, T., Ammon, C. J., Kanamori, H., Yamazaki, Y., Cheung, K. F., and Hutko, A. R. (2011). The 25 October 2010 Mentawai tsunami earthquake (Mw 7.8) and the tsunami hazard presented by shallow megathrust ruptures. *Geophys. Res. Lett.* 38, L06302. doi:10.1029/2010GL046552

Lay, T., Kanamori, H., Ammon, C. J., Nettles, M., Ward, S. N., Aster, R. C., et al. (2005). The great Sumatra-Andaman earthquake of 26 December 2004. *Science* 308, 1127–1133. doi:10.1126/science.1112250

Lay, T., and Kanamori, H. (1981). "An asperity model of large earthquake sequences," in *Earthquake prediction, an international review*. Editors D. W. Simpson and P. G. Richards (Maurice Ewing Book Series), Vol. 4, 579–592. doi:10.1029/ME004p0579

Lay, T., Kanamori, H., Ammon, C., Koper, K., Hutko, A., Ye, L., et al. (2012). Depth varying rupture properties of subduction zone megathrust faults. *J. Geoph. Res., Solid Earth* 117, B04311. doi:10.1029/2011JB009133

Lay, T., Kanamori, H., and Ruff, L. (1982). The asperity model and the nature of large subduction zone earthquakes. *Earthq. Pred. Res.* 1, 3–71. doi:10.1029/ME004p0579

Li, X. (2001). Vertical resolution: gravity versus vertical gravity gradient. *Lead. Edge.* 20, 901–904. doi:10.1190/1.1487304

Liu, C., Curray, J. R., and McDonald, J. M. (1983). New constraints on the tectonic evolution of the eastern Indian Ocean: *Earth Planet Sci. Lett.* 65, 331–342. doi:10.1016/0012-821X(83)90171-1

Llenos, A. L., and Mc Guire, J. J. (2007). Influence of fore-arc structure on the extent of great subduction zone earthquakes. *J. Geophys. Res.* 112, B09301. doi:10.1029/2007JB004944

Lorito, S., Romano, F., Piatanesi, A., and Boschi, E. (2008). Source process of the September 12, 2007, Mw 8.4 southern Sumatra earthquake from tsunami tide gauge record inversion. *Geophys. Res. Lett.* 35, L02310. doi:10.1029/2007GL032661

Lubis, A. M., Hashima, A., and Sato, T. (2013). Analysis of afterslip distribution following the 2007 September 12 Southern Sumatra earthquake using poroelastic and viscoelastic media. *Geophys. J. Int.* 192 (1), 18–37. doi:10.1093/gji/ggs020

McCloskey, J., Nalbant, S., and Steacy, S. (2005). Earthquake risk from co-seismic stress. *Nature* 434, 291. doi:10.1038/434291a

McGuire, J. J., Zhao, L., and Jordan, T. H. (2002). Predominance of unilateral rupture for a global catalog of large earthquakes. *Bull. Seismol. Soc. Am.* 92, 3309–3317. doi:10.1785/0120010293

Metois, M., Vigny, C., and Socquet, A. (2016). Interseismic coupling, megathrust earthquakes and seismic swarms along the Chilean subduction zone (38°-18°S). *Pure Appl. Geophys.* 173, 1431–1449. doi:10.1007/s00024-016-1280-5

Moreno, M. S., Melnick, D., Rosenau, M., Baez, J., Klotz, J., Oncken, O., et al. (2012). Toward understanding tectonic control on the Mw 8.8 2010 Maule Chile earthquake. *Earth Planet Sci. Lett.* 321–322, 152–165. doi:10.1016/j.epsl.2012.01.006

Müller, R. D., Sdrolias, M., Gaina, C., and Roest, W. R. (2008). Age, spreading rates, and spreading asymmetry of the world's ocean crust. *G-cubed* 9, 18–36. doi:10.1029/2007GC001743

Nalbant, S., McCloskey, J., Steacy, S., NicBhloscaidh, M., and Murphy, S. (2013). Interseismic coupling, stress evolution, and earthquake slip on the Sunda megathrust. *Geophys. Res. Lett.* 40, 4204–4208. doi:10.1002/grl.50776

Nalbant, S., Steacy, S., Sieh, K., Natawidjaja, D., McCloskey, J., et al. (2005). Earthquake risk on the Sunda trench. *Nature* 435, 756–757. doi:10.1038/nature435756a

Natawidjaja, D. H., Sieh, K., Chlieh, M., Galetzka, J., Suwargadi, B. W., Cheng, H., et al. (2006). Source parameters of the great Sumatran megathrust earthquakes of 1797 and 1833 inferred from coral microatolls. *J. Geophys. Res.* 111, B06403. doi:10.1029/2005JB004025

Natawidjaja, D. H., Sieh, K., Galetzka, J., Suwargadi, B. W., Cheng, H., Edwards, R. L., et al. (2007). Interseismic deformation above the Sunda Megathrust recorded in coral microatolls of the Mentawai islands, West Sumatra. *J. Geophys. Res.* 112, B02404. doi:10.1029/2006JB004450

Natawidjaja, D., Sieh, K., Ward, S., Cheng, H., Edwards, R. L., Galetzka, J., et al. (2004). Paleogeodetic records of seismic and aseismic subduction from central Sumatran microatolls, Indonesia. *J. Geophys. Res.* 109, B04306. doi:10.1029/2003JB0002398

Newcomb, K., and McCann, W. (1987). Seismic history and seismotectonics of the Sunda arc. *J. Geophys. Res.* 92, 421–439. doi:10.1029/JB092iB01p00421

Ni, S., Kanamori, H., and Helmberger, D. (2005). Energy radiation from the Sumatra earthquake. *Nature* 434, 582. doi:10.1038/434582a

Oleskevich, D. A., Hyndman, R. D., and Wang, K. (1999). The up-dip and down-dip limits to great subduction earthquakes: thermal and structural models of Cascadia, south Alaska, SW Japan, and Chile. *J. Geophys. Res.* 104, 14,965–14,991. doi:10.1029/1999JB900060

Pan, T. C., Megawati, K., Brownjohn, J. M. W., and Lee, C. L. (2001). The Bengkulu, southern Sumatra, earthquake of 4 June 2000 (Mw 7.7): another warning to remote metropolitan areas. *Seismol. Res. Lett.* 72, 171–185. doi:10.1785/gssrl.72.2.171

Panet, I., Mikhailov, V., Diament, M., Pollitz, F., King, G., de Viron, O., et al. (2007). Coseismic and post-seismic signatures of the Sumatra 2004 December and 2005 March earthquakes in GRACE satellite gravity. *Geophys. J. Int.* 171 (1), 177–190. doi:10.1111/j.1365-246X.2007.03525.x

Prawirodirdjo, L., Bocl, Y., McCaffrey, R., Genrich, J., Calais, E., Stevens, C., et al. (1997). Geodetic observations of interseismic strain segmentation at the Sumatra subduction zone, Geophys. *Res. Lett.* 24, 2601–2604. doi:10.1029/97GL52691

Prawirodirdjo, L., McCaffrey, R., Chadwell, C. D., Bock, Y., and Subarya, C. (2010). Geodetic observations of an earthquake cycle at the Sumatra subduction zone: role of interseismic strain segmentation. *J. Geophys. Res.* 115, B03414. doi:10.1029/2008JB006139

Reinen, L. A., Weeks, J. D., and Tullis, T. E. (1991). The frictional behaviour of serpentinite: implications for aseismic creep on shallow crustal faults. *Geophys. Res. Lett.* 18, 1921–1924. doi:10.1029/91GL02367

Rivera, L., Sieh, K., Helmberger, D., and Natawidjaja, D. (2002). A comparative study of the Sumatran subduction-zone earthquakes of 1935 and 1984. *Bull. Seismol. Soc. Am.* 92, 1721–1736. doi:10.1785/0120010106

Rummel, R., Yi, W., and Stummer, C. (2011). GOCE gravitational gradiometry. *J. Geodyn.* 85 (11), 777–790. doi:10.1007/s00190-011-0500-0

Sandwell, D. T., and Smith, W. H. F. (1997). Marine gravity anomaly from Geosat and ERS 1 satellite altimetry. *J. Geophys. Res.* 102, 10039–10054. doi:10.1029/96JB03223

Scholz, C. H. (1990). *The mechanics of earthquakes and faulting*. Cambridge, U.K: Cambridge University Press, 439.

Siebert, L., and Simkin, T. (2002). "Volcanoes of the world: an illustrated catalog of holocene volcanoes and their eruptions." Smithsonian Institution. Gloval volcanism program digital information series, GVP-3. Available at: www.volcano.si.edu/world (Accessed March 2020).

Sieh, K., and Natawidjaja, D. (2000). Neotectonics of the Sumatran fault, Indonesia. *J. Geophys. Res.* 105, 28295–28326. doi:10.1029/2000JB900120

Sieh, K., Natawidjaja, D., Chlieh, M., Galetzka, J., and Avouac, J.-P. (2004). "The giant subduction earthquakes of 1797 and 1833, West Sumatra: characteristic couplets, uncharacteristic slip," in Fall Meeting. American Geophysical Union, Vol. 85. [abstract:T12B-04].

Sieh, K., Natawidjaja, D. H., Meltzner, A. J., Shen, C.-C., Cheng, H., Li, K.-S., et al. (2008). Earthquake Supercycles inferred from sea-level changes recorded in the corals of West Sumatra. *Science* 322, 1674–1678. doi:10.1126/science.1163589

Sieh, K., Ward, S. N., Natawidjaja, D. H., and Suwargadi, B. W. (1999). Crustal deformation at the Sumatran subduction zone. *Geophys. Res. Lett.* 26, 3141–3144.

Simoes, M., Avouac, J. P., Cattin, R., and Henry, P. (2004). The Sumatra subduction zone: a case for a locked fault zone extending into the mantle. *J. Geophys. Res.* 109, B10402. doi:10.1029/2003JB002958

Sobiesiak, M. M., Meyer, U., Schmidt, S., Götze, H. J., and Krawczyk, C. (2007). Asperity generating upper crustal sources revealed by b-value and isostatic residual anomaly grids in the area of Antofagasta. *J. Geophys. Res.* 112, B12308. doi:10.1029/2006JB004796

Song, T. R., and Simons, M. (2003). Large trench-parallel gravity variations predict seismogenic behavior in subduction zones. *Science* 301, 630–633. doi:10.1126/science.1085557

Sparkes, R., Tilmann, F., Hovius, N., and Hillier, J. (2010). Subducted seafloor relief stops rupture in South American great earthquakes: implications for rupture behavior in the 2010 Maule, Chile earthquake. *Earth Planet Sci. Lett.* 298, 89–94. doi:10.1016/j.epsl.2010.07.029

Stein, S., and Okal, E. A. (2005). Speed and size of the Sumatra earthquake. *Nature* 434, 581–582. doi:10.1038/434581a

Tassara, A. (2010). Control of forearc density structure on megathrust shear strength along the Chilean subduction zone. *Tectonophysics* 495, 34–47. doi:10.1016/j.tecto.2010.06.004

Uieda, L., Barbosa, V., and Braitenberg, C. (2016). Tesseroids: forward-modeling gravitational fields in spherical coordinates. *Geophysics* 81, F41–F48. doi:10.1190/geo2015-0204.1

Vigny, C., Simons, W. J. F., Abu, S., Bamphenyu, R., Satirapod, C., Choosakul, N., et al. (2005). Insight into the 2004 Sumatra-Andaman earthquake from GPS measurements in southeast Asia. *Nature* 436, 201–206. doi:10.1038/nature03937

Wells, R. E., Blakely, R. J., Sugiyama, Y., Scholl, D. W., and Dinterman, P. A. (2003). Basin centered asperities in great subduction zone earthquakes: a link between slip, subsidence and subduction erosion?. *J. Geophys. Res.* 108 (B10), 2507–2536. doi:10.1029/2002JB002072

Wessel, P., Luis, J. F., Uieda, L., Scharroo, R., Wobbe, F., Smith, W. H. F., et al. (2019). The generic mapping tools version 6. *G-cubed* 20, 5556–5564. doi:10.1029/2019GC008515

Zachariasen, J., Sieh, K., Taylor, F. W., Edwards, R. L., and Hantoro, W. S. (1999). Submergence and uplift associated with the giant 1833 Sumatran subduction earthquake: evidence from coral microatolls. *J. Geophys. Res.* 104, 895–919. doi:10.1029/1998JB900050

Conflict of Interest: The authors declare that the research was conducted in the absence of any commercial or financial relationships that could be construed as a potential conflict of interest.

frontiers
in Earth Science

ORIGINAL RESEARCH
published: 25 February 2021
doi: 10.3389/feart.2021.596854

Strong Earthquakes Recurrence Times of the Southern Thessaly, Greece, Fault System: Insights from a Physics-Based Simulator Application

Christos Kourouklas[1], *Rodolfo Console*[2,3], *Eleftheria Papadimitriou*[1]*, *Maura Murru*[3] *and Vassilios Karakostas*[1]

[1]Geophysics Department, School of Geology, Aristotle University of Thessaloniki, Thessaloniki, Greece, [2]Center of Integrated Geomorphology for the Mediterranean Area (CGIAM), Potenza, Italy, [3]Istituto Nazionale di Geofisica e Vulcanologia, Sezione Roma 1 (Seismology and Tectonophysics), Rome, Italy

Edited by:
Debora Presti,
University of Messina, Italy

Reviewed by:
Jochen Woessner,
Risk Management Solutions, Switzerland
Maria Mesimeri,
The University of Utah, United States

***Correspondence:**
Eleftheria Papadimitriou
ritsa@geo.auth.gr

Specialty section:
This article was submitted to Solid Earth Geophysics, a section of the journal Frontiers in Earth Science

Received: *20 August 2020*
Accepted: *07 January 2021*
Published: *25 February 2021*

Citation:
Kourouklas C, Console R, Papadimitriou E, Murru M and Karakostas V (2021) Strong Earthquakes Recurrence Times of the Southern Thessaly, Greece, Fault System: Insights from a Physics-Based Simulator Application. Front. Earth Sci. 9:596854. doi: 10.3389/feart.2021.596854

The recurrence time, T_r, of strong earthquakes above a predefined magnitude threshold on specific faults or fault segments is an important parameter, that could be used as an input in the development of long-term fault-based Earthquake Rupture Forecasts (ERF). The amount of observational recurrence time data per segment is often limited, due to the long duration of the stress rebuilt and the shortage of earthquake catalogs. As a consequence, the application of robust statistical models is difficult to implement with a precise conclusion, concerning T_r and its variability. Physics-based earthquake simulators are a powerful tool to overcome these limitations, and could provide much longer earthquake records than the historical and instrumental earthquake catalogs. A physics-based simulator, which embodies known physical processes, is applied in the Southern Thessaly Fault Zone (Greece), aiming to provide insights about the recurrence behavior of earthquakes with $M_w \geq 6.0$ in the six major fault segments in the study area. The build of the input fault model is made by compiling the geometrical and kinematic parameters of the fault network from the available seismotectonic studies. The simulation is implemented through the application of the algorithm multiple times, with a series of different input free parameters, in order to conclude in the simulated catalog which showed the best performance in respect to the observational data. The detailed examination of the 254 $M_w \geq 6.0$ earthquakes reported in the simulated catalog reveals that both single and multiple segmented ruptures can be realized in the study area. Results of statistical analysis of the interevent times of the $M_w \geq 6.0$ earthquakes per segment evidence quasi-periodic recurrence behavior and better performance of the Brownian Passage Time (BPT) renewal model in comparison to the Poissonian behavior.

Keywords: strong earthquakes recurrence models, physics-based earthquake simulator, fault interaction, statistical analysis, southern Thessaly, Greece

INTRODUCTION

The study of the statistical behavior of strong earthquakes' occurrence above a given magnitude threshold (e.g., $M \geq 6.0$) on specific faults or faults segments is among the key components of the estimation of fault-based probabilistic seismic hazard assessment (PSHA). The main purpose of such studies is the determination of the mean recurrence time, T_r, between successive strong earthquakes and their variability, the latter of which can be used as an input in the application of either Poissonian or renewal (time-depended) long-term Earthquake Rupture Forecast (ERF) models in a specific time span (Field, 2015).

The accurate computation and evaluation of recurrence time statistical parameters is a prerequisite for both the better understating of its behavior and the precision of the forecast models. For this reason, the compilation of as many as possible records of strong earthquakes that occurred in individual fault segments is necessary. However, the amount of this observational data is limited, often between 3 and 10 observations (Ellsworth et al., 1999; Sykes and Menke, 2006), and the related catalogs (both historical and instrumental) are relatively short because of the earthquake cycle's long duration in each given segment. In addition, paleoseismological event dating (e.g., Biasi et al., 2015) and slip-rate constrains (Ogata, 2002; Biasi and Thompson, 2018) could refine the parameters' space when they are used in combination with alternative approaches, such as Bayesian inference methods (Fitzenz, 2018).

An alternative approach to support and improve the study of strong earthquakes' recurrence behavior is the development and application of physics-based simulator algorithms. These algorithms model the earthquake occurrence via numerical simulations using various approximations about the known physical processes concerning the stress transfer and frictional properties, along with kinematic and dynamic constraints (Tullis, 2012a). Starting from the early works of Rundle 1988 and Robinson and Benites 1996, the concept of physics-based simulators became popular during the last decade, due to their ability to model and reproduce long earthquake occurrence records (ranging from thousands to millions of years). Thus, a large number of such algorithms have been proposed (e.g., Yikilmaz et al., 2010; Richards-Dinger and Dieterich, 2012; Ward, 2012; Schultz et al., 2017) and applied (e.g., Robinson et al., 2011 and Christophersen et al., 2017 in New Zealand; Shaw et al., 2018 in California).

In this context, Console et al. 2015 introduced a physics-based simulator algorithm based on the modeling of the rupture growth, considering the long-term slip rate constraints on fault segments, which were firstly applied in the Corinth Gulf fault system in Greece. The simulated seismicity yielded satisfactory results on the magnitude distribution of the simulated catalog, which is consistent with the observations, and, again, with the realistic and consistent space time behavior (e.g., clustering of strong earthquakes and aftershock generation). Over the years, the simulation algorithm had a revolutionary improvement, comprising new parameters for the identification of successive ruptures (Console et al., 2017) and the inclusion of the afterslip process, modeled by a decaying Omori-like power law (Console et al., 2018a). These improved versions were successfully applied to simulate the seismicity of Calabria (Console et al., 2017; Console et al., 2018b) and Central Apennines (Console et al., 2018a) in Italy. The latest version of the algorithm incorporates the effect of the Rate and State Constitutive law proposed by Dieterich 1994 in the physical processes, leading to a stochastic manner of nucleation with applications in Central Italy (Console et al., 2020) and Greece (Mangira et al., 2020).

The current version is applied in the Southern Thessaly Fault Zone (STFZ) in Central Greece, which consists of part of the extensional back arc Aegean region and characterized by WNW-ESE to E-W normal faulting (Papazachos et al., 1998; Goldsworthy et al., 2002; **Figure 1B**). During the 20th century, a series of six strong and destructive ($M_w \geq 6.0$) earthquakes occurred in the study area (**Figure 1A** and **Table 1**). Papadimitriou and Karakostas 2003 showed that the stress transfer dominates the occurrence of strong earthquakes within the STFZ, which have been characterized as episodic since the active periods alternate with much longer quiescent periods. Although several strong earthquakes $M_w \geq 6.0$ had occurred since the 16th century in the broader Thessaly area, a rather complete historical record reveals (Papazachos and Papazachou, 2002) that only two of them that occurred during the 18th century are related with the STFZ (white stars of **Figure 1A** and **Table 1**). As a consequence, the study area could be characterized as an active area with strong earthquake occurrence during the instrumental period, however, het lack of a satisfactory number of $M_w \geq 6.0$ events per segment inhibits the identification of the corresponding mean recurrence time, T_r.

This fact provokes the detailed study of the long-term behavior of strong earthquakes via the application of the simulation algorithm with the ultimate goal of constructing built a large and representative strong earthquake record over a sufficient time span. This will form the basis for the statistical analysis of these earthquakes' recurrence time behavior.

SEISMOTECTONIC SETTING AND DEFINITION OF THE FAULT NETWORK OF THE SOUTHERN THESSALY FAULT ZONE

The active deformation in the broader Aegean region is dominated by the subduction of the oceanic lithosphere of the Eastern Mediterranean under the continental Aegean microplate, forming the Hellenic Arc and the extensional back arc region of the Aegean Sea (Papazachos and Comninakis, 1970; Papazachos and Comninakis, 1971; **Figure 1B**). The regional stress field of STFZ is characterized by a N-S extension, similar to the broader Aegean back arc area, with relatively moderate slip rates (about 4.6 ± 0.5 mm/yr) as derived from GPS measurements (Muller et al., 2013). The STFZ is composed of six sub-parallel major normal faults with an E-W to WNW-ESE strike (**Figure 1A** and **Table 2**), reaching maximum lengths of 15–25 km and typical dips for normal faulting equal to 45° (in agreement with Roberts,

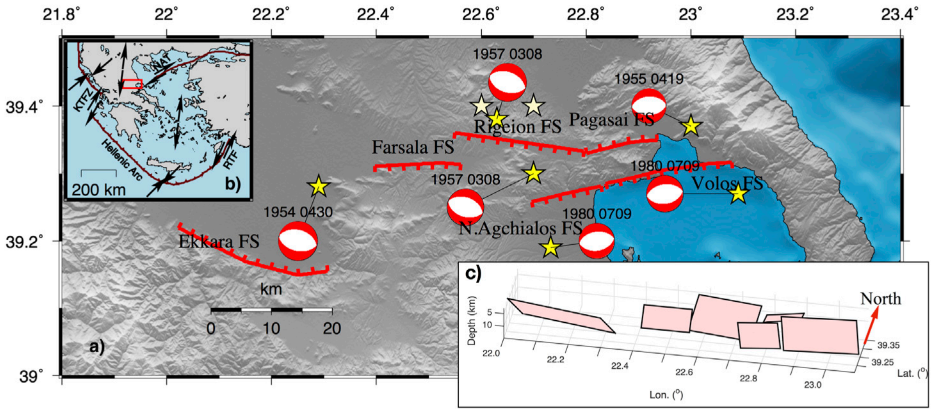

FIGURE 1 | (A) Strong earthquake ($M_w \geq 6.0$) occurrence in the Southern Thessaly Fault Zone. Yellow stars depict the $M_w \geq 6.0$ events during the 20th century, whereas the white stars depict the historical ones during the 18th century. The six major segments of the Southern Thessaly Fault System are represented with the red solid lines and their names are also given. Focal mechanisms are plotted as lower-hemisphere equal-area projections. The occurrence date of each event is annotated on the top of focal spheres. **(B)** Main seismotectonic properties of the broader Aegean area along with the relative plate motions represented by the black arrows, either side of the active boundaries depicted by the thick red lines. The study area is denoted with a rectangular red box. **(C)** Schematic 3D representation of the six fault segments of the Southern Thessaly Fault Zone, modeled as rectangular planes for the current simulator application.

TABLE 1 | Focal parameters of the $M_w \geq 6.0$ strong earthquakes that occurred in the Southern Thessaly Fault Zone since 1700.

Date	Epicentral coordinates		M_w (σM_w)	Ref
(yyyy-mm-dd)	Latitude	Longitude		
1743-02-12	39.40	22.60	6.6 (±0.3)	1
1773-03-15	39.40	22.70	6.4 (±0.3)	1,2
1954-04-30	39.28	22.29	7.0 (±0.3)	1,3
1955-04-19	39.37	23.00	6.2 (±0.3)	1,3
1957-03-08	39.30	22.70	6.5 (±0.3)	1,3
1957-03-08	39.38	22.63	6.8 (±0.3)	1,3
1980-07-09	39.27	23.09	6.5 (±0.2)	1,3,4
1980-07-09	39.19	22.73	6.1 (±0.2)	1,3,4

(1) Papazachos and Papazachou, 2002; (2) Ambraseys, 2009; (3) Ambraseys and Jackson, 1990; (4) geophysics.geo.autauth.gr/ss.

TABLE 2 | Geometrical and kinematic parameters of the fault network model used in the simulation application of the Southern Thessaly Fault Zone.

Fault segment	Upper left edge of segment		Seismogenic layer (km)	Strike(°)	Dip(°)	Rake(°)	L (km)	W (km)	Slip rate (mm/yr)	
	Lat(°)	Lon(°)							Geodetic	Seismic
Ekkara	39.154	224.306	3–15	285	45	−88	28	18	4.5 (±0.5)	3.0
Farsala	39.310	22.397	3–15	89	45	−90	14	10	4.5 (±0.5)	3.0
Rigeion	39.365	22.559	3–15	99	45	−90	19	14	4.5 (±0.5)	3.0
Pagasai	39.340	22.920	5–15	252	45	−90	12	10	4.5 (±0.5)	2.5
N.Agchialos	39.258	22.696	5–15	82	45	−90	12	10	4.5 (±0.5)	2.5
Volos	39.285	22.830	3–15	82	45	−90	21	14	4.5 (±0.5)	3.0

1996; Roberts and Ganas, 2000; Goldsworthy and Jackson, 2000). The thickness of the seismogenic layer along the fault zone is equal to 12 km, with earthquake focal depths ranging between 3 and 15 km (Hatzfeld et al., 1999). The stress is mainly accumulated on and released through the six major fault segments, whose dimensions (**Table 2**) are large enough to be comparable with the seismogenic thickness of the upper crust and capable of rupturing in $M_w \geq 6.0$ earthquakes (Goldsworthy and Jackson, 2000; Scholz, 2019).

The Ekkara fault segment with NW-SE strike (285°), NE dip, and length equal to 28 km is located at the westernmost part of the STFZ (**Figure 1A**), associated with the 1954 $M_w = 7.0$ earthquake (Papastamatiou and Mouyaris, 1986; Caputo and Pavlides, 1993). The 1954 event is the largest one known to have occurred in the study area and is also known as the Sofades earthquake due to the heavy damage caused by it in Sofades and neighboring villages (Ambraseys and Jackson, 1990; Papazachos and Papazachou, 2002; Papazachos et al., 2016).

Two distinctive groups of sub-parallel segments are its neighbors to the east. The fist group includes the Farsala, Rigeion, and Pagasai segments (**Figure 1A**). Farsala and Rigeion fault segments strike from E-W to ENE-WSW (89° and 99°, respectively), dip southwards, and extend in lengths of about 14 and 19 km, respectively (Caputo and Pavlides, 1993; Mountrakis et al., 1993). The third member of this group, the Pagasai fault segments strikes at 252°, dips north-northeastward, with a length equal to 12 km (Caputo and Pavlides, 1993; Galanakis et al., 1998). This group of fault segments is associated with a cluster of strong earthquakes from 1955 (just one year after the Ekkara main shock) up to 1957 that devastated the study area The 1955 M_w = 6.2 earthquake (Ambraseys and Jackson, 1990; Papazachos and Papazachou, 2002) occurred in the NE margin of the study area and is associated with the Pagasai fault segment. The activity continued by migrating westwards, filling in the gap between the 1954 and 1955 events, with the occurrence on the eighth of March 1957 doublet (with a time difference of 7 min; 12:14, M_w = 6.5 and 12:21, M_w = 6.8; Ambraseys and Jackson, 1990; Papazachos and Papazachou, 2002) causing heavy damage in the regions of Velestino, Farsala, and Volos. These two earthquakes, M_w = 6.5 and M_w = 6.8, are associated with the Farsala and Rigeion fault segments, respectively. It must be mentioned that, unless the M_w = 6.5 earthquake's initial location is quite far from the Farsala segment (about 15–16 km), it is more likely to be associated with it rather than with the Rigeion segment because the latter cannot bear two strong events simultaneously. Convincing support for this argument is found in that the macroseismic effects, although difficult to be discriminated between the two main shocks, can be ascribed to both fault segments and the epicentral misallocation of that period due to the seismological network limitations.

The second group of the eastern part of the study area encompasses the Nea Agchialos (Galanakis et al., 1998) and Volos fault segments (**Figure 1A**), also identified by the seismic reflection survey of Perissoratis et al. 1991. These two segments strike at 82°, dip to the SE and with lengths equal to 21 and 12 km, respectively (Caputo, 1996; Galanakis et al., 1998). The Volos and Nea Agchialos segments are linked with a second doublet of strong earthquakes that occurred on the 9th of July 1980, with magnitudes equal to M_w = 6.5 (02:11) and M_w = 6.1 (02:35) (Papazachos et al., 1983; Ambraseys and Jackson, 1990; Drakos et al., 2001).

Papadimitriou and Karakostas 2003 studied the episodic occurrence of strong earthquake occurrence in a larger area, including the STFZ, and concluded that the stress transfer among adjacent fault segments is the dominant pattern. In the study area during the 18th century, two earthquakes of M_w = 6.6 and M_w = 6.4 occurred in 1743 and 1773, respectively (**Table 1** and **Figure 1A**). These events are likely to be associated with the first group of easternmost faults segments (Farsala, Rigeion, Pagasai), but the lack of available historical information does not allow for a reliable linkage between them.

The available fault plane solutions show a rake angle equal to $\lambda = -88°$ for the 1954 earthquake (McKenzie, 1972) associated with the Ekkara segment and $\lambda = -90°$ for all the other fault segments (Papazachos et al., 2001). The thickness of the seismogenic layer along the fault zone is extended along 3 and 15 km (Hatzfeld et al., 1999), as already mentioned, except for the two smaller fault segments, namely the Pagasai and the Nea Agchialos, with lengths equal to 12 km, which are considered to be rooted in the middle of the seismogenic layer between the depths of 5 and 15 km.

The geodetic long-term slip rate equals 4.5 ± 0.5 mm/yr (Muller et al., 2013), is distributed homogenously along its segments, taking the larger part of the deformation. Taking into account that only the 60% of the total slip is released coseismically (Davis et al., 1997), the slip rate of each segment is assigned and given in **Table 2**. This estimate also agrees with Jenny et al. 2004 who concluded that the tectonic deformation in central Greece is not fully coupled but affected by aseismic creep. This conclusion is also supported by the recognition of anthropogenic-induced subsidence phenomena, as revealed by recent GNSS measurements (Argyrakis et al., 2020 and the references therein), which could be associated with the aseismic slip of the study area.

The slip rate values, corresponding to 60% percent of the total slip rate, are chosen to be equal to 3 mm/yr for the largest fault segments and 2.5 mm/yr for the smaller ones, rooted deeper in the seismogenic layer (Pagasai and Nea Agchialos; **Table 2**). These values are slightly higher and slightly lower, respectively, from the exact 60% (2.7 mm/yr), aiming to account in some way for the corresponding uncertainty of estimated values of the total slip.

All the aforementioned geometrical and kinematic parameters and data, as compiled from the previously mentioned studies, are taken into account in the definition of the fault network model for the study area, which is the main input of the simulation procedure, and are summarized in **Table 2**. The GreDass database (Caputo and Pavlides, 2013) and the 2020 updated version (v3.0) of NOA Faults (Ganas et al., 2013) are accessed in an attempt to compare the fault segments defined in this study and compare them with the ones defined in the two databases. This comparison (**Supplementary Appendix A**) revealed a good agreement between our definition with at least one of the databases. A systematic difference is observed at the dip angles, which in our study are taken to equal 45°, the typical value equal for normal faulting and in agreement with Roberts and Ganas 2000 and Goldsworthy and Jackson 2000.

The maximum expected magnitude, M_{max}, for each segment is also calculated by the application of a modified version of the method proposed by Pace et al. 2016, based on the combination of various scaling laws and the maximum observed magnitude per segment and the investigation of the consistency in this comparison. Four scaling relations (Wells and Coppersmith, 1994; Papazachos et al., 2004; Wesnousky, 2008; Leonard, 2010) were engaged, estimating the expected M_{max} and then its average value. The maximum observed magnitude per segment is also weighted in the final estimation of M_{max}.

The M_{max}, along with its ±1σ, was calculated as a function of each fault segment length, given the scaling relations, assuming that M_{max} corresponds to the full rupture length. The probability curve of M_{max} estimates for each relation is then drawn, using a normal distribution with mean and standard deviation equal to the estimated M_{max} and its corresponding ±1σ, respectively. Additionally, a fifth normal distribution is drawn considering the observed M_{max}, along with its corresponding ±1σ, as input parameters. The five probability density functions are then combined by summation. The summed curve is considered as the basis of the final normal fit, including both the calculated and the observed M_{max}, aiming to estimate the central value of the

TABLE 3 | Estimated M_{max} and its ±1σ as obtained from the Wells and Coppersmith (1994; W&C), Papazachos et al. (2004; Pap), Wesnouskly (2008; Wes), and Leonard (2010; Leo) scaling relations for each of the six segments of the Southern Thessaly Fault Zone, along with the observed M_{max} values (also listed in **Table 1**) used for the final estimation of the M_{max}. The final estimates and their corresponding error (last column) using the modified version of Pace et al. (2016) method are also given.

Fault segment	Scaling relations M_{Max} (±1σ)				Observed M_{max} (±1σ)	Estimated expected M_{max} (±1σ)
	W&C	Pap	Wes	Leo		
Ekkara	6.57 (±0.31)	6.61 (±0.26)	6.80 (±0.27)	6.65 (±0.46)	7.0 (±0.30)	6.72 (±0.36)
Farsala	6.11 (±0.31)	6.01 (±0.26)	6.66 (±0.27)	6.15 (±0.46)	6.5 (±0.30)	6.28 (±0.41)
Rigeion	6.31 (±0.31)	6.28 (±0.26)	6.72 (±0.27)	6.37 (±0.46)	6.8 (±0.30)	6.50 (±0.39)
Pagasai	6.00 (±0.31)	5.88 (±0.26)	6.63 (±0.27)	6.04 (±0.46)	6.2 (±0.30)	6.15 (±0.41)
Nea Agchialos	6.00 (±0.31)	5.88 (±0.26)	6.63 (±0.27)	6.04 (±0.46)	6.1 (±0.20)	6.13 (±0.40)
Volos	6.38 (±0.31)	6.36 (±0.26)	6.74 (±0.27)	6.44 (±0.46)	6.5 (±0.20)	6.48 (±0.34)

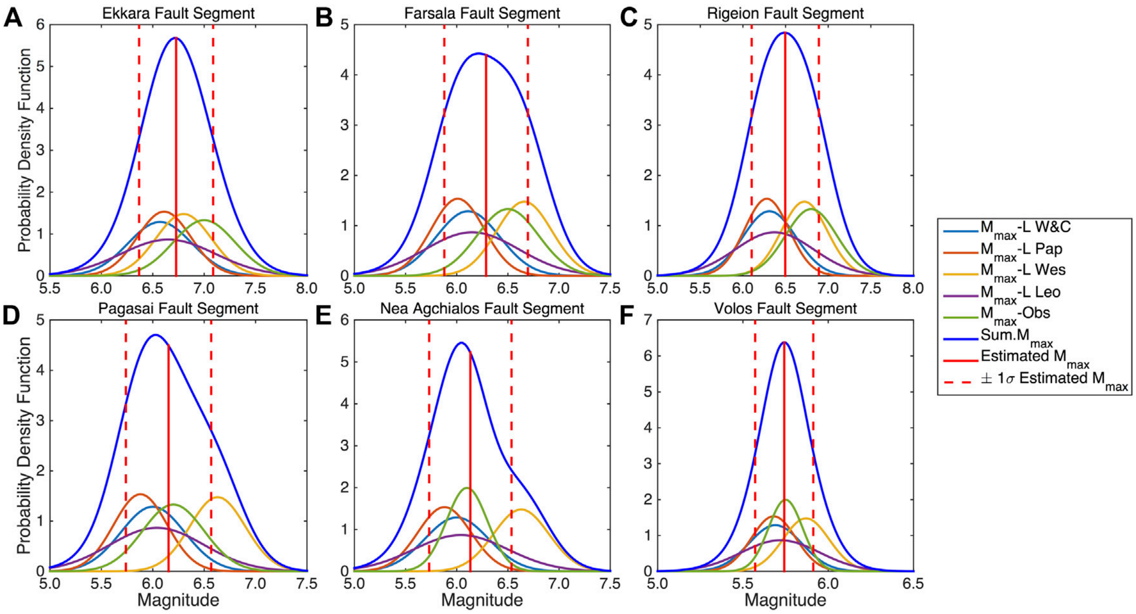

FIGURE 2 | Probability density functions considering the normal distribution with mean value and standard deviation, the estimated M_{max}, and its corresponding ±1σ as resulted from the (Wells and Coppersmith, 1994; light blue lines), (Papazachos et al., 2004; orange lines), (Wesnousky, 2008; yellow lines), and (Leonard 2010; magenta lines) scaling relations for normal faults using the fault segment length as input for each of the six segments of the Southern Thessaly Fault Zone. The green curves represent the normal distribution accrued from the observed M_{max} and its ±1σ based on the past strong earthquakes that occurred per segment. Blue curves depict the summed probability functions resulted from the combination of both scaling densities, along with the observational ones. The central values and their corresponding ±1σ of the summed densities after the application of the Gaussian fit are shown with solid and dashed red lines, respectively.

summed probability density and its standard deviation, which is assigned as the final expected M_{max} (**Table 3** and **Figure 2**).

A general remark concerning the estimates of the scaling relations is that Wesnousky's (2008) relation returns the largest values of M_{max} than the other 3, whose values are quite similar. For example, the M_{max} for the Ekkara fault segment equals to 6.80 with Wesnousky's (2008) relation, whereas the corresponding values using the Wells and Coppersmith 1994, Papazachos et al. 2004, and Leonard (2010) relations are equal to 6.57, 6.61, and 6.65, respectively. This fact slightly affects the +1σ part of the summed probability density (blue lines) in the cases of the Pagasai (**Figure 3D**) and Nea Agchialos (**Figure 3E**) fault segments.

The final estimates of M_{max}, resulted from the Gaussian fit of the summed density curves, show that the maximum expected magnitude values are slightly lower (but inside the +1σ confidence interval) than the observational ones in the cases of Ekkara (M_{max_exp} = 6.72 instead of M_{max_obs} = 7.0), Farsala (M_{max_exp} = 6.28 instead of M_{max_obs} = 6.5) and Rigeion (M_{max_exp} = 6.50 instead of M_{max_obs} = 6.8) fault segments. The estimates for Pagasai, Nea Agchialos, and Volos fault segments equal to M_{max_exp} = 6.15, M_{max_exp} = 6.13, and M_{max_exp} = 6.48, respectively, are in very good agreement with the observed ones (M_{max_obs} = 6.2, M_{max_obs} = 6.1, and M_{max_obs} = 6.5, respectively).

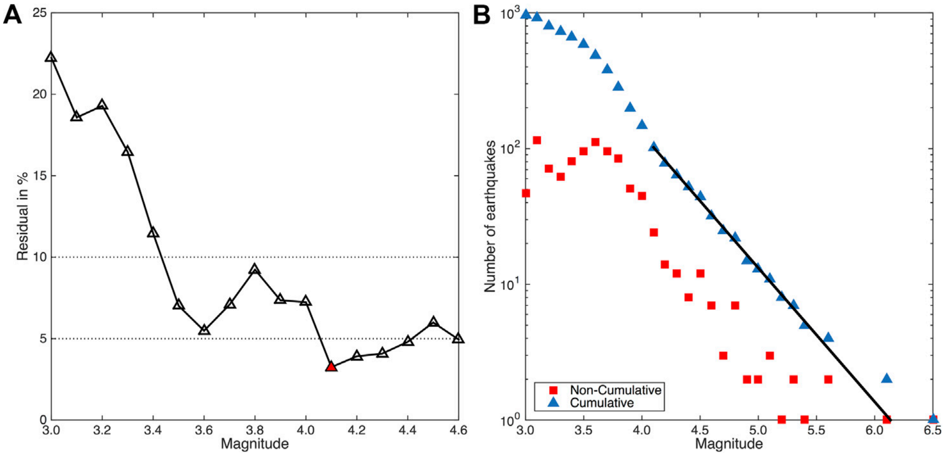

FIGURE 3 | Completeness magnitude, M_c, estimation through the GFT method for the Southern Thessaly Fault System during the period 1970–2020. **(A)** Residual in percentiles as function of the minimum magnitude bin of the observed catalog. Red triangle indicates the bin with residual below 5%. **(B)** Frequency-Magnitude Distribution (FMD) of incremental (red squares) and cumulative (blue triangles) number of the earthquakes. Straight black line represents the part of FMD above M_c.

In summary, the maximum expected magnitude evaluation using the estimates from scaling laws and constrained by the observed M_{max}, show the possible seismic potential of each fault segment. Some differences between the observed and the expected M values could possibly be related with some overestimation of the observed ones, due to the fact that these earthquakes occurred in the early instrumental period.

SIMULATOR ALGORITHM OUTLINE

The current simulation application is based on the algorithm developed and evolutionary improved by Console et al. 2015; Console et al. 2017; Console et al. 2018a; Console et al. 2020, where the main principles are analyzed in detail. In this section, a brief outline is presented about its main principles along with the improvement of the present version. The simulator algorithm comprises several physical constraints, including the geometry and the long-term slip rates of each segment of the 3-D fault model. Each fault segment is modeled as a quadrilateral plane source, onto which a normal grid of squared cells is superimposed. The long-term slip rate is distributed uniformly within a certain fault segment and could vary from one segment to the other. Each cell is initially assigned with a stress value taken from a random distribution, which then increases with time due to the slow tectonic loading in terms of a backslip model. The nucleation process is implemented by the contribution of the Rate and State Constitutive Law of Dieterich 1994, leading to a probabilistic manner of nucleation (Console et al., 2020).

Specifically, the seismicity rate, R, in each cell is calculated by:

$$R = \frac{r}{\left[\exp\left(-\left(\Delta CFF/A\sigma\right)\right)-1\right]\exp\left(-\left(\Delta t/\gamma_0 A\sigma\right)\right)+1} \tag{1}$$

where r is the reference seismicity rate of each cell (defined as the seismicity rate R when $\Delta CFF = 0$), ΔCFF is the change in Coulomb Failure Function due to the coseismic slip of previous earthquakes, $A\sigma$ is the constitutive parameter describing the response of the friction to a rate change caused by a stress step change (Toda and Stein, 2003), Δt is the time elapsed after the stress change on a given cell, and γ_0 is the inverse of the reference tectonic stressing rate, $\dot{\tau}_r$, $(\gamma_0 = (1/\dot{\tau}_r))$. Coulomb Stress Changes are computed by the equation:

$$\Delta CFF = \Delta\tau + \mu' \Delta\sigma_n \tag{2}$$

where $\Delta\tau$ is the shear stress change in the slip direction, $\Delta\sigma_n$ is the normal stress change, positive for extension normal to the observational fault plane, and μ' is the apparent coefficient of friction (Rice, 1992).

After the nucleation initiation, the strength of neighboring cells is reduced according to a constant value multiplied by the square root of the number of initially ruptured cells, resembling a weakening mechanism and promoting the growth of the rupture. The expansion of each rupture is limited by a factor equal to a given number of times the width of the fault segment, discouraging the rupture propagation over long distances. Rupture growth and termination are controlled by two free parameters in the algorithm, the Strength Reduction (*S-R*) coefficient and the Aspect Ratio (*A-R*), referring to the fault weakening and the discouragement of the rupture propagation over long distances, respectively.

During the coseismic stage of the process, the stress is decreasing by a constant stress drop, Δp (e.g., $\Delta p = 3$ MPa) in every cell that participates in the rupture, while in the surrounding cells the stress changes are given by the **Eq. 2**. A given cell is allowed to rupture more than once in the same event, when it is ruptured with a constant stress drop but with only a moderate amount of slip.

A rupture terminates when there are no more cells inside the searched area, in which the stress exceeds their strength. Coulomb stress changes also contribute to the interactions among the causative and receiving segments, allowing the expansion of a rupture to neighboring fault segments, which are located within a certain maximum distance (e.g., 5 km). This feature of the algorithm represents the ability of fault interactions to possibly produce fault linkage and coalescence phenomena, resulting in large earthquakes due to the simultaneous rupture of more than one segment (Scholz, 2019).

A critical point that affects the results of the simulation procedure is the input values of the three free parameters. The influence of the two of them, the *S-R* and *A-R*, was already analyzed by Console et al. (2015, 2017, 2018a). The Strength-Reduction coefficient (*S-R*) mainly controls the ratio between the number of small to large events. Small values of *S-R* produce simulated catalogs with much fewer large events than the large *S-R* values and visa versa. The effect of the Aspect-Ratio (*A-R*) value is mainly related with the maximum magnitude, not with the total number of events nor with the *b*-value of the simulated catalogs. Additionally, the effect of the product $A\sigma$ of the Rate and State law is mainly related with the probability of event's nucleation from the stress change due to the coseismic slip of previous events (Console et al., 2020).

APPLICATION OF THE SIMULATOR TO THE SOUTHERN THESSALY FAULT SYSTEM

The six fault segments of the fault model are rectangular planes, divided into 0.75 × 0.75 km squared cells (**Table 2** and **Figure 1C**). The 60% of the geodetically estimated slip, the values of rigidity, μ, and stress drop, Δp, equal to 40 GPa and 4 MPa, respectively, are considered for the simulator application. The minimum magnitude generated by the simulator is selected to be equal to 4.1 ($M_w = 4.1$), which corresponds to a two cells rupture.

An important step during the application of the simulator algorithm is the selection of the $A\sigma$, *S-R*, and *A-R* free input parameters. This step is very crucial because the final simulated catalog will be affected by their influence in terms of the total number of event and the ratio between the number of small to moderate and large earthquakes (effects of nucleation and fault weakening, related with the values of $A\sigma$ and *S-R*). The maximum magnitude that the simulator generates will also be influenced by the effect of the value of *A-R*. A wide range of $A\sigma$ values are reported, ranging from 0.0012 to 0.6 MPa, obtained from different earthquake sequences (Harris, 1998; Harris and Simpson, 1998). Mangira et al. 2020 tested values ranging between 0.04 and 0.09 MPa in the Central Ionian Islands (Greece), with a value equal to $A\sigma = 0.06$ MPa found to be the most appropriate. Console et al. 2020 used values between 0.01 and 1.0 Mpa concluding $A\sigma = 0.05$ MPa for Central Italy. Since the value of the product $A\sigma$ is not fixed, a range from 0.01 to 0.04 MPa with a step of 0.005 MPa is selected to be tested in this study [$A\sigma$ = (0.01 MPa–0.04 MPa)].

The relevant knowledge about the mechanism of fault weakening is based in indirect observations, such as past seismicity, and consequently is mainly undetermined A range of *S-R* values are tested, starting from a value of 0.1, which represents strong faults, and with a step of 0.05 up to the value 0.3, in which the weakening is enhanced [*S-R* = (0.1–0.3)]. The third parameter, *A-R*, is assigned after testing it for values equal to 2, 3, and 4, in accordance with the dimensions of the six segments. The effort for testing all possible values of the three free parameters resulted in 105 combinations stemming from the considered value ranges (**Supplementary Appendix B1**). The duration of each simulation is selected to be equal to 10 kyr with a warm-up period of 2 kyr, which were not taken into account in each final simulated catalog.

Each triplet of input parameters yielded a simulated catalog with different total number of events, maximum magnitude, and *b*-values. The number of events ranges from 9,309 to 40,056, whereas the *b*-values are fluctuated between 0.92 and 1.50 (**Supplementary Appendix B1**) affected by the different values of Strength-Reduction coefficient. Maximum magnitude is found to be between 6.6 and 6.8 because of the different Aspect-Ratio values, in good agreement with the maximum expected magnitude for each fault segment as obtained from the scaling relations (**Table 3**).

The selection of the most representative simulated catalog is made after comparison with observational data. The observational data are taken from the instrumental catalog of Geophysics Department at the Aristotle University of Thessaloniki, 1981 (http:/geophysics.geo.auth.gr/ss), based on the recordings of the Hellenic Unified Seismological Network (HUSN), and include all the available $M_w \geq 3.0$ earthquakes from 1970 to 2020. The complete magnitude of this catalog is investigated with the application of the Goodness of Fit method (GFT; Wiemer and Wyss, 2000), considering the 95% confidence level of residuals (**Figure 3A**), and was found to equal M_c = 4.1, with 102 earthquakes (**Figure 3B**). The maximum likelihood estimate (Aki, 1965) gave $b = 0.99$, and the parameter α equals $\alpha = 6.05$. A remarkable point arising from the FMD is the limited number of moderate to large earthquakes ($5.7 \leq M_w \leq 6.1$), implying the lack of the corresponding causative activated faults.

The comparison is implemented by assessing the performance of each simulated catalog against the observational one via the application of two non-parametric statistical tests, namely the two sample Kolmogorov—Smirnov (KS2) (Stephens, 1974) and the Wilcoxon Rank-Sum (WR-S) (Wilcoxon, 1945; Mann and Whitney, 1947), at a significance level equal to $\alpha = 0.05$. Specifically, the cumulative earthquake number N_i of a certain simulated catalog for each magnitude bin divided by the corresponding period (N_i/period, in years) is compared with the corresponding observations, under the null hypothesis that the two rates come from the same population against the alternative hypothesis that they come from different populations at a given significance level, α.

The two sample K-S test is a non-parametric goodness of fit test, which compares the differences between the empirical cumulative distribution functions (ecdf), F (*10*) and G (x), of two samples under the null hypothesis. The statistic of the test is defined as:

$$D = \max(|F(x) - G(x)|). \tag{3}$$

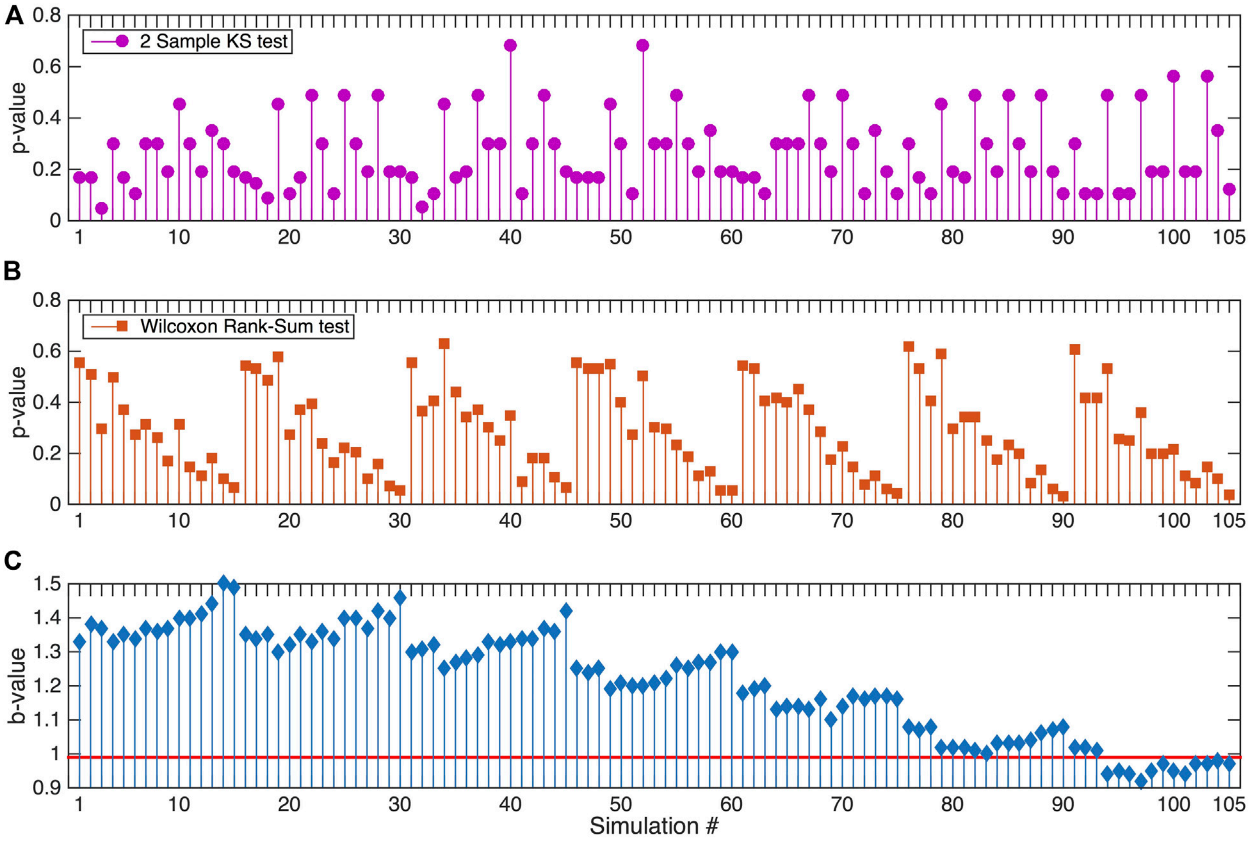

FIGURE 4 | Calculated *p*-values of the two Sample Kolmogorov-Smirnov **(A)** and the Wilcoxon Rank-Sum **(B)** tests for the 105 simulated catalogs at 0.05 level of significance ($\alpha = 0.05$). The *b*-values **(C)** of each simulated catalog (blue stems) are also presented vs. the observational catalog's one (solid red line).

The Wilcoxon Rank-Sum test compares two independent random variables, F and G, with sample sizes m and n, respectively, under the null hypothesis that the two samples come from the same distribution, similarly with the Mann-Whitney U-test. The samples are combined and ranked. The Wilcoxon statistic, T, is calculated from the sum of the ranks according to:

$$T_F = \sum_{i=1}^{m} R_{F_i} \tag{4}$$

and

$$T_G = \sum_{j=1}^{n} R_{G_j} \tag{5}$$

The number of times that $F_i > G_j$ is in an ordered arrangement, so the Mann-Whitney statistic U is defined as:

$$U = \min(U_F, U_G) \tag{6}$$

where

$$U_F = mn + \frac{m(m+1)}{2} - T_F \tag{7}$$

and

$$U_G = mn + \frac{n(n+1)}{2} - T_G. \tag{8}$$

The decision of rejecting or not the null hypothesis is based on the p-value returned by the test, compared with the significance level. If p-value is greater than α (p-value $> \alpha$) then the null hypothesis can not be rejected. On the contrary, if p-value is lower than α (p-value $< \alpha$) the null hypothesis can be rejected.

The results of the two statistical tests are shown in **Supplementary Appendix B1** and **Figure 4** in terms of their corresponding p-values, evidencing that in all cases their values are larger than the significance level, except for one case of the Wilcoxon Rank-Sum test, in which the p-value is equal to 0.032 (Simulation 90; **Supplementary Appendix B1** and **Figure 4**). More specifically, the p-values of the KS2 test range from 0.051 to 0.685, and those of WR-S between 0.032 and 0.630. Ideally, the best performed simulated catalog would be the one with the sufficiently largest p-values in both tests. The current results evidence a large number of candidate simulated catalogs as the best performed, since their p-values are quite large in both tests in respect to the others.

From a statistical point of view, each one of the simulated catalogs 19, 34, 52, 79, and 94 with values of free parameters ($A\sigma$/S-R/A-R) equal to 0.015 MPa/0.15/2, 0.02 MPa/0.15/2,

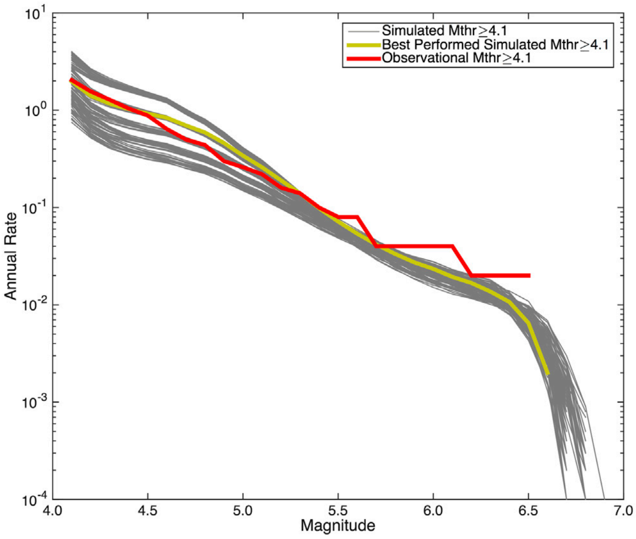

FIGURE 5 | Summary of annual occurrence rates of the 105 simulated catalogs (gray lines), using different combinations of the free input parameters ($A\sigma$, S-R, A-R; **Supplementary Appendix A1**). Annual occurrence rates of the best performed simulated catalog (Simulation 79; $A\sigma$ = 0.035 MPa, S-R = 0.15, A-R = 2) is represented by the yellow line, and the rates of the observational catalog with the red line.

0.025 MPa/0.2/2, 0.035 MPa/0.15/2, and 0.04 MPa/0.15/2, respectively, could be considered as the best performed, since their calculated p-values (**Supplementary Appendix B1** and **Figure 4**) are both large enough (e.g. p-values > 0.5) and quite close to each other. Four out of the five triplets showed a clear better performance of the values of S-R = 0.15 and A-R = 2. Simulation 52 (0.025 MPa/0.2/2) results in slightly higher p-values than the others (0.685 and 0.503 in KS2 and WR-S tests, respectively), but these results must be treated with caution before the final decision due to the sensitivity of statistical tests.

On the other hand, the best performed simulated catalog must also be representative in terms of the physical properties of the observational catalog, as expressed by the observed seismicity. The comparison among the calculated b-values of the simulated catalogs against the observational catalog, could be a reliable additional index for the final selection. The b-values of the simulated catalogs 19, 34, 52, and 94 are found to be equal to 1.30 (b_{sim19} = 1.30), 1.25 (b_{sim34} = 1.25), 1.20 (b_{sim52} = 1.20), and 0.94 (b_{sim94} = 0.94), respectively. These values considerably differ from the value of the observational catalog, which is equal to 0.99 (b_{obs} = 0.99). The b-value of the simulation 79 equals to 1.02 (b_{sim79} = 1.02) and is the one with the least difference in respect to the b_{obs}. It should be mentioned at this point that there are additional simulated catalogs with b-values close to the b_{obs} (eg, simulated catalogs 83 and 104 with b_{sim83} = 1.00 and b_{sim104} = 0.98, respectively; **Figure 4C**) but their statistical performance is poor.

Based on the above results, the simulated catalog 79 (yellow line in **Figure 5**) is considered as the best performed one in respect with the observed seismicity, identifying the catalog from which further recurrence time analysis will be accomplished.

The most representative simulated catalog is the one with $A\sigma$ = 0.035 MPa, S-R = 0.15, and A-R = 2, consisting of 19,740 events with $M_w \geq 4.1$ with a duration of 10 kyrs. The largest magnitude of the simulated catalog is equal to 6.6 (M_{w_max} = 6.6), which is considerably smaller than both the maximum observed magnitudes equal to 7.0 and 6.8 that occurred in the Ekkara and Rigeion fault segments. The maximum expected magnitude of this catalog agrees well with the maximum expected magnitude yielded by the empirical relations analysis. These discrepancies among the maximum observed and simulated magnitudes could be explained with the fact that the 1954 Sofades (M_w = 7.0) and the 1957 Rigeion (M_w = 6.8) earthquakes belong to the early instrumental period and their magnitudes could possibly have beenoverestimated, as already said. Looking at the ISC-GEM instrumental earthquake catalog, the estimated magnitudes of these events are equal to M_w = 6.66 and M_w = 6.40, respectively, in very good agreement with the largest magnitude estimated in the simulated catalog. The comparison among the maximum expected magnitudes and the simulated magnitudes for single segment ruptures (**Table 4**) allow to accept that this simulated catalog represents quite accurately the seismicity in the study area.

STRONG ($M_W \geq 6.0$) EARTHQUAKES OCCURRENCE AND RECURRENCE MODELING

The main purpose of the simulation application is the provision of an earthquake catalog of both long duration and seismicity physical properties, appropriate for investigating the recurrence behavior of strong events in each fault segment of STFZ after fulfilling a set of criteria, that must be specified. Firstly, the minimum magnitude threshold above which the strong earthquakes will be considered a characteristic one, must be specified. Considering the observed strong events that occurred per segment (**Figure 1**) and their magnitude uncertainties (**Table 1**), along with their dimensions, a unique magnitude threshold equal to 6.0 ($M_{thr} \geq 6.0$), corresponding to a group of at least 182 ruptured cells, is adopted.

Further, the contribution of each segment in a single earthquake must be specified. Each earthquake satisfying the

TABLE 4 | Summary of single and multiple ruptures for the $M_{thr} \geq 6.0$ for each of the six segments of the Southern Thessaly Fault Zone along with their maximum magnitude values obtained from the best performing 10 kyr simulated catalog (Simulation 79; $A\sigma$ = 0.035 MPa, S-R = 0.15, A-R = 2).

Fault segment	**M_{thr} ≥6.0**		**M_{max}**	
	Number of ruptures		**Single**	**Multiple**
	Single	**Multiple**		
Ekkara	71	–	6.62	–
Farsala	16	13	6.18	6.59
Rigeion	26	22	6.36	6.63
Pagasai	9	6	6.16	6.50
Nea Agchialos	6	17	6.16	6.61
Volos	41	27	6.48	6.63

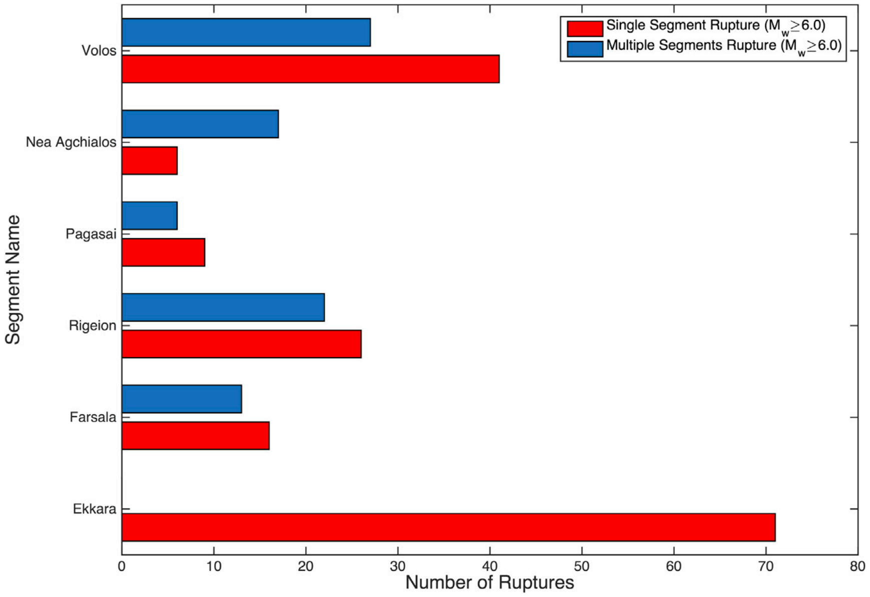

FIGURE 6 | Number of both single (red bars) and multiple (blur bars) ruptures of each segment of the Southern Thessaly Fault Zone obtained from the best performed simulated catalog for the $M_{thr} \geq 6.0$ characteristic earthquake magnitude threshold.

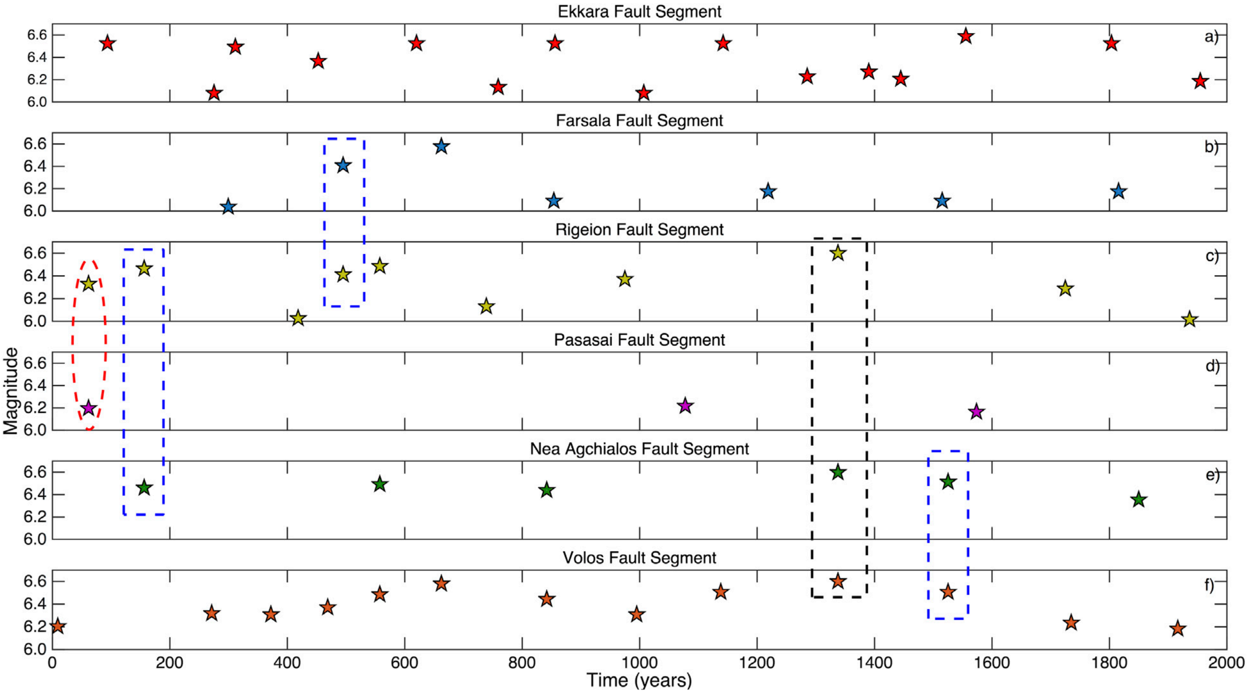

FIGURE 7 | Snapshot of the first 2 kyr temporal distribution of the $M_w \geq 6.0$ earthquakes of the best performed simulated catalog. Blue boxes indicate some of the combinations of the two segment ruptures, while the black one indicates one of the three cases of three segment ruptures. The red ellipse depicts a case of two individual fault segments ruptures (Mw = 6.3 for Rigeion fault segment and Mw = 6.2 for Pagasai fault segment) almost at the same time.

first criterion is initially assigned to the segment in which the nucleation starts. Moreover, an additional fault segment could also participate with many ruptured cells in the same earthquake. In this way, if the number of ruptured cells of another segment are at least 75% of the total number of its cells (in other words, the rupture covers more than 75% of the segment's area) or if they

TABLE 5 | Number of 2 and 3 segments' multiple ruptures for all the combinations of the participating fault segments of the Southern Thessaly Fault Zone.

2-Segments ruptures		3-Segments ruptures	
Fault segments	**Number of ruptures**	**Fault segments**	**Number of ruptures**
Farsala—Rigeion	9	Rigeion—Nea Agchialos—Volos	3
Rigeion—Pagasai	1		
Rigeion—Nea Agchialos	3		
Rigeion—Volos	5		
Farsala—Volos	2		
Nea Agchialos—Volos	12		
Pagasai—Volos	6		

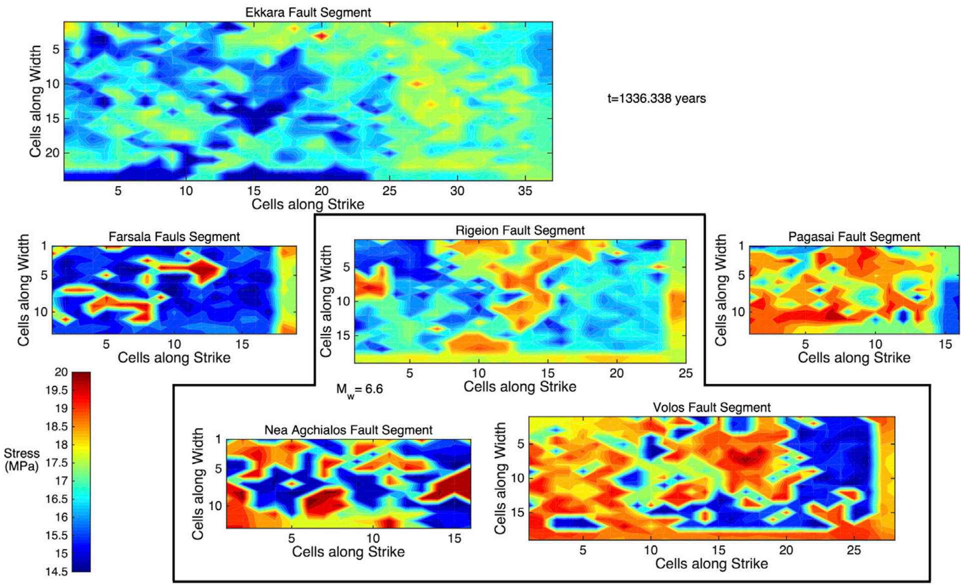

FIGURE 8 | The state of stress (in MPa) in the six fault segments of STFZ at time t = 1,336.338 years, when the Rigeion, Nea Agchialos, and Volos fault segments ruptures simultaneously (black polygon), resulting in a M_w = 6.6 earthquake. The stress value on each cell is depicted with the color bar, ranging from 14.5 MPa (dark blue) to 20 MPa (dark red).

exceed the minimum number of cells as defined previously, then this segment is also assigned to the respective earthquake.

Considering these criteria, 254 ruptures in total are reported in the simulated catalog. Out of them, 169 earthquakes are related with single segment ruptures and 85 are multi segmented ruptures during the 10 kyr of the simulation. The latter number of ruptures can be separated into 38 pairs of simultaneously failed segments and three triplets of multiple ruptures. From the analysis of the ruptures per segment (**Figure 6**), some interesting features are observed. The Ekkara segment is the only one that ruptured alone because it is located in the southwest boundary of STFZ, and it is rather isolated from the other segments. The other five segments (Farsala, Rigeion, Pagasai, Nea Agchialos, and Volos) participate in both single and multiple ruptures with values of maximum magnitude around 6.6 (**Table 4**).

It is worth mentioning that the simulated catalog includes earthquakes in which more than segment has failed. An example is illustrated in **Figure 7** for the first 2 kyr of the simulation and all the resulted multisegmented ruptures are given in **Table 5**. The main pattern of the two segment ruptures is that the neighbor fault segments are simultaneously failed in one earthquake, like the cases of Farsala–Rigeion and Nea Agchialos—Volos ones. There are some cases in which one segment of the northern group ruptured simultaneously with one from the southern group (e.g., the Pagasai—Volos ruptures), and in which the ruptured segments resulted in individual earthquakes with different magnitudes very close in time (e.g. within few seconds), as happened with Rigeion and Pagasai fault segments, that ruptured within a few seconds with magnitudes equal to M_w = 6.3 and M_w = 6.2, respectively (red ellipse in **Figure 7**).

An illustrated example of the state of stress at a certain time illustrates the stress evolution in the six segments of STZF (**Figure 8**). The snapshot is selected to depict the state of stress at t = 1,336.338 years, when the Rigeion, Nea Agchialos, and Volos fault segments ruptured simultaneously (black dashed box of **Figure 7**), resulting in a M_w = 6.6 earthquake. Stress values are rather high (warm colors) within the cells of each fault

TABLE 6 | Statistical parameters of the six segments of the Southern Thessaly Fault Zone as obtained from the best performing simulated catalog (Simulation 79; $A\sigma$ = 0.035 MPa, *S-R* = 0.15, *A-R* = 2) for the $M_{thr} \geq 6.0$ adopted for the recurrence modeling.

Fault segment	**$M_{thr} \geq 6.0$**			
	Obs	***Tr* (years)**	**σ (years)**	**C_v**
Ekkara	70	140.49	56.91	0.40
Farsala	28	350.92	166.46	0.47
Rigeion	47	205.02	109.13	0.53
Pagasai	14	673.88	398.10	0.60
Nea agchialos	22	448.28	275.25	0.62
Volos	67	147.19	53.27	0.36

segment that participate in the rupture (**Figure 8**). One additional remark derived from **Figure 8** is that the stress values of the Pagasai fault segment are also high, indicating that the Pagasai fault segment is also close to a failure. This latter fact was confirmed with a single segment rupture of Pagasai fault segment at $t = 1{,}574.264$ years, resulting in a $M_w = 6.2$ earthquake.

To study the earthquakes' recurrence behavior in each fault segment, the mean recurrence time, T_r, along with its standard deviation (σ) and the corresponding coefficient of variation (C_v) are calculated (**Table 6**). The mean T_r obtained for the $M_{thr} \geq 6.0$ earthquakes of the simulation procedure varies from almost 140–673 years, depending on the segment's long term slip rate values and interactions. The Ekkara, Farsala, Rigeion, and Volos segments exhibit lower values of T_r equal to 140.49, 350.92, 205.02, and 149.19, respectively, since their slip rates are slightly higher than the other ones. Pagasai and Nea Agchialos segments exhibit considerably less frequent strong earthquake occurrence. These two segments could likely be characterized as auxiliary ones, playing a supportive role in stress accumulation and rupture propagation. In all these cases, either for larger or intermediate mean T_r, the values of the coefficient of variation, which range between 0.36 and 0.62 (**Table 6**), show a quasi-periodic recurrence behavior with a slight trend to a less periodic one for the Pagasai and Nea Agchialos fault segments.

In the next step of the recurrence modeling, two different approaches are adopted, aiming to assess whether the strong earthquake occurrence in each segment is better described by a memoryless Poisson process or by a renewal one. The Poisson process can be expressed by the exponential distribution with probability density function (pdf):

$$f(t|T_r) = \frac{1}{T_r}\exp\left\{-\frac{t}{T_r}\right\} \tag{9}$$

where T_r is the mean recurrence time in each data sample. The cumulative density function (cdf) of the exponential distribution is then defined as:

$$F(t) = 1 - \exp\left\{-\frac{t}{T_r}\right\}. \tag{10}$$

For modeling the strong earthquake occurrence as a renewal process, the Brownian Passage Time (BPT) distribution (Matthews et al., 2002) is used. The pdf of the BPT model is given by:

$$f(t|T_r, \alpha) = \left(\frac{T_r}{2\pi\alpha^2 t^3}\right)^{1/2}\exp\left\{-\frac{(t - T_r)^2}{2T_r\alpha t}\right\} \tag{11}$$

where T_r is also the mean recurrence time and α is the aperiodicity, which can be considered as analogous of the coefficient of variation of the normal distribution and represents the level of the randomness model taking values between 0 and 1 ($0 \leq \alpha \leq 1$) to address the physical meaning of the recurrence of strong earthquakes, whereas the cdf is given by:

$$F(t) = \Phi[u_1(t)] + e^{2/a^2}\Phi[-u_2(t)] \tag{12}$$

where $\Phi(\cdot)$ is the cdf of the normal distribution, and u_1 and u_2 are defined as follows:

$$u_1 = a^{-1}\left[t^{1/2}T_r^{-1/2} - t^{-1/2\mathrm{T}_r^{1/2}}\right] \tag{13}$$

$$u_2 = a^{-1}\left[t^{1/2}T_r^{-1/2} + t^{-1/2\mathrm{T}_r^{1/2}}\right]. \tag{14}$$

The comparison of the models is made in terms of their Akaike (Akaike, 1974) Information Criterion given by

$$AIC = -2\ln L + 2k \tag{15}$$

where $\ln L$ and k stands for the value of the log-likelihood function and the number of parameters of the candidate model, respectively. The log-likelihood function of the Poisson process is defined by:

$$\ln L_P = (N-1)\ln\left(\frac{1}{T_r}\right) - \frac{t_0(N)}{T_r} \tag{16}$$

where N is the number of observations and t_0 (N) is the occurrence time of the most remote event of the data sample, whereas the log-likelihood function of the BPT (or any other renewal model) is given by:

$$\ln L_{\mathrm{BPT}} = \sum_{j=1}^{N-1}\ln\left\{\frac{f(\Delta t(j))}{1 - F(t \leq \Delta t(j))}\right\} - \frac{t_0(N)}{T_r} \tag{17}$$

where Δt (j) is the interevent time between the *jth* and the *jth* 1 events and f (Δt) and F ($t \leq \Delta t$) are the pdf and cdf of the BPT distribution, respectively (**Eqs 11**, **12**, respectively).

In this way, the two models are applied in each data sample of interevent times (ΔT) (**Figure 9**) and their corresponding log-likelihood values are calculated (**Table 7**). The results of these calculations reveal that the BPT model performs better than the Poisson model in all cases. In more detail, the BPT model is significantly better than the Poisson in the segments with larger numbers of observations, which are those with the lower values of T_r (Ekkara, Farsala, Rigeion, and Volos) and slightly better in the cases of large values of recurrence time and the larger values of C_v. This better performance of the renewal model adopted in this study suggests that an elastic rebound motivated behavior is more likely than the memoryless one.

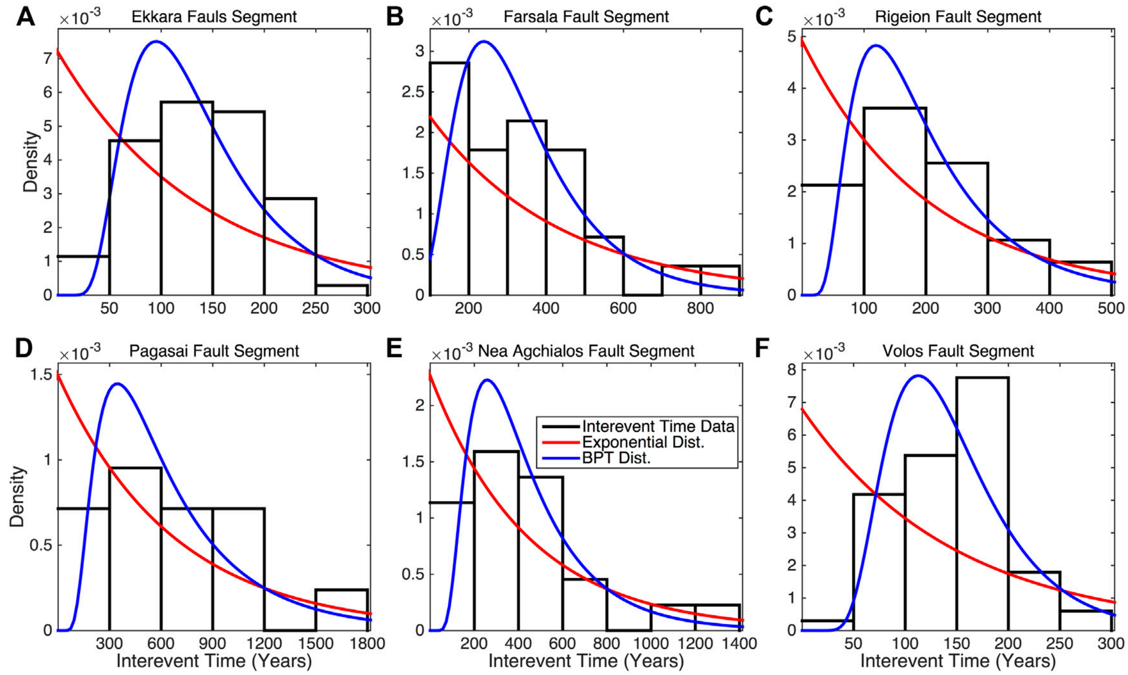

FIGURE 9 | Probability density functions of Poisson (red line) and BPT (blue line) models for the interevent times of strong earthquakes with $M_{thr} \geq 6.0$ for the Ekkara **(A)**, Farsala **(B)**, Rigeion **(C)**, Pagasai **(D)**, Nea Agchialos **(E)**, and Volos **(F)** fault segments. Black boxes indicate the density values of each bin of interevent times.

TABLE 7 | Log-likelihood and AIC calculated values of the Poisson and the Renewal models for the six segments of the Southern Thessaly Fault Zone for the $M_{thr} \geq 6.0$ adopted for the recurrence modeling. Subscripts *P* and *R* indicate the Poisson and the Renewal models, respectively.

Fault segment	lnL_P	lnL_R	AIC$_P$	AIC$_R$
Ekkara	−416.15	−390.48	834.30	784.96
Farsala	−192.09	−179.99	386.18	363.98
Rigeion	−297.18	−283.09	596.36	570.18
Pagasai	−105.18	−101.83	212.36	207.66
Nea agchialos	−156.31	−149.46	314.62	302.92
Volos	−401.44	−364.68	804.88	733.36

Additionally, an analysis of the implications of the BPT model in the strong earthquakes' occurrence per fault segment might be useful, highlighting also differences between the models in the forecasting of strong earthquakes in the near future. This analysis is based on the estimation of the hazard function, $H(t)$, for both the BPT and the Exponential models using the estimated mean recurrence time, T_r, and the corresponding coefficient of variation as obtained from the statistical analysis of the simulated catalog (**Table 5**). The hazard function of a given distribution can be easily evaluated using its corresponding probability density, $f(t)$, and cumulative density, $F(t)$, functions as follows:

$$h(t) = \frac{f(t)}{S(t)} = \frac{f(t)}{1 - F(t)} \tag{18}$$

where $S(t)$ is the survival function. Such an analysis is very useful for concluding future rupture scenarios. Specifically, the values of the hazard function or, in other words, the hazard rate, which is equivalent to the conditional probability estimate in a specific time span, could provide information on potential ruptures in the near future (Convertito and Faenza, 2014; Mangira et al., 2019).

In the current study, **Eq. 18** is applied for both models (**Eqs 9**, **10** for the Exponential and **Eqs 11**, **12** for BPT models, respectively) for each of the six segments of STFZ. The estimated hazard functions are shown in **Figure 10**. Setting $t = 0$ as the occurrence date of the $M_w \geq 6.0$ earthquake, it is derived that in all cases the values of the hazard function of the BPT model (blue lines) are very low soon after the occurrence of the earthquake and then they exhibit an increasing trend with time, taking its maximum value at some finite time close or soon after the mean recurrence time (black dashed lines).

In the cases of low to intermediate aperiodicity (Ekkara Fault Segment; $\alpha = 0.40$, Farsala Fault Segment; $\alpha = 0.47$, Rigeion Fault Segment; $\alpha = 0.53$ and Volos Fault Segment; $\alpha = 0.36$), showing high occurrence probabilities late in the earthquake cycle, flattening of the hazard function curve is achieved soon after the recurrence time. In the cases of higher aperiodicity, namely the Pagasai and Nea Agchialos Fault segments with aperiodicity equal to $\alpha = 0.60$ and $\alpha = 0.62$, respectively, the maximum value is temporally closest to the mean recurrence time, yielding higher values earlier in the seismic cycle. In contrast, the Exponential model returns a constant hazard rate independently of both the mean recurrence time and the calculated elapsed time (until 01–01-2020; green lines) since the last event in each segment.

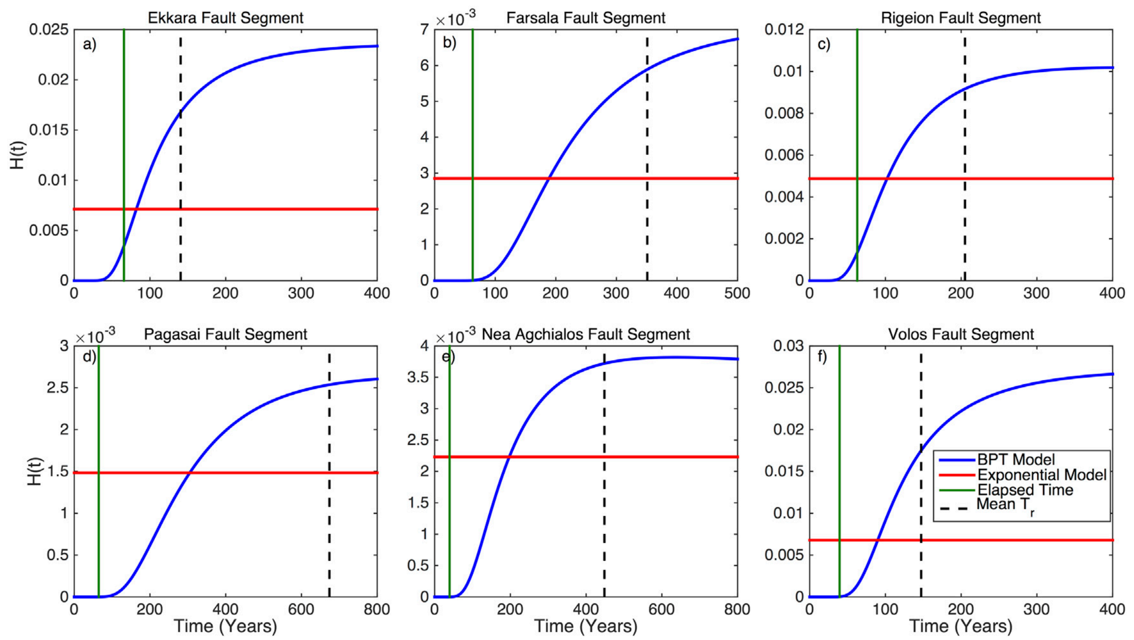

FIGURE 10 | Hazard functions, *h* (*t*), for the Ekkara **(A)**, Farsala **(B)**, Rigeion **(C)**, Pagasai **(D)**, Nea Agchialos **(E)**, and Volos **(F)** Fault SEgments according to the BPT renewal model (blue lines) against the memoryless exponential (red lines) one. Green lines represent the elapsed time since the last earthquake (t = 0), while the dashed black lines the mean T_r of the $M_w \geq 6.0$ as obtained from the statistical analysis of the simulated catalog (**Table 5**) for each one of the six segments.

Considering these results, along with the better performance of the renewal BPT model as resulted from the values of the Information Criteria (**Table 6**), the elastic rebound motivated rupture scenarios is clearly supported. Taking into account this remark and focusing on the mean recurrence time, and the elapsed time in each case, one can conclude that all six segments are far from a future rupture. This fact can be explained by the short elapsed time since the last event per segment, very short for the stress to be rebuilt and culminate in the next strong earthquake. Specifically, the hazard rate is almost zero and considerably far from their maximum values in the cases of Farsala, Pagasai, Nea Agchialos, and Volos fault segments, whereas for the corresponding values of the Ekkara and Rigeion fault segments, both are at the increasing part of their curves but far enough from their mean recurrence times (about 74 and 142 years, respectively) and their pick values.

DISCUSSION AND CONCLUSION

The application of the physics-based simulator algorithm in the STFZ produced a simulated seismic catalog lasting 10 kyr and containing 19,760 events with $M_w \geq 4.1$, from which the 254 corresponds with $M_w \geq 6.0$. This large number of simulated ruptures provides the ability of a thorough study of their recurrence properties o, since the number of observed ones is very limited. In the four out of the six fault segments only one observation is available. For example, only one earthquake with $M_w \geq 6.0$ is known to have occurred since 1700 in the Ekkara fault segment, which is the largest segment with the largest observed earthquake. The simulated catalog manages to resemble the observed seismicity successfully, as its b-value is very close with the value calculated from the observations.

Some mismatches are found between the maximum observed magnitude per segment and the one resulted by the simulation approach. These differences may be ascribed to the fact that the majority of strong earthquakes occurred in the study area in the early instrumental period, the magnitudes of which are possibly overestimated. Such cases are the magnitudes of the 1954 and 1958 earthquakes with M_w = 7.0 and M_w = 6.8 that occurred in the Ekkara and Rigeion segments, respectively. By assessing the ISC-GEM instrumental earthquake catalog, these earthquakes are found to be reported with magnitudes equal to M_w = 6.66 and M_w = 6.40, in agreement with those of the simulated catalog.

Emphasizing on the strong earthquakes, both single and multiple segment ruptures are found in the simulated catalog. The multiple segment ruptures can be distinguished into two and three segment ruptures, with the majority of them be composed of two segments. This fact could be ascribed to the similarity of their long-term slip rates that promotes the participation of more than one segment in simultaneous ruptures. This conclusion is in agreement with the study of Scholz 2019, who suggests that the fault synchronization and rupture jumping phenomena are more likely in segments with equal or similar slip rate values.

The mean recurrence time, T_r, for the selected magnitude threshold, $M_{thr\_} \geq 6.0$ can be separated in to classes, depending on the fault segments. The four segments with larger areas (larger L and W), namely the Ekkara, Farsala, Rigeion, and Volos, exhibit relatively moderate T_r values ranging from 140 to 350 years and values of C_v revealing a high periodic occurrence ($0.36 \leq C_v \leq$

0.53). The other class includes the two fault segments of Pagasai and Nea Agchialos, whose mean recurrence times are quite large. This latter class of segments could probably be characterized as auxiliary, since these segments participate more frequently in multiple ruptures. A remarkable feature of these two segments is that they exhibit more aperiodic behavior with values of C_v around 0.6 (**Table 6**). This behavior could be explained by the fact that the reset of stress possibly results in a delay in the strong earthquake occurrence.

The application of the Poisson model against the BPT model in interevent times of earthquakes with $M_{thr\_}\geq 6.0$ reveals a considerably better performance of the renewal BPT model than the memoryless Poisson model in all fault segments of the STFZ, which is in agreement with the elastic rebound theory (Reid, 1911, and a rather quasi-periodic recurrence behavior, as derived from the analysis of their hazard functions in combination with the elapsed time since the last event per segment. It should be mentioned that these results are independent from the algorithm itself, since its operates without any assumption related with the temporal occurrence of the earthquakes. As a consequence, the comparison among the statistical models are applied without a null hypothesis that could promote one model against the other.

DATA AVAILABILITY STATEMENT

The raw data supporting the conclusions of this article will be made available by the authors, without undue reservation.

AUTHOR CONTRIBUTIONS

CK has treated the data, applied the simulator algorithm and organized writing of the paper RC has developed the simulator algorithm, checked the application, interpreted the data and contributed to the writing of the paper EP has selected the study area and data, supervised the application, interpreted the data and contributed to the writing of the paper MM supervised the application, interpreted the data and contributed to the writing of the paper VK supervised the application, interpreted the data and contributed to the writing of the paper. All the authors contributed to the article and approved the submitted version.

FUNDING

The first author would like to acknowledge the financial support of the project "HELPOS—Hellenic System for Lithosphere Monitoring" (MIS 5002697) which is implemented under the Action "Reinforcement of the Research and Innovation Infrastructure", funded by the Operational Programme "Competitiveness, Entrepreneurship, and Innovation" (NSRF 2014-2020) and co-financed by Greece and the European Union (European Regional Development Fund).

ACKNOWLEDGMENTS

We greatly appreciate the editorial assistance of Prof. B. Presti, as well as the constructive comments of Dr. J. Woessner and Dr. M. Mesimeri that contributed to the improvement of the manuscript. The historical and instrumental earthquake catalogs of the Geophysics Department of the Aristotle University of Thessaloniki (http:/geophysics.geo.auth.gr/ss) and the instrumental ISC-GEM catalog provided by the International Seismic Centre, 2019 http://www.isc.ac.uk/iscgem/index are used in this study. The maps and graphs are generated using the GMT software (Wessel et al., 2013) and MATLAB software (http://www.mathworks.com/products/matlab). NOA active fault database (version 3.0; doi:10.5281/zenodo.4304613) is accessible from https://noa-beyondapps.maps.arcgis.com/. Fault plane solutions' data used in this paper came from resources listed in the References Section. Geophysics Department Contribution 942.

SUPPLEMENTARY MATERIAL

The Supplementary Material for this article can be found online at: https://www.frontiersin.org/articles/10.3389/feart.2021.596854/full#supplementary-material.

REFERENCES

Akaike, H. (1974). A new look at the statistical model identification. *IEEE Trans. Autom. Control, AC-* 19, 716–723. doi:10.1109/tac.1974.1100705

Aki, K. (1965). Maximum likelihood estimation of b in the formula log n = a − bm and its confidence limits. *Bull. Earthq. Res. Inst. Tokyo Univ.* 43, 237–239.

Ambraseys, N. (2009). *Earthquakes in eastern mediterranean and the Middle East: a multidisciplinary study of 2000 Years of seismicity*. Cambridge, U.K.: Cambridge University Press, 947.

Ambraseys, N. N., and Jackson, J. A. (1990). Seismicity and associated strain of central Greece between 1890 and 1988. *Geophys. J. Intell.* 101, 663–708. doi:10.1111/j.1365-246x.1990.tb05577.x

Argyrakis, P., Ganas, A., Valkaniotis, S., Tsioumas, V., Sagias, N., and Psiloglou, B. (2020). Anthropogenically induced subsidence in Thessaly, central Greece: new evidence from GNSS data. *Nat. Hazards* 102, 179–200. doi:10.1007/s11069-020-03917-w

Aristotle University of Thessaloniki (1981). Aristotle University of Thessaloniki seismological network. *Inter. Fed. Dig.Seis. Net.* doi:10.7914/SN/HT

Biasi, G. P., Langridge, R. M., Berryman, K. R., Clark, K. J., and Cochran, U. A. (2015). Maximum-likelihood recurrence parameters and conditional probability of a ground-rupturing earthquake on the southern Alpine fault, South Island, New Zealand. *Bull. Seismol. Soc. Am.* 105, 96–106. doi:10.1785/0120130259

Biasi, G. P., and Thompson, S. C. (2018). Estimating time-dependent seismic hazard of faults in the absence of an earthquake recurrence record. *Bull. Seismol. Soc. Am.* 108, 39–50. doi:10.1785/0120170019

Caputo, R., and Pavlides, S. (1993). Late Caenozoic geodynamic evolution of Thessaly and surroundings (central-northern Greece). *Tectonophysics* 223, 339–362. doi:10.1016/0040-1951(93)90144-9

Caputo, R., and Pavlides, S. (2013). *The Greek Database of seismogenic sources (GreDaSS), version 2.0.0: a compilation of potential seismogenic sources (Mw > 5.5) in the aegean region*. doi:10.15160/unife/gredass/0200

Caputo, R. (1996). The active Nea Anchiale fault system (Central Greece): comparison of geological, morphotectonic, archaeological and seismological data. *Ann. Geofisc.* 39, 557–574.

Christophersen, A., Rhoades, D. A., and Colella, H. V. (2017). Precursory seismicity in regions of low strain rate: insights from a physical-based earthquake simularor. *Geophys. J. Int.* 209, 1513–1525. doi:10.1093/gji/ggx104

Console, R., Carluccio, R., Papadimitriou, E., and Karakostas, V. (2015). Synthetic earthquake catalogs simulating seismic activity in the Corinth Gulf, Greece, fault system. *J. Geophys. Res.* 120, 326–343. doi:10.1002/2014JB011765

Console, R., Chiappini, M., Minelli, L., Speranza, F., Carluccio, R., and Greco, M. (2018b). Seismic hazard in southern Calabria (Italy) based on the analysis of a synthetic earthquake catalog. *Acta Geophys.* 66, 931–943. doi:10.1007/s11600-018-0181-7

Console, R., Murru, M., Vannoli, P., Carluccio, R., Taroni, M., and Falcone, G. (2020). Physics-based simulation of sequences with multiple mainshocks in Central Italy. *Geophys. J. Int.* 223, 526–542. doi:10.1093/gji/ggaa300

Console, R., Nardi, A., Carluccio, R., Murru, M., Falcone, G., and Parsons, T. (2017). A physics-based earthquake simulator and its application to seismic hazard assessment in Calabria (Southern Italy) region. *Acta Geophys.* 65, 243–257. doi:10.1007/s11600-017-0020-2

Console, R., Vannoli, P., and Carluccio, R. (2018a). The seismicity of Central Apennines (Italy) studied by means of a physics-based earthquake simulator. *Geophys. J. Int.* 212, 916–929. doi:10.1093/gji/ggx451

Convertito, V., and Faenza, L. (2014). "Earthquake recurrence," in *Encyclopedia of earthquake engineering*. Editors M. Beer, I. A. Kougioumtzoglou, E. Patelli, and I. Siu-Kui Au (Berlin, Germany: Springer), 1–22. doi:10.1007/978-3-642-36197-5-236-1

Davis, R., England, P., and Parsons, B. (1997). Geodetic strain of Greece in the interval 1892-1992. *J. Geophys. Res.* 102 (24), 571–624. doi:10.1029/97jb02378

Dieterich, J. H. (1994). A constitutive law for rate of earthquake production and its application to earthquake clustering. *J. Geophys. Res.* 99, 2601–2618. doi:10.1029/93jb02581

Drakos, A., Stiros, S. C., and Kiratzi, A. A. (2001). Fault parameters of the 1980 (Mw 6.5) Volos, Central Greece, earthquake from inversion of repeated leveling data. *Bull. Seismol. Soc. Am.* 91 (6), 1673–1684. doi:10.1785/0120000232

Ellsworth, W. L., Matthews, M. V., Nadeau, R. M., Nishenko, S. P., Reasenberg, P. A., and Simpson, R. W. (1999). A physically based earthquake recurrence model for estimation of long-term earthquake probabilities. *U.S. Geol. Surv. Open-File Rept.*, 99–522.

Field, E. H. (2015). Computing elastic-rebound-motivated earthquake probabilities in unsegments fault models: a new methodology supported by physics-based simulators. *Bull. Seismol. Soc. Am.* 105, 544–559. doi:10.1785/01201140094

Fitzenz, D. D. (2018). Conditional probability of what? Example of nankai interface in Japan. *Bull. Seismol. Soc. Am.* 108 (6), 3169–3179. doi:10.1785/0120180016

Galanakis, D., Pavlidis, S., and Mountrakis, D. (1998). Recent brittle tectonic in almyros-pagasitikos, Maliakos, N. Euboea and pilio. *Bull. Geol. Soc. Greece* XXXXII/1, 263–273.

Ganas, A., Oikonomou, I. A., and Tsimi, C. (2013). NOAFAULTS: a digital database for active faults in Greece. *Bull. Geol. Soc. Greece* 47 (2), 518–530. doi:10.12681/bgsg.11079

Goldsworthy, M., Jackson, J., and Haines, J. (2002). The continuity of active faults systems in Greece. *Geophys. J. Int.* 148, 596–618. doi:10.1046/j.1365-246x.2002.01609.x

Goldsworthy, M., and Jackson, J. A. (2000). Active normal fault evolution and interaction in Greece revealed by geomorphology and drainage patterns. *J. Geol. Soc. Lond.* 157, 967–981. doi:10.1144/jgs.157.5.967

Harris, R. A. (1998). Introduction to special section: stress triggers, stress shadows, and implications for seismic hazard. *J. Geophys. Res.* 103, 24. 346–24, 358. doi:10.1029/98JB01576/

Harris, R. A., and Simpson, R. W. (1998). Suppression of large earthquakes by stress shadows: a comparison of Coulomb and rate-and-state failure. *J. Geophys. Res.* 103, 24, 439–24,451. doi:10.1029/98JB00793.

Hatzfeld, D., Ziazia, M., Kementzetzidou, D., Hatzidimitriou, P., Panagiotopoulos, D., Makropoulos, K., et al. (1999). Microseismicity and focal mechanisms at the western termination of the North Anatolian Fault and their implications for continental tectonics. *Geophys. J. Int.* 137, 891–908. doi:10.1046/j.1365-246x.1999.00851.x

International Seismological Centre (2019). *ISC-GEM earthquake catalogue*. doi:10.31905/d808b825

Jenny, S., Goes, S., Giardini, D., and Kahle, H.-G. (2004). Earthquake recurrence parameters from seismic and geodetic strain rates in the eastern Mediterranean. *Geophys. J. Intell.* 157, 1331–1347. doi:10.1111/j.1365.246X.2004.02261.x

Mangira, O., Console, R., Papadimitriou, E., Murru, M., and Karakostas, V. (2020). The short-term seismicity of the Central Ionian Islands (Greece) studied by means of a clustering model. *Geophys. J. Int.* 220, 856–875. doi:10.1093/gji/ggz481

Mangira, O., Kourouklas, C., Chorozoglou, D., Iliopoulos, A., and Papadimitriou, E. (2019). Modeling the earthquake occurrence with time-dependent processes: a brief review. *Acta Geophys.* 67, 739–752. doi:10.1007/s11600-019-00284-4

Mann, H. B., and Whitney, D. R. (1947). On a test of whether one of two random variables is stochastically larger than the other. *Ann. Math. Stat.* 18 (1), 50–60. doi:10.1214/aoms/1177730491

McKenzie, D. (1972). Active tectonics of the mediterranean region. *Geophys. J. Int.* 30, 109–185. doi:10.1111/j.1365-246X.1972.tb02351.x

Mountrakis, D., Kilias, A., Pavlides, S., Zouros, N., Spyropoulos, N, Tranos, M., and Soulakelis, N. (1993). "Field study of the southern Thessaly highly active fault zone," in Proc. 2nd Congr. Hellenic Geophys. Union, 2, 603-614.

Leonard, M. (2010). Earthquake fault scaling: relating rupture length, width, average displacement, and moment release. *Bull. Seismol. Soc. Am.* 100(5A). 1971–1988. doi:10.1785/0120090189.

Muller, M. D., Geiger, A., Kahle, H.-G., Veis, G., Billiris, H., Paradissis, D., et al. (2013). Velocity and deformation fields in the North Aegean domain, Greece, and implications for fault kinematics, derived from GPS data 1993-2009, *Tectonophysics*, 597–598, 34–49. doi:10.1016/j.tecto.2012.08.003

Ogata, Y. (2002). Slip-size-dependent renewal process and Bayesian inferences for uncertainties. *J. Geophys. Res.* 107(B11). 2268. doi:10.1029/2001JB9000668

Pace, B., Visini, F., and Peruzza, L. (2016). FiSH: MATLAB Tools to turn fault data into seismic-hazard models. *Seismol Res. Lett.* 87, 374–386. doi:10.1785/0220150189

Papadimitriou, E., and Karakostas, V. (2003). Episodic occurrence of strong (Mw≥6.2) earthquakes in Thessalia area (central Greece). *Earth Planet Sci. Lett.* 215, 395–409. doi:10.1016/S0012-812X(03)00456-4

Papastamatiou, D., and Mouyaris, N. (1986). The earthquake of april 30, 1954, in Sofades (Central Greece). *J. R. Astron. Soc.* 87, 885–895. doi:10.1111/j.1365-246x.1986.tb01975.x

Papazachos, B., and Papazachou, C. (2002). *The earthquakes of Greece*. Ziti Publications.

Papazachos, B. C., and Comninakis, P. E. (1971). Geophysical and tectonic features of the Aegean arc. *J. Geophys. Res.* 76, 8517–8533. doi:10.1029/jb076i035p08517

Papazachos, B. C., and Comninakis, P. E. (1970). Geophysical features of the Greek island arc and eastern Mediterranean ridge. *Com. Ren. Des Sceances la Conf. Reunie a Madrid* 16, 74–75.

Papazachos, B. C., Hatzidimitriou, P. M., Karakaisis, G. F., Papazachos, C. B., and Tsokas, G. N. (1993). Rupture zones and active crustal deformation in southern Thessaly, central Greece. *Boll. Geof. Teor. Appl.* 139, 363–374.

Papazachos, B.C., Mountrakis, D.M., Papazachos, C.B., Tranos, M.D., Karakaisis, G.F., and Savvaidis, A.S., (2001). "The faults that caused the known strong earthquakes in Greece and surrounding areas during 5th century B.C. up to present,"in 2nd Conf. Earthq. Eng. Eng. Seism., September 2–30 2001, Thessaloniki, Greece, 17-26.

Papazachos, B. C., Panagiotopoulos, D. G., Tsapanos, T. M., Mountrakis, D. M., and Dimopoulos, G. Ch. (1983). A study of the 1980 summer seismic sequence in the Magnesia region of central Greece. *J. R. Astron. Soc.* 75, 155–168. doi:10.1111/j.1365-246x.1983.tb01918.x

Papazachos, B. C., Papadimitriou, E. E., Kiratzi, A. A., Papazachos, C. B., and Louvari, E. K. (1998). Fault plane solutions in the Aegean Sea and the surrounding area and their tectonic implications. *Boll. Geof. Teor. App.* 39, 199–218.

Papazachos, B. C., Scordilis, M. E., Panagiotopoulos, D. G., Papazachos, C. B., and Karakaisis, G. F. (2004). Global relations between seismic fault parameters and moment magnitude of earthquakes. *Bull. Geol. Soc. Greece* 36 (3), 1482–1489. doi:10.12681/bgsg.16538

Papazachos, G., Papazachos, C., Skarlatoudis, A., Kkallas, H., and Lekkas, E. (2016). Modelling macroseismic observations for historical earthquakes: the cases of the *M*=7.0, 1954 Sofades and *M*=6.8, 1957 Velestino events (central Greece). *J. Seismol.* 20, 151–165. doi:10.1007/s10950-015-9517-9

Perissoratis, C., Angelopoulos, I., Mitropoulos, D., and Michailidis, S. (1991). *Surficial sediment map of the Aegean Sea floorScale 1:200,000*. Athens: Pagasitikos sheet, IGME.

Reid, H. F. (1911). The elastic-rebound theory of earthquakes, Univ. *Calif. Pub. Bull. Dept. Geol. Sci.* 6, 413–444.

Rice, J. R. (1992). Fault stress states, pore pressure distributions, and the weakness of the San Andreas fault. In Fault mechanics and transport properties of rocks; a festschrift in honour of W. F. Brace. Editors *B. Evans and T. Wong.* . San Diego, CA, USA: Academic Press, 475–503.

Richards-Dinger, K., and Dieterich, J. H. (2012). RSQSim earthquake simulator. *Seismol Res. Lett.* 83, 983–990. doi:10.1785/0220120105

Roberts, G. P., and Ganas, A. (2000). Fault-slip directions in central and southern Greece measured from striated and corrugated fault planes: comparison with focal mechanism and geodetic data. *J. Geophys. Res.* 105 (23). 443–462. doi:10.1029/1999jb900440

Roberts, G. P. (1996). Variations in fault slip directions along active and segmented normal fault systems. *J. Struct. Geol.* 18, 835–845. doi:10.1016/s0191-8141(96)80016-2

Robinson, R., and Benites, R. (1996). Synthetic seismicity models for the Wellington Region, New Zealand: implications for the temporal distribution of large events. *J. Geophys. Res.* 101 (27), 833–844. doi:10.1029/96jb02533

Robinson, R., Van Dissen, R., and Litchfield, N. (2011). Using synthetic seismicity to evaluate seismic hazard in the Wellington region, New Zealand. *Geophys. J. Int.* 187, 510–528. doi:10.1111/j.1365-246X.2011.05161.x

Rundle, J. B. (1988). A physical model for earthquakes. 2. Application to southern California. *J. Geophys. Res.* 93, 6255–6274. doi:10.1029/jb093ib06p06255

Sachs, M. K., Yikilmaz, M. B., Heien, E. M., Rundle, J. B., Turcotte, D. L., and Kellogg, L. H. (2012). Virtual California earthquake simulator. *Seismol Res. Lett.* 83, 973–978. doi:10.1785/0220120052

Scholz, C. H. (2019). *The mechanics of earthquake and faulting*. 3rd edn. Cambridge University Press, 504.

Schultz, K. W., Yoder, M. R., Wilson, J. M., Heien, E. M., Sachs, M. K., Rundle, J. B., et al. (2017). Parametrizing physics-based earthquake simulations. *Pure Appl. Geophys.* 174, 2269–2278. doi:10.1007/s00024-016-1428-3

Shaw, B. E., Milner, K. R., Field, E. H., Richards-Dinger, K., Gilchrist, J. J., Dieterich, J. H., et al. (2018). A physics-based simulator replicates seismic hazard statistics in California. *Sci. Adv.* 4 (8). doi:10.1126/sciadv.aau0688

Stephens, M. A. (1974). EDF statistics for goodness of fit and some comparisons. *J. Am. Stat. Assoc.* 64 (374), 730–737. doi:10.2307/2286009

Sykes, L. R., and Menke, W. (2006). Repeat times of large earthquakes: implications for earthquake mechanics and long-term prediction. *Bull. Seismol. Soc. Am.* 96, 1569–1596. doi:10.1785/0120050083

Toda, S., and Stein, R. S. (2003). Toggling of seismicity by the 1997 Kagoshima earthquake couplet: a demonstration of time-dependent stress transfer. *J. Geophys. Res.* 108 (B12). 2567. doi:10.1019/2003JB002527

Tullis, T. E. (2012a). Preface to the focused issue on earthquake simulators. *Seismol Res. Lett.* 83, 957–958. doi:10.1785/0220120122

Ward, S. N. (2012). ALLCALL earthquake simulator. *Seismol Res. Lett.* 83, 964–972. doi:10.1785/0220120056

Wells, D. L., and Coppersmith, K. J. (1994). New empirical relationships among magnitude, rupture length, rupture width, rupture area, and surface displacement. *Bull. Seismol. Soc. Am.* 84, 974–1002.

Wesnousky, S. G. (2008). Displacement and geometrical characteristics of earthquake surface ruptures: Issues and implications for seismic hazard analysis and the process of earthquake rupture. *Bull. Seismol. Soc. Am.* 98(4). 1609–1632. doi:10.1785/0120070111

Wessel, P., Smith, W. H. F., Scharroo, R., Luis, J., and Wobbe, F., (2013). Generic mapping tools: improved version released. *EOS Trans. Am. Geophys. Union*, 94, 409-410. doi:10.1002/2013eo450001

Wiemer, S., and Wyss, M. (2000). Minimum magnitude of completeness in earthquake catalogs: examples from Alaska, the western United States, and Japan. *Bull. Seismol. Soc. Am.* 90, 859–869. doi:10.1785/0119990114

Wilcoxon, F. (1945). Individual comparison by ranking methods. *Biometrics* 1 (6), 80–83. doi:10.2307/3001968

Yikilmaz, M. B., Turcotte, D. L., Yakovlev, G., Rundle, J. B., and Kellog, L. H. (2010). Virtual California earthquake simulations: simple models and their application to an observed sequence of earthquakes. *Geophys. J. Int.* 180, 734–742. doi:10.1111/j.1365-246X.2009.04435

Conflict of Interest: The authors declare that the research was conducted in the absence of any commercial or financial relationships that could be construed as a potential conflict of interest.

frontiers
in Earth Science

ORIGINAL RESEARCH
published: 31 March 2021
doi: 10.3389/feart.2021.586152

Crustal Configuration and Seismic Stability of the Eastern Indian Shield and Adjoining Regions: Insights for Incidents of Great Earthquakes in the Nepal-Bihar-Sikkim Himalaya

Rashmi Singh and Prosanta Kumar Khan*

Department of Applied Geophysics, Indian Institute of Technology (Indian School of Mines) Dhanbad, Dhanbad, India

The Eastern Indian Shield (EIS) is comprised of the intracratonic (coal-bearing) Damodar Gondwana basin, rift-controlled extensional Lower Gangetic basin (LGB), and the downward flexed Indo-Gangetic basin (IGB). The present study involves the computations and mapping of the basement configuration, sediment thickness, Moho depth, and the residual isostatic gravity anomaly, based on 2-D gravity modeling. The sediment thickness in the area ranges between 0.0 and 6.5 km, and the Conrad discontinuity occurs at ∼17.0–20 km depth. The depth of the Moho varies between 36.0 and 41.5 km, with the maximum value beneath the Upper Gangetic basin (UGB), and the minimum of ∼36 km (uplifted Moho) in the southeastern part beneath the LGB. The maximum residual isostatic anomaly of +44 mGal in the southern part indicates the Singhbhum shear zone, LGB, and Rajmahal trap to be under-compensated, whereas the northern part recording the minimum residual isostatic anomaly of –87.0 mGal is over-compensated. Although the region experienced a few moderate-magnitude earthquakes in the past, small-magnitude earthquakes are sparsely distributed. The basement reactivation was possibly associated with a few events of magnitudes more than 4.0. Toward the south, in the Bay of Bengal (BOB), seismic activities of moderate size and shallow origin are confined between the aseismic 85 and 90°E ridges. The regions on the extreme north and south [along the Himalaya and the equatorial Indian Ocean (EIO)] are experienced moderate-to-great earthquakes over different times in the historical past, but the intervening EIS and the BOB have seismic stability. We propose that the two aseismic ridges are guiding the lithospheric stress fields, which are being further focused by the basement of the EIS, the BOB, and the N-S extended regional fault systems into the bending zone of the penetrating Indian lithosphere beneath the Himalaya. The minimum obliquity of the Indian plate and the transecting fault systems in the Foothills of the Himalaya channelize and enhance the stress field into the bending zone. The enhanced stress generates great earthquakes in the Nepal-Bihar-Sikkim Himalaya, and on being reflected back through the apparently stable EIS and BOB, the stress field creates deformation and great earthquakes in the EIO.

Keywords: gravity modeling, spectral analysis, crustal discontinuity, Eastern Indian Shield, isostasy

Edited by:
Sebastiano D'Amico,
University of Malta, Malta

Reviewed by:
Santanu Baruah,
North East Institute of Science and Technology (CSIR), India
Daniele Spatola,
University of Malta, Malta

****Correspondence:***
Prosanta Kumar Khan
khanprosanta1966@iitism.ac.in;
khanprosanta1966@gmail.com

Specialty section:
This article was submitted to Solid Earth Geophysics, a section of the journal Frontiers in Earth Science

Received: *22 July 2020*
Accepted: *09 March 2021*
Published: *31 March 2021*

Citation:
Singh R and Khan PK (2021) Crustal Configuration and Seismic Stability of the Eastern Indian Shield and Adjoining Regions: Insights for Incidents of Great Earthquakes in the Nepal-Bihar-Sikkim Himalaya. Front. Earth Sci. 9:586152. doi: 10.3389/feart.2021.586152

INTRODUCTION

Occasional incidents of major damaging earthquakes, such as 2015 (Mw 7.8) Nepal-Bihar, 2011 (Mw 6.9) Sikkim, 1988 (Mw 6.8) north Bihar, 1934 (Mw 8.0) north Bihar-Nepal, and 1833 (M_L 7.6) Nepal-Bihar, account continued accumulation and occasionally release of strain energy in the Nepal-Bihar-Sikkim part of the Himalayas (Ansari et al., 2014; Khan et al., 2017a; Singh et al., 2020). The adjacent area of the Eastern Indian Shield (EIS) also experienced a number of moderate-magnitude earthquakes, such as 1868 (M5.7) Manbhum, 1868 (M 5.0) Hazaribagh, 1963 (M 5.0) Ranchi, and 1969 (M5.7) Bankura (Chandra, 1977; Kayal et al., 2009; Gupta et al., 2014; Rastogi, 2016). The earthquakes occurring in the EIS and adjacent areas (**Figures 1**, **2**) are linked with the continued convergence of the Indian plate beneath the Himalaya (Khan et al., 2020; Singh et al., 2020). Toward the north, the Gangetic foredeep, the Himalayan Frontal Thrust (HFT), West Patna Fault (WPF), East Patna Fault (EPF), and Munger-Saharsa Ridge Fault (MSRF) are the main structural discontinuities; these run either parallel or orthogonal to the southern border of the Nepal Himalaya (**Figure 2**). A few of these features, along with other transecting faults, have shown strike-slip dominated movements during the Holocene period (Sastri et al., 1971; Valdiya, 1976; Ansari et al., 2014; Khan et al., 2014; Singh et al., 2020). Such operative dynamics and kinematics toward the south of the Himalayan Foothills, compatible with the back propagation of the compressive stress field, facilitated deformation in the EIS, and the effects were likely extended up to the Central Indian basin (McKenzie and Sclater, 1971; Minster and Jordan, 1978; Stein and Okal, 1978; Gordon et al., 1990; DeMets et al., 1994).

The present study was undertaken at the core of the EIS, which occupies portions of four Indian states—Bihar, Jharkhand, Orissa, and West Bengal—to investigate the link between the regional geodynamic processes and earthquake occurrences. Besides the tectonic features mentioned above, the eastern part of the EIS is associated with the Rajmahal Trap and several faults striking N-S (e.g., Pingla fault, Sainthia Bahamani fault, and GKGF faults). The core (central part) of the EIS has ∼ E-W striking regional shear zones such as the North Purulia, South Purulia, and Singhbhum (**Figure 2**). Thus, the area is tectonically very important for its location, and is essentially a geological corridor to the Eastern Himalaya and the Indo-Myanmar Ranges. The present study therefore was carried out to delineate the basement configuration and the Conrad and Mohorovičić (Moho) discontinuities based on analysis of the gravity anomalies. The detailed gravity modeling and mapping and the historical earthquake data available for the region were used for exploring the level of seismic stability at different locations of the study region.

The Moho depth for several small blocks of the EIS was determined by several studies (Choudhury, 1974; Verma et al., 1976, 1980; Bhattacharya and Shalivahan, 2002; Singh et al., 2004, 2015; Kayal et al., 2011; Sharma et al., 2015). All these investigations were constrained by an insufficient coverage of dataset and smaller sizes of the areas. The outcomes of these investigations provide valuable information regarding the crustal structure (discussed below).

The residual gravity analysis over the Raniganj Coalfield area (∼6 × 10^3 km^2) shows a gravity low of around –32 mGa1 associated with the Gondwana sediments, with a maximum estimated sediment thickness of ∼2 km (Verma et al., 1976). Gravity field analysis of North Singhbhum (∼36 × 10^3 km^2 area) could delineate the Bouguer anomalies of +4 to −62 mGal, with the estimated thickness of the basin, based on a 2D gravity model, of about 6–7 km (Verma et al., 1980). An analysis of free air, Bouguer, and isostatic anomalies over a part of the shield near the Gaya region shows a 6.6 km thick sediment layer underneath the Lower Gangetic basin (LGB). Compiling datasets from a few stations, a crustal thickness of 42.5 km underneath the northern part of the shield, 31.5 km underneath the Indo-Gangetic basin (IGB), and 81 km underneath the Higher Himalaya of Nepal-Bihar region were also estimated by Qureshy (1969). While the Bouguer gravity analysis, carried out by Choudhury (1974), for the Indo-Gangetic Plain and the northern Himalayan region, shows a crustal thickness of ∼35–37 and ∼70–72 km, respectively. A magnetotelluric study reports 40 km deeper Moho beneath the Singhbhum granite and adjoining regions (Bhattacharya and Shalivahan, 2002). Receiver function analysis of P-wave gives a depth of ∼41–42 km for the Moho and ∼20 km for the Conrad discontinuity below the IIT (ISM), Dhanbad seismic station (Kayal et al., 2011; Sharma et al., 2015). A 2D gravity modeling study shows that the Moho depth varies from ∼38 km below the Rajmahal Traps to ∼40 km near the Raniganj region (Singh et al., 2004). Lithospheric 3D mapping of the EIS shows that the Moho ranges from ∼35 to 40 km near Mahanadi, Damodar, and LGB (Singh et al., 2015). For a regional scale, Bouguer gravity anomalies can reflect the changes in mass disseminations between the lower crust and the upper mantle, and the isostatic stability (Tealeb and Riad, 1986). Bouguer anomalies and surface relief are also closely connected with the crustal thickness (Coron, 1969; Woollard, 1969; Pick et al., 1973; Riad et al., 1983; Riad and El-Etr, 1985). In the present study, the Bouguer gravity anomaly data and the geophysical parameters of various studies (Choudhury, 1974; Verma and Ghosh, 1977; Verma, 1985; Singh et al., 2004) were used to deduce the regional structural framework of the shallow basement, overlying sedimentary cover, and the Conrad and Moho discontinuities. The present study also attempts to visualize the crustal balance in terms of isostasy. Isostatic study of continents accounts for the mechanical balance of lithosphere at the time of loading (Watts et al., 1980; Djomani et al., 1992) and links to the deep-density structure, providing constraints on the geological model (Simpson et al., 1986).

TECTONIC SET-UP

The study area comprises the northern portion of the Singhbhum craton, the Chhotanagpur gneissic complex, and the southern portion of the Himalayas (**Figure 1**). The area is bounded by the Eastern Ghats mobile belt on the south and the Himalayan foothills on the north. The Gangetic alluvium and the

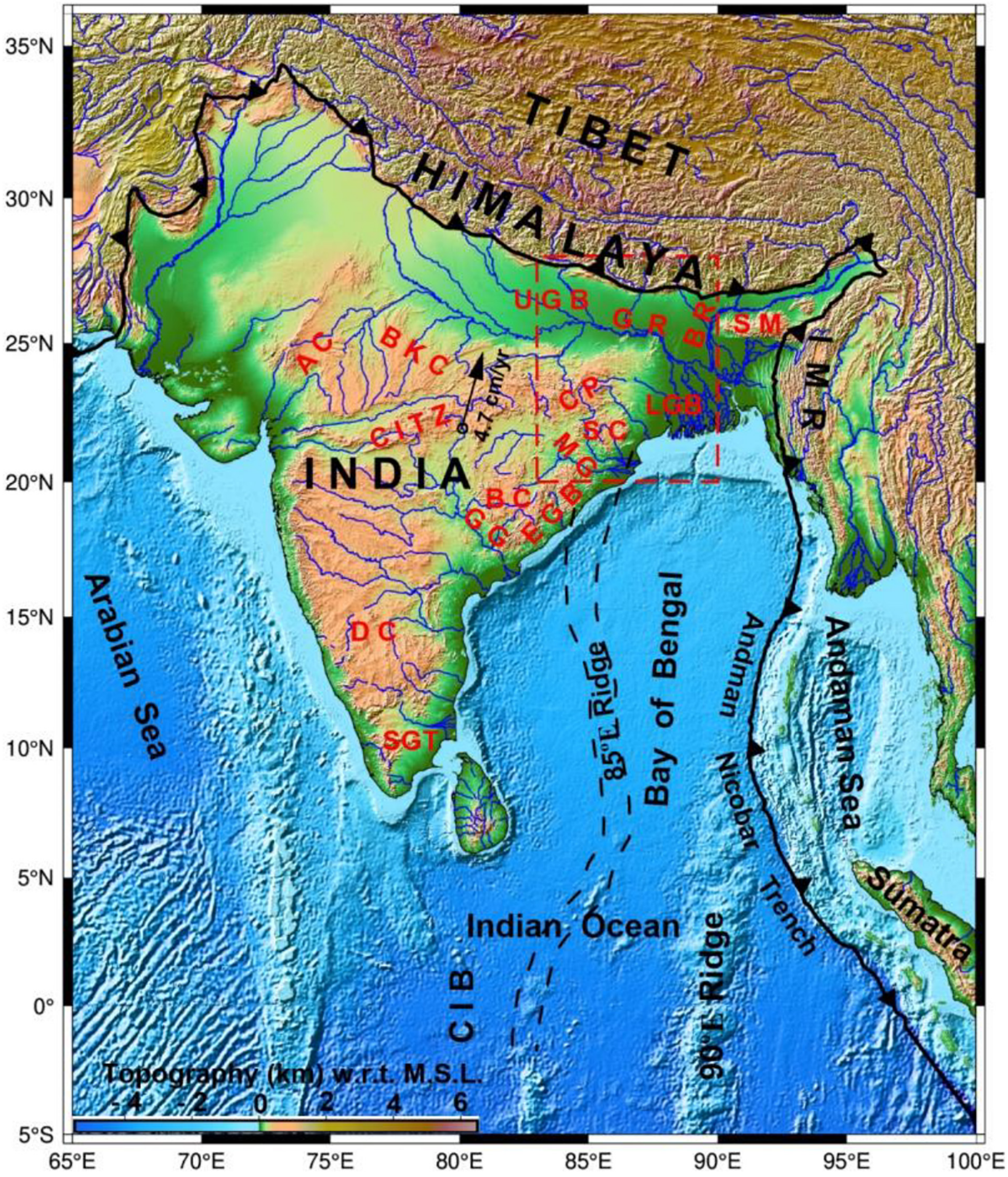

FIGURE 1 | Regional map (reconstructed after Khan et al., 2017b; Valdiya and Sanwal, 2017; Altenbernd et al., 2020) showing the location of the study area (rectangular block demarcated by red dashed line). Abbreviations: AC, Aravalli Craton; BKC, Bundelkhand Craton; CITZ, Central India Tectonic Zone; EGB, Eastern Ghats Belt; CP, Chhotanagpur Plateau; SC, Singhbhum Craton, BC, Bastar Craton; DC, Dharwar Craton; SGT, Southern Granulite Terrain; MG, Mahanadi Graben; GG, Godavari Graben; SM, Shillong Massif; IMR, Indo-Myanmar Range; GR, Ganga River; UGB, Upper Gangetic Basin; LGB, Lower Gangetic Basin; BR, Brahmaputra River.

Quaternary sediments of LGB border its eastern part, whereas the western part is bordered by the Gondwana sediments of the Sone-Mahanadi basin. The Upper Jurassic to lower Cretaceous basalts form the Rajmahal Traps, at the contact zone of the Chhotanagpur Gneiss Complex and the LGB. The Ganges River flows all along the north of the study area and was evolved during the bending of the Indian plate beneath the Himalaya (**Figures 1**, **2**). The rivers Subarnarekha and Koel pass through the southern part of the area, whereas the coal-bearing, faulted Damodar Valley transects the central part of the region from west to east.

The study area has variable relief, with the highest elevation in the Ranchi Plateau, situated at ∼610–1097 m from mean sea level (MSL) (Pandey et al., 2013). Several dissected hills with a number of hill stations constitute the adjacent Hazaribagh Plateau drained by the Damodar valley. The Chhotanagpur Plateau and the Hazaribagh Plateau have outcrops of gneisses, schists, and granite of Precambrian rocks (Ghose, 1983). Some other plateaus, like

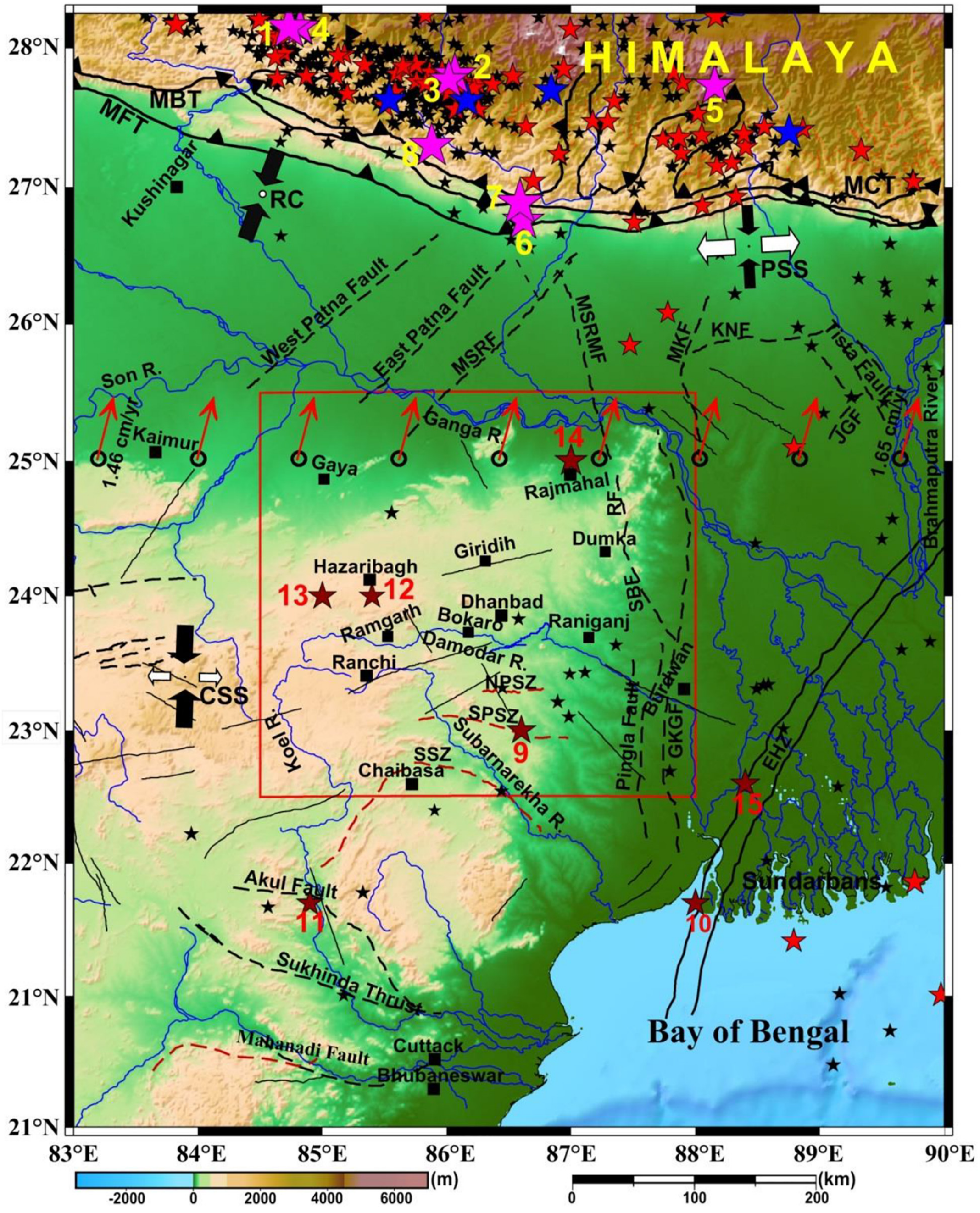

FIGURE 2 | Seismoteconics and topographic relief Map of EIS (EIS) and adjoining regions (after Dasgupta et al., 2000; Singh et al., 2020). The study area is marked by a red rectangular box. Black dashed lines represent faults, and black solid lines denote lineaments. Blue solid lines show the various permanent rivers. Black solid squares represent the locations of a few important areas. A combination of black and white solid arrows shows the stress regimes of that part within shallow depth (0–20 km). RC, radial compression; PSS, pure strike-slip; CSS, compressive strike-slip. Red arrows represent the Indian plate velocity motion direction with respect to the Eurasian plate. All stars show the seismicity since 1973 to May 2020 (from USGS Catalog). Magenta stars show the location of damaging earthquakes with magnitudes of $6.5 < M \leq 8.0$ (1: 2015 M 7.8 Nepal, 2: 2015 M 7.3 Nepal, 3: 2015 M 6.7 Nepal, 4 2015 M 6.6 Nepal 5: 2011 M 6.9 Sikkim, 6: 1988 M 6.9 Nepal-India Border, 7: 1934 M 8.0 Nepal-India Border, and 8: 1833 M 7.6 Nepal-India Region). Maroon stars represent the location of historical earthquakes that occurred in EIS and nearby regions within $5 < M \leq 6.3$ (9: 1969 M 5.7 Bankura, 10: 1964 M 5.5 Midnapur, 11: 1963 M 5.2 Thethanagar, SE Bihar, 12: 1868 M 5.5 Manbhum, 13: 1868 M 5.0 Hazaribagh, 14: 1866 M 6.3 Bengal, and 15: 1861 M 5.7 Calcutta). Blue stars show the epicenter location of earthquakes between 6 and 6.5 magnitude, red stars represent earthquake location within $5 \leq M < 6$, while the black stars denote epicenter locations of earthquakes within $4 \leq M < 5$. Abbreviations: MFT, Main Frontal Thrust; MBT, Main Boundary Thrust; MCT, Main Central Thrust; MSRF, Munger-Saharsa Ridge Fault; MSRMF, Munger-Saharsa Ridge Marginal Fault; GKGF, Garhmayna-Khandaghosh Fault; SBF, Sainthia Bahmani Fault; MKF, Malda-Kishanganj Fault; JGF, Jangipur-Gaibanda Fault; KNF, Katihar-Nailphamari Fault; CGG, Chhotanagpur gneissic complex terrain; SSZ, Singhbhum shear zone; NPSZ, North Purulia shear zone; SPSZ, South Purulia shear zone; R., River.

Kaimur Plateau and Rajmahal Hills, can be differentiated from each other by steep and narrow slopes known as scarps.

Mutual cyclic interactions of two converging microplates, i.e., Singhbhum and Chhotanagpur (Sarkar, 1982), during the Proterozoic times facilitated subduction, rifting, mantle plume activities, and mafic magmatism in the region (Pandey and Agarwal, 1999; Bose, 2008). The cyclic interactions happened in three consecutive stages with intervening quiescence (Sarkar, 1982), which further simplified the isostatic adjustments with coeval upliftment with intrusions of basic dyke swarms, erosion, and paralic sedimentation (Bose, 1999, 2009). During the Precambrian, the northward movement of the Singhbhum block toward the continental margin of the Chhotanagpur block produced a consuming plate boundary (**Figure 1**). The compressional stress produced by the plate merging caused N-S crustal shortening, resulting in the upliftment on the Chhotanagpur granite-gneissic terrain and beginning the basement reactivation and fresh rupture development (Sarkar and Saha, 1977).

The Chhotanagpur peneplain has been uplifted three times during the Cenozoic due to the flexural responses caused by the subduction of the Indian lithosphere toward the southern edge of the Himalayas, and gave rise to some familiar waterfalls, like Jonha and Hundru, on the scarps. During the Eocene to Oligocene period the first upliftment took place, forming the Pat region; the second one happened during the Miocene period which developed the Ranchi and Hazaribagh Plateau; and the third one took place during the Pliocene and Pleistocene period, which caused upliftment of the outer Chhotanagpur Plateau (Naqvi and Rogers, 1987; Weaver, 1990).

The Chhotanagpur plateau is comprised of high-grade gneisses and migmatites containing enclaves of meta-sediments, and mafic and ultramafic rocks. The basement of the Chhotanagpur plateau is represented by an uncategorized gneissic complex. Systems of Proterozoic fold belt occur as secluded patches within the Chhotanagpur Granite Gneissic terrain. Later, during late Palaeozoic and Mesozoic, Gondwana sediments were deposited in linear grabens in the Damodar valley. Irregular sedimentation above crystalline metamorphic rocks, harmonized subsidence, and sprinkled periodic accumulation of coal measures were greatly conditioned by climatic variation in the period of sedimentation in the Gondwana basin in the eastern part of the EIS (Sarkar, 1982). The maximum thickness of sediment filling in the basin is estimated to be 2.9 km in the central part (Verma et al., 1980). Intermittent periods of faulting and epeirogenic uplift of the margins of the master basin dismembered the master basin into several smaller sub-basins (Mahadevan, 2002). Various hot springs with numerous features are broadly dispersed over this area, and the area is apparently associated with several fault zones (Mahadevan, 2002). The Chhotanagpur Granite–Gneiss Complex (CGGC) mainly consists of granitic gneisses, migmatized porphyritic granite, and many meta-sedimentary enclaves. The Central CGGC gneisses and the western CGGC granites show almost similar ages of 1.7 Ga, whereas the migmatites and granulites, and granitic gneisses of northeastern CGGC (Dumka area), show ages of 1.5–1.6 Ga (Chatterjee et al., 2008).

DATA AND METHODOLOGY

Gravity Modeling and Validation

Gravity modeling is an important tool for delineation of crustal structures. Gravity data show an ordered link between crustal structure, density, and the surface altitude. In this line, a Bouguer anomaly map was reconstructed for the area covering a part of the Gangetic basin and EIS (i.e., between 22.5–25.5°N latitude and 84.5–88°E longitude) compiling the data from the second generation gravity map series of India (GMSI, 2006). An inaccuracy of about ± 0.5 mGal for the errors in elevation of 2–3 m was achieved in these data. The area of the new Bouguer anomaly map (**Figure 3**) has been divided into 99 square-grids, with a dimension of $1^\circ \times 1^\circ$. A shifting window with 75% overlapping area is used for inherent continuity of the data points and better resolution for delineating the basement and the Conrad discontinuity of the study area.

The Moho depth was computed by the spectral analysis (**Figure 4**) (Odegard and Berg, 1965; Bhattacharyya and Leu, 1975) over 12 blocks, by dividing the Bouguer anomaly map into smaller areas of dimension of $2^\circ \times 2^\circ$ in an overlapping adjacent grid. We have also computed the Moho depth based on the Airy-Heiskanen model at the same grid for better resolution and insufficient data points, as the GMSI (2006) gravity map is created from a grid of dimension 5.5×5.5 km^2. The 2D inverse gravity modeling was performed by adding layers incorporating its prior information as explained in **Figure 5** and **Table 1**. Error minimization between the observed and calculated gravity anomalies was followed at various steps of the iteration processes, to optimize the gravity model.

The inverse gravity modeling using Geosoft was done along 13 profiles, considering various Earth models (Choudhury, 1974; Verma et al., 1976; Verma and Ghosh, 1977; Verma, 1985; Singh et al., 2004). Power spectrum analysis was carried out to compute depths of the sharp density discontinuities appearing at the basement, Conrad, and Moho. The efficacy of this method has been demonstrated in the literatures (Spector and Grant, 1970; Green, 1972; Curtis and Jain, 1975; Tselentis et al., 1988; Djomani et al., 1992; Chavez et al., 1999; Ates and Kearey, 2000; Lefort and Agarwal, 2002; Rivero et al., 2002; Carbó et al., 2003; Gomez-Ortiz et al., 2005; Bansal et al., 2006). We have computed the crustal discontinuities based on the spectral analysis (**Figure 4**) of the Bouguer gravity field. The Moho depth (**Table 2**) has been computed from the slope of the energy spectrum at the lower end of the wave-number band, while the basement depth (**Table 3**) has been computed at a slightly higher wave-number band. Interface depths with different density contrasts are computed using the following equation:

$$\left|h\right| = -\frac{1}{4\pi}\frac{(logE_1 - logE_1)}{(k1 - k2)} \tag{1}$$

where h is the average interface depth and E_1 and E_2 are the power in the spectrum at wave-number (cycles/km) k_1

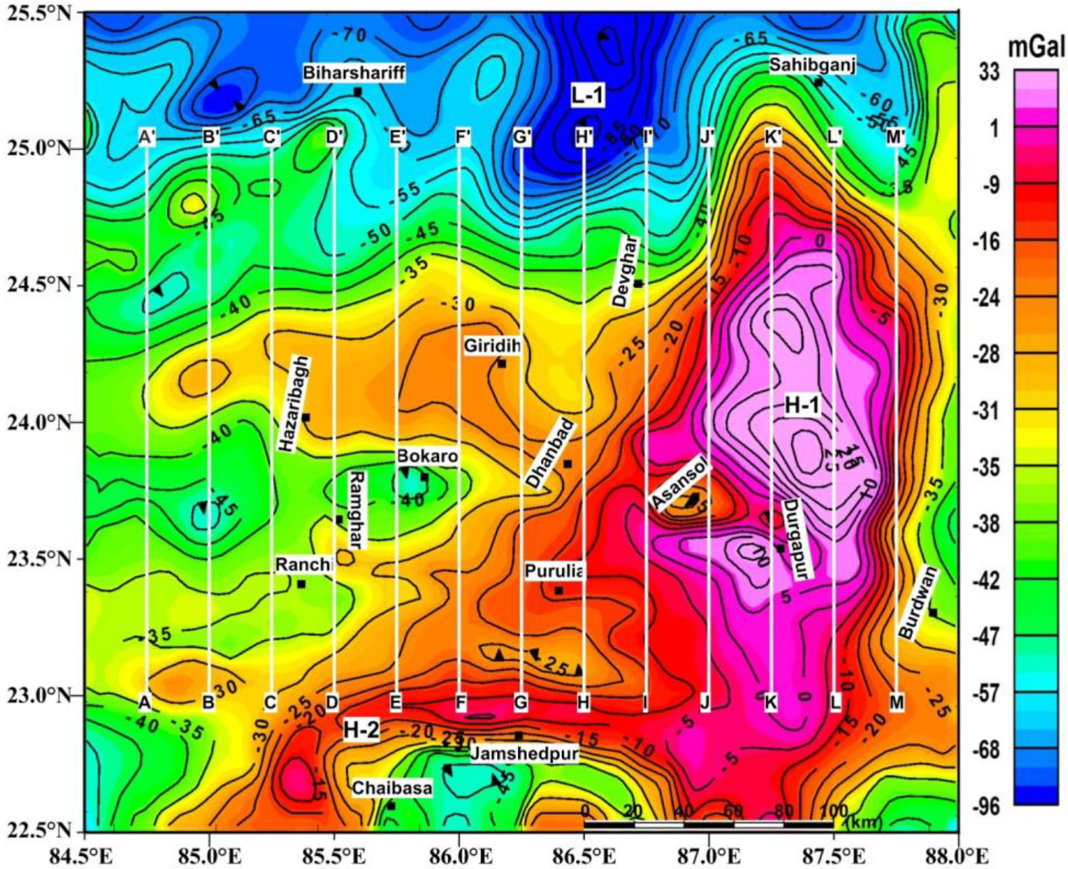

FIGURE 3 | Bouguer gravity anomaly map of the study area reconstructed from GMSI (2006). White vertical solid lines are the profiles, taken for the 2D gravity modeling. H-1 and H-2 represent the area associated with high Bouguer gravity anomalies, and L-1 represents the area with low Bouguer gravity anomaly.

and k_2 (cf. Spector and Grant, 1970; Karner and Watts, 1983; Maus and Dimri, 1995; Indriana, 2008; Bansal and Dimri, 2010; Chamoli et al., 2010).

Most of the geophysical methods, particularly the spectral analysis of potential field data, isostasy analysis, inversion of potential field data, receiver function, and seismic tomography, used for modeling and interpretation purposes, have some limitations as well as advantages. 2-D spectral analysis usually delivers spatially averaged depth for an undulated plane, i.e., an interface where density changes sharply, and depends on the gridding size of the data (Tselentis et al., 1988). In frequency domain, gravity anomalies generated from a multilayered source can be separated from each other by their own segments with the help of gravity anomaly spectrum and interpreted for the mean depth of the interface (Chamoli and Dimri, 2010). However, the spectral peak for each buried mass at different depths is not always sharp, and the overlapping of such peaks occasionally introduces ambiguity in the result. Refinement of higher wave-number components from noise is sometimes difficult due to its smaller amplitude, and the information loss can be minimized to < 10% by taking care of the window size of four to five times of the source depth (Regan and Hinze, 1976).

The Airy-Heiskanen isostatic technique results in reliable image gravity data on a continent-wide scale for the purpose of regional geologic interpretations. Isostatic residual gravity further enhances the short-wavelength anomalies produced by bodies at or near the surface and emphasizes the regional fabrics and trends in the gravity field. Isostatic anomaly gives information about the lateral mass distribution within the crust and mantle, having some geological interest (Simpson et al., 1986). However, crustal density variations are not considered for one fixed density for the entire crust. Gravity data alone cannot reveal the density inhomogeneity in the locally compensated crust. A solely isostatic model cannot provide the root geometry for a large continental region. There may be errors of less than 2 mGal in the calculation of isostatic residual anomaly because of the uncertainty present in gravity measurement, terrain correction, and station elevation (Chapin, 1996). The anomalies near the flanks are affected by the anomalies present at its neighborhood and become difficult to distinguish.

Gravity inversion method is well known for the derivation of appropriate anomalies due to Moho deflection (Prasanna et al., 2013), and its useful technique to detect Moho depth especially in a region where the availability of seismic data is insufficient. Moho interface can be delineated with the help of an iterative

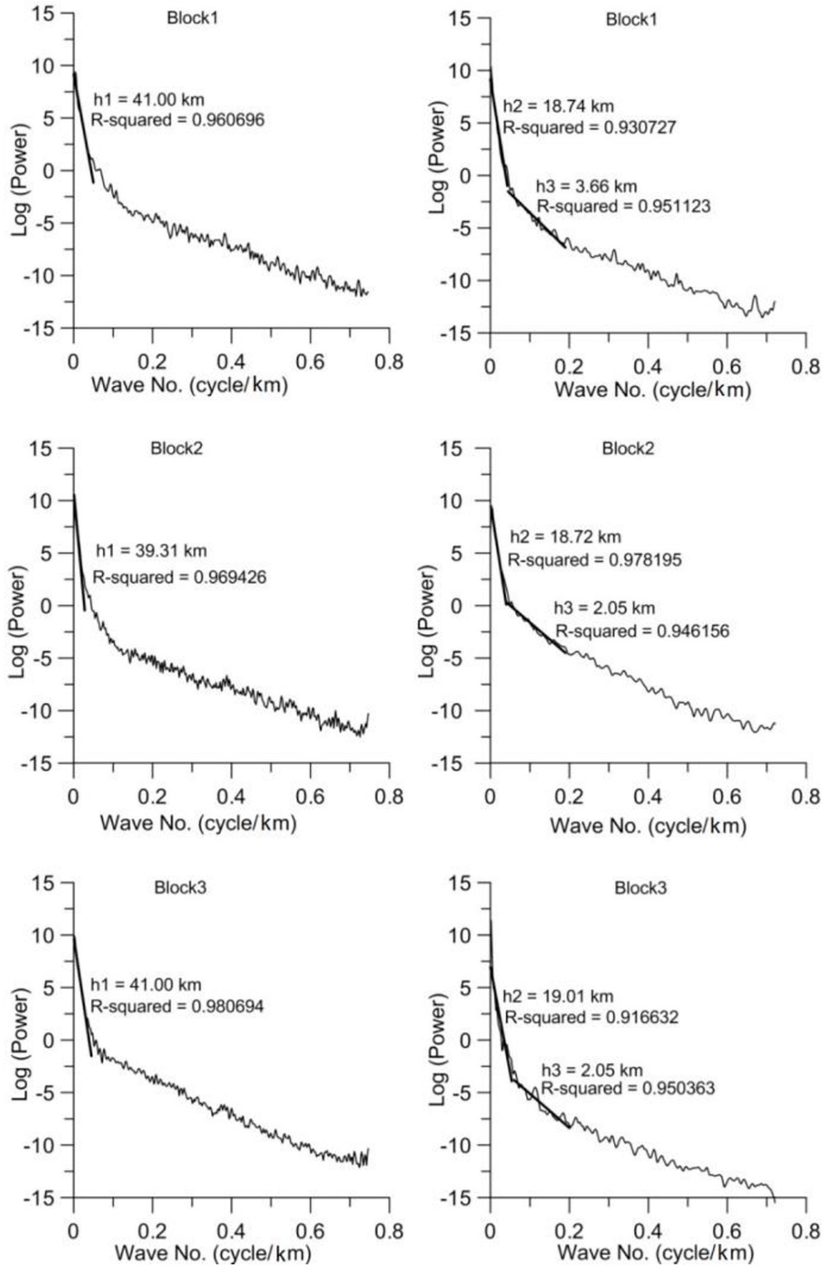

FIGURE 4 | Spectral analysis plots illustrating the estimation of interface depths at different grids. Wave number is plotted on the *X*-axis, and the corresponding power spectra of gravity are plotted on the *Y*-axis. Values of deepest density interface show Moho depth, and the shallowest interface shows sediment thickness.

process (Shin et al., 2007). However, the filtering of wavelength effects of gravity from crustal inhomogeneities and deep-seated sources is difficult and complex. Inhomogeneities in the intra-crustal density or noise can create a stability problem in inversion and provide a wrong estimation of depth.

Seismic receiver function is a simple and unambiguous method for the detection of 1D crustal structure beneath the seismic station. Receiver function consists of direct, reflected, and converted phases of seismic wave trains (Burdick and Langston, 1977; Ammon et al., 1990; Das et al., 2019). Converted phases and shallow surface multiples carry average crustal information about the surrounding of the receiver station. However, this method can only be applied to a nearly horizontal layer and works best for low incidence angles of seismic rays. Regionalization of Moho depth (2D crustal structure) estimation needs highly dense seismic networks. The seismic tomography can give the information of velocity structures, seismotectonics, and characterization of the source area for tectonically complex regions (Zhao et al., 1992). It gives a high-resolution image of the earth's interior. It can image the structures with different physical properties.

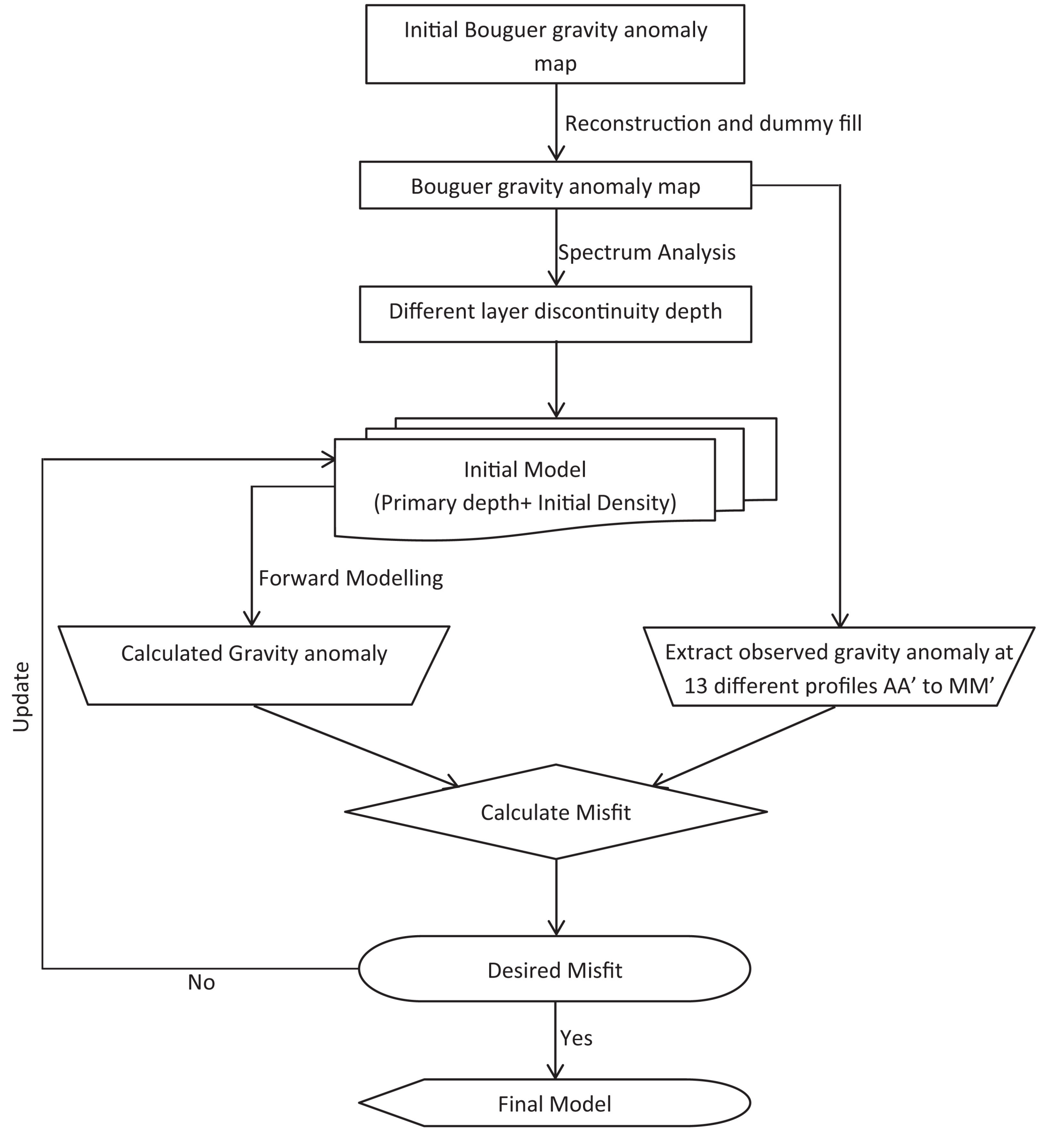

FIGURE 5 | Flowchart showing the various steps followed for the gravity modeling.

Seismic tomography can also be done using surface waves and full waveforms (Geller, 1991; Iyer and Hirahara, 1993). However, the resolution of seismic tomography depends on the wavelengths of seismic waves. Since a longer wavelength is used, deeper sources can be imaged, but small features cannot be resolved. Tomography results are also non-unique and need a good coverage of seismic stations with a huge amount of earthquake data, and hence are suitable for seismically active regions.

The EIS region is not very seismically active, and is located to the south of the seismically active Himalayan orogen. Thus, a good coverage of seismic network will be essential for delineation of the regional crustal structure of the study area. Ambient noise tomography is also another option for the detection of crustal structures in a seismically stable region like EIS region; however, it needs a dense network of seismic stations. Thus, the present results of gravity modeling were partially validated by the receiver function studies (Mandal and Biswas, 2016), and complied by the gravity study of Singh et al. (2015). Only two broadband seismic stations, located in the Chhotanagpur plateau, have been operative since 2007: Dhanbad [run by IIT (ISM)] and Bokaro [run by National Centre of Seismology (NCS), New Delhi]. The 1D crustal structure beneath Dhanbad and Bokaro stations has been estimated by several researchers using different initial velocity structures through receiver function analysis. Das et al. (2019) found 43 and 44 km crustal thickness beneath Dhanbad and Bokaro stations. Kosarev et al. (2013) found Moho at a

TABLE 1 | Density used in the 2D gravity modeling.

Layers	Depth (in km)	Initial density (gm/cm^3)	References	Final density (gm/cm^3)
Mantle	>36	3.30	Singh et al., 2004	3.28
Igneous Rajmahal trap material	38–39	3.02	Singh et al., 2004	3.02
Lower crust	20–40	2.90	Singh et al., 2004	2.90
Transitional layer (oceanic to continental crust)	12–20	2.80	Singh et al., 2004	2.80
Upper crust (granite gneiss)	5.5–12	2.69	Verma and Ghosh, 1977	2.70
Basement complex (granite)	0.0–7.5	2.67	Verma and Ghosh, 1977	2.67
Gondwana sediments in Damodar valley	0.0–3.0	2.45	Verma, 1985	2.42
Gondwana sediments near Bokaro Coalfield	0.0–3.0	2.55	Verma, 1985	2.56
Gondwana sediments near Jharia Coalfield	0.0–3.0	2.65	Verma, 1985	2.65
Gondwana sediments near Raniganj Coalfield	0.0–3.0	2.42	Verma, 1985	2.42
Alluvium sediments	0.0–2.6	2.40	Choudhury, 1974	2.20

TABLE 2 | 12 blocks of 2° × 2° grid with a 75% overlap with the adjacent grid for Moho depth calculation.

Area code (*i, j*)	Lat (*Y* in degree)/ long (*X* in degree)	Projection point (Y,X)	Moho depth (km)/R^2
(1,1)	(22.50–24.50), (84.50–86.50)	23.50, 85.50	40.38/0.945
(1,2)	(23.00–25.00), (84.50–86.50)	24.00, 85.50	40.72/0.984
(1,3)	(23.50–25.50), (84.50–86.50)	24.50, 85.50	38.80/0.982
(2,1)	(22.50–24.50), (85.00–87.00)	23.50, 86.00	38.70/0.877
(2,2)	(23.00–25.00), (85.00–87.00)	24.00, 86.00	37.99/0.970
(2,3)	(23.50–25.50), (85.00–87.00)	24.50, 86.00	37.70/0.968
(3,1)	(22.50–24.50), (85.50–87.50)	23.50, 86.50	37.01/0.951
(3,2)	(23.00–24.00), (85.50–87.50)	24.00, 86.50	37.00/0.928
(3,3)	(23.50–25.50), (85.50–87.50)	24.50, 86.50	37.50/0.961
(4,1)	(22.50–24.50), (86.00–88.00)	23.50, 87.00	36.70/0.981
(4,2)	(23.00–24.00), (86.00–88.00)	24.00, 87.00	37.10/0.977
(4,3)	(23.50–25.50), (86.00–88.00)	24.50, 87.00	37.11/0.968

R^2: coefficient of determination, i.e., fitness of the best fit line on spectrum.

45 km depth beneath the Bokaro station. Kumar et al. (2013) found 42 km depth for the Moho below this station. Kayal et al. (2011) found a depth of 41 km for the Moho beneath the Dhanbad station, whereas Kumar et al. (2001) found highly complicated crust below the Bokaro station with a Moho depth of 54 km. This wide variability of Moho depth was possibly due to considering the same Vp/Vs or Poison's ratio for the entire crust. The Moho depth computed under the present study varies from 37 to 41.5 km for the Chhotanagpur plateau and is ∼4–5 km shallower in comparison with the seismic methods. However, the Moho depth of ∼39 km near the Hazaribagh region (24.07°N and 85.38°E), ∼39.5–40 km in Ranchi (23.43°N and 85.43°E), and ∼40 km near Dumka (24.6°N and 87.08°E) are well correlated with the analysis of Mandal and Biswas (2016) (**Table 4**).

We use the Airy-Heiskanen model for the calculation of initial Moho depth assuming that the crust is isostatically being compensated. The isostatic imbalance and the delineation of many layers in the crust might be showing differences in Moho depth between the present study and results of receiver function studies. It is also found that the crustal structures obtained from seismic and gravimetric method are quite different depending on the geological and geophysical hypotheses, as well as different datasets (Reguzzoni et al., 2013). For example, well-known receiver function analysis starts their initial model by assuming a constant velocity and Vp/Vs, taking either a single or double layer of the crust for the calculation of 1D crustal structure (Dueker and Sheehan, 1997; Zhu, 2000; Zhu and Kanamori, 2000; Thompson et al., 2010; Kayal et al., 2011; Sharma et al., 2015; Mandal and Biswas, 2016; Song et al., 2017; Das et al., 2019). An incorrect or different initial seismic model may produce different or inaccurate crustal images, especially in the presence of heterogeneous medium with lateral velocity variations (Das et al., 2019). The calculation of crustal structure using the gravimetric method based on local and regional effect of Earth's crust provides important outputs (Woollard, 1969; Tsuboi, 1979; Chapin, 1996).

Isostasy Analysis

According to the theory of isostasy given by the Airy model, the excess mass or root zone around the base of the crust normally supports the topography. Regional-scale low-amplitude and long-wavelength anomalies are often observed in hilly terrain and near the continental shelves (i.e., edges of continents), and are often masked by anomalies due to upper crustal structures (Simpson et al., 1986). Enhancement of gravity anomalies by removing topography-induced regional effects caused by shallow geologic features is done by routine use of polynomial fitting or wavelength-filtering method. The main objectives of most kinds of geologic and tectonic studies are the density distribution in the upper crust and are more precisely revealed by isostatic residual gravity anomaly maps than any other gravity maps. Qureshy

TABLE 3 | Ninety-nine blocks of 1° × 1° grid, with a 75% overlap with the adjacent grid for basement and Conrad depth calculation.

Area code(i, j)	Lat (Y in degree.) Long (X in degree)	Projection point (Y, X)	Moho depth (km)	Transition layer depth (km)/R^2	Basement depth (km)/R^2
(1,1)	(22.50–23.50), (84.50–85.50)	23.00, 85.00	41.90	19.22/0.947	0.00/0.966
(1,2)	(22.75–23.75), (84.50–85.50)	23.25, 85.00	42.62	19.22/0.937	0.00/0.978
(1,3)	(23.00–24.00), (84.50–85.50)	23.50, 85.00	42.64	19.11/0.940	0.50/0.962
(1,4)	(23.25–24.25), (84.50–85.50)	23.75, 85.00	41.75	19.22/0.908	2.38/0.919
(1,5)	(23.50,24.50), (84.50–85.50)	24.00, 85.00	41.88	19.33/0.961	2.15/0.940
(1,6)	(23.75–24.75), (84.50–85.50)	24.25, 85.00	41.28	19.11/0.960	0.00/0.908
(1,7)	(24.00–25.00), (84.50–85.50)	24.50, 85.00	39.87	19.22/0.952	1.51/0.937
(1,8)	(24.25–25.25), (84.50–85.50)	24.75, 85.00	39.63	19.10/0.938	2.05/0.929
(1,9)	(24.50–25.50), (84.50–85.50)	25.00, 85.00	39.46	19.01/0.951	1.40/0.930
(2,1)	(22.50–23.50), (84.75–85.75)	23.00, 85.25	41.07	18.01/0.974	0.00/0.971
(2,2)	(23.00–23.50), (84.75–85.75)	23.25, 85.25	41.46	18.20/0.928	0.00/0.910
(2,3)	(23.00–24.00), (84.75–85.75)	23.50, 85.25	41.50	18.20/0.976	2.50/0.938
(2,4)	(23.25–24.25), (84.75–85.75)	23.75, 85.25	40.27	17.01/0.904	3.24/0.915
(2,5)	(23.50,24.50), (84.75–85.75)	24.00, 85.25	41.32	17.60/0.938	2.06/0.975
(2,6)	(23.75–24.75), (84.75–85.75)	24.25, 85.25	40.28	17.31/0.982	0.00/0.979
(2,7)	(24.00–25.00), (84.75–85.75)	24.50, 85.25	39.19	17.51/0.958	0.82/0.921
(2,8)	(24.25–25.25), (84.75–85.75)	24.75, 85.25	38.64	17.51/0.941	0.93/0.906
(2,9)	(24.50–25.50), (84.75–85.75)	25.00, 85.25	38.42	17.51/0.914	1.00/0.928
(3,1)	(22.50–23.50), (85.00–86.00)	23.00, 85.50	38.77	19.31/0.942	2.24/0.938
(3,2)	(22.75–23.75), (85.00–86.00)	23.25, 85.50	39.84	20.41/0.953	0.50/0.927
(3,3)	(23.00–24.00), (85.00–86.00)	23.50, 85.50	40.36	19.47/0.922	2.24/0.987
(3,4)	(23.25–24.25), (85.00–86.00)	23.75, 85.50	39.07	18.94/0.934	0.00/0.981
(3,5)	(23.50,24.50), (85.00–86.00)	24.00, 85.50	40.03	19.18/0.924	0.00/0.931
(3,6)	(23.75–24.75), (85.00–86.00)	24.25, 85.50	39.22	19.44/0.928	0.00/0.958
(3,7)	(24.00–25.00), (85.00–86.00)	24.50, 85.50	38.80	17.97/0.961	2.05/0.982
(3,8)	(24.25–25.25), (85.00–86.00)	24.75, 85.50	37.62	17.27/0.978	2.20/0.954
(3,9)	(24.50–25.50), (85.00–86.00)	25.00, 85.50	37.40	17.00/0.919	2.47/0.941
(4,1)	(22.50–23.50), (85.25–86.25)	23.00, 85.75	41.29	17.76/0.919	0.00/0.918
(4,2)	(22.75–23.75), (85.25–86.25)	23.25, 85.75	41.44	17.76/0.916	0.00/0.933
(4,3)	(23.00–24.00), (85.25–86.25)	23.50, 85.75	41.84	17.76/0.913	0.00/0.958
(4,4)	(23.25–24.25), (85.25–86.25)	23.75, 85.75	41.98	18.53/0.972	2.25/0.944
(4,5)	(23.50,24.50), (85.25–86.25)	24.00, 85.75	42.47	17.08/0.941	0.00/0.942
(4,6)	(23.75–24.75), (85.25–86.25)	24.25, 85.75	41.95	17.88/0.943	0.00/0.917
(4,7)	(24.00–25.00), (85.25–86.25)	24.50, 85.75	42.07	17.16/0.956	0.00/0.976
(4,8)	(24.25–25.25), (85.25–86.25)	24.75, 85.75	40.79	18.87/0.961	0.70/0.948
(4,9)	(24.50–25.50), (85.25–86.25)	25.00, 85.75	40.37	18.87/0.920	1.50/0.947
(5,1)	(22.50–23.50), (85.50–86.50)	23.00, 86.00	37.09	18.12/0.976	0.80/0.927
(5,2)	(22.75–23.75), (85.50–86.50)	23.25, 86.00	37.33	18.02/0.981	0.00/0.978
(5,3)	(23.00–24.00), (85.50–86.50)	23.50, 86.00	38.00	17.30/0.973	1.90/0.928
(5,4)	(23.25–24.25), (85.50–86.50)	23.75, 86.00	37.16	17.30/0.975	2.62/0.926
(5,5)	(23.50,24.50), (85.50–86.50)	24.00, 86.00	37.62	17.09/0.942	1.15/0.950
(5,6)	(23.75–24.75), (85.50–86.50)	24.25, 86.00	37.70	17.19/0.962	0.00/0.941
(5,7)	(24.00–25.00), (85.50–86.50)	24.50, 86.00	37.65	18.22/0.929	0.00/0.938
(5,8)	(24.25–25.25), (85.50–86.50)	24.75, 86.00	37.34	18.63/0.952	0.50/0.927
(5,9)	(24.50–25.50), (85.50–86.50)	25.00, 86.00	36.30	18.53/0.977	1.50/0.931
(6,1)	(22.50–23.50), (85.75–86.75)	23.00, 86.25	37.39	17.12/0.919	0.72/0.970
(6,2)	(22.75–23.75), (85.75–86.75)	23.25, 86.25	37.45	17.29/0.977	0.00/0.961
(6,3)	(23.00–24.00), (85.75–86.75)	23.50, 86.25	37.12	17.29/0.981	0.00/0.928
(6,4)	(23.25–24.25), (85.75–86.75)	23.75, 86.25	37.16	17.46/0.941	1.00/0.953
(6,5)	(23.50,24.50), (85.75–86.75)	24.00, 86.25	37.49	17.38/0.955	0.00/0.918
(6,6)	(23.75–24.75), (85.75–86.75)	24.25, 86.25	37.71	17.20/0.934	0.00/0.973
(6,7)	(24.00–25.00), (85.75–86.75)	24.50, 86.25	37.88	17.46/0.918	1.65/0.968
(6,8)	(24.25–25.25), (85.75–86.75)	24.75, 86.25	36.69	18.74/0.932	1.10/0.960
(6,9)	(24.50–25.50), (85.75–86.75)	25.00, 86.25	36.40	18.50/0.954	2.10/0.955
(7,1)	(22.50–23.50), (86.00–87.00)	23.00, 86.50	37.10	17.30/0.974	2.20/0.932

(Continued)

TABLE 3 | Continued

Area code(*i*, *j*)	Lat (*Y* in degree.) Long (*X* in degree)	Projection point (*Y*, *X*)	Moho depth (km)	Transition layer depth (km)/R^2	Basement depth (km)/R^2
(7,2)	(22.75–23.75), (86.00–87.00)	23.25, 86.50	37.08	17.30/0.935	0.00/0.970
(7,3)	(23.00–24.00), (86.00–87.00)	23.50, 86.50	37.03	17.30/0.917	0.00/0.949
(7,4)	(23.25–24.25), (86.00–87.00)	23.75, 86.50	37.05	17.71/0.936	1.50/0.923
(7,5)	(23.50,24.50), (86.00–87.00)	24.00, 86.50	37.05	17.30/0.910	0.72/0.918
(7,6)	(23.75–24.75), (86.00–87.00)	24.25, 86.50	37.59	17.89/0.958	0.87/0.944
(7,7)	(24.00–25.00), (86.00–87.00)	24.50, 86.50	37.41	19.05/0.964	0.00/0.921
(7,8)	(24.25–25.25), (86.00–87.00)	24.75, 86.50	37.28	19.56/0.918	0.00/0.922
(7,9)	(24.50–25.50), (86.00–87.00)	25.00, 86.50	36.65	18.53/0.915	3.14/0.917
(8,1)	(22.50–23.50), (86.25–87.25)	23.00,86.75	36.70	17.96/0.974	0.87/0.932
(8,2)	(22.75–23.75), (86.25–87.25)	23.25, 86.75	36.83	18.06/0.935	0.00/0.911
(8,3)	(23.00–24.00), (86.25–87.25)	23.50, 86.75	36.98	18.57/0.921	0.00/0.949
(8,4)	(23.25–24.25), (86.25–87.25)	23.75, 86.75	36.70	18.16/0.926	1.78/0.923
(8,5)	(23.50,24.50), (86.25–87.25)	24.00, 86.75	37.10	18.37/0.938	2.10/0.943
(8,6)	(23.75–24.75), (86.25–87.25)	24.25, 86.75	37.05	18.26/0.955	0.00/0.968
(8,7)	(24.00–25.00), (86.25–87.25)	24.50, 86.75	37.38	19.39/0.966	0.00/0.920
(8,8)	(24.25–25.25), (86.25–87.25)	24.75, 86.75	36.99	19.80/0.911	0.00/0.910
(8,9)	(24.50–25.50), (86.25–87.25)	25.00, 86.75	36.35	19.11/0.915	2.00/0.908
(9,1)	(22.50–23.50), (86.50–87.50)	23.00, 87.00	36.51	17.65/0.904	1.37/0.902
(9,2)	(22.75–23.75), (86.50–87.50)	23.25, 87.00	36.56	17.65/0.917	1.60/0.915
(9,3)	(23.00–24.00), (86.50–87.50)	23.50, 87.00	36.65	17.56/0.941	0.80/0.950
(9,4)	(23.25–24.25), (86.50–87.50)	23.75, 87.00	36.65	17.73/0.928	6.05/0.907
(9,5)	(23.50,24.50), (86.50–87.50)	24.00, 87.00	37.01	17.39/0.922	0.00/0.919
(9,6)	(23.75–24.75), (86.50–87.50)	24.25, 87.00	37.23	17.83/0.909	0.00/0.908
(9,7)	(24.00–25.00), (86.50–87.50)	24.50, 87.00	37.06	18.51/0.961	0.49/0.920
(9,8)	(24.25–25.25), (86.50–87.50)	24.75, 87.00	36.66	18.86/0.911	1.00/0.960
(9,9)	(24.50–25.50), (86.50–87.50)	25.00, 87.00	36.33	18.99/0.935	1.56/0.942
(10,1)	(22.50–23.50), (86.75–87.75)	23.00, 87.25	36.45	17.84/0.957	4.34/0.905
(10,2)	(22.75–23.75), (86.75–87.75)	23.25, 87.25	36.53	17.92/0.943	4.06/0.956
(10,3)	(23.00–24.00), (86.75–87.75)	23.50, 87.25	36.37	18.43/0.958	2.95/0.920
(10,4)	(23.25–24.25), (86.75–87.75)	23.75, 87.25	36.43	18.60/0.961	3.14/0.918
(10,5)	(23.50,24.50), (86.75–87.75)	24.00, 87.25	36.62	18.51/0.952	1.53/0.924
(10,6)	(23.75–24.75), (86.75–87.75)	24.25, 87.25	36.74	19.88/0.938	1.51/0.910
(10,7)	(24.00–25.00), (86.75–87.75)	24.50, 87.25	37.07	19.53/0.967	1.40/0.907
(10,8)	(24.25–25.25), (86.75–87.75)	24.75, 87.25	36.68	19.45/0.959	1.52/0.953
(10,9)	(24.50–25.50), (86.75–87.75)	25.00, 87.25	36.34	19.11/0.939	2.27/0.981
(11,1)	(22.50–23.50), (87.00–88.00)	23.00, 87.50	36.23	17.62/0.932	4.81/0.974
(11,2)	(22.75–23.75), (87.00–88.00)	23.25, 87.50	36.28	17.83/0.957	5.10/0.920
(11,3)	(23.00–24.00), (87.00–88.00)	23.50, 87.50	36.34	18.45/0.971	4.21/0.984
(11,4)	(23.25–24.25), (87.00–88.00)	23.75, 87.50	36.32	17.93/0.979	3.00/0.922
(11,5)	(23.50,24.50), (87.00–88.00)	24.00, 87.50	36.45	18.65/0.967	3.67/0.902
(11,6)	(23.75–24.75), (87.00–88.00)	24.25, 87.50	36.78	18.24/0.981	3.54/0.916
(11,7)	(24.00–25.00), (87.00–88.00)	24.50, 87.50	36.64	19.87/0.958	2.80/0.932
(11,8)	(24.25–25.25), (87.00–88.00)	24.75, 87.50	37.00	19.87/0.962	3.01/0.952
(11,9)	(24.50–25.50), (87.00–88.00)	25.00, 87.50	36.78	19.68/0.978	4.71/0.909

R^2: coefficient of determination, i.e., fitness of the best fit line on spectrum.

and Warsi (1980) and Kumar et al. (2020) reconstructed the Airy-Heiskanen isostatic anomaly map over the Indian shield and adjoining regions using the world gravity map (Bonvalot et al., 2012). Several other workers reconstructed the isostatic anomaly maps for the Himalayas and IGB (Qureshy, 1969), Ninety-East Ridge (Tiwari, 2003), Deccan Trap (Qureshy, 1981), and for the Indian continent (Mishra et al., 2004). However, this is the first attempt to reconstruct the isostatic anomaly map for the EIS and adjacent regions using land gravity data (GMSI, 2006). Airy isostatic anomalies were computed from the difference between the gravity effect of topography and a crustal root from the Bouguer corrected anomaly, with the Parker (1972) series up to degree 4 to take care of the nonlinear effects (e.g., Lyons et al., 2000). We fixed the Moho depth to 38 km and formed an average

TABLE 4 | Thickness of the crust of different shield areas around the globe and the present study area.

Age	Region	Name of the terrain	Average crustal thickness (km)	References
Paleoproterozoic	Southern Africa	Limpopo Belt	40 ± 3	Tugume et al., 2013
Paleoproterozoic	Southern Africa	Kheis Province Okwa Province	39 ± 3 43	Tugume et al., 2013
Paleoproterozoic	Eastern Africa	Ubendiain Belt Usagaran Belt	43 ± 5 37 ± 3	Tugume et al., 2013
Mesoproterozoic	Eastern Africa	Kibaran Belt Rwenzori Belt	40 ± 3 38 ± 2	Tugume et al., 2013
Neoproterozoic	Arabia	Asir Belt Nabitah Belt Af-Rayn Belt	39 ± 1 39 ± 1 43	Tugume et al., 2013
Paleoproterozoic	Eastern Indian Shield and Singhbhum Craton	Chhotanagpur Gneiss Complex Singhbhum Craton Damodar Gondwana Basin	40 35–38 ∼37	Singh et al., 2015
Paleoproterozoic	Dhanbad (23.82°N and 86.44°E), Eastern India	Chhotanagpur plateau	43 42 37–37.5	Das et al., 2019 Kayal et al., 2011 Present study
Paleoproterozoic	Bokaro (23.8°N and 85.9°E), Eastern India	Chhotanagpur plateau	44 45 42 54 37.5–38	Das et al., 2019 Kosarev et al., 2013 Kumar et al., 2013 Kumar et al., 2001 Present study
Paleoproterozoic	Different locations within Eastern India Ranchi (23.43°N and 85.43°E),	Chhotanagpur plateau	41.5 39.5–40	Mandal and Biswas, 2016 Present study
	Hazaribagh (24.07°N and 85.38°E)		40.5 39.5	Mandal and Biswas, 2016 Present study
	Nirsa (23.86°N and 86.66°E)		41.4 37–37.5	Mandal and Biswas, 2016 Present study
	Dumka (24.60°N and 87.08°E)		40.1 40–40.5	Mandal and Biswas, 2016 Present study

of the spectrum analysis result. The density contrasts between surface and MSL and between mantle and crust are presumed to be 1470 and 400 kg/m^3, respectively.

GRAVITY PROFILING AND CRUSTAL LAYER MAPPING

The depths to the gravity sources in the sub-surface can be estimated from the shapes of the anomalies or the shapes of the power spectra (**Figure 4**) computed from the potential field data (Spector and Grant, 1970; Curtis and Jain, 1975; Djomani et al., 1992; Chavez et al., 1999; Lefort and Agarwal, 2002; Rivero et al., 2002; Gomez-Ortiz et al., 2005; Bansal et al., 2006). 2D spectral analysis for 1° × 1° and 2° × 2° to ensemble basement, Conrad depth, and Moho depth was carried out for archiving reliable information of the subsurface (**Tables 2–4**).

In the present study, 13 gravity profiles (AA′ to MM′, **Figure 3**) were selected to investigate the configurations of the crustal layers. Most of the profiles are orthogonal to the regional trend of the gravity anomaly. These profiles run from south to north, extending over ∼225 km, and were selected following the general structural trends of the various shear zones, except profiles 3–4 on the east, which are parallel to the trend of the Bouguer gravity anomaly. Profiles 1–4 (AA′ to DD′, **Figure 6**), located over the low Bouguer gravity anomaly (−35 to −60 mGal), are associated with the Ranchi-Hazaribagh plateau and UGB, while the profiles 9–13 (II′ to MM′) lie over the highest Bouguer gravity anomaly (i.e., −20 to +33 mGal), associated with the Rajmahal Trap and surrounding areas. The initial model along profiles AA′ to II′ was considered on the basis of spectrum analysis, studies of Verma et al. (1976); Verma (1985), Ismaiel et al. (2019), and Krishna et al. (2019), and other geological background data (Mahadevan, 2002). The final model was selected through minimization of error during optimization of the layer parameters and corresponding densities.

The 2D gravity modeled parameters for the study area (84.75–87.75°E and 23.0–25°N) covered by all the 13 profiles (AA′ to MM′) were used for the computation of parameters of different crustal layers. The results of the 2D gravity modeling were integrated into two maps for the Moho discontinuities and sediment thickness mapping (**Figures 7**, **8**). The mapping of the Conrad discontinuity was not carried out because of its apparent uniformity over the area. The isostatic anomaly

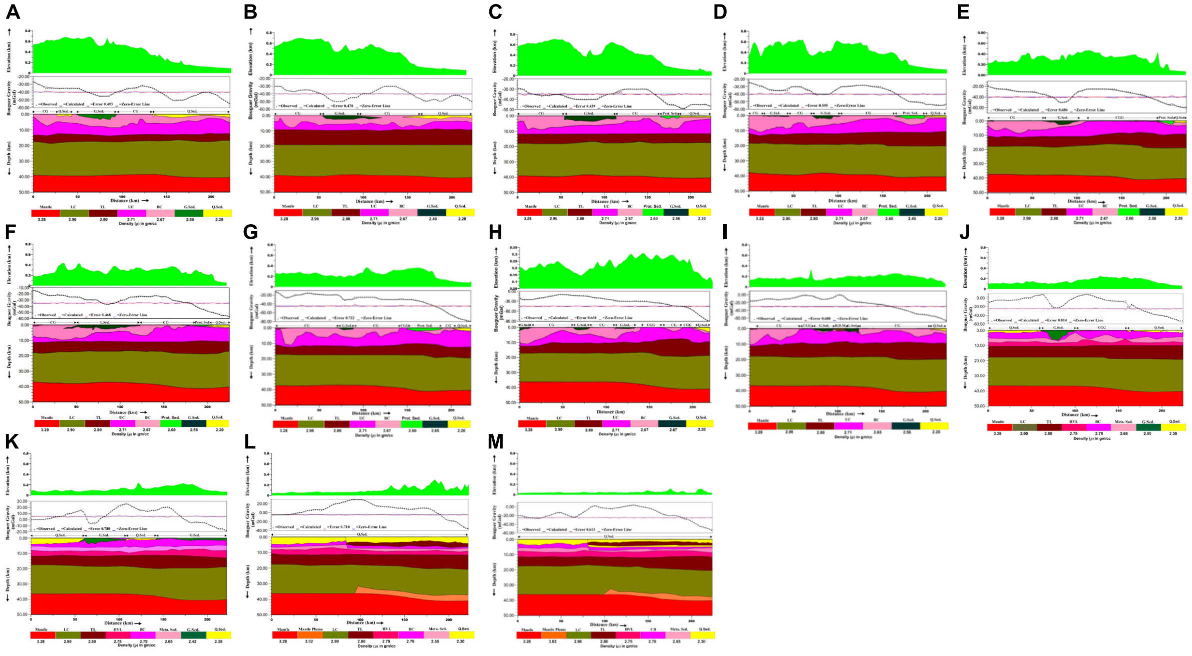

FIGURE 6 | (A) 2D gravity model along profile AA′ (at longitude 84.75°E), location of the profile is shown in **Figure 3**. Abbreviations: CG, Chhotanagpur granite; CGG, Chhotanagpur granite gneiss; Q. Sed., quaternary sediment; G. Sed., Gondwana sediment; Prot. Sed., proterozoic sediment; LC, lower crust; TL, transition layer; UC, upper crust; BC, basement complex. **(B)** 2D gravity model along profile BB′ (at longitude 85.00°E), location of the profile is shown in **Figure 3**. **(C)** 2D gravity model along profile CC′ (at longitude 85.25°E), location of the profile is shown in **Figure 3**. **(D)** 2D gravity model along profile DD′ (at longitude 85.50°E), location of the profile is shown in **Figure 3**. **(E)** 2D gravity model along profile EE′ (at longitude 85.75°E), location of the profile is shown in **Figure 3**. **(F)** 2D gravity model along profile FF′ (at longitude 86.00°E), location of the profile is shown in **Figure 3**. **(G)** 2D gravity model along profile GG′ (at longitude 86.25°E), location of the profile is shown in **Figure 3**. **(H)** 2D gravity model along profile HH′ (at longitude 86.50°E), location of the profile is shown in **Figure 3**. **(I)** 2D gravity model along profile II′ (at longitude 86.75°E), location of the profile is shown in **Figure 3**. **(J)** 2D gravity model along profile JJ′ (at longitude 87.00°E), location of the profile is shown in **Figure 3**. **(K)** 2D gravity model along profile KK′ (at longitude 87.25°E), location of the profile is shown in **Figure 3**. **(L)** 2D gravity model along profile LL′ (at longitude 87.50°E), location of the profile is shown in **Figure 3**. **(M)** 2D gravity model along profile MM′ (at longitude 87.75°E), location of the profile is shown in **Figure 3**.

(**Figure 9**) was computed based on the differences between the Bouguer gravity anomalies and the gravity values of the computed root zones estimated from the topography (Heiskanen and Vening Meinesz, 1958).

The Moho depth map (**Figure 7**) was generated by the U.S. Geological Survey program called AIRYROOT (Simpson et al., 1983). Moho depth was also computed by 2D spectral analysis, sub-dividing the Bouguer anomaly map into 12 zones of dimension 2° × 2° (Regan and Hinze, 1976) with a uniform 75% overlap with the adjacent grid (**Table 2**). The sediments depth map (**Figure 8**) was generated by 2D spectral analysis, sub-dividing the Bouguer anomaly map into 99 zones of 1° × 1° dimension (**Table 3**) with a uniform 75% overlap with adjacent grid (Regan and Hinze, 1976) for better resolution and continuity of data points.

RESULTS

Sub-surface Structures Along the Gravity Profiles

The profiles on the west (AA′ to DD′) selected over a relatively lower Bouguer gravity anomaly (**Figures 6A–D**), brought out six layers with some pockets of sediments. The first layer from 0 to 3.5 km comprises the Gondwana sediment with a density of 2.40–2.65 gm/cm^3 and quaternary sediment of density 2.20 gm/cm^3 (Choudhury, 1974). The maximum thickness found in the Damodar valley area corroborates the observation proposed by Verma (1985). The thickness of the second layer consisting of a granitic basement complex with a density of 2.67 gm/cm^3 varies from 0 to ∼10 km, showing thinning toward the north. In some places, the sediments are almost absent, exposing the basement on the surface. The third layer of granite gneiss with a density of 2.71 gm/cm^3 occurs from 2 to 10 km depths, thickening toward the north. The fourth layer of density 2.80 gm/cm^3 is apparently a transition layer between the continental and oceanic crust. Ismaiel et al. (2019) and Krishna et al. (2019) also observed a similar layer at ∼8–13 km depth. The boundary between the lower crust (average density: 2.90 gm/cm^3) and the transition layer is found at ∼17–20 km depths. The Moho depth along these profiles is found to vary between ∼38 and 40 km, corroborating the observations of Singh et al. (2015) and Mandal and Biswas (2016). Beneath the Moho, the density of the upper mantle is found to be 3.28 gm/cm^3.

Profiles 5–8 (EE′ to HH′) lie over the intermediate Bouguer gravity anomaly (i.e., −80 to −15 mGal), and pass through

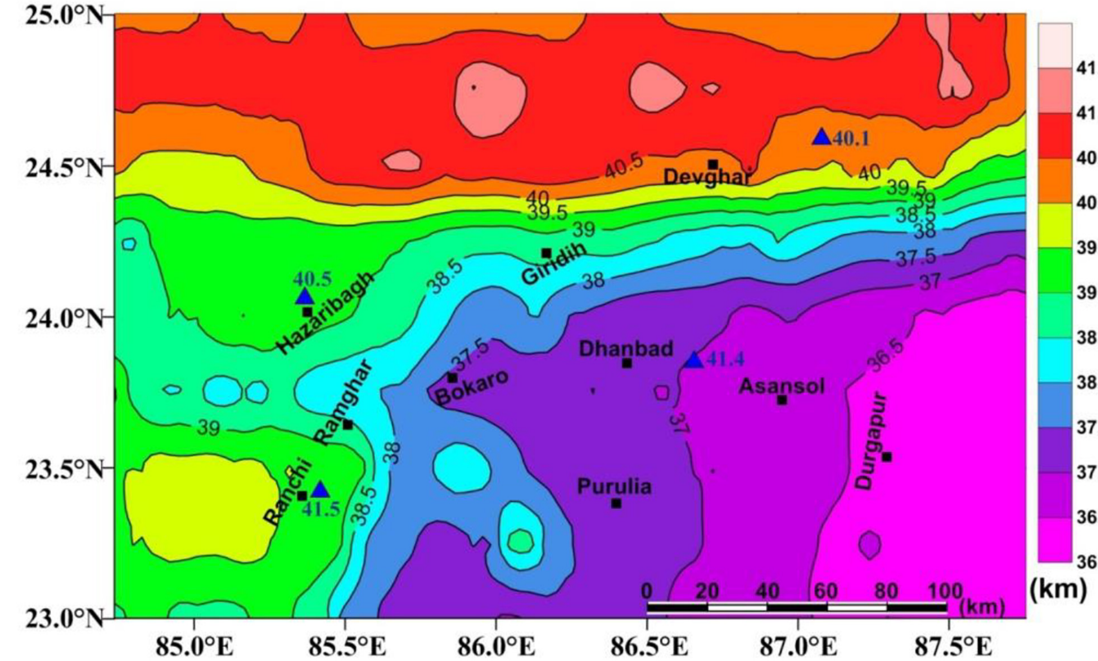

FIGURE 7 | Moho depth map deduced from spectral analysis technique and AIRYROOT program using a contour interval of 0.5 km (with color-coded index on the east). Blue triangle represents the location of broadband seismic stations in the EIS region and below their blue color texts represent the value of Moho depth calculated by receiver function analysis (Mandal and Biswas, 2016).

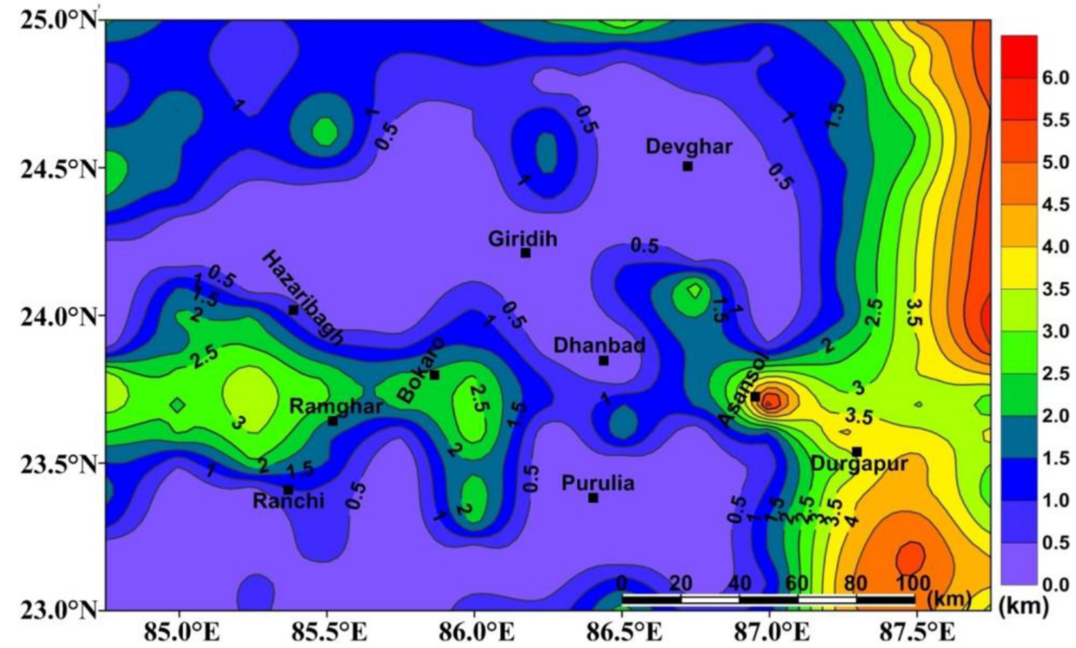

FIGURE 8 | Sediment depth map deduced from spectral analysis, with a contour interval of 0.5 km.

the Bokaro-Dhanbad coal field and the Purulia shear zone. The only difference is the upper crust exposed on the surface at each profile. Here, sediment thickness is 0–2.5 km and the Moho varies from ∼37 to 41 km. The observations corroborate the observations of Verma (1985), Sharma et al. (2015), and Das et al. (2019). Profile 9 (II′) runs through the Raniganj coalfield. The deposition of the Gondwana sediments (i.e., 2.42 gm/cm^3) is laterally continued from 75 to 125 km of the profile. Occasionally, the sediment is punctuated by patches of high density (2.80 gm/cm^3) material. Here, Moho is found at a depth of 37–40 km, dipping toward the north. This observation is corroborated by the studies of Verma et al. (1976), Singh et al. (2015), and Mandal and Biswas (2016).

Profiles toward the east (JJ′ to MM′) pass over the relatively higher Bouguer gravity anomaly (**Figures 6J–M**). A total of six layers with an additional high velocity crystalline basement of density 2.75 gm/cm^3 are identified along these profiles. Alluvium/sediment forming 0–4 km thick layer, with patches of Gondwana sediments, are found overlain on a 2–6 km thick layer of basement complex. A depression in the Bouguer gravity anomaly, noted at 75 km along the profile JJ′, is interpreted to be associated with ∼4–5 km basin of Gondwana sediments (density: 2.42 gm/cm^3) in the Raniganj coalfield area. The profile KK′ shows a merger of ∼0.5–2 km thick Gondwana sediments with the alluvium/sediment of LGB (Verma et al., 1976). We find a high velocity layer at ∼6–8 km depth. A metasediment layer with a density of 2.65 gm/cm^3 is sandwiched between the basement complex and the high velocity layer. A transition layer is identified at ∼10–12 km depth. Along profiles LL′ and MM′, a ∼3–6 km thick layer of alluvium/sediment is identified, which corroborates the observations of Qureshy (1969, 1970) and Singh et al. (2004). We have identified a fault extending from the surface to 8 km depth, at ∼80 km distance toward the south. In profile LL′, a high density (2.80 gm/cm^3) material is found intruding the basement complex, but the same intruded materials are sandwiched between two sedimentary layers in the profile MM′; the high-density materials are apparently associated with the Rajmahal traps. In these areas (profiles JJ′ to MM′), Moho varies from ∼36 to 41 km.

Variation of Crustal Structure

The Moho depth (**Table 4** and **Figure 7**) is found to vary from 40 to 41.5 km in the northern part near the IGB, apparently corroborating the observation of Singh et al. (2015), but differs from Qureshy (1969), who reported the crustal thicknesses beneath the IGB to be 37.5 km. The Damodar Gondwana basin shows moderate to low Moho depth of 37–39 km, whereas the Ranchi plateau shows a maximum depth of ∼39–40 km for the Moho; this result is well corroborated by the study of Mandal and Biswas (2016) (**Table 4**). The Moho depth varies from ∼37 to 37.5 km beneath the Dhanbad and Bokaro region. This observation differs from Singh et al. (2015), who found the Moho at depths between 36 and 40 km in this region. The LGB in the region of Bengal shows a minimum depth of Moho to be 36.5 km, which agrees with the Moho depth of 35–36 km computed by Singh et al. (2015). Mitra et al. (2008) found the Moho boundary at ∼37.5 km depth near the LGB. Kaila et al. (1992) also found the Moho at ∼35 km depth. We further compared the depth of Moho beneath other continents of a similar age around the world (**Table 4**) and found compatible results.

The map (**Figure 8**) illustrates that the thicknesses of sediments vary between 0.0 and 6.5 km. A strip-like region of ∼160 km lateral extent (∼23.5 to ∼24 °N) and a sediment thickness of 0.5–3.0 km is found to be associated with the Damodar Gondwana basin (Verma and Ghosh, 1977). Sediment thickness varies from 0 to 2 km toward the north near the UGB. Qureshy (1969) and Choudhury (1974) also reported similar thicknesses of the Quaternary sediments in these areas. The eastern part of the region exhibits a maximum thickness of sedimentary cover, reaching more than 6.0 km, particularly in the LGB, and corroborates the observations of Kaila et al. (1992, 1996), Mall et al. (1999), and Singh et al. (2004). At several places, on both sides of the Damodar Gondwana basin, the basement is exposed on the surface, usually found in the Achaean terrain (Verma, 1985; Veevers and Tewari, 1995; Bhattacharya and Bhattacharya, 2015; Acharyya, 2018a).

Isostatic anomaly is found to be varied from −87 to 44 mGal (**Figure 9**), and the minimum value is found on the northern and eastern part, where the elevation from the MSL is minimum, indicating over-compensation along the UGB. The maximum value of 44 mGal, representing the under-compensation, is identified toward the east and south near the LGB, Rajmahal trap, and Singhbhum shear zone. The coal-rich Damodar Gondwana basin (i.e., Bokaro, Dhanbad, and Asansol areas) shows −1 to −30 mGal isostatic anomalies, indicating over-compensation because of subsiding basement of the areas. The Ranchi and Hazaribagh Plateaus show almost compensated parts with values of isostatic anomalies of 0–5 mGal.

DISCUSSION

The reconstructed map of the study area is characterized by extensively low regional gravity in the range of −40 to −10 mGal (**Figure 3**), with some highs in the central part in the form of oxbow-shape and the well-defined shear zones characterized by high Bouguer gravity of values around −20 mGal at the southern part. A region in the UGB, elongated from west to east between 24° and 25°N in the northern part of the study area, is characterized by relatively low Bouguer value of −50 mGal. A very low anomaly of about −80 mGal has been noted toward the northern part of this region, and might be associated with the downward flexing of the Indian basement beneath the Himalayan Foothills. The Rajmahal trap and LGB show some high Bouguer gravity, ranging between −10 and +33 mGal.

Three individual discontinuities (i.e., basement, Conrad, and Moho) show a varying sediment thickness of zero to 6.2 km with significant lateral density variation from 2.2 gm/cm^3 (approximated to be alluvial sediments) to 2.40 gm/cm^3 (for Gondwana sediments). The upper crustal layer with an average density of about 2.67 gm/cm^3 is followed by the crystalline basement of density 2.75 gm/cm^3 and transitional layer of 2.80 gm/cm^3. The Conrad layer at ∼17 and 20 km is marked by a sharp increase in density of the lower crustal layer (average density is 2.90 gm/cm^3). The model indicates that the crust-mantle boundary (i.e., Moho) ranges from ∼36 km in the southeastern part of the LGB to ∼42 km toward north, possibly due to the stretching and thinning of the crust toward the south. The mean density is taken as 3.28 gm/cm^3 for the upper mantle layer (**Table 1**).

Elevation of the study area varies from zero to ∼700 m with the highest value observed at its southwest part, and the northern

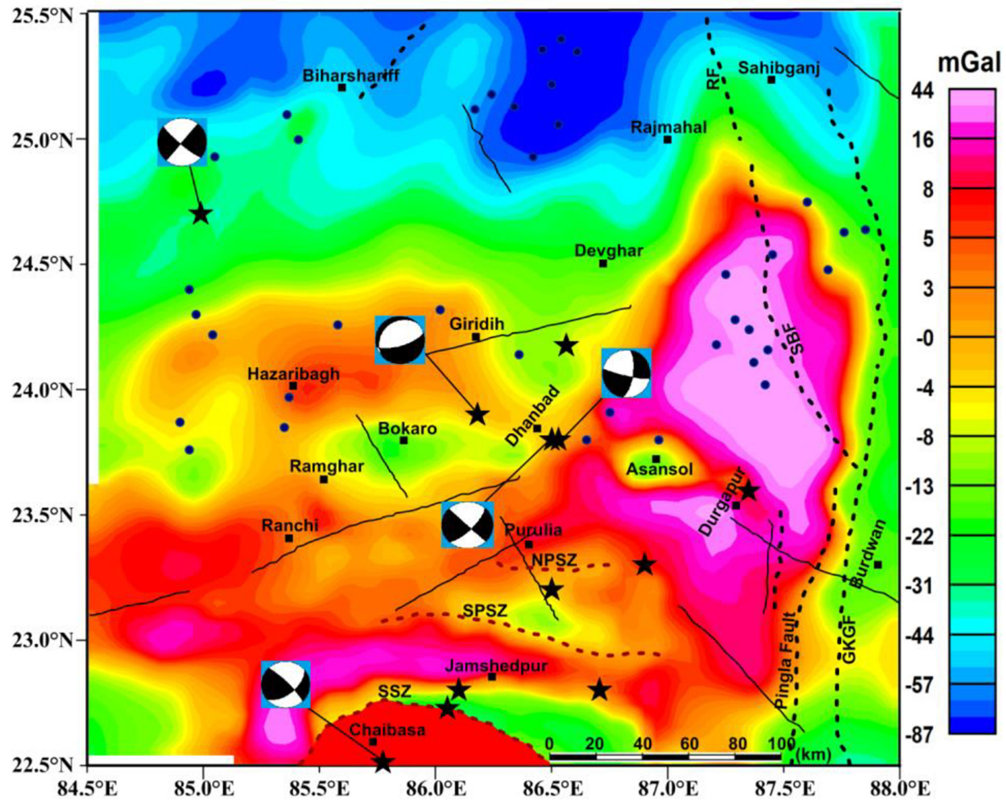

FIGURE 9 | Airy Isostatic anomaly map of the study area, generated by removing the gravity effect of topography and its root (Airy) from the Bouguer gravity anomaly. Dark blue solid circles represent the location of the hot springs (after Sankar et al., 1991). Black stars represent the location of local earthquakes with magnitude M > 2.0, and beach balls show the focal mechanisms of some events.

and eastern parts associated with the LGB show minimum elevation (**Figure 1**). Moho depth varies from ∼36 to 41.5 km with minimum value found in the southeast corner of the study area, near the LGB, but the northern part has a maximum depth of Moho at ∼40.5–41.5 km (**Figure 7**). Moho dips toward the southeast near LGB, whereas toward the north the Moho is dipping more sharply than other parts of the study area. Sediment thickness varies from 0 to 6 km beneath the study area. Maximum area shows zero sediment thickness, i.e., the basement is exposed on the surface. A few pockets of sediments are found to be associated with coal-bearing Gondwana basin. The eastern part of the study area shows a high accumulation of sediment (**Figure 8**).

Bouguer and Isostatic Anomalies and the Vertical Stability of the Study Area

Isostatic anomaly is the difference between the Bouguer gravity anomaly and the computed anomaly of root zone computed from the topography. Isostasy anomaly in the study area varies from −87.0 mGal to a maximum of +44.0 mGal (**Figure 9**). The northern part of the study area (i.e., UGB) is associated with a strong negative Bouguer anomaly (∼−55 to −96 mGal) and moderate to high negative isostatic anomaly (∼−44 to −87 mGal) with minimum elevation of topography. This apparently accounts for the over-compensation, and is presumably caused by a deficit of rock-mass in the basin (Abbas and Subramanian, 1984; Lyon-Caen and Molnar, 1985). The UGB was explained to be a down warping foredeep of the Himalayan orogen, and the sediments in this basin, subducted along with the converging Indian plate against the Eurasian plate, evolved into the Siwalik Hills, which further resulted in the flexing zone into the over-compensated area (Lyon-Caen and Molnar, 1985). Maximum positive isostatic anomaly (H-1 and H-2; +5 to +44 mGal) is observed toward the southeast near the LGB and southern part of the study area near the Singhbhum shear zone and South Purulia shear zone. Here, the low to moderate elevation of topography records little negative (∼−16 mGal) to moderate positive values (∼+33 mGal) Bouguer gravity anomalies. The positive Bouguer gravity anomaly may be due to the presence of high-density material in the shear zones, Raniganj Coal-field, and Rajmahal trap, and the positive isostatic anomaly indicates under-compensation in the region. It is clear from the sediment map that the eastern part is loaded with enormous amounts of sediments (Sengupta, 1966; Abbas and Subramanian, 1984; Alam et al., 2003; Roy and Chatterjee, 2015; Ghosh, 2018). The coal-bearing Damodar Gondwana basin accommodated the E-W extending Damodar River (Verma, 1985; Acharyya, 2018b) where the isostatic anomaly varies from ∼−22 to +5 mGal and Bouguer gravity anomaly varies from ∼−47 mGal to −24 mGal. Moderately negative Bouguer anomaly and moderately negative to slightly positive isostatic gravity anomalies account for either over-isostatic compensation or near to zero-compensation for the region. Within the drainage area, it collects huge amounts of sediments denudated from the adjacent Ranchi and Hazaribagh plateaus (i.e., under-compensated), which makes some areas over-compensated. Ranchi and Hazaribagh plateaus have a maximum elevated topography (∼700 m) and show moderate Bouguer gravity anomaly (∼−38 to −31 mGal) with little positive isostatic anomaly (+4 to +8 mGal). This apparently accounts for the little under-compensation of the area. To inquire into the overall stability, both positive and negative values of isostatic anomalies are apparent over the study area (**Figure 9**). Negative value within UGB corresponds to the over-compensation, reflecting higher value in Moho depth up to ∼41 to 41.5 km, whereas positive value of isostatic anomaly reflects under-compensation and less Moho depth up to 36 km in the LGB. The western part, near the Ranchi and Hazaribagh plateau, apparently falls under positive isostatic anomaly with a normal Moho depth of 39–39.5 km (**Table 4**). Overall, the Moho is uplifted in the southeast part, whereas it is subsided toward the north of the study area because of the down-going basement beneath the foreland Gangetic basin.

Earthquake Activities and Seismic Stability of the EIS and Adjoining Regions

The study area is tectonically very significant, comprising mainly the EIS and the Singhbhum craton, starting from the northern end of the Eastern Ghats Belt (EGB) and Bengal estuary to the bending zone beneath the IGB. A geophysical study carried out by Sengupta (1966) indicates the disappearance of the Achaean basement of the shield area below the alluvial plain of the LGB. The exposed Achaean basement in the Shillong plateau in the northeast is apparently a continuation of the Peninsular shield through the Garo-Rajmahal gap (Evans, 1964). A series of faults and fractures pass all through the western margin of the LGB (**Figure 2**) and are likely continued in the Himalayas toward north (Valdiya, 1976). The buried ridges of this area are likely to be isolated in the LGB in the east. A recent study (Khan et al., 2020) shows that the lithospheric deformation in the deeper part of the area is apparently active. Further, numerous hot springs in the Damodar Gondwana basin and adjacent areas near the crest of the flexural bulging of the Indian plate are facilitating reactivation of the crust through the triggering of small magnitude earthquakes because of the strain weakening processes (Mahadevan, 2002; Bilham et al., 2003).

The study area experienced a number of moderate magnitude earthquakes in the past (discussed in section "Introduction") (**Figure 2**). A recent study (Singh et al., 2020) has shown that the faulting processes in the EIS are apparently dominated by strike-slip movements. It was further transformed into extension in the northeast part of the area between the junction of the Ganga and the Brahmaputra River basins. The compression tectonics dominated by thrust faulting presumably triggered many great damaging earthquakes in the Nepal-Bihar segment of the Himalayas (**Figure 2**). Stretching of the basement toward the northeast of the present study area is also quite active, and likely continued with the subduction of the Indian plate toward the east beneath the Myanmar microplate (Khan, 2005; Singh et al., 2020). The present earthquakes are mostly of shallow origin and low magnitude, occasionally reaching to more than 4.0 magnitude, and few occur in the lower crust (Singh et al., 2020). It is found that the depths of 20 events are very shallow (<20 km), associated with the upper crust and likely caused by reactivation processes in the basement. The role of high heterogeneities of the crust (Khan et al., 2016, 2020; Singh et al., 2019) can also be the reason for the occurrences of low to moderate magnitude earthquakes in this part of Eastern India. The recent 2011 M 6.9 Sikkim and 2015 M 7.8, 7.3 Nepal-Bihar earthquakes, and the great aftershocks of magnitudes more than 6.0, encouraged earthscientists to review the seismotectonics of the Nepal-Bihar-Sikkim segment and its southern shield areas.

Toward the southeastern side of the study area, the Indian oceanic plate is subducting below the Eurasian plate along the Andaman-Nicobar margin (Khan et al., 2020) and beneath the Myanmar microplate toward east (Khan, 2005). This has made the Bay of Bengal (BOB) seismically active with incidents of earthquakes of magnitudes (m_b) 5.5, 5.7, and 5.2 in 1964, 1989, and 1992, respectively. The 1964 Midnapore earthquake was dominated by thrust-faulting (Chandra, 1977), and the other two earthquakes were dominated by strike-slip faultings (Rao et al., 2015). An analysis of earthquakes during 1900–2011 reveals that the older structural features and weak zones near the BOB and adjacent regions were reactivated by regional stress field (Murthy et al., 2010; Rao et al., 2015). The NW-SE trending fracture zones in the BOB are found to be correlated with strike-slip faultings. The seismicity in the southern and eastern parts of the BOB is dominated by thrust faulting due to a predominant N-S compression, which had back-propagated stress from the Himalayan orogen (Biswas and Majumdar, 1997).

Himalayan tectonics are likely linked with the zone of intense deformation of the oceanic lithosphere near the equatorial Indian Ocean (EIO) Basin (Geller et al., 1983; Cloetingh and Wortel, 1986). An east-west extended structural break in this area of the northern Indian Ocean is particularly associated with the diffuse segment (DeMets et al., 1990), and has isolated the Australian plate and the Indian plate in the south to southwest. The intense seismic activities, along with the occurrences of great earthquakes, operative stress fields, and the high heat flow of the area, also support this observation (Weissel et al., 1980; Geller et al., 1983; Bergman and Solomon, 1984; Weins, 1985). The ∼N-S striking aseismic 85 and 90°E ridges divide the BOB into three main sub-basins (Gopala Rao et al., 1997), apparently guiding the active stress of the lithosphere, linking the Himalayan operative tectonics through the EIS, Singhbhum craton, and the IGB. Several faults and lineaments on both sides of the Munger-Saharsa ridge are intersecting the Foothills of the Himalaya, and these geo-fractures are likely extended all through the Gangetic basin, concentrating and raising the stress in the flexing zone of the subducting Indian crust (Sibson, 1980; Marshak and Paulsen, 1997; Godin and Harris, 2014; Khan et al., 2017a; Khan et al., 2021). The plate obliquity of 0° to less than

10° of the Nepal-Bihar-Sikkim area (Khan et al., 2014) further enhances and confines the stress field around the flexing zone through interacting fractures and triggering great earthquakes by the stress build-up processes.

CONCLUSION

The Bouguer gravity anomaly map indicates that the study area is characterized by low (−96 mGal) to moderate (+33 mGal) regional anomalies with the maximum value over the Rajmahal trap, the LGB in the east, and over the well-defined shear zone in the south (**Figure 3**). The minimum Bouguer gravity anomaly values of −50 to −96 mGal are associated with the UGB, elongated along east-west between 24.5° and 25.5°N in the northern part of the study area. Such a low anomaly in the area is possibly associated with the downward flexing of the Indian basement beneath the Himalayan Foothills. Ranchi, Hazaribagh, Giridih, Bokaro, Ramgarh, and the western part of the study area are found to be associated with ∼−30 to −40 mGal anomalies. Further, a few pockets recorded low anomalies of ∼−40 to −50 mGal, as seen in Chaibasa in the extreme south. The 2D gravity modeling (**Figure 5**) shows a sediment layer of thicknesses of ∼0–6.5 km, with a significant density variation of 2.2–2.65 gm/cm^3, underlain by a basement of a density of 2.67 gm/cm^3. The Conrad is marked by an increase in density from ∼2.67 to 2.90 kg/m^3 at depths between 17 and 20 km. The average density of the upper mantle layer is computed to be ∼3.28 gm/cm^3. A ∼2–3 km thick high density (3.02 gm/cm^3) material overlies the Moho toward the east and is apparently connected with the Rajmahal trap (Singh et al., 2004). The maximum depth of the Moho is found to be ∼40.5–41.5 km toward the north (UGB), while Moho near the LGB has the lowest depth of ∼36 km. Ranchi and Hazaribagh plateau are underlain by Moho at ∼39–39.5 km depths. The uplifted Moho and the maximum deposition of alluvium sediments are found beneath the LGB in the southeastern part (**Table 4**).

A residual isostatic map provides the status of stability of any study area. Based on isostatic anomaly (**Figure 9**), it is found that the northern part (Gangetic basin), a down-warping fore-deep of the Himalayan orogen, is over-compensated. Eastern and southern parts, comprising the LGB and shear zones (e.g., Singhbhum and North and South Purulia, **Figure 1**), have predominant records of under-compensation. While the coal-bearing Damodar Gondwana basin is partially over-compensated, the Ranchi and Hazaribagh plateau have achieved partial under-compensation. The present study also shows that the exposed Achaean basement of the shield area at various locations disappears below the Gangetic basin and is affected by active stretching toward the northeast of India (Singh et al., 2020). Seismic activities of this region are mostly of shallow origin, particularly associated with the basement within the upper crust. Although the region experienced a few moderate magnitude earthquakes in the historical past (**Figure 2**), occasional incidents of recent earthquakes have magnitudes less than 5.0. Occasional events are also found in the deeper part and might be related to the reactivation processes in the lower crust. The eastern part of the study area is also activated seismically due to the subduction processes of the Indian plate beneath the Myanmar microplate.

The long-term observations of occurrences of moderate to low magnitude earthquakes in the EIS, Singhbhum craton, and the BOB apparently account for seismic stability of the region, extending from the diffused EIO to the Nepal-Bihar-Sikkim Himalayan region. Lithospheric stress in the BOB is guided by the aseismic 85 and 90°E ridges, partially accumulated along the different fault-guided zones or other tectonic elements and triggering low-magnitude events. Sometimes, the ∼N-S striking regional fault systems (e.g., EPF, WPF, PF, MSRF, MSRMF, etc., **Figure 2**) also guide the stress field, concentrating and raising it in the bending zones of the downward migrating Indian lithosphere, are triggering occasional great earthquakes in the Himalaya. The back-propagation stress from the Himalayan Mountain possibly facilitates deformation in the EIO basin (Weissel et al., 1980; Geller et al., 1983; Cloetingh and Wortel, 1986; DeMets et al., 1990). The pure compression in the foothills of the Nepal Himalaya and the minimum obliquity of the converging Indian plate corroborate the observation of stress enhancement in the flexing zone of the down-going plate. We propose that the prevailing stress fields in the converging Indian lithosphere, guided by the aseismic 85 and 90°E ridges, are migrating through the low-to-moderately stable BOB and EIS. The migrating enhanced stress (because of minimum Indian plate obliquity, Figure 9 of Khan et al., 2014) is further guided by the foothill transecting fault systems to be concentrated in the bending zone of the penetrating lithosphere beneath the Himalaya. This increasing accumulated stress occasionally triggers great earthquakes in the Nepal-Bihar-Sikkim sector of the Himalaya.

DATA AVAILABILITY STATEMENT

The raw data supporting the conclusions of this article will be made available by the authors, without undue reservation.

AUTHOR CONTRIBUTIONS

All authors listed have made a substantial, direct, and intellectual contribution to the work, and approved it for publication.

ACKNOWLEDGMENTS

RS is thankful to the Director of the Indian Institute of Technology (ISM), Dhanbad, for financial support to complete the present work and Dhananjay Singh, Geophysicist, M & CSD, Geological Survey of India, Kolkata, West Bengal, India, for his useful and critical suggestions during the computation of 2D gravity modeling. Thanks to both of the reviewers for their valuable comments, which improved the manuscript greatly. The authors are grateful to S. P. Mohanty for thorough revision and correction and improvement of the English of the whole manuscript.

REFERENCES

Abbas, N., and Subramanian, V. (1984). Erosion and sediment transport in the Ganges River basin (India). *J. Hydro.* 69, 173–182. doi: 10.1016/0022-1694(84)90162-8

Acharyya, S. K. (2018b). "Development of Gondwana Basins in Indian Shield," in *Tectonic Setting and Gondwana Basin Architecture in the Indian Shield*, ed. S. K. Acharyya (Berlin: Elsevier), 17–29. doi: 10.1016/b978-0-12-815218-8.00003-0

Acharyya, S. K. (2018a). "Chapter 1 – **Introduction**," in *Tectonic Setting and Gondwana Basin Architecture in the Indian Shield*, Vol. 4, ed. S. K. Acharyya (Berlin: Elsevier), 1–5. doi: 10.1016/b978-0-12-815218-8.00001-7

Alam, M., Alam, M. M., Curray, J. R., Chowdhury, M. L. R., and Gani, M. R. (2003). An overview of the sedimentary geology of the Lower Gangetic basin in relation to the regional tectonic framework and basin-fill history. *Sed. Geol.* 155, 179–208. doi: 10.1016/s0037-0738(02)00180-x

Altenbernd, T., Wilfried, J., and Wolfram, H. G. (2020). The bent prolongation of the 85°E Ridge south of 5°N – Fact or fiction? *Tectonophysics* 785:228457. doi: 10.1016/j.tecto.2020.228457

Ammon, C. J., Randall, G. E., and Zandt, G. (1990). On the non-uniqueness of receiver function inversions. *J. Geophys. Res.* 95, 15303–15318. doi: 10.1029/jb095ib10p15303

Ansari, M. A., Khan, P. K., Tiwari, V. M., and Banerjee, J. (2014). Gravity anomalies, flexure, and deformation of the converging Indian lithosphere in Nepal and Sikkim–Darjeeling Himalayas. *Int. J. Earth Sci.* 103, 1681–1697. doi: 10.1007/s00531-014-1039-0

Ates, A., and Kearey, P. (2000). Interpretation of gravity and aeromagnetic anomalies of the Kenya region, south central Turkey. *J. Balkan Geophys. Soc.* 3, 37–44.

Bansal, A. R., and Dimri, V. P. (2010). Scaling spectral analysis: A new tool for interpretation of gravity and magnetic data. *Earth Sci. India* 3, 54–68.

Bansal, A. R., Dimri, V. P., and Sagar, G. V. (2006). Depth estimation from gravity data using the maximum entropy method (MEM) and the multi taper method (MTM). *Pure Appl. Geophys.* 163, 1417–1434. doi: 10.1007/s00024-006-0080-8

Bergman, E. A., and Solomon, S. C. (1984). Source mechanisms of earthquakes near mid-ocean ridges from body waveform inversion: implications for the early evolution of oceanic lithosphere. *J. Geophys. Res.* 89, 11415–11441. doi: 10.1029/jb089ib13p11415

Bhattacharya, B. B., and Shalivahan, S. S. (2002). The electric Moho underneath Eastern Indian Craton. *Geophys. Res. Lett.* 29:1376.

Bhattacharya, H. N., and Bhattacharya, B. (2015). Lithofacies architecture and palaeogeography of the Late Paleozoic glaciomarine Talchir formation, Raniganj Basin, India. *J. Palaeogeog.* 4, 269–283. doi: 10.1016/j.jop.2015.08.006

Bhattacharyya, B. K., and Leu, L.-K. (1975). Spectral analysis of gravity and magnetic anomalies due to two dimensional structures. *Geophys* 40, 993–1013. doi: 10.1190/1.1440593

Bilham, R., Bendick, R., and Wallace, K. (2003). Flexure of the Indian plate and intraplate earthquakes. *Proc. Indian Aca. Sci. Earth Planet. Sci.* 112, 315–329. doi: 10.1007/bf02709259

Biswas, S., and Majumdar, R. K. (1997). Seismicity of the BOB: evidence for intraplate deformation of the northern Indian plate. *Tectonophysics* 269, 323–336. doi: 10.1016/s0040-1951(96)00168-0

Bonvalot, S., Balmino, G., Briais, A., Kuhn, M., Peyrefitte, A., Vales, N., et al. (2012). *World Gravity Map. Commission for the Geological Map of the World.* ed. BGI-CGMW-CNES-IRD. Paris: CGMW.

Bose, M. K. (1999). Geochemistry of the metabasics and related rocks from the eastern part of the Proterozoic Singhbhum mobile belt, eastern India—Petrogenitic implications. *Indian J. Geol.* 71, 213–234.

Bose, M. K. (2008). "Petrology and geochemistry of Proterozoic 'Newer Dolerite' and associated ultramafic dykes within Singhbhum granite pluton, eastern India," in *Indian Dykes: Geochemistry, Geophysics and Geochronology,* eds. R. K. Srivastava, C. Sivaji, and N. V. Chalapathi Rao (New Delhi: Narosa Publishing House Pvt. Ltd.), 413–445.

Bose, M. K. (2009). Precambrian mafic magmatism in the Singhbhum craton, Eastern India. *J. Geol. Soc. India* 73, 13–135. doi: 10.1007/s12594-009-0002-3

Burdick, L. J., and Langston, C. A. (1977). Modeling crustal structure through the use of converted phases in teleseismic body-wave forms. *Bull. Seismol. Soc. Am.* 67, 677–691.

Carbó, A., Muñoz-Martín, A., Llanes, P., Álvarez, J., and Eez Working Group. (2003). Gravity analysis offshore the Canary Islands from a systematic survey. *Mar. Geophys. Res.* 24, 113–127. doi: 10.1007/1-4020-4352-x_5

Chamoli, A., and Dimri, V. P. (2010). "Spectral analysis of gravity data of NW Himalaya," in *Proceedings of the EGM 2010 International Workshop, Apr 2010, cp-165-00048*, Capri.

Chamoli, A., Swaroopa Rani, V., Srivastava, K., Srinagesh, D., and Dimri, V. P. (2010). Wavelet analysis of the seismograms for tsunami warning. *Nonlin. Process. Geophys.* 168, 569–574. doi: 10.5194/npg-17-569-2010

Chandra, U. (1977). Earthquakes of Peninsular India–a seismotectonic study. *Bull. Seismol. Soc. Am.* 67, 1387–1413.

Chapin, D. (1996). A deterministic approach toward isostatic gravity residuals—a case study from South America. *Geophys* 61, 1022–1033. doi: 10.1190/1.1444024

Chatterjee, N., Crowley, J. L., and Ghose, N. C. (2008). Geochronology of the 1.55 Ga Bengal anorthosite and Grenvillian metamorphism in the Chhotanagpur gneissic complex, eastern India. *Precambrian Res.* 161, 303–316. doi: 10.1016/j.precamres.2007.09.005

Chavez, R. E., Lazaro-Mancilla, O., Campos-Enriquez, J. O., and Floresmarquez, E. L. (1999). Basement topography of the Mexicali valley from spectral and ideal body analysis of gravity data. *J. South Am. Earth Sci.* 12, 579–587. doi: 10.1016/s0895-9811(99)00041-3

Choudhury, S. K. (1974). Gravity and crustal thickness in the Indo-Gangetic basins and Himalayan region. *India. Gcophys. J. R. Astron. Soc.* 40, 441–452. doi: 10.1111/j.1365-246x.1975.tb04141.x

Cloetingh, S., and Wortel, R. (1986). Stress in the Indo-Australian plate. *Tectonophysics* 132, 49–67. doi: 10.1016/0040-1951(86)90024-7

Coron, S. S. (1969). "Gravity anomalies as function of elevation. Some results of Western Europe," in *The Earth's Crust and Upper Mantle. Geophysical Monograph*, 13, ed. P. J. Hart (Washington, DC: American Geophysical Union), 304–312. doi: 10.1029/gm013p0304

Curtis, C. E., and Jain, S. (1975). Determination of volcanic thickness and underlying structures from aeromagnetic maps of the Silet area of Algeria. *Geophys* 40, 79–90. doi: 10.1190/1.1440517

Das, M. K., Agrawal, M., Gupta, R. K., and Gautam, J. L. (2019). Lithospheric seismic structure beneath two broadband station sites of the Eastern part of Chhotanagpur plateau: new constraints from receiver functions and dispersion curves. *Phys. Earth Planet. Inter.* 287, 51–64. doi: 10.1016/j.pepi.2019.01.004

Dasgupta, S., Pande, P., Ganguly, D., Iqbal, Z., Sanyal, K., Venkataraman, N. V., et al. (2000). *Seismotectonic Atlas of India and its Environs. Special Publication Series 59.* Kolkata: Geological Survey of India, 87.

DeMets, C., Gordon, R. G., Argus, D. F., and Stein, S. (1990). Current plate motions. *Geophys. J. Int.* 101, 425–478. doi: 10.1111/j.1365-246x.1990.tb06579.x

DeMets, C., Gordon, R. G., Argus, D. F., and Stein, S. (1994). Effect of recent revision to the geomagnetic reversal time scale on estimates of current plate motions. *Geophys. Res. Lett.* 21, 2191–2194. doi: 10.1029/94gl02118

Djomani, Y. H. P., Diament, M., and Albouy, Y. (1992). Mechanical behaviour of the lithosphere beneath the Adamawa Uplift (Cameroon, West Africa) based on gravity data. *J. African Earth Sci.* 15, 81–90. doi: 10.1016/0899-5362(92)90009-2

Dueker, K. G., and Sheehan, A. F. (1997). Mantle discontinuity structure from midpoint stacks of converted P to S waves across the Yellowstone hotspot track. *J. Geophys. Res.* 102, 8313–8327. doi: 10.1029/96jb03857

Evans, P. (1964). The tectonic frame work of Assam. *J. Geol. Soc. India* 5, 80–96.

Geller, G. A., Weissel, J. K., and Anderson, R. N. (1983). Heat transfer and intraplate deformation in the central Indian Ocean. *J. Geophys. Res.* 88, 1018–1032. doi: 10.1029/jb088ib02p01018

Geller, R. J. (1991). Supercomputers in seismology: determining 3-D earth structure. *SIAM News* 24:5.

Ghose, N. C. (1983). Geology, tectonics and evolution of Chotanagapur granite-gneiss complex. Eastern India. *Recent Res. Geol.* 10, 211–247.

Ghosh, S. C. (2018). "Nature of boundary and other faults in Raniganj Gondwana rift basin", in *Tectonic Setting and Gondwana Basin Architecture in the Indian Shield*, ed. S. K. Acharyya (Amsterdam: Elsevier) 4, 33–44. doi: 10.1016/b978-0-12-815218-8.00005-4

GMSI (2006). *Gravity Map Series of India (GMSI)*. Hyderabad: National Geophysical Research Institute and Geological Survey of India.

Godin, L., and Harris, L. B. (2014). Tracking basement cross-strike discontinuities in the Indian crust beneath the Himalayan orogen using gravity data – relationship to upper crustal faults. *Geophys. J. Int.* 198, 198–215. doi: 10.1093/gji/ggu131

Gomez-Ortiz, D., Tejero-Lopez, R., Babin-Vich, R., and Rivas-Ponce, A. (2005). Crustal density structure in the Spanish Central System derived from gravity data analysis (Central Spain). *Tectonophysics* 403, 131–149. doi: 10.1016/j.tecto.2005.04.006

Gopala Rao, D., Krishna, K. S., and Sar, D. (1997). Crustal evolution and sedimentation history of the BOB since the Cretaceous. *J. Geophys. Res.* 102, 17747–17768. doi: 10.1029/96jb01339

Gordon, R. G., DeMets, C., and Argus, D. F. (1990). Kinematic constraints on distributed lithospheric deformation in the equatorial Indian Ocean from present motion between the Australian and Indian plates. *Tectonics* 9, 409–422. doi: 10.1029/tc009i003p00409

Green, A. G. (1972). Magnetic profile analysis. *Geophys. J. R. Astron. Soc.* 30, 393–403. doi: 10.1111/j.1365-246x.1972.tb05823.x

Gupta, S., Mohanty, W. K., Mandal, A., and Misra, S. (2014). Ancient terrane boundaries as probable seismic hazards: a case study from the northern boundary of the Eastern Ghats Belt, India. *Geosci. Fron.* 5, 17–24. doi: 10.1016/j.gsf.2013.04.001

Heiskanen, W. A., and Vening Meinesz, F. A. (1958). *The Earth and Its Gravity Field*, Vol. 97. New York, NY: McGraw Hill Book Co. Ltd, 86–86.

Indriana, R. D. (2008). Estimasi ketebalan sedimen dan kedalaman diskontinuitas Mohorovicic daerah Jawa Timur dengan analisis power sectrum dan data anomlai gravitasi. *Berkala Fisika* 11, 67–74.

Ismaiel, M., Krishna, K., Srinivas, K., Mishra, J., and Saha, D. (2019). Crustal architecture and Moho topography beneath the eastern Indian and Bangladesh margins – new insights on rift evolution and continent-ocean boundary. *J. Geol. Soc.* 176, 553–573. doi: 10.1144/jgs2018-131

Iyer, H. M., and Hirahara, K. (1993). *Seismic Tomography: Theory and Practice*. Upper Saddle River, NJ: Prentice Hall.

Kaila, K. L., Murthy, P. R., MadhavaRao, N., Rao, I. B. P., Rao, P. K., Sridhar, A. R., et al. (1996). Structure of the crystalline basement in the West Lower Gangetic basin, India, as determined from deep seismic sounding studies. *Geophys. J. Int.* 124, 175–188. doi: 10.1111/j.1365-246x.1996.tb06362.x

Kaila, K. L., Reddy, P. R., Mall, D. M., Venkateswarlu, N., Krishna, V. G., and Prasad, A. S. S. S. R. S. (1992). Crustal structure of the West Lower Gangetic basin, India, from deep seismic sounding investigations. *Geophys. J. Int.* 111, 45–66. doi: 10.1111/j.1365-246x.1992.tb00554.x

Karner, G. D., and Watts, A. B. (1983). Gravity anomalies and flexure of the lithosphere at mountain ranges. *J. Geophys. Res.* 88, 10449–10477. doi: 10.1029/jb088ib12p10449

Kayal, J. R., Srivastava, V. K., Bhattacharya, S. N., Khan, P. K., and Chatterjee, R. (2009). Source parameters and focal mechanisms of local earthquakes: single broadband observatory at ISM Dhanbad. *J. Geol. Soc. India* 4, 413–419. doi: 10.1007/s12594-009-0144-3

Kayal, J. R., Srivastava, V. K., Kumar, P., Chatterjee, R., and Khan, P. K. (2011). Evolution of crustal 869 and upper mantle structures using receiver function analysis: ISM broad band 870 observatory data. *J. Geol. Soc. India* 78, 76–80. doi: 10.1007/s12594-011-0069-5

Khan, P. K. (2005). Variation in dip-angle of the Indian plate subducting beneath the Burma plate and its tectonic implications. *Geosci. J.* 9, 227–234. doi: 10.1007/bf02910582

Khan, P. K., Ansari, A., and Singh, D. (2017a). Insights into the great Mw 7.9 Nepal earthquake of 25 April 2015. *Curr. Sci.* 113, 2014–2020. doi: 10.18520/cs/v113/i10/2014-2020

Khan, P. K., Ansari, M. A., and Mohanty, S. (2014). Earthquake source characteristics along the arcuate Himalayan belt: geodynamic implications. *J. Earth Sys. Sci.* 123, 1013–1030. doi: 10.1007/s12040-014-0456-6

Khan, P. K., Bhukta, K., and Mandal, P. (2020). Estimation of source parameters of local earthquakes based on inversion of waveform data. *Curr. Sci.* 119:7.

Khan, P. K., Bhukta, K., and Tarafder, G. (2016). Coda Q in EIS. *Acta Geod. Geophys.* 51, 333–346.

Khan, P. K., Mohanty, S. P., Chakraborty, P. P., and Singh, R. (2021). Earthquake shocks around Delhi-NCR and the adjoining himalayan front: a seismotectonic perspective. *Front. Earth Sci.* 9:598784. doi: 10.3389/feart.2021.598784

Khan, P. K., Shamim, Sk, Mohanty, M., Kumar, P., and Banerjee, J. (2017b). Myanmar-Andaman-Sumatra subduction margin revisited: insights of arc-specific deformations. *J. Earth Syst. Sci.* 28, 683–694. doi: 10.1007/s12583-017-0752-6

Kosarev, G. L., Oreshin, S. I., Vinnik, L. P., Kiselev, S. G., Dattatrayam, R. S., Suresh, G., et al. (2013). Heterogeneous lithosphere and the underlying mantle of the Indian subcontinent. *Tectonophysics* 592, 175–186. doi: 10.1016/j.tecto.2013.02.023

Krishna, K. S., Ismaiel, M., Srinivas, K., and Saha, D. (2019). Ancient ocean floor hidden beneath Bangladesh. *Curr. Sci.* 117, 916–917.

Kumar, M. R., Saul, J., Sarkar, D., Kind, R., and Shukla, A. (2001). Crustal structure of the Indian shield; new constraints from teleseismic receiver functions. *Geophys. Res. Lett.* 28, 1339–1342. doi: 10.1029/2000gl012310

Kumar, N., Singh, A. P., and Tiwari, V. M. (2020). Gravity anomalies, isostasy and density structure of the Indian Continental Lithosphere. *Episod* 43, 609–621. doi: 10.18814/epiiugs/2020/020040

Kumar, P., Kumar, M. R., Srijayanthi, G., Arora, K., Srinagesh, D., Chadha, R. K., et al. (2013). Imaging the lithosphere-asthenosphere boundary of the Indian plate using converted wave technique. *J. Geophys. Res.* 118, 5307–5319. doi: 10.1002/jgrb.50366

Lefort, J. P., and Agarwal, B. N. P. (2002). Topography of the Moho undulations in France from gravity data: their age and origin. *Tectonophysics* 350, 193–213. doi: 10.1016/s0040-1951(02)00114-2

Lyon-Caen, H., and Molnar, P. (1985). Gravity anomalies, flexure of the Indian plate, and the structure, support and evolution of the Himalaya and Ganga Basin. *Tectonics* 4, 513–538. doi: 10.1029/tc004i006p00513

Lyons, S. N., Sandwell, D. T., and Smith, W. H. F. (2000). Three-dimensional estimation of elastic thickness under the Louisville ridge. *J. Geophys. Res.* 105:252.

Mahadevan, T. M. (2002). *Geology of Bihar and Jharkhand*. Bangalore: Geological society of India.

Mall, D. M., Rao, V. K., and Reddy, P. R. (1999). Deep sub-crustal features in the Lower Gangetic basin: Seismic signatures for plume activity. *Geophys. Res. Lett.* 26, 2545–2548. doi: 10.1029/1999gl900552

Mandal, P., and Biswas, K. (2016). Teleseismic receiver functions modeling of the eastern Indian craton. *Phys. Earth Planet. Inter.* 258, 1–14. doi: 10.1016/j.pepi.2016.07.002

Marshak, S., and Paulsen, T. (1997). Structural style, regional distribution, and seismic implications of midcontinent fault-and-fold zones, United States. *Seismol. Res. Lett.* 68, 511–520. doi: 10.1785/gssrl.68.4.511

Maus, S., and Dimri, V. P. (1995). Potential field power spectrum inversion for scaling geology. *J. Geophys. Res.* 100, 12605–12616. doi: 10.1029/95jb00758

McKenzie, D., and Sclater, J. G. (1971). The evolution of the Indian Ocean since the Late Cretaceous. *Geophys. J. Int.* 24, 437–528. doi: 10.1111/j.1365-246x.1971.tb02190.x

Minster, J. B., and Jordan, T. H. (1978). Present-day plate motions. *J. Geophys. Res.* 83, 5331–5354. doi: 10.1029/jb083ib11p05331

Mishra, D. C., Laxman, G., and Arora, K. (2004). Large-wavelength gravity anomalies over the Indian continent: indicators of lithospheric flexure and uplift and subsidence of Indian peninsular shield related to isostasy. *Curr. Sci.* 86, 861–867.

Mitra, S., Bhattacharya, S. N., and Nath, S. K. (2008). Crustal structure of the Western Lower Gangetic basin from joint analysis of teleseismic receiver functions and Rayleigh wave dispersion. *Bull. Seismol. Soc. Am.* 98, 2715–2723. doi: 10.1785/0120080141

Murthy, K. S. R., Subrahmanyam, V., Subrahmanyam, A. S., Murty, G. P. S., and Sarma, K. V. L. N. S. (2010). Land-ocean tectonics (LOTs) and the associated seismic hazard over the Eastern continental margin of India (ECMI). *Nat. Hazards* 55, 167–175. doi: 10.1007/s11069-010-9523-8

Naqvi, S. M., and Rogers, J. J. W. (1987). *Precambrian Geology of India*. New York, NY: Oxford University Press Inc, 223.

Odegard, M. E., and Berg, J. W. (1965). Gravity interpretation using the Fourier integral. *Geophys* 33, 424–438. doi: 10.1190/1.1439598

Pandey, A. C., Kumar, A., and Jeyaseelan, A. T. (2013). Urban built-up area assessment of Ranchi Township using Cartosat-I stereopairs satellite images. *J. Indian Soc. Remote Sens.* 41, 141–155. doi: 10.1007/s12524-012-0209-4

Pandey, O. P., and Agarwal, P. K. (1999). Lihtospheric mantle deformation beneath the Indian cratons. *J. Geol.* 107, 683–692. doi: 10.1086/314373

Parker, R. L. (1972). The rapid calculation of potential anomalies. *Geophys. J. R. Astron. Soc.* 31, 447–455. doi: 10.1111/j.1365-246x.1973.tb06513.x

Pick, M., Picha, J., and Vyskocil, V. (1973). *Theory of the Earth's Gravity Field*. Prague: Academia.

Prasanna, H. M. I., Chen, W., and İz, H. B. (2013). High resolution local Moho determination using gravity inversion: a case study in Sri Lanka. *J. Asian Earth. Sci.* 74, 62–70. doi: 10.1016/j.jseaes.2013.06.005

Qureshy, M. N. (1969). Thickening of a basalt layer as a possible cause for the uplift of the Himalayas-A suggestion based on gravity data. *Tectonophysics* 7, 137–157. doi: 10.1016/0040-1951(69)90003-1

Qureshy, M. N. (1970). "Relation of gravity to elevation, geology and tectonics of India," in *Proceedings of the II UMP Symp*, Hyderabad, 1–23. doi: 10.1007/978-3-642-96785-6_1

Qureshy, M. N. (1981). Gravity anomalies, isostasy and crust-mantle relations in the Deccan Trap and contiguous regions. *India. Geol. Soc. India Mem.* 3, 184–197.

Qureshy, M. N., and Warsi, W. E. K. (1980). A Bouguer anomaly map of India and its relation to broad tectonic elements of the subcontinent. *Geophy. J. Roy. Astron. Soc.* 61, 235–242. doi: 10.1111/j.1365-246x.1980.tb04314.x

Rao, G. S., Radhakrishna, M., and Murthy, K. S. R. (2015). A seismotectonic study of the 21 May 2014 BOB intraplate earthquake: evidence of onshore-offshore tectonic linkage and fracture zone reactivation in the northern BOB. *Nat. Hazards* 78, 895–913. doi: 10.1007/s11069-015-1750-6

Rastogi, B. K. (2016). Seismicity of Indian Stable continental region, 2016. *J. Earthquake. Sci. Eng.* 3, 57–93.

Regan, R. D., and Hinze, W. J. (1976). The effect of finite data length in the spectral analysis of ideal gravity anomalies. *Geophys* 41, 44–55. doi: 10.1190/1.1440606

Reguzzoni, M., Sampietro, D., and Sanso, F. (2013). Global Moho from the combination of the CRUST2.0 model and GOCE data. *Geophys. J. Int.* 195, 222–237. doi: 10.1093/gji/ggt247

Riad, S., and El-Etr, H. A. (1985). Bouguer anomalies and lithosphere-crustal thickness in Uganda. *J. Geodyn.* 3, 169–186. doi: 10.1016/0264-3707(85)90027-4

Riad, S., Fouad, A., Refai, E., and Ghalib, M. (1983). "Preliminary interpretation of regional gravity anomalies of Egypt," in *Proceedings of the IUGG Interdisciplinary Symposium Hamburg*, Hamburg.

Rivero, L., Pinto, V., and Casas, A. (2002). Moho depth structure of the eastern part of the Pyrenean belt derived from gravity data. *J. Geodyn.* 33, 315–332. doi: 10.1016/s0264-3707(01)00073-4

Roy, A. B., and Chatterjee, A. (2015). Tectonic framework and evolutionary history of the Lower Gangetic basin in the Indian subcontinent. *Curr. Sci.* 109, 271–279.

Sankar, R., Guha, S. K., Seth, N. N., Muthuraman, K., Pitale, U. L., Jangi, B. L., et al. (1991). Geothermal Atlas of India. *Geol. Sur. India* 19:144.

Sarkar, A. N. (1982). Precambrian tectonic evaluation of eastern India: a model of converging microplates. *Tectonophysics* 86, 363–397. doi: 10.1016/0040-1951(82)90180-9

Sarkar, S. N., and Saha, A. K. (1977). Present status of the Precambrian stratigraphy, tectonics and geochronology of Singhbhum, Keonjhar, Mayurbhanj region, Eastern India. *Indian J. Earth Sci.* 4, 37–55.

Sastri, V. V., Bhandari, L. L., Raju, A. T. R., and Datta, A. K. (1971). Tectonic framework and subsurface stratigraphy of the Ganga basin. *J. Geol. Soc. India* 12, 222–233.

Sengupta, S. (1966). Geological and geophysical studies in western part of Lower Gangetic basin, India. *Am. Assoc. Petrol. Geolog. Bull.* 50, 1001–1017.

Sharma, N. K., Khan, P. K., and Bhukta, K. K. (2015). Nature of the Moho in the mid-eastern part of the Chhotanagpur Plateau, India, from a receiver function perspective. *Arabian J. Geosci.* 8, 5669–5675. doi: 10.1007/s12517-014-1648-8

Shin, Y. H., Xu, H., Braitenberg, C., Fang, J., and Wang, Y. M. (2007). Moho undulations beneath Tibet from GRACE-integrated gravity data. *Geophy. J. Int.* 170, 971–985. doi: 10.1111/j.1365-246x.2007.03457.x

Sibson, R. H. (1980). Transient discontinuities in ductile shear zones. *J. Struct. Geol.* 2, 165–171. doi: 10.1016/0191-8141(80)90047-4

Simpson, R. W., Jachens, R. C., and Blakely, R. J. (1983). AIRYROOT: A FORTRAN program for calculating the gravitational attraction of an Airy isostatic root out to 166.7 km. *U.S. Geol. Surv. Open File Rep.* 8:66.

Simpson, R. W., Jachens, R. C., and Blakely, R. J. (1986). A New Isostatic Residual Gravity Map of the conterminous United States with a Discussion on the Significance of Isostatic Residual Anomalies. *J. Geophys. Res.* 91, 8348–8372. doi: 10.1029/jb091ib08p08348

Singh, A. P., Kumar, N., and Singh, B. (2004). Magmatic underplating beneath the Rajmahal traps: gravity signatures and derived 3-D configuration. *Proc. Indian Acad. Sci.* 113, 759–769. doi: 10.1007/bf02704035

Singh, A. P., Kumar, N., and Zeyen, H. (2015). Three-dimensional lithospheric mapping of the EIS: A multi-parametric inversion approach. *Tectonophysics* 665, 164–176. doi: 10.1016/j.tecto.2015.09.038

Singh, R., Khan, P. K., and Singh, A. P. (2020). Earthquake source dynamics and kinematics of the EIS and adjoining regions. *Acta Geophys.* 68, 337–355. doi: 10.1007/s11600-020-00418-z

Singh, R., Sharma, S., Mitra, S., and Khan, P. K. (2019). Mapping of coda-wave attenuation and its frequency dependency Over EIS. *Pure Appl. Geophys.* 176, 5291–5313. doi: 10.1007/s00024-019-02284-3

Song, P., Zhang, X., Liu, Y., and Teng, J. (2017). Moho imaging based on receiver function analysis with teleseismic wavefield reconstruction: application to South China. *Tectonophysics* 718, 118–131. doi: 10.1016/j.tecto.2017.05.031

Spector, A., and Grant, F. S. (1970). Statistical models for interpreting aeromagnetic data. *Geophys.* 35, 293–302. doi: 10.1190/1.1440092

Stein, S., and Okal, E. A. (1978). Seismicity and tectonics of the Ninetyeast Ridge area: Evidence for internal deformation of the Indian plate. *J. Geophys. Res.* 83, 2233–2245. doi: 10.1029/jb083ib05p02233

Tealeb, A., and Riad, S. (1986). "Regional gravity anomalies of western Saudi Arabia and their geological significance," in *Proceedings of the 5 Ann. The Meeting of E. G. S*, Cairo, 50–89. doi: 10.4324/9781003074601-3

Thompson, D. A., Bastow, I. D., Helffrich, G., Kendall, J. M., Wookey, J., Snyder, D. B., et al. (2010). Precambrian crustal evolution: seismic constraints from the Canadian Shield, Earth Planet. *Sci. Lett.* 297, 655–666. doi: 10.1016/j.epsl.2010.07.021

Tiwari, V. M. (2003). Analysis of satellite gravity and bathymetry data over Ninety-East Ridge: variation in the compensation mechanism and implication for emplacement process. *J. Geophy. Res.* 108, ETG 13-1-16. doi: 10.1029/2000JB000047

Tselentis, G. A., Drakopoulos, J., and Dimitriadis, K. (1988). A spectral approach to Moho depths estimation from gravity measurements in Epirus (NW Greece). *J. Phys. Earth* 36, 255–266. doi: 10.4294/jpe1952.36.255

Tsuboi, C. (1979). *Gravity*. Crows Nest: George Allen & Unwin (Publishers) Ltd. (1983 English translation).

Tugume, F., Nyblade, A., Julià, J., and van der Meijde, M. (2013). Precambrian crustal structure in Africa and Arabia: Evidence lacking for secular variation. *Tectonophysics* 609, 250–266. doi: 10.1016/j.tecto.2013.04.027

Valdiya, K. S. (1976). Himalaya transverse faults and their parallelism with subsurface structures of North Indian planes. *Tectonophysics* 32, 353–386. doi: 10.1016/0040-1951(76)90069-x

Valdiya, K. S., and Sanwal, J. (2017). "The dynamic Indian crust," in *Neotectonism in the Indian Subcontinent - Landscape Evolution*, (Amsterdam: Elsevier), 458. doi: 10.1016/b978-0-444-63971-4.00001-3

Veevers, J. J., and Tewari, R. C. (1995). Gondwana Master Basin of Peninsular India between Tethys and the Interior of the Gondwanaland Province of Pangea. *GSA Mem.* 187, 1–73.

Verma, R. K. (1985). "Gravity field and tectonics of Gondwana basins of Peninsular India," in *Gravity Field, Seismicity and Tectonics of the Indian Peninsula and the Himalayas* (Solid Earth Sciences Library), Vol. 3, ed. R. K. Verma (Dordrecht: Springer), 44–60.

Verma, R. K., Bandyopadhyay, T. K., and Mukhopadhyay, M. (1980). Gravity field, structure and tectonics of the Raniganj coalfield three dimensional model. *J. Geol. Soc. India* 21, 117–127.

Verma, R. K., and Ghosh, D. (1977). "Gravity field, structure and tectonics of some Gondwana basins of Damodar valley India," in *Geophysical Case Histories of India*, Vol. 1, ed. V. L. S. Bhimsamkasam (Hyderabad: AEG), 97–112.

Verma, R. K., Majumdar, R., Ghosh, D., Ghosh, A., and Gupta, N. C. (1976). Results of gravity survey over Raniganj Coalfield. *India. Geophys. Prosp.* 24, 19–30. doi: 10.1111/j.1365-2478.1976.tb00382.x

Watts, A. B., Bodine, J. H., and Ribe, N. M. (1980). Observations of flexure and geological evolution of the Pacific Ocean basin. *Nature* 283, 532–537. doi: 10.1038/283532a0

Weaver, B. L. (1990). "Early Precambrian basic rocks of India," in *Early Precambrian Basic Magmatism*, eds R. P. Hall and D. J. Hughes (Glasgow: Blackie), 339–351. doi: 10.1007/978-94-009-0399-9_15

Weins, D. A. (1985). Historical seismicity near Chagos: a complex deformation zone in the equatorial Indian Ocean. *Earth Planet. Sci. Lett.* 76, 350–360. doi: 10.1016/0012-821x(86)90086-5

Weissel, J. K., Andreson, R. N., and Geller, C. A. (1980). Deformation of the Indo–Australian plate. *Nature* 287, 284–291. doi: 10.1038/287284a0

Woollard, G. P. (1969) "Regional variations in gravity. The earth's crust and upper mantle,"in *Geophysical Monograph Series,* Vol. 13, (National Academy of Sciences-National Research Council Publication 1708), ed. P. J. Hart, (Washington, DC: AGU), 320–341.

Zhao, D., Hasegawa, A., and Horiuchi, S. (1992). Tomographic Imaging of P and S wave velocity structure beneath northeast Japan. *J. Geophys. Res.* 97:928.

Zhu, L. P. (2000). Crustal structure across the San Andreas fault, southern California from teleseismic converted waves. *Earth Planet. Sci. Lett.* 179, 183–190. doi: 10.1016/s0012-821x(00)00101-1

Zhu, L. P., and Kanamori, H. (2000). Moho depth variation in southern California from teleseismic receiver functions. *J. Geophys. Res.* 105, 2969–2980.

Conflict of Interest: The authors declare that the research was conducted in the absence of any commercial or financial relationships that could be construed as a potential conflict of interest.

frontiers
in Earth Science

ORIGINAL RESEARCH
published: 12 July 2021
doi: 10.3389/feart.2021.667501

Recent Seismicity in the Area of the Major, 1908 Messina Straits Earthquake, South Italy

Giancarlo Neri, Barbara Orecchio, Debora Presti, Silvia Scolaro and Cristina Totaro*

Department of Mathematics, Computer Sciences, Physics, and Earth Sciences, University of Messina, Messina, Italy

High-quality non-linear hypocenter locations and waveform inversion focal mechanisms of recent, shallow earthquakes of the Messina Straits have allowed us to obtain the following main results: 1) seismicity has occurred below the east-dipping north-striking fault proposed by most investigators as the source of the 1908, magnitude 7.1 Messina earthquake, while it has been substantially absent in correspondence of the fault and above it; 2) earthquake locations and related strain space distributions do not exhibit well defined trends reflecting specific faults but they mark the existence of seismogenic rock volumes below the 1908 fault representing primary weakness zones of a quite fractured medium; 3) focal mechanisms reveal normal and right-lateral faulting in the Straits, reverse faulting at the southern border of it (Ionian sea south of the Ionian fault), and normal faulting at the northern border (southeastern Tyrrhenian sea offshore southern Calabria); 4) these faulting regimes are compatible with the transitional character of the Messina Straits between the zone of rollback of the in-depth continuous Ionian subducting slab (southern Calabria) and the collisional zone where the subduction slab did already undergo detachment (southwest of the Ionian fault); 5) the whole seismicity of the study area, including also the less recent earthquakes analyzed by previous workers, is compared to patterns of geodetic horizontal strain and uplift rates available from the literature. We believe that the joint action of Africa-Europe plate convergence and rollback of the Ionian subducting slab plays a primary role as regard to the local dynamics and seismicity of the Messina Straits area. At the same time, low horizontal strain rates and large spatial variations of uplift rate observed in this area of strong normal-faulting earthquakes lead us to include a new preliminary hypothesis of deep-seated sources concurring to local vertical dynamics into the current debate on the geodynamics of the study region.

Keywords: hypocenter locations, focal mechanisms, earthquake source, regional geodynamics, messina straits, Italy

Edited by:
Claudia Piromallo,
Istituto Nazionale di Geofisica e Vulcanologia (INGV), Italy

Reviewed by:
Simone Cesca,
Helmholtz Centre Potsdam, Germany
Gianfranco Vannucci,
Istituto Nazionale di Geofisica e Vulcanologia (INGV), Italy

****Correspondence:***
Debora Presti
dpresti@unime.it

Specialty section:
This article was submitted to Solid Earth Geophysics, a section of the journal Frontiers in Earth Science

Received: *13 February 2021*
Accepted: *24 June 2021*
Published: *12 July 2021*

Citation:
Neri G, Orecchio B, Presti D, Scolaro S and Totaro C (2021) Recent Seismicity in the Area of the Major, 1908 Messina Straits Earthquake, South Italy. Front. Earth Sci. 9:667501. doi: 10.3389/feart.2021.667501

PREMISE

The Messina Straits area is well known to be one of the areas with the highest seismic risk in the Mediterranean region. The December 28, 1908 earthquake was one of the most devastating seisms of the past century with huge damage and 80,000 fatalities in Northeastern Sicily and Southern Calabria. Other major seisms which occurred in the previous centuries in Southern Calabria (February 1783) and Southeastern Sicily (January 1693) have also produced remarkable damage and victims on both sides of the Messina Straits.

Many geophysical and geological investigations have been performed on the 1908 earthquake with the purpose of identifying its source and relationship with the regional geodynamics. As discussed in a later Section, the intense efforts made by the scientific community to retrieve the source properties from the geodetic and seismic data available for the earthquake have allowed to obtain a family of solutions lying in an acceptably limited range concerning location, geometry and mechanism of the generating fault. The most convincing source appears to be a normal fault striking between N10W and NNE, east-dipping with a relatively low dip angle around 40°, and with the top located a few km beneath the Sicilian side of the Straits and the bottom beneath the Calabrian side (De Natale and Pingue, 1987; De Natale and Pingue, 1991; Capuano et al., 1988; Boschi et al., 1989; Bottari et al., 1989; Amoruso et al., 2002; Amoruso et al., 2006).

In the present study we analyze the local seismic activity recorded in the last twenty years in the Messina Straits area. We take benefit of the seismic network improvements occurred in this area during the 90's of the last century, making good databases available to researchers interested in high resolution analyses of local seismicity (Amato and Mele, 2008). We also take benefit of 1) recent improvements of algorithms for hypocenter location (Presti et al., 2004 and Presti et al., 2008) and focal mechanism computation (D'Amico et al., 2010 and D'Amico et al., 2011) and 2) increasing accuracy of the seismic velocity structure of this region (Neri et al., 2012; among others). On these grounds, we have started the present work confident to be able to furnish incremental knowledge on the seismicity of this area and relationships with the regional geodynamics.

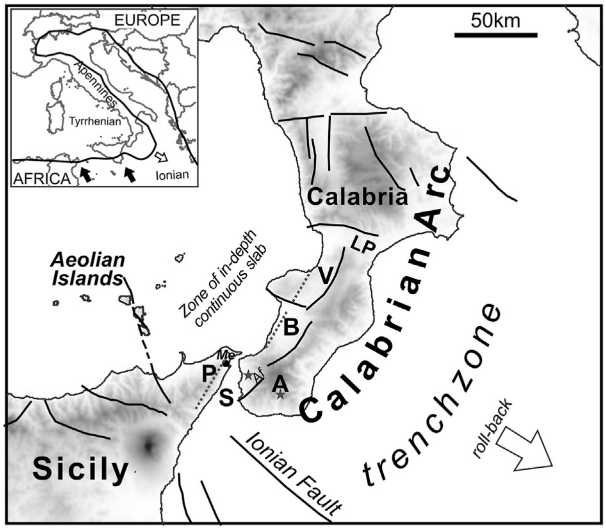

FIGURE 1 | Geodynamic sketch with main fault systems and topography of the Calabrian Arc region. In the upper-left inset, a simplified representation of the plate margin in the central Mediterranean region (black line) is shown. Full arrows indicate the present-day Africa motion with respect to Europe according to Nocquet (2012), and references therein. The white arrow in the main plate shows the sense of the gravity-induced subducting slab rollback. The dotted segments in the southern Calabria and Messina Straits area indicate the east-dipping blind faults proposed by several authors (see, e.g., DISS Working Group, 2018) as the seismogenic sources of the strong earthquakes of December 28, 1908 and February 5 and 7, 1783 discussed in the text. The stars indicate the epicenters of the 1908 Messina Straits and 1978 Aspromonte earthquakes according to Rovida et al. (2020) and Orecchio et al. (2019), respectively. A = Aspromonte, Af = Armo fault, B = Gioia Basin, Me = Messina,P=Peloritani, S = Messina Straits, V = Mesima Valley, LP = Lamezia Plain.

THE MESSINA STRAITS IN THE CALABRIAN ARC GEODYNAMIC FRAMEWORK

We have described the main geodynamic features of the Calabrian Arc region in previous studies, to which we address the reader interested in more details on the argument (see, e.g., Presti et al., 2013; Orecchio et al., 2015; Presti, 2020). Useful references may also be the basic continental-scale geodynamic reconstructions by Malinverno and Ryan (1986), Faccenna et al. (1996), and Rosenbaum et al. (2002). A widely shared geodynamic model of the Calabrian Arc region assumes the co-existence of 1) NNW–SSE convergence of Africa and Europe plates and 2) gravity-induced south-eastward rollback of a Ionian lithospheric slab subducting to northwest beneath the Tyrrhenian lithosphere (**Figure 1**). Plate convergence velocity is of the order of 3–5 mm/yr (see, e.g., D'Agostino and Selvaggi, 2004; Devoti et al., 2008), rollback of the subducting slab is also very slow (a couple of mm/yr; see, e.g., Hollestein et al., 2003; Devoti et al., 2008; Nocquet, 2012).

The Calabrian Arc presents strongly contrasting vertical movements, such as mountain chain uplifting of the order of 1–2 mm/yr since Middle Pleistocene and relative-to-chain subsidence in the major tectonic basins located on the western side of the chain (**Figure 1**; Monaco et al., 1996; Ferranti et al., 2007; Ferranti et al., 2010; Faccenna et al., 2011). Focusing on the Calabrian side of the Messina Straits area, Ferranti et al. (2007) estimated that the Late Holocene uplift is equally partitioned between steady and stick-slip coseismic contributions. On their hand, Ferranti et al. (2010) suggested a deep-seated contribution to remarkable uplift of Calabria, based on spatial correspondence between the uplifting area and the location of the Ionian subducting slab. It is worth mentioning that in the early phase of the debate on the Calabrian uplift, Negredo et al. (1999) proved by Finite Element Modeling that coexistence of plate convergence and roll-back of an in-depth continuous subducting slab beneath the Calabrian Arc is compatible with chain uplift observed in Calabria. More recently, strong spatial variation of vertical movements in the Arc area was detected by GPS data (Serpelloni et al., 2013) with maximum uplift rate into the chain and maximum subsidence into the basins.

Normal faults located around the basins west of the chain are considered to be major seismogenic faults, with particular reference to the NE-trending fault systems of the Messina Straits, Gioia Basin and Mesima Valley (S, B and V in **Figure 1**). It can be remarked that the strongest earthquakes of the S, B and V basins of **Figure 1** (magnitude 7.1 of Dec 28, 1908 in S; magnitude 7.1 of Feb 5, 1783 in B; and magnitude 6.7. of Feb 7, 1783 in V) have been imputed to west-dipping faults located on the eastern border of the basin by

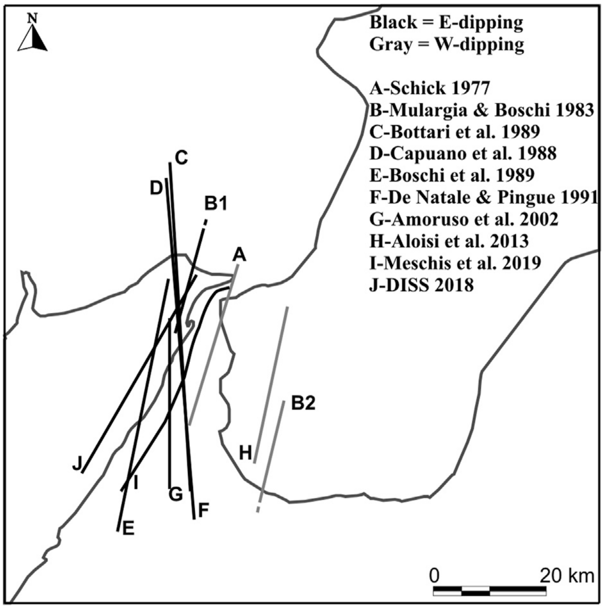

FIGURE 2 | Graphical summary of the sources proposed by different authors for the 1908 Messina Straits earthquake (legend). The traces A–J corresponding to the different sources indicate the intersection of the prolongation of the respective sources (fault planes) with the earth surface. Black and gray lines indicate E-dipping and W-dipping sources, respectively.

some authors (e.g. Monaco and Tortorici, 2000; Jacques et al., 2001) and to east-dipping faults on the western border of the basin by others (e.g. Valensise and D'Addezio, 1994; Pizzino et al., 2004; DISS Working Group, 2018).

Analyses of different geophysical data have led Neri et al. (2009) and Neri et al. (2012) to propose that the Ionian subducting slab is still continuous over depth beneath the central part of Calabrian Arc (southern Calabria, between Messina Straits and Lamezia Plain; **Figure 1**), while detachment of the deepest portion of subducting lithosphere has already occurred beneath the Arc edges, i.e. beneath Northern Calabria (north of Lamezia Plain) and Northeastern Sicily (southwest of Messina Straits), respectively. The Messina Straits area (**Figure 1**) is transitional between the zone of rollback of the in-depth continuous Ionian subducting slab (southern Calabria) and the collisional zone where the subduction slab did already undergo detachment, southwest of the Ionian fault zone (Neri et al., 2012; Totaro et al., 2016; among others). In contrast to the mentioned spatial variation of vertical movements, the Southern Calabria Messina Straits area is characterized by quite low values of horizontal strain rate, of the order of 0–15 nanostrain/yr (Palano, 2015).

THE SOURCE OF THE 1908 EARTHQUAKE

In the first paper of the most recent epoch of seismological research concerning the 1908 earthquake source, Schick (1977) proposed a fault located in the middle of the Messina Straits, with a strike approximately along a north-south direction and dipping to the west (**Figure 2**). This conclusion was partly based on an analysis only qualitative of the original geodetic data gathered by Loperfido (1909) who measured vertical displacements on both sides of the Straits between two campaigns performed before and soon after the December 28, 1908 earthquake, respectively.

Mulargia and Boschi (1983) presented a graben-shaped model assuming that the earthquake was generated by joint activation of two faults, a east-dipping one with top between the Sicilian side of the Straits and a west-dipping one with top beneath the Calabrian side (B1 and B2 in **Figure 2**).

The studies that followed demonstrated that a single east-dipping fault located in the middle of the Straits may explain the main features of the levelling data (De Natale and Pingue, 1987; De Natale and Pingue, 1991; Capuano et al., 1988; Boschi et al., 1989; Bottari et al., 1989; Amoruso et al., 2002; Amoruso et al., 2006). The source models proposed by these authors differed one from the other in terms of the fault length and small differences in strike orientation between N10°W and NNE. All analyses, whether seismological or geodetic or joint seismological/geodetic, indicated normal faulting.

Valensise and Pantosti (1992) and D'Addezio et al. (1993) analyzed recent geologic and geomorphic features on both sides of the Messina Straits and compared the distribution and deformation patterns with the displacement fields produced by different fault models that were proposed by several authors for the 1908 earthquake. They concluded that the long-term evolution of the Straits is strongly affected by the repetition of coseismic deformation episodes related to the occurrence of 1908 –type earthquakes represented by Boschi et al.'s (1989) NNE-trending east-dipping source. A main product of these investigations is the 1908 earthquake source reported in the Database of Individual Seismogenic Sources (DISS Working Group, 2018).

By analysis of the original seismograms, Pino et al. (2000) inferred that the 1908 earthquake was generated by unilateral rupture, with northwards directivity along a 43-km-long fault in the Straits. The extensional nature of the faulting, which involved rupturing of a roughly N-S striking plane, was confirmed.

A nonlinear joint inversion of P wave first-motion polarities and coseismic surface displacement data of the great earthquake allowed Amoruso et al. (2002) to propose a very stable solution according to which the earthquake was generated by a fault oriented ca. N-S located beneath the Straits, dipping to east at an angle of 40° and characterized by normal mechanism with a minor dextral lateral component.

In a more recent paper, Aloisi et al. (2013) proposed that the original levelling data do not allow reliable discrimination of the fault plane and claimed that an antithetic plane dipping westwards at a high angle provides an almost equivalent solution. Based on geological considerations, they suggested the Armo fault, located on-shore east of the Straits in Southern Calabria (**Figure 1**), as the source of the 1908 earthquake. They argued that southern Calabria represents the locus of major deformation in the region and reported on the documented activity of the Armo fault during the late Holocene. Nevertheless, they did not provide any element that demonstrates that the only 18-km long Armo fault was activated during the 1908 earthquake. Some inconsistencies in this study were, however, contested by De Natale and Pino (2014) concerning, in particular, the use of the levelling data.

Convertito and Pino (2014) tested three typologies of sources among those proposed in the literature (Boschi et al., 1989; De Natale and Pingue, 1991; Aloisi et al., 2013) by computing synthetic seismograms from the respective sources and comparing the PGA and PGV values to the macroseismic intensity field available for the earthquake. They concluded that, among the tested models, the one characterized by an east-dipping fault, with strike oriented NS slightly rotated clockwise, better explains the observed macroseismic field of the 1908 Messina Straits earthquake. Then, they identified the fault proposed by Boschi et al. (1989) as the best fitting one.

In the last years several efforts have been made to find evidence of the 1908 earthquake source on the sea bottom of the Messina Straits. High-resolution swath bathymetry of the Messina Straits has led Ridente et al. (2014) to conclude that intense erosional and depositional processes superimposed on active tectonic deformation hinder the distinction between tectonic and sedimentary features, so that fault systems compatible with the source of the 1908 earthquake could not be identified. Based on multibeam sonar, chip profiler and seismic reflection data, Goswami et al. (2014) explored the seabed morphology of the Messina Straits and detected mass wasting processes around fault escarpments previously identified by Selli et al. (1978) on the Calabrian side of the Straits. No conclusion was, however, drawn in this connection concerning eventual seismic activity. More recently, Fu et al. (2017) discovered a major east-trending fault zone at the southern border of the Messina Straits, highlighted by a prominent 60 m high escarpment on the Ionian seafloor. Fu et al. (2017) proposed this fault zone as a potential source of seismic and tsunami hazard, but they excluded a role of it as source of the 1908 earthquake for incompatibility with the seismic data of this earthquake.

A couple of years ago, Meschis et al. (2019) tested the compatibility between the IGM levelling data of Loperfido (1909) with the NNE-SSW fault (I in **Figure 2**) reported by Doglioni et al. (2012) on the basis of geomorphic elements and acoustic data obtained by previous investigators in the Ionian offshore of Northeastern Sicily. Meschis et al. (2019) found the best fit of levelling data with this fault when assuming a east-ward dip of 70° and 5 m of maximum slip at depth. The authors have not, however, compared their source with the seismic data. Finally, during the phase of revision of the present article, a new paper appeared in the literature (Barreca et al., 2021) proposing a NNE-trending SE-dipping fault in the Messina Straits as the source of the 1908 earthquake, with the peculiar feature of a northeast-ward rotation of the northernmost part of the fault and possible continuation across southern Calabria mainland.

On the basis of the wide series of studies available in the literature, the largely most convincing source of the 1908 Messina Straits earthquake appears to be a low-angle east-dipping normal fault striking between N10W and NNE, with the top located a few km beneath the Sicilian side of the Straits. Analogue modeling allowed Bonini et al. (2011) to state that high-angle, very shallow normal faults detected over all the Messina Straits area can be interpreted as minor structures related to the activity of this low-angle east-dipping, deeper normal fault believed to have generated the 1908 earthquake.

METHODS OF ANALYSIS, DATA AND RESULTS

We perform estimates of hypocenter locations in the present study by the Bayloc Bayesian non-linear location algorithm (Presti et al., 2004 and Presti et al., 2008). Starting from seismic phase arrival times at the recording stations, Bayloc computes for an individual earthquake a probability cloud marking the hypocenter location uncertainty and defines the point-location of the earthquake as the point of maximum probability in the cloud. Then, Bayloc estimates the spatial distribution of probability relative to a set of earthquakes by summing the probability densities of the individual events. This procedure has been shown to help detection of seismogenic structures through better hypocenter location and more accurate estimation of location errors compared to linearized methods (Presti et al., 2008). More details on methodological aspects of Bayloc can be found in Presti et al. (2004) and Presti et al. (2008).

We have applied Bayloc to the earthquakes of magnitude greater than two occurred at depth less than 30 km in the area of **Figures 3A–C** during the period 2000–2020. We have taken the P- and S-wave arrival times of these earthquakes from the Italian national seismic database (http://terremoti.ingv.it/) and selected the subset of earthquakes for which a minimum of six P-wave arrival times at stations with epicentral distance <150 km were available. A map of the stations used for these hypocenter locations is shown in **Figure 3D**. The 3D velocity model estimated for the study area and surroundings by Neri et al. (2012) has been used for locations. Based on completeness analyses of the seismic database performed by previous authors (Schorlemmer et al., 2010), we are confident that our sample of shallow earthquakes of magnitude over 2.0 in the Messina Straits area is substantially complete. The results of our hypocenter locations are shown in the maps of **Figures 3A–C**, reporting the cumulative probability density of the earthquakes (A), the corresponding point-locations (B) and the seismic energy density relative to plot A (C). With the same types of representation, the **Figure 4** reports the maps (A, C and E) and the W-E vertical sections (B, D and F) of the seismicity located in the sector of the 1908 earthquake source. All plots A-to-F show the trace of the 1908 earthquake fault of Amoruso et al. (2002), more precisely the intersection of the prolongation of the fault with the earth surface is reported in the map views. In addition, the low-right insets in the plots C and D of **Figure 4** show the Bayloc's barycentric distributions representing the average uncertainty volume of the located earthquakes in the map and section views (Presti et al., 2008). The relatively small

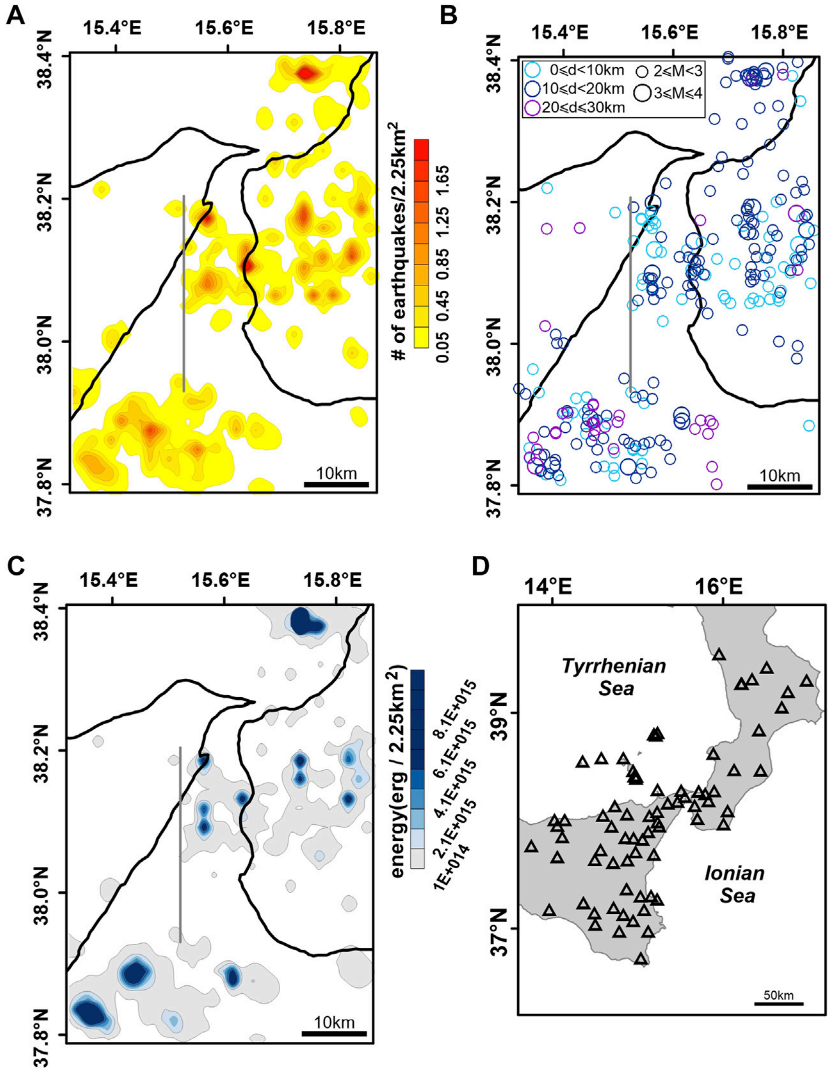

FIGURE 3 | Epicentral maps obtained by the Bayloc probabilistic location method for M ≥ 2 earthquakes occurred at depth less than 30 km in the period 2000–2020. For comparison, the 1908 earthquake source of Amoruso et al. (2002) is reported in plots A-to-C (gray line): the trace corresponds to the intersection between the fault plane prolongation and the earth surface. Bayloc locations are reported both in terms of cumulative probability density **(A)** and point-locations, i.e. points of maximum probability **(B)**. The graphical representation in plot **(B)** allows for differentiation of earthquakes according to depth d and magnitude M (legend). Plots **(C)** and **(D)** show the seismic energy density relative to plot A and a map of the stations used for hypocenter locations, respectively.

extent of the average uncertainty volume of hypocenters, corresponding to ERH and ERZ values of the order of 0.7 and 1 km, respectively, represent a basic pre-condition for the forthcoming analysis and discussion of the earthquake space distributions. Finally, **Figure 5** displays the cross-section views of the hypocenters of earthquakes of **Figure 4** along profiles perpendicular to the orientations of the east-dipping sources of the 1908 earthquake proposed by different authors (Boschi et al., 1989; De Natale and Pingue, 1991; Amoruso et al., 2002; DISS Working Group, 2018). This family of east-dipping sources is here intended as a sort of range of uncertainty of the 1908 source.

Hypocenter locations obtained by Bayloc have been used as starting data for computation of focal mechanisms. For this, we have used the Cut and Paste (CAP) waveform inversion method by Zhao and Helmberger (1994), and Zhu and Helmberger (1996). Each waveform is broken up into Pnl and surface wave segments, which are given different weights during inversion. The same frequency bands have been used to filter synthetic and observed ground velocities, in detail 0.02–0.1 Hz for surface waves and 0.05–0.3 Hz for Pnl waves. Diversely from other waveform inversion methods of current use in the literature which are known to be effective when the earthquake magnitude exceeds a threshold of 3.5–4 (Pondrelli et al., 2006; Ekstrom et al., 2012), CAP has shown to be very effective also for earthquakes of magnitude in the range 2.5–3.5 (more details on CAP and its applications can be found in Zhao and Helmberger, 1994; Zhu and Helmberger, 1996; D'Amico et al., 2010; D'Amico et al., 2011; Scolaro et al., 2018).

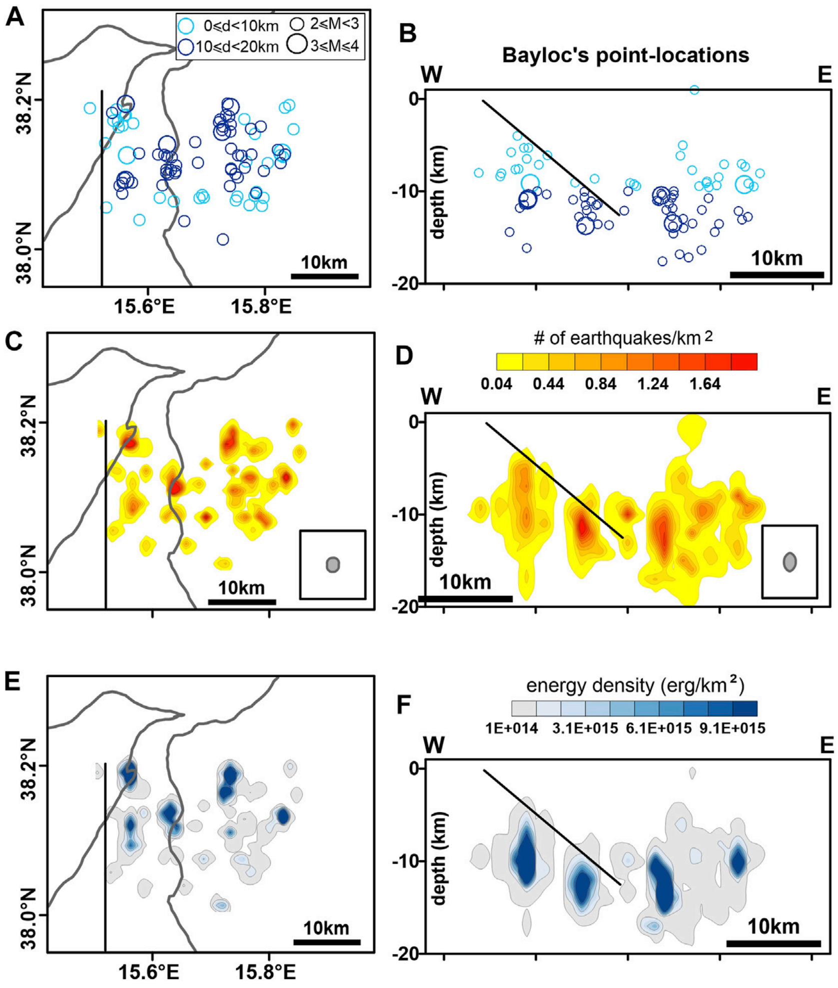

FIGURE 4 | Epicentral maps (left) and E-W oriented vertical sections (right) of recent earthquakes located in the sector of the 1908 earthquake source. For comparison, the 1908 earthquake source of Amoruso et al. (2002) is reported in all plots (black line): in the maps the trace corresponds to the intersection between the fault plane prolongation and the earth surface, in the vertical sections the trace shows the location of the circa north-striking east-dipping source. Top **(A–B)**: earthquake point-locations with differentiation of earthquakes according to depth d and magnitude M (legend). Middle **(C–D)**: distribution of the cumulative probability density. The average epicentre and hypocentre uncertainties expressed in terms of "barycentric map" and "barycentric vertical section" (see text, and Presti et al., 2008) are also reported in the low-right insets of C and D plots. Bottom **(E–F)**: seismic energy density distribution. All the earthquakes reported in the maps **(A,C,E)** are projected onto the cross-sections **(B,D,F)**.

We have applied the CAP method to seismic waveforms available in the database EIDA, http://orfeus-eu.org/webdc3/, for the shallow earthquakes that occurred in the study area since 2005. A greater number of waveforms is generally available in the database for the most recent earthquakes, and this has led us to obtain well constrained solutions in large majority for earthquakes occurred in the last few years. The earth structure used for the Green's Functions computation was properly calibrated for the study area by D'Amico et al. (2011). The most stable focal mechanisms obtained by CAP in the present study are reported in **Figure 6** and **Table 1**. The stability of the solutions has been carefully checked by means of tests and procedures widely described in D'Amico et al. (2011) and Scolaro et al. (2018). For conciseness, we report in **Figures 7A–D** the comparison between synthetic and observed waveforms relative to the earthquakes n. 1, 5, 10 and 14 of **Figure 6** sampling the different sectors of the study area. An overally good fit of waveforms can be observed at almost all the recording stations, the map of which is given in **Figure 6**. In addition to the best solution obtained for the individual earthquake, each of the four sections of **Figures 7A–D** reports in the top the solutions obtained by moving the hypocenter of the event in all directions within the Bayloc's uncertainty volume of the event itself. The focal mechanisms of the events 1, 5, 10 and 14 appear very stable. Similar levels of stability have been obtained for the other events of **Figure 6**. Finally, we note that the earthquake of October 6, 2006 in **Table 1** (n. 13) was also present in the list of earthquakes analysed in the previous paper by Presti et al. (2013), indicated as n. 97 in their **Table 1** and **Figure 4**. Slight differences of fault parameters between the respective solutions, resulting from difference between

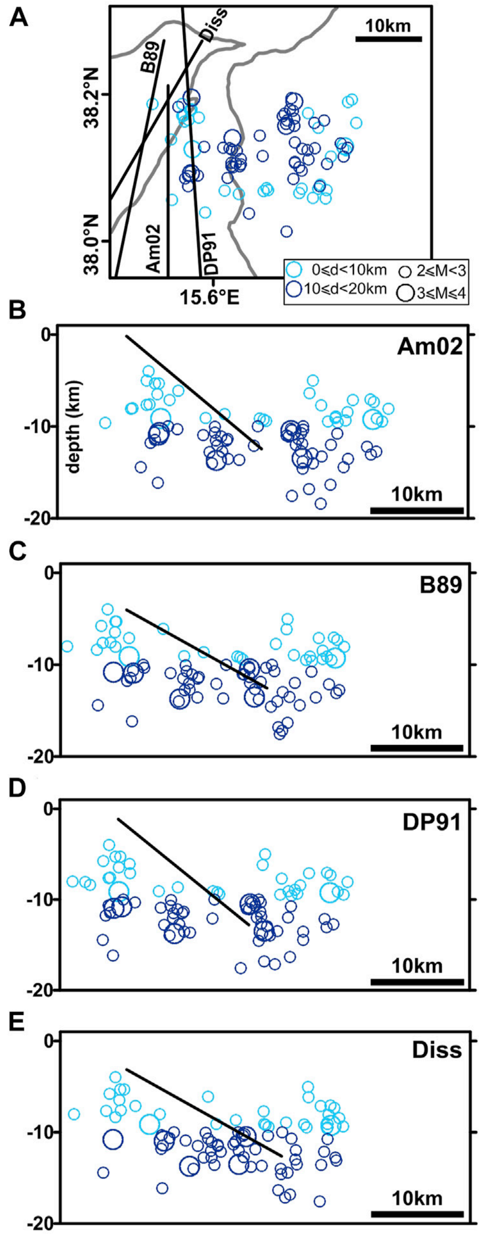

FIGURE 5 | Plot **(A)** reproduces the epicentral map of **Figure 4A** reporting also the traces of the east-dipping sources of the 1908 earthquake proposed by different authors: Am02, B89, DP91 and Diss stand for Amoruso et al. (2002), Boschi et al. (1989), De Natale and Pingue (1991) and DISS Working Group (2018), respectively. Plots B-to-E display the cross-section views of the earthquakes of plot **(A)** along profiles perpendicular to the orientations of the different sources. All the earthquakes reported in the map **(A)** are projected onto the cross-sections **(B–E)**. This family of east-dipping sources is here intended as a sort of range of uncertainty of the 1908 source.

1) Bayloc's earthquake location used for CAP inversion in the present study and 2) Italian bulletin's earthquake location used for CAP estimates reported in Presti et al. (2013), highlight substantial stability of this mechanism also varying the location of the event according to different procedures.

DISCUSSION

Figure 3 shows the epicenter map of the earthquakes shallower than 30 km which occurred in the Messina Straits area during the last 20 years. Seismicity has been mainly located in the Straits, in the Calabrian on-shore east of it, and in two offshore sectors located NE and SW of it, respectively. A maximum magnitude of 4.0 has been recorded in the whole area during the study period. A quite low seismicity level (both as number and energy of earthquakes) was recorded on the Sicilian on-shore of the Straits. Higher and lower activity recorded on the Calabrian

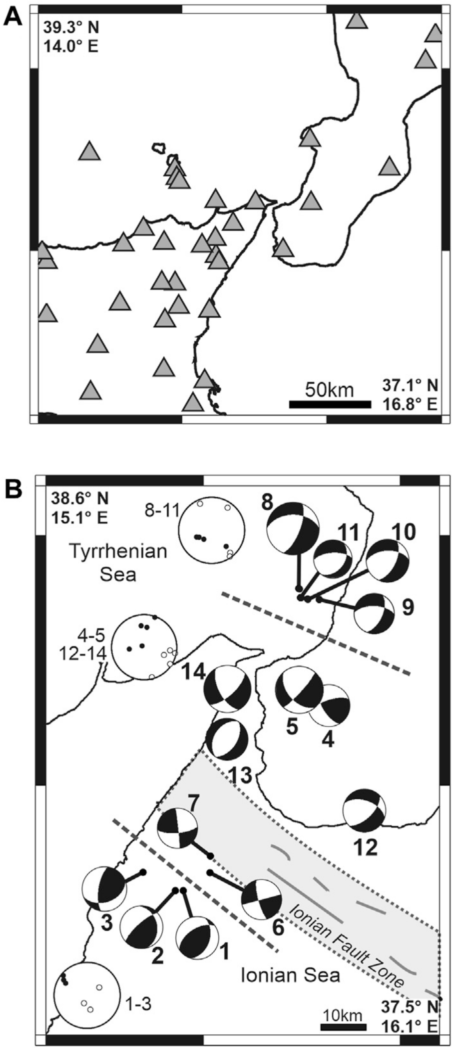

FIGURE 6 | (A) Seismic stations used for focal mechanism computations. **(B)** Waveform inversion focal mechanisms computed by the CAP method for earthquakes occurred at depths less than 30 km in the Messina Straits area between 2005 and 2020. Numerical values of earthquake parameters are reported in **Table 1**. Polar plots of P- and T-axes for three different subsets of our FMs (1–3; 4–5 and 12–14; 8–11) are also reported, with the standard representation black = P and white = T. Dashed lines help recognizing the different compartments discussed in the text. The NW-SE striking gray belt in the Ionian Sea shows the location of the Ionian Fault Zone (see Polonia et al., 2016, among others).

TABLE 1 | Identity number, date and origin time, hypocenter coordinates, fault parameters and moment magnitude of the earthquakes reported in **Figure 6**. The number of traces used for each focal mechanism computation is also reported in the last column.

ID	YYYY-MM-DD	hh:mm	sec	Lat (°N)	Lon (°E)	Depth (km)	Strike (°)	Dip (°)	Rake (°)	Mw	no. of traces
1	2015-12-22	02:13	39	37.79	15.45	18.11	19	42	60	3.3	12
2	2015-12-22	05:35	9	37.79	15.43	22.38	348	28	33	3.3	9
3	2016-02-11	01:38	50	37.83	15.35	26.87	189	68	56	3.4	4
4	2016-11-18	17:14	1	38.16	15.82	20.10	251	68	28	3.2	6
5	2018-02-10	02:16	17	38.19	15.75	12.64	42	82	–41	3.6	13
6	2018-02-27	12:35	13	37.83	15.52	14.74	255	90	13	3.1	6
7	2018-02-27	12:44	18	37.86	15.52	15.00	85	71	3	3.1	6
8	2018-09-28	05:24	31	38.40	15.74	17.00	269	46	–31	4.0	23
9	2018-10-03	01:23	1	38.37	15.79	20.72	272	59	–39	3.1	7
10	2018-11-14	15:01	2	38.37	15.76	18.00	267	51	–42	3.3	12
11	2018-11-14	15:15	3	38.38	15.75	18.00	267	63	–61	2.9	7
12	2019-08-14	23:26	22	37.95	15.91	16.00	289	51	–39	3.3	13
13	2006-10-06	21:16	23	38.09	15.56	11.00	33	51	–90	3.2	6
14	2013-12-23	04:20	38	38.19	15.56	11.00	48	67	–32	3.6	11

and Sicilian sides of the Straits, respectively, correspond to higher and lower degree of surface faulting and associated deformation (rate of geological moment release) estimated in the respective sectors by Ghisetti (1992). The **Figure 4** allows us to better focus on the seismicity located in the upper 20 km in the Straits and the Calabrian on-shore east of it, in particular we may look at the events occurring in the sector of the 1908 earthquake fault as reconstructed by Amoruso et al. (2002). All plots A-to-F in **Figure 4** show, in fact, the trace of Amoruso et al.'s 1908 earthquake fault, more precisely the trace in the map representations corresponds to the intersection between the fault plane prolongation and the earth surface. In the cross-section views, the trace shows the location of the circa north-striking east-dipping Amoruso et al.'s source. A striking feature appearing from **Figure 4** is that the recent seismicity occurred in the Straits is nearly all located below and east of the Amoruso et al.'s 1908 fault plane, with some events only located close above the bottom edge of the fault. This feature is highlighted by the great accuracy of hypocenter locations already discussed in the previous Section. Non-linear locations performed by the Bayloc algorithm, and the use of the robust dataset of the last 2 decades, have allowed us to obtain hypocenter distributions accurate enough for comparison between recent earthquake activity and the 1908 source. Less accurate locations performed with linearized methods applied to databases as long as 4 decades (including poorer network geometries) result in very noisy distributions of hypocenters (see, e.g., Barreca et al., 2021). The plots of **Figure 4** show also several clusters of earthquakes below the 1908 fault, more or less concentrated, but they do not display any clear evidence of trends indicating seismogenic faults. The findings of **Figure 4** suggest that a huge portion of the rock volume located above the 1908 fault is quite inactive from the seismic point of view. This could mean that the rock fracturing level is relatively low in it. The events located close above the bottom edge of the 1908 fault and east of it mark the (Calabrian) eastern boundary of the low-fractured block standing over the fault. **Figure 5** displays the hypocenter vertical sections of the recent seismicity occurred in the 1908 earthquake fault area, taken perpendicular to the orientations of the east-dipping sources proposed by different authors in the literature. The Figure shows that the conclusions drawn by comparing the recent earthquake locations to the location of the Amoruso et al. (2002) source of the 1908 earthquake are confirmed when considering the other sources, in particular most of the hanging wall of the 1908 fault is a low-fractured block.

The **Figure 6** displays the waveform inversion focal mechanisms estimated in the present study for the recent shallow earthquakes occurred in the study area of **Figure 3**. The figure shows reverse mechanisms at the southern border of the area (earthquakes n. 1–3), extensional ones at the northern border (8–11), and a mixture of extensional and right-lateral mechanisms in the Straits and the Calabrian on-shore of it (4–5 and 12–14). The earthquakes n. 6 and 7, located near the right-lateral Ionian fault zone corresponding to the southwestern edge of the Ionian subducting slab (shadowed belt in **Figure 6**; see also Polonia et al., 2016), show dextral strike-slip mechanisms compatible with the kinematics of same fault zone. The distribution of mechanisms of **Figure 6** (see also the polar plots of P and T axes relative to the different compartments) matches well with the geodynamic model of the study area assuming that the Messina Straits area is transitional between the zone of rollback of the in-depth continuous Ionian subducting slab (southern Calabria) and the collisional zone where the subduction slab did already undergo detachment (southwest of the Ionian fault zone) (Neri et al., 2012; Orecchio et al., 2014; among others). Normal faulting earthquakes in the Tyrrhenian sea offshore southern Calabria (FMs n. 8–11) are compatible with southeast-ward rollback and trench retreat of the subducting Ionian slab. Reverse mechanisms in the Ionian sea southwest of the Ionian fault zone (FMs n. 1–3) are compatible with the collisional domain existing southwest of the subducting slab edge. The transitional character of the Messina Straits implies reasonably the coexistence of normal faulting and right-lateral mechanisms, the latter accommodating the internal deformation of the overriding unit subjected to differential southeast-ward advance onto the subducting one (this mechanism is schematized

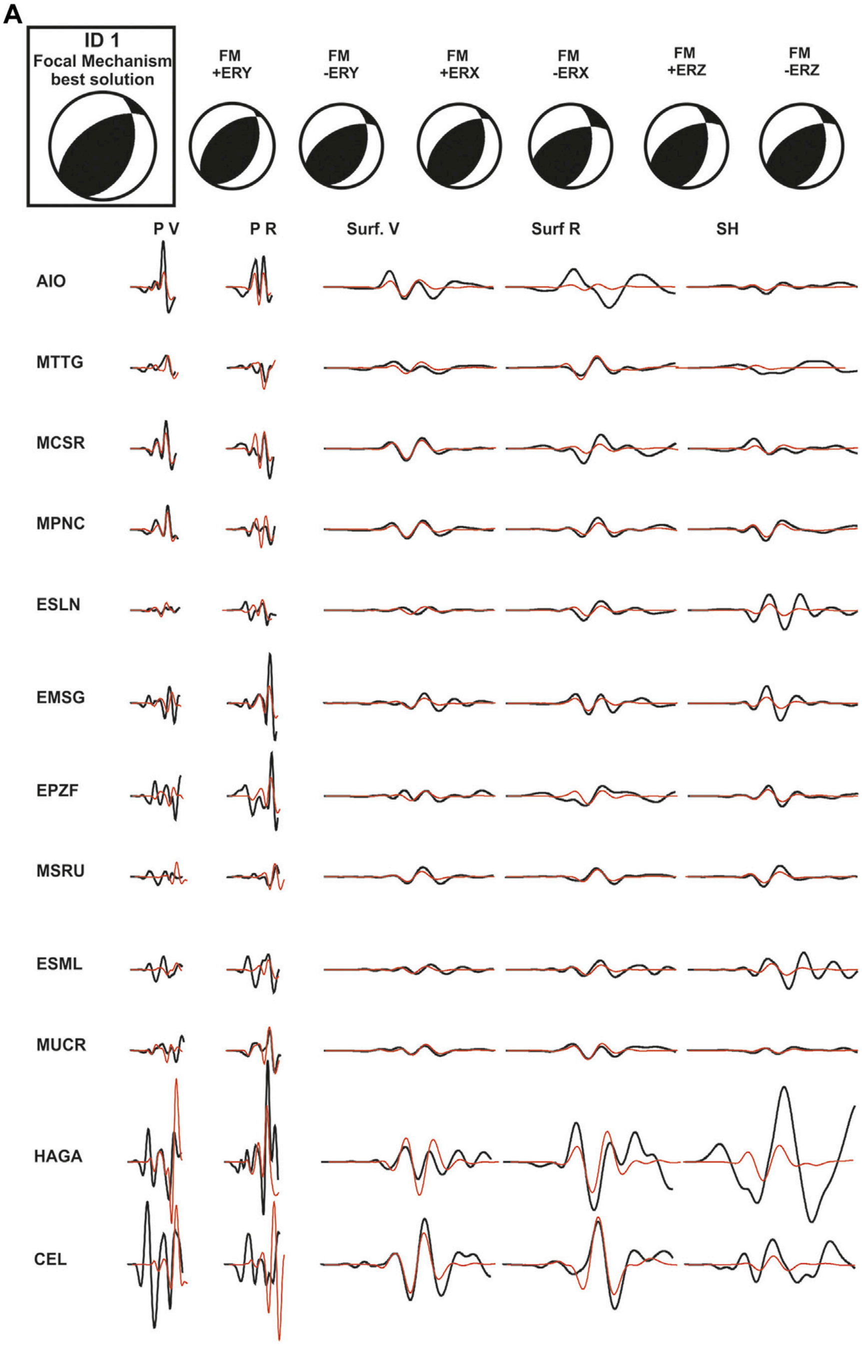

FIGURE 7 | Plots **(A–D)** show waveform inversion results obtained in the present study for the earthquakes n. 1, 5, 10 and 14 of **Figure 6** and **Table 1**. For each event we report the best focal mechanism solution (top-left, in the box), the relative waveform fits (observed-black vs predicted-red; main part of the figure), and some stability tests of the solution performed by moving the hypocenter in all directions within the Bayloc's uncertainty volume of the event itself (top of the plot, to the right of the best solution).

in the forthcoming **Figure 9A**). Coexistence of normal faulting and right-lateral mechanisms is just what we obtain in the present study by analysis of focal mechanisms in the Messina Straits and the Calabrian onshore east of it (FMs n. 4–5 and 12–14 in **Figure 6**). The quality of the focal mechanisms (some examples of stability tests are given in **Figure 7**) supports our interpretation of themselves in the frame of the above mentioned geodynamic model.

We show in **Figure 8A** the map of present-day uplift rate values reported by Serpelloni et al. (2013) for a ca. NW-trending rectangular sector including southern Calabria (south of Lamezia Plain) and the Messina Straits. The GPS stations used by

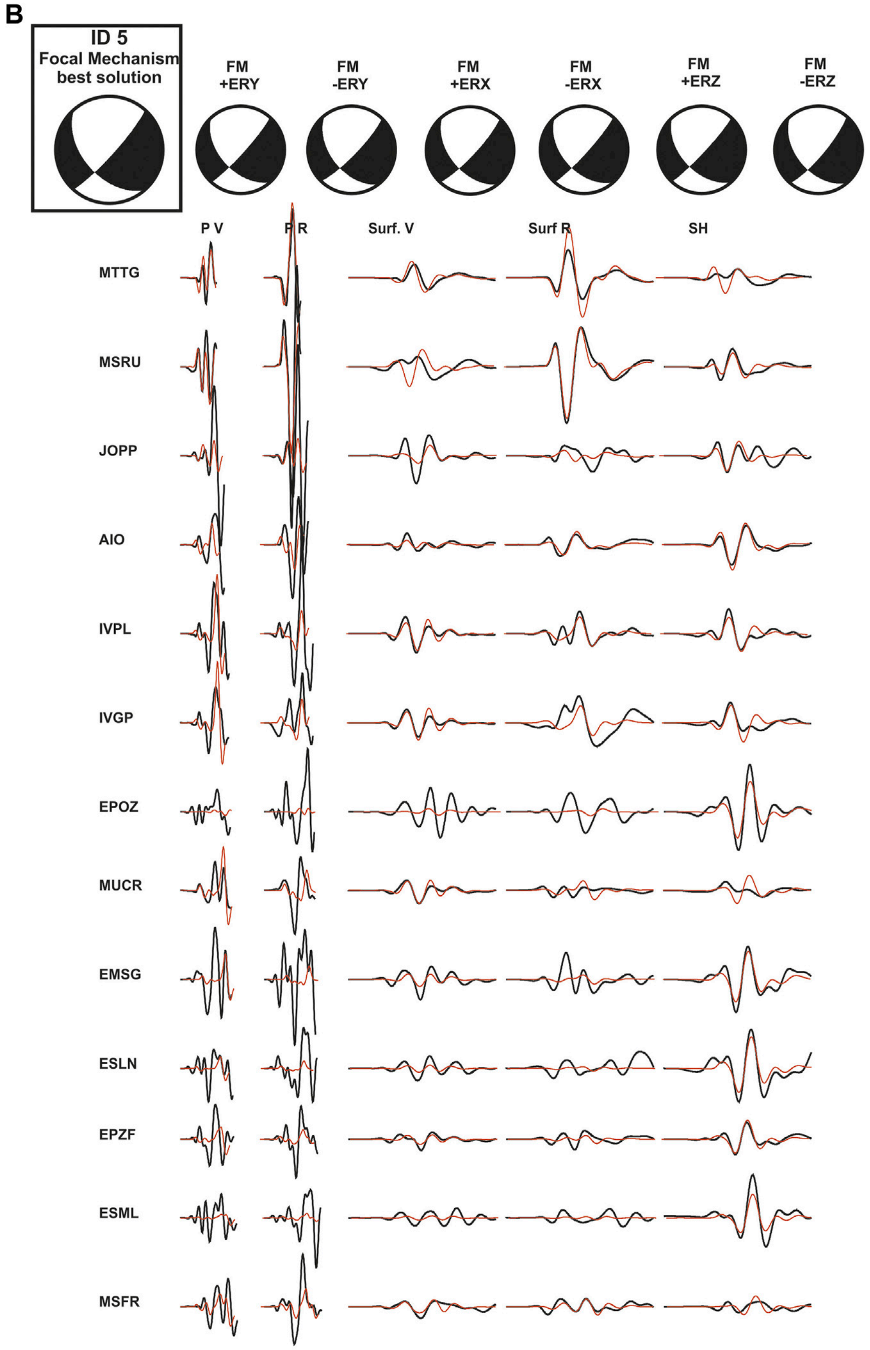

Figure 7. | (Continued).

Serpelloni et al. (2013) for their study are almost all concentrated in the southwestern half of the rectangle, more precisely in the sector of the Arc comprising the basins of Gioia Tauro and Messina Straits. We may consider the cross-section view of the same data (**Figure 8B**, taken from Serpelloni et al.'s Figure 13) as representative of the uplift rate pattern along profile crossing (from SE to NW) the Aspromonte chain, the basins (Gioia Tauro and Messina Straits), and the eastern Aeolian Islands in the southeastern Tyrrhenian sea. The profile of our **Figure 8B** (taken from Figure 13 of Serpelloni et al., 2013) shows the maximum value of uplift rate in southeastern Calabria (0.8 mm/yr; southeast of the top of the chain indicated by T) and a rapid drop to a minimum of—0.8 mm/yr moving to NW in the basins' area (Ba). Northwest of the minimum, the profile shows a NW-ward increasing uplift rate from—0.8 mm/yr to circa 0 mm/yr. This pattern indicates a SE-ward progressive subsidence in the

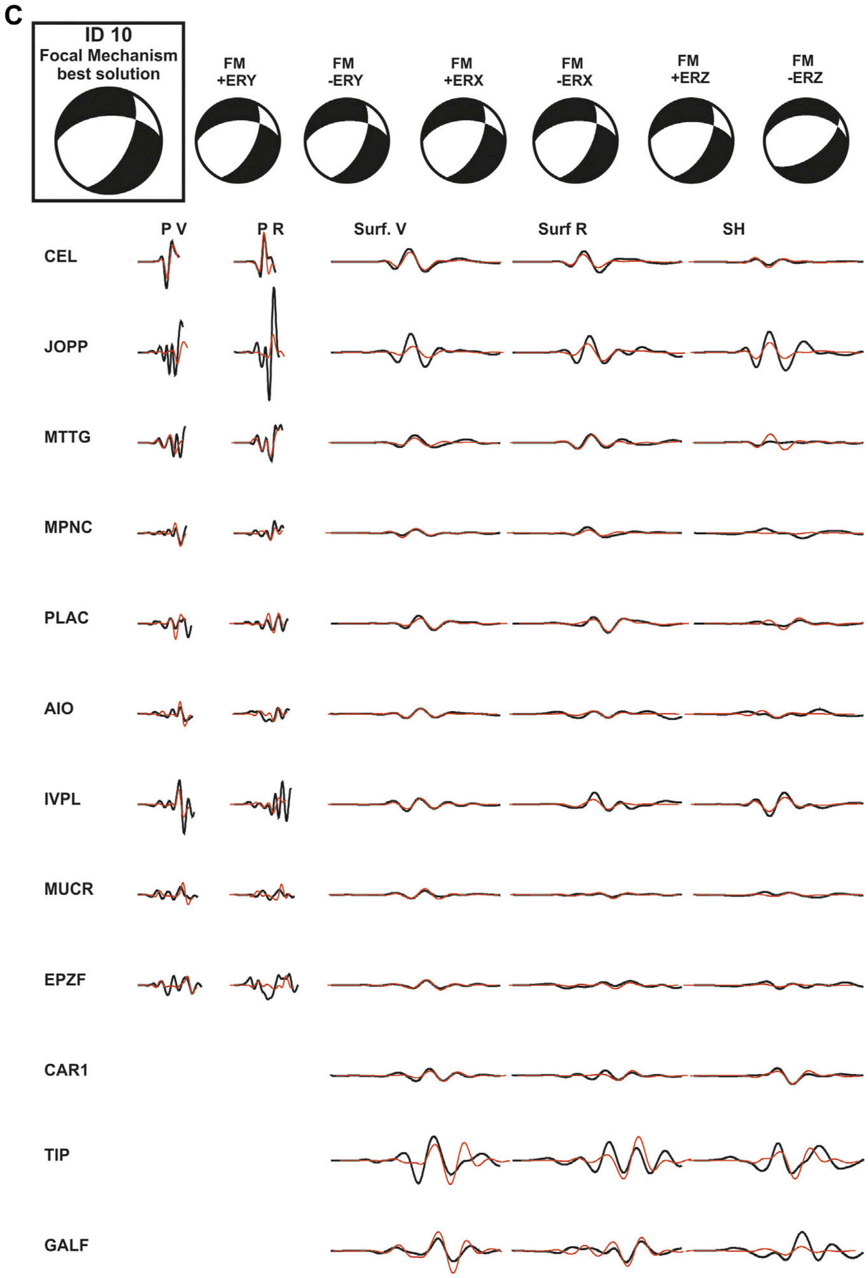

Figure 7. | (Continued).

area of the basins (Gioia Tauro and Messina Straits). Even if future data acquisition is needed for a more robust analysis of the uplift rate pattern in this area, in particular in the Messina Straits area, we take from Serpelloni et al.'s data a preliminary indication of a possible phenomenon of east-ward progressive subsidence in the Messina Straits. We may also note from **Figure 8** that 1) the maximum uplift rate of 0.8 mm/yr corresponds to the eastern boundary of the Aspromonte chain and 2) the rapid drop of uplift rate observed moving to NW contains the location (E) of the March 11, 1978, magnitude 4.7 earthquake investigated by Orecchio et al. (2019). For this earthquake, Orecchio et al. (2019) estimated a depth of 8 km and a normal-faulting mechanism on a high-dip NNE-trending fault plane dipping to WNW (**Figure 8C**). On the basis of these data, we tend to believe that the March 1978 Aspromonte earthquake may have derived from differential uplift into the chain area.

We suggest the following geodynamic processes to explain the findings of the present study concerning recent seismicity of the Messina Straits and the information available from literature concerning 1) the 1908 earthquake and 2) other geophysical features of the southern Calabrian Arc. A primary process is the

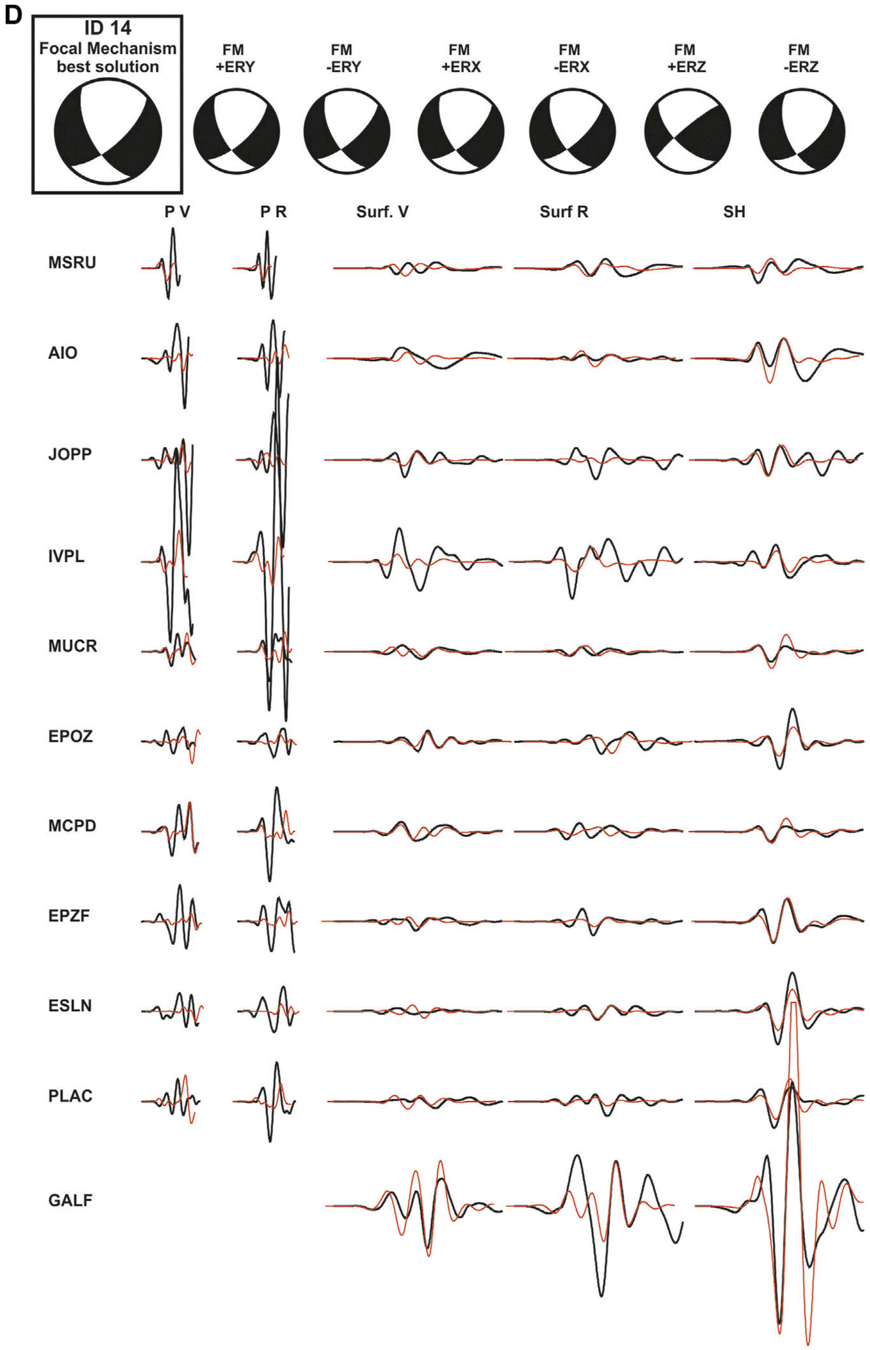

Figure 7. | (Continued).

widely shared coexistence in the study region of 1) Africa-Europe NNW-trending plate convergence and 2) SE-ward residual rollback of the Ionian lithospheric slab subducting underneath the Tyrrhenian-Calabria unit. As said above, the Messina Straits area can be considered as transitional between the zone of rollback of the in-depth continuous subducting slab (southern Calabria) and the collisional zone where the subduction slab did already undergo detachment (southwest of the Ionian fault zone) (Neri et al., 2012; Orecchio et al., 2014). This transitional character of Messina Straits would produce the observed coexistence of normal faulting and right-lateral mechanisms (**Figure 6**), the latter accommodating the internal deformation of the overriding unit due to the decreasing trench retreat when approaching the slab edge. As said in a previous Section, the coexistence of Africa-Europe convergence and rollback of the Ionian subducting lithosphere was shown to be able to produce

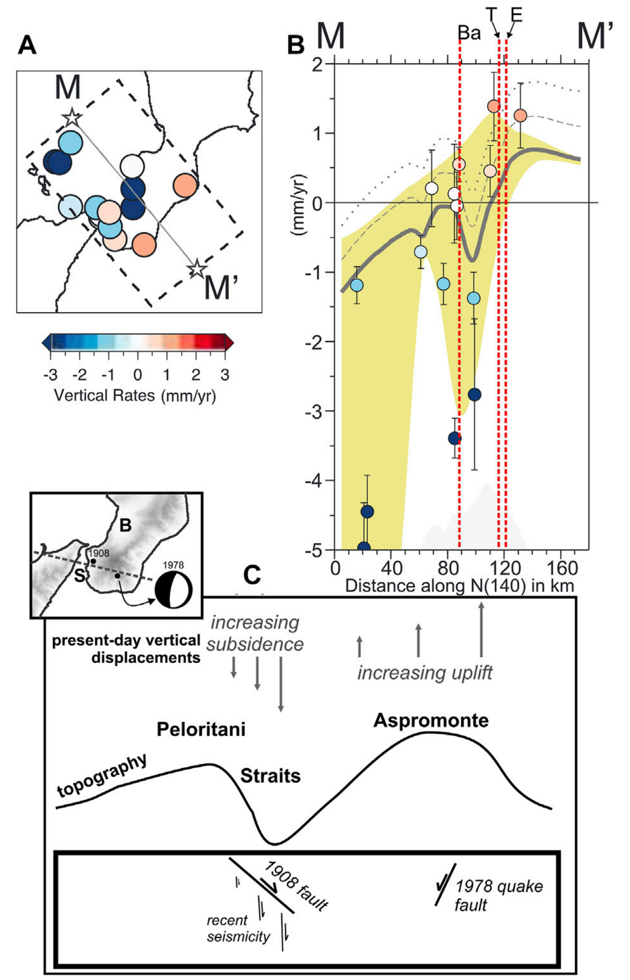

FIGURE 8 | Map plot **(A)** and related cross-section view plot **(B)** of the present-day uplift rate values estimated by Serpelloni et al. (2013) in a ca. NW-trending rectangular sector including southern Calabria and the Messina Straits (redrawn from Serpelloni et al., 2013). "Ba", "T" and "E" in the plot **(B)** indicate, respectively, the basins' area (Gioia Tauro basin and Messina Straits), the top of the mountain chain and the location of the 1978 Aspromonte earthquake. Serpelloni et al.' s (2013) gray curve indicating the uplift rate pattern along the MM' profile in plot **(B)** evidences that the maximum of the present-day uplift rate is located southeast of the top of the chain and of the 1978 Aspromonte earthquake. The plot **(C)** (with the inset showing the Aspromonte-Peloritani profile and the focal mechanism of the 1978 Aspromonte earthquake) furnishes sketch representations of 1) present-day vertical displacements across the Messina Straits area desumed from the patterns of plots **(A)** and **(B)**, 2) topography, and 3) the locations and kinematics of the faults which generated the earthquakes of 1908 (magnitude 7.1) and 1978 (magnitude 4.7). In the same plot **(C)**, "increasing subsidence" indicates the approximate location of the descending pattern of the gray curve that can be noted in the basin's area (Ba) in plot **(B)**, while "increasing uplift" marks the location of the gray curve growing pattern between the basin and the zone of maximum uplift rate. As explained in the text, future checks of these uplift/subsidence patterns should be performed by acquisition of new data especially in the offshore sectors.

uplift of southeastern Calabria (Negredo et al., 1999), and this is in agreement with Serpelloni et al.'s (2013) uplift rate pattern that we have reported in **Figure 8**. The above discussed phenomenon of east-ward progressive subsidence in the Messina Straits inferred from Serpelloni et al.'s uplift pattern reproduced in **Figure 8**, if it will confirmed in the future by a more robust

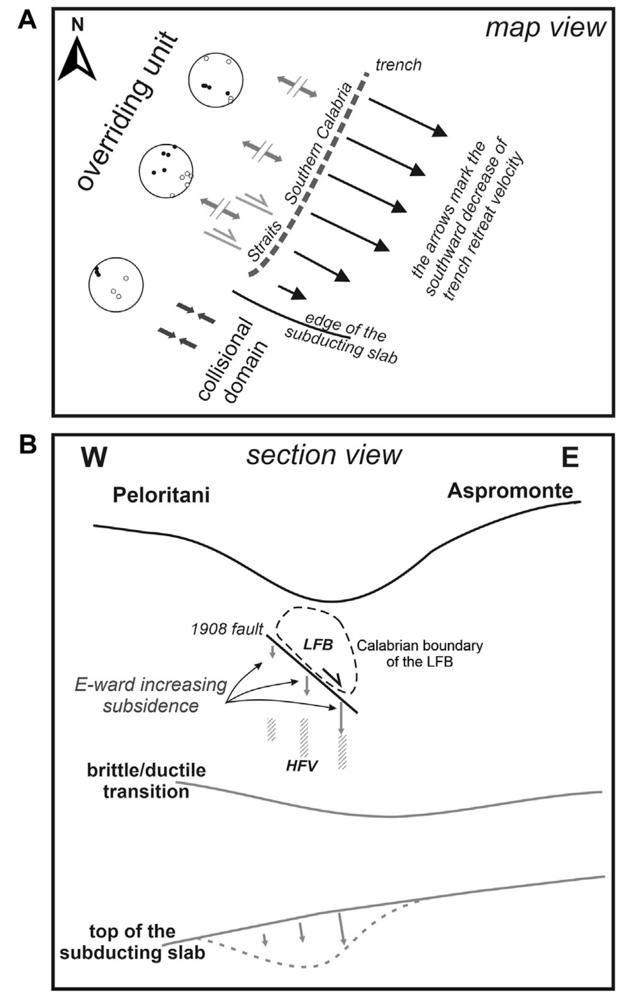

FIGURE 9 | Sketch representation of geodynamic engines producing seismicity in the Messina Straits area. The map view of plot **(A)** shows the progressive reduction of trench retreat velocity from northeast to southwest along the southern Calabrian Arc (southern Calabria–Straits) when approaching the southern edge of the Ionian subducting slab. This process produces internal deformation of the Messina Straits transitional zone between the extensional domain of southern Calabria and the collisional one of Sicily, southwest of the slab edge. Internal deformation of the Messina Straits is accommodated by dextral strike-slip mixed to normal faulting mechanisms (**Figure 6B**). The same polar plots of P- and T-axes reported in **Figure 6B** are also shown in this Figure for easier comparison. The representation of processes given in the section view of plot **(B)** is based on the preliminary evidence of east-ward progressive subsidence in the Messina Straits inferred from Serpelloni et al.'s (2013) uplift pattern reproduced in **Figure 8**. If this east-ward progressive subsidence will be confirmed in the future by new data including sea bottom measurements, this scheme will offer a new possible explanation of the loading mechanism of the 1908 fault. The east-ward increasing subsidence, eventually imputable to instabilities in the top of the subducting slab of the type suggested for the study region in previous papers (Orecchio et al., 2014; Presti et al., 2019), could drive the huge low-fractured block LFB resting on the fault to slide episodically onto the high-fractured volume HFV representing the footwall of the fault.

set of data including sea bottom measurements, could offer a new explanation of the loading mechanism of the 1908 fault. The east-ward increasing subsidence, eventually imputable to instabilities in the top of the subducting slab of the type suggested for the study region in previous papers (Orecchio et al., 2014; Presti et al., 2019), could drive the huge low-fractured block resting on the fault to slide episodically onto the more fractured basement representing the footwall of the fault (**Figure 9**). We offer this purely speculative hypothesis to the currently intense debate on local seismicity (Tiberti et al., 2017; Carafa et al., 2017; Presti et al., 2017; Neri et al., 2020; among others) and to future plans of data acquisition in the study region, also considering that vertical dynamics of the type suggested here would represent a simple and rather appropriate model for an area of strong normal-faulting earthquakes and relatively low horizontal strain rates like the Messina Straits.

CONCLUSION

The recent crustal seismicity in the area of the major, 1908 Messina Straits earthquake has mainly occurred below the east-dipping north-striking fault proposed by most investigators as the source of the 1908 earthquake, while it has been substantially absent in correspondence of the fault and above it (**Figures 4**, **5**). This distribution of seismicity suggests the existence of a huge, low-fractured shallow block resting on a somewhat fractured medium, with the separation surface between them roughly corresponding to the fault which generated the 1908 earthquake (**Figure 9B**).

The focal mechanisms of recent earthquakes (**Figure 6**) furnish a convincing picture of the transition from the extensional domain of southern Calabria (where southeast-ward trench retreat is still active, although slow) to the compressional domain of Sicily (where detachment of the subducting slab has already occurred), see **Figure 9A**. The progressive reduction of trench retreat from northeast to southwest produces internal deformation of the Messina Straits transitional zone and this deformation is accommodated by dextral strike-slip faulting mixed to normal faulting.

Starting from the above findings, we state that the joint action of Africa-Europe plate convergence and rollback of the Ionian subducting slab can be considered a major engine of seismicity in the Messina Straits area. A remarkable feature of the Messina Straits and the nearby southernmost Calabria is the occurrence of strong normal-faulting earthquakes (like 1908 and 1783) associated to evidence of relatively low horizontal strain rate furnished by GPS data of the last few decades (Palano, 2015). Different hypotheses have been proposed to explain this feature (Carafa et al., 2017; Presti et al., 2017; Tiberti et al., 2017; Neri et al., 2020). Starting also from strong spatial variations of geodetic uplift rate estimated by Serpelloni et al. (2013), we believe that hypotheses of deep-seated sources of stress concurring to local vertical dynamics (see, e.g., Orecchio et al., 2014) may reasonably be part of the ongoing debate on the study area. The apparent east-ward progressive subsidence in correspondence with the basin area (Serpelloni et al.'s Figures 10, 13 and our **Figure 8**), if confirmed in the future by acquisition of new data with particular reference to offshore areas, will furnish a new possible interpretation of the loading mechanism of the 1908 fault: the east-ward increasing subsidence would drive the huge low-fractured shallow block to slide episodically onto the more fractured basement in the Straits area (**Figure 9B**).

DATA AVAILABILITY STATEMENT

Publicly available datasets were analyzed in this study. These data can be found here: www.ingv.it; http://orfeus-eu.org/webdc3/.

AUTHOR CONTRIBUTIONS

GN and DP: coordination of the study. BO, SS, and CT: data collection and analysis, and contributions to interpretation of results.

FUNDING

This research has benefited from funding provided by Italian Project PRIN 2017KT2MK.

ACKNOWLEDGMENTS

The authors are grateful to the Editor Claudia Piromallo and the Reviewers Simone Cesca and Gianfranco Vannucci for their suggestions which helped to improve the manuscript.

REFERENCES

Aloisi, M., Bruno, V., Cannavò, F., Ferranti, L., Mattia, M., Monaco, C., et al. (2013). Are the Source Models of the M 7.1 1908 Messina Straits Earthquake Reliable? Insights from a Novel Inversion and a Sensitivity Analysis of Levelling Data. *Geophys. J. Int.* 192 (3), 1025–1041. doi:10.1093/gji/ggs062

Amato, A., and Mele, F. (2008). Performance of the INGV National Seismic Network from 1997 to 2007. *Ann: Geophys-Italy*. 51 (2-3). doi:10.4401/ag-4454

Amoruso, A., Crescentini, L., Neri, G., Orecchio, B., and Scarpa, R. (2006). Spatial Relation between the 1908 Messina Straits Earthquake Slip and Recent Earthquake Distribution. *Geophys. Res. Lett.* 33, 17. doi:10.1029/2006GL027227

Amoruso, A., Crescentini, L., and Scarpa, R. (2002). Source Parameters of the 1908 Messina Straits, Italy, Earthquake from Geodetic and Seismic Data. *J. Geophys. Res.* 107, 4–1. doi:10.1029/2001JB000434

Barreca, G., Gross, F., Scarfì, L., Aloisi, M., Monaco, C., and Krastel, S. (2021). The Strait of Messina: Seismotectonics and the Source of the 1908 Earthquake. *Earth-Science Rev.* 218, 103685. doi:10.1016/j.earscirev.2021.103685

Bonini, L., Bucci, D. D., Toscani, G., Seno, S., and Valensise, G. (2011). Reconciling Deep Seismogenic and Shallow Active Faults through Analogue Modelling: the

Case of the Messina Straits (Southern Italy). *J. Geol. Soc.* 168 (1), 191–199. doi:10.1144/0016-76492010-055

Boschi, E., Pantosti, D., and Valensise, G. (1989). *Modello di sorgente per il terremoto di Messina del 1908 ed evoluzione recente dell'area dello Stretto*. Roma: Atti VIII Convegno GNGTS, 245–258.

Bottari, A., Capuano, P., De Natale, G., Gasparini, P., Neri, G., Pingue, F., et al. (1989). Source Parameters of Earthquakes in the Strait of Messina, Italy, during This century. *Tectonophysics* 166 (1-3), 221–234. doi:10.1016/0040-1951(89)90215-1

Capuano, P., De Natale, G., Gasparini, P., Pingue, F., and Scarpa, R. (1988). A Model for the 1908 Messina Straits (Italy) Earthquake by Inversion of Levelling Data. *Bull. Seism. Soc. Am.* 78 (6), 1930–1947.

Carafa, M. M. C., Valensise, G., and Bird, P. (2017). Assessing the Seismic Coupling of Shallow continental Faults and its Impact on Seismic hazard Estimates: a Case-Study from Italy. *Geophys. J. Int.* 209 (1), ggx002–47. doi:10.1093/gji/ggx002

Convertito, V., and Pino, N. A. (2014). Discriminating Among Distinct Source Models of the 1908 Messina Straits Earthquake by Modelling Intensity Data through Full Wavefield Seismograms. *Geophys. J. Int.* 198 (1), 164–173. doi:10.1093/gji/ggu128

D'Addezio, G., Pantosti, D., Valensise, G., and Cinti, F. (1993). Investigating the Seismic Potential of Hidden and Semi-hidden Faults: the 1908 Messina Staits and the 1980 Irpinia Earthquakes (Southern Italy). *Z.* Geomorphol. *Supp.* 94, 119–135.

D'Amico, S., Orecchio, B., Presti, D., Gervasi, A., Zhu, L., Guerra, I., et al. (2011). Testing the Stability of Moment Tensor Solutions for Small Earthquakes in the Calabro–Peloritan Arc Region (Southern Italy). *Boll. Geof. Teor. Appl.* 52, 283–298. doi:10.4430/bgta0009

D'Amico, S., Orecchio, B., Presti, D., Zhu, L., Herrmann, R. B., and Neri, G. (2010). Broadband Waveform Inversion of Moderate Earthquakes in the Messina Straits, Southern Italy. *Phys. Earth Planet. In.* 179, 97–106. doi:10.1016/j.pepi.2010.01.012

D'Agostino, N., and Selvaggi, G. (2004). Crustal Motion along the Eurasia-Nubia Plate Boundary in the Calabrian Arc and Sicily and Active Extension in the Messina Straits from GPS Measurements. *J.* Geophys. Res.-Sol. Ea. 109 (B11). doi:10.1029/2004JB002998

De Natale, G., and Pino, N. A. (2014). Comment on 'Are the Source Models of the M 7.1 1908 Messina Straits Earthquake Reliable? Insights from a Novel Inversion and Sensitivity Analysis of Levelling Data' by M. Aloisi, V. Bruno, F. Cannavò, L. Ferranti, M. Mattia, C. Monaco and M. Palano. *Geophys. J. Int.* 197 (3), 1399–1402. doi:10.1093/gji/ggu063

De Natale, G., and Pingue, F. (1987). *Inversione di dati geodetici per modelli di faglia a dislocazione variabile. Applicazione al terremoto di Messina del 1908 Atti 6°Conv*. GNGTS.

De Natale, G., and Pingue, F. (1991). A Variable Slip Fault Model for the 1908 Messina Straits (Italy) Earthquake, by Inversion of Levelling Data. *Geophys. J. Int.* 104 (1), 73–84. doi:10.1111/j.1365-246X.1991.tb02494.x

Devoti, R., Riguzzi, F., Cuffaro, M., and Doglioni, C. (2008). New GPS Constraints on the Kinematics of the Apennines Subduction. *Earth Planet. Sci. Lett.* 273, 163–174. doi:10.1016/j.epsl.2008.06.031

DISS Working Group (2018). Database of Individual Seismogenic Sources (DISS), .version 3.2.1: a compilation of potential sources for earthquakes larger thanM 5.5 in Italy and surrounding areas (Rome: Istituto Nazionale di Geofisica e Vulcanologia). Available at: http://diss.rm.ingv.it/diss/

Doglioni, C., Ligi, M., Scrocca, D., Bigi, S., Bortoluzzi, G., Carminati, E., et al. (2012). The Tectonic Puzzle of the Messina Area (Southern Italy): Insights from New Seismic Reflection Data. *Sci. Rep.* 2 (1), 1–9. doi:10.1038/srep00970

Ekström, G., Nettles, M., and Dziewoński, A. M. (2012). The Global CMT Project 2004-2010: Centroid-Moment Tensors for 13,017 Earthquakes. *Phys. Earth Planet. In.* 200, 1–9. doi:10.1016/j.pepi.2012.04.002

Faccenna, C., Davy, P., Brun, J.-P., Funiciello, R., Giardini, D., Mattei, M., et al. (1996). The Dynamics of Back-Arc Extension: an Experimental Approach to the Opening of the Tyrrhenian Sea. *Geophys. J. Int.* 126, 781–795. doi:10.1111/j.1365-246X.1996.tb04702.x

Faccenna, C., Molin, P., Orecchio, B., Olivetti, V., Bellier, O., Funiciello, F., et al. (2011). Topography of the Calabria Subduction Zone (Southern Italy): Clues for the Origin of Mt. Etna. *Tectonics* 30, TC1003. doi:10.1029/2010TC002694

Ferranti, L., Antonioli, F., Anzidei, M., Monaco, C., and Stocchi, P. (2010). The Timescale and Spatial Extent of Vertical Tectonic Motions in Italy: Insights from Relative Sea-Level Changes Studies. *J. Virtual Explorer* 36, 30. doi:10.3809/jvirtex.2009.0025510.3809/jvirtex.2010.00255

Ferranti, L., Monaco, C., Antonioli, F., Maschio, L., Kershaw, S., and Verrubbi, V. (2007). The Contribution of Regional Uplift and Coseismic Slip to the Vertical Crustal Motion in the Messina Straits, Southern Italy: Evidence from Raised Late Holocene Shorelines. *J. Geophys. Res.* 112 (B6). doi:10.1029/2006JB004473

Fu, L., Heidarzadeh, M., Cukur, D., Chiocci, F. L., Ridente, D., Gross, F., et al. (2017). Tsunamigenic Potential of a Newly Discovered Active Fault Zone in the Outer Messina Strait, Southern Italy. *Geophys. Res. Lett.* 44 (5), 2427–2435. doi:10.1002/2017GL072647

Ghisetti, F. (1992). Fault Parameters in the Messina Strait (Southern Italy) and Relations with the Seismogenic Source. *Tectonophysics* 210 (1-2), 117–133. doi:10.1016/0040-1951(92)90131-o

Goswami, R., Mitchell, N. C., Argnani, A., and Brocklehurst, S. H. (2014). Geomorphology of the Western Ionian Sea between Sicily and Calabria, Italy. *Geo-mar. Lett.* 34 (5), 419–433. doi:10.1007/s00367-014-0374-2

Hollenstein, C., Kahle, H.-G., Geiger, A., Jenny, S., Goes, S., and Giardini, D. (2003). New GPS Constraints on the Africa-Eurasia Plate Boundary Zone in Southern Italy. *Geophys. Res. Lett.* 30 (18). doi:10.1029/2003GL017554

Jacques, E., Monaco, C., Tapponnier, P., Tortorici, L., and Winter, T. (2001). Faulting and Earthquake Triggering during the 1783 Calabria Seismic Sequence. *Geophys. J. Int.* 147, 499–516. doi:10.1046/j.0956-540x.2001.01518.x

Loperfido, A. (1909). Livellazione geometrica di precisione eseguita dall'IGM sulla costa orientale della Sicilia, da Messina a Catania, a Gesso ed a Faro Peloro e sulla costa occidentale della Calabria da Gioia Tauro a Melito di Porto Salvo Relazione della Commissione Reale incaricata di designare filezone più adatte per la ricostruzione degli abitati colpiti dal terremoto del 28 dicembre 1908 o da altri precedenti, 131–156.

Malinverno, A., and Ryan, W. B. F. (1986). Extension in the Tyrrhenian Sea and Shortening in the Apennines as Result of Arc Migration Driven by Sinking of the Lithosphere. *Tectonics* 5 (2), 227–245. doi:10.1029/TC005i002p00227

Meschis, M., Roberts, G. P., Mildon, Z. K., Robertson, J., Michetti, A. M., and Faure Walker, J. P. (2019). Slip on a Mapped normal Fault for the 28th December 1908 Messina Earthquake (Mw 7.1) in Italy. *Sci. Rep.* 9 (1), 1–8. doi:10.1038/s41598-019-42915-2

Monaco, C., and Tortorici, L. (2000). Active Faulting in the Calabrian Arc and Eastern Sicily. *J. Geodyn.* 29 (3-5), 407–424. doi:10.1016/S0264-3707(99)00052-6

Monaco, C., Tortorici, L., Nicolich, R., Cernobori, L., and Costa, M. (1996). From Collisional to Rifted Basins: An Example from the Southern Calabrian Arc (Italy). *Tectonophysics* 266 (1/4), 233–249. doi:10.1016/S0040-1951(96)00192-8

Mulargia, F., and Boschi, E. (1983). The 1908 Messina Earthquake and Related Seismicity, *Earthquakes: observation, Theor. interpretation*, 493–518.

Negredo, A. M., Carminati, E., Barba, S., and Sabadini, R. (1999). Dynamic Modelling of Stress Accumulation in central Italy. *Geophys. Res. Lett.* 26, 13, 1945–1948. doi:10.1029/1999GL900408

Neri, G., Marotta, A. M., Orecchio, B., Presti, D., Totaro, C., Barzaghi, R., et al. (2012). How Lithospheric Subduction Changes along the Calabrian Arc in Southern Italy: Geophysical Evidences. *Int. J. Earth Sci. (Geol Rundsch)* 101, 1949-1969. doi:10.1007/s00531-012-0762-7

Neri, G., Orecchio, B., Scolaro, S., and Totaro, C. (2020). Major Earthquakes of Southern Calabria, Italy, into the Regional Geodynamic Context. *Front. Earth Sci.* 8, 579846. doi:10.3389/feart.2020.579846

Neri, G., Orecchio, B., Totaro, C., Falcone, G., and Presti, D. (2009). Subduction beneath Southern Italy Close the Ending: Results from Seismic Tomography. *Seismological Res. Lett.* 80, 63–70. doi:10.1785/gssrl.80.1.63

Nocquet, J.-M. (2012). Present-day Kinematics of the Mediterranean: A Comprehensive Overview of GPS Results. *Tectonophysics* 579, 220–242. doi:10.1016/j.tecto.2012.03.037

Orecchio, B., Presti, D., Totaro, C., D'Amico, S., and Neri, G. (2015). Investigating Slab Edge Kinematics through Seismological Data: The Northern Boundary of the Ionian Subduction System (South Italy). *J. Geodynamics* 88, 23–35. doi:10.1016/j.jog.2015.04.003

Orecchio, B., Presti, D., Totaro, C., and Neri, G. (2014). What Earthquakes Say Concerning Residual Subduction and STEP Dynamics in the Calabrian Arc Region, South Italy. *Geophys. J. Int.* 199 (3), 1929–1942. doi:10.1093/gji/ggu373

Orecchio, B., Scolaro, S., Batlló, J., Ferrari, G., Presti, D., and Stich, D. (2019). A Reappraisal of the 1978 Ferruzzano Earthquake (Southern Italy) from New Estimates of Hypocenter Location and Moment Tensor Inversion. *Phys. Earth Planet. Interiors* 289, 34–44. doi:10.1016/j.pepi.2019.02.003

Palano, M. (2015). On the Present-Day Crustal Stress, Strain-Rate fields and Mantle Anisotropy Pattern of Italy. *Geophys. J. Int.* 200 (2), 969–985. doi:10.1093/gji/ggu451

Pino, N. A., Giardini, D., and Boschi, E. (2000). The December 28, 1908, Messina Straits, Southern Italy, Earthquake: Waveform Modeling of Regional Seismograms. *J. Geophys. Res.* 105 (B11), 25473–25492. doi:10.1029/2000JB900259

Pizzino, L., Burrato, P., Quattrocchi, F., and Valensise, G. (2004). Geochemical Signatures of Large Active Faults: The Example of the 5 February 1783, Calabrian Earthquake (Southern Italy). *J. Seismology* 8, 363–380. doi:10.1023/B:JOSE.0000038455.56343.e7

Polonia, A., Torelli, L., Artoni, A., Carlini, M., Faccenna, C., Ferranti, L., et al. (2016). The Ionian and Alfeo-Etna Fault Zones: New Segments of an Evolving Plate Boundary in the central Mediterranean Sea? *Tectonophysics* 675, 69–90. doi:10.1016/j.tecto.2016.03.016

Pondrelli, S., Salimbeni, S., Ekström, G., Morelli, A., Gasperini, P., and Vannucci, G. (2006). The Italian CMT Dataset from 1977 to the Present. *Phys. Earth Planet. Interiors* 159 (3-4), 286–303. doi:10.1016/j.pepi.2006.07.008

Presti, D., Billi, A., Orecchio, B., Totaro, C., Faccenna, C., and Neri, G. (2013). Earthquake Focal Mechanisms, Seismogenic Stress, and Seismotectonics of the Calabrian Arc, Italy. *Tectonophysics* 602, 153–175. doi:10.1016/j.tecto.2013.01.030

Presti, D., Neri, G., Orecchio, B., Scolaro, S., and Totaro, C. (2017). The 1905 Calabria, Southern Italy, Earthquake: Hypocenter Location, Causative Process, and Stress Changes Induced in the Area of the 1908 Messina Straits Earthquake. *Bull. Seismol. Soc. Am.* 107 (6), 2613–2623. doi:10.1785/0120170094

Presti, D., Orecchio, B., Falcone, G., and Neri, G. (2008). Linear versus Non-linear Earthquake Location and Seismogenic Fault Detection in the Southern Tyrrhenian Sea, Italy. *Italy.* Geophys. J. Int. 172, 607–618. doi:10.1111/j.1365-246X.2007.03642.x

Presti, D. (2019). Seismicity Supports the Theory of Incipient Rifting in the Western Ionian Sea, central Mediterranean. *Ann. Geophys-italy* 62 (2), 225. doi:10.4401/ag-8360

Presti, D., Totaro, C., Neri, G., and Orecchio, B. (2019). New Earthquake Data in the Calabrian Subduction Zone, Italy, Suggest Revision of the Presumed Dynamics in the Upper Part of the Subducting Slab. *Seismol. Res. Lett.* 90 (5), 1994–2004. doi:10.1785/0220190024

Presti, D., Troise, C., and De Natale, G. (2004). Probabilistic Location of Seismic Sequences in Heterogeneous media. *Bull. Seismological Soc. America* 94, 2239–2253. doi:10.1785/0120030160

Ridente, D., Martorelli, E., Bosman, A., and Chiocci, F. L. (2014). High-resolution Morpho-Bathymetric Imaging of the Messina Strait (Southern Italy). New Insights on the 1908 Earthquake and Tsunami. *Geomorphology* 208, 149–159. doi:10.1016/j.geomorph.2013.11.021

Rosenbaum, G., Lister, G. S., and Duboz, C. (2002). Reconstruction of the Tectonic Evolution of the Western Mediterranean since the Oligocene. *J.Virt.Ex* 08 (6). doi:10.3809/jvirtex.2002.00053

Schick, R. (1977). Eine seimotektonische Bearbeitung des Erdbedens von Messina aus dem Jahre 1908. Geol. Jb. *E-* 11, 3–74.

Schorlemmer, D., Mele, F., and Marzocchi, W. (2010). A Completeness Analysis of the National Seismic Network of Italy. *J. Geophys. Res.* 115 (B4). doi:10.1029/2008JB006097

Scolaro, S., Totaro, C., Presti, D., D'Amico, S., Neri, G., and Orecchio, B. (2018). Estimating Stability and Resolution of Waveform Inversion Focal Mechanisms. In *Moment Tensor Solutions*. Springer, 93–109. doi:10.1007/978-3-319-77359-9_5

Selli, R., Colantoni, P., Fabri, A., Rossi, S., and Borsetti, A. M. (1978). Marine Geological Investigations on the Messina Strait and its Approaches. *Giorn. Geol.* 42 (2).

Serpelloni, E., Faccenna, C., Spada, G., Dong, D., and Williams, S. D. P. (2013). Vertical GPS Ground Motion Rates in the Euro-Mediterranean Region: New Evidence of Velocity Gradients at Different Spatial Scales along the Nubia-Eurasia Plate Boundary. *J. Geophys. Res. Solid Earth* 118 (11), 6003–6024. doi:10.1002/2013JB010102

Tiberti, M. M., Vannoli, P., Fracassi, U., Burrato, P., Kastelic, V., and Valensise, G. (2017). Understanding Seismogenic Processes in the Southern Calabrian Arc:A Geodynamic Perspective. *Ijg* 136 (3), 365–388. doi:10.3301/IJG.2016.12

Totaro, C., Orecchio, B., Presti, D., Scolaro, S., and Neri, G. (2016). Seismogenic Stress Field Estimation in the Calabrian Arc Region (South Italy) from a Bayesian Approach. *Geophys. Res. Lett.* 43 (17), 8960–8969. doi:10.1002/2016GL070107

Valensise, G., and D'Addezio, G. (1994). *Il contributo della geologia di superficie all'individuazione delle strutture sismogenetiche della Piana di Gioia Tauro*, Istituto Nazionale di Geofisica internal publication No., 559, 21 pp.

Valensise, G., and Pantosti, D. (1992). A 125 Kyr-Long Geological Record of Seismic Source Repeatability: the Messina Straits (Southern Italy) and the 1908 Earthquake (Ms7/2). *Terra Nova* 4 (4), 472–483. doi:10.1111/j.1365-3121.1992.tb00583.x

Zhao, L. S., and Helmberger, D. V. (1994). Source Estimation from Broadband Regional Seismograms. *Bull. Seismol. Soc. Am.* 84 (1), 91–104.

Zhu, L., and Helmberger, D. (1996). Advancement in Source Estimation Technique Using Broadband Regional Seismograms. *Bull. Seismol. Soc. Am.* 86, 1634–1641.

Conflict of Interest: The authors declare that the research was conducted in the absence of any commercial or financial relationships that could be construed as a potential conflict of interest.

frontiers in Earth Science

ORIGINAL RESEARCH
published: 04 August 2021
doi: 10.3389/feart.2021.521220

Deep Dehydration as a Plausible Mechanism of the 2013 Mw 8.3 Sea of Okhotsk Deep-Focus Earthquake

Hao Zhang[1,2]*, *Suzan van der Lee*[2], *Craig R. Bina*[2] *and Zengxi Ge*[3]

[1]University of Utah Seismograph Stations, University of Utah, Salt Lake City, UT, United States, [2]Department of Earth and Planetary Sciences, Northwestern University, Evanston, IL, United States, [3]School of Earth and Space Sciences, Peking University, Beijing, China

The rupture mechanisms of deep-focus (>300 km) earthquakes in subducting slabs of oceanic lithosphere are not well understood and different from brittle failure associated with shallow (<70 km) earthquakes. Here, we argue that dehydration embrittlement, often invoked as a mechanism for intermediate-depth earthquakes, is a plausible alternative model for this deep earthquake. Our argument is based upon the orientation and size of the plane that ruptured during the deep, 2013 Mw 8.3 Sea of Okhotsk earthquake, its rupture velocity and radiation efficiency, as well as diverse evidence of water subducting as deep as the transition zone and below. The rupture process of this earthquake has been inferred from back-projecting dual-band seismograms recorded at hundreds of seismic stations in North America and Europe, as well as by fitting *P*-wave trains recorded at dozens of globally distributed stations. If our inferences are correct, the entirety of the subducting Pacific lithosphere cannot be completely dry at deep, transition-zone depths, and other deep-focus earthquakes may also be associated with deep dehydration reactions.

Keywords: deep dehydration, multi-array, multiband back projection, multi-subevent model, rupture velocity, P wave, 2013 okhotsk deep-focus earthquake

OPEN ACCESS

Edited by:
Sebastiano D'Amico,
University of Malta, Malta

Reviewed by:
Piero Poli,
Université Grenoble Alpes, France
Daniela Farrugia,
University of Malta, Malta

Correspondence:
Hao Zhang
zhang@seis.utah.edu

Specialty section:
This article was submitted to
Solid Earth Geophysics,
a section of the journal
Frontiers in Earth Science

Received: *18 December 2019*
Accepted: *29 June 2021*
Published: *04 August 2021*

Citation:
Zhang H, van der Lee S, Bina CR and Ge Z (2021) Deep Dehydration as a Plausible Mechanism of the 2013 Mw 8.3 Sea of Okhotsk Deep-Focus Earthquake.
Front. Earth Sci. 9:521220.
doi: 10.3389/feart.2021.521220

INTRODUCTION

Deep-focus earthquakes occur in subducting slabs of lithosphere at depths greater than 300 km. The mechanisms of these earthquakes must be fundamentally different from the brittle failure associated with earthquakes on the shallow (<70 km) megathrust plate interface because of the vast differences in pressure, temperature, and composition (Frohlich, 2006; Green and Houston, 1995; Kirby et al., 1996). Three previously proposed rupture mechanisms for deep-focus earthquakes include a phase transformation in the olivine polymorphs (Green and Burnley, 1989; Kirby et al., 1991; Green et al., 2015), thermal shear instabilities (Kanamori et al., 1998; Wiens, 2001), and embrittlement resulting from devolatilization (e.g., dehydration) of volatile-bearing phases present over a suitable spatial extent (Jung et al., 2004). The last mechanism is widely invoked to explain intermediate-depth earthquakes between 70 and 300 km (Peacock, 2001; Hacker et al., 2003).

The May 24, 2013, Mw 8.3, 609 km deep, Sea of Okhotsk earthquake provides a new perspective in understanding the rupture mechanism of the deep-focus earthquakes on account of its unusually large magnitude and the rapidly increased density of seismic stations at the Earth's surface. Previous studies of the rupture process of this earthquake revealed important aspects of the earthquake's mechanics, but did not agree with each other in all important respects (Wei et al., 2013; Ye et al., 2013; Chen et al., 2014; Meng et al., 2014; Zhan et al., 2014). As found by Ruiz et al. (2017), it is of

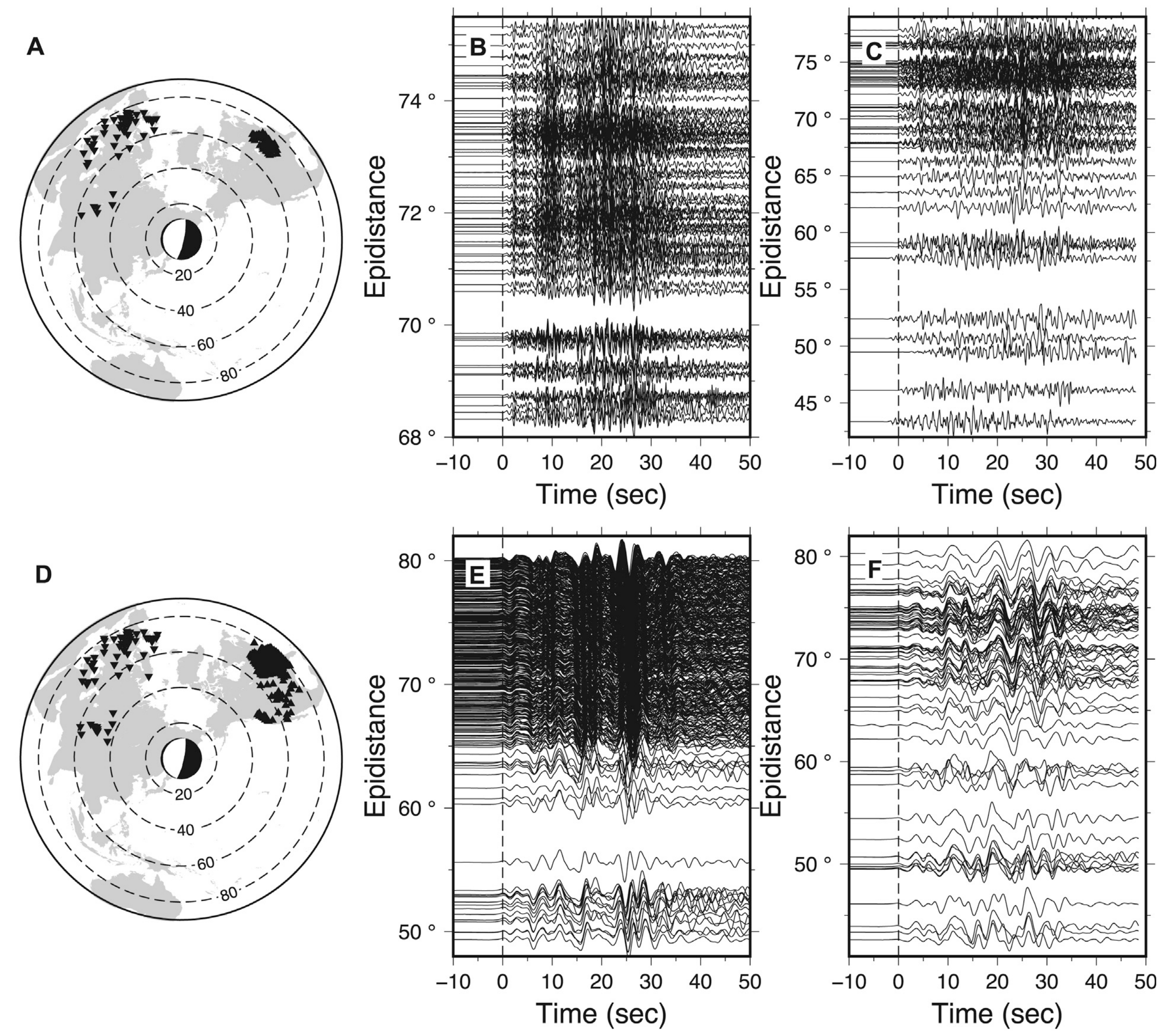

FIGURE 1 | Station distribution of the TA (triangles) and the EU (inverse triangles) arrays for **(A)** the high- and **(D)** low-frequency bands. *P*-wave trains are aligned with the first arrival (dashed lines) at the TA filtered in **(B)** the high- (0.5–2 Hz) and **(E)** low- (0.1–0.5 Hz) frequency bands, and at the EU in **(C)** the high- and **(F)** low-frequency bands. The *P* waveform's polarities are reversed at the TA. The GCMT focal mechanism is placed at the epicenter of the 2013 Sea of Okhotsk deep-focus earthquake.

importance to identify the correct orientation of the causative faults of the deep earthquakes since incorrect assumption of the faults' orientation could result in biased parameters, and thus may lead to misinterpretation to the mechanisms of the deep earthquakes. The 2013 Okhotsk earthquake was found to rupture sequentially on a subvertical plane by inverting teleseismic *P*, *SH*, and depth phases (*pP* and *sSH*) (Chen et al., 2014), but was discovered to rupture a subhorizontal fault plane using teleseismic *P* waves (Wei et al., 2013; Ye et al., 2013). Moreover, the subhorizontal fault as the causative fault is also supported by the *P* and *pP*-wave single-array back-projection (BP) imaging (Meng et al., 2014). In addition, the single-array back projection typically has the uncertainties of the subevents approximately 20 km (Zhang et al., 2015). In this study, the multi-array BP imaging is used to dramatically increase the resolution of the images as detailed in *A Synthetic Test for the Causative Fault's Orientation and BP Images' Resolution*.

To infer a comprehensive model for the rupture of the 2013 deep Okhotsk earthquake, we combined two different rupture-assessment methods: one is the multi-array BP method (Kiser and Ishii, 2012; Zhang et al., 2016), modified from the BP method (Ishii et al., 2005; Xu et al., 2009; Zhang and Ge, 2010; Zhang et al., 2011), and the other one is the multi-subevent inversion (Kikuchi and Kanamori, 1991). The back-projection analyses were carried out in two different frequency bands (Koper et al., 2011; Wang and Mori, 2011; Lay et al., 2012; Yao et al., 2013; Fan and Shearer,

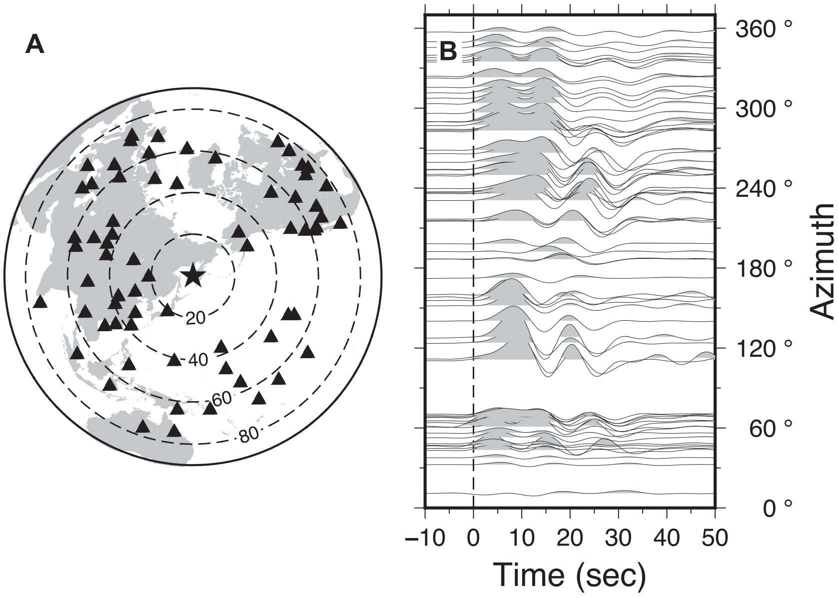

FIGURE 2 | Station distribution and seismic waveforms using in the multi-subevent inversion. **(A)** GSN station distribution and **(B)** *P*-waves aligned with the first arrivals (vertical dashed line). Stations at the GSN in the epidistance range of 20°–80° are used in the inversion. Triangles represent the GSN stations and the star indicates the epicenter of the earthquake. Polarities of the waveforms with azimuths greater than 180° are reversed.

2015) using data from USArray (TA) and European seismic network (EU) (**Figure 1**), while the multi-subevent inversion was performed using the data from the Global Seismic network (GSN) (**Figure 2**). Next, we integrated the back-projection and multi-subevent models with the local curved strike of the subducting Pacific slab. Additionally, to identify the orientation of the causative fault of the earthquake and resolution of the BP images, a synthetic test composed of two seismic point sources has been performed. Finally, we discuss the source properties of the earthquake and their implications for the mechanics of the earthquake on the basis of the resulting rupture models.

DATA AND METHODOLOGY

Multi-Array, Multi-Frequency-Band Back-Projection Analysis

P-wave trains from two seismic networks TA and EU were back-projected to the source region (Zhang et al., 2016; Zhang et al., 2017; Zhang and Ge, 2017) in two adjacent frequency bands (0.1–0.5 Hz and 0.5–2.0 Hz, **Figure 1**). We developed the final back-projection rupture model in the following three steps.

The first step was to separately generate single-array back-projection imaging for each frequency band and each array. Because signal coherence is a critical factor in successful back projection, we only retained traces having a cross-correlation coefficient greater than 0.6 with the trace of a reference station near the array's center. This culling reduced the number of used traces to 74 high-frequency and 377 low-frequency traces for the TA array (**Figures 1B,E**). Likewise, for the EU array, we retained 57 high-frequency and 69 low-frequency traces (**Figures 1C,F**). The low-frequency data at the TA have better azimuthal coverage than the high-frequency data, whereas the azimuthal coverage for the EU is independent of the frequency band (**Figures 1A,D**).

The global Centroid Moment Tensor (GCMT) implies two possible fault planes: one (strike 189°, dip 11°, and rake −93°) is subhorizontal, and the other one (strike 12°, dip 79°, and rake −89°) is subvertical (**Figures 1A,D**). As elucidated by Meng et al. (2014), a subhorizontal plane agrees better with both the *P* and *pP*-waves back-projection imaging as well as our back-projection models. Moreover, the subhorizontal plane as the causative fault is evidently supported by a synthetic test done with two seismic point sources separating 20 km vertically as detailed in *A Synthetic Test for the Causative Fault's Orientation and BP Images' Resolution*. We approximated this subhorizontal fault plane by a horizontal plane centered around the USGS hypocenter (54.87°N, 153.28°E, and 609 km). The plane is larger than the area that contains the aftershocks (**Supplementary Figure 1**) and is gridded into 101 × 101 0.05° × 0.05° fault patches. A grid search was conducted to identify slip on those fault segments that correspond to stacking slownesses that maximize stacked *P* wave energy in 6-s-long time windows for the first 50 s of *P* arrivals (**Figure 1**).

In a second step, and for both frequency bands, the two sets of *P*-wave trains from the TA and EU arrays were jointly back-projected together. To equalize the contribution of the two arrays, stacked *P* amplitude distributions were normalized with their respective maxima. The multi-array back-projection imaging was

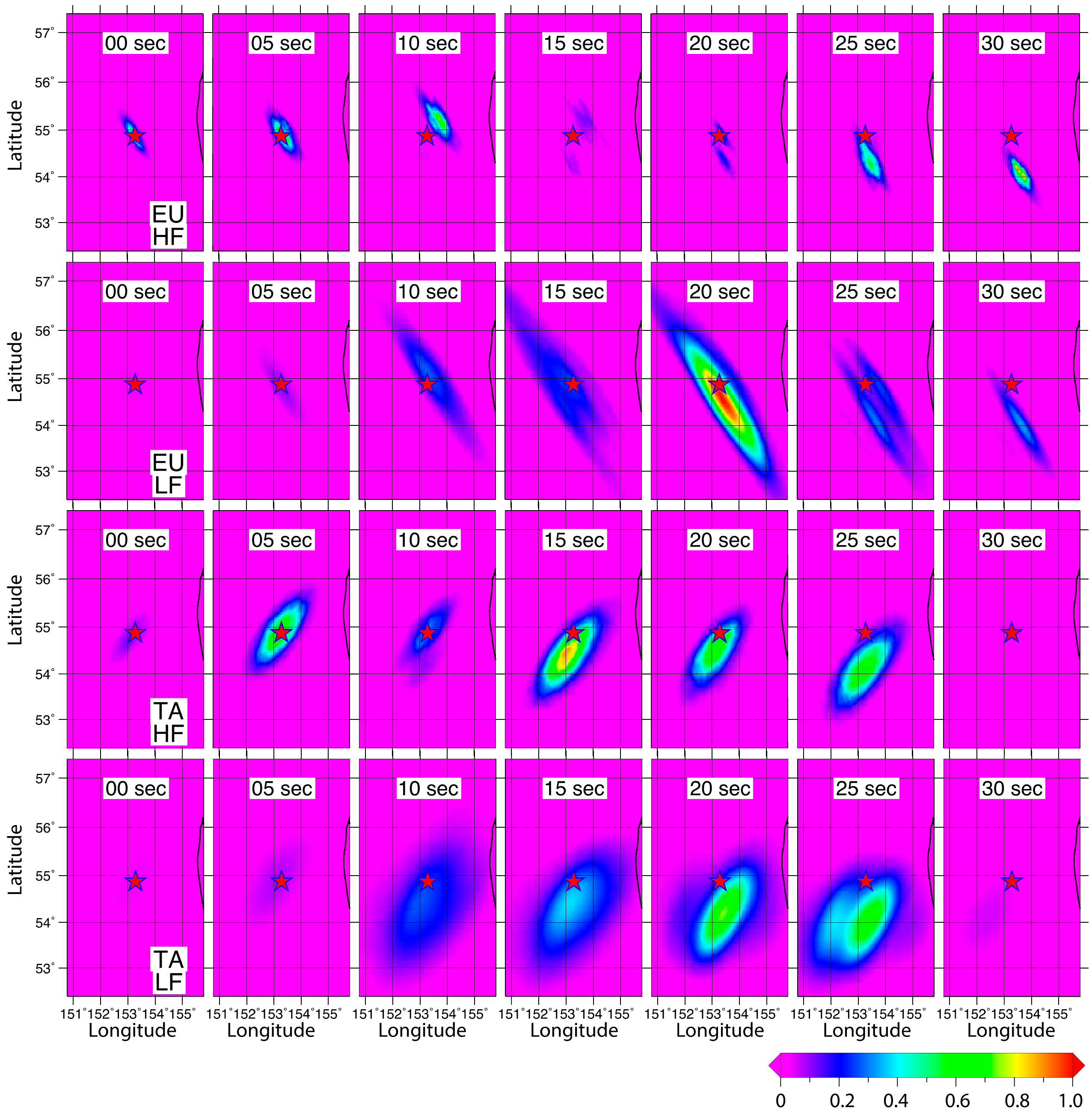

FIGURE 3 | Rupture evolution of the earthquake by back-projecting *P*-waves from the arrays TA and EU in the high- (HF) and low-(LF) frequency bands. The color bar denotes the normalized power of potential subevents. The potential subevents with the maximum power at each time frame are viewed as the true subevents. Red star indicates the hypocenter.

then done by summing up the normalized single-array distributions and identifying the subevents for both frequency bands.

The third step back-projected the high-frequency and low-frequency data sets simultaneously. As before, the stacked *P* amplitude distributions for the two frequency bands were normalized with their respective maxima before stacking. Thus, the four sets of P-wave trains, from the TA and EU arrays and both frequency bands, were back-projected together to image slip evolution on the fault plane and in time (**Figure 3**). We eliminated the artifacts from the subevents at the same locations by retaining the subevents with the maximum energy. The rupture time of a subevent was obtained by averaging those derived from both arrays. Thus, the remaining subevents comprise the final back-projection rupture model as shown in **Figure 4**.

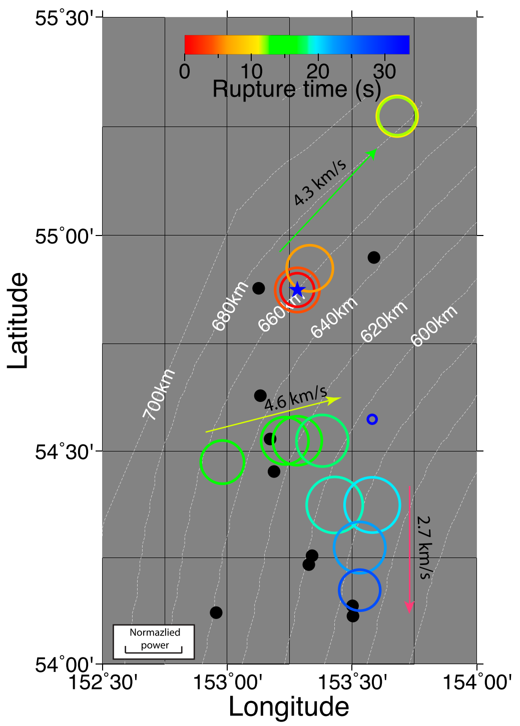

FIGURE 4 | The final back-projection rupture model. The colored circles indicate the subevents. Their areas are proportional to the normalized power, which is indicated by the scale bar. The color bar represents the rupture times of the subevents. The black dots depict the aftershocks, while the blue star indicates the hypocenter. The white dashed lines are depth contours of the subducting Pacific slab (Hayes et al., 2012). The arrows indicate the rupture directions.

Global, Low-Frequency Waveform Inversion

Low-passed *P*-wave trains (2–100 mHz) from the Global Seismic Network (GSN) were inverted for seismic moments of the Okhotsk earthquake's subevents, using the method of Kikuchi and Kanamori (1991). The *P* waves are from 69 GSN stations with epicentral distances in the teleseismic window for a deep source from 20° to 80° (**Figure 2A**), avoiding involvement of *P* wave triplications and *P* waves in shadow zone. *P*-wave peak values in traces along the strike do not vary significantly with time (**Figure 2B**), implying that all subevents may have similar nodal planes and thus focal mechanisms. In addition, the shortest duration of the *P* waveforms in the azimuthal range of 120°–180° represents rupture directivity associated with the southward rupture of the earthquake.

The subhorizontal fault plane as the causative fault, indicated by the BP synthetic test detailed in *A Synthetic Test for the Causative Fault's Orientation and BP Images' Resolution*, was gridded into 19 × 13 patches, each 10 km long along the strike and 5 km wide, respectively. Based on the subevents imaged in the final back-projection model, we chose to subdivide the rupture and slip evolution into a number of discrete subevents and found that a source model with 12 subevents (**Supplementary Figure 1**) produces well-fitting waveforms except for those with azimuths close to the strikes of nodal planes, such as station COLA (**Supplementary Figure 2**), and captures the complexity of the rupture pattern. Increasing the number of subevents improves the waveform fits but yields unrealistically high seismic moments (**Supplementary Figure 3**). To be consistent with the final back-projection rupture model, we removed subevents 40 s after the origin time, leading to a well correspondence of the remaining subevents to those in the multi-array, multi-frequency-band back-projection rupture model, except for three subevents northwest of the epicenter and the southernmost subevent (**Figure 4** and **Supplementary Figure 1**). Because the contribution of these four subevents to the waveform fits is very small (**Supplementary Figure 2, 4**), we removed them from the final multi-subevent model (**Figure 5A**). The resulting model has a seismic moment of 2.3 × 10^{21} Nm (equivalent to a moment magnitude of M_w 8.2), providing a lower-bound for the seismic moment of the earthquake.

This multi-subevent model estimates moment release of the earthquake's subevents. Rupture areas of the subevents in the slip model can be inferred from their seismic moments. The seismic moment is defined as $M_0 = \mu \overline{u} A$ (Aki, 1966), where μ is the shear modulus at the focal depth, $\overline{u}$ is the slip, and A is the rupture area. Assuming subevents rupture circularly gives $A = \pi R^2$, where R is the radius of the ruptured fault patch. For the earthquake, the average stress drop $\Delta\sigma$ is estimated to be 12–15 MPa (Ye et al., 2013), which is compatible with the stress drop in a range of 5–50 MPa for 14 large deep earthquakes (Tibi et al., 2003). For a circular rupture, the rupture radius can then be estimated from the seismic moment as follows (Eshelby, 1957):

$$R = \sqrt[3]{\frac{7M_o}{16\Delta\sigma}} \tag{1}$$

The estimated rupture radii of the subevents range from 15.0 to 27.1 km (**Figure 5A**). Estimating the rupture radii is important for evaluating the fault dimensions and inferring the source mechanism of the earthquake.

A SYNTHETIC TEST FOR THE CAUSATIVE FAULT'S ORIENTATION AND BP IMAGES' RESOLUTION

To determine the orientation of the causative fault (subhorizontal or subvertical), a BP synthetic test was carried out for the arrays TA and EU. The *P* waves were synthesized from two seismic point sources separating 20 km vertically with a 5-s bursting difference using the orthonormal propagator method (Wang, 1999) and were filtered in the frequency band of 0.1–0.5 Hz as shown in **Figure 6**. We performed the single-array BP as above mentioned for both arrays and then combined them. The BP images of the two point sources were derived as shown in **Figure 7**. The second source is imaged right at the same location of the first one in the combined BP image. This indicates that the vertical resolvability of the multi-array BP imaging is too low to discriminate the depth differences of the subevents, but the depth differences of the subevents have no effect on the multi-array BP imaging on the horizontal plane. If

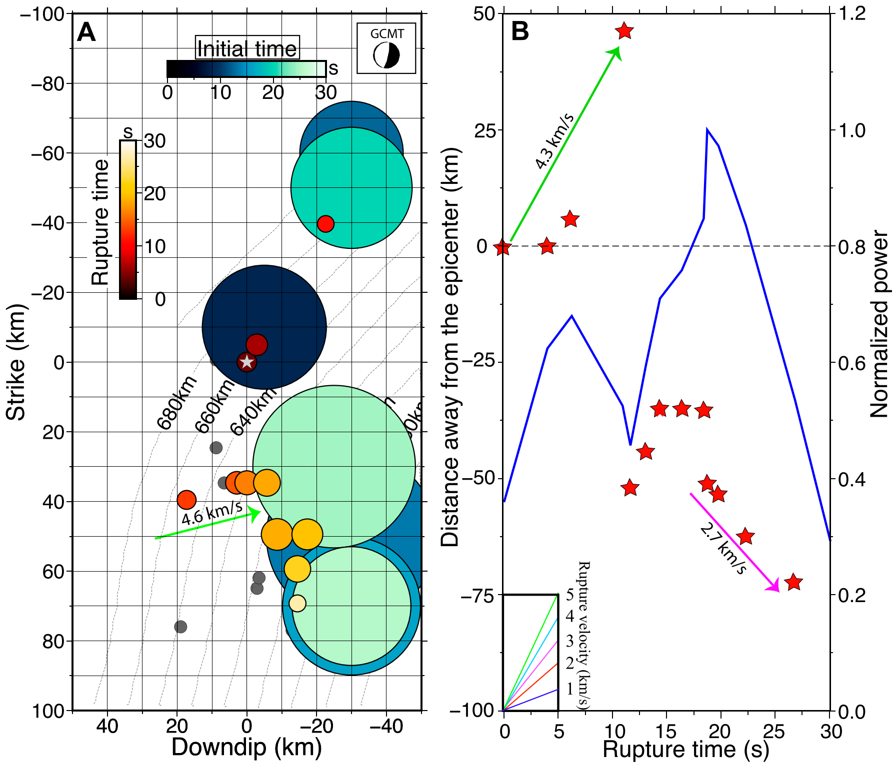

FIGURE 5 | Multi-array, multiband back-projection and multi-subevent rupture models. **(A)** Integration of the two source models. The ocean color bar in the final inversion source model indicates initial times of the subevents, while the hot color bar in the back-projection model represents rupture times of the subevents. Circles indicate the subevents, whose areas are estimated in the Data and Methodology section and are proportional to the normalized power for the back-projection method. White star depicts the epicenter and gray dots denote aftershocks. Dashed curved lines indicate the depth contours of the subducting slab (Hayes et al., 2012). The inset shows the GCMT focal mechanisms of the earthquake. **(B)** Distances away from the epicenter varying with rupture time (red stars) and normalized power of subevents varying with rupture time (blue line). Moment releases peaks at 6 s and 18 s. Blue, red, purple, cyan, and green lines in the inset represent rupture velocities of 1–5 km/s.

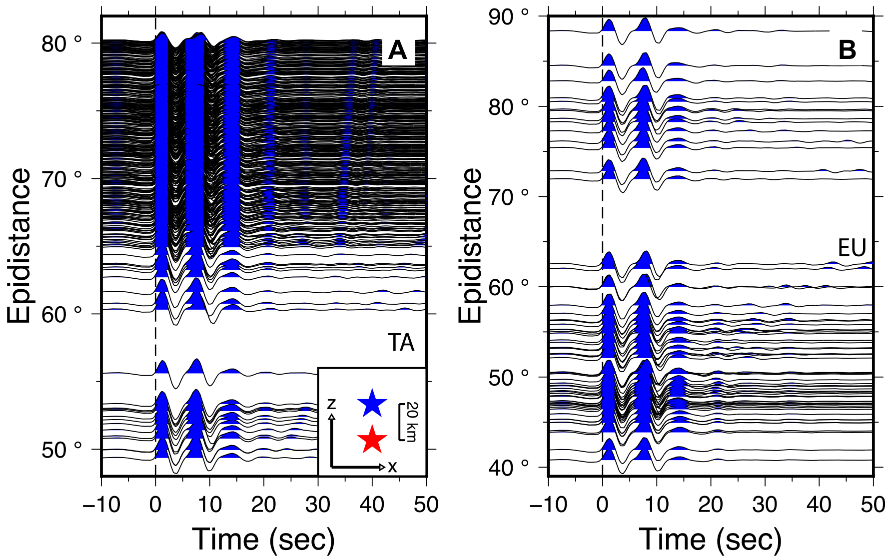

FIGURE 6 | Synthetic waveforms for **(A)** TA and **(B)** EU arrays in a frequency band of 0.1–0.5 Hz. Inset of **(A)**. The first seismic source (red star) initiates at 0 s and the second one (blue star) bursts at 5 s and 20 km above the first one.

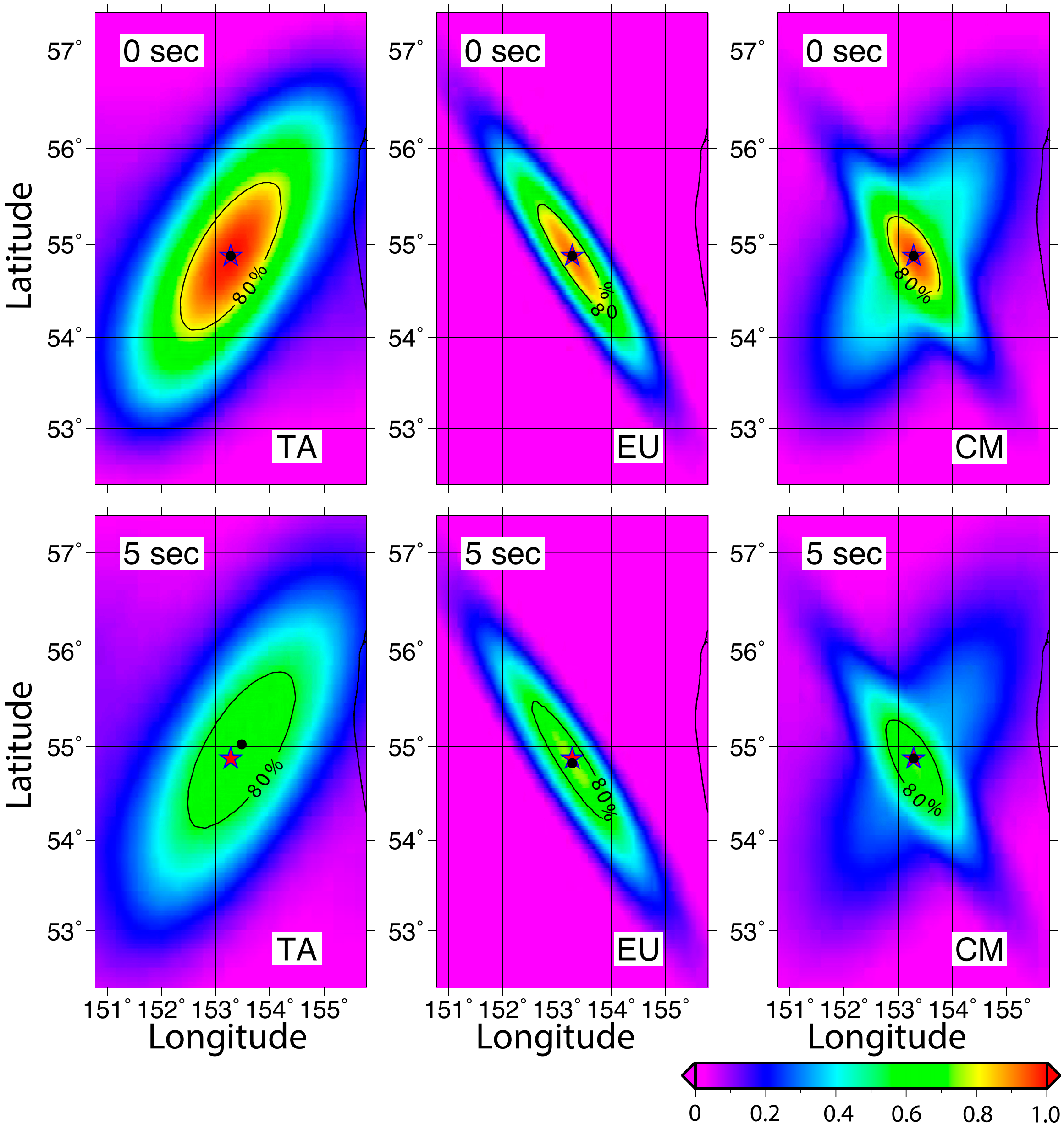

FIGURE 7 | Rupture imaging of the two seismic sources by back-projecting synthesized *P*-waves from the TA (left panels) and the EU (middle panels) in the low-frequency band and the combined imaging (right panels). The color bar denotes the normalized power of potential subevents. Red stars indicate the epicenters. The contour shows the 80% of the maximum normalized power.

the rupture of the earthquake is on the subvertical plane, the width of the causative plane could be much greater than 121 km, given the dip angle of approximately 80° from GCMT and the rupture width of ~21 km projected to the horizontal plane during the second rupture stage (**Figure 4**). The shallow intraslab M > 8 earthquakes such as 1933 Mw 8.5 Sanriku earthquake (Okal et al., 2016) and 2017 Mw 8.2 Chiapas, Mexco earthquake (Zhang and Brudzinski, 2019) typically have rupture widths less than 100 km. Moreover, compared to the shallow earthquakes, the deep-focus earthquakes have faster rise times (Houston and Williams, 1991) and hence compacter rupture dimensions. The extremely wide rupture seems to be unlikely for the deep-focus earthquake. Therefore, the orientation of the causative fault of the 2013 Okhotsk earthquake is likely to be subhorizontal.

Besides confining the orientation of the causative fault, the synthetic test shows the resolution of the BP images. For the TA and EU, the second source is imaged ~20 km northeast and ~5 km south to the real location, respectively. However, for the combined image, the second source is imaged right to its real location. This indicates that the multi-array BP images have a high resolution less than 1 km, which is much better than those

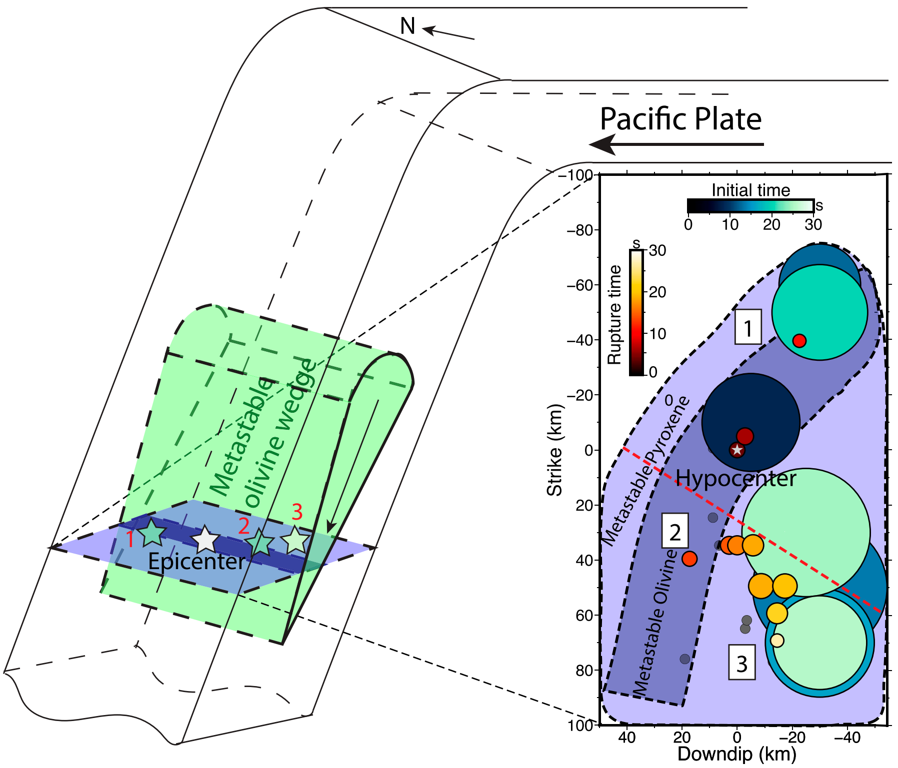

FIGURE 8 | Schematic diagram illustrating the rupture of the 2013 Okhotsk earthquake outside the possible metastable olivine wedge (dark purple) but inside the metastable pyroxene wedge (light purple) (Bina, 2013). Three rupture segments are labeled 1, 2, and 3 respectively. (Inset) Overlap the final back-projection and inversion models with the possible MOW and metastable pyroxene wedge (MPW). Numbers one to three depict the first, second, and third rupture segments, respectively. Dark purple area denotes the MOW, and the light purple area indicates the MPW. The red dashed line just crosses the slab.

from the single-array BP. This is the reason why we take multi-array, multi-band, BP imaging in this study.

RESULTS

Our multi-array, multi-frequency-band back-projected rupture imaging and the inverted multiple subevents show that the deep earthquake's asymmetrical, bilateral rupture occurred within 30 s on a subhorizontal, curved fault plane (**Figure 5A**). The rupture could be separated into three principal segments at rupture velocities of 2.7–4.6 km/s, 47–84% of shear velocity (Fukao and Obayashi, 2013) at the focal depth (**Figures 4**, **5B**). The rupture velocity is constrained from the multi-array, multi-frequency BP. The first segment ruptured northwards and somewhat down-dip on the subhorizontal fault plane at a high rupture velocity of 4.3 km/s, 78% of shear velocity at the focal depth. Unsurprisingly, this segment radiated strong high-frequency seismic energy. After a transitional second segment ruptured, the third segment started on the other (south) side of the nucleation point and ruptured in the reverse direction: southwards and somewhat up-dip at a velocity of 2.7 km/s, 47% of shear velocity at the focal depth, while radiating low-frequency seismic energy. For the first and third segments, the considerable slab-normal components of the rupture are 23 and 31 km wide, which are estimated from the multi-subevent inversion. The slab-normal component of the second segment is constrained to 19 km using the rupture length of the BP image. The wide slab-normal rupture has also been observed by Meng et al. (2014). Each of the rupture distances is wider than the thickness of the metastable olivine wedge (MOW) (less than 15 km estimated by Kirby et al. (1996) or approximately 15 km constrained by Marone and Liu (1997)) using numerical modeling unless the slab at the focal depth is contorted. Additionally, if there exists the MOW, the nucleation of the earthquake would occur near the bottom of the MOW as shown in the inset of **Figure 8** since there stores more strain energy for the occurrence of large earthquakes. Besides the high resolution of the multi-array, multi-frequency BP images, the location of the MOW relative to the rupture of the earthquake has an uncertainty less than 5 km.

To confirm the rupture beyond the possible metastable olivine wedge, a source model with 12 subevents (**Supplementary Figure 5B**) is inverted on a curved plane with the method of Kikuchi and Kanamori (1991) using the data in **Figure 2B**. The curved plane is designed parallel to the strike of the subducting slab. The resulting misfit of the waveforms is 0.56, which is much larger than that derived from the final multi-subevent model in **Figure 5A** and **Supplementary Figure 5A**. The better fitting of waveforms for the final multi-subevent model can be seen in

Supplementary Figure 4, 6. This emphasizes the necessity of the rupture beyond the possible MOW.

Intriguingly, the rupture in the first 13 s extends northwards of the hypocenter, followed by the fourth subevent that bursts 44 km southwest of the epicenter with an azimuth of approximately 200°, without subevents to spatially connect the two energy bursts (**Figure 8A**). The body wave incident on the location of the 13-secend subevent has a takeoff angle of approximately 90°. Given the subhorizontal fault (strike 189°, dip 11°, and rake −93°), the *P*-to-*S* amplitude ratio is only 0.082 according to radiation pattern (Aki and Richards, 2002), so triggering of the rupture by *p* waves is unlikely. The shear velocity at the depth of the hypocenter (609 km) is approximately 5.5 km/s in the velocity model AK135 (Kennett et al., 1995). The first *S* arrival at the 13-s subevent from the hypocenter is 8 s after the commence of the earthquake. The onset of the post-13-s subevent to the southwest is consistent with the arrival of *S*-waves from the preceding subevents. The appropriate timing and large amplitude of the *S*-waves thus indicate that the occurrence of the post-13-s subevent is dynamically triggered by the running *S*-waves. The coseismic dynamic triggering was also discovered in the 2012 Mw 8.6 Sumatra offshore earthquake (Zhang et al., 2012).

COMPARISON WITH PREVIOUS STUDIES

The rupture models in this study are basically consistent with those using single-array back-projection methods and/or inversion techniques (Wei et al., 2013; Ye et al., 2013; Meng et al., 2014; Zhan et al., 2014). For the fault plane, Wei et al. (2013) exclude the near-vertical fault plane based on the strong directivity effect along the azimuth of 165°, which significantly deviates from the strike (12° given by the GCMT) of this fault plane. The trending of subevents significantly off the strike of the subvertical fault plane leads Zhan et al. (2014) to choose the subhorizontal fault as the causative fault. Also, the subhorizontal fault plane is preferred by Ye et al. (2013) according to the single-array back-projection models and finite fault models. Additionally, the bilateral rupture in our rupture models agrees with another back-projection study by Meng et al. (2014).

The second largest subevent ruptures backward to the north relative to the largest subevent (**Figure 5A**). The rupture feature is confirmed by removing the two subevents in the new inversion model, respectively. The synthetic waveforms are significantly affected by the two subevents and show that the largest subevent radiates the first amplitude peak (**Supplementary Figure 7**), and the second largest one generates the second amplitude peak (**Supplementary Figure 8**). The locations and rupture times of the largest two energy-releasing peaks in our results agree reasonably well with other groups' such as Zhan et al. (2014). This feature may be explained as a barrier, corresponding to the second largest subevent, is unbroken when the rupture first reaches it but eventually breaks down due to stress transferring. This intriguing rupture reversal has also been observed by prior studies (Wei et al., 2013; Zhan et al., 2014).

A profound difference between the models obtained in this study and by Ye et al. (2013) and Wei et al. (2013) is that the southernmost rupture is spatially shorter, resulting in this study's more compact rupture area and lower rupture velocity. The compact rupture area in our model is the result of jointly back projecting seismic data from two arrays at different azimuths, reducing artifacts related to "smearing" of energy along the event-array azimuth (Zhang et al., 2016; Zhang et al., 2017; Zhang and Ge, 2017; Zhang and Brudzinski, 2019). The source model (**Supplementary Figure 5C**) by Zhan et al. (2014) lacks subevents in the northernmost, down-dip portion of our rupture models probably due to inversion of the displacement waveforms for a limited number of subevents.

DISCUSSION

The estimated extent of Okhotsk rupture does not favor simple transformational faulting in metastable olivine as the primary instability mechanism, because the rupture extent exceeds the likely plausible thermo-spatial extent of metastable olivine in the slab. Likewise, both the large seismic efficiency of 0.6 determined by Ye et al. (2013) and fast rupture velocities in the first two rupture segments preclude (Tibi et al., 2003) a thermal shear instability (Ogawa, 1987; Hobbs and Ord, 1988) as the rupture mechanism. The simplest explanation of the earthquake would be that dehydration embrittlement, associated with intermediate-depth earthquakes, still operates at these great depths (Omori et al., 2004). Three more speculative seismogenic options include: 1) another form of transformational faulting, perhaps transformation of metastable pyroxene to metastable akimotoite; 2) nucleation by transformational faulting in the metastable olivine wedge that propagates into surrounding rock by shear melting (Green, 2017), perhaps aided by latent heat release (Bina, 1998); 3) unusual slab contortions that completely enclose the rupture plane within a flattened MOW (Stein, 1995).

Option 1) may seem plausible given its exothermicity (Green et al., 2015) and the broader thermal range of pyroxene metastability (Bina, 2013) as shown in **Figure 8** due to slow rates of diffusion-controlled pyroxene-garnet transformation in the transition zone (Nishi et al., 2013; Van Mierlo et al., 2013). However, it has not been observed in the laboratory, and both the low abundance of pyroxene in the peridotitic bulk of the slab (<20% by volume (Ringwood, 1991) and the generally displacive nature of metastable pyroxene transitions (Dera et al., 2013) also disfavor this mechanism. The arguments that the earthquake has a high seismic efficiency and fast rupture velocity V_r already advanced against thermal instability also disfavor a melt-related mechanism such as option 2) for the first two rupture segments. Although the third rupture segment ruptures somewhat more slowly, the radiation efficiency η_R of 0.42, calculated via the equation $\eta_R = 1 - \sqrt{\frac{1-V_r/\beta}{1+V_r/\beta}}$ (Venkataraman and Kanamori, 2004), where β is shear velocity at the focal depth (5.5 km/s, Kennett et al., 1995), is much larger than 0.02, typical radiation efficiency of the thermal-induced earthquakes (Prieto et al., 2013). This precludes option 2) as the mechanism of the third rupture segment. Option 3) remains speculative because the 2013 Okhotsk and three prior transition-zone earthquakes reveal the

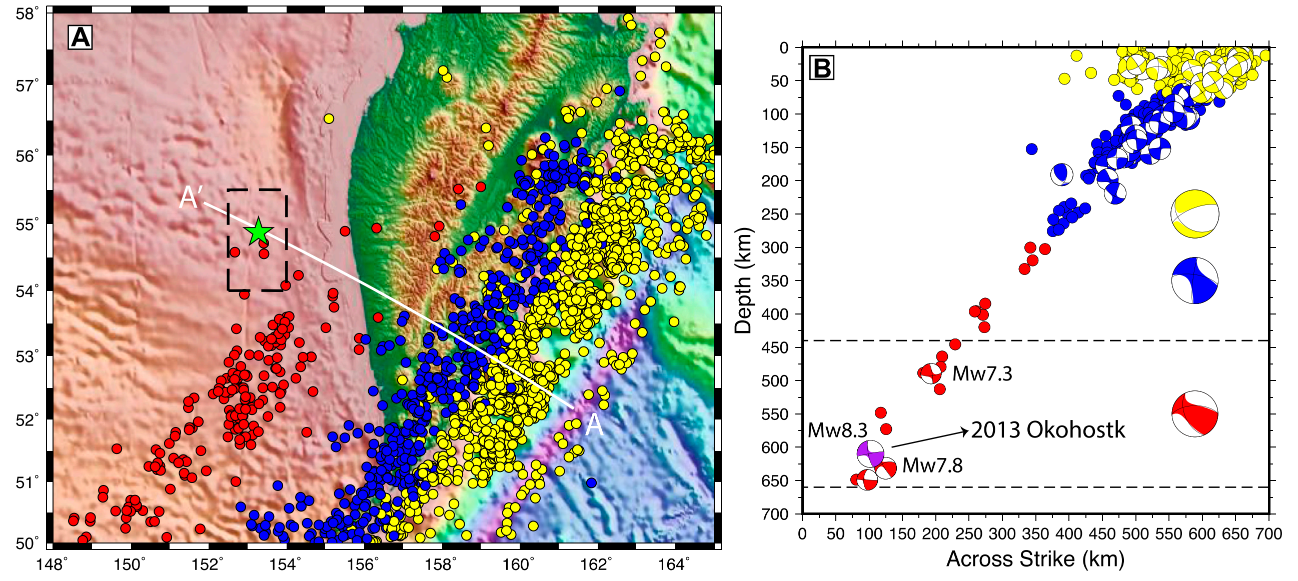

FIGURE 9 | Seismicity in North Kamchatka subduction zone. **(A)** Seismicity distribution from the EHB Bulletin, ISC (1960–2008, http://www.isc.ac.uk/ehbbulletin/search/bulletin/). The shallow, intermediate, and deep-focus earthquakes are depicted by yellow, blue, and red dots, respectively. Green star indicates the epicenter of the 2013 Okhotsk earthquake. Black dashed frame represents the study region, while white line AA' denotes the cross section in **Figure 7B**. **(B)** Seismicity of the subducting Pacific oceanic slab within 120 km around the cross-section AA'. The beach balls, in a side view from southwest to northeast, indicate the GCMT focal mechanisms of the earthquakes along the cross-section AA' since 1976 (http://www.globalcmt.org/CMTsearch.html). They are colored with yellow, blue, and red for the shallow, intermediate, and deep-focus earthquakes, respectively. The focal mechanism of the 2013 Okhotsk earthquake is indicated by a purple beach ball, which has the same *P* axis as two other deep-focus earthquakes (M_w 7.3 and M_w 7.8). The three larger beach balls on the right-hand side from top to bottom indicate the normalized, summed focal mechanisms of the shallow, intermediate, and deep-focus earthquakes, respectively.

same down-dip compressional stress regime in their focal mechanisms as that governing the intermediate-depth earthquakes (**Figure 9**). There is also no evidence of slab contortions in the seismicity, which displays a steadily dipping Wadati-Benioff zone (**Figure 9**), and seismic tomography suggests that the subducting Okhotsk slab proceeds into the lower mantle with roughly the same dip orientation (Fukao and Obayashi, 2013).

We consider the simplest plausible explanation to be that dehydration embrittlement (Green and Houston, 1995; Kirby, 1995; Houston, 2015) remains operable under conditions of deep-focus seismicity (Jung et al., 2004; Zhang et al., 2004). Jung et al. (2004) show that faulting due to dehydration can occur even at pressures so high that the volume change of reaction becomes negative and this mechanism can attain a near-critical state susceptible to stress change. This indicates that dehydration embrittlement does not require the evolution of a free fluid with a positive volume change to allow slip to occur. Ferrand et al. (2017) find that faults are experimentally produced by stress transfer driven by volume change of dehydration even under a partially hydrated condition (with only 5% volume of antigorite). Moreover, Green et al. (2015) and Green (2017) argue that it is nanometric crystallization of product phases, whether from hydration-dehydration reactions or from metastable transformations, which induce the formation of a fault zone. Deep dehydration has been invoked to interpret the rupture mechanism of the November 24, 2015 Mw 7.6 Peru deep-focus earthquake doublet (Zahradník et al., 2017).

Rüpke et al. (2006) demonstrate that at least 10% of water contained within the oceanic lithosphere upon subduction could survive passage through the mantle wedge en route to the mantle transition zone and lower mantle. While common hydrous minerals such as serpentine and chlorite would break down in the uppermost mantle, dense hydrous magnesium silicates can carry the water deeper and are stable in cool slabs down to at least as far as the top of the lower mantle (Komabayashi, 2006). Once these break down in/near the transition zone, the nominally anhydrous olivine polymorphs in the ambient mantle can absorb this water without melting (Smyth, 1994; Smyth and Jacobsen, 2006, studies in: Jacobsen and Van der Lee, 2006). Moreover, dehydration reactions in hydrated subducting slabs closely correlate with the depth-distribution of subduction-zone earthquakes, indicating dehydration embrittlement as a universal mechanism for intermediate and deep earthquakes (Omori et al., 2004; Barcheck et al., 2012; Shirey et al., 2019). In addition, there is evidence from deep diamond inclusions (Pearson et al., 2014) and indirect evidence from magneto-telluric studies, seismic tomography, and studies of seismic discontinuities (studies in Jacobsen and Van der Lee, 2006) that water indeed resides and cycles through the transition zone. Omori and Komabayashi (2007) propose one of several pathways by which subducting lithospheric slabs bring some of all subducted water to depth beyond the mantle wedge in dense hydrous magnesium silicates, which transform and dehydrate in the deep transition zone to help form less hydrous ringwoodite. Van der Lee et al. (2008) and Wang et al. (2018) show that hydrous ringwoodite is consistent with lowered rigidity imaged by seismic tomography in some places. The amounts by which the rigidity and density are lowered in ringwoodite are consistent with the volume of water supplied by a slab traversing the transition zone. Van der Lee et al. (2008) propose that a less-dense, hydrated transition zone provides a mechanism for water to return to the surface and that this deep water cycle may be responsible for many present and past plate-tectonic events. Shirey et al. (2019) invoke a similar deep water cycle to explain the deep diamond inclusions of Pearson et al. (2014). In other words, a deep upper-mantle water cycle is more consistent with diverse geophysical observations than a dry deep upper mantle.

Furthermore, Silver et al. (1995) suggested that the subhorizontal fault plane of the deep 1994 Mw 8.3 Bolivia earthquake could represent the reactivation of a fault that formed at the oceanic outer rise through bending of the subducting lithosphere, as is also argued for intermediate-depth seismicity (Jiao et al., 2000; Chen et al., 2004; Kiser et al., 2011). Warren et al. (2015) associated many such deep earthquakes with similar subhorizontal fault planes or their conjugate fault planes. Faulting at the oceanic outer rise has also been identified as an effective mechanism to hydrate the deep crust and mantle of the lithosphere before subduction (Rüpke et al., 2006). Moreover, due to the hydrated outer-rise normal fault, the amount of the subducted water is assessed to be one order of magnitude higher than previous estimation (Garth and Rietbrock, 2014; Cai et al., 2018), making these subhorizontal fault planes and their conjugates prime candidates for dehydration reactions and related embrittlement-induced and earthquake rupture.

If indeed dehydration played a role in the deep Okhotsk earthquake, the entirety of the subducting Pacific lithosphere cannot be completely dry even at these great depths in the mantle transition zone.

CONCLUSION

The 2013 Mw 8.6 Sea of Okhotsk deep-focus earthquake is found to rupture at different speeds to the north and the south, respectively, of the epicenter. This rupture model is constrained by a multi-array and multi-frequency combined back-projection method as well as a global *P*-wave train inversion technique for discrete subevents. The earthquake asymmetrically ruptures bilaterally a subhorizontal curved fault (150 km long, 70 km wide) in three stages. In the first 13 s, the rupture extends northwestwards on the downdip portion of the fault for approximately 55 km at a velocity of approximately 4.3 km/s. Afterward, a subevent at approximately 44 km southwest of the epicenter may be triggered by the passage of *S*-waves from previous faulting in the northwest and rupture continues eastward at a speed of 4.6 km/s. At the last stage, the rupture propagates up dip in a southeastward direction at a velocity of approximately 2.7 km/s until it ends at approximately 85 km SSE of the epicenter. The high rupture speeds indicate high seismic radiation efficiencies during the earthquake. Moreover, sizes of the subevents in the three rupture segments are beyond those of the possible MOW (**Figure 8**), which are not distorted as focal mechanisms of the nearby deep-focus earthquakes are subject to the similar down-dip compressional stress regime and seismicity is distributed regularly in the subducting slab. Thus, these findings together with diverse evidence of water subducting as deep as the transition zone and below suggest dehydration as the mechanism of the deep-focus earthquake.

KEY POINTS

- The 2013 M_w 8.3 Sea of Okhotsk deep-focus Earthquake bilaterally ruptured over 160 km in 30 s in three stages.
- The deep earthquake ruptured fast and its rupture area extends beyond the inferred metastable olivine wedge.
- The deep earthquake's rupture mechanism is consistent with it being the result of dehydration of deeply subducted oceanic lithosphere.

DATA AVAILABILITY STATEMENT

The datasets generated for this study are available on request to the corresponding author.

AUTHOR CONTRIBUTIONS

All authors listed have made a substantial, direct, and intellectual contribution to the work and approved it for publication.

ACKNOWLEDGMENTS

We thank Trevor Bollmann, Michael Witek, and Emily Wolin for polishing this manuscript as well as Harry Green II, Emile A. Okal, Anthony Sladen, Zhongwen Zhan, and Heidi Houston for constructive comments and helpful discussion. We also thank Wessel and Smith (1995), as all the figures in this manuscript were plotted using their Generic Mapping Tools (GMT). Waveform data at the European (doi:10.14470/TR560404), USArray Transportable Array Seismic Networks (https://doi.org/10.7914/SN/TA), and the Global Seismic Network (https://doi.org/10.7914/SN/IU) were downloaded from the IRIS-DMC (http://ds.iris.edu). Ge Z. is supported by National key research and development program (Grant No. 2018YFC1504203) and the National Science Foundation of China (Grant No. 41774047).

SUPPLEMENTARY MATERIAL

The Supplementary Material for this article can be found online at: https://www.frontiersin.org/articles/10.3389/feart.2021.521220/full#supplementary-material

REFERENCES

Aki, K. (1966). Generation and Propagation of G Waves from the Niigata Earthquake of June 14, 1964. Part 2. Estimation of Earthquake Moment, Released Energy and Stress-Strain Drop from G Wave Spectrum. *Bull. Earthq. Res. Inst.* 44, 73–88.

Aki, K., and Richards, P. G. (2002). *Quantitative Seismology*, 2nd Edition, New York: University Science Books.

Barcheck, C. G., Wiens, D. A., Hacker, P. E., and van Keken, B. R. (2012). The Relationship of Intermediate- and Deep-Focus Seismicity to the Hydration and Dehydration of Subducting Slabs. *Earth Planet. Sci. Lett.* 349-350, 153–160. doi:10.1016/j.epsl.2012.06.055

Bina, C. R. (1998). A Note on Latent Heat Release from Disequilibrium Phase Transformations and Deep Seismogenesis. *Earth Planet. Sp* 50, 1029–1034. doi:10.1186/bf03352197

Bina, C. R. (2013). Garnet Goes Hungry. *Nat. Geosci*. 6 (5), 335–336. doi:10.1038/ngeo1804

Cai, C., Wiens, D. A., Shen, W., and Eimer, M. (2018). Water Input into the Mariana Subduction Zone Estimated from Ocean-Bottom Seismic Data. *Nature* 563, 389–392. doi:10.1038/s41586-018-0655-4

Chen, P.-F., Bina, C. R., and Okal, E. A. (2004). A Global Survey of Stress Orientations in Subducting Slabs as Revealed by Intermediate-Depth Earthquakes. *Geophys. J. Int.* 159 (2), 721–733. doi:10.1111/j.1365-246x.2004.02450.x

Chen, Y., Wen, L., and Ji, C. (2014). A Cascading Failure during the 24 May 2013 Great Okhotsk Deep Earthquake. *J. Geophys. Res. Solid Earth* 119, 3035–3049. doi:10.1002/2013jb010926

Dera, P., Finkelstein, G. J., Duffy, T. S., Downs, R. T., Meng, Y., Prakapenka, V., et al. (2013). Metastable High-Pressure Transformations of Orthoferrosilite Fs82. *Phys. Earth Planet. Interiors* 221, 15–21. doi:10.1016/j.pepi.2013.06.006

Eshelby, J. D. (1957). The Determination of the Elastic Field of an Ellipsoidal Inclusion, and Related Problems. *Proc. R. Soc. Lond. A.* 241, 376–396. doi:10.1098/rspa.1957.0133

Fan, W., and Shearer, P. M. (2015). Detailed Rupture Imaging of the 25 April 2015 Nepal Earthquake Using Teleseismic P Waves. *Geophys. Res. Lett.* 42 (14), 5744–5752. doi:10.1002/2015GL064587

Ferrand, T. P., Hilairet, N., Incel, S., Deldicque, D., Labrousse, L., Gasc, J., et al. (2017). Dehydration-driven Stress Transfer Triggers Intermediate-Depth Earthquakes. *Nat. Commun.*, 8(15247), 1–11. doi:10.1038/ncomms15247

Frohlich, C. (2006). *Deep Earthquakes*. Cambridge, England: Cambridge University Press.

Fukao, Y., and Obayashi, M. (2013). Subducted Slabs Stagnant above, Penetrating through, and Trapped below the 660 Km Discontinuity. *J. Geophys. Res. Solid Earth* 118 (11), 5920–5938. doi:10.1002/2013jb010466

Garth, T., and Rietbrock, A. (2014). Order of Magnitude Increase in Subducted H_2O Due to Hydrated normal Faults within the Wadati-Benioff Zone. *Geology* 42 (3), 207–210. doi:10.1130/g34730.1

Green, H. W., II, and Burnley, P. C. (1989). A New Self-Organizing Mechanism for Deep-Focus Earthquakes. *Nature* 341, 733–737. doi:10.1038/341733a0

Green, H. W., II, and Houston, H. (1995). The Mechanics of Deep Earthquakes. *Ann. Rev. Earth Planet. Sci.* 23, 169–214. doi:10.1146/annurev.ea.23.050195.001125

Green, H. W., II (2017). Phase-transformation-induced Lubrication of Earthquake Sliding. *Phil. Trans. R. Soc. A.* 375, 20160008. doi:10.1098/rsta.2016.0008

Green, H. W., II, Shi, F., Bozhilov, K., Xia, G., and Reches, Z. (2015). Phase Transformation and Nanometric Flow Cause Extreme Weakening during Fault Slip. *Nat. Geosci.* 8, 484–498. doi:10.1038/ngeo2436

Hacker, B. R., Peacock, S. M., Abers, G. A., and Holloway, S. D. (2003). Subduction Factory 2. Are Intermediate-depth Earthquakes in Subducting Slabs Linked to Metamorphic Dehydration Reactions? *J. Geophys. Res. Solid Earth* 108 (B1). doi:10.1029/2001jb001129

Hayes, G. P., Wald, D. J., and Johnson, R. L. (2012). Slab1.0: A Three-Dimensional Model of Global Subduction Zone Geometries. *J. Geophys. Res.* 117, B01302. doi:10.1029/2011jb008524

Hobbs, B. E., and Ord, A. (1988). Plastic Instabilities: Implications for the Origin of Intermediate and Deep Focus Earthquakes. *J. Geophys. Res.* 93 (B9), 10521–11054. doi:10.1029/jb093ib09p10521

Houston, H. (2015). Deep Earthquakes, in *Treatise on Geophysics* 2nd Ed., editor-in-chief G. Schubert, Oxford, Elsevier, 4, 329–354. doi:10.1016/b978-0-444-53802-4.00079-8

Houston, H., and Williams, Q. (1991). Fast Rise Times and the Physical Mechanism of Deep Earthquakes. *Nature* 352, 520–522. doi:10.1038/352520a0

Ishii, M., Shearer, P. M., Houston, H., and Vidale, J. E. (2005). Extent, Duration and Speed of the 2004 Sumatra-Andaman Earthquake Imaged by the Hi-Net Array. *Nature* 435, 933–936. doi:10.1038/nature03675

Jacobsen, S. D., and Van der Lee, S. (2006). Earth's Deep Water Cycle. *Geophys. Monogr. Ser.* 168. doi:10.1029/GM168

Jiao, W., Silver, P. G., Fei, Y., and Prewitt, C. T. (2000). Do intermediate- and Deep-Focus Earthquakes Occur on Pre-existing Weak Zones? an Examination of the Tonga Subduction Zone. *J. Geophys. Res.* 105, 28125–28138. doi:10.1029/2000jb900314

Jung, H., Green, H. W., II, and Dobrzhinetskaya, L. F. (2004). Intermediate-depth Earthquake Faulting by Dehydration Embrittlement with Negative Volume Change. *Nature* 428 (6982), 545–549. doi:10.1038/nature02412

Kanamori, H., Anderson, D. L., and Heaton, T. H. (1998). Frictional Melting during the Rupture of the 1994 Bolivian Earthquake. *Science* 279, 839–842. doi:10.1126/science.279.5352.839

Kennett, B. L. N., Engdahl, E. R., and Buland, R. (1995). Constraints on Seismic Velocities in the Earth from Traveltimes. *Geophys. J. Int.* 122 (1), 108–124. doi:10.1111/j.1365-246x.1995.tb03540.x

Kikuchi, M., and Kanamori, H. (1991). Inversion of Complex Body Waves--III. *Bull. Seism. Soc. Am.* 81 (6), 2335–2350.

Kirby, S. H., Durham, W. B., and Laura, A. S. (1991). Mantle Phase Changes and Deep-Earthquake. *Science* 252, 216–225. doi:10.1126/science.252.5003.216

Kirby, S. H., Stein, S., Okal, E. A., and Rubie, D. C. (1996). Metastable Mantle Phase Transformations and Deep Earthquakes in Subducting Oceanic Lithosphere. *Rev. Geophys.* 34, 261–306. doi:10.1029/96rg01050

Kiser, E., and Ishii, M. (2012). Combining Seismic Arrays to Image the High-Frequency Characteristics of Large Earthquakes. *Geophys. J. Int.* 188 (3), 1117–1128. doi:10.1111/j.1365-246x.2011.05299.x

Kiser, E., Ishii, M., Langmuir, C. H., Shearer, P. M., and Hirose, H. (2011). Insights into the Mechanism of Intermediate-Depth Earthquakes from Source Properties as Imaged by Back Projection of Multiple Seismic Phases. *J. Geophys. Res. Solid Earth* 116 (B6). doi:10.1029/2010jb007831

Komabayashi, T. (2006). Phase Relations of Hydrous Peridotite: Implications for Water Circulation in the Earth's Mantle. *Earth's Deep Water Cycle*, 29–43.

Koper, K. D., Hutko, A. R., Lay, T., Ammon, C. J., and Kanamori, H. (2011). Frequency-dependent Rupture Process of the 2011 M(w) 9.0 Tohoku Earthquake: Comparison of Short-Period P Wave Backprojection Images and Broadband Seismic Rupture Models. *Earth Planets Space* 63 (7), 599–602. doi:10.5047/eps.2011.05.026

Lay, T., Kanamori, H., Ammon, C. J., Koper, K. D., Hutko, A. R., Ye, L., et al. (2012). Depth-varying Rupture Properties of Subduction Zone Megathrust Faults. *J. Geophys. Res.* 117 (B4). doi:10.1029/2011jb009133

Marone, C., and Liu, M. (1997). Transformation Shear Instability and the Seismogenic Zone for Deep Earthquakes. *Geophys. Res. Lett.* 24 (15), 1887–1890. doi:10.1029/97GL01851

Meng, L., Ampuero, J.-P., and Burgmann, R. (2014). The 2013 Okhotsk Deep-Focus Earthquake: Rupture beyond the Metastable Olivine Wedge and Thermally Controlled Rise Time Near the Edge of a Slab. *Geophys. Res. Lett.* 41 (1), 3779–3785. doi:10.1002/2014gl059968

Nishi, M., Kubo, T., Ohfuji, H., Kato, T., Nishihara, Y., and Irifune, T. (2013). Slow Si-Al Interdiffusion in Garnet and Stagnation of Subducting Slabs. *Earth Planet. Sci. Lett.* 361, 44–49. doi:10.1016/j.epsl.2012.11.022

Ogawa, M. (1987). Shear Instability in a Viscoelastic Material as the Cause of Deep Focus Earthquakes. *J. Geophys. Res.* 92, 13801–13810. doi:10.1029/jb092ib13p13801

Okal, E. A., Kirby, S. H., and Kalligeris, N. (2016). The Showa Sanriku Earthquake of 1933 March 2: a Global Seismological Reassessment. *Geophys. J. Inter.* 206, 1492–1514. doi:10.1093/gji/ggw206

Omori, S., Komabayashi, T., and Maruyama, S. (2004). Dehydration and Earthquakes in the Subducting Slab: Empirical Link in Intermediate and Deep Seismic Zones. *Phys. Earth Planet. Inter.* 146 (1), 297–311. doi:10.1016/j.pepi.2003.08.014

Omori, S., and Komabayashi, T. (2007). "Subduction Zone: The Water Channel to the Mantle," in *Superplumes: Beyond Plate Tectonics*. Editors D. A. Yuen, S. Maruyama, S. I. Karato, and B. F. Windley (Dordrecht: Springer), 113–138. doi:10.1007/978-1-4020-5750-2_5

Peacock, S. M. (2001). Are the Lower Planes of Double Seismic Zones Caused by Serpentine Dehydration in Subducting Oceanic Mantle? *Geology* 29 (4), 299–302. doi:10.1130/0091-7613(2001)029<0299:atlpod>2.0.co;2

Pearson, D. G., Brenker, F. E., Nestola, F., McNeill, J., Nasdala, L., Hutchison, M. T., et al. (2014). Hydrous Mantle Transition Zone Indicated by Ringwoodite Included within diamond. *Nature* 507 (7491), 221–224. doi:10.1038/nature13080

Prieto, G. A., Florez, M., Barrett, S. A., Beroza, G. C., Pedraza, P., Blanco, J. F., et al. (2013). Seismic Evidence for thermal Runaway during Intermediate-depth Earthquake Rupture. *Geophy. Res. Lett.* 40, 6064–6068. doi:10.1002/2013GL058109

Ringwood, A. E. (1991). Phase Transformations and Their Bearing on the Constitution and Dynamics of the Mantle. *Geochim. Cosmochim. Act* 55, 2083–2110. doi:10.1016/0016-7037(91)90090-r

Ruiz, S., Tavera, H., Poli, P., Herrera, C., Flores, C., Rivera, E., et al. (2017). The Deep Peru 2015 Doublet Earthquakes. *Earth Planet. Sci. Lett.* 478, 102–109. doi:10.1016/j.epsl.2017.08.036

Rüpke, L., Morgan, J. P., and Dixon, J. E. (2006). Implications of Subduction Rehydration for Earth's Deep Water Cycle. *Earth's Deep Water Cycle* 168, 263–276. doi:10.1029/168gm20

Shirey, S. B., Wagner, L. S., Walter, M. J., Van Keken, P. E., and Pearson, G. (2019). *Deep Focus Earthquakes, Deep Slab Fluids, and Superdeep Diamonds*, 100. Washington, DC: Eos, Transactions of the American Geophysical Union. Fall Meeting supplement.

Silver, P. G., Beck, S. L., Wallace, T. C., Meade, C., Myers, S. C., James, D. E., et al. (1995). Rupture Characteristics of the Deep Bolivian Earthquake of 9 June 1994 and the Mechanism of Deep-Focus Earthquakes. *Science* 268, 69–73. doi:10.1126/science.268.5207.69

Smyth, J. R. (1994). A Crystallographic Model for Hydrous Wadsleyite (β-Mg2 SiO4): Ad Ocean in the Earth's interior? *Am. Mineral.* 79, 1021–1024.

Smyth, J. R., and Jacobsen, S. D. (2006). Nominally Anhydrous Minerals and Earth's Deep Water Cycle. *Earth's Deep Water Cycle*, 1–11. doi:10.1029/168gm02

Stein, S. (1995). Deep Earthquakes: a Fault Too Big? *Science* 268, 49–50. doi:10.1126/science.268.5207.49

Tibi, R., Bock, G., and Wiens, D. A. (2003). Source Characteristics of Large Deep Earthquakes: Constraint on the Faulting Mechanism at Great Depths. *J. Geophys. Res.* 108 (B2). doi:10.1029/2002jb001948

Van der Lee, S., Regenauer-Lieb, K., and Yuen, D. A. (2008). The Role of Water in Connecting Past and Future Episodes of Subduction. *Earth Planet. Sci. Lett.* 273 (1), 15–27. doi:10.1016/j.epsl.2008.04.041

Van Mierlo, W. L., Langenhorst, F., Frost, D. J., and Rubie, D. C. (2013). Stagnation of Subducting Slabs in the Transition Zone Due to Slow Diffusion in Majoritic Garnet. *Nat. Geosci.* 6 (5), 400–403. doi:10.1038/ngeo1772

Venkataraman, A., and Kanamori, H. (2004). Observational Constraints on the Fracture Energy of Subduction Zone Earthquakes. *J. Geophy. Res.* 109, B05302. doi:10.1029/2003JB002549

Wang, D., and Mori, J. (2011). Frequency-dependent Energy Radiation and Fault Coupling for the 2010 Mw 8.8 Maule, Chile, and 2011 Mw 9.0 Tohoku, Japan, Earthquakes. *Geophys. Res. Lett.* 38 (22), L22308. doi:10.1029/2011gl049652

Wang, F., Barklage, M., Lou, X., van der Lee, S., Bina, C. R., and Jacobsen, S. D. (2018). HyMaTZ: A Python Program for Modeling Seismic Velocities in Hydrous Regions of the Mantle Transition Zone. *Geochem. Geophys. Geosystems* 19, 2308–2324. doi:10.1029/2018gc007464

Wang, R. (1999). A Simple Orthonormalization Method for Stable and Efficient Computation of Green's Functions. *Bull. Seismol. Soc. Am.* 89 (3), 733–741.

Warren, L. M., Baluyut, E. C., Osburg, T., Lisac, K., and Kokkinen, S. (2015). Fault Plane Orientations of Intermediate-depth and Deep-focus Earthquakes in the Japan-Kuril-Kamchatka Subduction Zone. *J.* Geophys.l Res. Solid Earth 120 (12), 8366–8382. doi:10.1002/2015jb012463

Wei, S., Helmberger, D., Zhan, Z., and Graves, R. (2013). Rupture Complexity of the Mw 8.3 Sea of Okhotsk Earthquake: Rapid Triggering of Complementary Earthquakes? *Geophys. Res. Lett.* 40 (19), 5034–5039. doi:10.1002/grl.50977

Wessel, P., and Smith, W. H. F. (1995). New Version of Generic Mapping Tools Released. *EOS Trans. AGU* 76, 329. doi:10.1029/95eo00198

Wiens, D. A. (2001). Seismological Constraints on the Mechanism of Deep Earthquakes: Temperature Dependence of Deep Earthquake Source Properties, *Phy. Earth Planet. Inter.* 127 (1), 145–163. doi:10.1016/s0031-9201(01)00225-4

Xu, Y., Koper, K. D., Sufri, O., Zhu, L., and Hutko, A. R. (2009). Rupture Imaging of the Mw 7.9 12 May 2008 Wenchuan Earthquake from Back Projection of Teleseismic P Waves. *Geochem. Geophys. Geosyst.* 10 (4), Q04006. doi:10.1029/2008gc002335

Yao, H., Shearer, P. M., and Gerstoft, P. (2013). Compressive Sensing of Frequency-dependent Seismic Radiation from Subduction Zone Megathrust Ruptures. *Proc. Natl. Acad. Sci. U.S.A* 110 (12), 4512–4517. doi:10.1073/pnas.1212790110

Ye, L., Lay, T., Kanamori, H., and Koper, K. D. (2013). Energy Release of the 2013 Mw 8.3 Sea of Okhotsk Earthquake and Deep Slab Stress Heterogeneity. *Science* 341, 1380–1384. doi:10.1126/science.1242032

Zahradník, J., Čížková, H., Bina, C. R., Sokos, E., Janský, J., Tavera, H., et al. (2017). A Recent Deep Earthquake Doublet in Light of Long-Term Evolution of Nazca Subduction. *Scientific Rep.* 7, 45153. doi:10.1038/srep45153

Zhan, Z., Kanamori, H., Tsai, V. C., Helmberger, D. V., and Wei, S. (2014). Rupture Complexity of the 1994 Bolivia and 2013 Sea of Okhotsk Deep Earthquakes. *Earth Planet. Sci. Lett.* 385, 89–96. doi:10.1016/j.epsl.2013.10.028

Zhang, H., and Brudzinski, M. (2019). Evidence for Rupture through a Double Benioff Zone during the 2017 Mw 8.2 Chiapas, Mexico Earthquake. *Geophys. Res. Lett.* 46 (2), 652–660. doi:10.1029/2018gl080009

Zhang, H., Chen, J., and Ge, Z. (2012). Multi-fault Rupture and Successive Triggering during the 2012 Mw 8.6 Sumatra Offshore Earthquake. *Geophys. Res. Lett.* 39 (22). doi:10.1029/2012gl053805

Zhang, H., Ge, Z., and Ding, L. (2011). Three Sub-events Composing the 2011 off the Pacific Coast of Tohoku Earthquake (Mw 9.0) Inferred from Rupture Imaging by Back-Projecting Teleseismic P Waves. *Earth, planets and space* 63 (7), 595–598. doi:10.5047/eps.2011.06.021

Zhang, H., and Ge, Z. (2017). Stepover Rupture of the 2014 Mw7.0 Yutian, Xinjiang Earthquake. *Bull. Seismol. Soc. Am.* 107 (2), 581–591. doi:10.1785/0120160099

Zhang, H., and Ge, Z. (2010). Tracking the Rupture of the 2008 Wenchuan Earthquake by Using the Relative Back-Projection Method. *Bull. Seism. Soc. Am.* 100 (5B), 2551–2560. doi:10.1785/0120090243

Zhang, H., Koper, K. D., Pankow, K., and Ge, Z. (2017). Imaging the 2016 Mw 7.8 Kaikoura, New Zealand, Earthquake with Teleseismic P Waves: A Cascading Rupture across Multiple Faults. *Geophys. Res. Lett.* 44, 4790–4798. doi:10.1002/2017gl073461

Zhang, H., van der Lee, S., and Ge, Z. (2016). Multiarray Rupture Imaging of the Devastating 2015 Gorkha, Nepal Earthquake Sequence. *Geophys. Res. Lett.* 43. doi:10.1002/2015GL066657

Zhang, J., Green, H. W., Bozhilov, K., II, and Jin, Z. (2004). Faulting Induced by Precipitation of Water at Grain Boundaries in Hot Subducting Oceanic Crust. *Nature* 428, 633–636. doi:10.1038/nature02475

Conflict of Interest: The authors declare that the research was conducted in the absence of any commercial or financial relationships that could be construed as a potential conflict of interest.

Advantages of publishing in Frontiers

OPEN ACCESS
Articles are free to read
for greatest visibility
and readership

FAST PUBLICATION
Around 90 days
from submission
to decision

HIGH QUALITY PEER-REVIEW
Rigorous, collaborative,
and constructive
peer-review

TRANSPARENT PEER-REVIEW
Editors and reviewers
acknowledged by name
on published articles

Frontiers
Avenue du Tribunal-Fédéral 34
1005 Lausanne | Switzerland

Visit us: www.frontiersin.org
Contact us: frontiersin.org/about/contact

REPRODUCIBILITY OF RESEARCH
Support open data
and methods to enhance
research reproducibility

DIGITAL PUBLISHING
Articles designed
for optimal readership
across devices

FOLLOW US
@frontiersin

IMPACT METRICS
Advanced article metrics
track visibility across
digital media

EXTENSIVE PROMOTION
Marketing
and promotion
of impactful research

LOOP RESEARCH NETWORK
Our network
increases your
article's readership